THE ELASTIC ANALYSIS OF LOAD DISTRIBUTION IN WIDE-FACED HELICAL GEARS

BY

CHARLES D. HADDAD

A thesis submitted to

The University of Newcastle upon Tyne

for

The Degree of Doctor of Philosophy

OCTOBER 1991

TEXT BOUND CLOSE TO THE SPINE IN THE ORIGINAL THESIS

VOLUME CONTAINS CLEAR OVERLAYS

OVERLAYS HAVE BEEN SCANNED SEPERATELY AND THEN AGAIN OVER THE RELEVANT PAGE

DECLARATION

This thesis consists of the original work of the author except where specific reference to the work of others is made, and has not been previously submitted for any other degree or qualification.

ACKNOWLEDGEMENTS

This work was carried out at the Mechanical Engineering Department, University of Newcastle upon Tyne, Newcastle upon Tyne, U.K., under the supervision of Mr. J.A. Pennell, to whom I am grateful for continued and constructive technical guidance and support throughout the project.

I would like to point out that this project was made possible by the continued moral and financial support of the University of Birzeit, West Bank, and the prompt financial support received from the "Arab Student Aid International", USA. Other financial contributors to whom I am also grateful are the "United Nations Development Project" and the "British Council".

I would also like to extend my gratitude to the following people: Mr. D.A. Hofmann, Director of the Design Unit, for supplying most of the experimental rig's basic components, and for his technical advice and financial assistance towards the end of the project; Mr. M.E. Norman, for his expert advice on micro-computer software; Mr. Rob Frazer, for his expertise in gear metrology; Mr. Norman Baty, for his drafting expertise, and the remaining members of the Design Unit staff, particularly Mrs. J. McLean, Mrs. D. Graham and Mrs. S. Stone for their meticulous typing of this thesis.

I should also like to thank the Design Unit technicians, Mr. Colin Kirby and Mr. David Clipperton, and the departmental technicians, Mr. Bill Young, Mr. Richard Warhurst and Mr. Steve Smith for their assistance and skilled workmanship during the development of the experimental rig.

Finally, special thanks to Mr. Eddie Small for supplying the proper quarters in the Department, without which it would have been very difficult to work.

ABSTRACT

For a gear designer, the meshing gear tooth root bending stresses, and contact stresses are of major importance. To be able to obtain accurate values of these stresses, it is essential to determine the actual load distribution along the contact lines of the meshing gear tooth pairs. The objective of this work is to predict this load distribution.

In the current gear design standards such as AGMA 2001[1], BS436[2], DIN3990[3] and ISO-DIS6336[4] the contact line load distribution is estimated by using a two-dimensional "thin slice" model of the meshing gear teeth. Clearly, this cannot account accurately for maldistribution of loading across the tooth face width, which is essentially a three-dimensional phenomenon. As a result, the effects of tooth lead, profile and pitch deviations are inadequately modelled.

In this work, the elastic compliance of wide-faced helical gears of standard tooth form, zero addendum modification, and between 10 and 100 teeth, was determined using a 3-D finite element elastic model of the whole gear. These results were incorporated into a micro-computer program which calculates the load distribution across the meshing tooth pair faces.

The effects of a number of parameters such as U, Z, b, and β^* on the load distribution and contact stresses of an error-free gear were also investigated using the micro-computer program and the results were compared with other published data and those obtained from the standards[2,3,4], Vedmar[5] and Simon[43]. The load peaks near the start and end of contact, attributed by some[6,7] to the resistance of the unloaded portion of the tooth beyond the shorter contact lines in those regions, is very clearly demonstrated by Vedmar[5], others[6,7] and this work, but certainly not by the standards (this effect is usually referred to as the "buttressing" effect). The thin slice model largely over estimates the tooth mesh stiffness c_γ since the convective effects of loading are completely ignored.

The effects of lead deviations such as helix angle error and face crowning (barrelling), profile deviations such as profile angle error, profile crowning and tip

* See list of Notation

relief, and pitch deviations such as adjacent base pitch error, were also studied. Their effect on the load distribution factors $K_{H\beta}$, $K_{H\alpha}$ and the overall load distribution factor K_H, were obtained from the micro-computer program and compared with the results from the standards[2,3,4]. As expected, the standards considerably overestimate these factors due to their overestimation of mesh stiffness. Nevertheless, the pattern of variation in the load distribution factors was similar.

The theoretical predictions were compared with experimental results measured on wide-faced test gears (specifications given in Table 5.1) with known (measured) mounting and tooth form errors. Measurement of tooth root strains to determine the load distribution along the simultaneous contact lines showed that the experimental and theoretical results agreed on the average to within 3.5% (end of tooth results not included). Also the total applied load upon comparison with theory agreed to within 6%. Experimental absolute values of transmission error "f_t" were not available, however, the pattern of variation of "f_t" during meshing showed excellent consistency with the theoretical results (variations were very small anyway and within the error band). A separate test however, which gave the approximate absolute transmission error (tooth misalignments and form errors not included) agreed to within 1% with theory.

NOTATION

The notation presented below applies to the symbols used in the main text of this work. Identical symbols may appear in the accompanying Appendices, and in works quoted from other authors in the main text which may retain the same meaning, or have a totally different meaning, in which case these symbols are defined locally with the aid of diagrams when applicable.

A, A', A_0, A'_0	Points
a	Centre distance, influence factor
$B, B' B_0, B'_0$	Points
$b (b_0 = b/m_n)$	Gear face width (non-dimensional)
b'	Gear tooth length
C_f, C_g	Constants
c_{ay}	Tip relief
c_c	Face crowning (barrelling)
c_e	End relief
c_{fy}	Root relief
$c_{\alpha a}$	Addendum profile crowning
$c_{\alpha f}$	Dedendum profile crowning
c	Point on tooth central surface
c_n	Clearance along load line direction
c_t	Clearance along base tangent
c'	Single tooth stiffness
c_γ	Overall mesh stiffness in the normal plane
c'_γ	Instantaneous mesh stiffness in the normal plane
$c'_{\gamma t}$	Instantaneous mesh stiffness in the transverse plane
d	Reference diameter
d_a	Tooth tip diameter
d_b	Base diameter
d_s	Shaft diameter
d_y	Arbitrary tooth diameter
e	Gear tooth root strain, eccentricity
E	Modulus of elasticity, base tangent point
$F (F_0 = F/E.m^2)$	Normal tooth load (non-dimensional), bending deflection master curve fitting function
F_{cal}	Calibration point load value
F_f	Total profile error
F_p	Cumulative pitch error
$F_{\beta y}$	Mesh misalignment

F^*	Load intensity (experimental)
f	Loaded point on tooth flank, fillet
f_f	Profile form error
$f_{H\alpha}$	Profile angle error
$f_{H\beta}$	Helix angle error
f_p	Adjacent pitch error
f_{pb}	Normal base pitch error
f_t	Transmission error
f_{yz}	Twist
G	Modulus of rigidity, bending deflection non-master curve fitting function
G_F	Gain factor
h(h'=h/L)	Tooth surface to centre-line distance along normal to tooth surface (non-dimensional)
h_{a0}	Tool addendum
I	Moment of inertia
i	Number
J	Polar moment of inertia
j	Number
K	Maximum number of simultaneously engaged teeth
$K_{F\alpha}$	Transverse load distribution factor for bending stress
$K_{F\beta}$	Longitudinal load distribution factor for bending stress
K_g	Gain
K_H	Overall load distribution factor for contact stress
$K_{H\alpha}$	Transverse load distribution factor for contact stress
$K_{H\beta}$	Longitudinal load distribution factor for contact stress
K_{tb}	Bending deflection influence function
k	Number, tip diameter modification coefficient
L	Half Hertzian contact width
ℓ	Number, shaft length, length
m	Number of Gauss intervals across gear face width
m_n	Normal module
m_t	Transverse module
n	Number
O	Gear centre of rotation
p	Arbirtrary point on tooth flank
p_{bt}	Transverse base pitch
p_ℓ	Point on succeeding adjacent tooth flank
p_r	Point on preceding adjacent tooth flank
r_{a0}	Tool fillet radius

$\bar{r}_o$	Mean reference ring radius
r_{if}	Radius at involute–fillet transition
s	Gauss point spacings
s_{yn}	Tooth thickness in the normal plane at a diameter dy
s_{yt}	Tooth thickness in the transverse plane at a dyameter dy
T	Torque, reference point for phase of mesh measurement.
t	Shim thickness
U	Gear ratio
V_o	Output voltage
V_i	Input supply voltage
w	Load intensity (theoretical)
w_{max}	Peak load intensity at a particular instant for a real gear
w_{max0}	Peak load intensity at a particular instant for a perfect gear
x	Cartesian coordinate
x_n	Addendum modification factor
y	Cartesian coordinate
Z	Number of teeth
z	Axial Cartesian coordinate
z_F	Start of a contact line
z_L	End of a contact line
$\bar{z}$	Axial coordinate measured from the loaded point f
α	Angle contained by base diameter and line of centres of gears
α_n	Normal pressure angle at the reference diameter
α_{yn}	Normal pressure angle at an arbitrary diameter d_y
α_t	Transverse pressure angle at the reference diameter
α_{yt}	Transverse pressure angle at an arbitrary diameter d_y
α_{wt}	Working transverse pressure angle
β	Helix angle at reference diameter
β_b	Helix angle at base diameter
β_y	Helix angle at an arbitrary diameter d_y
γ	Torsional strain, angle
Δ	Gauss interval in axial direction
Δ'	Gauss interval along tooth direction
Δr_m	Measured run-out reading
$\Delta\bar{r}$	Mean of measured run-out readings
δ_e	Tooth errors
δ_h	Shaft horizontal misalignment
δ_{ht}	Component of shaft horizontal misalignment along base tangent

δ_r	Absolute variation of actual ring radius from nominal (theoretical) radius
δ_s	Shaft torsion and bending and shear deflection
δ_t	Tooth bending (and shear) and contact deflection
δ_{tb}	Tooth bending (and shear) deflection
δ_{tc}	Tooth contact deflection
δ_v	Shaft vertical misalignment
δ_{vt}	Component of shaft vertical misalignment along base tangent
ϵ	Strain
ϵ_α	Transverse contact ratio for a rigid perfect gear pair
$\epsilon_{\alpha 0}$	Transverse contact ratio for an extended plane of mesh
ϵ_β	Overlap ratio
ϵ_γ	Total contact ratio for a rigid perfect gear pair
$\epsilon_{\gamma 0}$	Total contact ratio for an extended plane of mesh
θ_{ht}	Horizontal angular misalignment component of shaft along base tangent
θ_{vt}	Vertical angular misalignment component of shaft along base tangent
θ_t	Sum of horizontal and vertical angular misalignment components of shaft along base tangent
$(\theta_t)_{mod}$	θ_t modified to account for reference ring imperfections
ν	Poisson's ratio
ρ	Radius of curvature of tooth profile at a contact point
ρ_{eff}	Effective relative radius of curvature of a pair of meshing teeth at a contact point
σ_H	Hertzian contact stress for a real gear
σ_{H0}	Hertzian contact stress for a perfect gear
σ_{Hmax}	Peak contact stress at a particular instant for a real gear
σ_{Hmax0} gear	Peak contact stress at a particular instant for a perfect
τ	Torsional shear stress
φ	angle from arbitrary reference to point of peak eccentricity "e" on reference ring surface
φ_y	Angle
φ_z	Phase of mesh at a Gauss point
φ_{z0}	Reference tooth phase of mesh
ψ	Tooth thickness half angle at reference diameter
ψ_p, ψ_y	Tooth thickness half angle at an arbitrary diameter dp,dy

Indices

0	Perfect gears, non-dimensional, extended plane of mesh
1	Pinion
2	Gear
a	Addendum
b	Base, bending and shear, blunt end of tooth
c	Contact, point on tooth central surface
ccw	Counter clockwise
cw	Clockwise
e	Error
f	Loaded point on tooth flank, master curve function coefficient, tooth root fillet
g	Gear, non-master curve function coefficient
h	Horizontal
H	Hertzian, Haddad
i	Input
i,j,k	Numbers, points
ℓ	Succeeding adjacent tooth
m	Measured
n	Normal
o	Output
p	Pinion, arbitrary point on tooth flank
r	Preceding adjacent tooth
s	Shaft, sharp end of tooth, shear
t	Transverse, tooth, torsion
v	Vertical
V	Vedmar
w	Working
x	Cartesian coordinate
y	Cartesian coordinate, arbitrary point on tooth flank
z	Cartesian coordinate

KEY TO PHOTOGRAPHIC PLATES

1	Helical pinion
2	Helical wheel
3	Pinion shaft
4	Wheel shaft
5,6,7,8*	Main bearings (Fig.5.3)
9	Spur pinion
10	Spur wheel
11	Torsion bar
12	Torque setting assembly
13	Bearing retainer
14	Bearing retainer
15	Bearing retainer and ROD 800 mounting frame
16	Bearing retainer
17,18	Bearing caps
19	Zero datum jig
20	Spring table assembly
21,22	Friction disks
23	Lower gear casing
24	Friction disk bearing housing
25	Heidenhain encoder ROD 270
26	Heidenhain encoder ROD 800
27	Ringfeder housing
28	Fine pitch driving screw
29	Locking base plate and driving screw clamp support
30	Driving screw clamp
31 - 34	Reference bands (rings)
35	UPM 60 multipoint measuring instrument
36	IEEE 488-78 data logger
37	Heidenhain bi-directional VRZ counter
38	Avometer
39	Fylde amplifier
40	Klingelnberg evaluation electronics PEW 02
41	Hewlett-Packard plotter
42	Strain gauge cables and wiring
43	Torque restraining arm
44	Gear driving clamp
45	Ringfeder

* not shown in photographs

CONTENTS

APPENDICES

CHAPTER 1

GEAR ELASTIC MESH AND STIFFNESS MODELS

1.1 Introduction

Proper design of gears of appropriate size, material, finish and reliability for a specific application requires an accurate estimation of both the contact stresses between the surfaces of the meshing gear tooth pairs and of the bending stresses in the tooth root, where fatigue fracture is most likely to occur. These stresses may easily be calculated, once the load distribution across the contact lines of the meshing gear tooth pairs has been determined.

Many attempts by a number of authorities on the subject have been made to determine the load distribution along the contact lines of meshing helical gear teeth, some of which will be mentioned in this chapter. The method used in the gear rating standards[1,2,3,4] is discussed first, then the different elastic models developed by authors are discussed in a separate section as they are extensively used by many gear designers so that their validity must be checked particularly thoroughly.

1.2 The Gear Rating Standards

1.2.1 Introduction

Practical gear designers usually make use of one of the modern gear rating standards such as AGMA[1], BS[2], DIN[3] or ISO[4] to analyse gear tooth stresses. These all adopt a fundamentally similar approach to gear stress analysis particularly BS, DIN and ISO which are discussed here. The factors governing the load distribution are identified, and the methods of calculating the load distribution factors are presented in detail to facilitate the comparisons made in Ch.4 with the author's results.

The standards all adopt a basically 2-D mesh model in which the gear is considered to be divided into a number of "thin slices" which are assumed to be free to deflect in the transverse plane independently of one another. A loaded point on an individual slice is thus deflected only by that load and is unaffected by loading on any of the other slices. The "convective" effect of loading is thus ignored, as is the so-called "buttressing" effect[5,6,7] of the unloaded adjacent portions of helical teeth, which gives rise to sharp peak loads. The "thin slice" model used in the standards also ignores the effects on tooth deflections of loads applied to adjacent teeth, which Steward[30] has shown to be quite significant.

1.2.2 Contact Stress Analysis

The mechanism of pitting failure is not yet fully understood, so that a rigorous surface fatigue failure analysis is not yet possible. However, the maximum value of the Hertzian contact stress σ_H is usually assumed to be the main factor affecting surface fatigue strength, and the value of σ_H at the pitch point is used as the basis for the pitting strength calculations in the standards [2,3,4].

The contacting tooth flanks at the pitch point are assumed to be equivalent to two cylindrical bodies in elastic contact. This problem was first studied by Hertz[8] in 1895. Using the notation shown in Figure 1.1, the peak (compressive) contact stress at the reference diameter contact of a pair of geometrically perfect spur gears is given by:

$$\sigma_{H0} = \left[\frac{E}{2\pi\ (1-\nu^2)} \cdot \frac{w}{\rho_{eff}} \right]^{\frac{1}{2}} \qquad 1.1$$

where

$$\rho_{eff} = \frac{\rho_1 \cdot \rho_2}{\rho_1 + \rho_2} \qquad 1.2$$

is the effective combined radius of relative curvature of the two contacting flanks, and w is the local load intensity (N/mm). If w is expressed in terms of the tangential load F_t (assumed distributed uniformly along the contact lines), and ρ_{eff} is determined from the gear geometry, we obtain

$$\sigma_{H0} = \left[\frac{F_t}{d_1 . b} \cdot \frac{U + 1}{U} \right]^{\frac{1}{2}} \cdot Z_H . Z_E . Z_\epsilon \qquad 1.3$$

where

- σ_{H0} - is the pitch point contact stress for a "perfect" gear set.
- F_t - mean tangential component of the load at the reference cylinder.
- U - gear ratio = Z_2/Z_1
- d_1 - pinion reference diameter
- b - gear face width
- Z_H - zone factor accounting for flank curvatures (ρ_{eff}) at the pitch point, given by

$$Z_H = \left[\frac{2.\cos\beta_b \cdot \cos\alpha_{tw}}{\cos^2\alpha_t \cdot \sin\alpha_{tw}} \right]^{\frac{1}{2}}$$

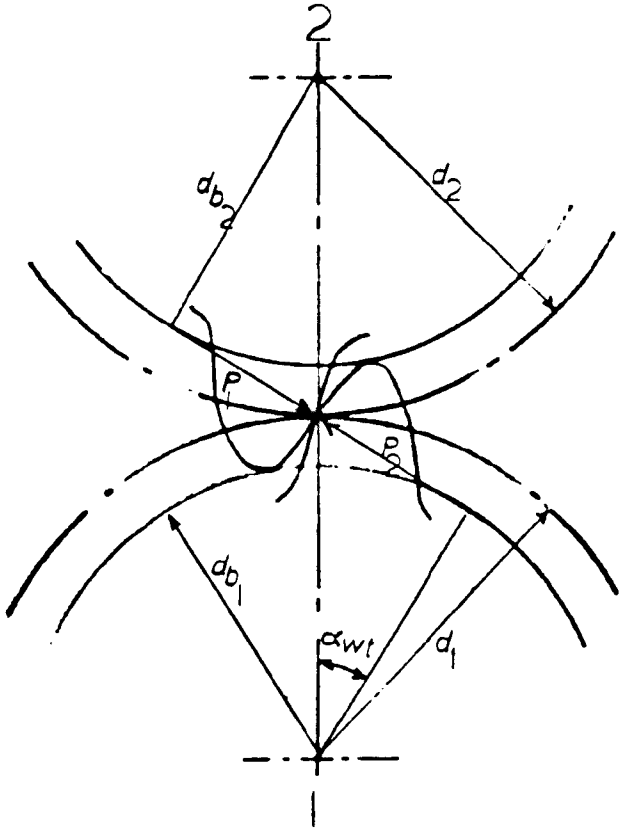

Fig. 1.1 Notation for Contact Stress Analysis

Z_E - elasticity factor accounting for gear material properties, given by

$$Z_E = \left[\frac{1}{\left[\frac{1-\nu_1^2}{E_1} + \frac{1-\nu_2^2}{E_2} \right]} \right]^{\frac{1}{2}}$$

Z_ϵ - contact ratio factor accounting for mean total length of contact

For spur gears

$$Z_\epsilon = \left[\frac{4 - \epsilon_\alpha}{3} \right]^{\frac{1}{2}}$$

For helical gears

$$Z_\epsilon = \left[\left[\frac{(4 - \epsilon_\alpha)}{3} \cdot (1 - \epsilon_\beta) \right] + \frac{\epsilon_\beta}{\epsilon_\alpha} \right]^{\frac{1}{2}} \text{for } \epsilon_\beta < 1$$

and

$$Z_\epsilon = \left[\frac{1}{\epsilon_\alpha} \right]^{\frac{1}{2}} \text{for } \epsilon_\beta \geq 1$$

Eqn. 1.3 is valid for spur gears. In the standards [2,3,4], the calculations for helical gears are based on the geometry of the "equivalent" spur gears, so that Eqn. 1.3 must be modified to account for the effects of the helix angle, since even for perfect helical gears, the load intensity actually varies along each contact line as will be shown later. To allow for this, an empirical helix angle factor Z_β was introduced into the BS[2], ISO[3] and DIN[4] rating procedures (see Figure 1.2):

$$Z_\beta = [\cos\beta]^{\frac{1}{2}} \qquad 1.4$$

so that equation 1.3 finally becomes:

$$\sigma H_0 = \left[\frac{F_t}{d_1 . b} \cdot \frac{U+1}{U} \right]^{\frac{1}{2}} \cdot Z_H \cdot Z_E \cdot Z_\epsilon \cdot Z_\beta \qquad 1.5$$

In BS436[2], an additional allowance for the non-uniformity of loading along helical gear contact lines is also introduced via the factor $K_{H\alpha}$ (see below) for which a minimum value of 1.15 is assumed. The logic of this procedure is not clear, since, as shown below, $K_{H\alpha}$ was a factor originally introduced to allow for the effect of tooth errors

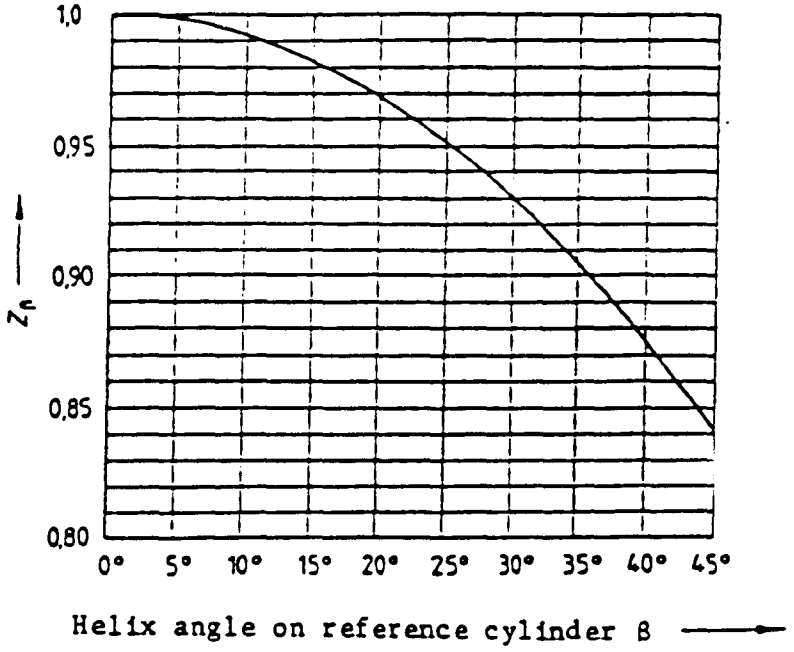

Fig. **1.2** Helix angle factor Z_β

or deviations and in the ISO and DIN standards is thus, by definition, equal to 1.0 for "perfect" gears.

Real gears cannot be perfect and do not operate under precisely uniform torque. There will always be combinations of errors and/or tooth modifications, as well as dynamic effects which will modify the tooth loads and stresses. To allow for such imperfections, the standards [2,3,4] include four additional factors, and Eqn. 1.5 thus becomes:

$$\sigma_H = \sigma_{H0} \cdot [K_A \cdot K_V \cdot K_{H\alpha} \cdot K_{H\beta}]^{\frac{1}{2}} \qquad 1.6$$

where:

σ_{H0} - is the stress for "perfect" gears operating under the "nominal" load F_t.

K_A - is the load application factor accounting for load fluctuations caused by sources external to the gear system. It is obtained either from measurements on similar existing gear systems, or from empirical data provided by the equipment manufacturer.

K_V - is the dynamic load factor accounting for dynamic load fluctuations arising from the gear system itself, due to contact conditions during the mesh cycle. It is calculated using semi-empirical expressions suitable for each particular application.

$K_{H\beta}$ - is the longitudinal (face) load distribution factor for surface pressure. It accounts for the local increases in specific load ω, due to maldistribution of the load across the face-width of the gear arising from shaft torsional, bending and shear deflections, tooth misalignment due to manufacturing and mounting errors, or tooth modifications such as end relief or face-crowning, or any combination of these.

$K_{H\alpha}$ - is the transverse load distribution factor for surface pressure. It accounts for changes in the pattern of load sharing between adjacent pairs of teeth in mesh arising from manufacturing errors, such as profile and pitch error, or tooth modification such as tip and root relief or profile crowning, or any combination of these.

$K_{H\alpha}$ and $K_{H\beta}$ are the prime concern of the present study, as is also the factor Z_β which allows for the non-uniformity of the load distribution along the contact lines of "perfect" helical gears. In all the gears studied, K_A and K_V can be assumed to be unity since only quasi-static meshing of gears under a known constant torque is considered. As a result, Eqn. 1.6 reduces to:

$$\sigma_H = \sigma_{H0} \cdot [K_{H\alpha} \cdot K_{H\beta}]^{\frac{1}{2}} \qquad 1.7$$

Clearly, an overall load distribution factor can be defined, where

$$K_H = K_{H\alpha} \cdot K_{H\beta} = (\sigma_H/\sigma_{H0})^2 \qquad 1.8$$

and for a perfect gear $K_H = 1.0$.

In Eqn. 1.8, if there are no lead deviations, $K_{H\beta}$ is unity and

$$K_H = K_{H\alpha} = (\sigma_H/\sigma_{H0})^2 \qquad 1.9$$

Likewise, if there are no profile deviations, $K_{H\alpha}$ is unity and equation 1.8 reduces to:-

$$K_H = K_{H\beta} = (\sigma_H/\sigma_{H0})^2 \qquad 1.10$$

As will be seen later, Eqns. 1.8 to 1.10 provide a convenient basis for comparing the author's results with those predicted by the standards. However, this is not the only basis for comparison. The standards [2,3,4] also define $K_{H\beta}$ as the ratio of peak to mean specific load. From Fig. 1.3, this gives

$$K_{H\beta} = w_{max}/w_m \qquad 1.11$$

where

w_m - is the mean specific load on the contact lines.

w_{max} - is the peak specific load on the contact lines of a "real" gear.

In the standards, w is assumed to vary linearly as shown in Fig.1.3, giving,

for light load and/or large $F_{\beta y}$

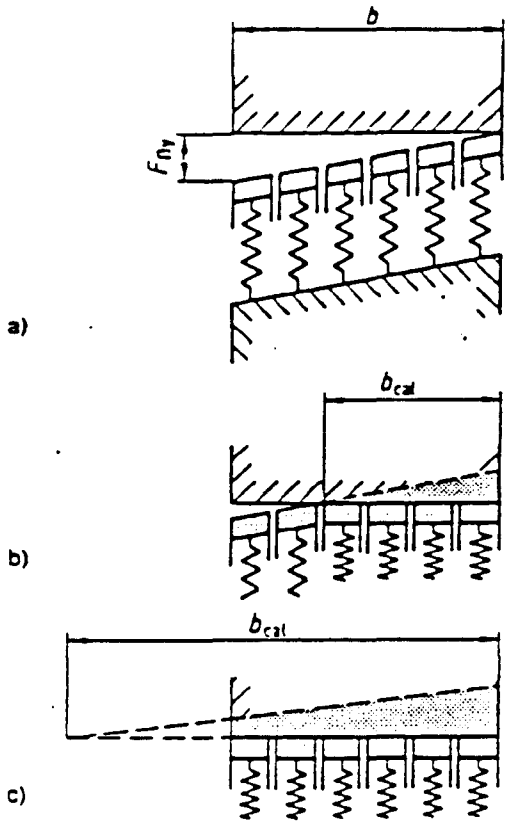

a) Without load

b) With light load and/or high mesh alignment error (large value of $F_{\beta y}$)

c) With heavy load and/or small mesh alignment error (small value of $F_{\beta y}$)

Fig. **1.3a** Distribution of longitudinal load with linear mesh misalignment (illustration of principle)

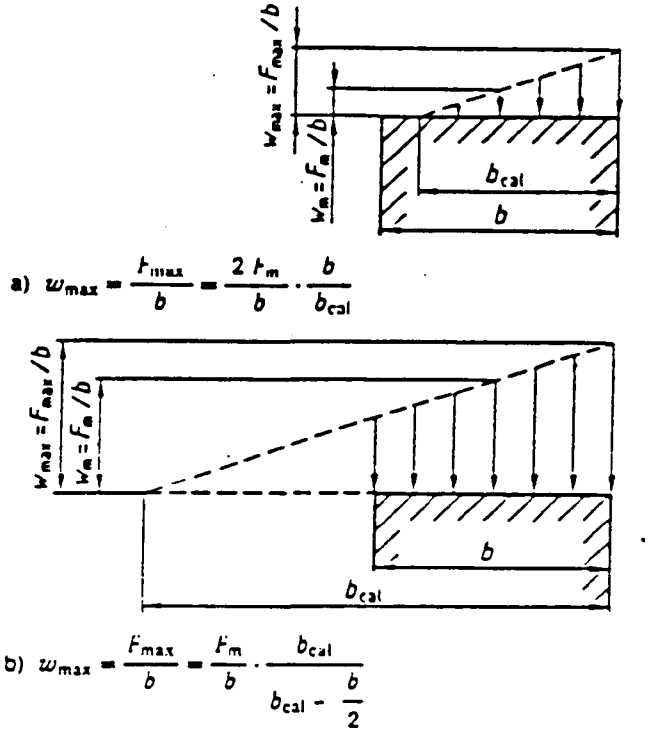

a) Light load and/or large value of $F_{\beta y}$ $b_{cal}/b < 1$

b) Heavy load and/or small value of $F_{\beta y}$, $b_{cal}/b > 1$

Fig. **1.3b** Calculation of the maximum line loading $(F/b)_{max}$ with linear distribution of the longitudinal loading.
$F_m = F_t \cdot K_A \cdot K_v$

$$b_{cal/b} = \left[\frac{2.Fm/b}{F_{\beta y}.c_\gamma} \right]^{\frac{1}{2}} < 1 \qquad 1.12a$$

and

$$K_{H\beta} = 2(b/b_{cal}) = \left[\frac{2.F_{\beta y}.c_\gamma}{F_m/b} \right]^{\frac{1}{2}} > 2 \qquad 1.12b$$

For heavy load and/or small $F_{\beta y}$

$$b_{cal/b} = \left[0.5 + \frac{F_{m/b}}{F_{\beta y}.c_\gamma} \right] > 1 \qquad 1.13a$$

and

$$K_{H\beta} = \frac{b_{cal}}{b_{cal} - b/2} = \left[1 + \frac{F_{\beta y}.c_\gamma}{2.F_m/b} \right] > 2 \qquad 1.13b$$

where, for $K_A = K_V = 1.0$,

$$F_m = K_A.K_V.F_t = F_t \qquad 1.13c$$

and $F_{\beta y}$ is the resultant misalignment and c_γ the mesh stiffness (see 1.2.4).

The elastic mesh model developed in Ch.2 yields values of ω_{max} and σ_{Hmax} at any instant during the mesh cycle, so that, using either Eqns. 1.10 or 1.11, values of $K_{H\beta}$ can be calculated for comparison with those given by Eqns. 1.12 or 1.13. These comparisons are presented in Ch. 4.

Next consider $K_{H\alpha}$ as calculated by the standards[2,3,4]. It was shown earlier that $K_{H\alpha}$ may be found from Eqn. 1.9 if the stresses are known. The standards also define $K_{H\alpha}$ as the factor which accounts for the uneven distribution of the load on several gear tooth pairs meshing simultaneously, and resulting from pitch and/or profile deviations and the elasticity of the gears. In that sense, $K_{H\alpha}$ is defined as the ratio of the peak contact load on all the meshing tooth pairs at near zero rpm of the meshing gear pair, to the corresponding peak contact load of a perfect gear pair with identical specifications.

$$K_{H\alpha} = w_{max}/w_{max0} \qquad 1.14$$

Again Eqn. 1.14 will later on be very useful for comparison purposes. Based on this definition of $K_{H\alpha}$, the standards devise the following empirical expressions,

For $\epsilon_\gamma \leqslant 2$:

$$K_{H\alpha} = \tfrac{1}{2} \cdot \epsilon_\gamma \cdot \left[0.9+0.4 \frac{c_\gamma \cdot (fpe - y_\alpha)}{F_{tH}/b}\right] \qquad 1.15a$$

For $\epsilon_\gamma > 2$:

$$K_{H\alpha} = 0.9+0.4 \left[\frac{2.(\epsilon_\gamma-1)}{\epsilon_\gamma}\right]^{\frac{1}{2}} \frac{c_\gamma \cdot (f_{pe} - y_\alpha)}{F_{tH}/b} \qquad 1.15b$$

With the limiting condition,

if $K_{H\alpha} > \epsilon_\gamma/\epsilon_\alpha . Z_\epsilon{}^2$ then

$$K_{H\alpha} = \epsilon_\gamma/\epsilon_\alpha . Z_\epsilon{}^2 \qquad 1.15c$$

and

if $K_{H\alpha} < 1.0$ then

$$K_{H\alpha} = 1.0 \qquad 1.15d$$

where

c_γ - mesh stiffness in accordance with section 1.2.4 (appearing in Eqns. 1.12, 1.13 and 1.15).

fpe - maximum mesh pitch error of pinion or wheel.

y_α - running in allowance, causing a reduction in the original equivalent mesh deviation. y_α varies for varying material types, but for the type of gears used in this work (case hardened or carburised teeth)

$y_\alpha = 0.075$. fpe for all velocities with the restriction:

$(y_\alpha)_{max} = 3\mu m$; $(fpe)_{max} = 40\ \mu m$

and where pinion and wheel materials differ

$y_\alpha = (y_{\alpha 1} + y_{\alpha 2})/2$

F_{tH} - equivalent tangential load in the transverse section

$F_{tH} = F_t . K_A . K_V . K_{H\beta}$

Clearly $K_{H\alpha}$ does depend on $K_{H\beta}$ as can be seen from the definition of F_{tH}. In other words, if lead deviations of any form are introduced, $K_{H\alpha}$ will be affected. This is demonstrated in Chapter 4. The standards

assume that fpe accounts for the total effect of all gear deviations which influence $K_{H\alpha}$. If however the single pitch deviation (profile form error) f_f is greater than fpe, then f_f should replace fpe in Eqns. 1.15a and 1.15b.

From the above discussion so far, it is evident that multiplying the values of $K_{H\alpha}$ and $K_{H\beta}$ obtained independently will not give the same result as Eqn. 1.8, and this is demonstrated later on in Chapter 4.

1.2.3 Bending Stress Analysis

In the present work, no attempt has been made to calculate bending stresses due to space and time limitations. However, the standards[2,3,4] equations for bending stress calculations are presented in this section for completeness. A procedure whereby "exact" values of the bending stresses may be determined from the calculated load distribution is also presented.

The nominal root bending stress is calculated at the outermost point of single tooth pair engagement of the equivalent spur gears. The gear tooth is assumed to be a simple cantilever beam in bending under the corresponding tangential component of the load as shown in Figure 1.4, with the critical section for bending stress assumed to be at the 30° tangent points. Application of simple engineering bending theory then gives the nominal bending stress as

$$\sigma_F = \frac{6.h_F.\ F_{et}}{b.S_{FN}^2} = \frac{6.h_f.\ F_t.\ \cos(\alpha_{en})}{b.S_{FN}^2\ .\cos\ (\alpha_n)} \qquad 1.16$$

where

F_t – is the tangential component of the load in the transverse section at the pitch point.

F_{et} – is the tangential component of the load in the transverse section at the outermost point of single tooth pair contact.

F – is the total load in the normal section

The form factor is defined as:

$$Y_F = \frac{6.h_F.\ \cos(\alpha_{en}).m_n}{S_{F_n}^2\ .\ \cos\ (\alpha_n)} \qquad 1.17$$

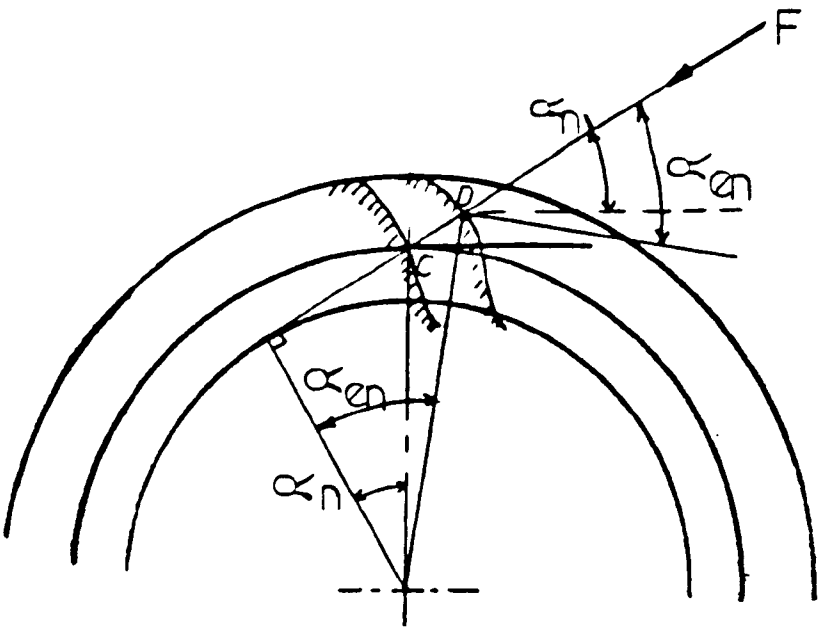

Transverse Section

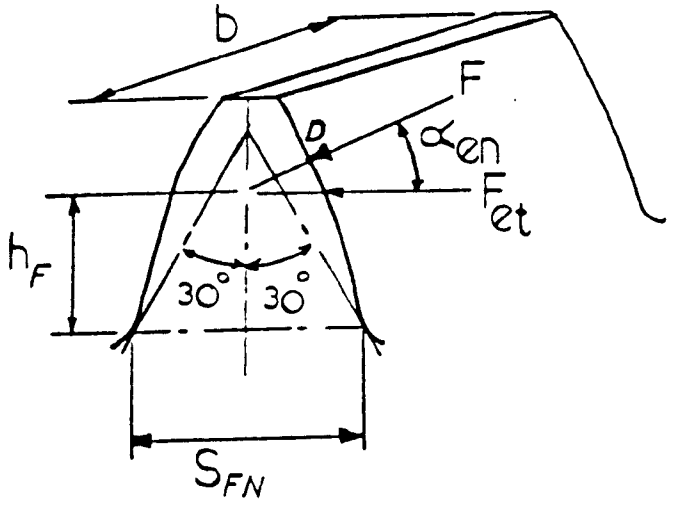

Fig. 1.4 Notation for Bending Stress Analysis of the Equivalent Spur Gear (D is the Outermost point of Single Tooth Pair Contact & C is the Pitch Point)

From equations 1.16 and 1.17

$$\sigma_F = \frac{F_t}{b.m_n} \cdot Y_F \qquad 1.18$$

The maximum bending stress in the root fillet at the 30° tangent point is given as:

$$\sigma_F = \frac{F_t}{b.m_n} \cdot Y_F \cdot Y_S \qquad 1.19$$

where,

Y_S - is a stress concentration factor.

Values of Y_S are based on strain gauge measurements carried out by Hirt[9], as well as finite element analysis and "exact" solutions of the 2-D elasticity problem by conformal mapping by Cardou and Tordion[10]. Earlier works on the bending stresses in gear teeth were based on a different approach originally proposed by Lewis[11], with the stress concentration factor based on photoelastic data such as that given by Dolan and Broghammer[12], and Heywood[13]. These methods have however been shown to underestimate considerably the peak tooth root bending stresses.

Eqn. 1.19 gives relatively accurate estimates of the tooth root peak bending stress in "perfect" spur gears. In such cases, the contact lines are assumed parallel to the gears axes, and the tooth loading is assumed to be uniformly distributed across the face width. For helical gears, however, contact lines run obliquely across the tooth, giving reduced bending stresses based on Eqn. 1.19, while the load is generally not uniformly distributed across either the face width or along the actual oblique contact lines.

To allow for these differences, a semi-empirical helix angle factor Y_β has been introduced, so that for perfect gears,

$$\sigma_F = \frac{F_t}{b.m_n} \cdot Y_F \cdot Y_S \cdot Y_\beta \qquad 1.20$$

Finally, the factors K_A, K_V, $K_{F\beta}$ and $K_{F\alpha}$ are introduced. These are the equivalents of K_A, K_V, $K_{H\beta}$ and $K_{H\alpha}$ respectively, discussed earlier in Section 1.2.2 for contact stress. Therefore, Eqn. 1.20 now becomes:

$$\sigma_F = \frac{F_t}{b.m_n} \cdot Y_F \cdot Y_S \cdot Y_\beta \cdot K_A \cdot K_V \cdot K_{F\beta} \cdot K_{F\alpha} \quad 1.21$$

As for contact stress, the conditions of quasi-static loading at uniform torque set both K_A and K_V to unity.

The longitudinal load distribution factor $K_{F\beta}$ takes account of the effect of the load distribution across the gear face width, on the stress on the gear tooth root. It is somewhat less than $K_{H\beta}$. This may be explained by the fact that the contact loads at the most heavily loaded section of the tooth flank are actually supported by root bending stresses over some finite width of the tooth flank on either side of the loaded section. Some averaging of the contact load distribution thus occurs, producing a flatter root bending stress distribution rendering $K_{F\beta}$ less than $K_{H\beta}$,

$$K_{F\beta} = (K_{H\beta})^{N_F} \quad 1.22$$

$$N_F = \frac{1}{1 + h/b + (h/b)^2}$$

where,

b/h is the face width to tooth height ratio, where the smaller of b_1/h_1 and b_2/h_2 is used in place of b/h.

The transverse load distribution factor $K_{F\alpha}$ takes account of the effect of the uneven distribution of load on several gear tooth pairs meshing simultaneously, on the root stress. In the absence of further information.

$$K_{F\alpha} = K_{H\alpha} \quad 1.23a$$

with the limiting condition that if

$$K_{F\alpha} > \frac{\epsilon_\gamma}{\epsilon_\alpha \cdot Y_\epsilon} \quad \text{then}$$

$$K_{F\alpha} = \frac{\epsilon_\gamma}{\epsilon_\alpha \cdot Y_\epsilon} \quad 1.23b$$

and if $K_{F\alpha} < 1.0$ then

$$K_{F\alpha} = 1.0 \quad 1.23c$$

where

where

$Y\epsilon$ - is the contact ratio for root bending stress and is given by

$$Y\epsilon = 0.25 + \frac{0.75}{\epsilon_{\alpha n}}$$

From the above discussion, it is clear that the criteria set out for $K_{H\beta}$ and $K_{H\alpha}$ also apply to $K_{F\beta}$ and $K_{F\alpha}$, and the overall factor K_F accounts for both effects resulting from the combined effect of lead and profile deviations.

1.2.4 Stiffness Analysis

1.2.4.1 Introduction

The tooth stiffness constant is defined as the "normal" tooth load along the line of action in the transverse section required to deform by 1mm along the line of action, one or more meshing perfect (error-free) tooth pairs of 1mm face width. This deformation is the arc length along the base circle corresponding to the angle by which the axis of one gear would rotate under load due to elastic deflection of the meshing teeth if the other were rigidly constrained.

Two such stiffness constants are used in the standards: c' - the stiffness of a single tooth pair in contact at the pitch point, and c_γ - the so-called mean mesh stiffness.

1.2.4.2 Single Stiffness c'

For spur gears, c' is the maximum tooth stiffness of one tooth pair and is approximately the stiffness of the pair when they make contact at the pitch point. According to the DIN standard[3] c' is given, for $(F_t/b)K_A > 100$ N/mm, by

$$c' = c'_{th} \cdot C_M \cdot C_R \cdot C_B \cdot \cos\beta \qquad 1.24$$

where

c'_{th} is the theoretical single stiffness for "solid" spur gears of standard basic rack profile. For helical gears, c'_{th} is the theoretical single stiffness of the equivalent spur gear.

C_M is a correction factor which accounts for the difference between the measured results obtained by Winter and Podlesnik[14], and the results of the calculations in accordance with Weber and Banaschek[15] for solid disk wheels. The standard assumes

$$C_M = 0.8$$

C_R is a wheel blank factor which accounts for the flexibility of the tooth rim and the web in accordance with results obtained by Winter and Podlesnik[14]. The C_R values given by the standards[2,3,4], are average values which should only be used if the mating pinion is of equal or greater blank stiffness

$$C_R = 1.0 \text{ for solid disk wheels}$$

$$C_R = \frac{1 + \ln(b_s/b)}{5.e^{S_R/(5.m_n)}} \quad \text{for webbed wheels}$$

where for $\frac{bs}{b} < 0.2$ use $\frac{bs}{b} = 0.2$

and for $\frac{bs}{b} > 1.2$ use $\frac{bs}{b} = 1.2$

and for $\frac{S_R}{m_n} < 1$ use $\frac{S_R}{m_n} = 1$

C_B is the basic rack tooth profile factor which accounts for the deviations of the basic rack tooth profile from the "standard" profile. From Winter and Podlesnik[14] results:

$$C_B = [1 + 0.5(1.25-h_{fp}/m_n)].[1-0.02(20-\alpha_{pn})]$$

where h_{fp} - is the standard basic rack dedendum = $1.25m_n$

α_{pn} - is the standard basic rack normal pressure angle=20°

$C_B = 1$ if $h_{fp} = 1.25m_n$, and $\alpha_{pn} = 20°$.

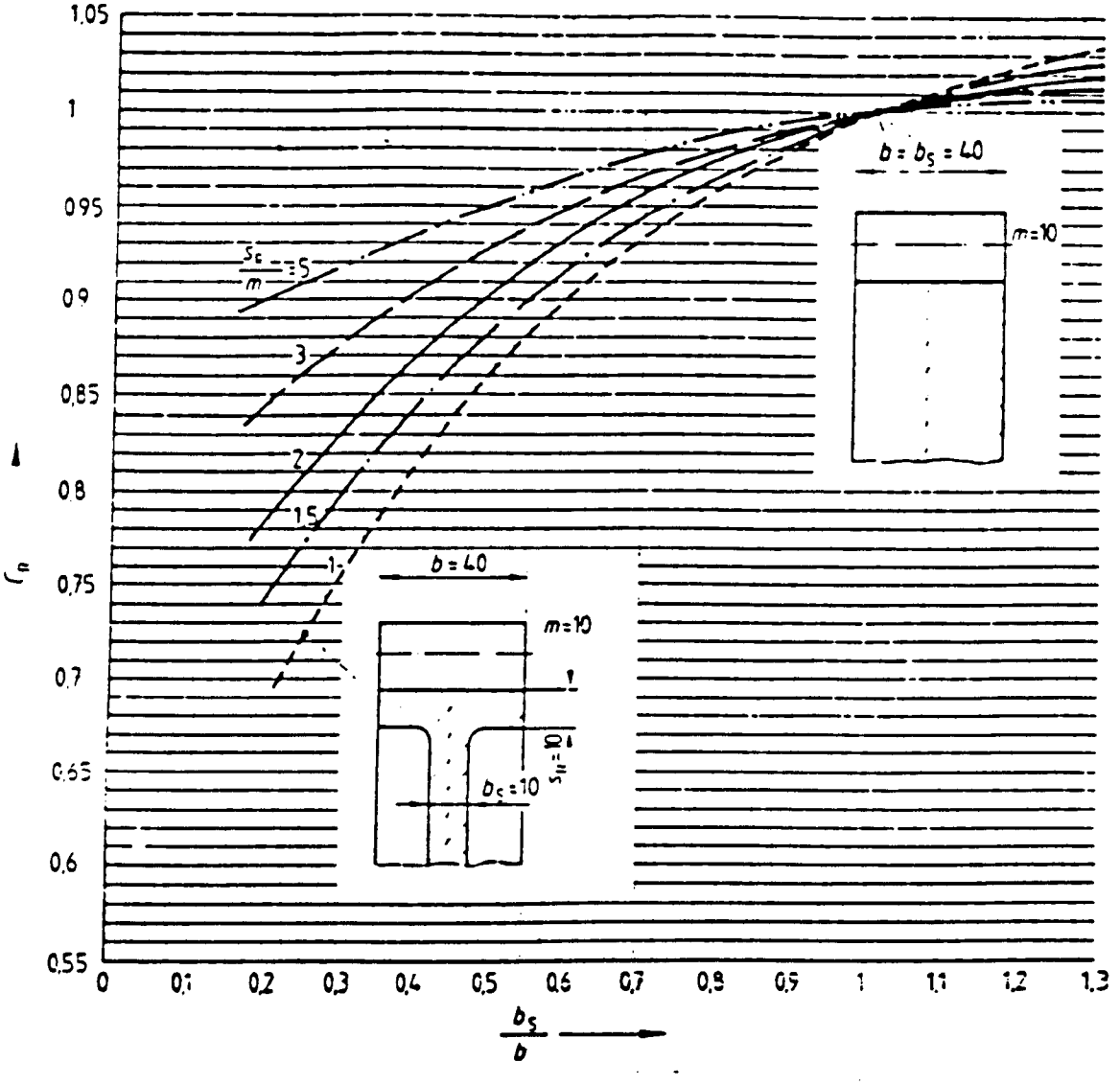

Fig. 1.5 Wheel blank factor C_R, mean values in accordance with (9/2) for counterwheels of equal or stiffer wheel blank form

If h_{fp} differs for pinion and wheel then,

$$C_B = \frac{C_{B1} + C_{B2}}{2}$$

The theoretical single pair stiffness c'_{th} is calculated from the relation

$$c'_{th} = \frac{1}{q'} \qquad 1.25$$

where

q' - is the minimum value for the flexibility of one spur gear tooth pair.

It is calculated from the semi-empirical relation

$$q' = 0.04723 + 0.15551/Z_{n1} + 0.25791/Z_{n2} - 0.00635.x_1 - 0.11654.x_1/Z_{n1} - 0.00193.x_2 - 0.24188.x_2/Z_{n2} + 0.00529.x_1^2 + 0.00182.x_2^2 \qquad 1.26$$

where

x - is the addendum modification factor

Z_n - is the number of teeth of the equivalent spur gear

$$Z_n = Z/\cos^3\beta$$

Eqns. 1.25 and 1.26 are valid for

$$Z_{n1} > Z_{n2} \qquad 1.27a$$

and

$$x_1 \geqslant x_2 - 0.5 \leqslant x_1 + x_2 \leqslant 2.0 \qquad 1.27b$$

Finally, the factor $\cos\beta$ in Eqn. 1.24 is introduced to convert the theoretical single stiffness of the straight gear pair of the equivalent spur gearing in the normal plane into the theoretical single stiffness of the actual helical gear pair in the normal plane.

For $(F_t/b)K_A < 100$ N/mm, it is assumed that c' decreases linearly to zero as $F_t \to 0$, so, in this case,

$$c' = c'_{th}.C_M.C_R.C_B.\cos\beta.(F_t.K_A/b)/100 \qquad 1.28$$

1.2.4.3 Mesh Stiffness c_γ

The mesh stiffness c_γ is defined as the mean (time averaged) value of the total tooth stiffness in the transverse section, and is needed for the calculation of K_V, $K_{H\beta}$, $K_{F\beta}$, $K_{H\alpha}$ and $K_{F\alpha}$ discussed earlier. For spur gears with $\epsilon_\alpha \geq 1.2$, and for helical gears with $\beta \leq 45^\circ$, the mesh stiffness is calculated by the equation

$$c_\gamma = c'.\ (0.75.\epsilon_\alpha + 0.25) \qquad 1.29$$

where c' is given by Eqn. 1.24 (or equation 1.28 for $(F_t/b).K_A < 100$ N/mm). For $\epsilon_\alpha < 1.2$, c_γ is typically up to 10% less than the value given by Eqn. 1.29.

1.2.5 **Limitation of the Gear Rating Standards**

The gear rating standards[2,3,4] are inadequate in many ways. In Stewards's[30] discussion of their application to spur gears and in the present work in both spur and helical gears, the following shortcomings are noted:

1 - Due to the 2-D "thin slice" model assumed, the standards fail to model properly the maldistribution of the load across the gear tooth face width, which is actually an essentially 3-D phenomenon.

2 - The "thin slice" model does not account for the so-called "buttressing" effect of the unloaded adjacent portions of the tooth in helical gearing. This tends to produce a flatter load distribution than that predicted by the 3-D model. The adjacent tooth effect is also not accounted for (see Sec. 1.2.1).

3 - The linear variation of the load intensity assumed in the standards to estimate $K_{H\beta}$ (see Fig. 1.3), makes it impossible to model the effects of non-linear tooth deviations such as parabolic face crowning, or any other type of non-linear lead correction. These can nowadays be readily applied to gear teeth by the CNC hobbers and grinders at the gear designer's disposal.

4 - The standards 2-D model ignores the gear body deformations altogether, and as a result, the overall gear tooth compliance is underestimated.

5 - The actual contact compliance near the tooth tips is greater than that calculated from the Hertzian theory used by the standards. (See equation 1.54 and the corresponding discussion).

6 - The load distribution factors $K_{H\beta}$ and $K_{H\alpha}$, and also $K_{F\beta}$ and $K_{F\alpha}$, are assumed in the standards to be multiplicative. (See Eqn. 1.8 and last paragraph of Sec.1.2.3). However, there is very little evidence to confirm that nonuniformities in the longitudinal and transverse load distribution can be superposed in this way to predict the effects of (e.g.) combined lead and profile deviations.

7 - The standards analyse a helical gear as an "equivalent" spur gear. This does not lead to exact results, especially for large helix angles, so that the semi-empirical factors Z_β and Y_β (see Eqns. 1.5, 1.21, 1.22 and 1.23) are needed to account for the full effect of the helix angle. These factors are rather insecurely based on a very limited amount of experimental data obtained by Brossmann[16] and need further research.

8 - In estimating $K_{H\alpha}$, the standards assume that any type of profile deviation may simply be treated as an equivalent profile form error or base pitch error, and that the effect of combined form and pitch errors is the same as that of the larger error by itself. This makes it impossible to model properly the effect of individual deviations such as profile crowning and tip or root relief, or any combination of profile deviations and pitch errors.

1.3 Other 2-D Models

1.3.1 Introduction

In Section 1.2, the 2-D "thin slice" model used in the standards was examined in detail, since it is used later when the stiffness and load distribution factors obtained in the present work are compared with those given by the standards. For the sake of completeness, other published 2-D models are very briefly summarised below.

1.3.2 Existing 2-D Models

In 1942, Merrit[17] used a 2-D model to determine the deformations of loaded spur gear teeth and used these results to develop a thin slice model of helical gears. He assumed that the helical teeth behave as if they consisted of a large number of independent thin (spur gear) slices, at different phases of their mesh cycle. Having made a rough estimate of the relative flexibility of slices loaded at different

heights above the tooth root, he then concluded that the peak load intensity on a major or full line of contact is in the middle, near the pitch point.

In 1949 Weber[18], and later in 1950 Weber and Banascheck[19], applied a more rigorous approach to the 2-D compliance model adopted by Merrit. They derived analytical expressions for the compliance of spur gear teeth, in which the contact compliance was derived using Hertzian 2-D theory for cylinders in contact. The tooth bending radial and shear deformations were obtained by equating the strain energy resulting from the applied bending moment M, the shear force Q, and the radial force N, shown in Figure 1.6, to the work of deformation. An estimate of the gear body deformation was also obtained by assuming the gear body to be equivalent to part of a semi-infinite plane loaded by the reactions M, Q and N. The Hertzian contact deformations were assumed to extend to the tooth centreline, and the semi-infinite gear body was assumed to extend to a point "a few modules" beneath the pitch point. The equations presented in section 1.2.4 for c', c_γ and q are essentially those developed by Weber and Banascheck, modified to bring the values into closer agreement with Winter and Podlesnik's experimental results[14].

In 1973, Wilcox and Coleman[21] also developed a formula for determining tooth root fillet stresses, and in 1974, Chabert and Dang and Mathis[22] also developed formulae for tooth deformations and stresses. These workers all used 2-D finite element analysis to obtain their results which agree well with those reported above.

In 1973, Schmidt[23] used equations of the same form as Weber and Banascheck's[19] to estimate the combined compliance of a pinion and wheel in mesh. However, the constants in the equations were slightly altered to allow for additional wheel flexibility. This acknowledged for the first time the greater gear body deflections of large diameter wheels. Nevertheless, this additional compliance was still based on the Weber-Banascheck semi-infinite plane assumption for the wheel body, which, as shown by Steward[30], underestimates the overall compliance. The compliance values thus obtained were then incorporated in a 3-D stiffness model of the type developed by Kagawa[24] (see below).

In 1980 and 1981, Terauchi and Nagamura[25,26,27] determined the deflection of various spur gear teeth by using a 2-D elastic theory and a conformal mapping function (See Fig.1.7). They derived a simplified formula for the tooth deflection based on the results from the elastic

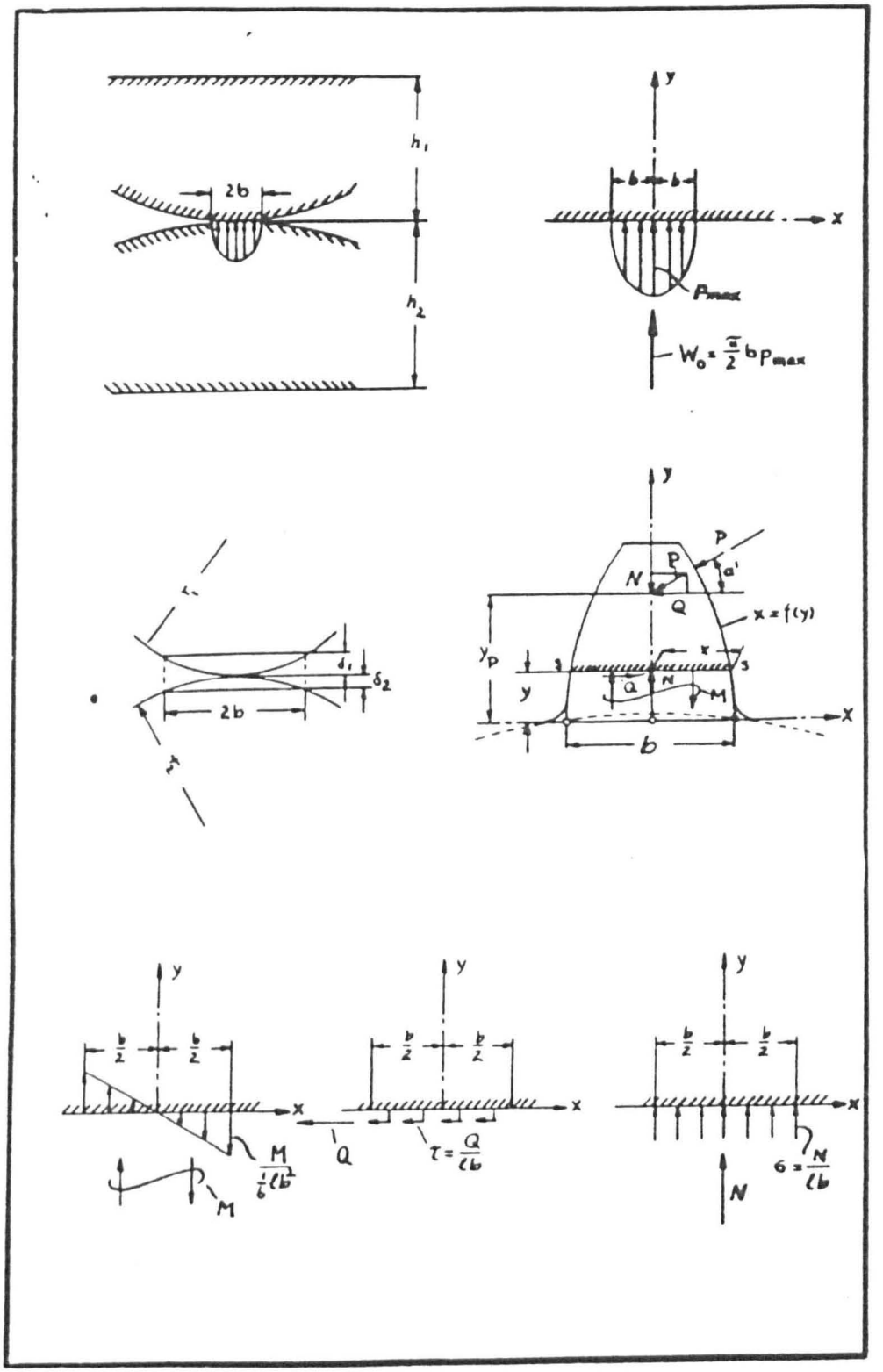
h1
2b
h2
y
x
b
b
Pmax
W0 = π/2 b pmax
y
P
N
P
a'
Q
x = f(y)
yp
x
s
y
Q
N
M
x
b
d1
δ2
2b
y
b/2
b/2
x
M
M/(1/6 lb²)
y
b/2
b/2
x
Q
τ = Q/lb
y
b/2
b/2
x
N
δ = N/lb

Fig. 1.6 Weber

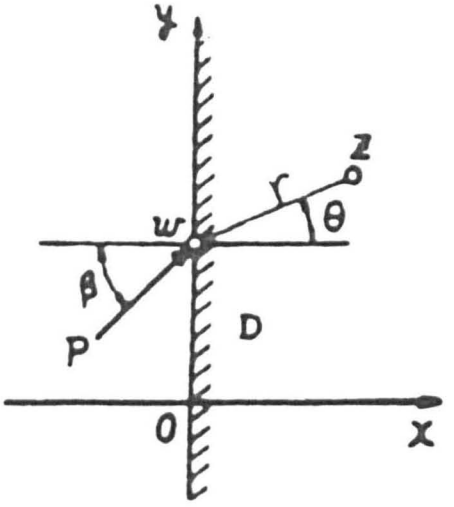

a) Applied load at a point on boundary of semi-infinite plate

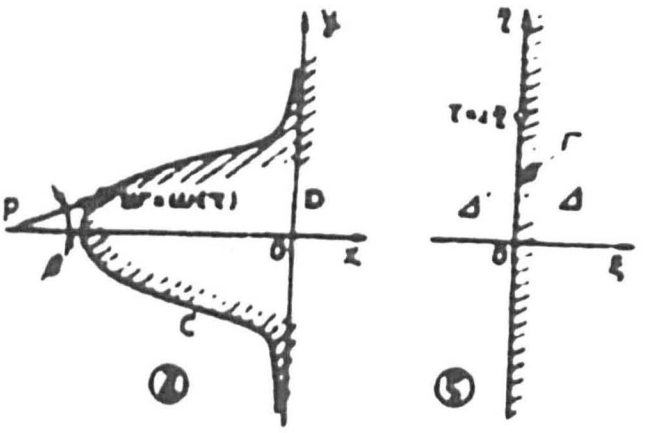

b) Conformal transformation

Fig.1.7 Terauchi & Nagamura

theory. Gear body deformations and Hertzian deformations were also accounted for, although the gear body component was again essentially the semi-infinite plane value obtained by Weber and Banaschek.

1.4 3-D Models

1.4.1 Introduction

So far, only 2-D "thin slice" meshing and compliance models have been discussed. In Chapter 2, a 3-D elastic mesh model is developed, but this is partly based on earlier models published by several authors. These are described below.

To model accurately the meshing behaviour of a gear pair under load, 3-D elastic mesh models must meet the following criteria:-

1. The load and deflection at any point on one contact line is affected by the loads and deflections at all the other points along that contact line, and by those at points along the contact lines of the adjacent simultaneously meshing tooth pairs. This "convective" effect of loads, including the "adjacent tooth" effects must be fully taken into account.
2. The actual gear tooth geometry must be accurately modelled. This cannot be done by using "plate theory", or approximating the tooth by a rack. In helical gears, the effect of tooth twist must also be allowed for.
3. All possible contact conditions must be allowed for, including the possibility of tip or edge contacts outside the "theoretical" contact region for perfect, rigid gears.
4. The effect of the axial component of the load in helical gears should be fully accounted for. The "thin-slice" approach ignores the effect of axial force components.
5. Gear body deformations must be included in the overall analysis of the gear deflections, since it can contribute a significant proportion of the overall tooth deformation on large diameter gears.

The various 3-D elastic mesh models, so far published, all fail to meet one or more of these conditions.

The model developed in Chapter 2 meets all the conditions and is thus potentially superior to the others which are described in detail below.

1.4.2 Approximate 3-D Models

Models based on tooth compliance values not derived from actual gear teeth are termed "approximate" 3-D models in this work. This is because an actual gear tooth has a very complex geometry, particularly in the case of helical gears. Representing it by a semi-infinite plate or a straight rack-shaped tooth is inadequate.

The earliest attempts to study the 3-D "convective" effect of tooth loads were based on the work carried out by Jaramillo[28] in 1950, who used exact solutions for an infinitely wide cantilever plate with point loads applied along the free edge. This solution was subsequently extended by Wallauer and Seireg[29] in 1960 to predict the behaviour of finite width gear teeth by means of the approximate "moment image" method.

This was (and still is) extensively used as a practical calculation procedure in the USA, and is described in detail by Steward[30] who shows that while the method correctly models the bending boundary conditions at the tooth ends on spur gears, it does not satisfy the shear boundary conditions. Its use for helical gear analysis is even less justifiable due to the lack of symmetry about mid-face point. Moreover, the moment image method originally proposed by Wellauer and Seireg bases the "infinite width" stiffness on Jaramillo's[28] thin plate results, which are unreliable since shear deformations and the effects of variable thickness (tooth taper) will clearly be significant on real gear teeth.

In 1961, Kagawa[24] assumed that each gear tooth was equivalent to a beam, with its axis along the tooth trace, and having an elastic support k_1 (representing the cantilever bending stiffness of each "thin slice" section normal to the beam axis) and a torsional stiffness k_2 as shown in Fig. 1.8. Semi-theoretical solutions for the load distribution were also developed to allow for the semi-elastic foundation of the built-in edge of the plate. This model provided a basis for the improved 3-D model developed by Schmidt[23] and discussed in Section 1.3.2. This model, like Schmidt's, predicted the occurrence of sharp load 'spikes' near the ends of some contact lines, and provided the first analytical confirmation of this so-called "buttressing effect", which had long been a controversial topic. This buttressing effect is shown clearly in Figs. 3.21 to 3.24 in Chapter 3.

In 1963, Hyashi[31] used a constant-thickness cantilever plate with a built-in edge, to represent an actual loaded gear tooth. He determined the plate deflections and root strains experimentally, and

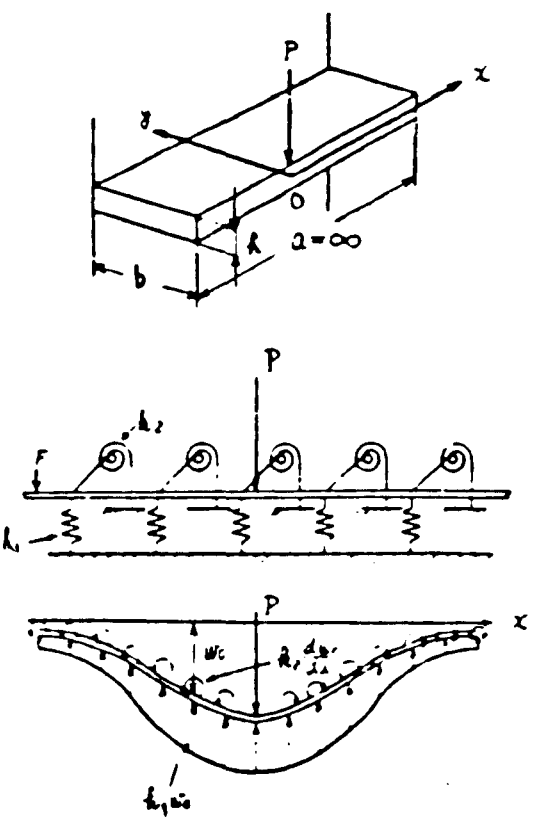

Fig. 1.8 Kagawa

incorporated these results in a mesh model which led to an integral equation which he solved numerically to obtain the load distribution on helical gear contact lines.

In 1963, Hyashi and Sayama[33] extended Hyashi's[31] model by incorporating into it experimentally determined deflections for a rack tooth, 240mm wide and 8mm module. It was concluded that the cantilever plate adequately represented an actual rack tooth as part of an encaster block. In 1967, Hyashi and Umezawa and Kajiyama and Uchibori[6] carried out further work on the subject. Again, the buttressing effect was revealed.

In 1967, Seager[34] modified the "thin slice" model and developed semi-empirical tooth bending deflection equations to account for convective effects. The contact deformations were assumed to be localized and hence without convective effects. Tests carried out on a model rack-shaped tooth provided the coefficients for the relevant differential equations, which were then solved by numerical methods. The buttressing effect was again evident but on a very small scale. Gear body deflections were not properly modelled.

In 1972 and 1973, Umezawa[35,36,37] developed finite-difference solutions for the deflections of a rack-shaped cantilever. Experiments carried out on a rack-shaped cantilever projecting from a large block, agreed very well with the numerical solutions once the effect of the deformations of the built-in end of the cantilever had been removed. This work was, in fact, a refinement of the earlier work carried out by Hayashi and Sayama[33] in 1963. The buttressing effect was again evident.

In 1981, Inoue and Tobe[38] used the finite element method to include the effect of transverse shear on tooth deformation. The actual gear tooth was approximated by a number of thin rectangular plates of varying width up the (rack-shaped) tooth. These results were later improved by Inoue and Tobe[39], including the effect of the elastic built-in end of the tooth. This, however, only accounted for part of the gear body deformation evident in real gears with a large number of teeth. Buttressing effects were again revealed.

In all the 3-D models discussed above, and referring to the conditions necessary for developing a good 3-D model in Section 1.4.1, condition 1 is only partially satisfied since the convective effects of the adjacent simultaneously meshing tooth pairs has been ignored. Condition 2 is also not satisfied since all the models discussed apply the analysis to either a cantilever plate or a built-in rack-shaped tooth. Condition

4 has certainly not been satisfied as the loading was always applied in the transverse section of the gear. Step 5 has been either totally unsatisfied or partially in the cases where the elastic built-in edge deformations were considered, as these represent only a small portion of the total gear body deformation of an actual gear. Clearly then, none of the 3-D models discussed so far adequately or accurately represents the actual meshing conditions of real gears.

1.4.3 Exact 3-D Models

1.4.3.1 Introduction

In this section, 3-D models which base their stiffness analysis on actual gear teeth are discussed. Since the true geometry of a gear tooth is modelled, these 3-D models will be termed "exact" models.

Three recently-published models of this type are discussed here in detail, to provide the basis for comparison with the model developed in Chapter 2.

1.4.3.2 Vedmar's Model

Tooth Geometry and Meshing Conditions

In Vedmar's[5] work in 1981, actual involute gear teeth were modelled. The involute profile and trochoidal fillet coordinates were calculated point by point from exact equations which are given in Appendix 1A.

Figure 1.9 shows the gear meshing region assumed by Vedmar, Ap and A'g are the "theoretical" outermost limits of contact on the pinion and gear (wheel) respectively and were assumed to define the start and end of contact during mesh. Any contact outside this region was ignored.

Contact Deformation

Vedmar assumed, as did the present author, that contact lines are straight, and are always located in the base tangent plane, as would be the case for perfect rigid gears with no profile or lead modifications.

Like Weber and Banaschek[40] and most other workers in this field, Vedmar assumed that contact deflections were localized ("non-convective"), and that they could be calculated using 2-D Hertzian contact theory.

His expression for the deflection of the centre of the loaded contact region relative to that of a point a distance h below the surface is

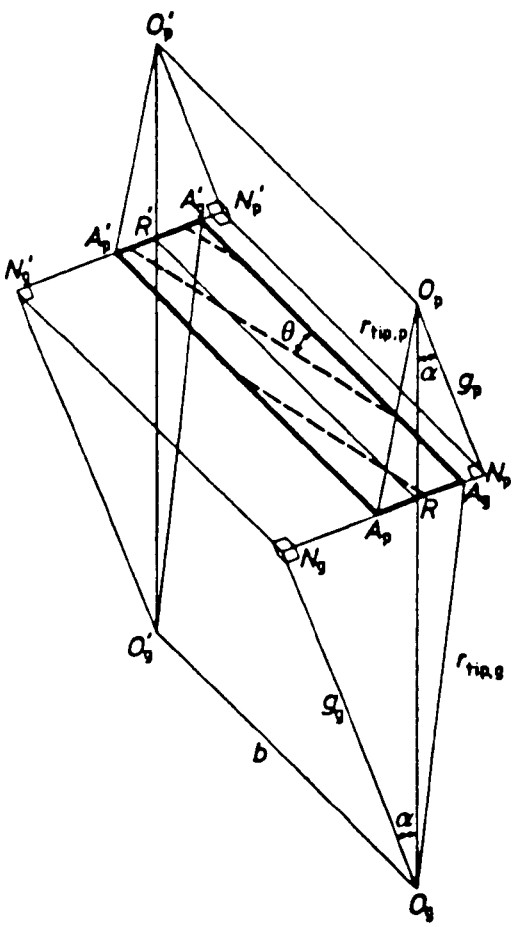

Fig. 1.9 Gear meshing region

$$u_c = 2.\frac{(1-\nu^2)}{\pi E} \cdot w\left[\ell n\left[h'+\sqrt{1+(h')^2}\right] - \frac{\nu}{1-\nu}(h')\left[\sqrt{1+\left(\frac{1}{h'}\right)^2}-1\right]\right]$$

1.30

where,

$h' = h/L$

and L is the semi-width of the contact region (Fig.1.11) given by

$$L = \left[8.\frac{1-\nu^2}{\pi.E}.w.\rho_{eff}\right]^{\frac{1}{2}} = \left[7.28.\frac{w}{\pi.E}.\rho_{eff}\right]^{\frac{1}{2}} \qquad 1.31$$

Vedmar non-dimensionalized Eqn.1.30 by multiplying by $E.m_n/F$, giving (with $\nu = 0.3$ for steel gears):

$$u_{c0} = \frac{1.82}{\pi}.m_n.\frac{w}{\eta F}\left[\ell n\left[h'+\sqrt{1+(h')^2}\right]-0.42857(h')^2\left[\sqrt{1+\left(\frac{1}{h'}\right)^2}-1\right]\right]$$

1.32

where F is the applied point load normal to the tooth flank in the normal plane (see below).

As explained in section 2.4, it proves necessary to "correct" Vedmar's deflection values to compare them with the author's. This requires calculations of the <u>increment</u> in contact deflection Δu_c between two <u>different</u> depths h_1 and h_2.

By substituting $h = h_1$ and $h = h_2$ in Eqn. 1.32, we can calculate

$$\Delta u_c = u_{c1} - u_{c2} \qquad 1.33$$

However, if $h >> L$, Eqns. 1.30 and 1.32 reduce to the simpler expressions

$$u_c = \frac{1.82}{\pi E} \cdot w \cdot \left[\ell n(2h') - 3/14\right] \qquad 1.34a$$

$$u_{c0} = \frac{1.82}{\pi}.m_n.w/F.\left[\ell n\,(2h') - 3/14\right] \qquad 1.34b$$

whence

$$\Delta u_c = \frac{1.82}{\pi E} \cdot w \cdot \ell n\,[h_1/h_2] \qquad 1.35$$

F.E. Model and Bending Deformation

The "bending" of the tooth was calculated using the F.E. mesh shown in Fig. 1.10. Tooth deformations were obtained at points along the contact line with a "point" load applied at various axial positions on the tooth flank.

The F.E. mesh used was relatively coarse, and thus incapable of modelling accurately the deformations near the "point" load. This problem was resolved by extracting the tooth bending (and shear) deformations at a considerable depth (0.5mn) beneath the surface, to exclude the inaccurately modelled surface region. The additional "contact deflections" were then added in, using the analytical expression given in Eqn. 1.34, so that (c.f. Fig. 1.11)

F.E. bending + Shear + contact Deformation	−	Incorrect F.E. Contact Deformation	+	Approximate Analytical Contact Deformation	=	Calculated Surface Deflection

1.36

The bending and shear deflections 0.5 m_n below the tooth surface extracted by Vedmar from his F.E. results represent the first two terms of Eqn. 1.36. Since these deflections were only available at a few nodal points for point loads applied at a few positions on the tooth flank, Vedmar curve-fitted the F.E. data to allow calculation of deflections anywhere along any contact line, with loads applied at any point across the tooth face. The approximating function so derived took the form

$$\alpha(\zeta_F,\eta_F,\zeta,\eta) = [\psi(\zeta_F,\eta_F).\ \psi(\zeta,\eta)]^{\frac{1}{2}} \cdot \Gamma(|\zeta-\zeta_F|),\eta.\eta_F,\ \eta+\eta_F,\ \eta^2+\eta_F^2) \qquad 1.37$$

where

- α − bending (and shear) compliance function
- ψ − "end effect" function
- Γ − "master" function
- ζ − axial co-ordinate of point where deformation is desired
- ζ_F − axial co-ordinate of loaded point
- η − radial co-ordinate of point where deformation is measured. (η = 0 at tooth tip)

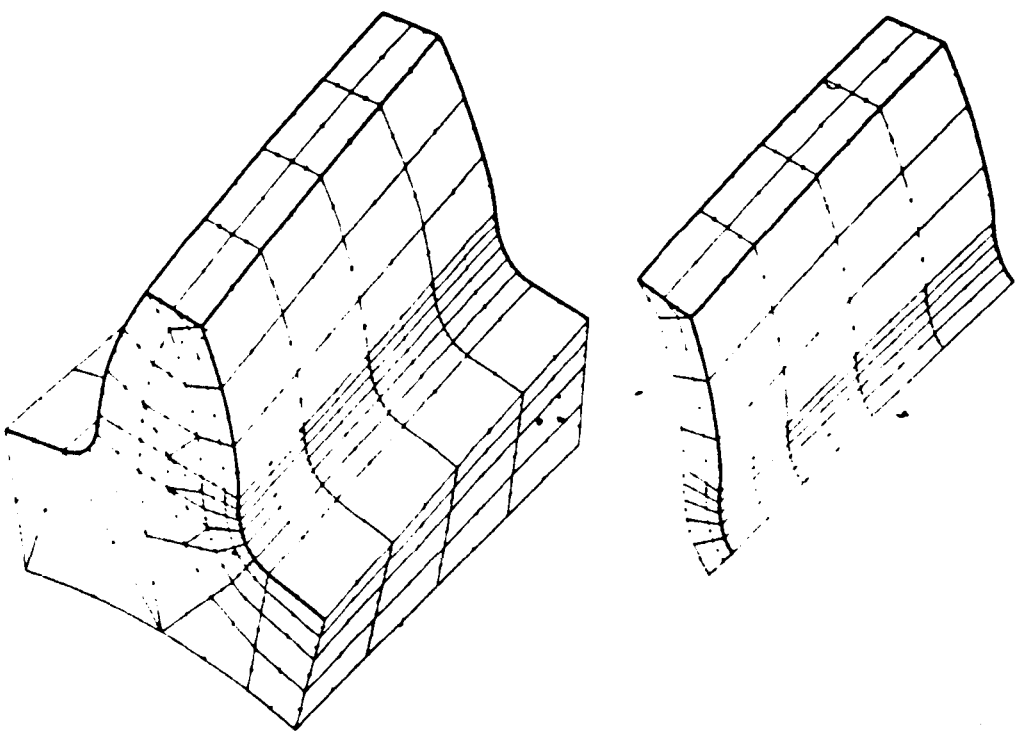

Fig.1.10 Helical gear tooth and contact zone divided into finite elements

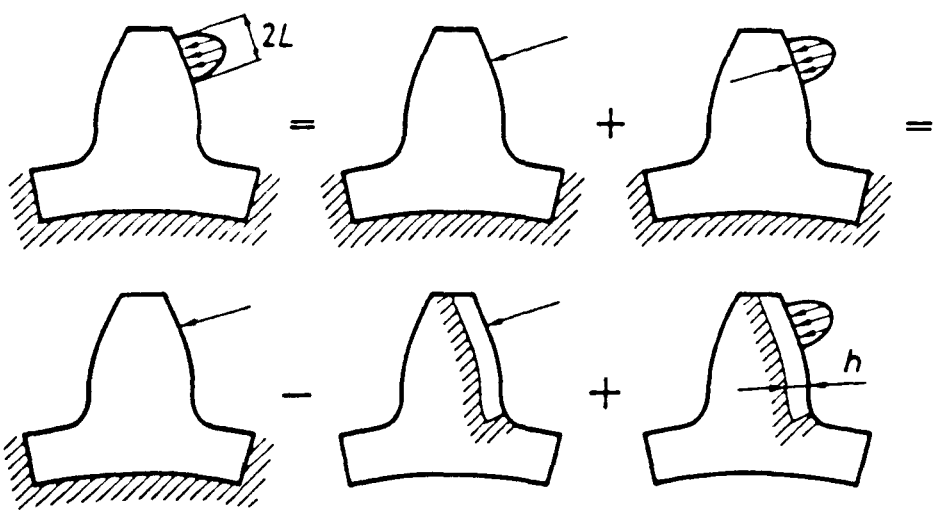

Fig. **1.11** Dividing into bending and contact conditions

η_F - value of η at the loaded point

(α, ζ nd η are non-dimensional)

The master function Γ models the gear tooth compliance for an "infinitely" wide gear or at points far from the ends of the teeth, where end effects are of no consequence. For finite width gears Γ must be used as shown in conjunction with the end effect function ψ to account for the additional tooth end compliance which is significant, particularly for end loading. Vedmar gives

$$\Gamma(|\zeta-\zeta_F|,\eta.\eta_F,\eta+\eta_F,\eta^2+\eta_{2F}) =$$

$$e^{-(A_1+A_2(\eta+\eta_F)+A_3.\eta.\eta_F+A_4.(\eta^2+\eta_F^2)+A_5.\eta.\eta_F.(\eta+\eta_F)+A_6.\eta^2.\eta_F^2}$$

$$. (|\zeta-\zeta_F|)^B \qquad 1.38$$

Where A_i and B are independent of η and ζ.

The end effect function ψ was assembled from two functions, each depending on the distance from one of the free ends of the gear. Since the F.E. data was obtained for a face width where these functions are independent of each other, the function ψ is given by

$$\psi(\zeta,\eta) = A_{11}+A_{12}e^{-A_{13}\cdot\eta}+(B_{11}+B_{12}\cdot e^{-B_{13}\cdot\eta}).e^{-(C_{11}+C_{12}\cdot\eta).\zeta}$$
$$+(B_{21}+B_{22}\cdot e^{-B_{23}.\eta}).e^{-(C_{21}+C_{22}\cdot\eta).(b_0-\zeta)} \qquad 1.39$$

where $b_0 = b/m_n$, and, as for Γ the A_{ij} and Bij coefficients are independent of radial location η.

Vedmar tabulates values of the coefficients A_{ij} and B_{ij} etc. for $\beta = 0^\circ$, 10° and 20° for teeth with standard basic rack profile, zero addendum modification, and values of Z from 15 to 160.

Compatibility Condition

Fig. 1.12 shows the mesh area near the base tangent plane (c.f. Fig. 1.9). For contact between the two gears at any axial section

$$e = e_p + e_g = g_p . \Delta\varphi - \delta . m_n \qquad 1.40$$

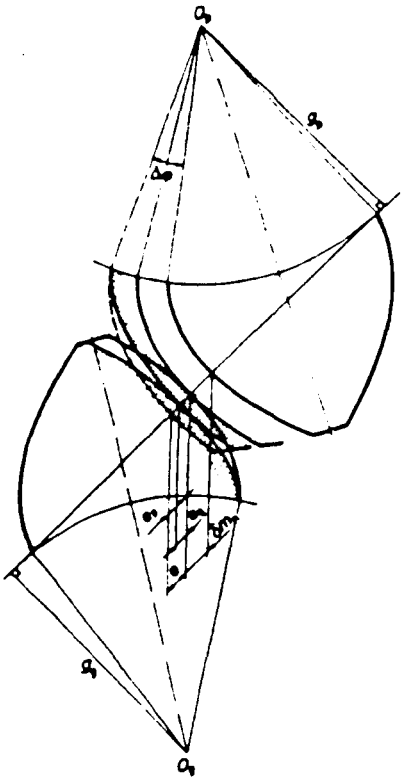

a) Deformation of a pair of teeth in contact

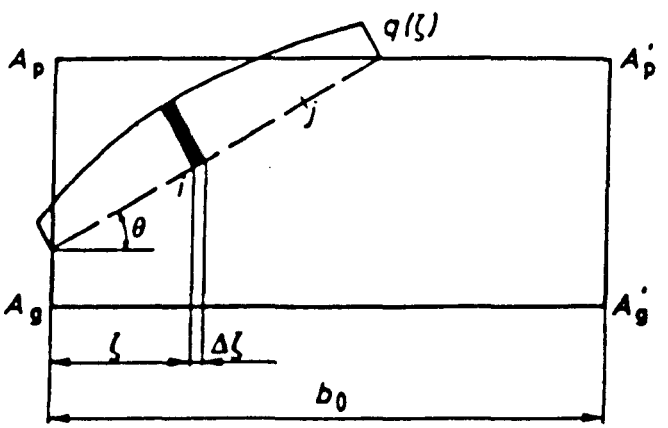

b) Force acting on a contact line

Fig. 1.12 Condition of Deformation

where

e – combined non-dimensional displacement of pinion and gear teeth.

δ – combined flank error

$\Delta\varphi$ – rotation of the pinion from the unloaded position if the gear is assumed fixed. (All measured in the transverse plane along the base tangent).

Since $\Delta\varphi$ (the transmission error) is independent of the axial position of the point considered, then, for each contact point

$$e + \delta \cdot m_n = g_p.\Delta\varphi = \text{constant} \qquad 1.41$$

Introducing the displacement u_i normal to the tooth flank, Vedmar obtains

$$\frac{u_i}{\cos\theta} + \delta_i m_n = \Delta m_n \qquad 1.42$$

where Δ is a non-dimensional constant, and θ is the base helix angle as labelled by Vedmar.

Load Distribution Solution

The static load distribution along the contact lines of meshing gear teeth is determined from the stiffness characteristics of the gears. The tooth bending/shear and contact deformation at a point i due to loads F_j applied at points j is given by

$$u_{\tilde{i}} = \sum_{\tilde{j}=1}^{n} \alpha_{\tilde{i}\tilde{j}} \cdot F_{\tilde{j}} + uc_{\tilde{i}} \qquad 1.43$$

where

n – number of contact points on all simultaneous contact lines

$\alpha_{\tilde{i}\tilde{j}}$ – combined bending compliance influence function for pinion and gear obtained from Eqns. 1.37 – 1.39, with $(\eta,\zeta) = (\eta_i,\zeta_i)$, $(\eta_F,\zeta_F) = (\eta_j,\zeta_j)$.

The contact deflection u_{ci} is assumed to be caused entirely by the load F_i at $\tilde{i}$ and is unaffected by loadings $F_{\tilde{j}}$ at $\tilde{j} \neq \tilde{i}$. This is a valid assumption since the contact deformations are highly localised as shown

in Fig. 1.13, (which also shows the bending deflection distribution for comparison).

The total force acting on all simultaneous lines of contact K in the meshing plane is given by

$$F = \sum_{k=1}^{K} \int_{0}^{b_0} w^{(k)}(\zeta).m_n.\frac{d\zeta}{\cos\theta} = \sum_{k=1}^{K} \sum_{j=1}^{nk} F_j^{(k)} \qquad 1.44$$

where $w(\zeta)$ is along the base tangent direction.

Substituting for $u_{c\tilde{i}}$ from Eqn. 1.34a and non-dimensionalising using

$$\begin{aligned} u_{\tilde{i}} &= u_{0\tilde{i}} \cdot \frac{F}{E.m_n} \\ \alpha_{\tilde{i}\tilde{j}} &= \frac{\alpha_{o\tilde{i}\tilde{j}}}{E.m_n} \\ w_{\tilde{i}} &= w_{0\tilde{i}} \cdot \frac{F}{m_n} \\ h' &= h'_0 \cdot m_n \end{aligned} \qquad 1.45$$

Eqn. 1.43 becomes,

$$u_{0\tilde{i}} = \sum_{\tilde{j}=1}^{n} \alpha_{0\tilde{i}\tilde{j}} \cdot \frac{F_{\tilde{j}}}{F} + \frac{1.82}{\pi} \cdot w_{0\tilde{i}} \cdot [\ell n(2.h'_0 \cdot m_n)^{-3.14}] \qquad 1.46$$

Dividing Eqn. 1.44 through by F

$$\sum_{k=1}^{K} \sum_{\tilde{j}=1}^{nk} F_{\tilde{j}}^{(k)}/F = 1 \qquad 1.47$$

where

k - is the contact line number

nk - is the number of contact points on line k

K - is the number of simultaneous contact lines

and introducing

$$F_{\tilde{j}} = \sum_{\ell=1}^{n} \varphi_{\tilde{j}\ell} \cdot w_\ell \qquad 1.48$$

where $\varphi_{\tilde{j}\ell} = m_n \cdot \varphi_{0j\ell}$ is a <u>weighting</u> function (=0 for $|\ell-j|>2$) which decides what proportion of each of w_1 to w_ℓ must be included in summing up the force at point $\tilde{j}$, where for $|\ell-\tilde{j}|>2$ w is too far from point $\tilde{j}$ and the multiplier φ is zero.

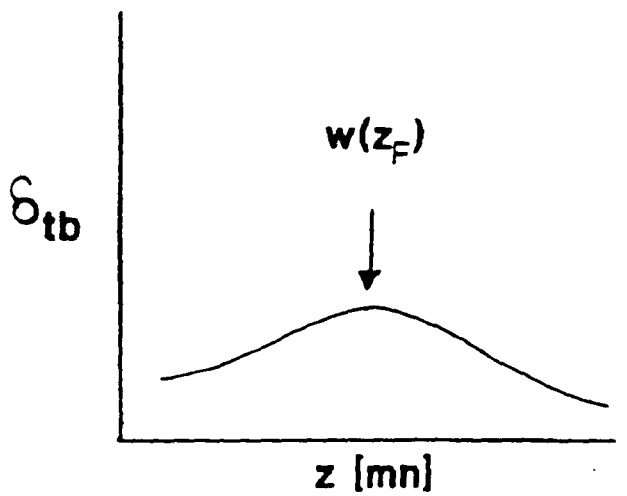

a) Bending Deflection

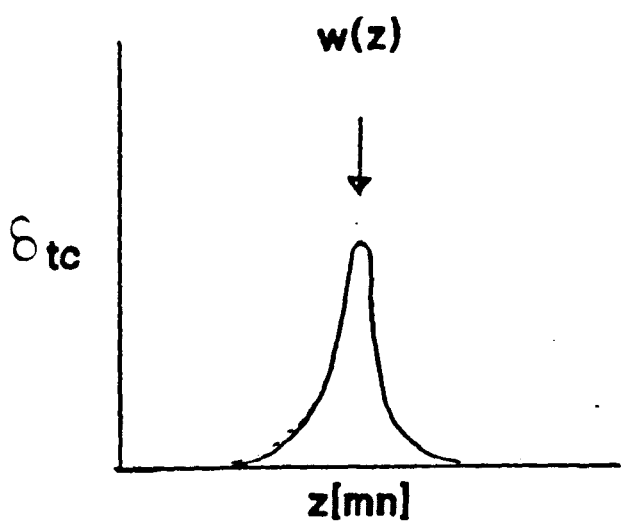

b) Contact Deflection

Fig. 1.13 Contact & Bending Deflection Distribution

Substituting for $F_{\tilde{j}}$ from Eqn. 1.48 into Eqn. 1.46 finally becomes

$$u_{0\tilde{i}} = \sum_{\tilde{j}=1}^{n} \sum_{\ell=1}^{n} \alpha_{0i\ell} \cdot \varphi_{0\ell\tilde{j}} \cdot w_{0\tilde{j}} + \frac{1.82}{\pi} \cdot w_{0\tilde{i}} \cdot [\ell_n(2.h'_0.m_n) - \frac{3}{14}] \qquad 1.49$$

where ℓ and $\tilde{j}$ are interchangeable as both have the same limits. Next considering the condition $|\ell - \tilde{j}| > 2$, then for φ not to be zero, the limit of ℓ may be narrowed down as

$$u_{0\tilde{i}} = \sum_{\tilde{j}=1}^{nk} w_{0\tilde{j}}^{(k)} \sum_{\ell=\tilde{j}-2}^{\tilde{j}+2} \alpha_{0\tilde{i}\ell}^{(k)} \cdot \varphi_{0\ell\tilde{j}}^{(k)} + \frac{1.82}{\pi} \cdot w_{0\tilde{i}}^{(k)} \cdot [\ell_n(2h'_0 \cdot m_n) - \frac{3}{14}] \qquad 1.50$$

where k representing the k^{th} contact line has been introduced.

Substituting Eqn. 1.48 into Eqn. 1.47 and introducing non-dimensionality while keeping in mind that ℓ and $\tilde{j}$ are interchangeable we get

$$\sum_{k=1}^{K} \sum_{\tilde{j}=1}^{nk} \left[w_{0\tilde{j}}^{(k)} \cdot \sum_{\ell=\tilde{j}-2}^{\tilde{j}+2} \varphi_{0\ell\tilde{j}}^{(k)} \right] = 1 \qquad 1.51$$

Rearranging Eqn. 1.42 and using the non-dimensional form of u from Eqn. 1.45, then

$$u_{0\tilde{i}} = (\Delta - \delta_{\tilde{i}}^{(k)}) \cdot \cos\theta / F_0 \qquad 1.52$$

Substituting for u_{0i} from Eqn. 1.50 into Eqn. 1.52, then

$$\sum_{\tilde{j}=1}^{nk} w_{0\tilde{j}}^{(k)} \sum_{\ell=\tilde{j}-2}^{\tilde{j}+2} \alpha_{0\tilde{i}\ell}^{(k)} \cdot \varphi_{0\ell\tilde{j}}^{(k)} + \frac{1.82}{\pi} \cdot w_{0\tilde{i}}^{(k)} \cdot [\ell n(2h'_0.m_n) - \frac{3}{14}] = \frac{(\Delta - \delta_{\tilde{i}}^{(k)}) \cdot \cos\theta}{F_0} \qquad 1.53a$$

Eqns. 1.51 and 1.53a may be solved simultaneously since Eqn. 1.53a must be satisfied at all contact points giving an equal number of equations, and Eqn. 1.51 gives a number of equations equal to the number of unknowns. One method of solution is to divide Eqn. 1.53a by Δ to give

$$\sum_{\tilde{j}=1}^{nk} w_{0\tilde{j}/\Delta}^{(k)} \sum_{\ell=\tilde{j}-2}^{\tilde{j}+2} \alpha_{0\tilde{i}\ell}^{(k)} \cdot \varphi_{0\ell\tilde{j}}^{(k)} + \frac{1.82}{\pi} \cdot w_{0\tilde{i}/\Delta}^{(k)} \cdot \left[\frac{\ell}{n} (2h'_0 . m_n) - \frac{3}{14}\right]$$

$$= \frac{(1-\delta_{\tilde{i}/\Delta}^{(k)}) . \cos\theta}{F_0} \qquad 1.53b$$

and knowing F_0 and k, and assuming a reasonable value for $w_0^{(k)}/\Delta$, Eqn. 1.53b may be solved by iteration, each time using the newly calculated value of $w_0^{(k)}/\Delta$ until convergence occurs, and equation 1.53b is satisfied. If separation does take place at any contact position $\tilde{i}$, then $u_{0\tilde{i}}$ is zero since as separation "just" begins $\delta_{\tilde{i}}^{(k)} = \Delta$ and beyond that $u_{0\tilde{i}}$ must also be set to zero.

1.4.3.3 Steward's Model

Tooth Geometry and Meshing Conditions

In Steward's[30] work in 1988, actual involute gear teeth were again modelled. The involute profile and trochoidal fillet were developed from Buckingham's[41] equations for spur gears, which correspond exactly to the equations in Appendix 1A used by Vedmar[5] and in this work.

Fig.1.15 shows the mesh region assumed by Steward (Figure 1.14 represents a perfect and rigid gear). AA' and BB' are the theoretical limits of mesh for perfect rigid gears (defined, as in Fig. 1.9, by the intersection of the effective tip circules of the two gears with the base tangent plane). Steward assumed that, due to the combined effect of gear errors, corrections and elastic deformation, contact was actually possible within the region $A_0A'_0B'_0B$, with contact outside the theoretical limits taking the form of edge contacts (not in the base tangent plane). Appendix 2A describes in detail how the location of contact points in this region is determined for both spur and helical gears, using a procedure derived from Steward's work on spur gears.

As in Vedmar's work and the author's, Steward assumed that the contact lines are straight and in the same base tangent plane, regardless of tooth errors, corrections and elastic distortions. For relatively accurate gears, this is a reasonable assumption unless Z_1 and Z_2 are both large.

l _ a line of contact
j _ a Gauss point

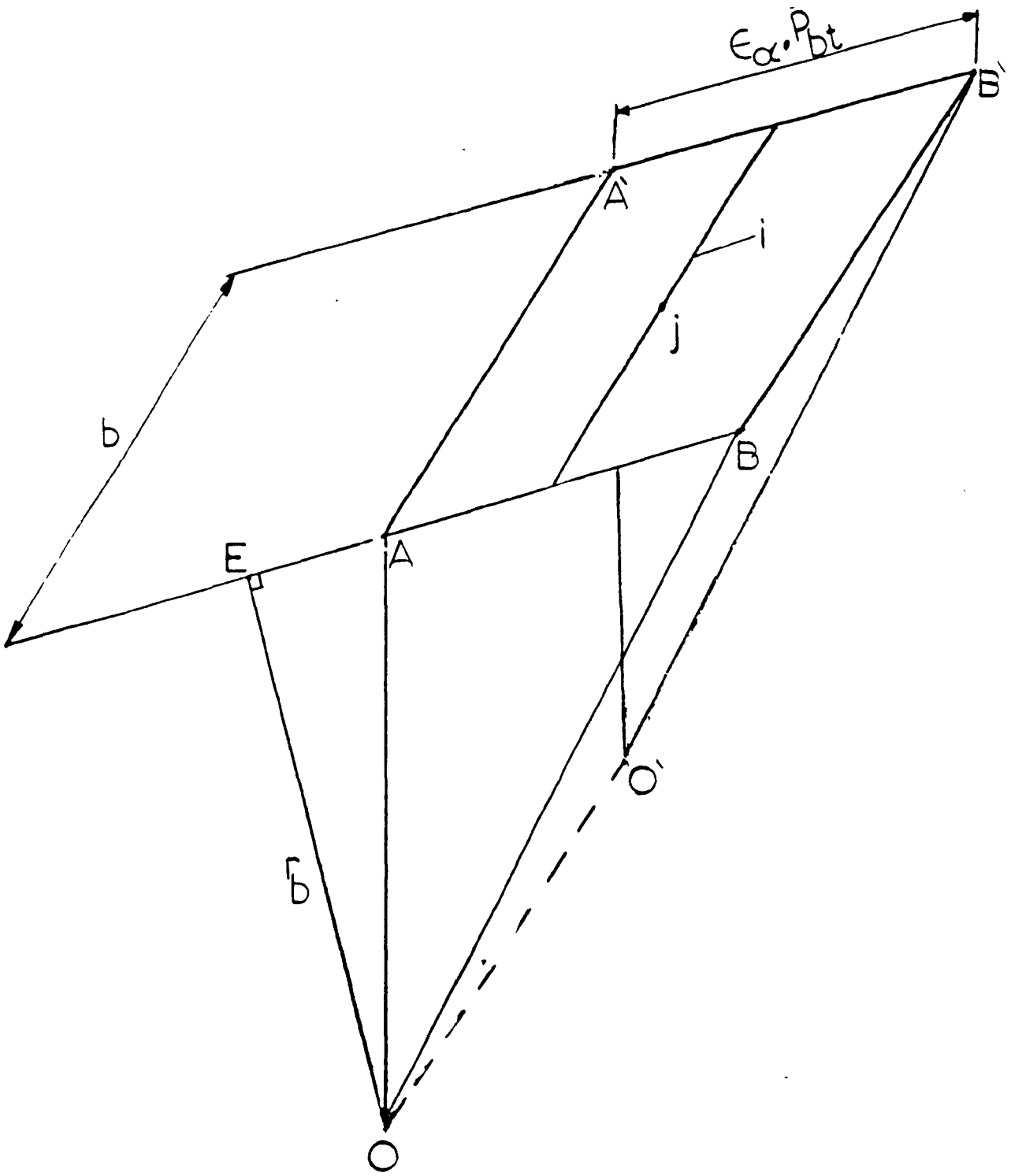

Fig. 1.14 Plane of Action ABB'A' of a Perfect Spur Gear

i – a line of Contact
j – a Gauss point

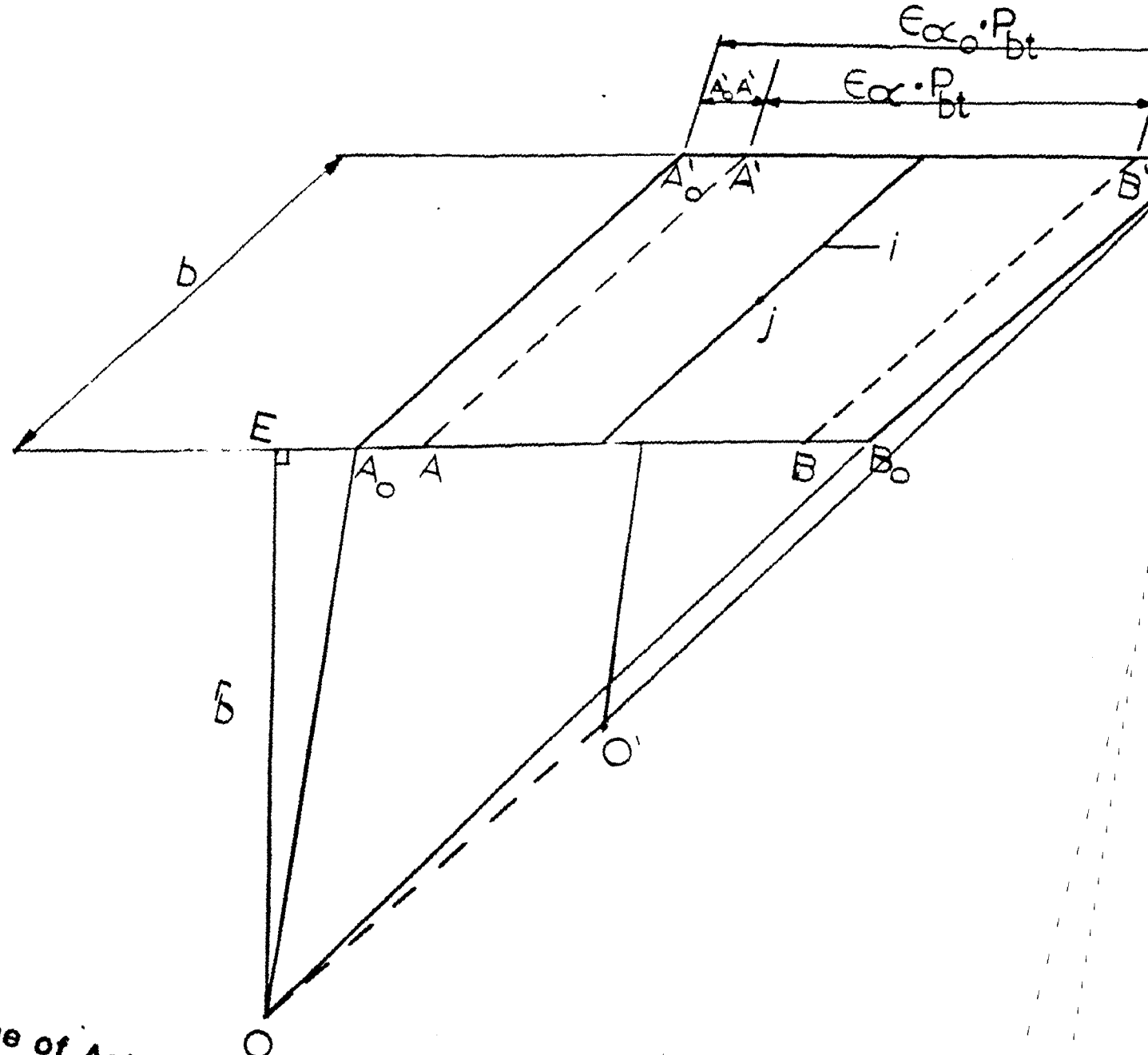

5 Plane of Action $A_oB_oB_o' A_o'$ of an actual Spur Gear

Contact Deformation

Steward calculated contact deformations using the same basic equations as Vedmar (Section 1.4.3.2). However, there are two important differences in his approach which are discussed below.

As previously explained, Vedmar[5] extracted his FE "bending" deformations at a constant depth of $0.5m_n$ beneath the tooth surface. Steward[30] used, instead, the deflections at the tooth centre line derived from FE modelling of the whole gear. This is an improvement on Vedmar's work since at this greater depth (at the tooth centre-line), the effect of inadequately-modelled contact deformation is much reduced. Only at the tooth tips is Vedmar's depth sometimes comparable to Steward's.

Steward also investigated the additional compliance of contacts near the tooth tip by carrying out a 2-D FE study of a rack profile subjected to Hertzian pressure distributions at various distances from the tip.

The corner contact compliance was found to be much greater than that predicted by Hertzian theory (Eqn. 1.34a), as a result of which Steward introduced a correction factor M given by

$$M = 1.627 - 0.282 \,.\, y_t + 0.03338 \,.\, y_t^2 \qquad 1.54$$

where

$$y_t = \frac{(da - dy)/2}{b.\cos(\alpha y)}$$

Such that the actual contact compliance is given by

$$(u_c)_{tip} = M.(u_c) \qquad 1.55$$

where u_c is the value given by Eqn. 1.34a.

Steward also carried out a very important investigation to check the validity of "separating" the "contact" and "bending" components of tooth deflection. This has been the basis of nearly every published method for predicting tooth compliance in both 2-D and 3-D mesh models, but does not appear to have been previously checked.

To do this, Steward first established an FE mesh geometry that would satisfactorily model the compliance of "classical" Hertzian contacts

between "semi infinite" solids, then, using this fine mesh at the points of contact, he modelled a gear tooth in 2-D, with three different loading positions (Fig. 1.16). In this way the contact region was modelled with sufficient accuracy to yield reliable values for the actual deflection of the flanks relative to the tooth centreline.

Steward's results are shown in Table 1.1 in which the FE deflections at the tooth flank are compared with those obtained by adding the Hertzian deflection calculated from Eqn. 1.34a to the FE tooth centreline deflections. The maximum discrepancy of less than 3% shows that separate treatment of the contact compliance is reasonable.

FE Model and Bending Deformation

Unlike Vedmar[5] who modelled only the loaded tooth and a very small portion of the gear body (Fig.1.10) Steward[30] modelled the loaded tooth, the two directly adjacent teeth, the whole gear body and a length of shaft (approximately half a shaft diameter) at each end of the gear as shown in Fig. 1.17. The shaft was simply supported at both ends, and torsionally restrained at one end so that tooth loads could be reacted in a realistic way. For each gear modelled, the shaft diameter used was given by

$$d_s = 0.8.d = 0.8.m_n.Z \qquad 1.56$$

To ensure that this is a "typical" diameter for larger gears, Steward suggested a cut-off point at $d = 25\ m_n$ as shown in Fig. 1.18.

Having established that it was reasonable to add separately-calculated contact deflections to the tooth centre line deflections, Steward then investigated the effect on the accuracy of the predicted deflections of using relatively coarse meshes, (since it was no longer necessary to attempt to model the contact region accurately). The coarse tooth meshes shown in Fig.1.19 (cf. the fine meshes of Fig. 1.16) were found to be adequate.

Steward then determined how much of the gear body it was necessary to model, by analysing the three meshes shown in Fig. 1.19. Even on the small (14 tooth) gear studied, the gear body deflections were very significant, as the table shows, and Steward concluded that modelling of the whole gear was necessary.

Based on the above, a 3-D model with a relatively coarse mesh was developed based on 20-noded isoparametric brick elements and to a much lesser extent 15-noded triangular prism elements for easy fitting.

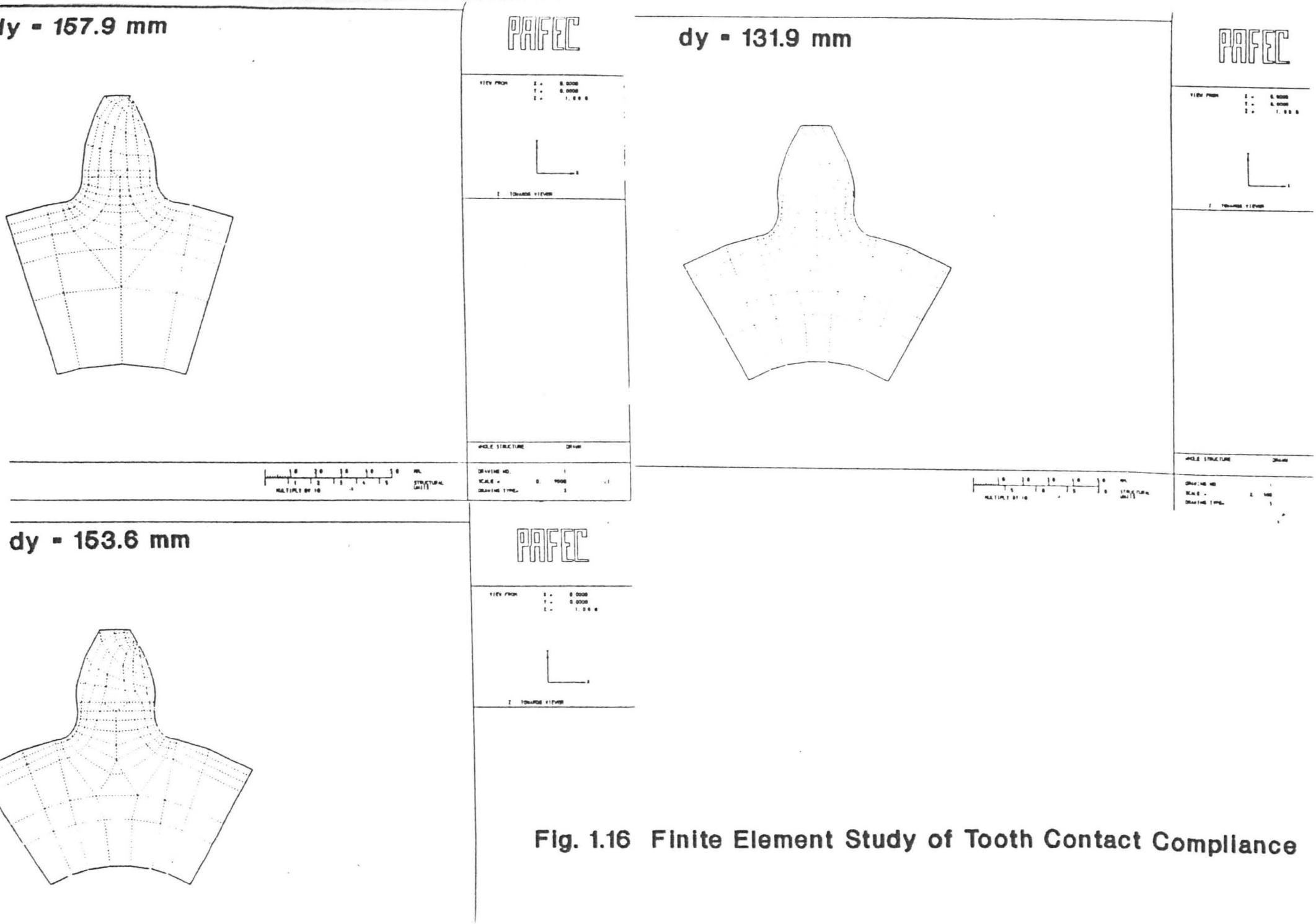

Fig. 1.16 Finite Element Study of Tooth Contact Compliance

dy [mm]	del1 [um]	del2 [um]	error [%]
157.9	80.121	78.051	-2.60
153.6	69.888	68.562	-1.90
131.94	35.062	34.349	-1.90

dy _ loading diameter
del1 _ FE tooth flank deflection
del2 _ FE tooth centre_line deflection
error _ (del2-del1)*100/del2

Table 1.1 Comparison of Analytical & FE Tooth Contact Deflections

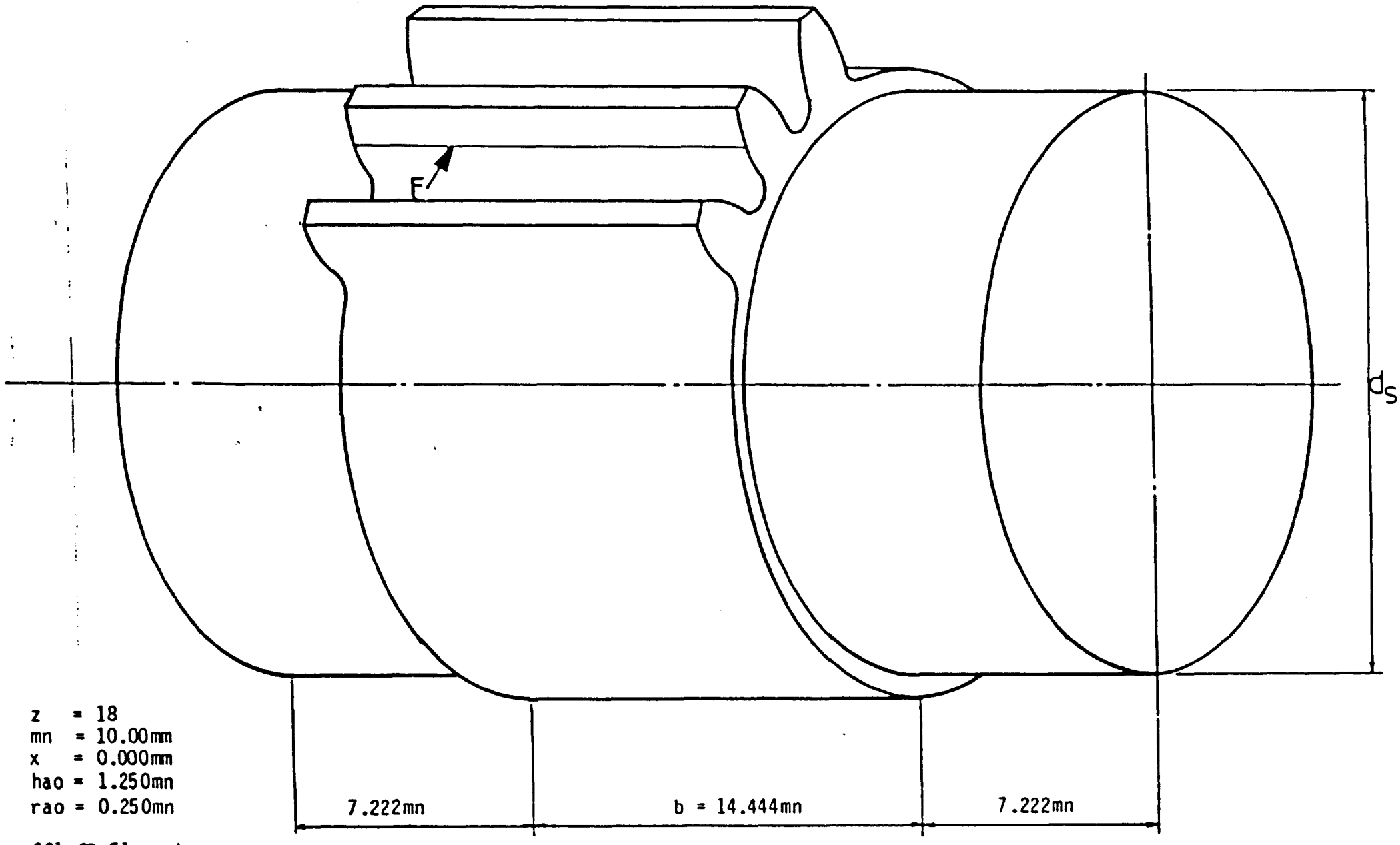

Fig. 1.17 Finite Element Modelling of Tooth Centre_Line Deflections

Fig. 1.18 Shaft Diameter For Spur Gear FE Model

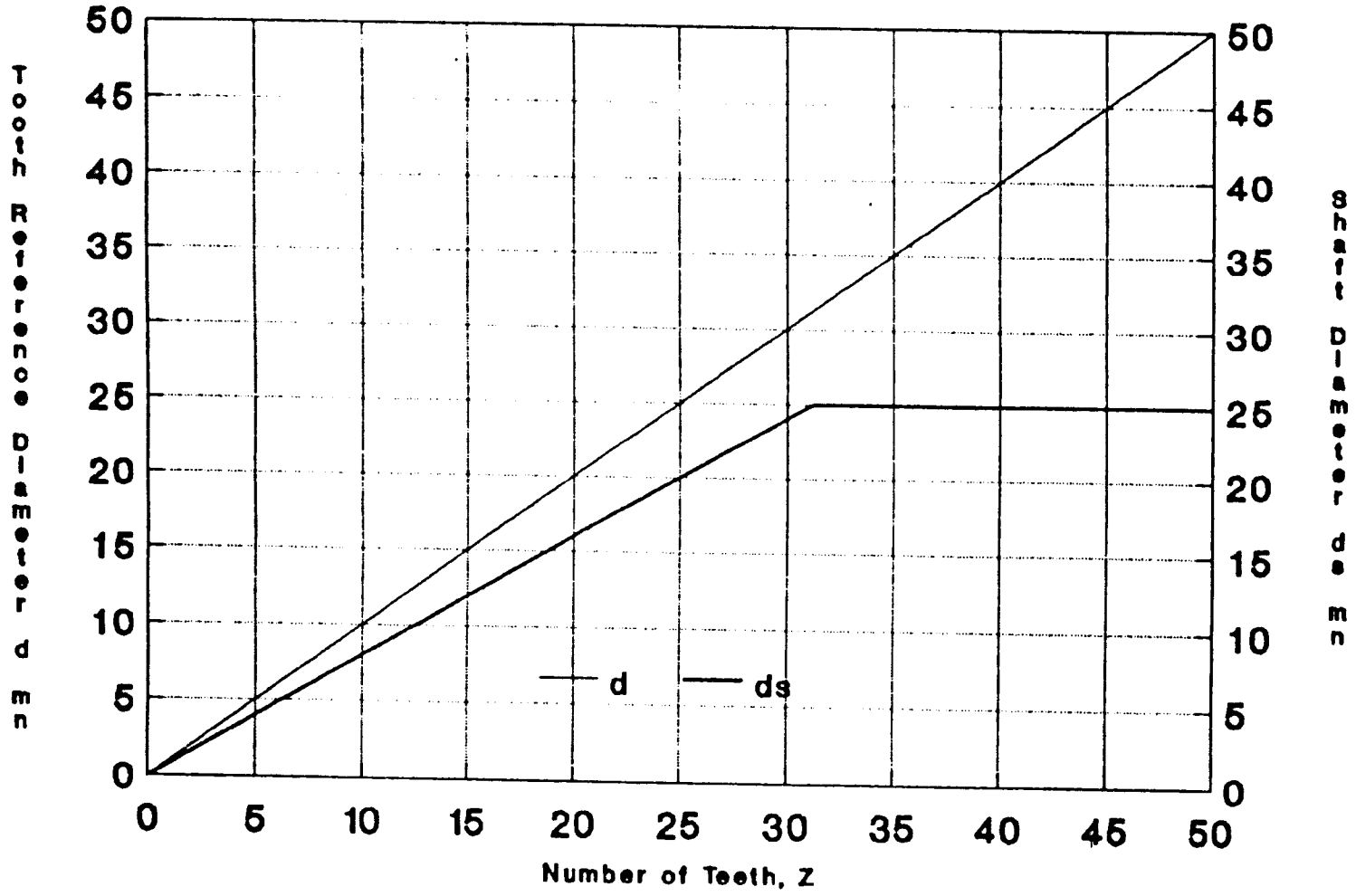

mn=10 mm

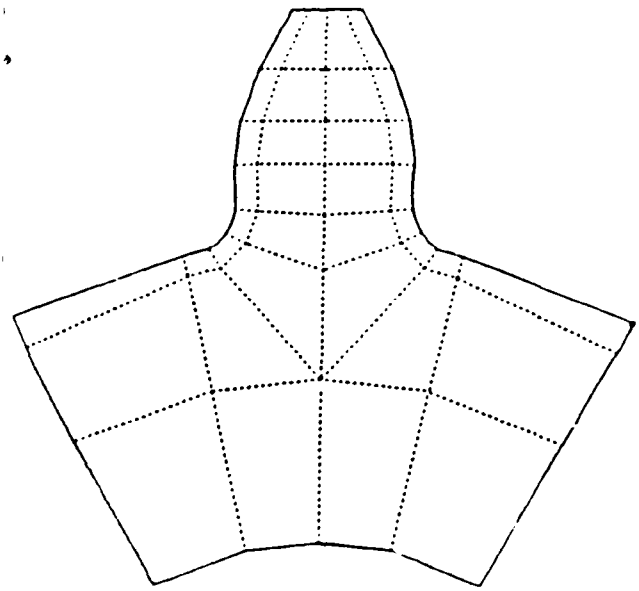

Model 1

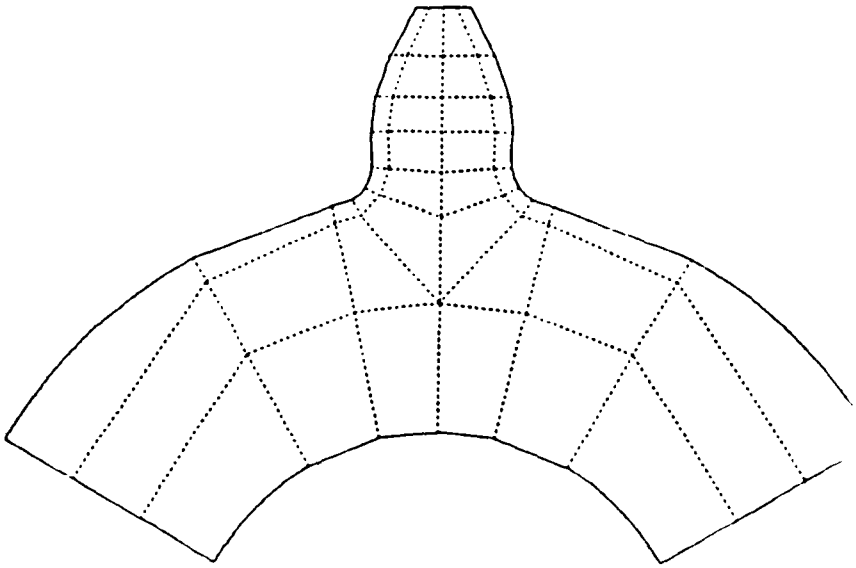

Model 2

z = 14
mn = 10.00mm
x = 0.000mm
hao = 1.200mn
rao = 0.304mn

F.E. Model	$\frac{\delta_{tb}}{\omega}$ [mu/N/mm]
1	0.0248
2	0.0286
3	0.0313

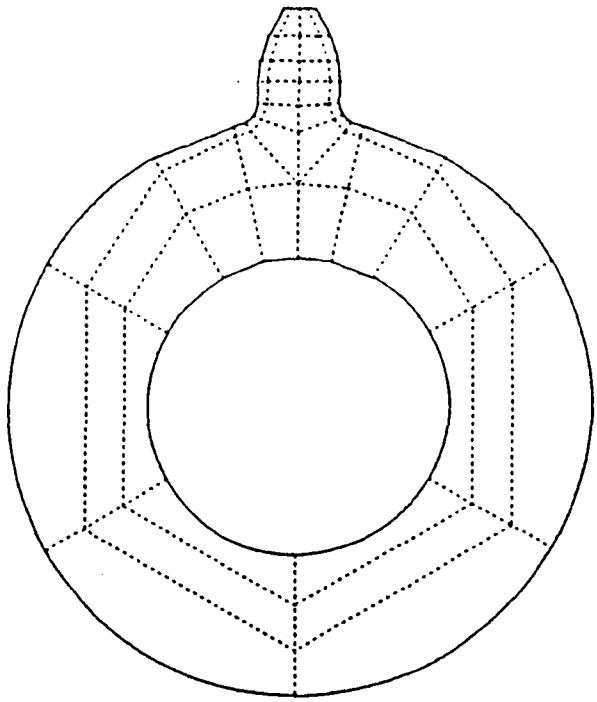

Model 3

Fig. 1.19 Winter's Experimental Gear 2_D FE Models

These elements are shown in Fig. 1.20. "Point" loads normal to the tooth flank were applied at the reference radius, and at points $0.5m_n$ and $1.0\ m_n$ at each of five axial loactions ($0.25m_n$, $0.75m_n$, $1.25m_n$, $2.50m_n$, $6.0m_n$) from one end of the gear. Due to symmetry (since b = $12m_n$) of spur gears, there was no need to apply any loads on the other half. For each axial loading position, the axial divisions were arranged to give a finer mesh near the points of loading, where stress gradients are largest (see Fig. 2.6).

To simulate a point load as closely as possible, and to minimize the effect of "spreading" of the load over adjacent elements, the loads were applied to mid-side nodes rather than corner nodes as shown in Fig. 1.21b. This is equivalent to a parabolic distribution in the axial direction, and due to the characteristics of the FE solution is equivalent to a sharply peaked distribution over two elements in the radial direction as shown. The "point" loads were thus distributed over a rectangular patch $0.5m_n$ x $1.0m_n$ (Fig.1.21b) rather than $1.0m_n$ x $1.0m_n$ (Fig. 1.21a). From Fig. 1.21b, most of the load is concentrated on the shaded area $0.5m_n$ x $0.5m_n$.

As mentioned earlier, the FE tooth centreline deflections exclude the effect of the FE contact deformations under the point loads. The centre-line deformations were obtained at the points where the load-line intersects the tooth centre-line (for spur gears this point is in the same transverse plane as the loaded point). To simplify the analysis, the FE mesh was designed so that these intersection points fell on mid-side nodes in the mid-plane of the tooth.

The deflections thus obtained included tooth bending and shear deformation, gearbody and shaft deformations. Steward used simple engineering theory to calculate shaft bending, torsional and shear deformations (which compared very well with FE shaft deformations). These were then subtracted from the tooth centre-line deflections to give the combined tooth bending shear and gear body deflection at each point.

Steward also investigated the deflection of teeth adjacent to the loaded tooth. There are no contact loads and so no contact deflections to consider, so the FE deformations on the surfaces of the flanks could be used. These deformations were shown to be independent of radial loading position and were identical for the "preceding" and "succeeding" adjacent teeth (see Fig. 2.9).

The loaded and adjacent tooth deformations so obtained were approximated by exponential functions. For the loaded tooth, these

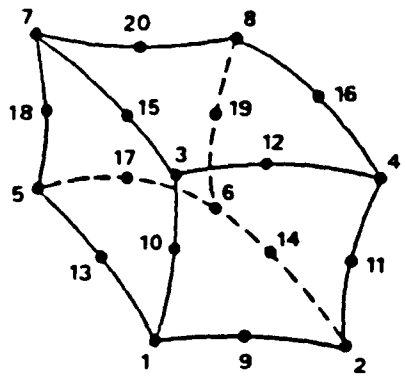

a) Isoparametric Brick Element

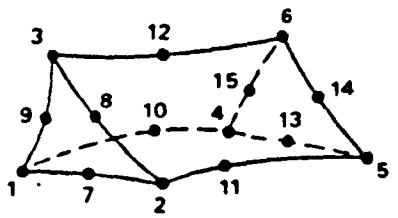

b) Triangular Prism Element

Fig. 1.20 Element Types Used in Steward's 3_D FE Model

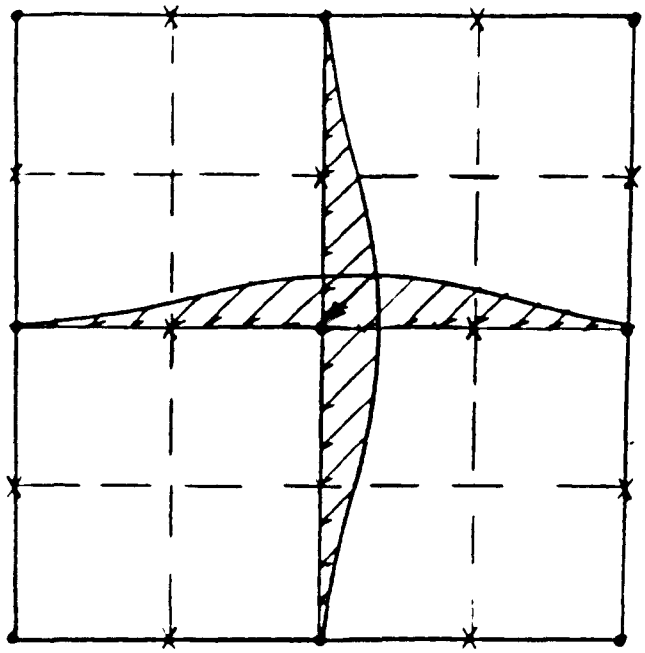

a) Corner Node Loading

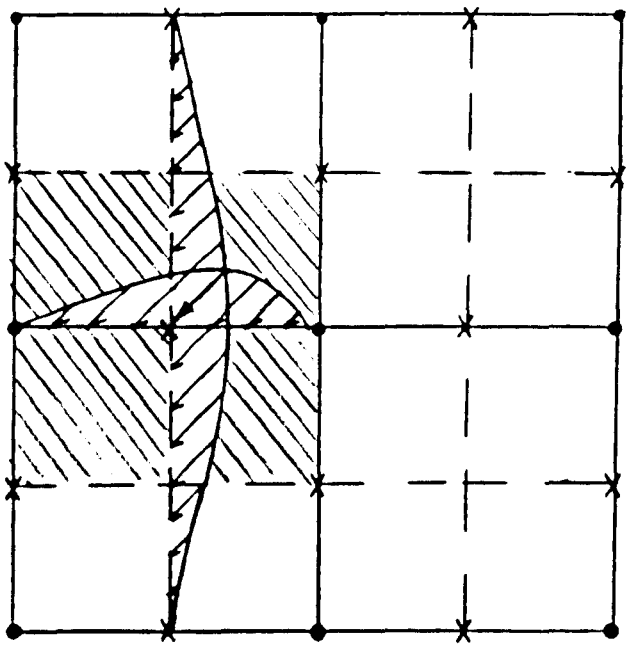

b) Mid_Side Node Loading

● corner nodes × mid_side nodes

Fig. 1.21 Advantage of Mid_Side Node Loading

were similar to those developed by Vedmar[5] (Eqn. 1.37) and take the general form

$$K_{tb}[z_F,z,r_F]=[G[z_F,r_F]\cdot G[z,r_F]]^{\frac{1}{2}}\cdot F[\bar{z},r_F] \qquad 1.57$$

$$\bar{z} = z - z_F \qquad 1.58$$

where

K_{tb} - bending and shear of tooth plus gear body compliance.
F - master function
G - end-effect (non-master) function
z - axial coordinate of point where deformation is desired.
z_F - axial coordinate of loaded point
r_F - loading radius.

The master function represents the "convective" effect of the applied load at z_F on all points sufficiently far (approximately $> 5.m_n$) from the tooth ends. For such points, $G(z,r_F)$ and $G(z_F,r_F)$ both approach unity and Eqn. 1.57 reduces to

$$K_{tb}\ (z_F,z,r_F) = F(\bar{z}.r_F) \qquad 1.59$$

For the master function, Steward used the following equation, (cf. Eqn. 1.39)

$$F(\bar{z},r_F)= C_{f1}\cdot\left[e^{-C_{f2}\cdot|\bar{z}|} - C_{f3}\cdot e^{-25.|\bar{z}|}\right] + C_{f4} \qquad 1.60$$

The coefficients C_{fi} were determined for each radial loading position r_F using the curve-fitting routine described in detail in Steward's work[30]. The first two terms account for tooth bending and shear effects, the last for the gear body deformation.

The end-effect function modifies $F(\bar{z},r_F)$ whenever either the loaded point z_F or the point of interest z are near the more flexible ends of a tooth. This function was found to be symmetrical about the tooth face width for spur gears, although Vedmar[5] showed that this symmetry is destroyed for helical gears.

Steward[30] used the function

$$G(z,r_F) = C_{g1} + C_{g2}\cdot\left[e^{-C_{g3}\cdot z} + e^{-C_{g3}\cdot(b-z)}\right] \qquad 1.61$$

Clearly, away from the ends of wide teeth the last two terms are both small leaving

$$G(z, r_F) \cong C_{g1} \qquad 1.62$$

where, in view of Eq. 1.59, $C_{g1} \simeq 1.0$.

In Vedmar's curve-fitting equations (Eqns.1.37...1.39) the coefficients A and B are independent of radial loading position. Variations in η_F (and η) are allowed for by including η and η_F in the exponential terms. In Steward's Eqns. 1.60 and 1.61, however, the coefficients C_f and C_g respectively do depend on radial loading position. Steward generated coefficient values for each of the five radial loading positions analysed and used a cubic spline interpolation procedure to generate values for intermediate positions. He also obtained satisfactory fits for the deflection of the (unloaded) preceding and succeeding adjacent teeth, in each case using an equation of the form

$$K_{tb}(z_F,z)_{adj} = C_{a1} + C_{a2}\cdot\left[e^{-C_{a3}(z_F+z)} + e^{-C_{a3}(2b-(z_F+z))}\right] \qquad 1.63$$

where, as mentioned above, the C_{ai} coefficients were found to be independent of radial loading position.

Compatibility Equation

Steward developed an equation similar to Vedmar's equation 1.40, viz.

$$f_t = \delta_{tb} + \delta_{tc} + \delta_s - \delta_e + c_t \qquad 1.64$$

where

f_t – is the transmission error, i.e. the angular displacement measured at the base circle of one gear relative to the other from the position it would occupy if the teeth were assumed to be rigid perfect involutes.

δ_{tc} - local contact deformation of loaded tooth (determined analytically from Eqn. 1.55), see figure 1.22a.

δ_{tb} - gear tooth bending and shear deflection including gear body deflection, figure 1.22b (obtained from the curve fits of the FE results).

δ_s - shaft bending, torsion and shear deflection.

δ_e - deviations of the tooth from its ideal (involute) form due to manufacturing errors or deliberate modifications/corrections.

c_t - initial separation between perfect, rigid teeth when contact is outside the theoretical limits (see Figure 1.15 and Appendix 2A) (c_t = 0 otherwise).

All the parameters in equation 1.64 were, of course, for spur gears, defined in the "transverse" plane and measured along the base tangent. For helical gears however, all the parameters should be defined in a direction normal to the tooth flank at the contact points (cf. Vedmar's use of u instead of e in Eqn. 1.42).

Steward assumed that the bending and shear deflection δ_{tb} in Eqn.1.64 is given by

$$\delta_{tb}(z) = \int_0^b K_{tb}(z,z_F).w(z_F).\,dz_F \qquad 1.65$$

where

$K_{tb}(z,z_F)$ - is an influence function such that, by Maxwell's[42] reciprocal theorem

$$K_{tb}(z,z_F) = K_{tb}\,(z_F,z) \qquad 1.66$$

(The function of Eqn.1.59 satisfies this equation).

From Eqn.1.65, δ_{tb} is clearly a function of the load distribution along the whole contact length thus including the "convective" terms (see Fig. 1.13a) which are discussed in greater detail in Chapter 2. The contact deflection δ_{tc} is however highly localized (see Fig.1.13b) and is consequently assumed to be only a function of the "local" load intensity at the point of interest.

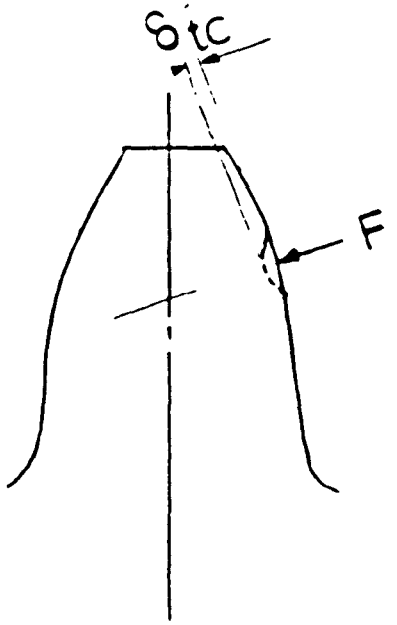

a) Tooth Flank Contact Def'n

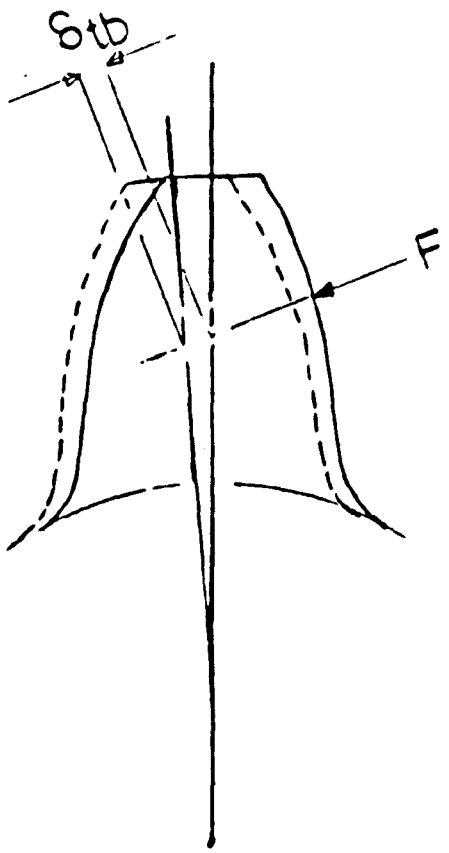

b) Tooth Centre_Line Bending Def'n

Fig. 1.22 Components of Gear Tooth Deflection in the Loading Plane

Thus

$$\delta_{tc}(z) = K_{tc}(z).\ w(z) \qquad 1.67$$

Substituting for δ_{tb} and δ_{tc} from Eqns. 1.65 and 1.67 into Eqn. 1.64 then gives

$$f_t = \int_0^b K_{tb}(z,z_F).w(z_F).dz + K_{tc}(z).w(z)+\delta_s(z)-\delta_e(z)+c_t(z) \qquad 1.68$$

where all the parameters on the RHS are also functions of the radial position of the point being analysed.

Load Distribution Solution

For equilibrium with the applied torque T the total load normal to the tooth flank is

$$F = \frac{T}{(d_b/2)} = \int_0^b w(z_F)\ .\ dz_F \qquad 1.69$$

Steward solved Eqns. 1.68 and 1.69 for the unknowns w(z) and f_t by replacing the integrals by numerical approximations based on a finite number of values of the unknown load distribution $w(z_i)$, using an iterative method to allow for the non-linearity of the contact compliance K_{tc} (in both the Hertzian and non-contacting regions). This procedure was also used in the present work and is described in greater detail in Chapter 2.

Since no exact analytical expression is possible yet, Eqns. 1.68 and 1.69 are solved using numerical integration methods (2-point Gauss integration as explained in Chapter 2 in more detail).

By the method described above, the load intensities are determined at all the Gauss points of integration along the contact length. The load intensities at the ends of the contact lines however are of special interest, and Steward determines those by using a modified version of Hyashi's[31] method, and is expressed by rearranging Eqn. 1.68 and replacing the first term on the right by δ_{tb} giving for a Gauss point at z

$$w(z) = \frac{f_t - \delta_{tb}(z) - \delta_s(z) + \delta_e(z) - c_t(z)}{K_{tc}(z)} \qquad 1.70$$

The improvement over Hyashi's[31] method was replacing the first term on the right of Eqn. 1.68 by δ_{tb}. Although the compliance

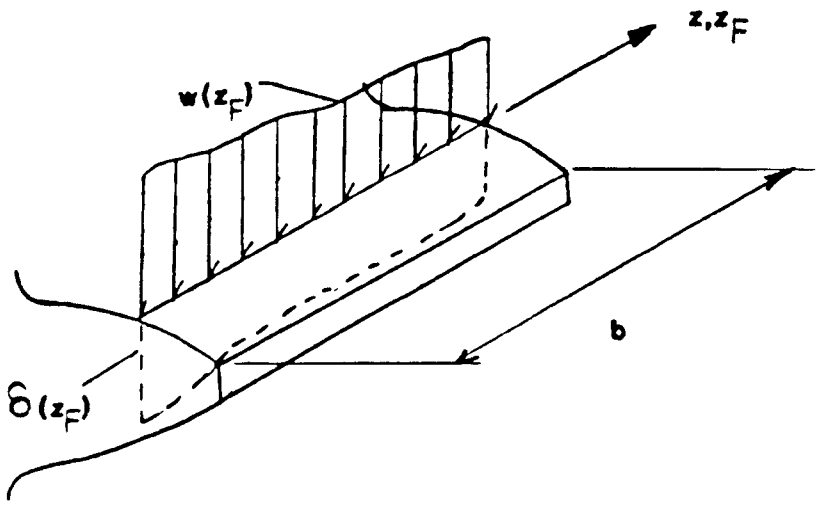

Fig. 1.23 Load Distribution Along a Spur Gear's Contact Line

function of bending and shear K_{tb} changes sharply at the ends of the contact lines, the bending deflection itself δ_{tb} remains smooth. This ensures that the extrapolated end deflections are reasonably accurate giving better results than Hyashi's, who extrapolated for the unstable function K_{tb} at the ends. The extrapolated end point load intensities were determined by using a cubic spline fitting routine. δ_{tb} values at the Gauss points were determined from the curve fitting routines described earlier in this section.

Contact and Bending Stresses

Once the load intensity w(z) has been determined as discussed above, the contact stress $\sigma_H(z)$ can be found by using equations 1.1 and 1.2. The appropriate values of ρ_1 and ρ_2 are easily found from the position of the point of interest on the tooth flank.

The bending stress at any point in the root fillet will, like the tooth deflection, be a linear function of all the loads on the gear, so that we can write

$$\sigma_F(z) = \int_0^b K_{tF}(z, z_F) \cdot w(z_F) \cdot dz_F \qquad 1.71$$

where K_{tF} is a bending stress influence function of the type first introduced by Wellaur and Seireg[29] and subsequently used by several other authors for gear stress analysis.

Replacing the integral of Eqn. 1.71 by an equivalent numerical integral then gives

$$\sigma_F(z_{\bar{i}}) = \frac{\Delta}{2} \cdot \sum_{\bar{j}=1}^{n} K_{tF}(\bar{i}, \bar{j}) \cdot w(z\bar{j}) \qquad 1.72$$

where

$\bar{i}$ - is the point along the tooth root where the stress is desired.

$\bar{j}$ - is the point on the tooth flank where the load is applied

Δ - is the interval of Gauss integration used and $w(z_j)$ is determined by the method described earlier in this section. Therefore, if K_{tF} is known (maybe obtained from FE bending stress results in some fashion as K_{tb} was obtained from FE bending deflection results) then σ_F can be easily calculated.

1.4.3.4 Simon's Model

Geometry and Meshing Conditions

In 1988, Simon[43] developed a 3-D FE gear model to analyse the load distribution along the contact lines of meshing helical gears. This model is generally similar to those published by Vedmar[5] and Steward[30]. An actual involute profile was modelled. The contact lines of instantaneously engaged teeth were divided into segments as shown in Fig. 1.24c and the tooth loads acting on a segment were approximated by a concentrated load ΔF acting at its mid-point. The relative separation of the meshing teeth flanks was assumed to consist of the geometrical separation plus the effect of teeth modifications (Fig. 1.24a), both defined along the normal to the tooth flank (in the normal plane).

$$s_{(i_t,i_z)} = p_{m1} \cdot \frac{r_{p1}-(r_{k1}-h_{m01})}{h_{m01}} + p_{m2} \cdot \frac{r_{p2}-(r_{k2}-h_{m02})}{h_{m02}} + (c_{r1}+c_{r2}) \cdot \frac{|z| - z_{cr0}}{b_{f/2} - z_{cr0}} \qquad 1.73$$

where i_t - is the tooth pair identification number

i_z - is the segment identification number

and the negative terms have to be omitted. Figure 1.24b shows the load intensity along each of the simultaneously engaged tooth pair contact lines.

Contact Deformation

The exact expressions for contact deflection used by Vedmar[5] and Steward[30] (Eqns. 1.34 and 1.35) were also used by Simon[43] to calculate w_c. Like Steward[30], Simon[43] used the tooth centre-line as the reference datum for determining the contact deformation. There is a slight difference however, since Steward takes the distance from the surface to the centre-line as that along the load line, whereas Simon takes it to be half the tooth (arc)thickness at the contact radius. Simon made no correction for tip contact (factor M of Eqn. 1.54).

FE Model and Bending Deformation

Simon's[43] 3-D FE model accounts only for bending and shear deformation w_t of the tooth, to which the calculated contact deflection w_c is added. The "gear body" bending and torsion deflections w_{bs} (including those of the supporting shafts) were calculated using the expressions developed by Tobe and Inoue[44]. These give only the shaft compliance, so that no gear body deflections (of the type considered by Steward) are included in w_{bs}.

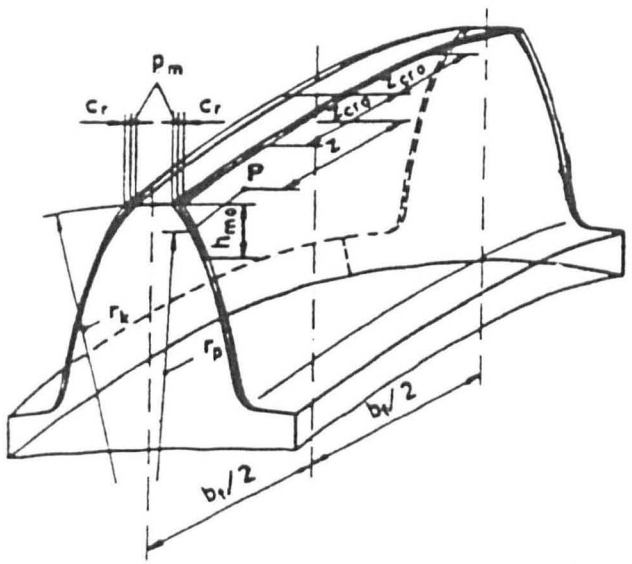

a) Tooth Profile Modifications & Crowning

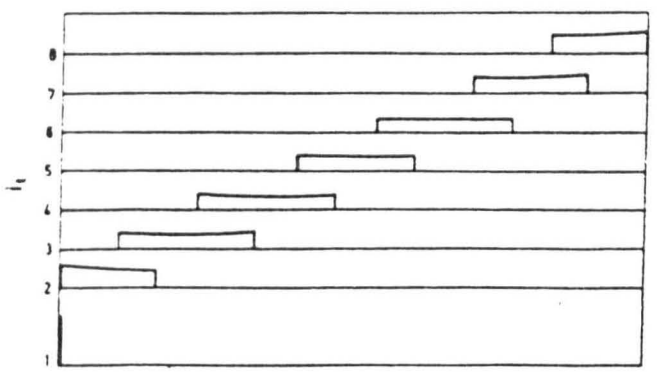

b) Load Distribution Along Simultaneous Contact Lines

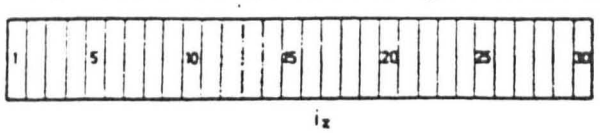

c) Contact Lines Divisions

Fig. 1.24 Meshing Conditions & Load Distribution According to Simon

To calculate w_t, Simon[43] developed from his FE results an empirical expression for a tooth bending and shear influence function K_D in the form

$$K_D = \left[\frac{1515.37}{E.m} \right] . f_1.f_2.f_3. Z^{-1.0622} . \left(\frac{\alpha_0}{20}\right)^{-0.3879} . \left(1 + \frac{\beta_0}{10}\right)^{0.8219} . (1+x_p)^{-0.2165} . \left(\frac{h_f}{m}\right)^{0.5563} . \left(\frac{h_k}{m}\right)^{0.6971} . \left(\frac{r_{fil}}{m}\right)^{0.00043} . \left(\frac{b_f}{m}\right)^{-0.6040} \quad 1.74$$

where

- f_1 – is a factor of the position of the loaded surface point p (see Figure 1.25).
- f_2 – is a factor of the relative position of point p to point D (point where deflection is desired) in the "radial" direction.
- f_3 – is a factor of the relative position of the point p to point D in the "axial" direction.
- Z – number of teeth
- α_0 – transverse plane pressure angle (deg.)
- β_0 – reference helix angle (deg.)
- m – transverse module (m)
- h_f – dedendum height (m)
- h_k – addendum height (m)
- r_{fil} – fillet radius (m)
- b_f – face width (m)
- x_p – addendum modification factor.

The relation between K_D and w_t is expressed later on in Eqn. 1.80. The factor f_3 accounts for the diminished deformation away from the loading point, and is given by

$$f_3 = 1 + b_3 . \frac{|z_p - z_D|}{z_{w0}} + c_3 . \frac{|z_p - z_D|^2}{z_{w0}} \quad 1.75$$

where b_3, c_3 and z_{w0} were determined empirically as

$$b_3 = -1.8874 + 1.004.10^{-2} . b_{f/m} - 6.0468.10^{-5} . (b_{f/m})^2 \quad 1.76a$$

$$c_3 = 0.8874 - 1.004.10^{-2} . b_{f/m} + 6.0468.10^{-5} (b_{f/m})^2 \quad 1.76b$$

for $b_{f/m} < 20.75$, and

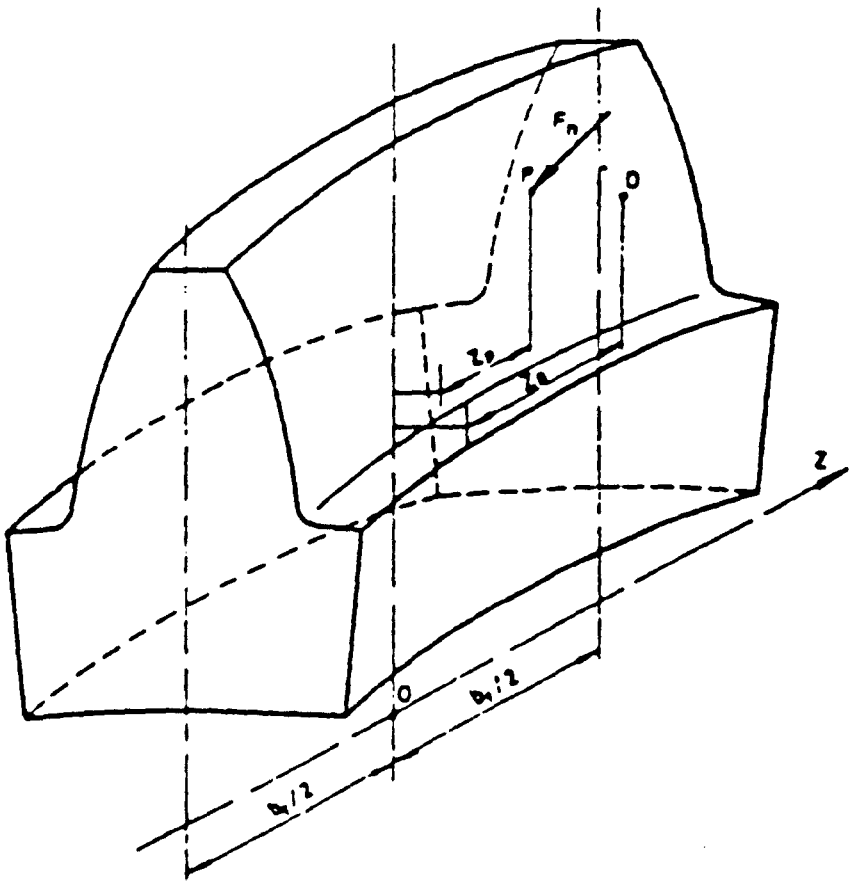

Fig. 1.25 Relative Position of Loaded Tooth Surface Point P to Point D in Which the Deflection is Calculated

$$b_3 = -1.4707 \qquad 1.76c$$

$$c_3 = 0.4707 \qquad 1.76d$$

for $b_{f/m} \geq 20.75$, and

$$z_{w0} = [1.2070 - 4.0256.10^{-4}.b_{f/m} + 5.0261.10^{-4}.(b_{f/m})^2].\frac{b_f}{2} \qquad 1.77$$

Clearly by inspection of Eqs. 1.75 and 1.76, if $|z_p - z_D| = z_{w0}$, $f_3 \to 0$ and $K_D \to 0$. This means that for $|z_p - z_D| \geq z_{w0}$, a concentrated load at p has no effect on point D. Note that Eq. 1.74 is the analogue of Eqns. 1.37 and 1.57 used by Vedmar[5] and Steward[30] respectively.

Compatibility Condition

The analogue to Eqns.1.42 and 1.64 used by Vedmar and Steward respectively is

$$w_t + w_c + w_{bs} = [\Delta y - e] \cdot \cos\beta_b + s \qquad 1.78$$

where

- Δy – is the rotational delay of the driven gear relative to the driving gear, measured along the base tangent line in the transverse plane (i.e. the transmission error).
- e – is the composite error at point D (sum of all manufacturing and mounting errors plus tooth modifications), along the base tangent in the transverse plane.
- β_b – is the base helix angle (deg.)

and the other parameters are as defined earlier in this section. Note the presence of the factor $\cos\beta_b$ which transforms Δy and e into components normal to the tooth flank in the normal plane (i.e. parallel to w_t, w_c, w_{bs} and s).

Load Distribution Solution

Applying Eqn. 1.78 to a single segment $\tilde{\imath}_z$ of a particular contact line $\tilde{\imath}_t$ gives

$$w_t(i_t,i_z)+w_c(i_t,i_z)+w_{bs}\ (i_t,i_z)=[\Delta y(\tilde{\imath}_t)-e\ (\tilde{\imath}_t,\tilde{\imath}_z)].\cos\beta_b+s(i_t.i_z) \qquad 1.79$$

where $(1 \leqslant i_t \leqslant N_t)$ and $(1 \leqslant i_z \leqslant N_z)$.

The tooth bending and shear deformation w_t is calculated from the influence function K_D (Eq. 1.74) as

$$w_t\ (i_t, i_z) = \sum_{\tilde{\imath}_{zp-1}}^{N_z} \Delta F_{(i_t,\tilde{\imath}_{zp})} \cdot K_{D(i_t, i_{zp})} \qquad 1.80$$

and the tooth contact deflection $w_c(\tilde{\imath}_t,i_z)$ is calculated from Eqn.1.34, replacing the term w by

$$(\Delta F(i_t,i_z)/\Delta z)$$

where

Δz – is the length of each segment across the face width.

The "gear body" and shaft deformations $w_{bs}(i_t,i_z)$ and the tooth separation $s(i_t,i_z)$ were calculated as previously described.

The transmitting load F in the normal plane (Fig.1.25) is given by (cf. Vedmar's Eqn.1.44)

$$F = \sum_{i_t=1}^{N_t} \int_{L_{i_t}} \frac{p(z).dz}{\cos\beta_b} = \sum_{i_t=1}^{N_t} \sum_{i_z=1}^{N_z} \frac{\Delta F(i_t, i_z)}{\cos\beta_b} \qquad 1.81$$

where

$p(z)$ – is the load intensity at z, measured along the base tangent line in the transverse plane.

N_t – number of instantaneously engaged tooth pairs (number of instantaneous contact lines)

L_{it} – geometrical length of the line of contact for tooth pair i_t.

For the segments which are not instantaneously in contact $\Delta F(\tilde{i}_t,i_z)$ is assumed to be zero.

Simon calculated the load distribution by solving the system of non-linear numerical integral Eqns.1.79 and 1.81, using, like Vedmar, an iterative procedure to allow for the effects of non-linear contact compliance.

A discussion of results obtained using Simon's formulae is given in Chapter 3.

Contact and Bending Stresses

As in Steward's work[30], Eqns.1.1 and 1.2 were then used to calculate the contact stress $\sigma_H(\tilde{i}_t,\tilde{i}_z)$ with w again replaced by

$$\Delta F(i_t,i_z)/\Delta z$$

The bending stress calculated from the loads $\Delta F(i_t,i_z)$ using an expression similar to Eqn.1.71 given by

$$\sigma_F(i_t,i_z) = \sum_{\tilde{i}_{zp}=1}^{N_z} K_{D\sigma}(\tilde{i}_t,\tilde{i}_{zp}) \cdot \Delta F(i_t,i_{zP}) \qquad 1.82$$

where $K_{D\sigma}$ is an influence factor for bending stress determined like K_D (Eq.1.74) by an empirical expression of the form

$$K_{D\sigma} = \left(\frac{700.51}{m}\right) . f_{1\sigma} . f_{2\sigma} . z^{-1.0960} . \left(\frac{\alpha_0}{20}\right)^{-0.7123} . \left(1+\frac{\beta_0}{10}\right)^{0.0974}$$
$$. (1+x_p)^{-0.2800} . \left(\frac{h_f}{m}\right)^{0.1309} . \left(\frac{h_k}{m}\right)^{0.2276} . \left(\frac{r_{fil}}{m}\right)^{-0.0986}$$
$$. \left(\frac{b_f}{m}\right)^{-0.9544} \qquad 1.83$$

where, for $|z_p-z_D| \geq b_f/4$, $f_{2\sigma}$ and $K_{D\sigma}$ are both zero.

1.5 Objectives of the Present Work

In each of the models for helical gears described so far, one or more defects were pointed out. Shortcomings of the 2-D "thin slice" models were discussed in Section 1.2.5, and the requirements for an accurate 3-D mesh model listed in Section 1.4.1. All of the mesh models for helical gears discussed so far fail to meet one or more of these requirements.

The objective of the present work was to develop and validate experimentally a mesh model for helical gears, based on Steward's spur gear model, that did meet all these criteria.

To this end, the following work was carried out:

1. A 3-D FE elastic gear model of helical gears was developed using PAFEC software, running on the University of Newcastle AMDAAL 6000 system. The model included the loaded tooth, the two directly adjacent teeth, the whole gear body and a section of shaft at each end of the gear, and was supported and loaded in a realistic manner.
2. A two-dimensional interpolation scheme was developed to allow calculation of tooth centre-line deflections at the correct point on the load line from the FE results obtained from (1) above.
3. Shaft deformations predicted by the FE analysis were subtracted from the FE deflections to give net gear deformations relative to the shaft, which thus comprised tooth bending and shear deflections, as well as gear body bending, torsion and shear deflections.
4. Curve fitting equations for the deflections obtained in (3) above were developed to allow calculation of tooth deflections at any point along an arbitrary contact line for gears with any helix angle or number of teeth.
5. Micro-computer based software was developed to calculate the load and stress distribution on pairs of loaded helical gears at successive points through the mesh cycle. The program allows for contact outside the normal phase of mesh caused by gear tooth imperfections, mounting errors, corrections and elastic behaviour, and allows input of the common elemental errors and corrections.
6. Numerous runs were made using this program to analyse a range of geometrically "perfect" gears. The results obtained were compared with those predicted by other methods and the causes of any discrepancies identified. The effects on performance of different numbers of teeth, face widths and helix angles were also studied systematically.
7. A further set of results was obtained for gears of a particular geometry to study the effects of manufacturing and mounting errors, and design corrections on load distribution and contact stress. In particular, the load distribution factors $K_{H\alpha}$ and $K_{H\beta}$ were studied and compared with other published data.
8. An experimental rig was designed, and instrumented to allow measurement of static transmission error and load distribution in a pair of loaded helical gears.
9. Results obtained from this test rig were compared with values predicted using the software described above.

CHAPTER 2

HELICAL GEAR ELASTIC MESH AND STIFFNESS MODEL

2.1 Introduction

In chapter 1, the various 2-D and 3-D mesh and stiffness gear models were discussed with emphasis on the 2-D "thin-slice" model used in the standards [2,3,4], and the 3-D "exact" models devised by Vedmar[5] and Simon[43] for spur and helical gears and by Steward[30] for spur gears only.

In this chapter, Steward's model is extended for helical gears. The gear geometry and the F.E. model are first modified to account for the more complex geometry and loading of helical gears, then, based on the new F.E. model, the gear tooth deformations are obtained and curve-fitted. Finally, a micro-computer program incorporating the curve-fitted F.E. data is developed to allow calculation of the load and stress distribution along the simultaneous contact lines of the meshing gear pair.

2.2 Helical Gear Tooth Geometry

To obtain accurate values for tooth compliance and bending stresses, the actual involute tooth flanks and trochoidal tooth root fillet must be modelled exactly. We thus require co-ordinates for the following:

1. points on the loaded and adjacent tooth involute flanks
2. points on the loaded and adjacent tooth trochoidal root fillets.

Involute co-ordinates were calculated using the equations given by Buckingham[41] (see Appendix 1A). The Oxyz axis system used has its origin at the centre of rotation O of the gear, Oz along the gear axis, and the y-axis coincident with the loaded tooth centre-line at the datum section of the gear in the transverse plane.

The trochoidal root fillet co-ordinates were calculated using Vedmar's[5] "exact" equations which are also given in Appendix 1A. These equations avoid the approximations introduced by using the profile of the equivalent spur gears.

In calculating the position of contact lines on the active flanks of the gears, the effects of the (small) errors, tooth corrections and elastic deformations have been ignored. The equations used are thus those for rigid perfect involute flanks, and 'normal' contact is therefore assumed to occur in the base tangent plane as shown in Fig. 2.1. (c.f. Steward's Fig. 1.15 for spur gears).

2.3 Helical Gear Meshing Conditions

The theoretical start of contact for a rigid and perfect gear is the point A', and the theoretical end of contact is the point B, (the plane of action shown in Fig.2.1 represents the mating of a right hand helix driver with a left hand helix driven gear).

At a particular instant of mesh, a contact line 'k' is shown where $z_f(k)$ (=0) and $z_\ell(k)$ (=b) represent the end locations of this contact line. The "phase" of this contact line is defined at the distance $\varphi_{z0}(k)$ shown, in base pitches and describes the position of this contact line in the mesh cycle. It is only necessary to know the phase of one of the simultaneous lines of contact, since they are all spaced by the transverse base pitch p_{bt} in the plane of mesh. To describe the "phase of mesh" it is thus only necessary to specify the phase of one 'master' contact line (k = K) say. The phase of all other lines is then

$$\varphi_{z0}(k) = \varphi_{z0}(K) \pm (k - K) \qquad 2.1$$

where

$$1 \leq k \leq 2.K-1$$

and the positive sign is valid for Fig. 2.1 with start of contact near A_0' or A'. If the opposite end of the tooth flank was loaded, then the negative sign in Eqn.2.1 is valid as the contact lines will proceed from the opposite end.

As in Fig. 1.15, the regions $A_0AA'A_0'$ and $B_0BB'B_0'$ in Fig. 2.1 allow for possible mesh outside the theoretically defined limits due to gear imperfections and elastic behaviour. The widths of these regions are made equal to simplify calculation, and their magnitude depends on the maximum likely elastic deformation, and the anticipated maximum deviations of the teeth

ABB'A' - Perfect Gear
$A_0B_0A_0'B_0'$ - Actual Gear

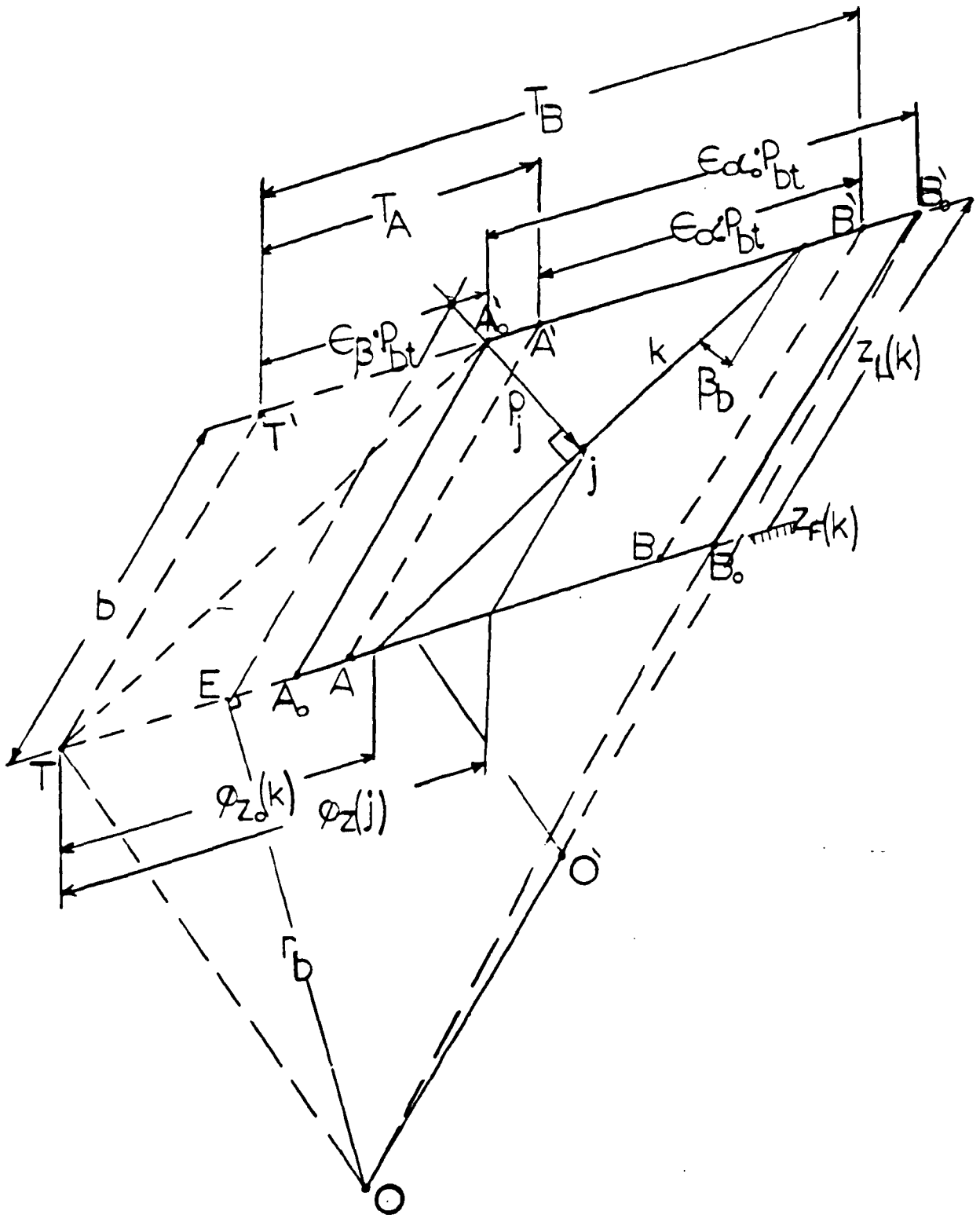

Fig. 2.1 Plane of Action

from the ideal involute form. In the present work A_0A and B_0B were both set to 0.35 p_{bt}. No contacts outside this region occurred in any of the gear sets analysed.

In order to determine whether a particular tooth pair k is potentially in contact, it is only necessary to check whether the line crosses the "mesh region" $A_0A_0'B_0'B_0$ of Fig. 2.1. This condition is satisfied if $\varphi_{z0}(k)$ is such that

$$0 < \varphi_{z0}(k) < \epsilon_{\alpha 0} + \epsilon_{\beta}$$

where $\epsilon_{\alpha 0}$ is the 'extended' transverse contact ratio defined in Fig. 2.1.

Considering, now, a particular point j at axial positions z_j on contact line k as shown, it is first necessary to find whether it lies in the 'normal' or the 'extended' contact region. The phase of the point j is

$$\varphi_z(j) = \varphi_{z0}(k) + \frac{z_j.\tan\beta_b}{p_{bt}}$$

and if

$$T_A/p_{bt} < \varphi_z\,(j) < T_B/p_{bt}$$

it lies in the normal contact region AA'B'B

If this condition is not satisfied, the point lies in the (potential) extended contact region, and tip contact can be expected (on the wheel in region $A_0A_0'A'A$, on the pinion in region $B_0B_0'B'B$). In this case, there would be an initial clearance c_t between perfect rigid teeth as shown in Fig. 2.2. The point of nearest approach of the two teeth (where contact under load may occur) then no-longer lies in the base tangent plane. Contact occurs on the tip circle of one gear and at a radius $d_y/2$ on the other. Exact formulae derived by Steward[30] for calculating c_t and d_y for spur gears are modified to apply to helical gears and are given in Appendix 2A. These agree well with values derived from the approximate expression used by Seager[34] and Munro[47]. In the 'normal' contact region AA'B'B, $c_t = 0$.

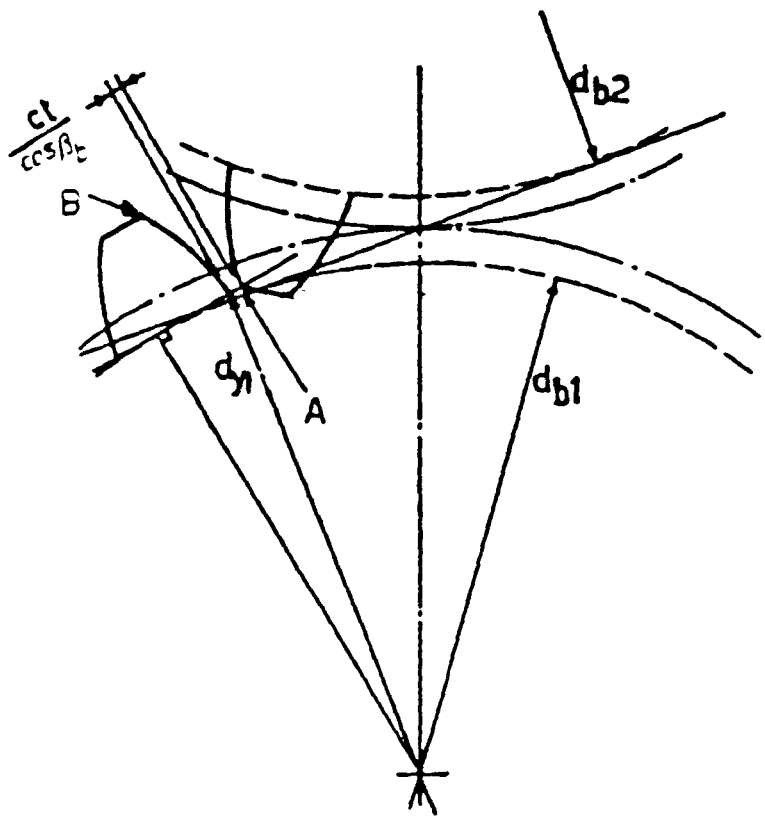

Fig. 2.2 Start of Engagement Outside the Theoretical Limit

2.4 Contact Deformation

Vedmar's equation (Eqn. 1.33)[5] modified by Steward's factor M (Eqn. 1.54)[30] to correct for tip and near-tip loading is used in the present work. The datum depth 'h' used by Steward in Eqn. 1.33 is

$$h = \frac{s_{y/2}}{\cos\alpha_y} \qquad 2.2$$

This is (approximately) the depth to the tooth centre plane in the transverse section. For helical gears, the loading plane is the normal plane as shown in Fig. 2.3. However, the same expression can be used if s_y and α_y are replaced by s_{yn} and α_{yn} respectively.

As in Steward's[30] FE model, the FE mesh consists of radial spacings up the tooth flank of $0.5m_n$, which is the radial width of the elements, and as discussed in section 1.4.3.3, and clearly shown in Fig. 1.21 the load is distributed radially over two elements. This gives a Hertzian contact width 2L equal to $1.0m_n$ and L equal to $0.5m_n$. It now becomes easy to verify that the depth of the tooth centre-line is sufficient, thus Eqn. 1.31 is used to calculate δ_{c0} (u_{c0} by Vedmar's notation) using both the present work's h'(h/L) and that of Vedmar's. For simplicity, h is calculated at reference diameter loading for a standard gear (x=0) and a 20° pressure angle.

$$h = \frac{\pi . m_n/4}{\cos\alpha_n} = 0.8358.m_n \qquad 2.3$$

and h'(h/L) becomes 1.6716, and based on Vedmar's[5] depth ($h=0.5m_n$) then h' is 1.0. From Eqn. 1.31, the corresponding contact deflections are $0.6305.m_n.w/F$ and $0.4078.m_n.w/F$ and the difference is $0.2227.m_n.w/F$. Assuming a mean load w = F/b, the difference becomes $0.2227.m_n/b$. Using values of 10mm and 120mm for m_n and b respectively, the non-dimensional contact deflection difference is 0.01856, which shows that beyond a depth of $0.5m_n$, the difference is insignificant making the tooth centre line a very safe datum to use.

It was shown in section 1.4.3.2 that Eqns. 1.30 and 1.32 may be simplified to give Eqns. 1.34 when $h' >> 1$. In the example above, h' is 1.6716 based on this work, and 1.0 based on Vedmar's work and so $h' >> 1$ is not satisfied. Yet calculating the difference in the contact deformation using the approximated equation (Eqn. 1.34) results in a value of 0.0248. Clearly this is a good approximation when compared with the exact value of 0.01856, verifying the validity of Eqn. 1.34 considering that h' is not much greater than 1.

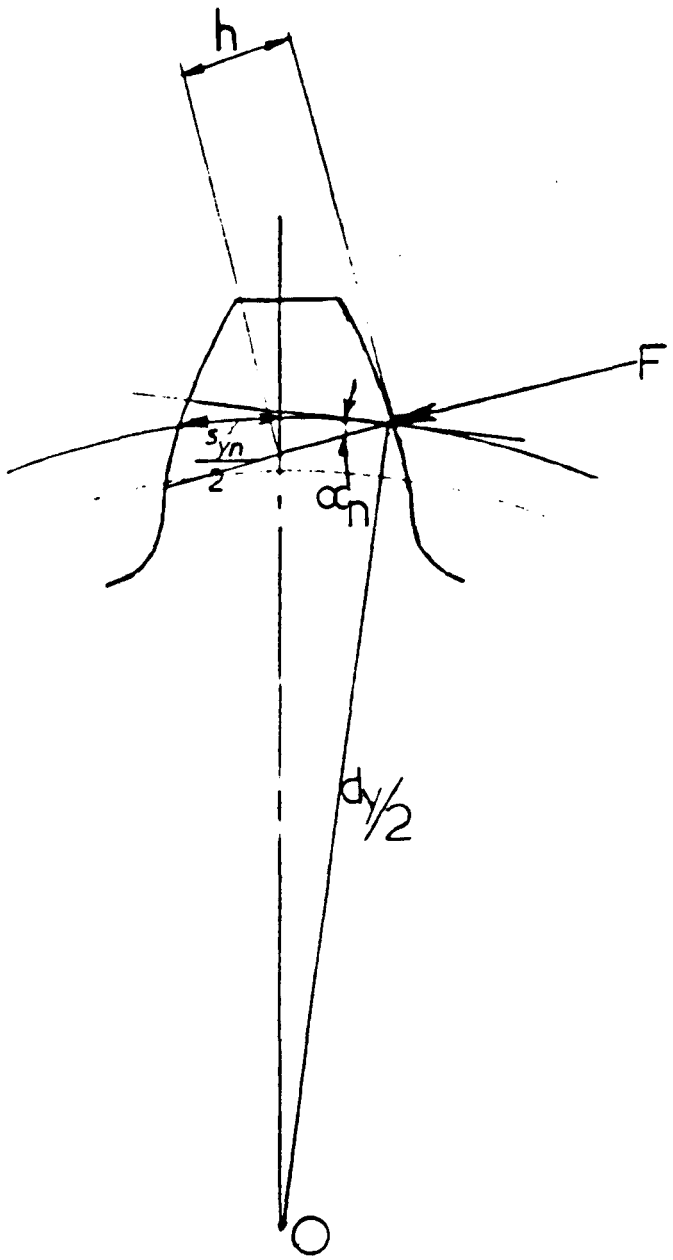

Fig. 2.3 Calculation of Tooth Surface_To_Centre_line Depth "h" in the Normal Plane

2.5 Helical Gear F.E. Model and Resulting Tooth Deformations

A "twisted" version of the F.E. mesh developed by Steward (Fig. 1.17) was used in the present work, and the actual F.E. meshes of the 18-tooth and 40-tooth gears respectively are shown in Figs. 2.4a and 2.4b. Fig. 2.4a shows the external elements only, while Fig. 2.4b shows the internal lines also.

Simple supports at both ends of the shaft, with torque restraint at one end were simulated by applying radial constraints only to all nodes at one end, and constraints in the x and y directions to all nodes at the other end. In addition, the central node at this end was also restrained axially to react the axial component of the tooth load.

Steward's equation[30] for the recommended shaft diameter was modified for helical gears to give

$$d_s = 0.8 \cdot m_n \cdot z/\cos\beta \qquad 2.4$$

with Steward's cut-off diameter "d_s" of $25m_n$ also increased by the factor $1/\cos\beta$. Fig. 2.5 (c.f. Fig. 1.18) shows the plot of d_s against Z for gears with $\beta = 30^{\circ}$.

As discussed in section 1.4.3.3, Steward verified the accuracy of a relatively coarse F.E. mesh for determining the loaded tooth centre-line deformations and the adjacent tooth surface deformations. He also verified the significance of gear body rotations. The same relatively coarse mesh was therefore used to model the whole gear with the loaded tooth, and the two directly adjacent teeth, (Figs 2.4(c), (d)). Based on this, F.E. models for standard helical gears with b=120mm, m_n=10mm, β=30°, a BS436[2] standard rack profile ($h_{a0} = 1.0m_n$, $h_{f0} = 1.25m_n$, $r_{a0} = 0.39m_n$) and 18, 40 and 100 teeth were analysed. The model used the same 20-node 'brick' elememts used by Steward (Fig. 1.20) with 'point' loads applied to the mid-side nodes rather than to corner nodes as explained in section 1.4.3.3, and clarified in Fig. 1.21. Co-ordinates of both the corner and mid-side surface nodes were specified using the equations given in Appendix 1A to ensure accurate modelling of the teeth geometry with the relatively coarse mesh.

The same radial loading positions selected by Steward[30] were used: at the reference radius and at $0.5m_n$ and $1.0m_n$ above and below it. Unlike

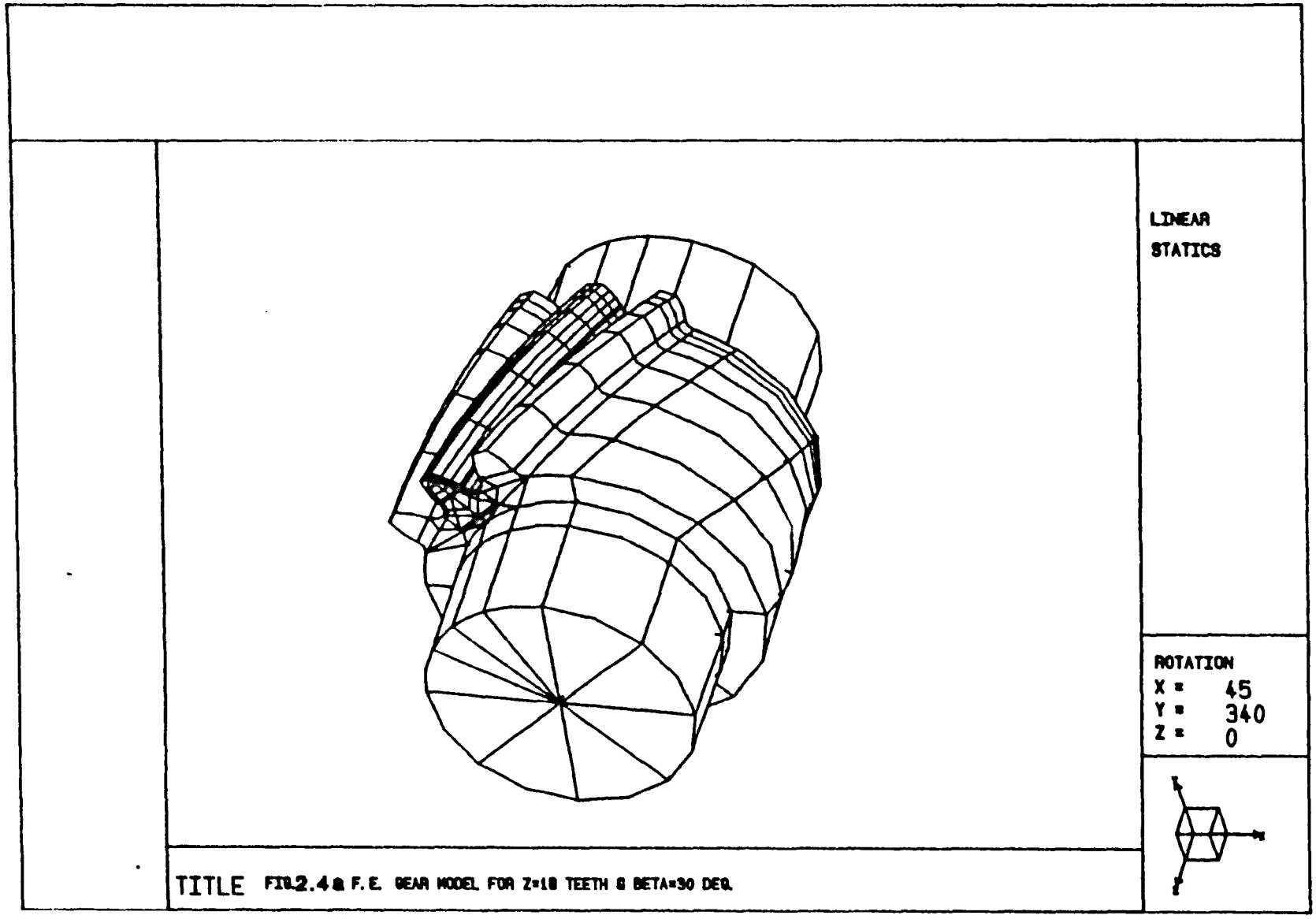
LINEAR
STATICS
ROTATION
X = 45
Y = 340
Z = 0
TITLE FIG.2.4 a F.E. GEAR MODEL FOR Z=18 TEETH & BETA=30 DEG.

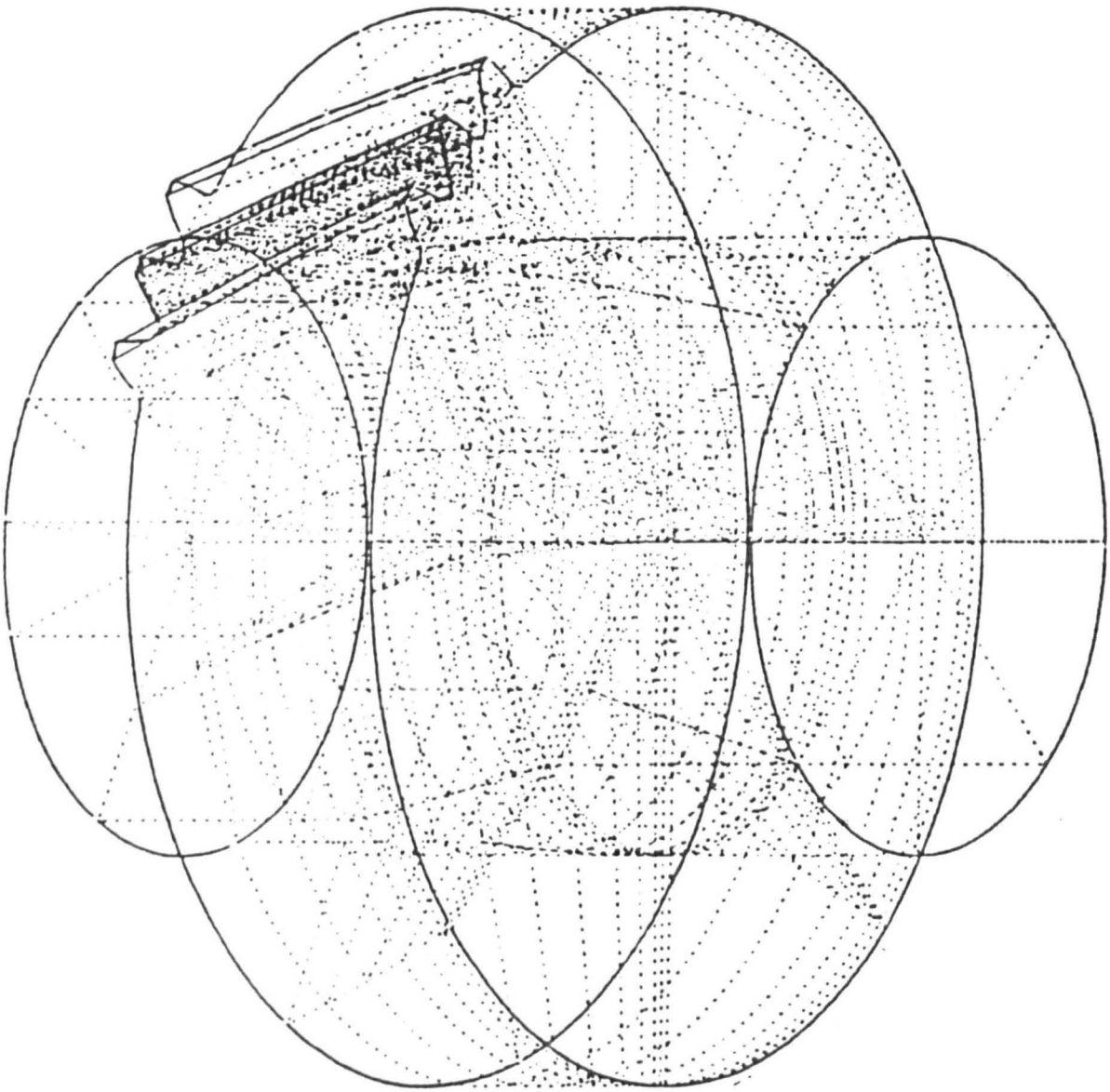

Fig. 2.4b FE GEAR MODEL FOR Z=40 TEETH & BETA=30 DEG.

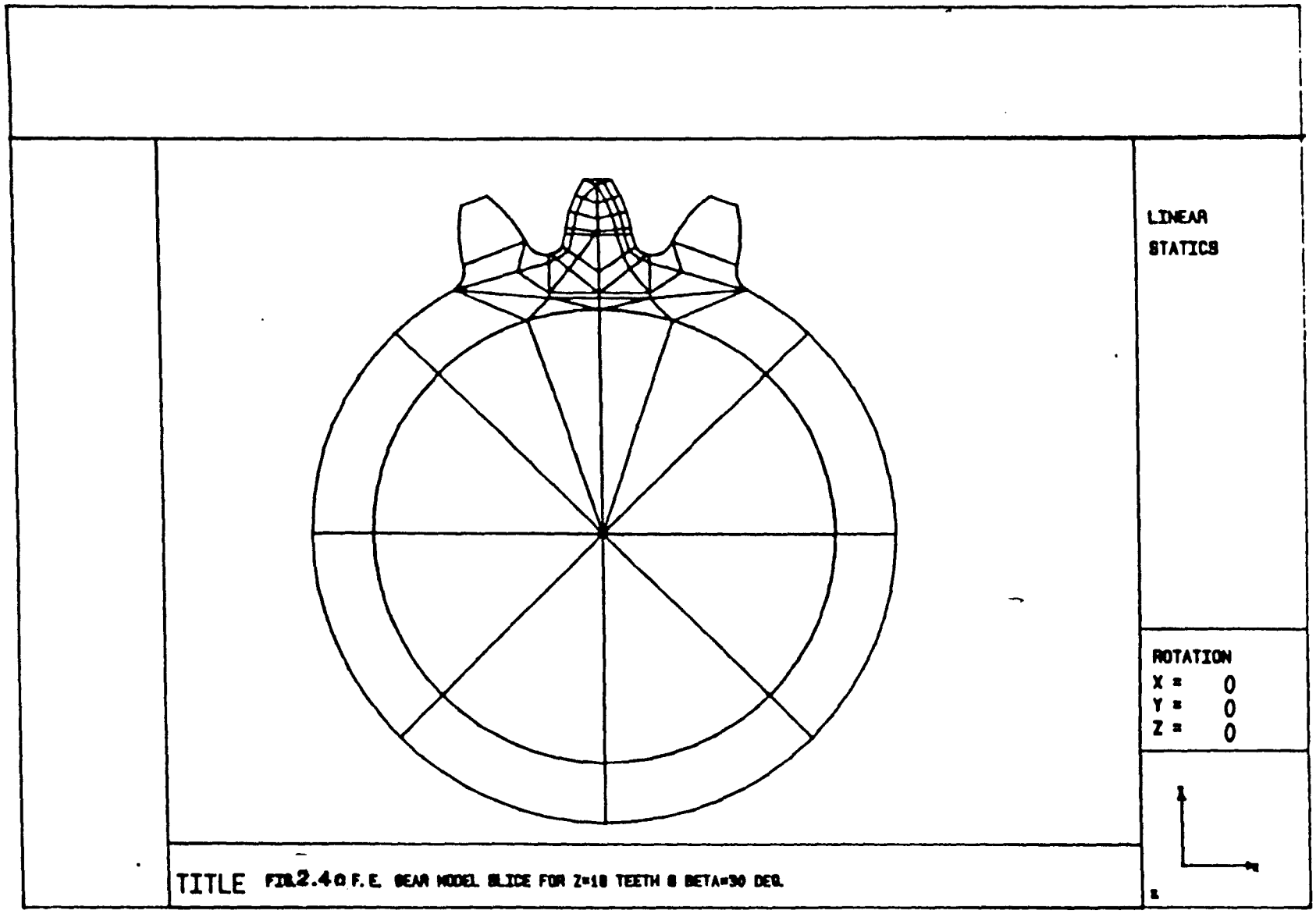
LINEAR
STATICS
ROTATION
X = 0
Y = 0
Z = 0
TITLE FIG.2.4 O F.E. GEAR MODEL SLICE FOR Z=18 TEETH & BETA=30 DEG.

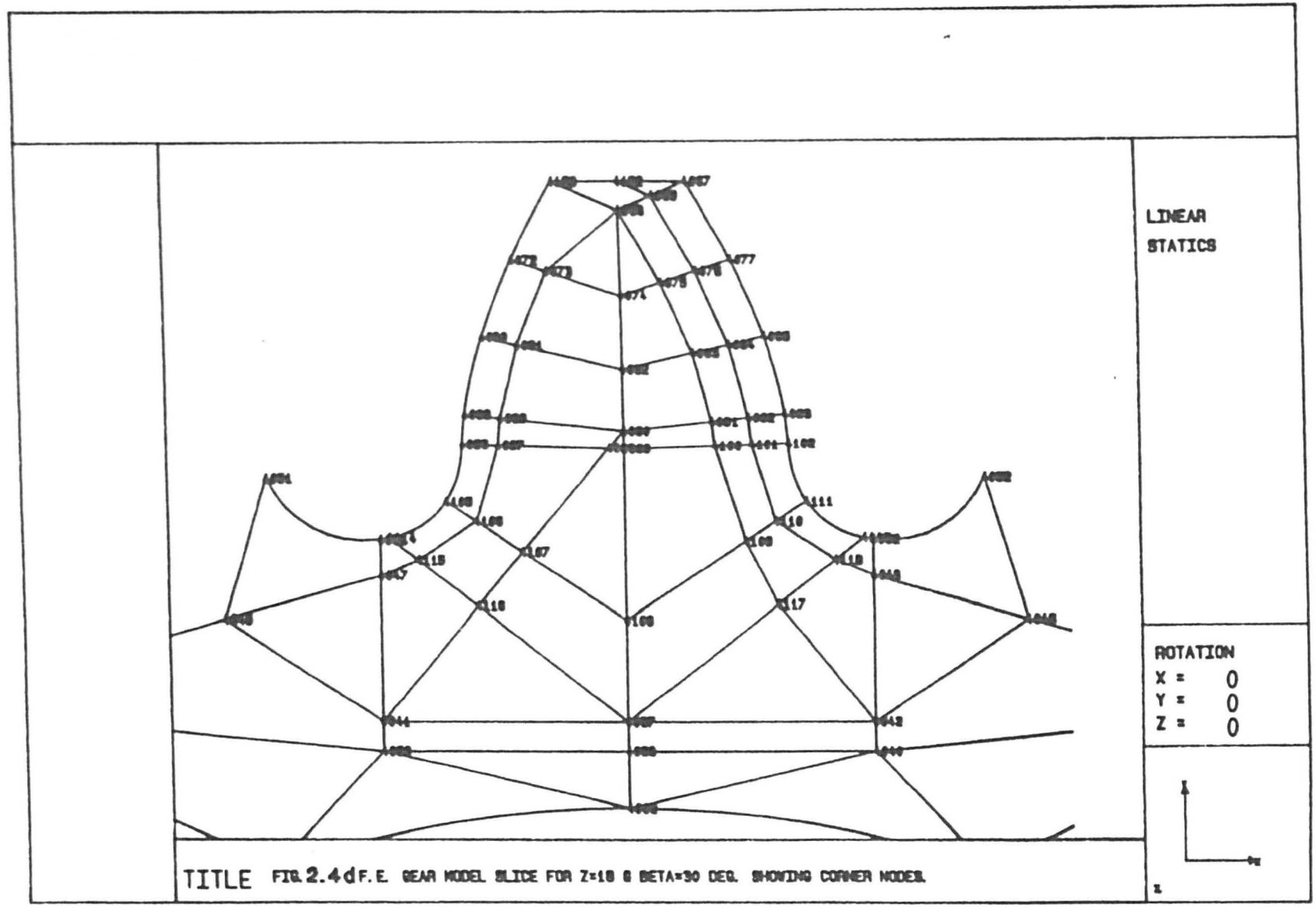
LINEAR
STATICS
ROTATION
X = 0
Y = 0 0
Z = 0
TITLE FIG. 2.4d F.E. GEAR MODEL SLICE FOR Z=18 & BETA=30 DEG. SHOWING CORNER NODES.

Fig. 2.5 Shaft Diameter For Helical Gear FE Model

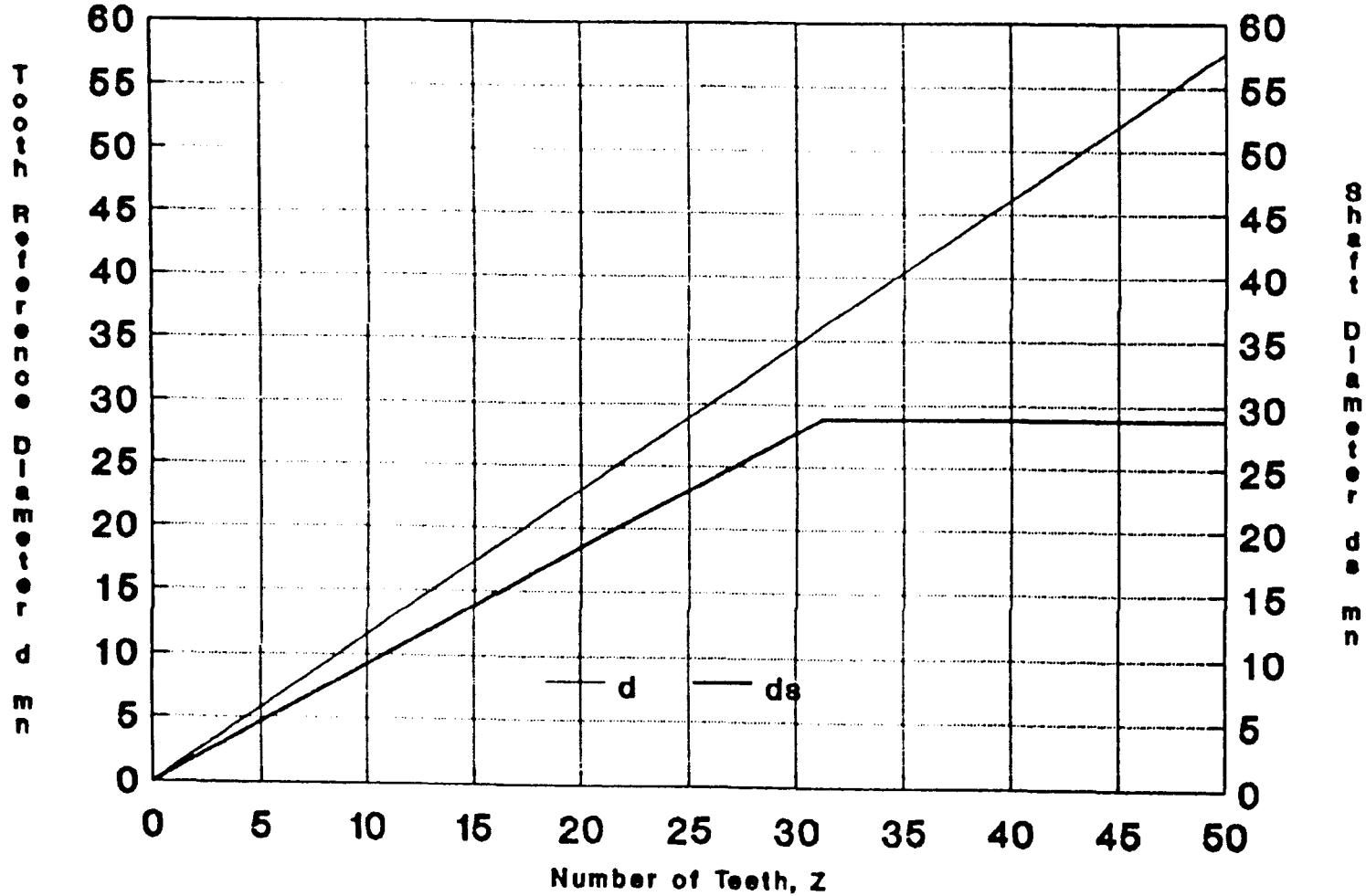

mn=10 mm Beta=30 Degrees

spur gears, however, helical gears exhibit no symmetry about the middle of the face-width, and it was therefore necessary to apply the 'point' loads at axial locations across the whole face width. The 7 axial locations chosen, measured along the axis of the shaft, from one end of the gear face were 0.25, 0.75, 2.5, 6.0, 9.5, 11.25 and $11.75m_n$ giving, in all, 35 loading cases to be analysed for each gear. As for spur gears, the axial pitch of the F.E. mesh was, in each case, reduced near the loading position where the stress gradients are largest. Not only does this improve modelling accuracy, it also better simulates a 'point' load by reducing the flank area effectively under load, (see Fig. 1.21). Fig. 2.6 shows the F.E. mesh axial spacings used for all seven axial loading positions.

As discussed in section 1.4.3.3 for spur gears, the 'loaded' tooth deflections are defined at the tooth centre-line to eliminate the incorrectly modelled F.E. contact deformation. These centre-line deflections, made up of tooth bending and shear, gear body and shaft deflections, must be those at a point in the tooth central surface, lying on the line of action of the applied 'point' load, normal to the tooth flank (i.e. in the normal plane). For spur gears (section 1.4.3.3), this point lies at the same axial location as the loading point (in the same transverse plane). For helical gears however, this is no longer the case.

Referring to Fig. 2.7, the points 'c' on the central surface, corresponding to surface points 'p' or 'f', lie on the surface normal at 'p' or 'f'. Their axial co-ordinates z_c differ from z_p or z_f. The point 'c' corresponding to the point 'f' for each loading position was deliberately made to fall on the edges of particular mesh elements. This simplified the axial interpolation required to determine the deflection of 'c' from the nodal deflections output by the PAFEC software. On the other hand, the position of points 'c' corresponding to unloaded points 'p' along the oblique contact line through 'f' could not be so arranged, and interpolation of the F.E. results in two directions was necessary. The procedures used are set out in Appendix 2B.

To check the accuracy of this process, the tooth surface deflections at points 'p' far from the point of load application 'f' were compared with the tooth centre-line deflections at the corresponding point 'c'. The agreement was excellent, as would be expected, since there is clearly no contact deflection at these positions.

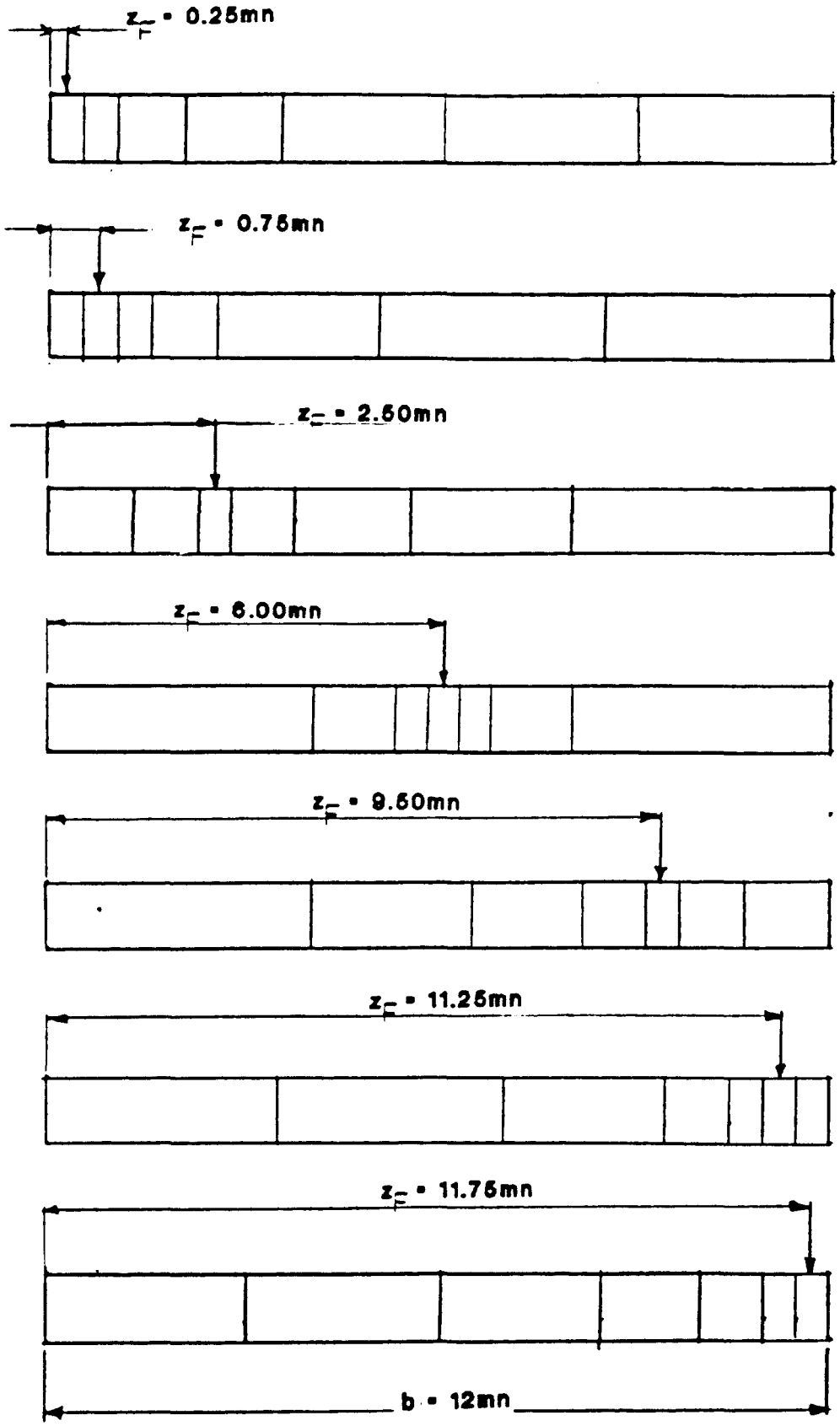

Fig. 2.6 FE Mesh Model Axial Spacing of Elements for all Loading Positions "z_F"

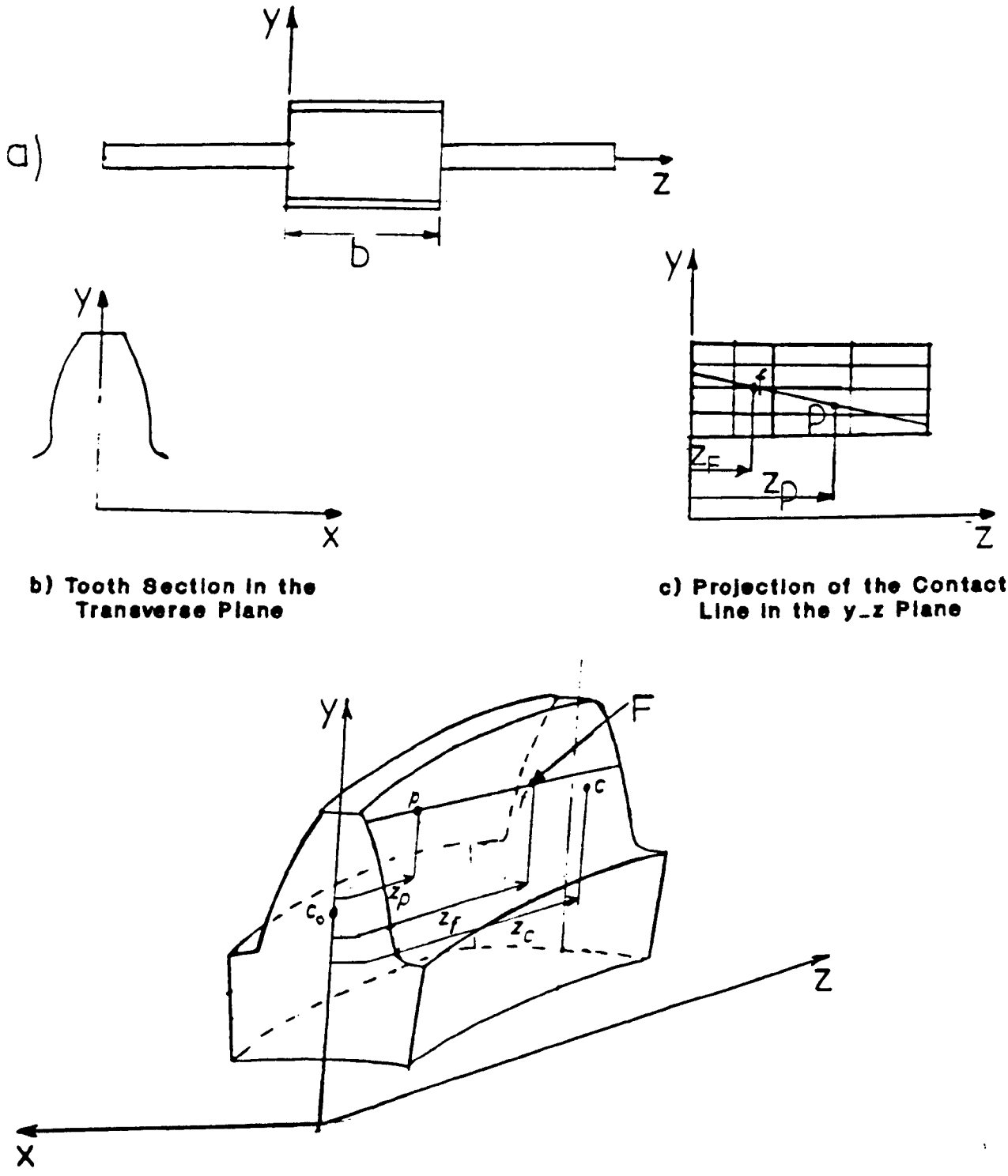

b) Tooth Section in the Transverse Plane

c) Projection of the Contact Line in the y_z Plane

d) 3_D View of Tooth

c _ is the intersection of the Normal at "p" or "f" with the Tooth Central Surface

f _ Point on Flank Where Load is Applied

p _ Point on Flank Where Def'n is Desired

Fig. 2.7 Locating Point "c" on Tooth Central Surface

So far only the 'loaded' tooth deformations have been discussed. For each point of load application 'f', however, simultaneous contact lines corresponding to the loaded tooth contact line, occur on adjacent teeth, so that for each point 'p' along the loaded tooth contact line (and for point 'f'), deflections at the corresponding points on the 'preceding' and 'succeeding' adjacent tooth contact lines must be determined as shown in Fig. 2.8. Since the adjacent teeth are not directly loaded in the F.E. analyses, they have no contact deformations, so that their 'surface' deformations at points along these contact lines can be extracted directly from the F.E. nodal deformations. The interpolation procedure required is also detailed in Appendix 2B.

As with spur gears (see section 1.4.3.3), these adjacent tooth deformations for helical gears show very little dependence on the radial position at which the load is applied as shown later in this section. For spur gears, Steward[30] also demonstrated nearly identical deformations for the 'preceding' and 'succeeding' adjacent teeth (Fig. 2.9), but for helical gears, the results obtained show that separate treatment of the two teeth is necessary, as explained below.

The 'loaded' tooth and 'adjacent' teeth F.E. deformations thus obtained, include the shaft bending, torsion and shear deflections. As in Steward's work [30], these shaft-specific deflections must be subtracted to yield the net gear tooth deflections. In this work, the actual F.E. shaft deformations at each axial section z_j were subtracted. As in Steward's work, these were virtually identical with the deformations obtained from simple Engineering Theory (See Appendix 2C).

Results

The net 'loaded' tooth centre-line F.E. deflections (excluding shaft deflections) are plotted in Figs. 2.11 to 2.25 for the 18, 40 and 100 tooth gears at each radial loading position 'r_f', and each axial loading position 'z_f'. The deflections have been non-dimensionalised by multiplying them by '$E.m_n/F$' showing larger deformations.

The curves are largely self explanatory with larger deformations for tip loading (larger r_f) and towards the tooth ends which are less well 'supported' than mid-face sections, particularly at the 'sharp' end (Fig. 2.10a) which shows much larger deformations than the 'blunt' end.

Fig. 2.10b shows how the point loads were applied at the various axial

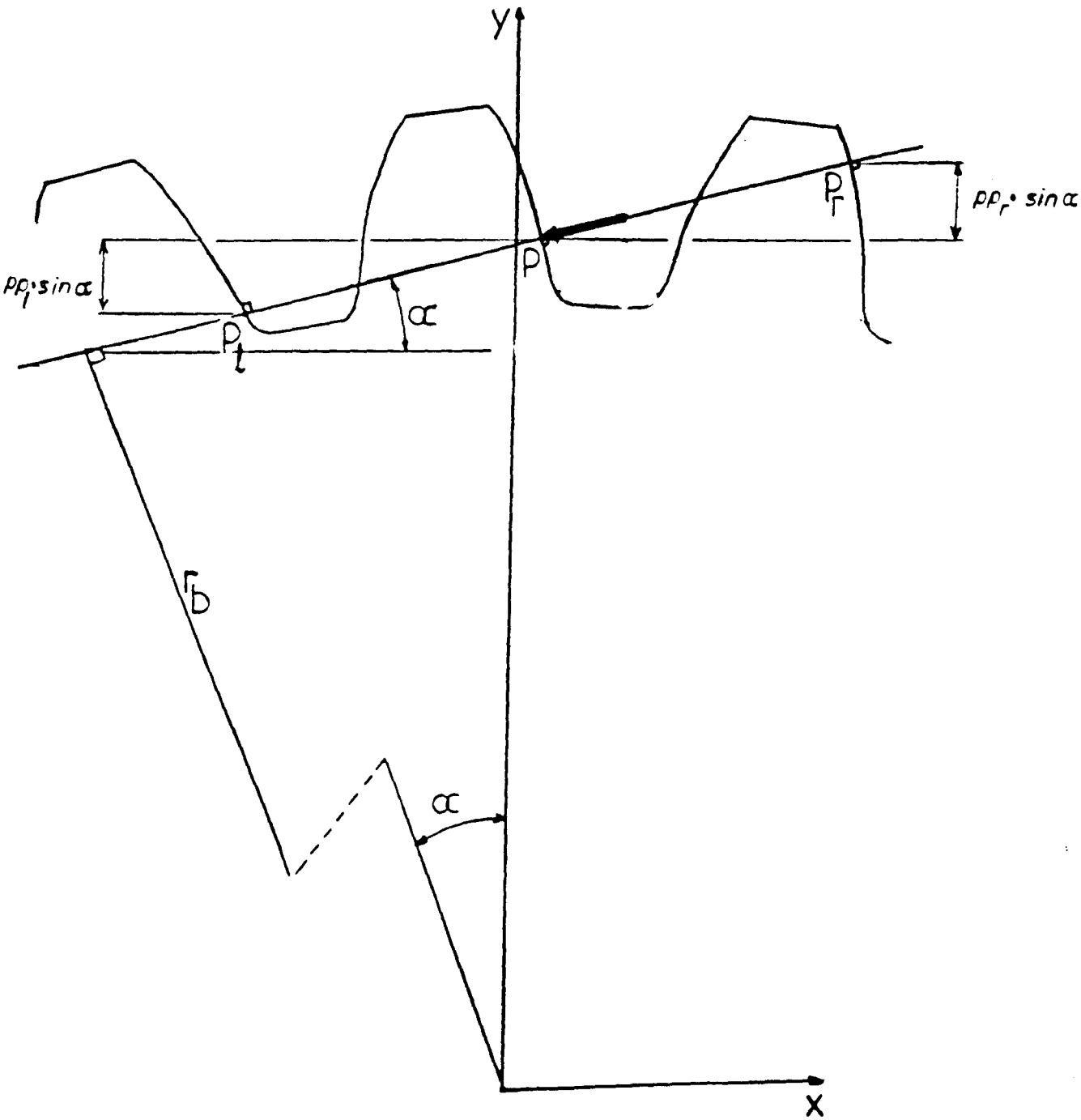

Transverse Section Through Point "p"

Fig. 2.8 Adjacent Teeth Contact Line Coordinates

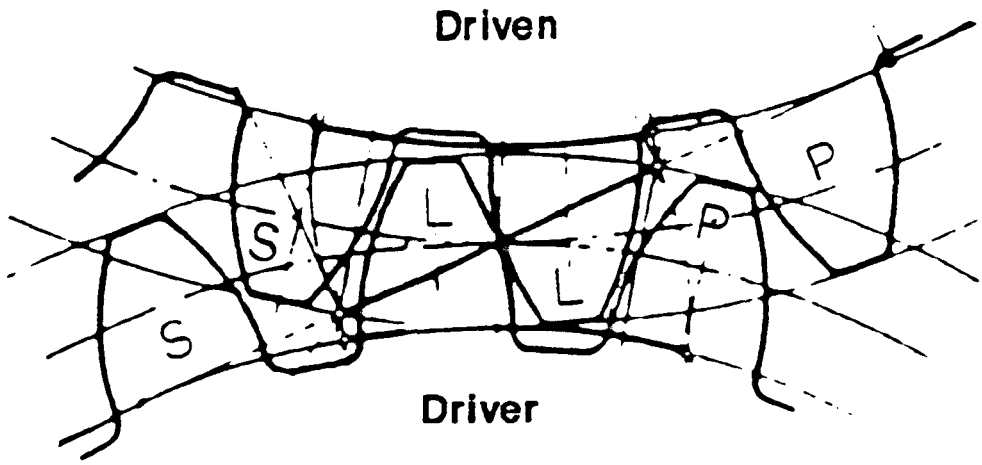

L _ Loaded Tooth
S _ Succeeding Tooth
P _ Preceeding Tooth

Fig. 2.9 Convention Used for Identifying Adjacent Teeth

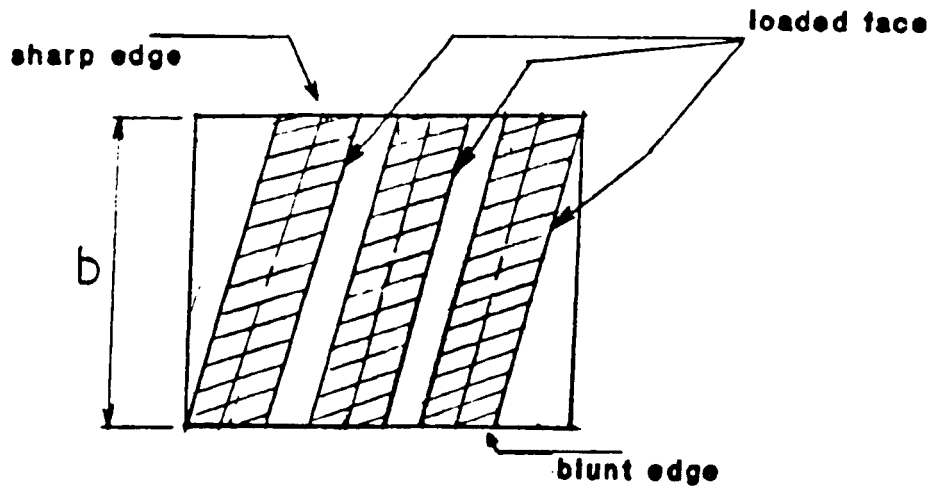

a) Sharp & Blunt End of a RH Gear

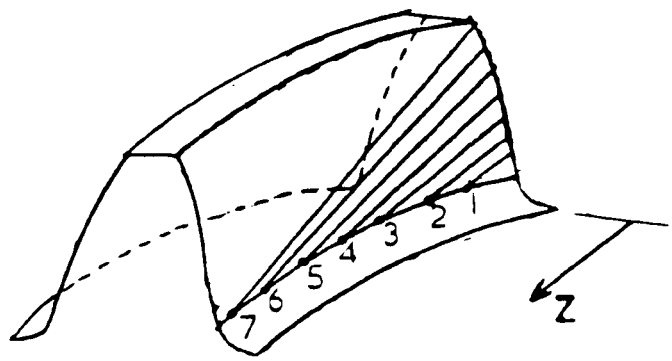

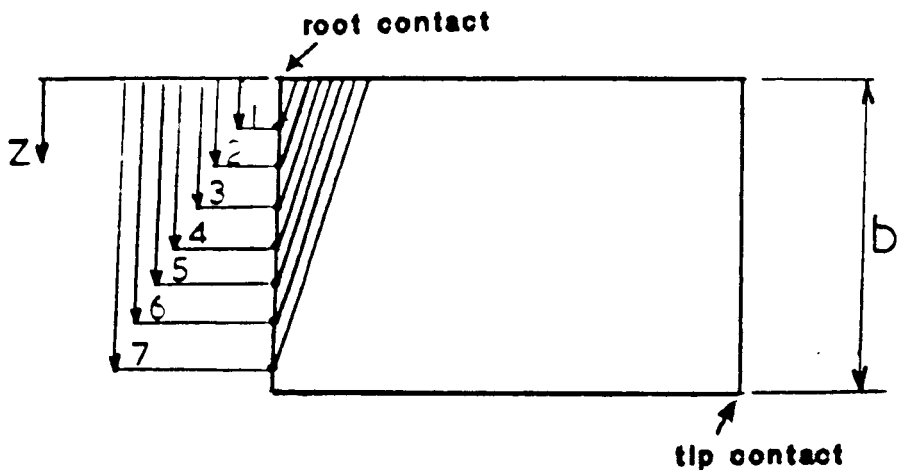

b) Contact Lines Corresponding to Point Loads Applied to a RH Driver at Points 1..7 Near the Root

Fig. 2.10

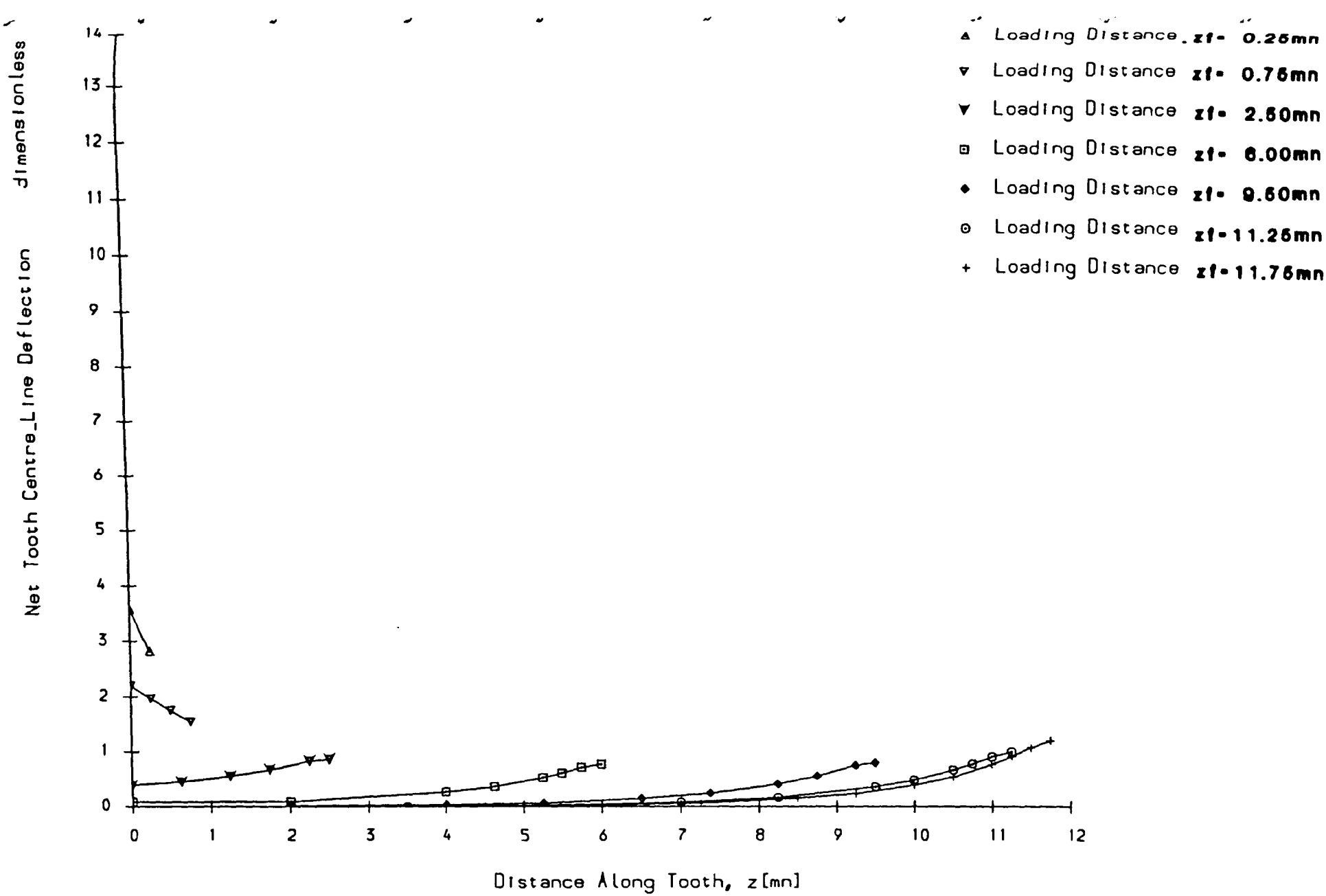

Fig. 2.11 F.E. Loaded Tooth Net Centre_Line Deflection Curves, ry=96.916 mm **Z=18**

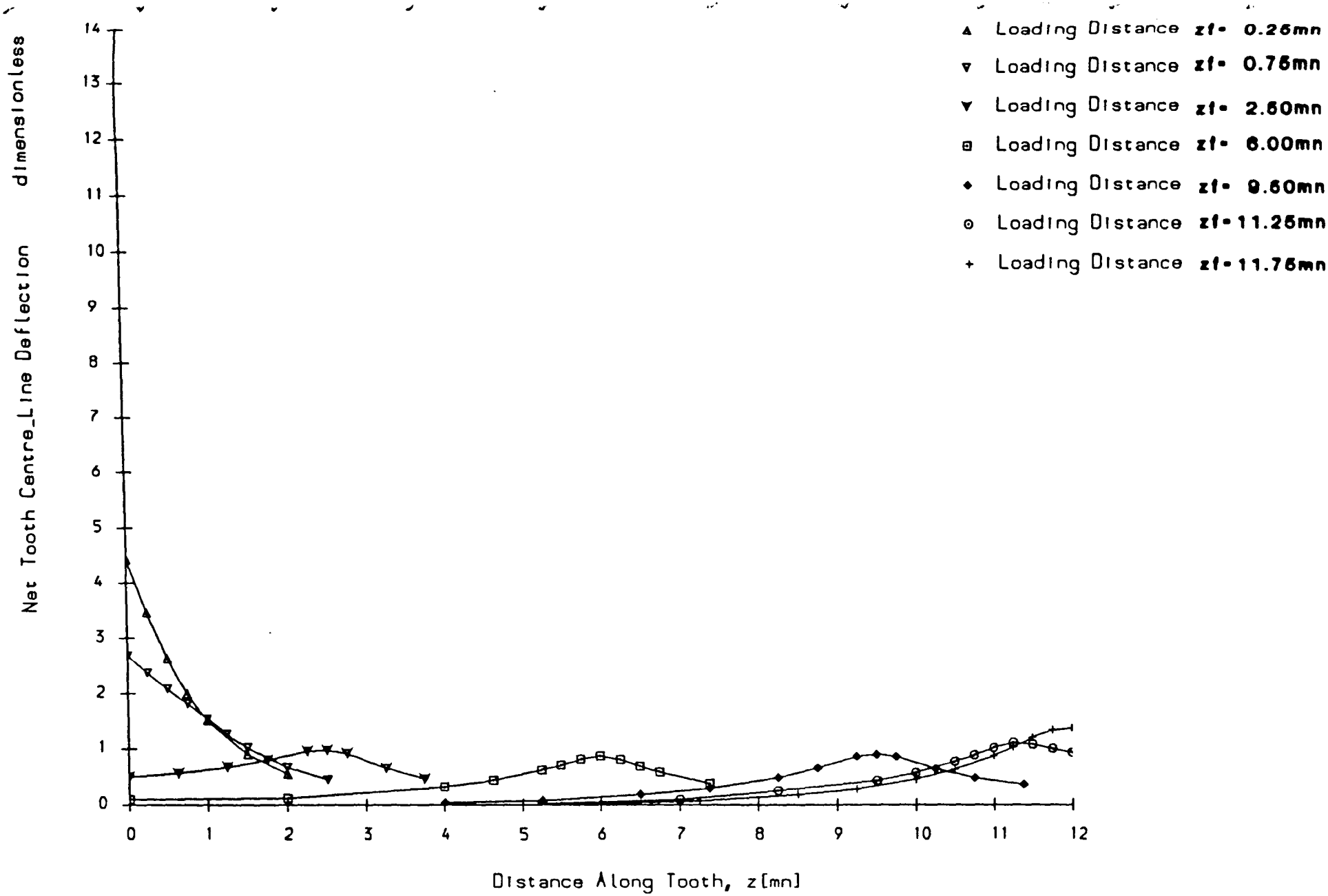

Fig. 2.12 F.E. Loaded Tooth Net Centre_Line Deflection Curves, ry=98.923 mm **Z=18**

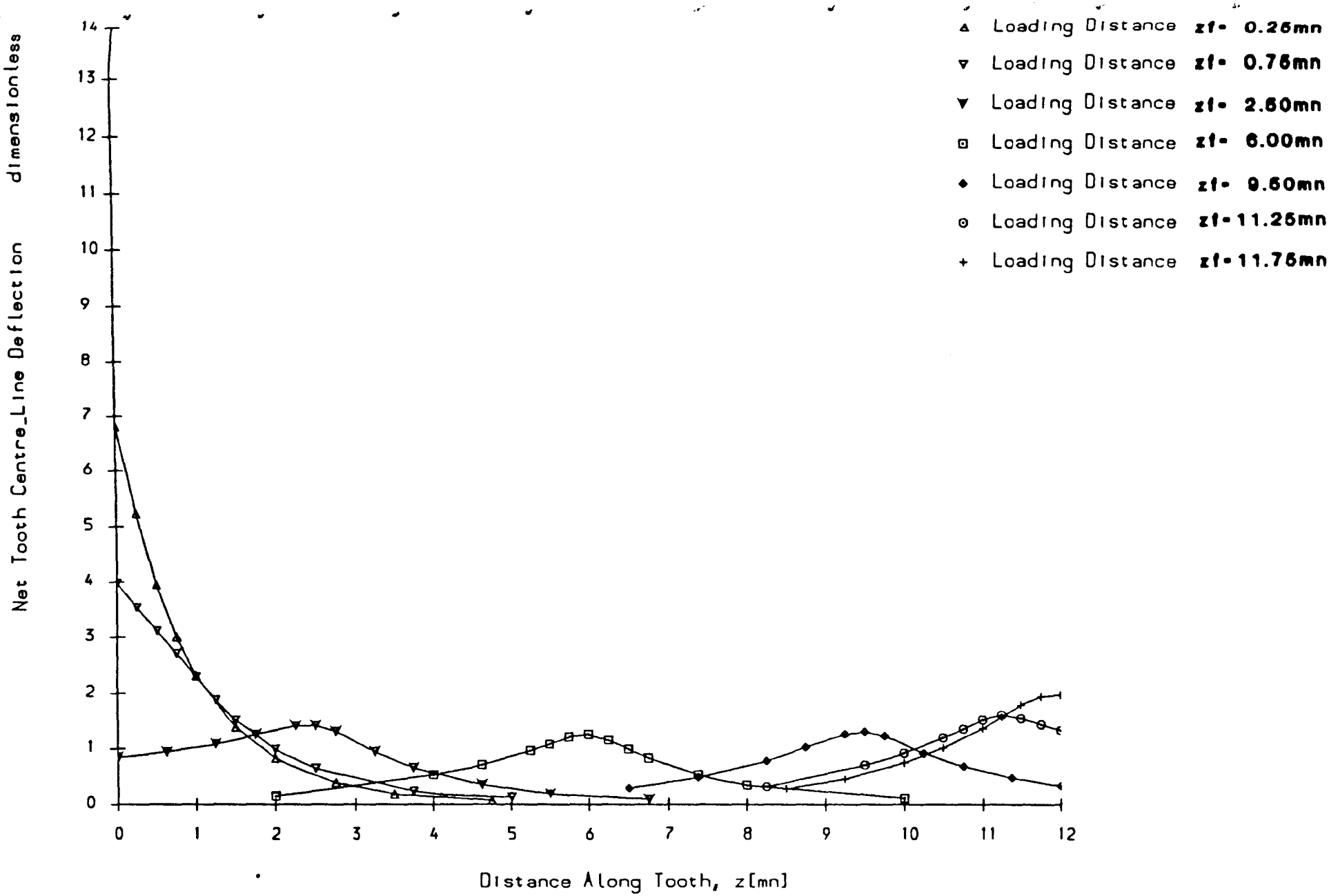

Fig. 2.13 F.E. Loaded Tooth Net Centre_Line Deflection Curves, ry=103.923mm **Z=18**

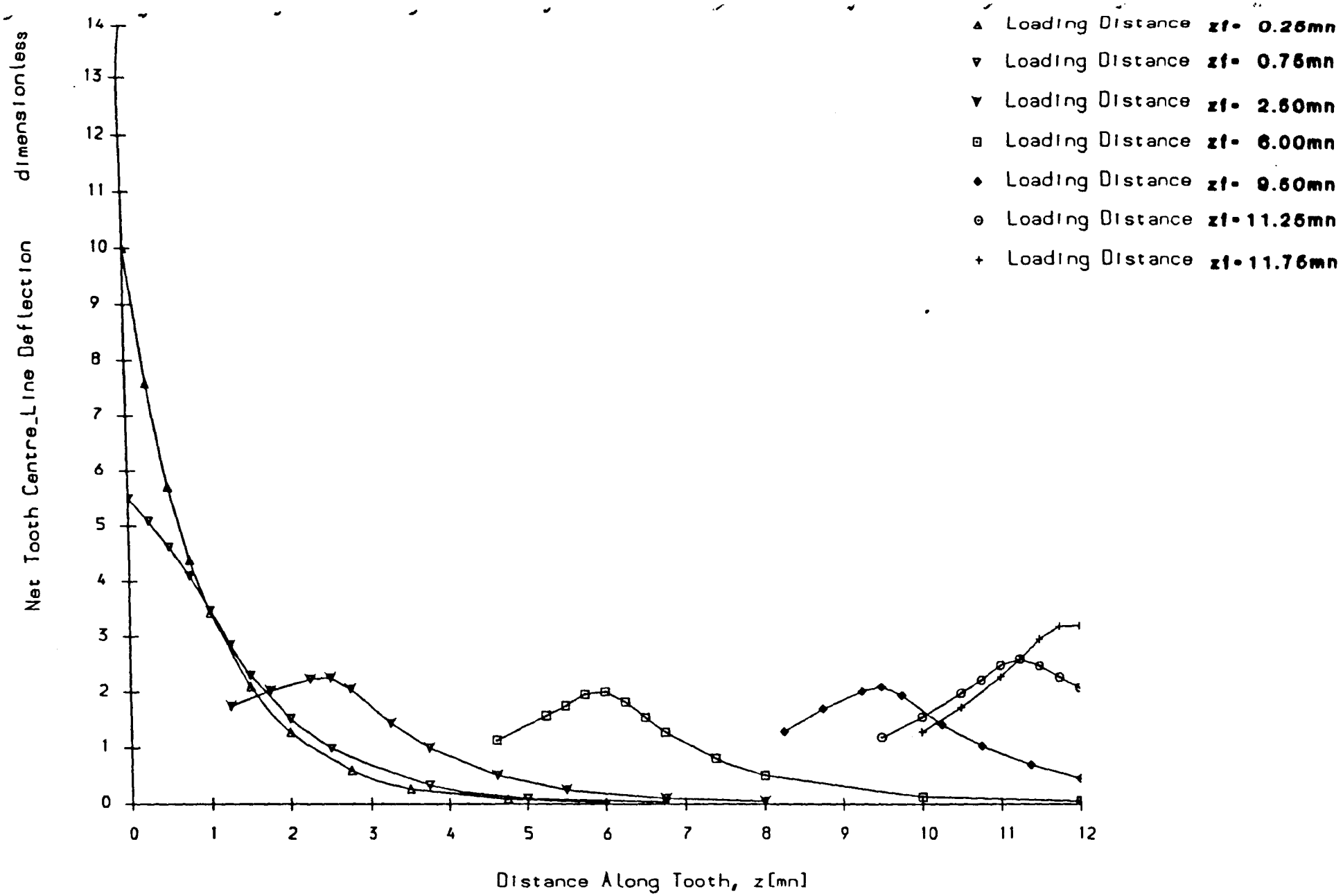

Fig. 2.14 F.E. Loaded Tooth Net Centre_Line Deflection Curves, ry=108.923mm **Z=18**

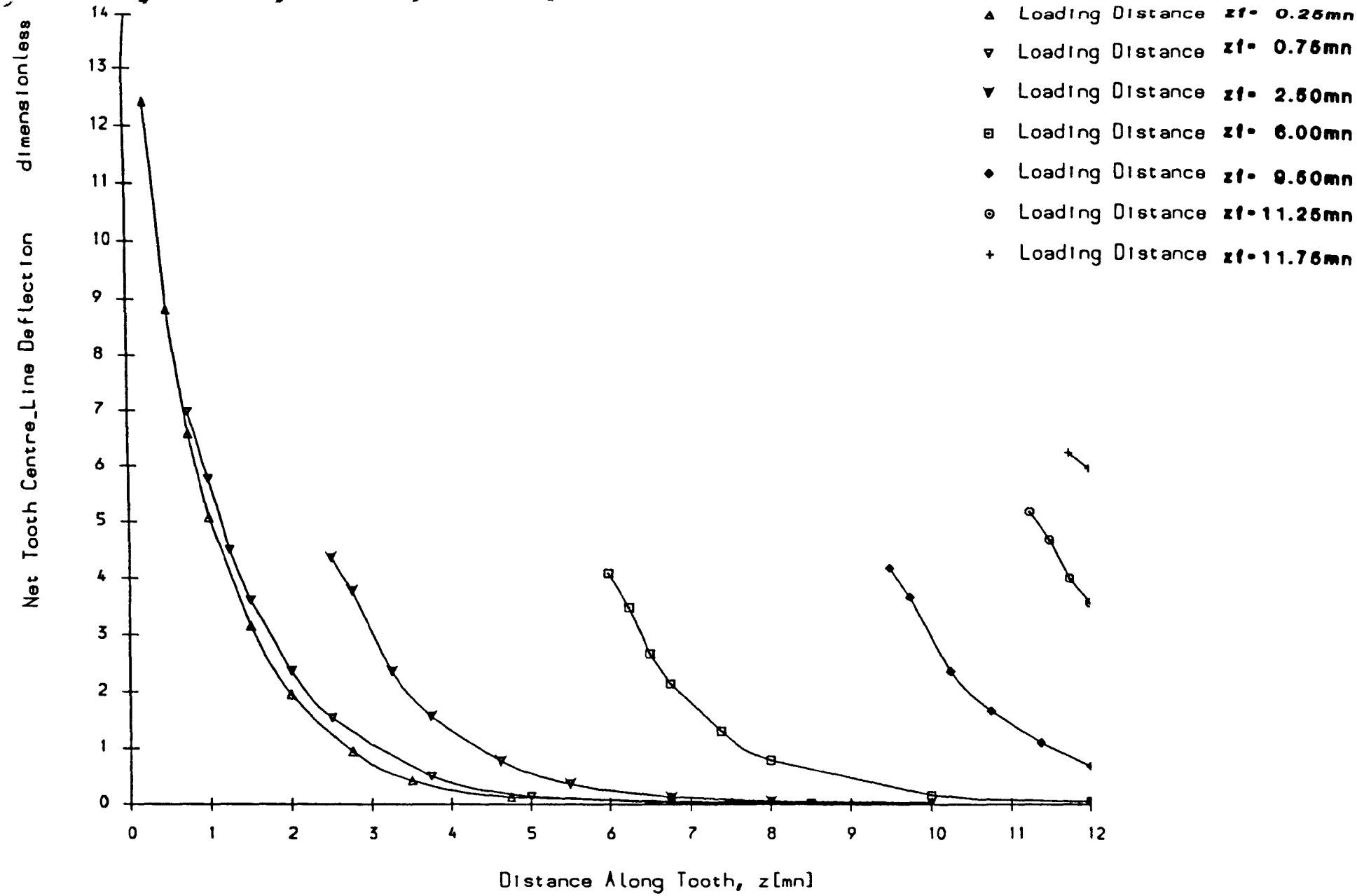

Fig. 2.16 F.E. Loaded Tooth Net Centre_Line Deflection Curves, ry=113.923mm **Z=18**

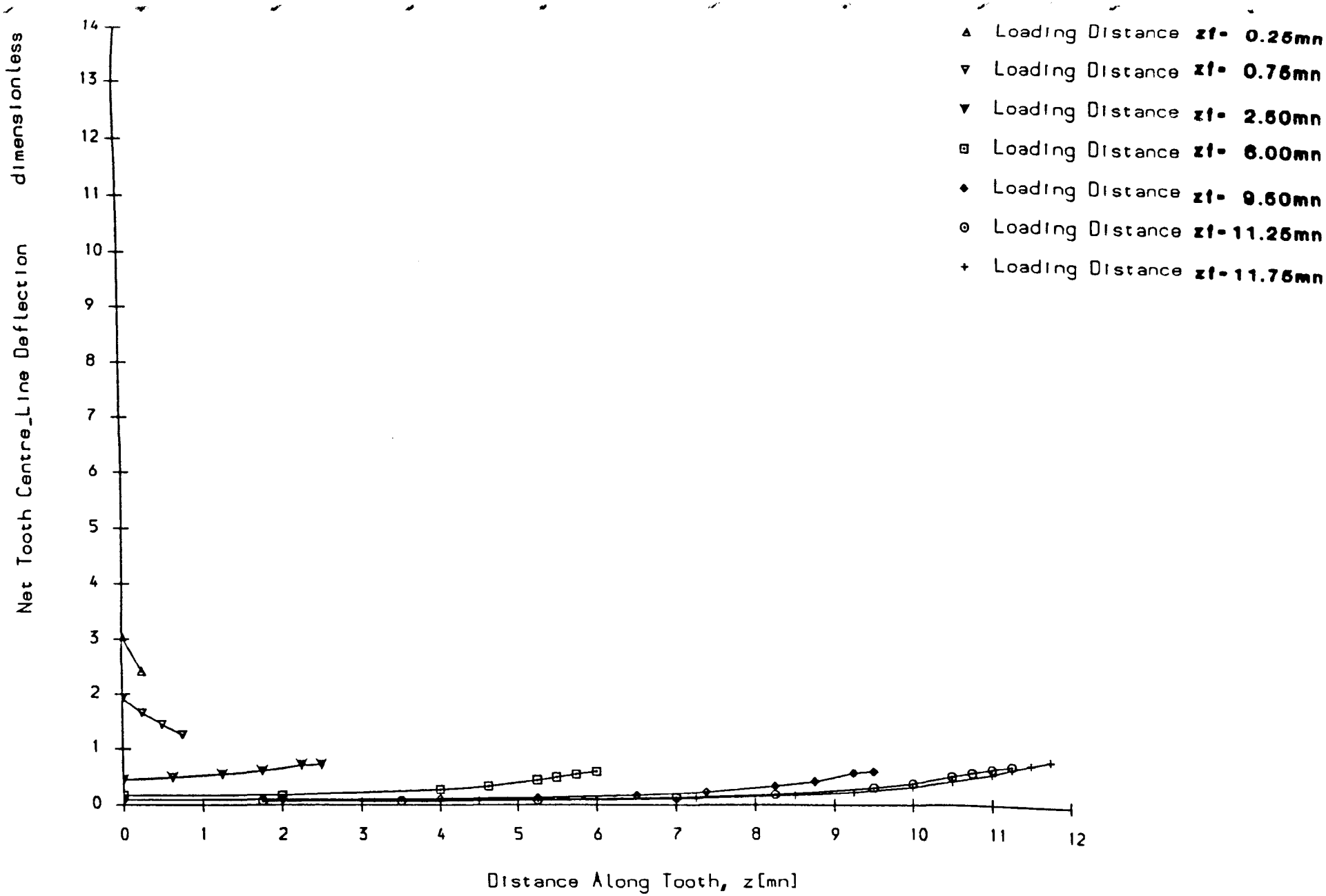

Fig. 2.16 F.E. Loaded Tooth Net Centre_Line Deflection Curves, ry=222.267mm **Z=40**

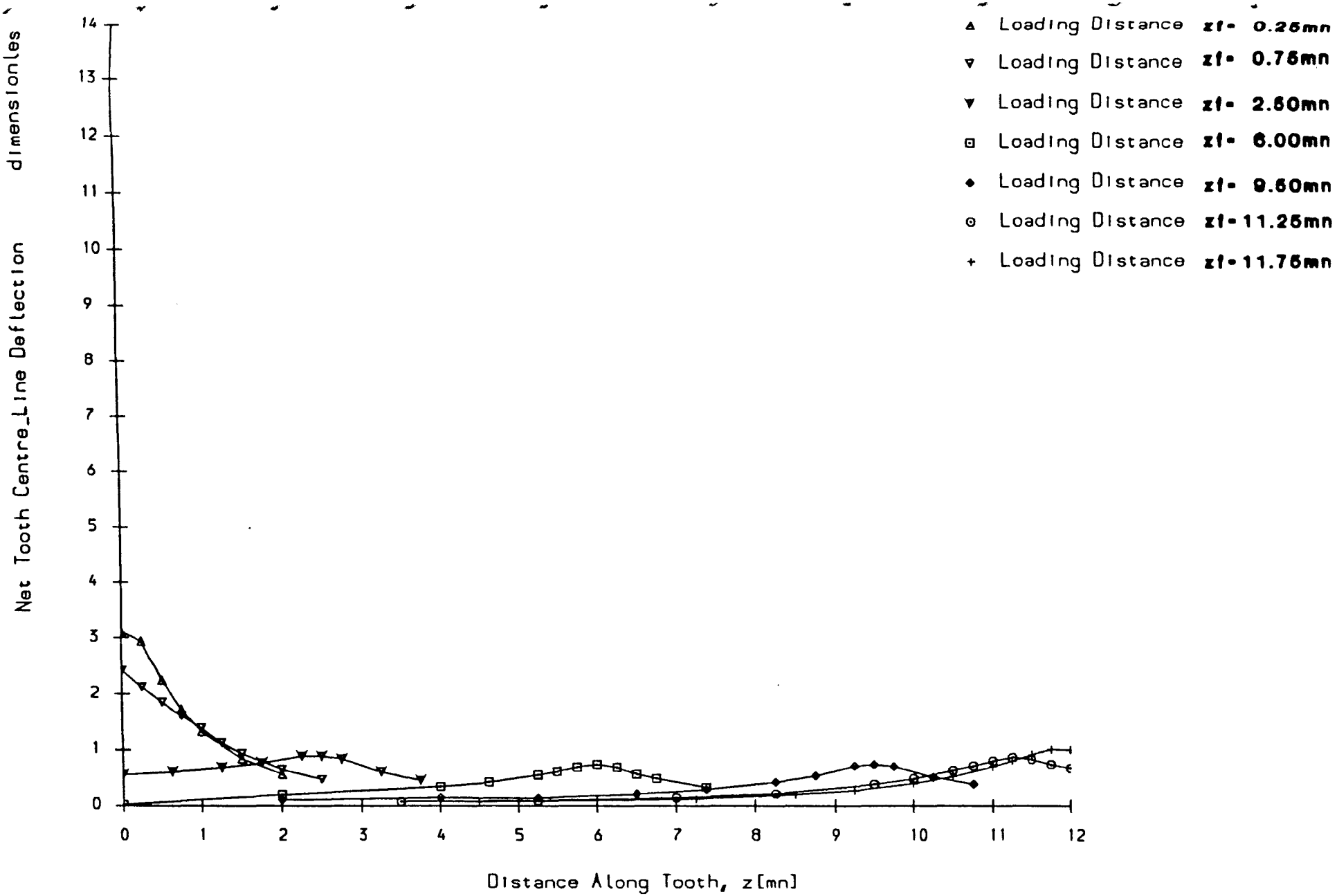

Fig. 2.17 F.E. Loaded Tooth Net Centre_Line Deflection Curves, ry=225.166mm **Z=40**

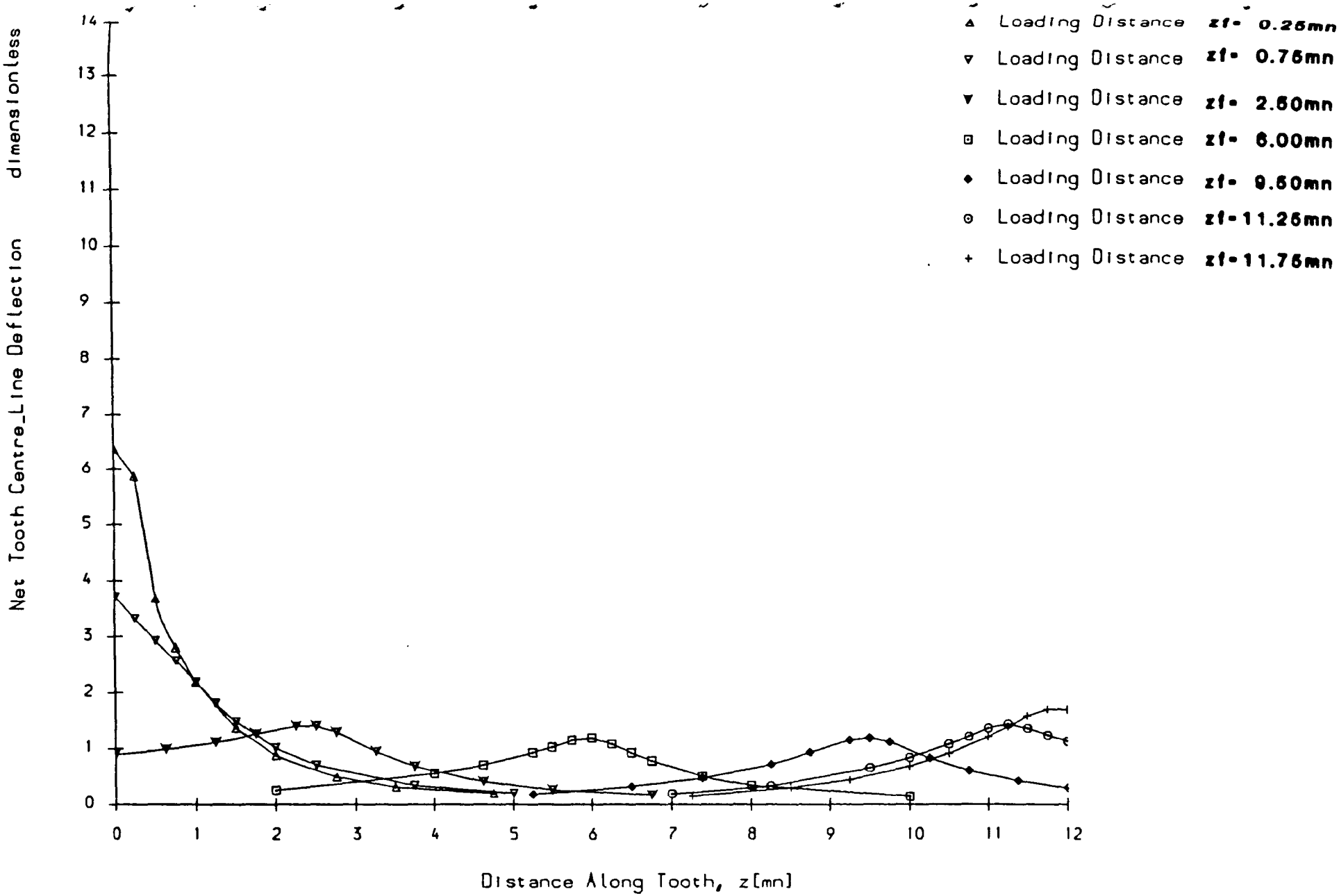

Fig. 2.18 F.E. Loaded Tooth Net Centre_Line Deflection Curves, ry=230.940mm **Z=40**

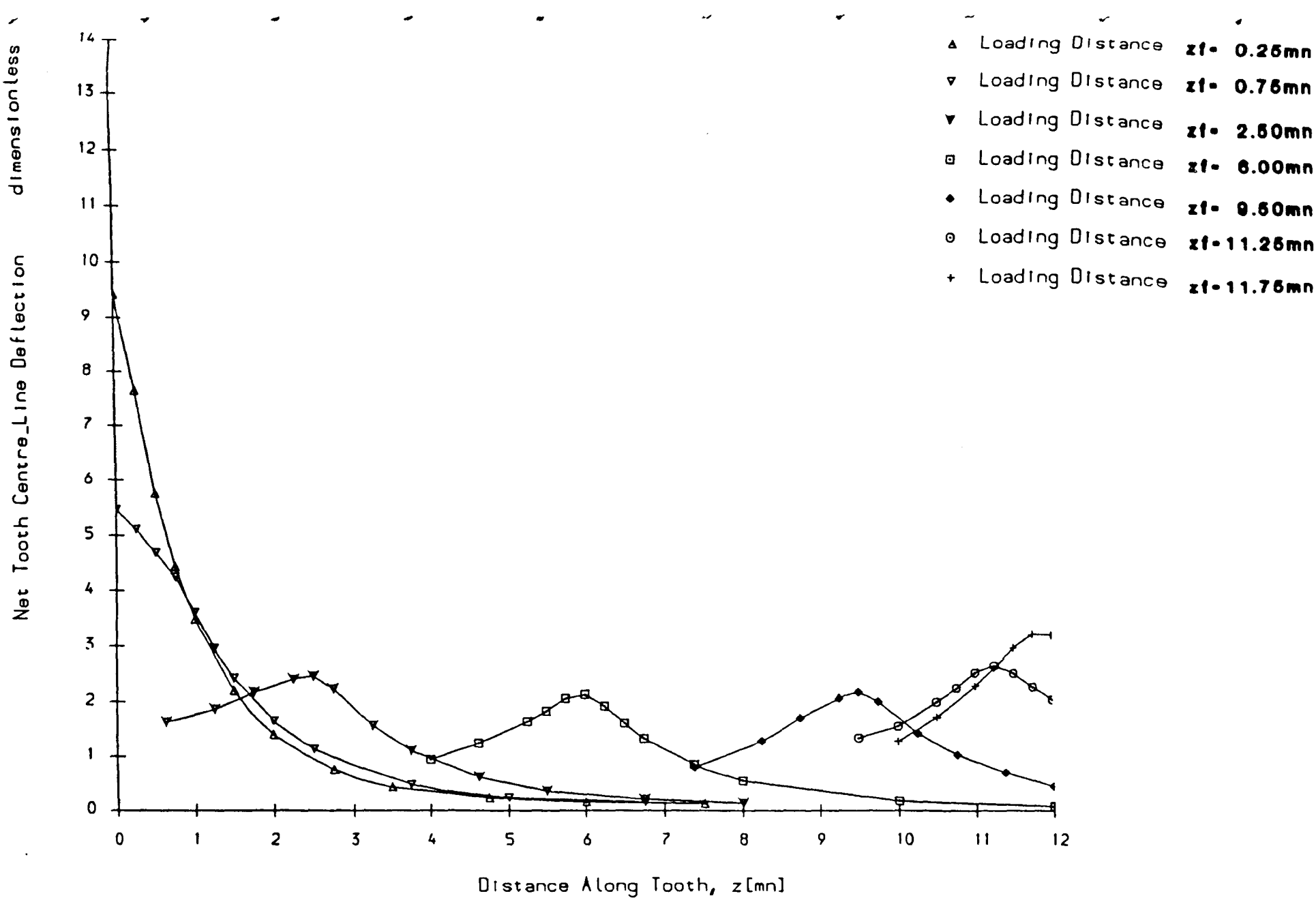

Fig. 2.19 F.E. Loaded Tooth Net Centre_Line Deflection Curves, ry=236.713mm **Z=40**

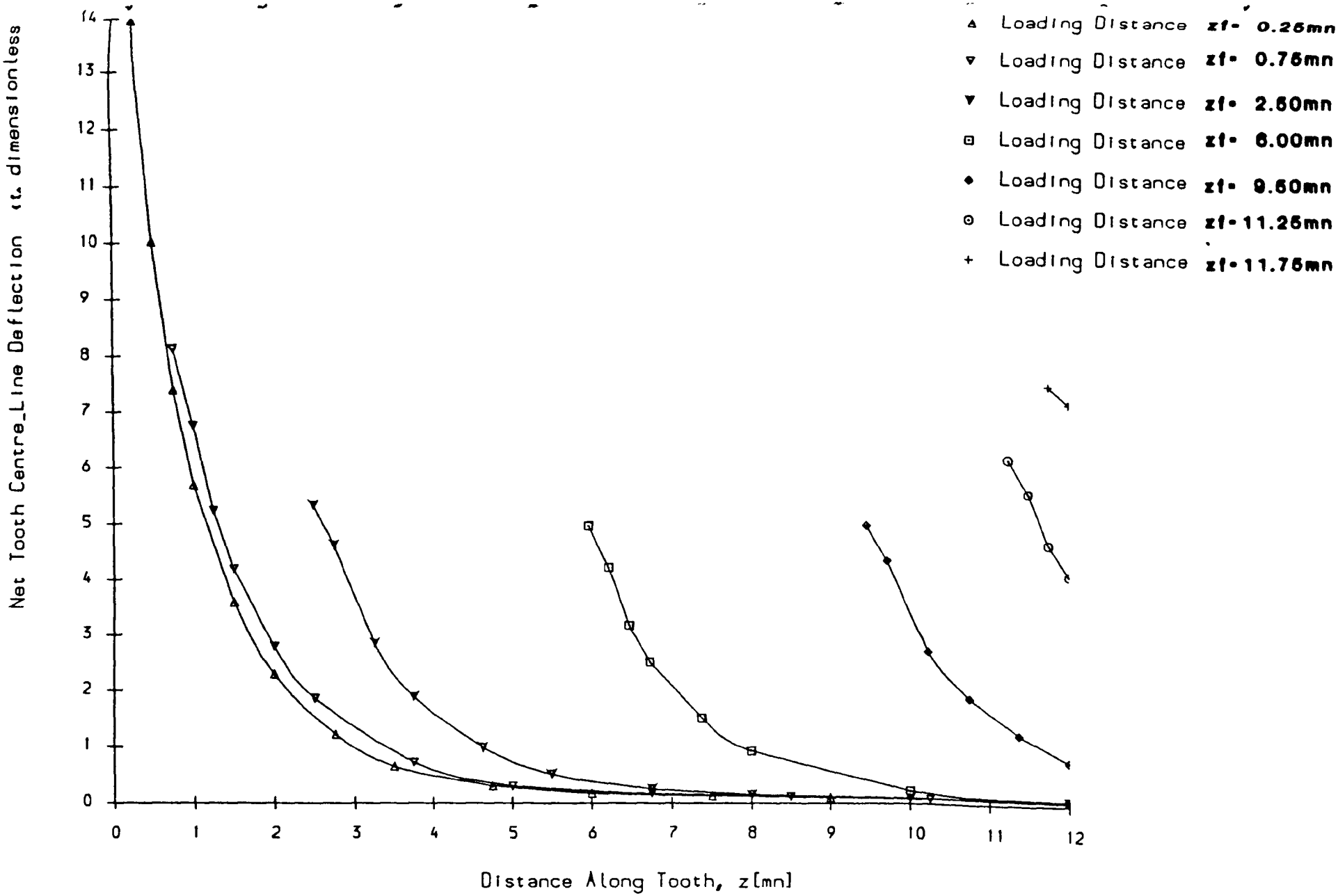

Fig. 2.20 F.E. Loaded Tooth Net Centre_Line Deflection Curves, ry=242.487mm' **Z=40**

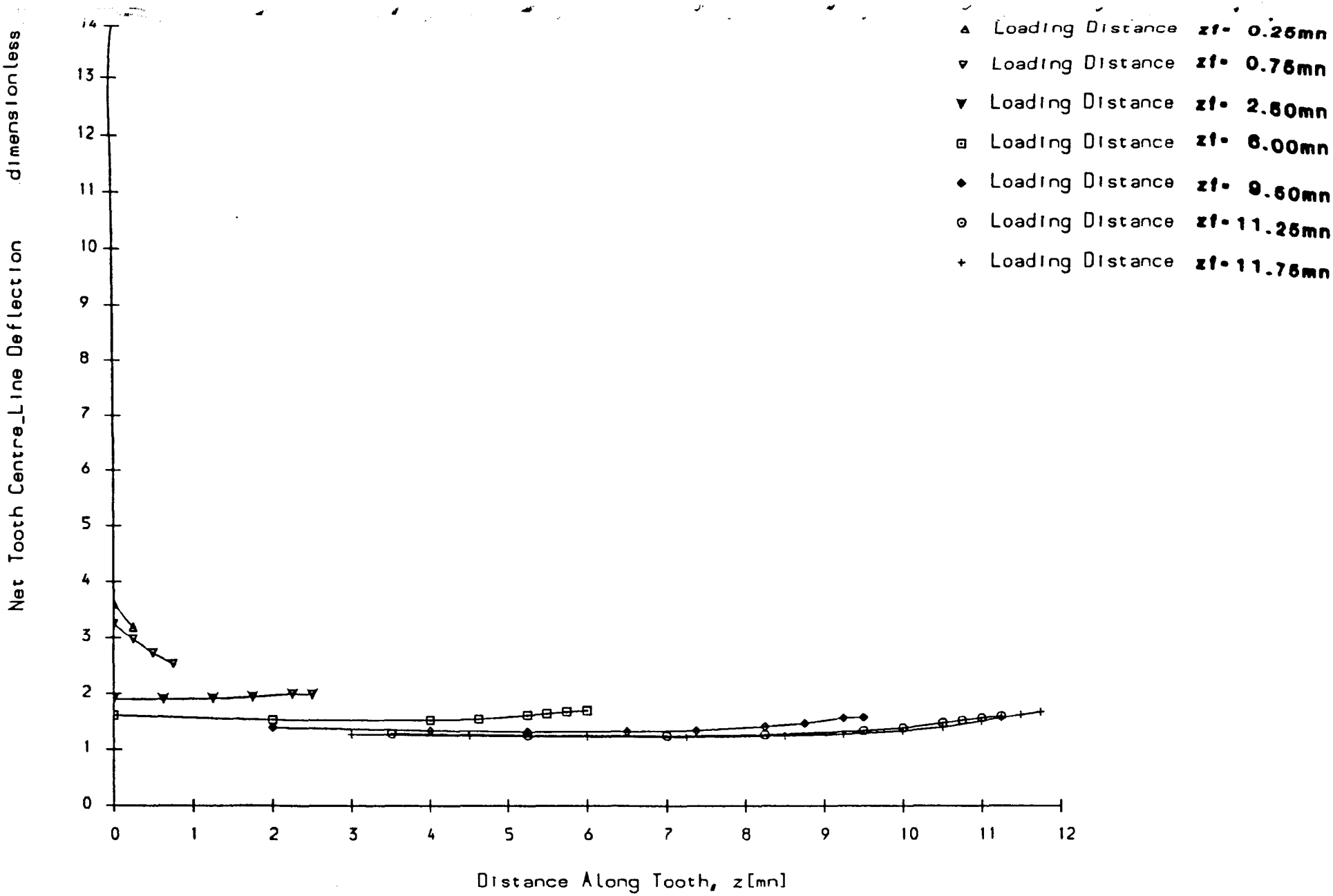

Fig. 2.21 F.E. Loaded Tooth Net Centre_Line Deflection Curves, ry=567.908mm **Z=100**

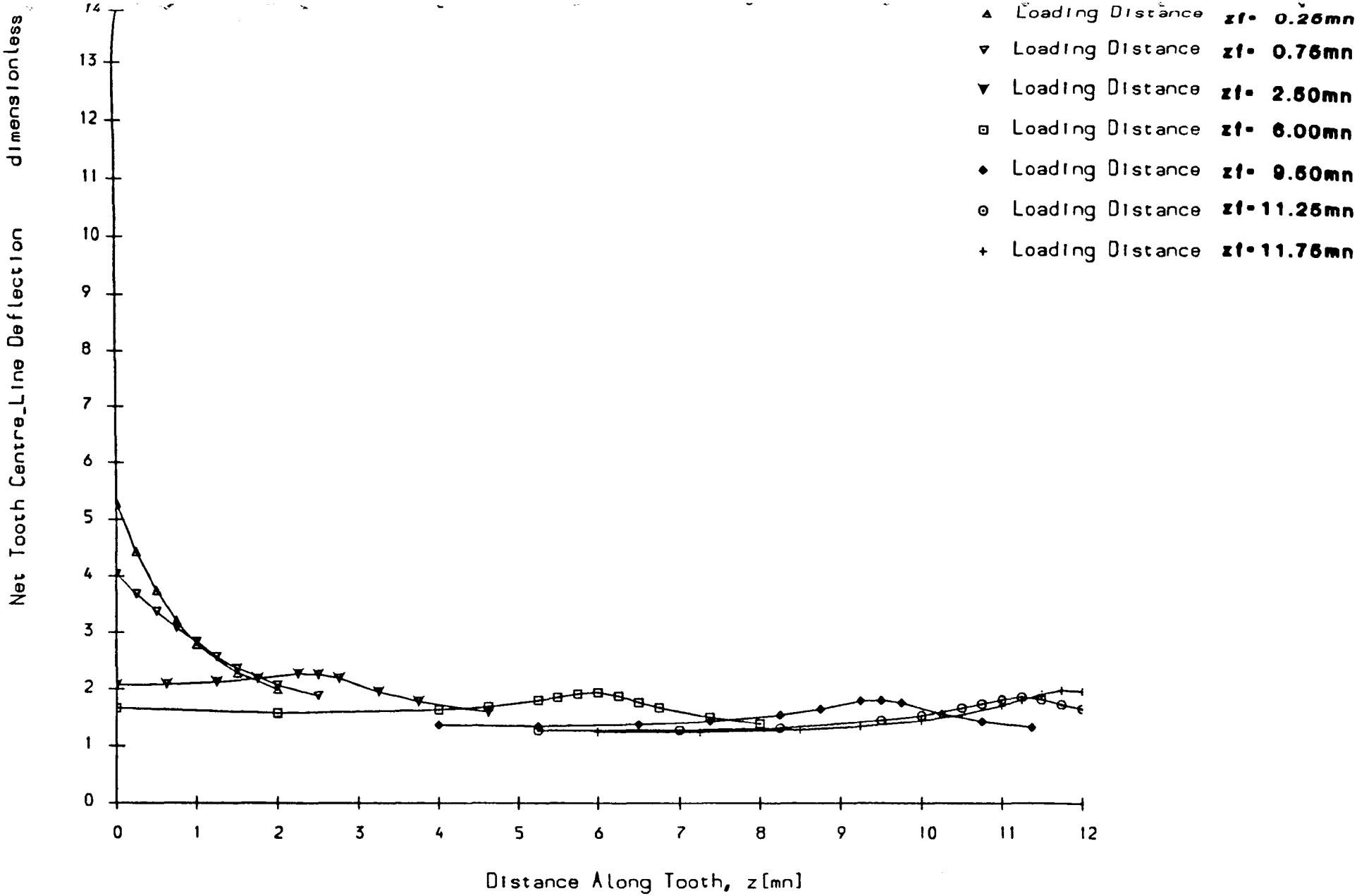

Fig. 2.22 F.E. Loaded Tooth Net Centre_Line Deflection Curves, ry=572.350mm **Z=100**

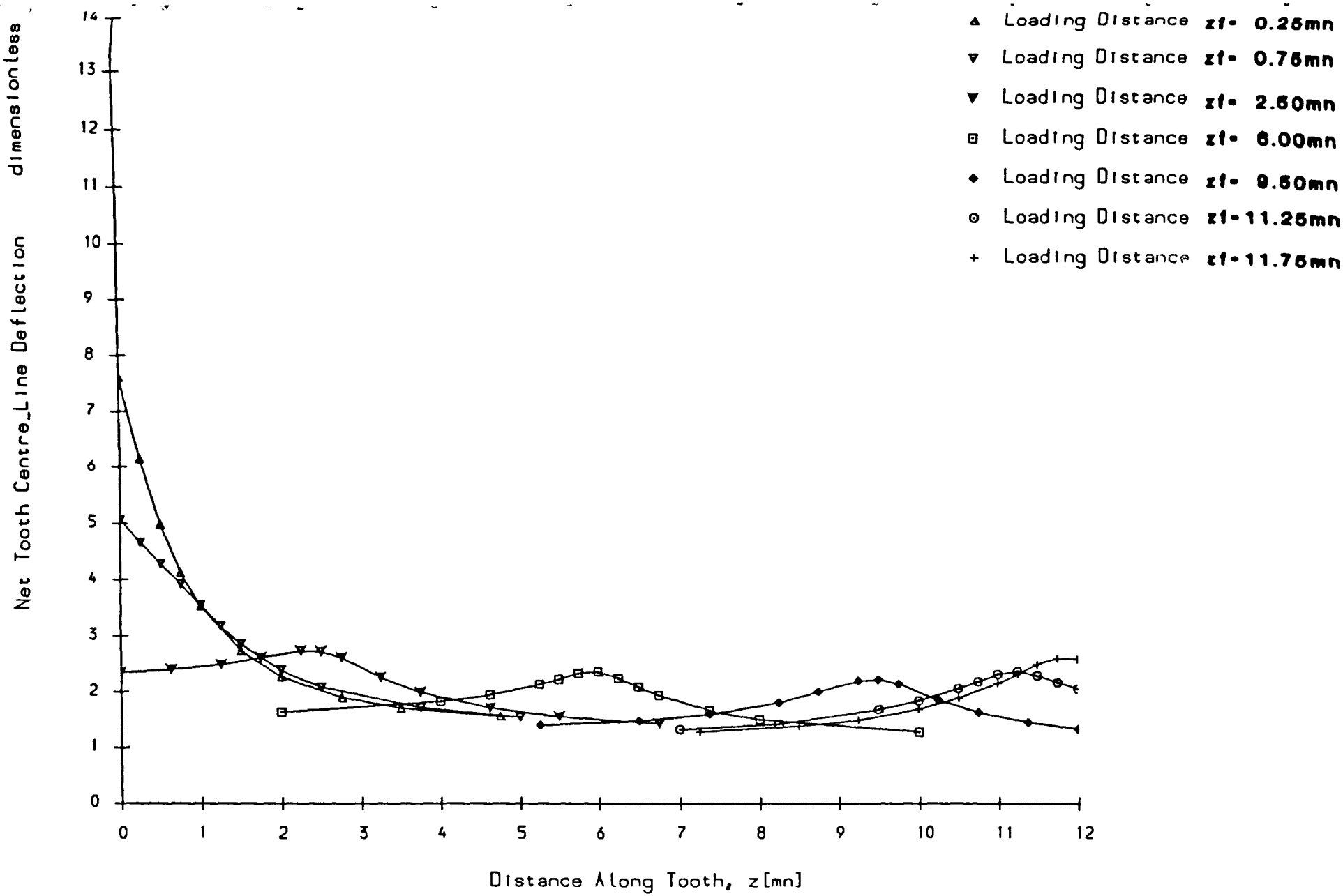

Fig. 2.28 F.E. Loaded Tooth Net Centre_Line Deflection Curves, ry=577.350mm **Z=100**

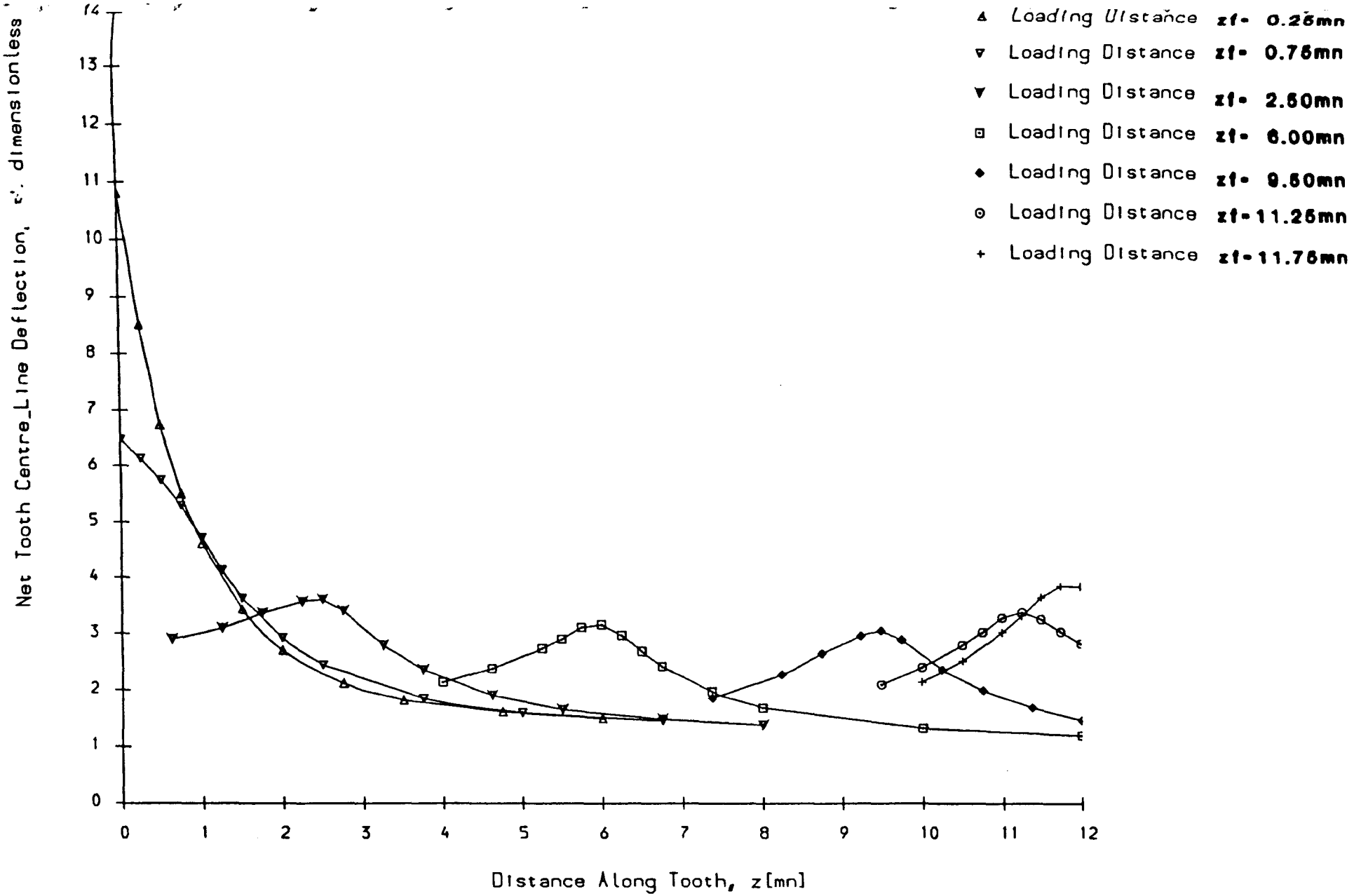

Fig. 2.24 F.E. Loaded Tooth Net Centre_Line Deflection Curves, ry=582.350mm **Z=100**

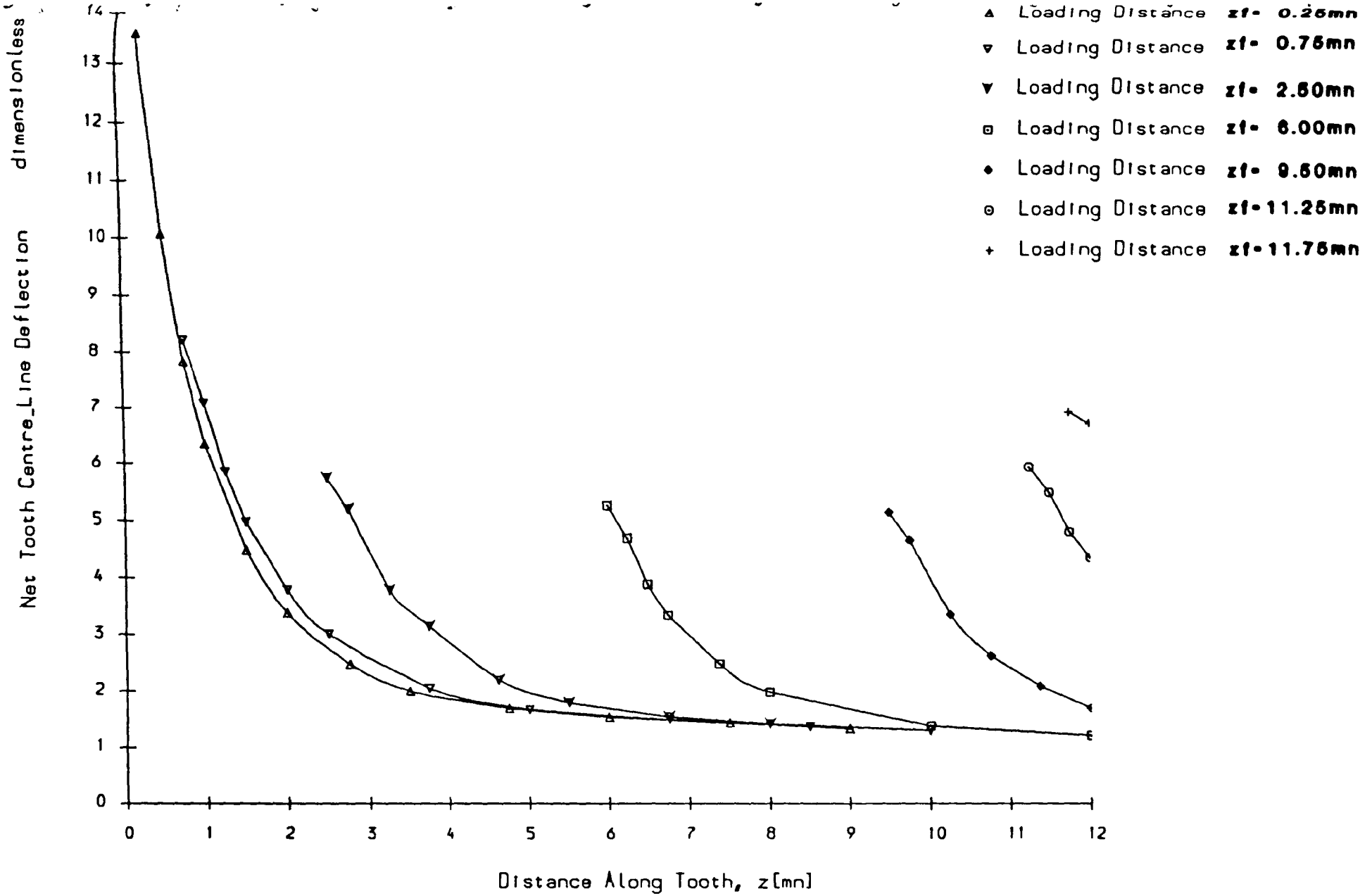

Fig. 2.25 F.E. Loaded Tooth Net Centre_Line Deflection Curves, ry=587.350mm **Z=100**

loading (position z_f), for the particular case of near root loading. Loading positions 1 to 7 on Fig. 2.10b correspond to axial loading positions of 0.25, 0.75, 2.5, 6.0, 9.5, 11.25 and $11.75m_n$ respectively.

Some interesting points emerge from a comparison of the 'loaded' tooth deflections (at corresponding loading diameters), for the 18 and 40 tooth gears. First, for loading near or below the reference diameter, the 18-tooth gear generally deforms more than the 40-tooth gear. Although the larger gear has greater gear body deformations, these are not significant, for most of the deflections are thus, for both gears, due to tooth bending/shear, which, for the 'weaker' 18-tooth profile is greatest.

However, the results for loading positions at and near the tip, show that, in this case, the 40-tooth gear generally deforms more than the 18-tooth gear. A possible reason for this is that at large loading diameters, the gears body deformations relative to the shaft centre become rather more significant, so that they more than compensate for the lower tooth compliance of the 40-tooth gear. However, since the contact lines run obliquely across the face, some of the deflected points are much further from the tip than others, and experience lower gear body deflections. At such points, the 18-tooth deflections again prove to be larger. These effects are clearly seen if the corresponding curves for both gears are superposed.

The 'loaded' tooth deflections of the 100-tooth gear are, as expected, much greater than the deflections of the other two gears. This is due to the much greater gear body deformations, which more than offset the reduced compliance of the teeth themselves.

In fact, superposing the graphs for all three gears (for corresponding loading diameters) shows that the deflections for the 18-tooth and 40-tooth gears are almost identical, implying that for small gears, gear body deformations are insignificant. However, the curve for the 100-tooth gear is consistently shifted vertically relative to the other two curves by about 1.3 units. That this shift is almost entirely due to the extra gear body deformation on the larger 100-tooth gear is confirmed by a study of the adjacent tooth deflection curves in Figs 2.32 and 2.33 (see below). These (which must be mainly due to gear body effects since there is no loading on the adjacent teeth) are also typically at least 1.3 units.

Considering now the results for the 'adjacent' teeth deformations, it has

already been pointed out that for helical gears the adjacent teeth deformations show very little dependence on radial loading position. This is clearly demonstrated in Figs. 2.26 and 2.27 for the preceding and succeeding teeth respectively (only shown for the 40-tooth gear, and one axial loading position due to space limitations). For spur gears, points of contact 'p_ℓ' and 'p_r' on the adjacent teeth (Fig. 2.8) lie on straight contact lines which run right across the face-width at constant heights above the tooth root.

On helical gears, however, the contact lines through the points 'p_ℓ' and 'p_r' are oblique, so that all the points are at different heights up the tooth. The contact lines on the preceding and succeeding teeth thus have different positions radially and axially so that the deformation curves for these two teeth are significantly different.

Figs. 2.28 to 2.33 show this quite clearly, although the curves for preceding and succeeding teeth do seem to be near 'mirror-images' of one another for opposite loading positions. For instance, loading at the 'sharp' end gives a 'preceding' tooth deflection curve which is nearly a mirror-image of the deflection curve for the 'succeeding' tooth resulting from loading at the 'blunt' end.

The increasing contribution of gear body deflections to the total tooth deflection on larger gears has already been mentioned. Steward[30] found that for a 100-tooth spur gear, the peak adjacent tooth deflections at reference diameter loading, varied from 29% to 47% of the corresponding peak deflection of the loaded tooth. For the 100-tooth helical gear, Figs. 2.32-2.33 show corresponding values between 25% and 72%. The larger percentages in the case of helical gears, may be attributed to the even greater gear body deflections due to the greater diameter (by a factor $1/\cos\beta$) of the helical gear.

2.6 Curve Fitting of F.E. Compliance Data

2.6.1 Introduction

The emprical compliance function K_{tb} developed by Steward[30] for the 'loaded' tooth (Eq. 1.57) for standard spur gears, is used in the same general form and applied to helical gears in the present work. However, the master function 'F' and the non-master function 'G' both require modification. Steward's adjacent tooth curve fitting function

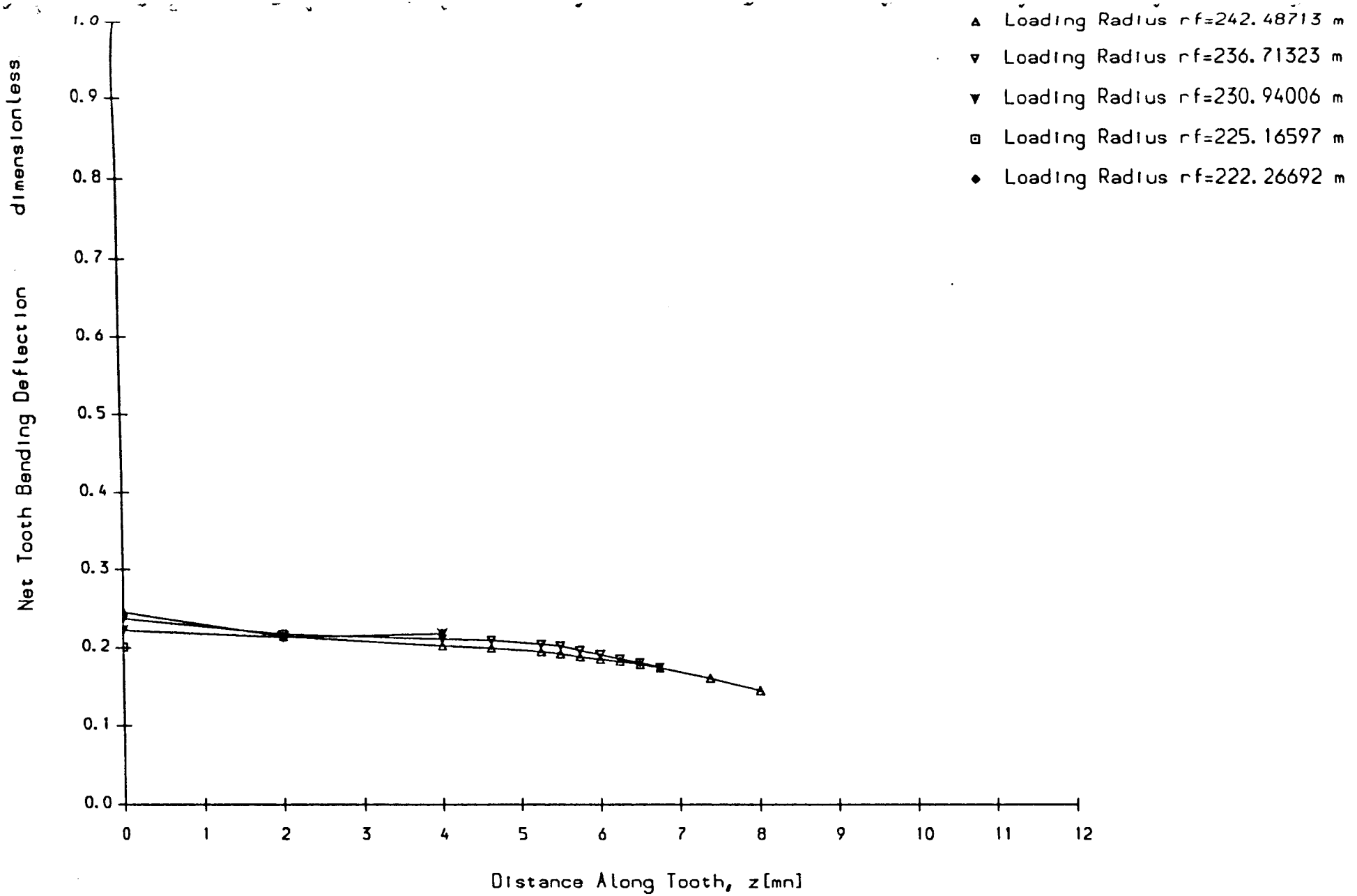

Fig. 2.26 F.E. Succeeding Tooth Net Bending Deflection Curves, **zf=6.0mn Z=40**

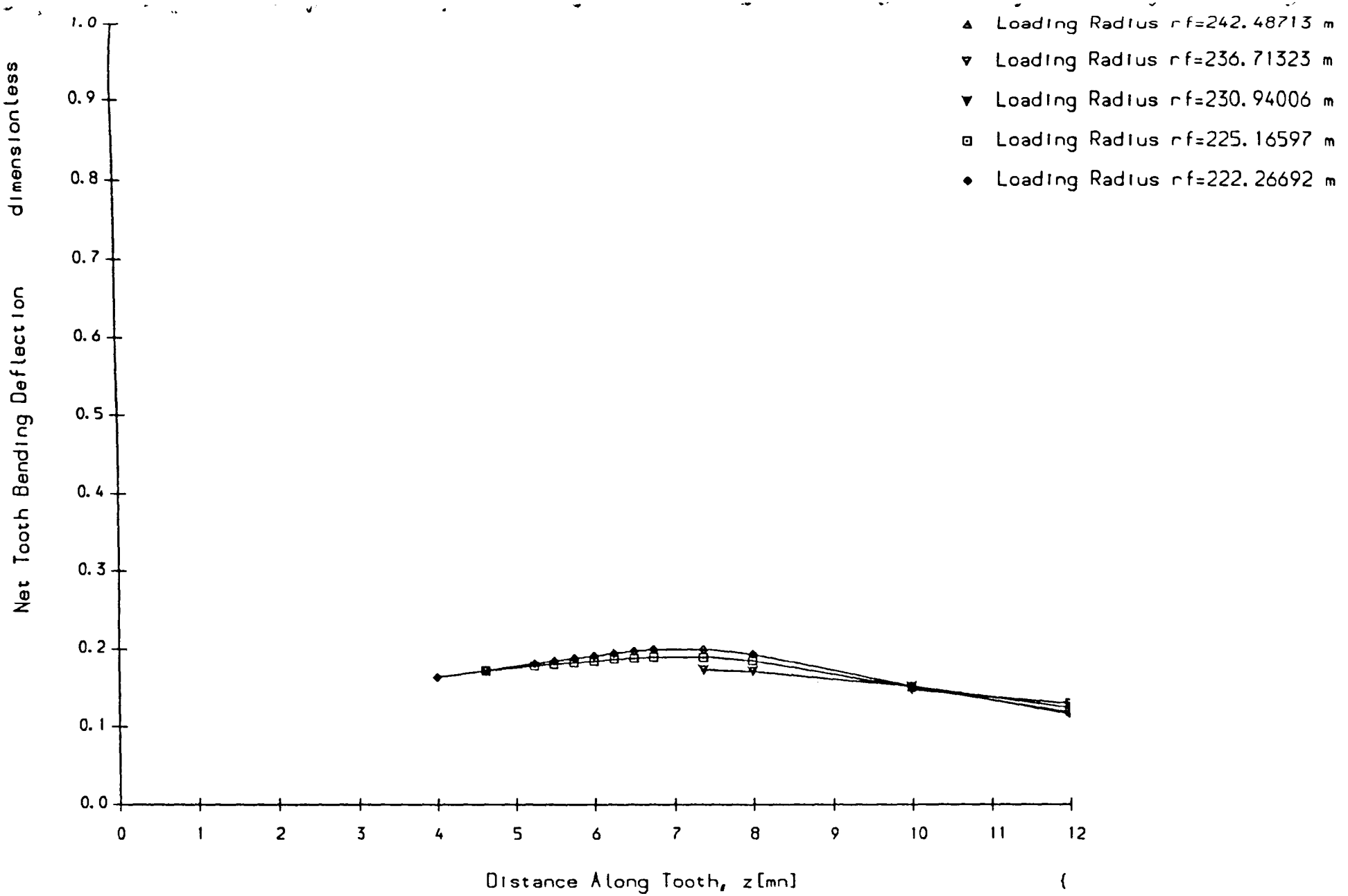

Fig. 2.27 F.E. Preceeding Tooth Net Bending Deflection Curves, **zt=6.0mn Z=40**

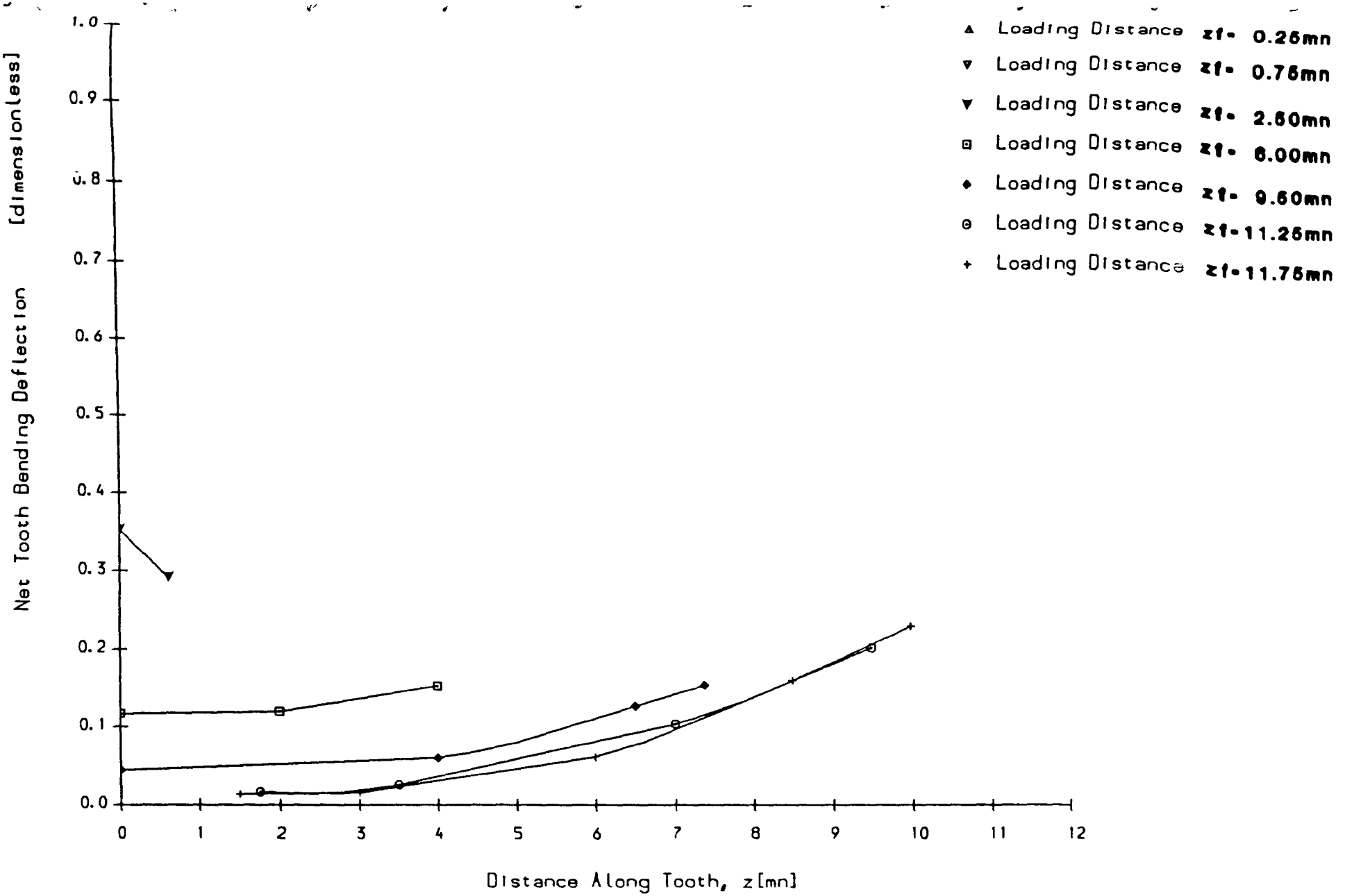

Fig. 2.28 F.E. Succeeding Tooth Net Bending Deflection Curves, ry=103.923mm **Z=18**

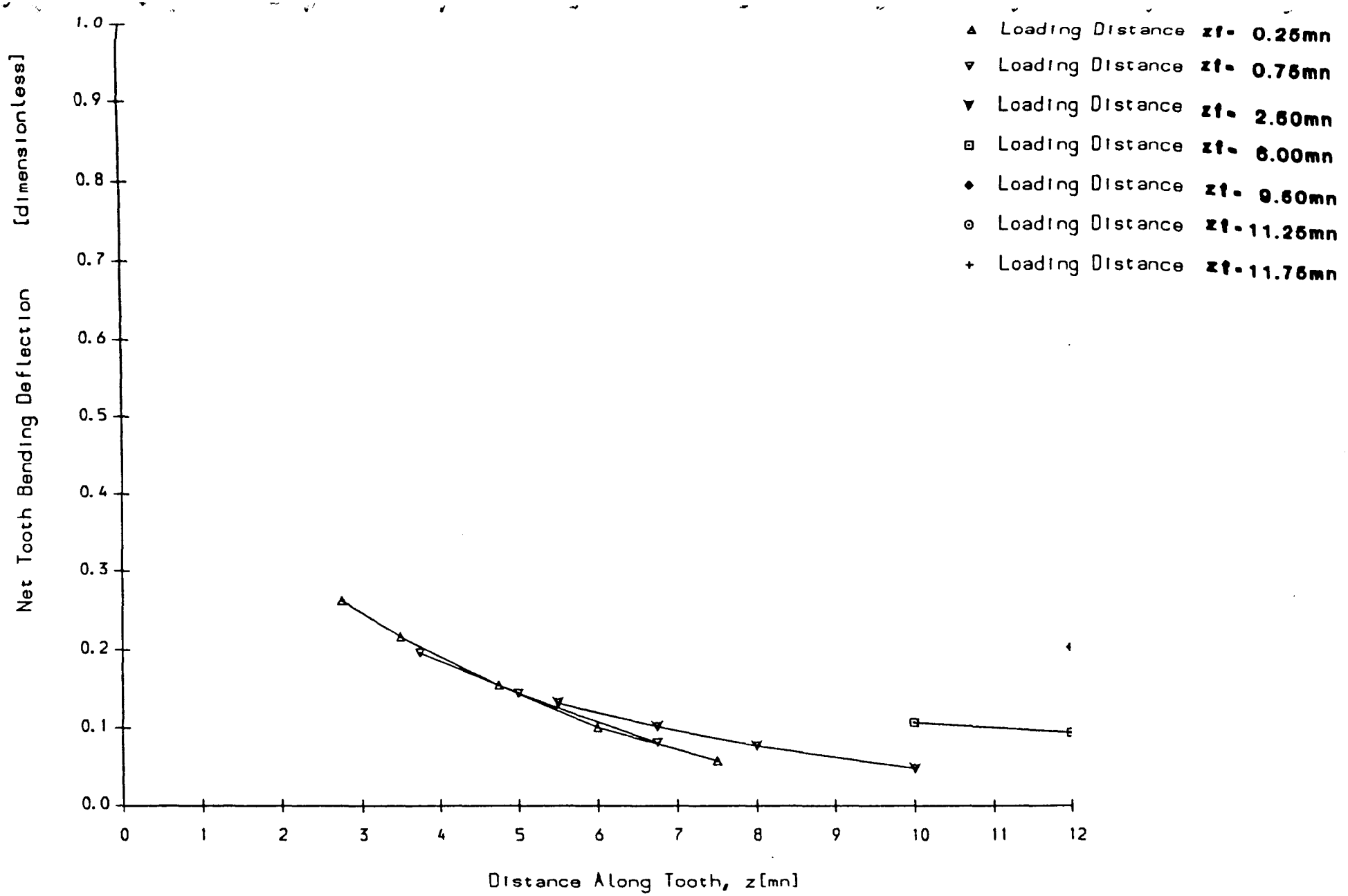

Fig. 2.29 F.E. Preceeding Tooth Net Bending Deflection Curves, ry=103.923mm **Z=18**

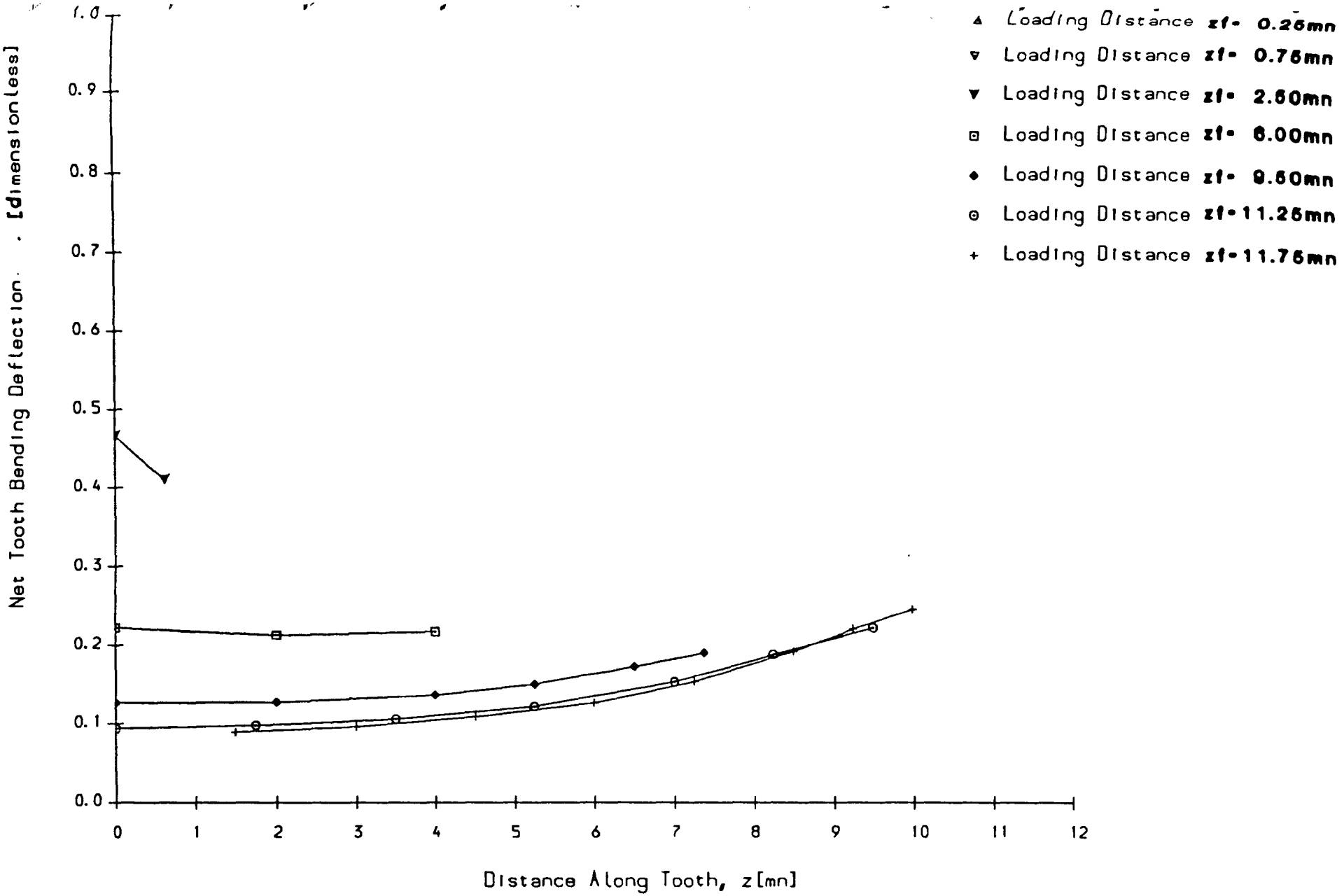

Fig. 2.30 F.E. Succeeding Tooth Net Bending Deflection Curves, ry=230.940mm **Z=40**

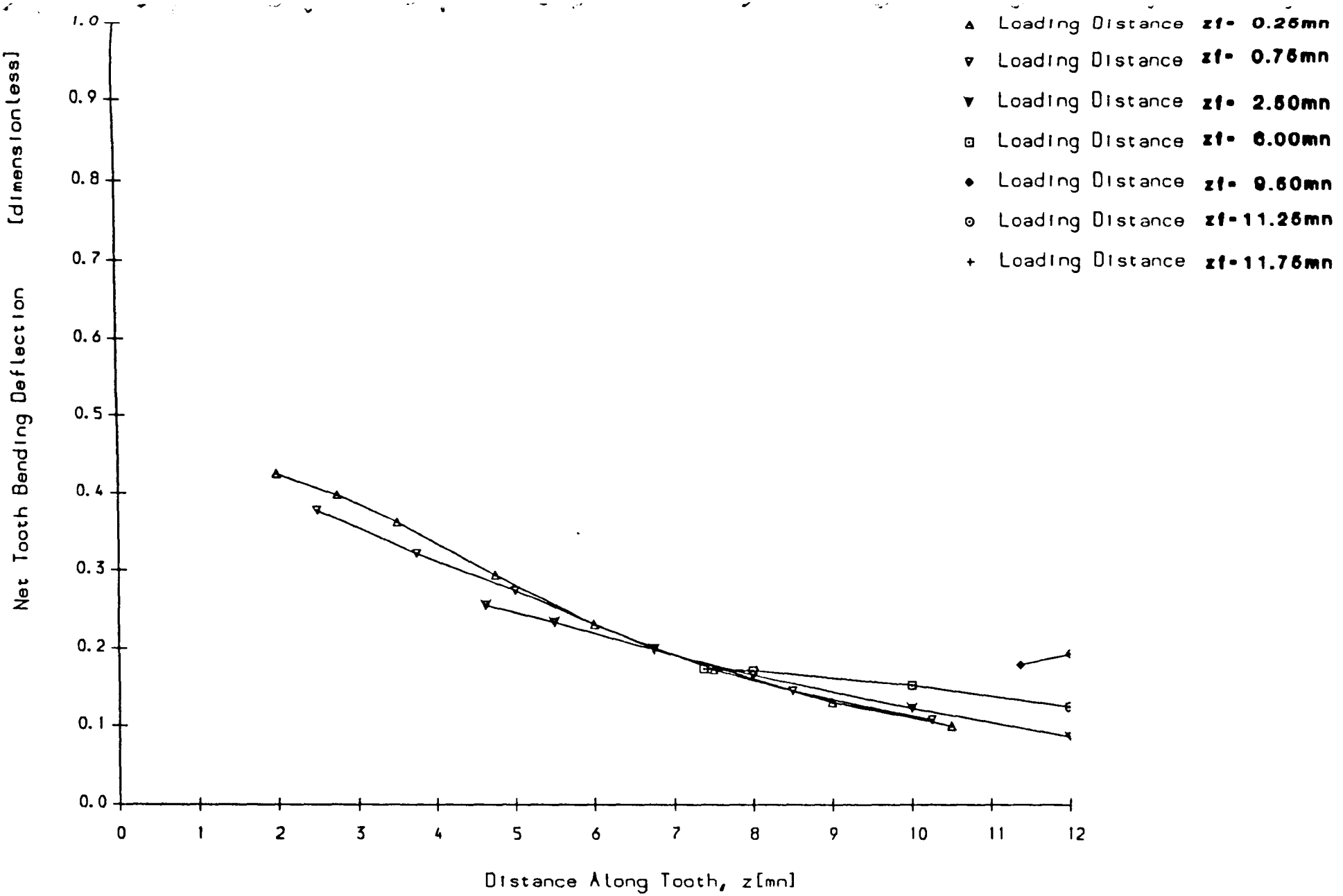

Fig. 2.31 F.E. Preceeding Tooth Net Bending Deflection Curves, ry=230.940mm **Z=40**

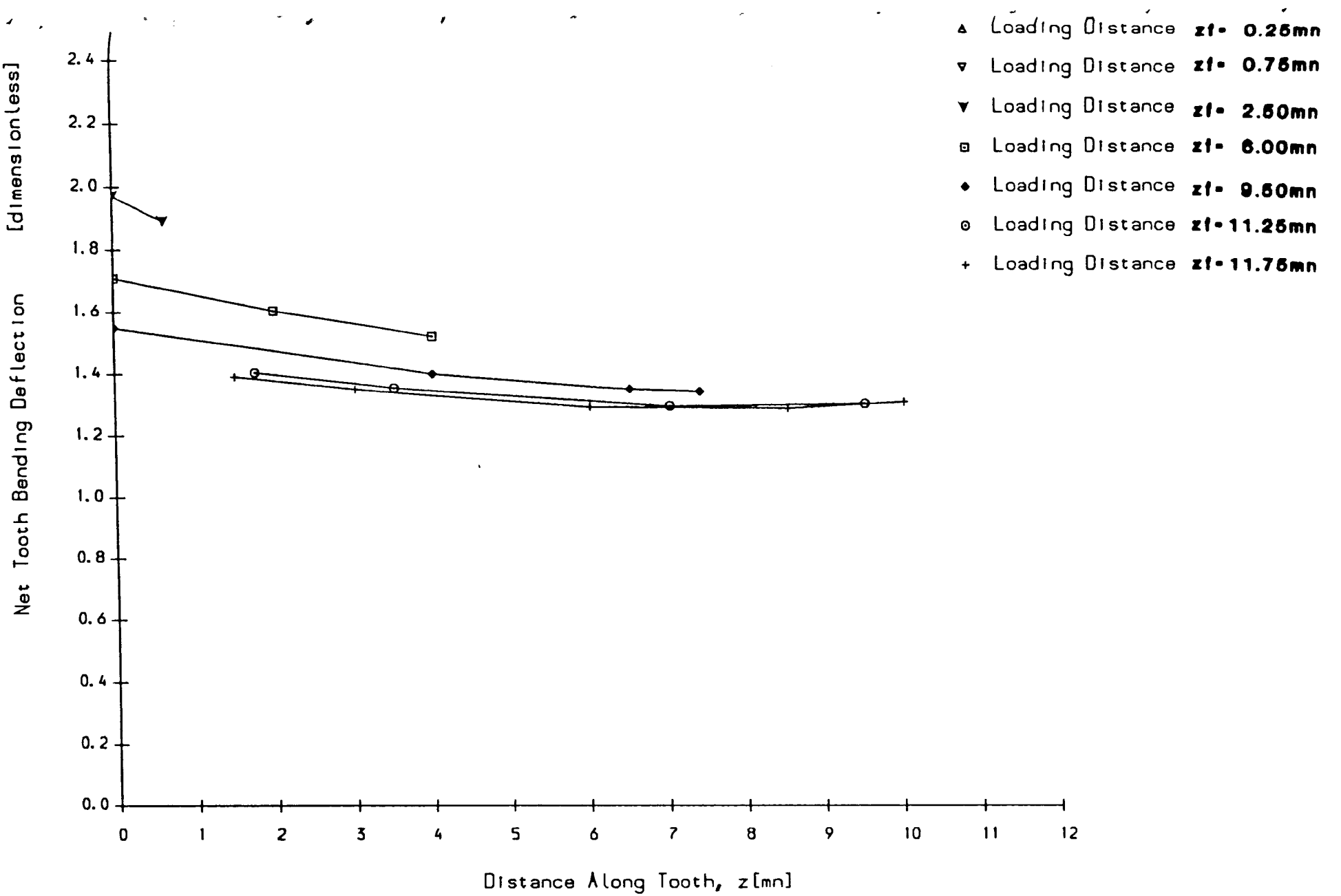

Fig. 2.32 F.E. Succeeding Tooth Net Bending Deflection Curves, ry=577.350mm **Z=100**

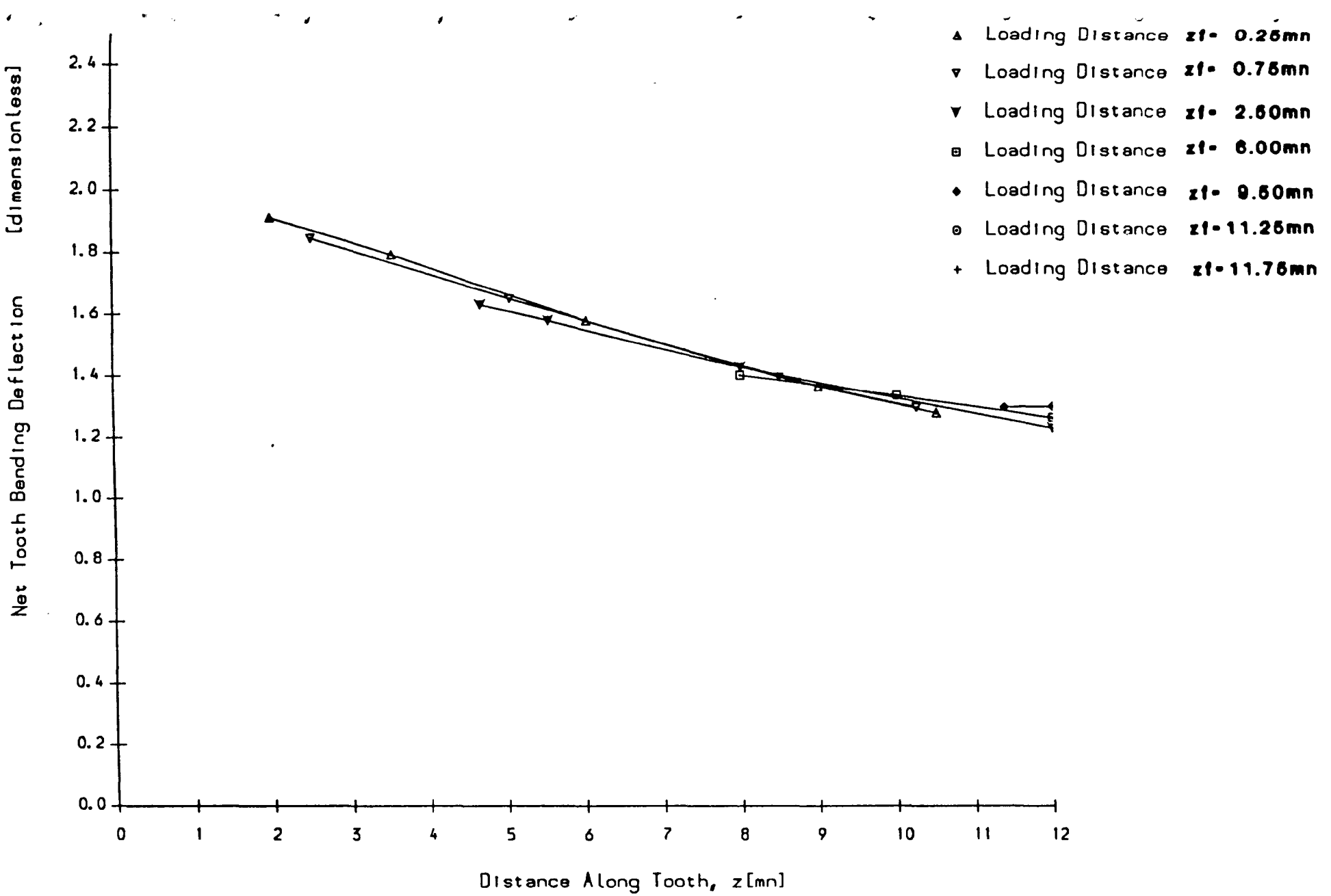

Fig. 2.33 F.E. Preceeding Tooth Net Bending Deflection Curves, ry=577.350mm **Z=100**

$(K_{tb})_{adj}$ (Eq. 1.63) has also been modified to apply to helical gears.

2.6.2 Curve Fitting of Loaded Tooth Deflections

To determine the best form of the function 'F' for helical gears, attempts were first made to fit the F.E. loaded tooth deflection results given in Figs 2.38 to 2.40 by exponential functions of the type proposed by Steward and given in Eq. 1.60. Best fit values of the function coefficients C_{fi} were determined by minimising the mean squared error between the actual F.E. data points and the exponential approximation, for each value of r_f, z_f and z, by using the non-linear optimisation software developed by Steward for this purpose.

However, Steward's function (Eq. 1.60) gave very poor fits for $F(\bar{z},r_f)$, since, as shown in Fig. 2.34, the master function $F(\bar{z},r_f)$ for helical gears is non-symmetric with respect to the point z_f, and cannot be approximated well by a symmetric function of the type which fitted Steward's spur gear results so well.

This assymmetry is caused partly by the axial component of the tooth load, which not only causes localised axial deflections of the tooth, but also 'tips' it (Fig. 2.34) due to bending of the gear body. This tipping effect increases as the gear diameter is increased as shown in Figs. 2.35, 2.36 and 2.37 for the 18, 40 and 100-tooth gears. A further cause of assymmetry in the $F(\bar{z},r_f)$ function is the oblique position of the contact lines on the tooth flank. Points p(z,r) on one side of the loaded point $p(z_f,r_f)$ are thus higher up the teeth than the loaded point, and so tend to deflect more, while points on the other side are lower down the teeth than the loaded point and so deflect less.

To allow for this effect and the additional gear body deflection caused by the axial component of the load, equation 1.60 was modified to give

$$F(\bar{z},r_f) = C_{f1}\cdot\left[e^{-C_{f2}\cdot|\bar{z}|-C_{f6}\cdot\bar{z}} - C_{f3}\cdot e^{-25.|\bar{z}|}\right]+C_{f4}+C_{f5}\cdot\bar{z} \qquad 2.5$$

where the term $C_{f5}.\bar{z}$ allows for the additional 'gear body' deflection at points far from the loaded point, and the terms in C_{f2} and C_{f6} allow for the slight assymmetry of the master curves on each side of z_f (i.e. for positive and negative values of $\bar{z} = z-z_f$). It is worth mentioning at this point that the term $C_{f5}.\bar{z}$ will give unrealistically large values of $F(\bar{z},r_f)$ as $\bar{z}$ approaches infinity, so that for <u>very</u> wide gears (perhaps >

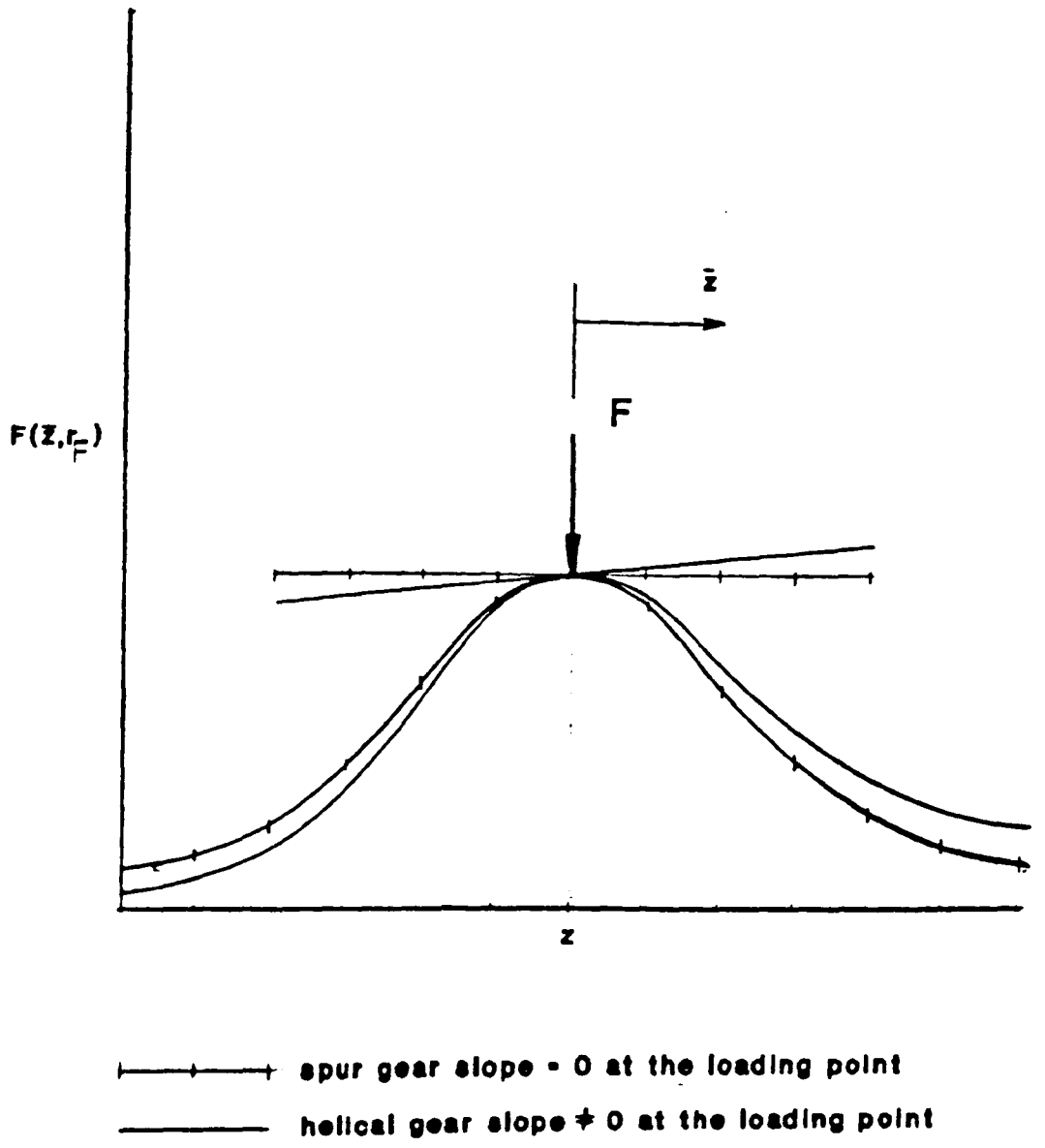

Fig. 2.34 Tipping Effect Apparant in Helical Gears

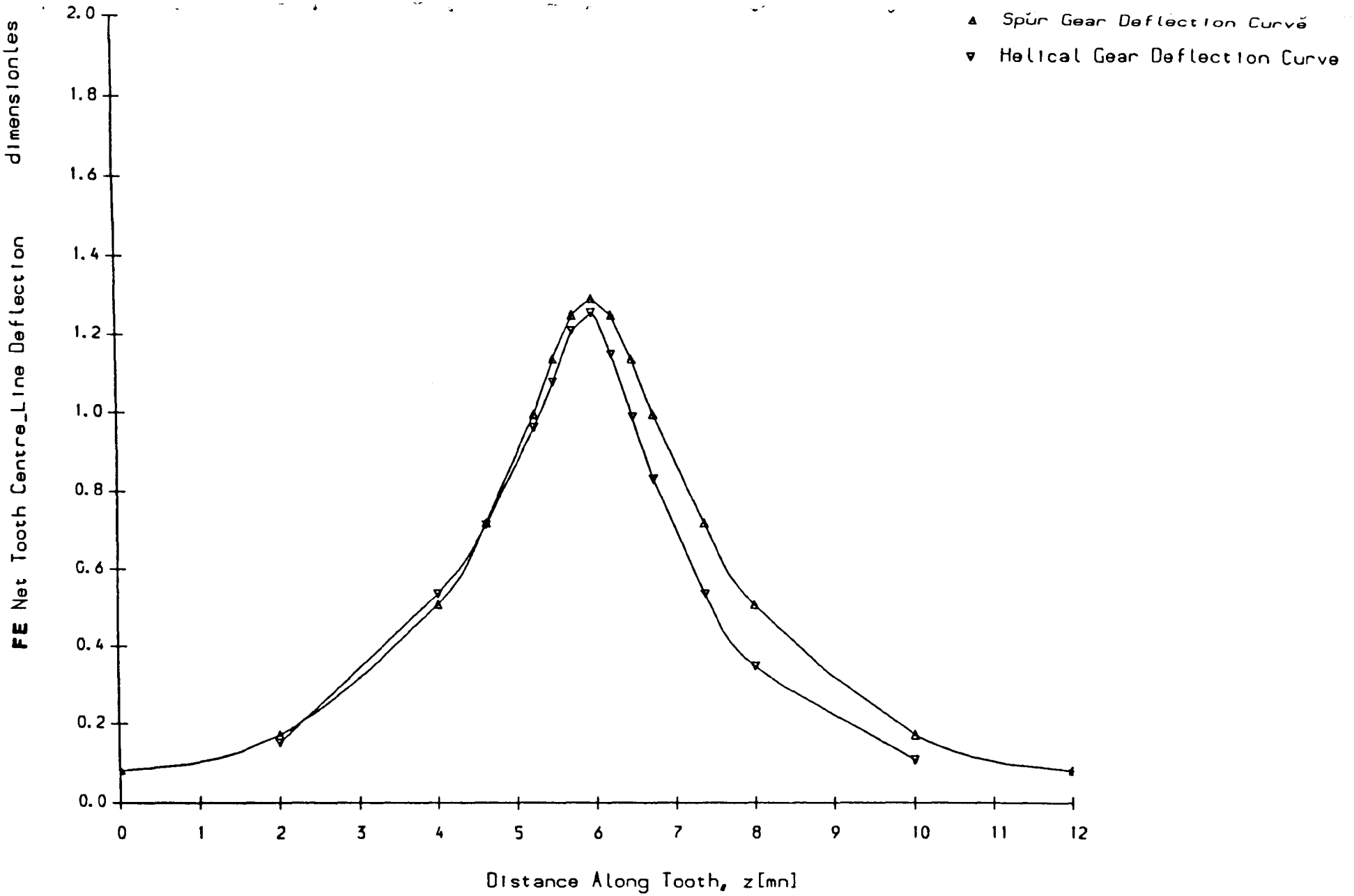

Fig. 2.35 Tipping Effect Shown For the 18 Tooth Gear at Ref. dia. loading

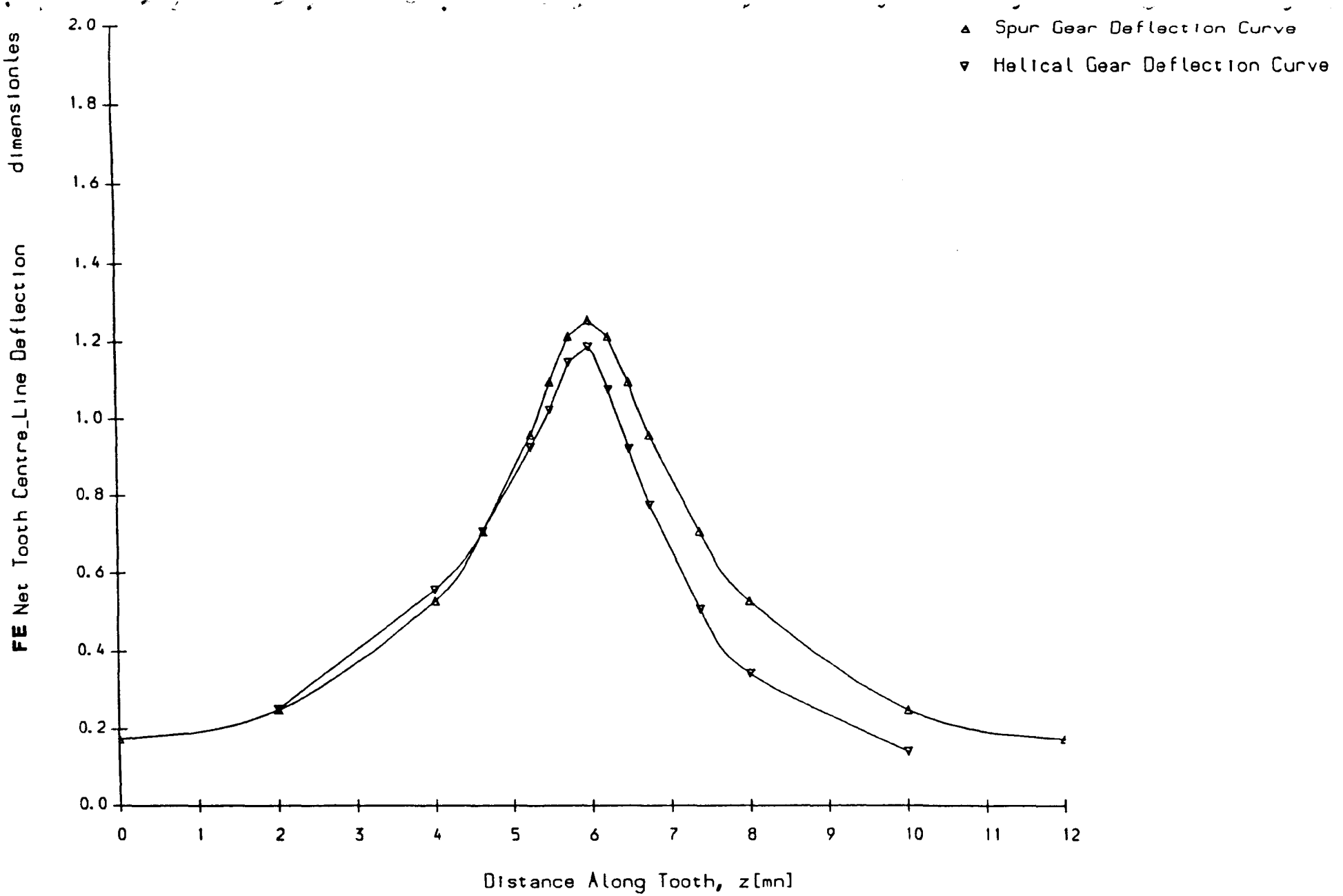

Fig. 2.36 Tipping Effect Shown For the 40 Tooth Gear at Ref. dia. loading

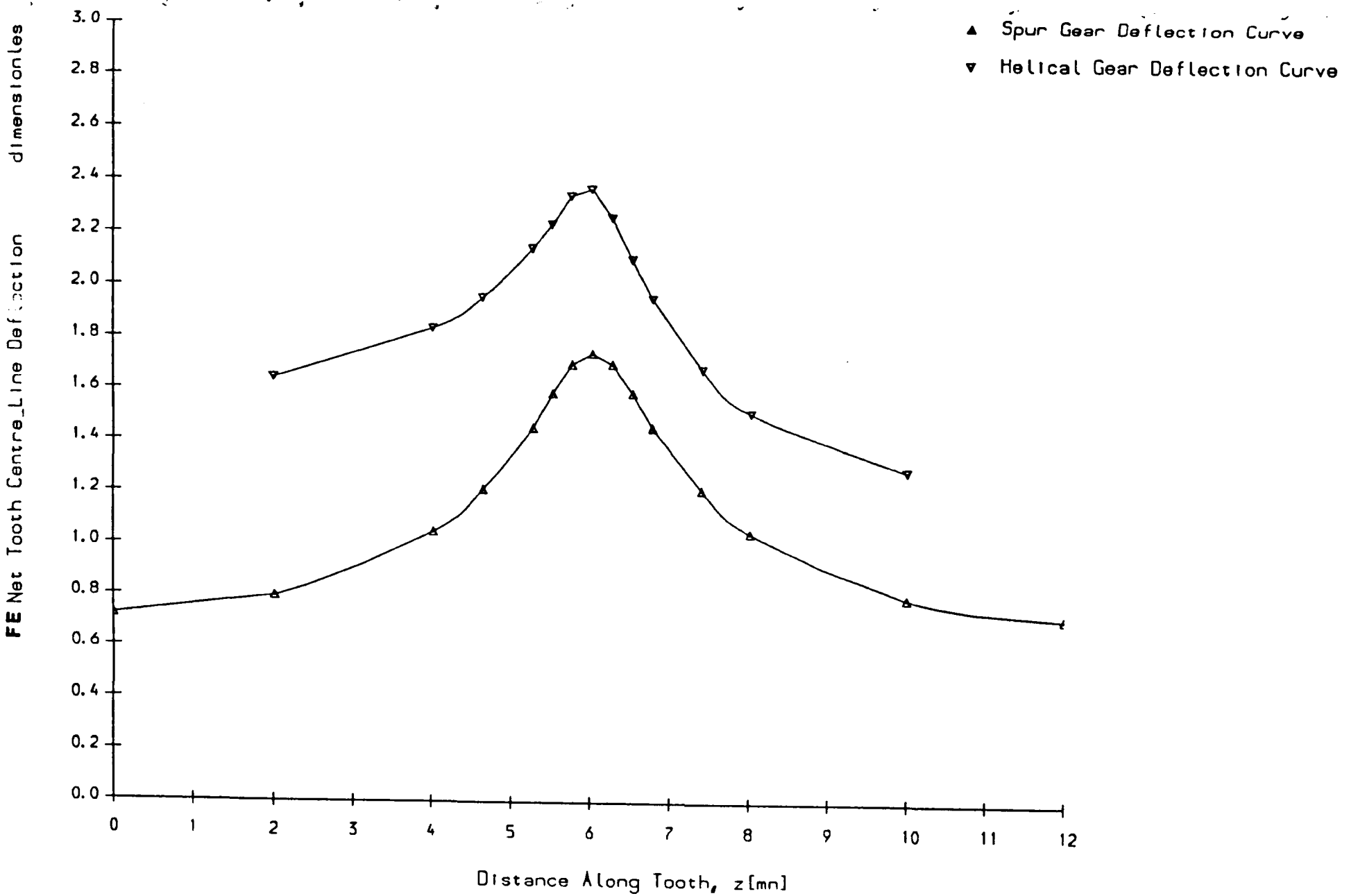

Fig. 2.37 Tipping Effect Shown For the 100 Tooth Gear at Ref. dia. loading

15 m_n), it might be sensible to replace $C_{f5}.\bar{z}$ by a 'slow' negative exponentail factor (such as $C_{f5}.e^{-\bar{z}/10}.\bar{z}$). This option was not pursued, since no data was available for wider gears.

As in Steward's attempts to curve-fit the function $F(\bar{z},r_f)$ using equation 1.60, the results from equation 2.5 were found to be very insensitive to the value of the second exponent ($-25.1\bar{z}1$). So this value was retained as in equation 1.60.

Next, considering the non-master (end-effect) function 'G', the symmetric form used by Steward (Eq. 1.61) for spur gears was again modified to apply to helical gears, where symmetry is, in this case, destroyed by the different flexibility at the 'sharp' and 'blunt' ends of the tooth (Fig. 2.10a). Different 'end-effect' terms were thus required for each end of the tooth, so equation 1.61 was modified to give

$$G(z,r_f) = C_{g1} + C_{g2}.\, e^{-C_{g3}.z} + C_{g4}.\, e^{-C_{g5}.(b-z)} \qquad 2.6$$

The second and third terms vanish at points sufficiently far from the tooth ends, and since equation 1.57 must then reduce to the master function $F(\bar{z},r_f)$ it follows that $C_{g1} \cong 1.0$ is required.

Neverthless, C_{g1} was retained as a 'free' coefficient in the curve fitting optimisation, to improve the quality of fit. Note that, from equations 1.61 and 2.5, for spur gears, $C_{g2} = C_{g4}$ and $C_{g3} = C_{g5}$.

Figs. 2.38 to 2.40 show a comparison between the master curve fitting function of equation 2.5 and the mid-face values (at $z_F = 6.0m_n$) from the F.E. analysis for reference diameter loading for the 18, 40 and 100-tooth gears. The fit achieved using equation 2.6 is clearly excellent.

Figs. 2.41 to 2.61 show a comparison between the overall fitting equation (Eq. 1.57), which combines the 'F' and 'G' functions to give the fitted tooth compliance K_{tb}, and the original F.E. values at reference diameter loading for the 18, 40 and 100-tooth gears already given in Figs. 2.13, 2.18 and 2.23. The results for the other radial loading positions were not shown due to space limitations, but show equally good agreement with the F.E. data.

To improve the accuracy of the fits obtained, it seemed worthwhile to separate out the 'gear body' compliance components (represented by $C_{f4} + C_{f5}.\bar{z}$ in Eq. 2.5) from the gear tooth master function $F(\bar{z},r_f)$ in equation 1.57. This reduces equation 2.5 to

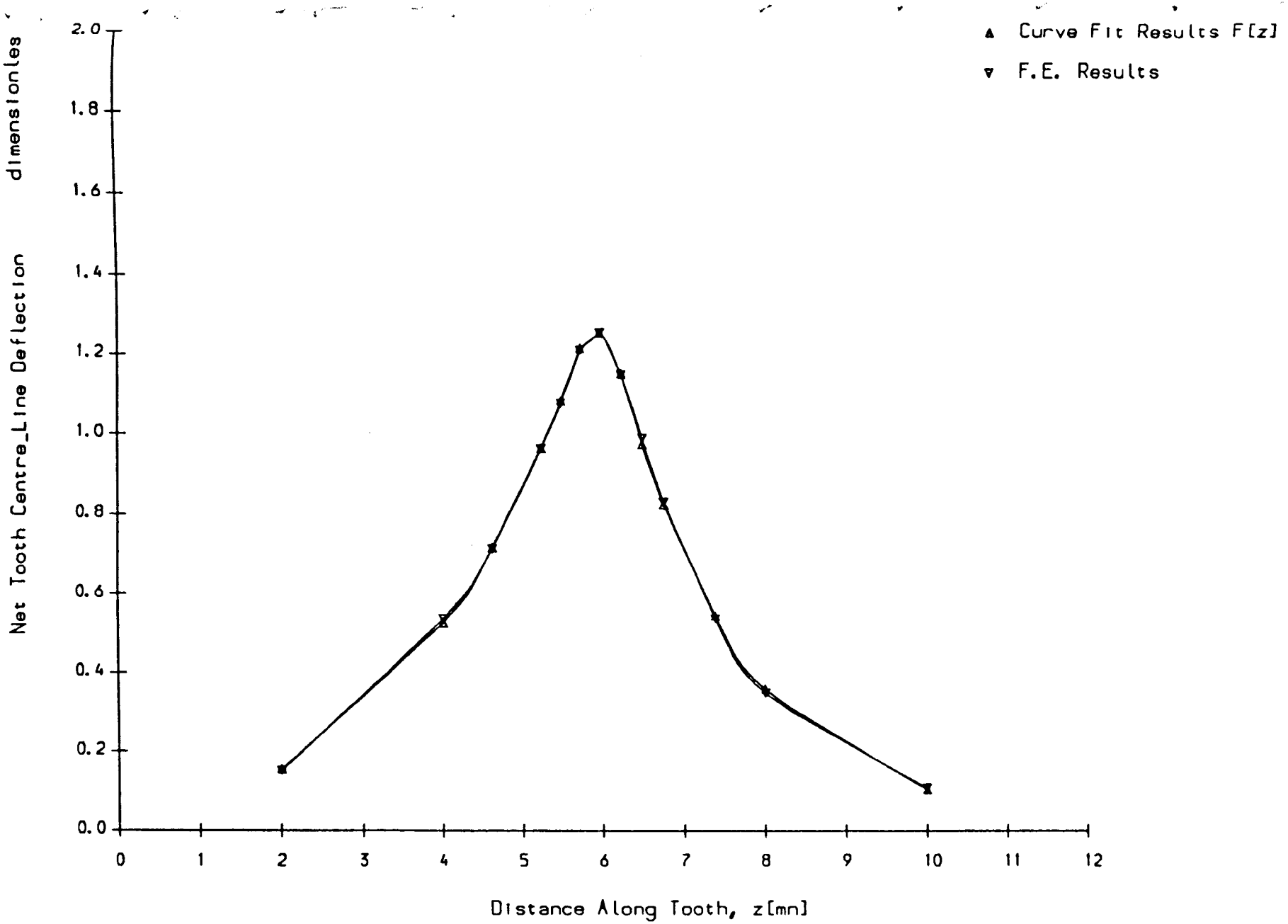

Fig. 2.38 Master Curve FE & Curve Fit Results at Ref. Dia. loading & **Z=18**

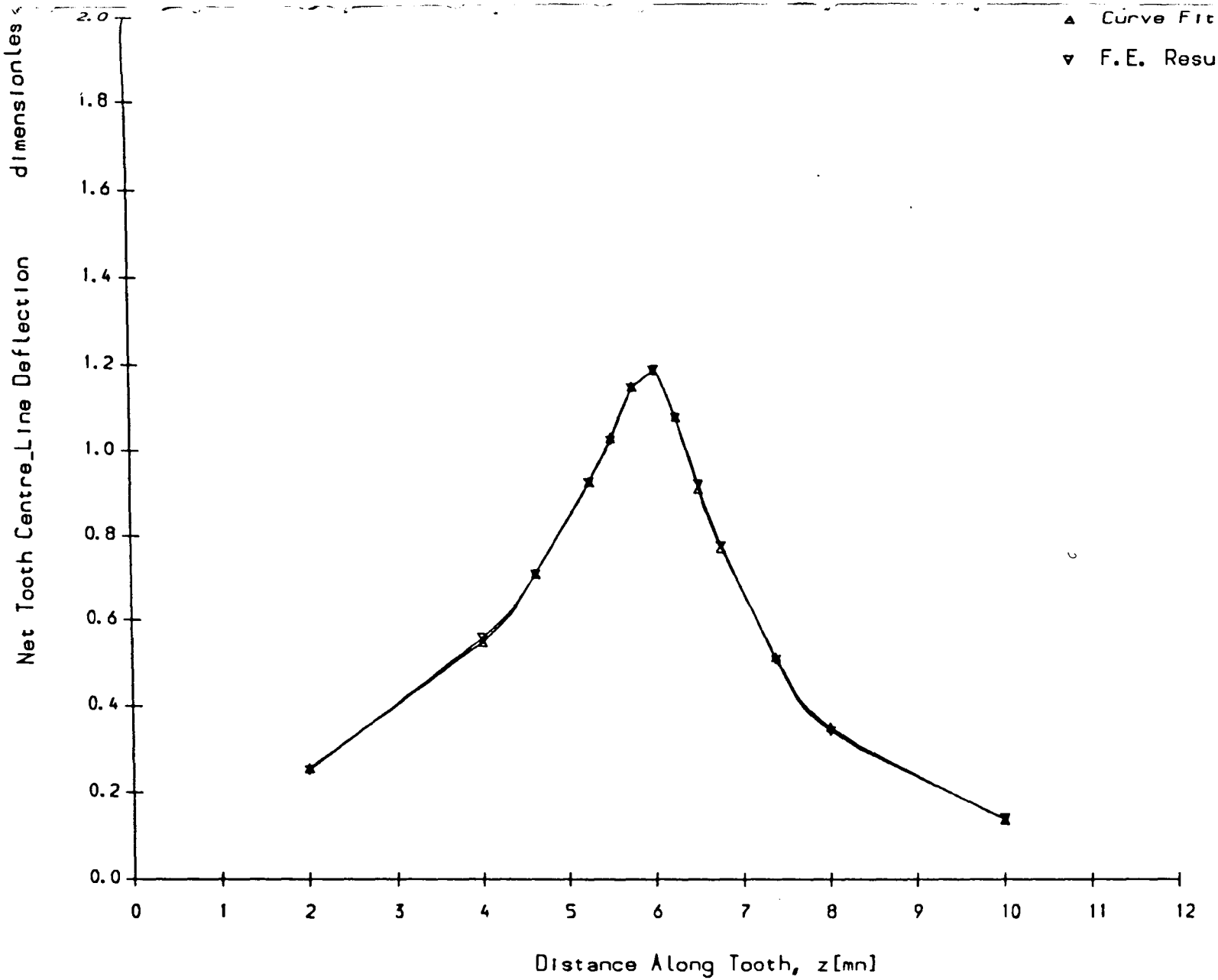

Fig. 2.89 Master Curve FE & Curve Fit Results at Ref. Dia. loading & **Z=40**

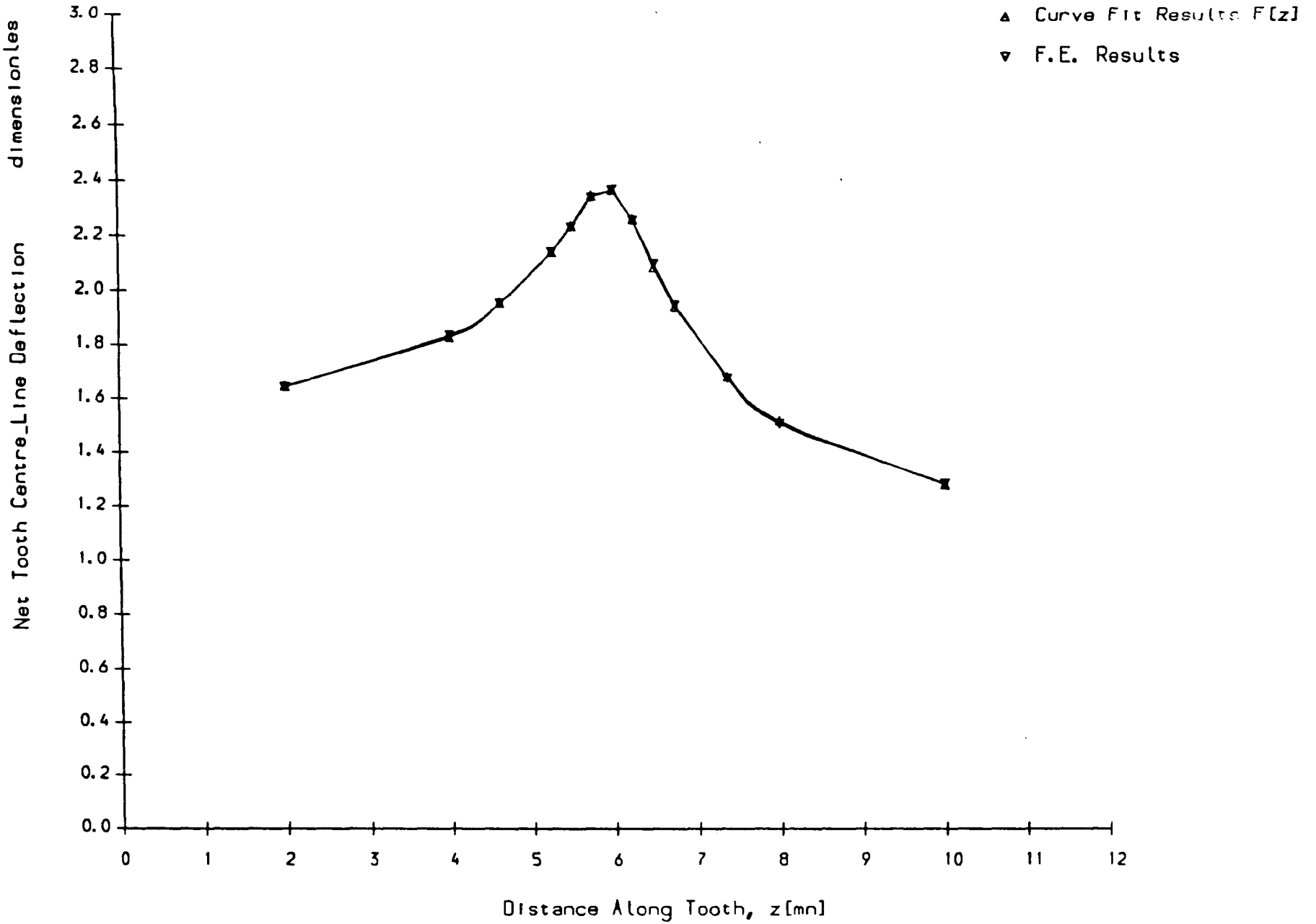

Fig. 2.40 Master Curve FE & Curve Fit Results at Ref. Dia. loading & **Z=100**

$$F(\bar{z},r_f) = C_{f1}\cdot\left[e^{-C_{f2}\cdot|\bar{z}|-C_{f6}\cdot\bar{z}} - e^{-25.|\bar{z}|}\right] \qquad 2.7$$

the 'gear body' deflection terms could then be added separately, to give (c.f. Eqn. 1.57)

$$K_{tb}(z_f,z,r_f) = [G(z_f,r_f).\ G(z,r_f)]^{\frac{1}{2}}\ .\ F(\bar{z},r_f)+C_{f4}+C_{f5}.\bar{z} \qquad 2.8$$

This seems more reasonable, since the gear body terms are not then 'modified' by the tooth 'end effect' function $[G(z_f,r_f).G(z,r_f)]$. Note however, that in this form $K_{tb}(z_f,z,r_f)$ would no longer precisely satisfy equation 1.66.

The whole optimisation procedure described earlier was repeated using equations 2.7 and 2.8, and new values for the coefficients $C_{f\tilde{i}}$ and $C_{g\tilde{i}}$ and the fit values of $K_{tb}(z_f,z,r_f)$ were obtained and compared with the F.E. results represented in Figs. 2.11 to 2.25.

For small numbers of teeth (z = 18,40), the gear body terms are small, and the fit results differed insignificantly from those given by equations 1.57 and 2.5. For larger gears (z = 100) however, where the gear body compliance is greater, the fits obtained from equations 2.7 and 2.8 were marginally better than those shown in Figs. 2.55 to 2.61, especially at the tooth ends. This suggests that it would, in fact, be worthwhile to separate-out the gear body deflections as in Eqn. 2.8. This would also allow the inclusion of 'modified' gear body deflections for e.g. gears with a thin rim/web, etc.

In spite of this conclusion, it was nevertheless decided that the simpler equations 1.57 and 2.5 would be used to generate $K_{tb}(z_f,z,r_f)$ since they are fully compatible with Steward's equations for spur gear compliance, making interpolations between the two sources for the intermediate values of β much easier. It may, nevertheless, be worthwhile to try reprocessing Steward's data using equations analogues to equations 2.7 and 2.8 to obtain an even better fit. Unfortunately, there was insufficient time available to allow this.

It is worthwhile noting at this point that the equations for 'F' and 'G' above were developed based on loading the right side of line 'k' in Fig. 2.1 with the flexible end at $z_\ell(k)$ and the rigid one at $z_f(k)$. If the loading (or helix angle) is reversed, then the term $(\bar{z})$ must be replaced by $(-\bar{z})$ in the function 'F', and (z_f) and (z) should be replaced by $(b-z_f)$ and (b-z) in the function 'K_{tb}', effectively reversing

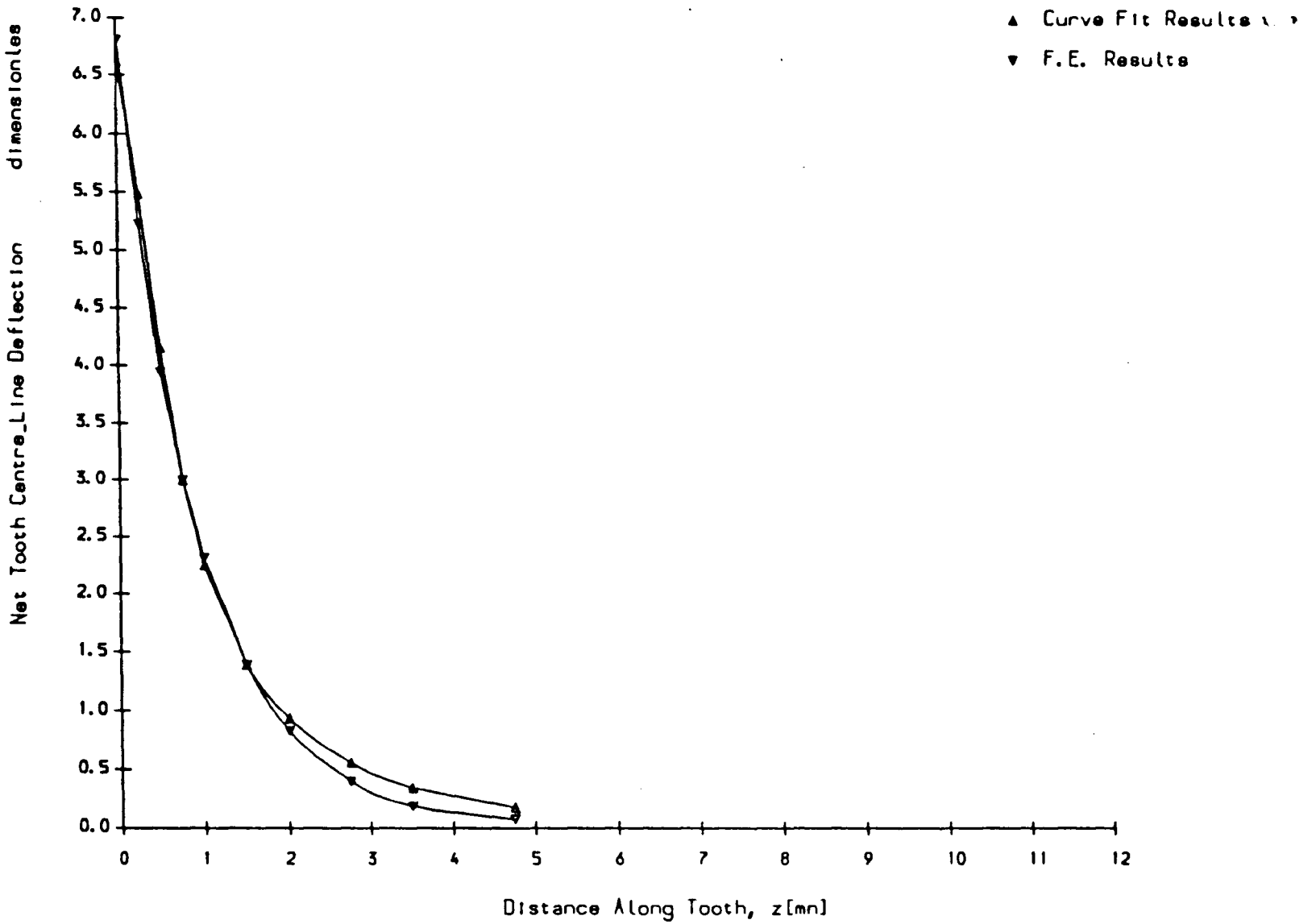

Fig. 2.41 Ktb for Loading at Ref Dia & zf=0.25mn, Z=18

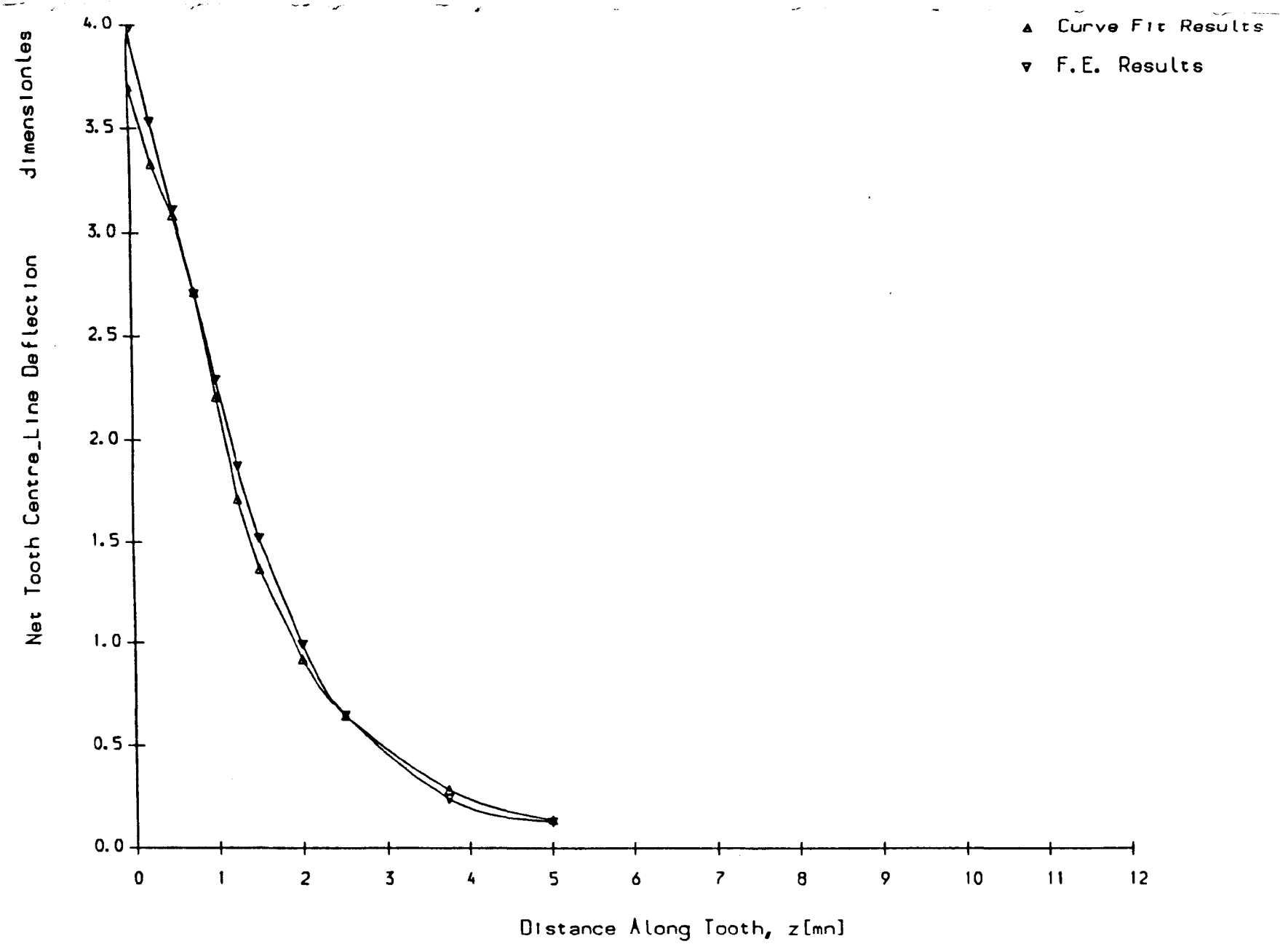

Fig. 2.42 Ktb for Loading at Ref Dia & zf=0.75mn, Z=18

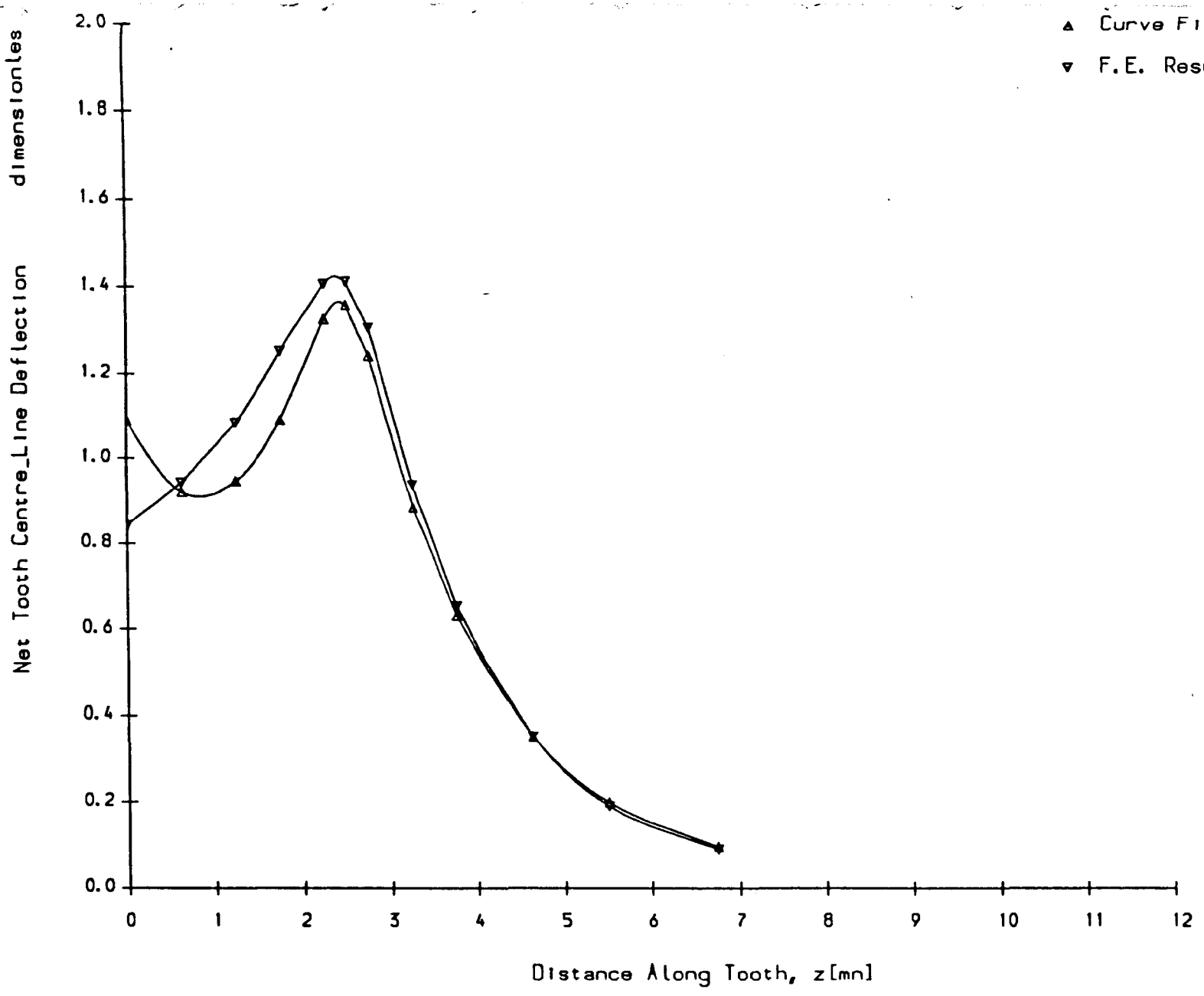

Fig. 2.43 Ktb for Loading at Ref Dia & zf=2.50mn, Z=18

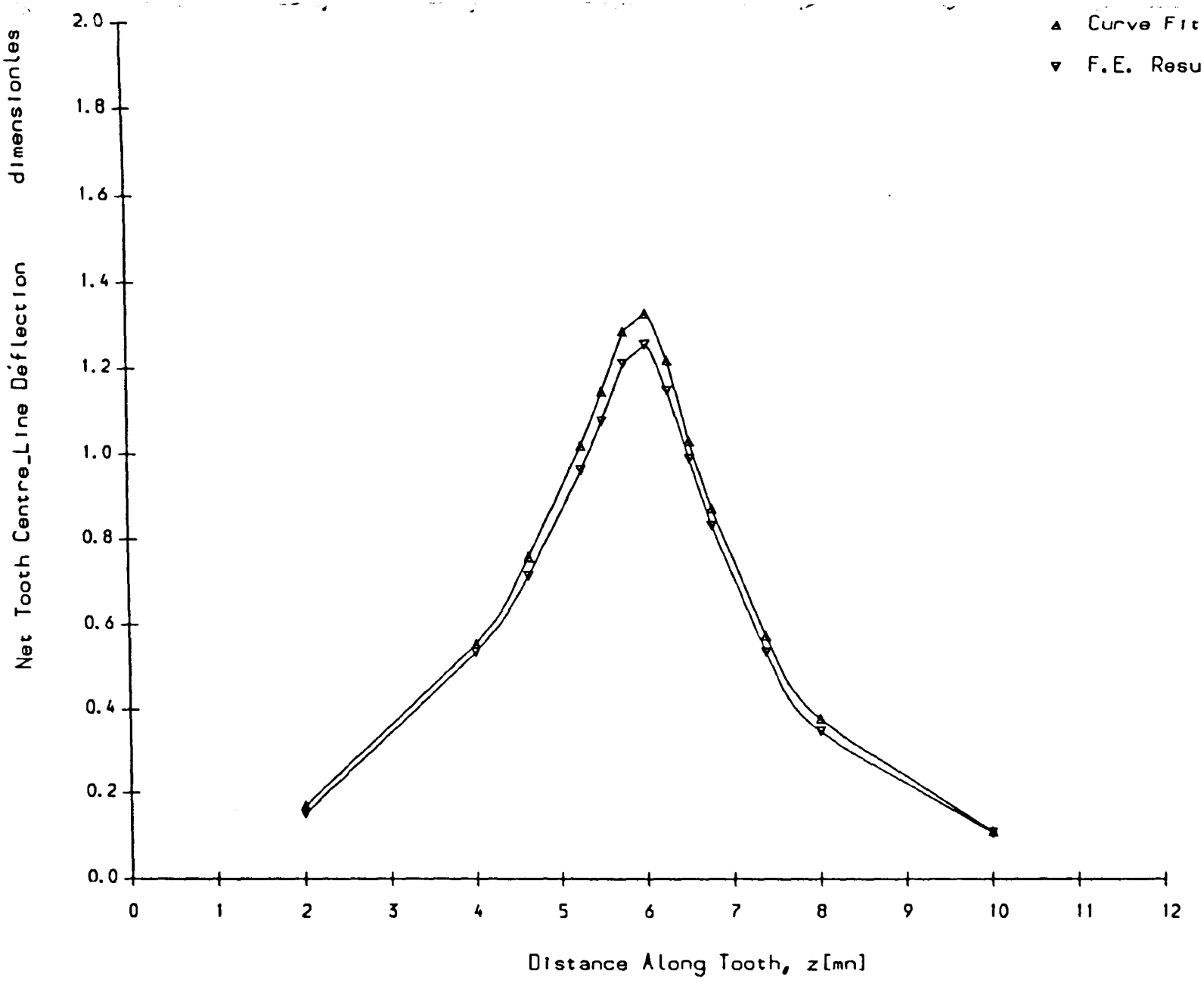

Fig. 2.44 Ktb for Loading at Ref Dia & zf-6.00mn, Z-18

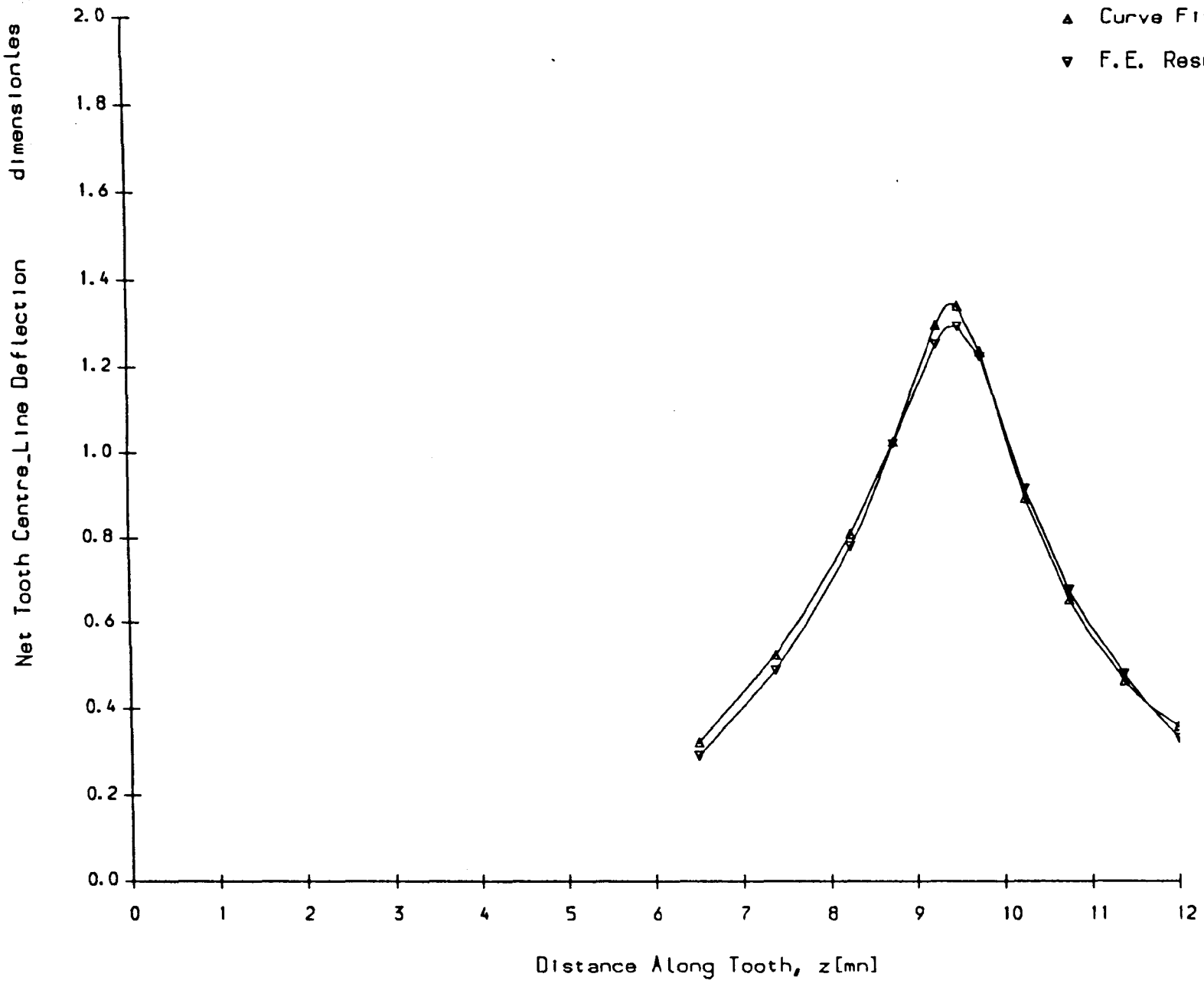

Fig. 2.46 Ktb for Loading at Ref Dia & z1=9.50mn, Z=18

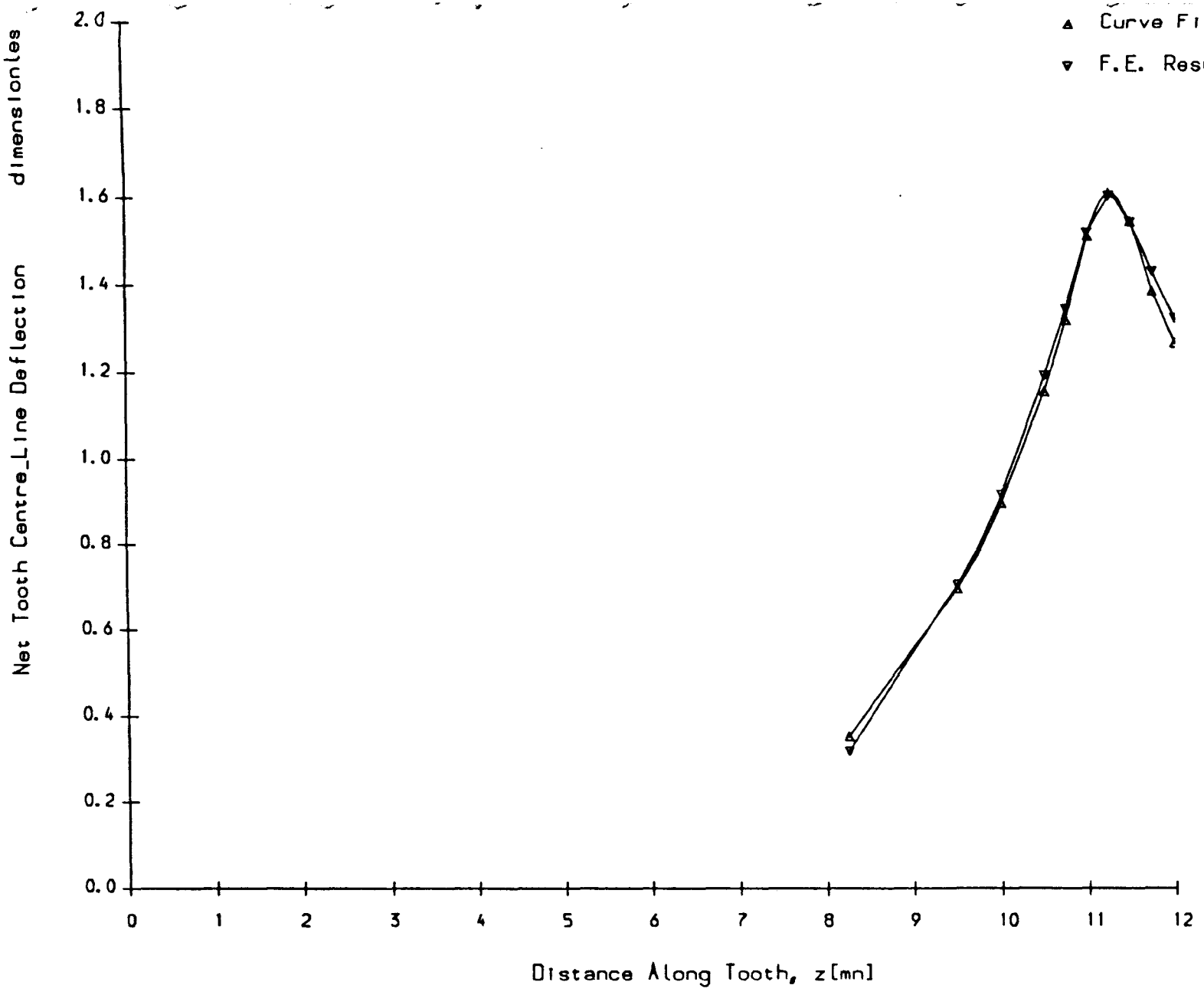

Fig. 2.46 Ktb for Loading at Ref Dia & zf=11.25mn, Z=18

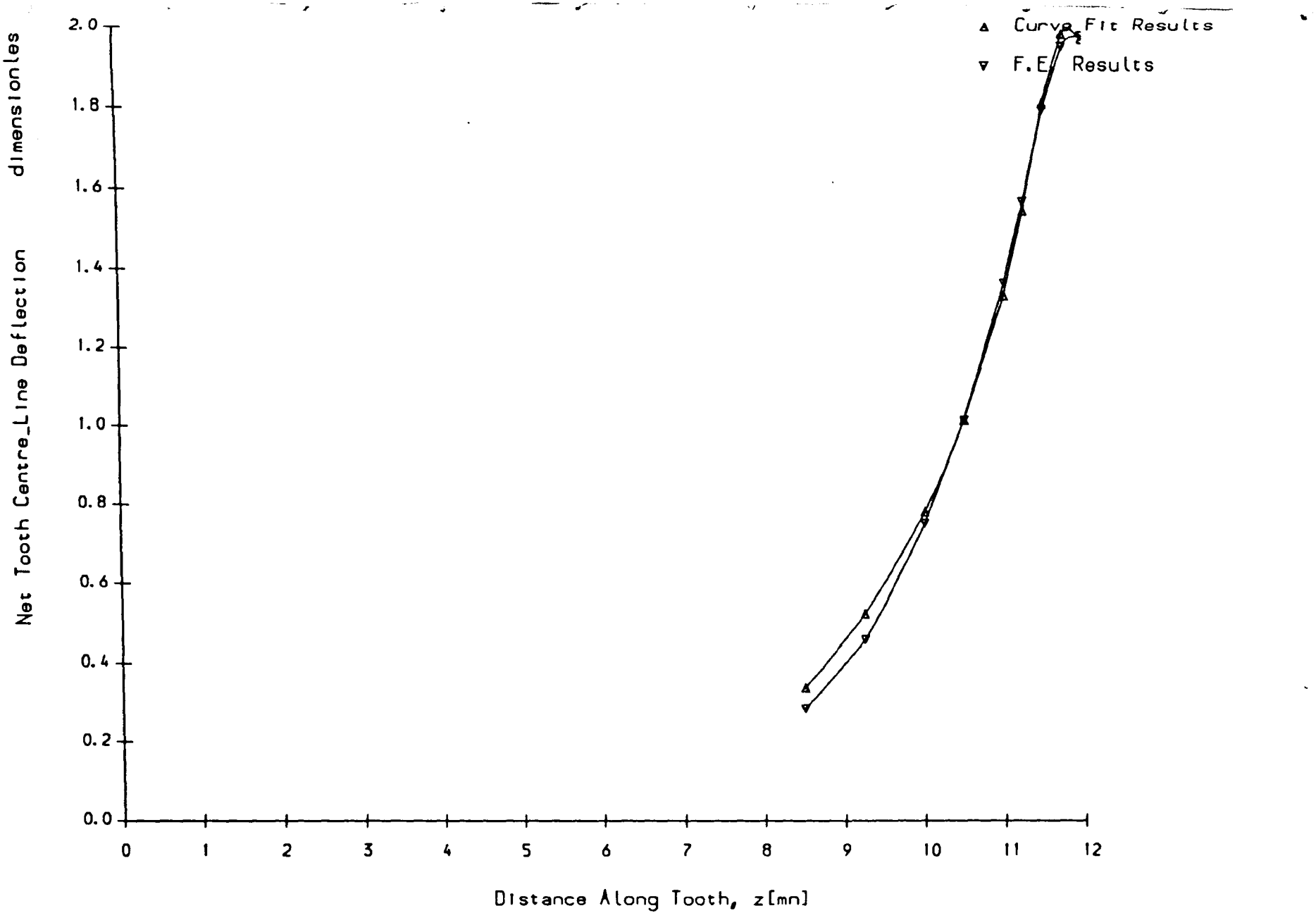

Fig. 2.47 Ktb for Loading at Ref Dia & zf=11.75mn, Z=18

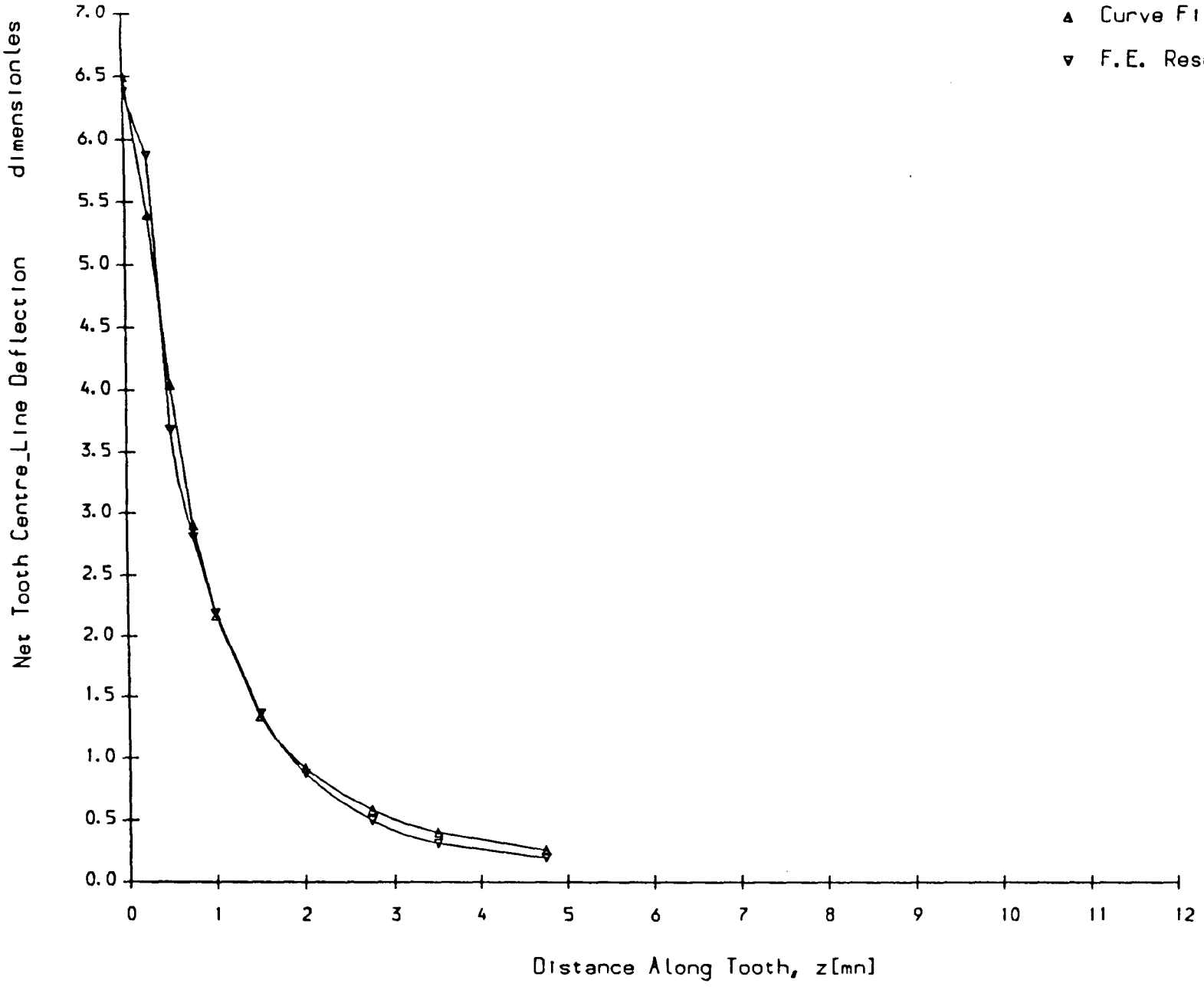

Fig. 2.48 Ktb for Loading at Ref Dia & zf=0.26mn, Z=40

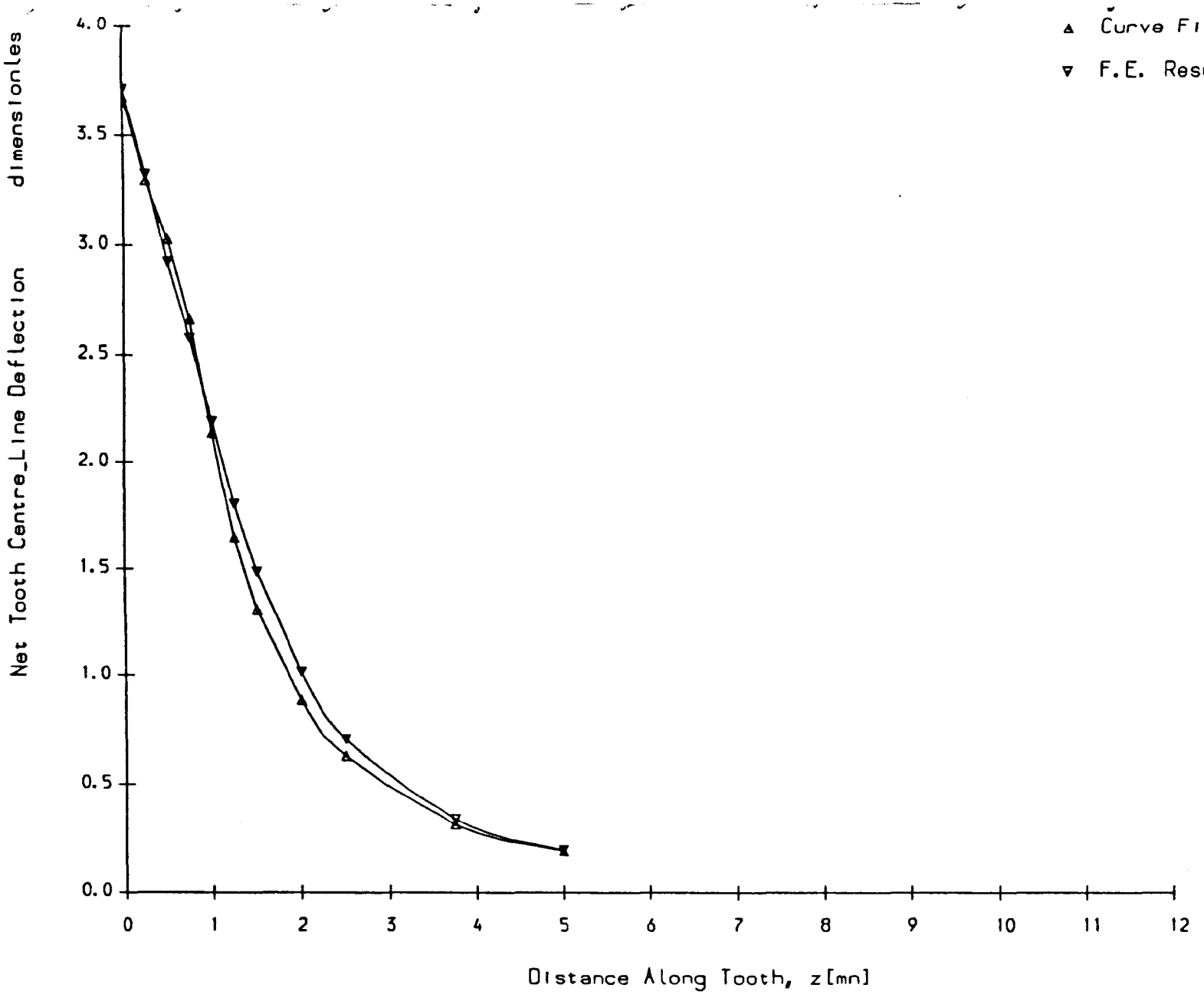

Fig. 2.49 Ktb for Loading at Ref Dia & zf=0.75mn, Z=40

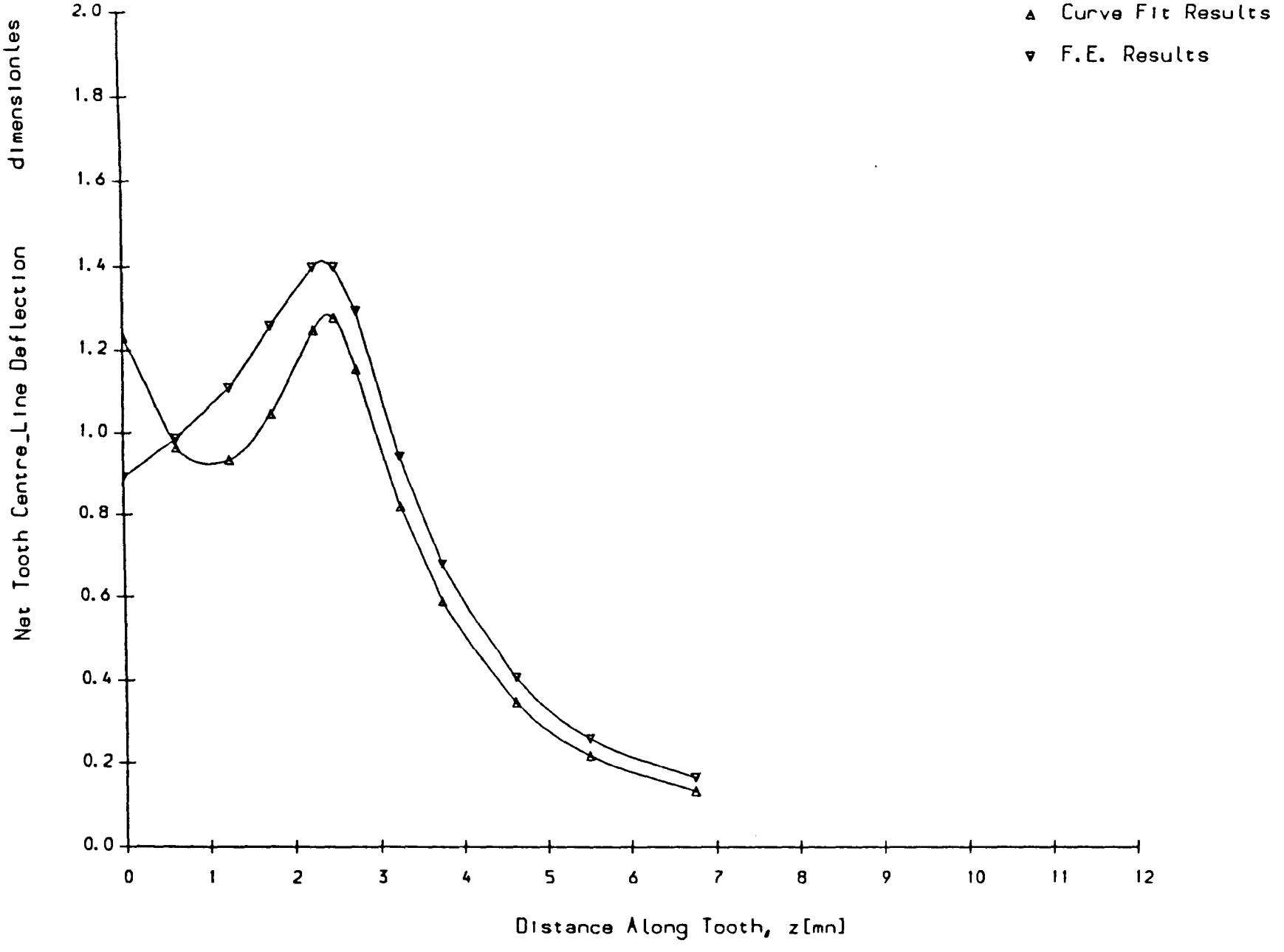

Fig. 2.50 Ktb for Loading at Ref Dia & zi-2.50mn, Z-40

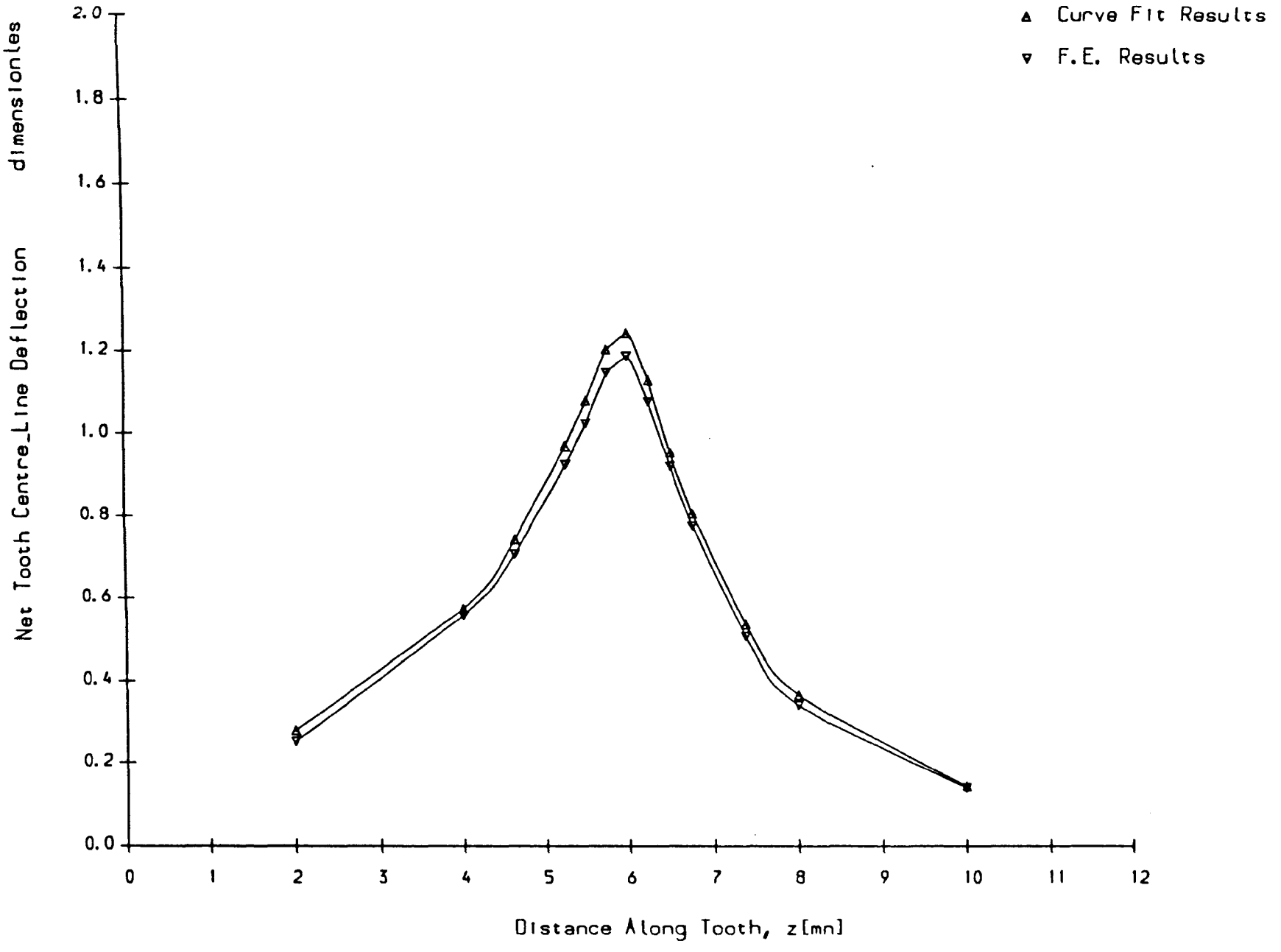

Fig. 2.61 Ktb for Loading at Ref Dia & zf=6.00mn, Z=40

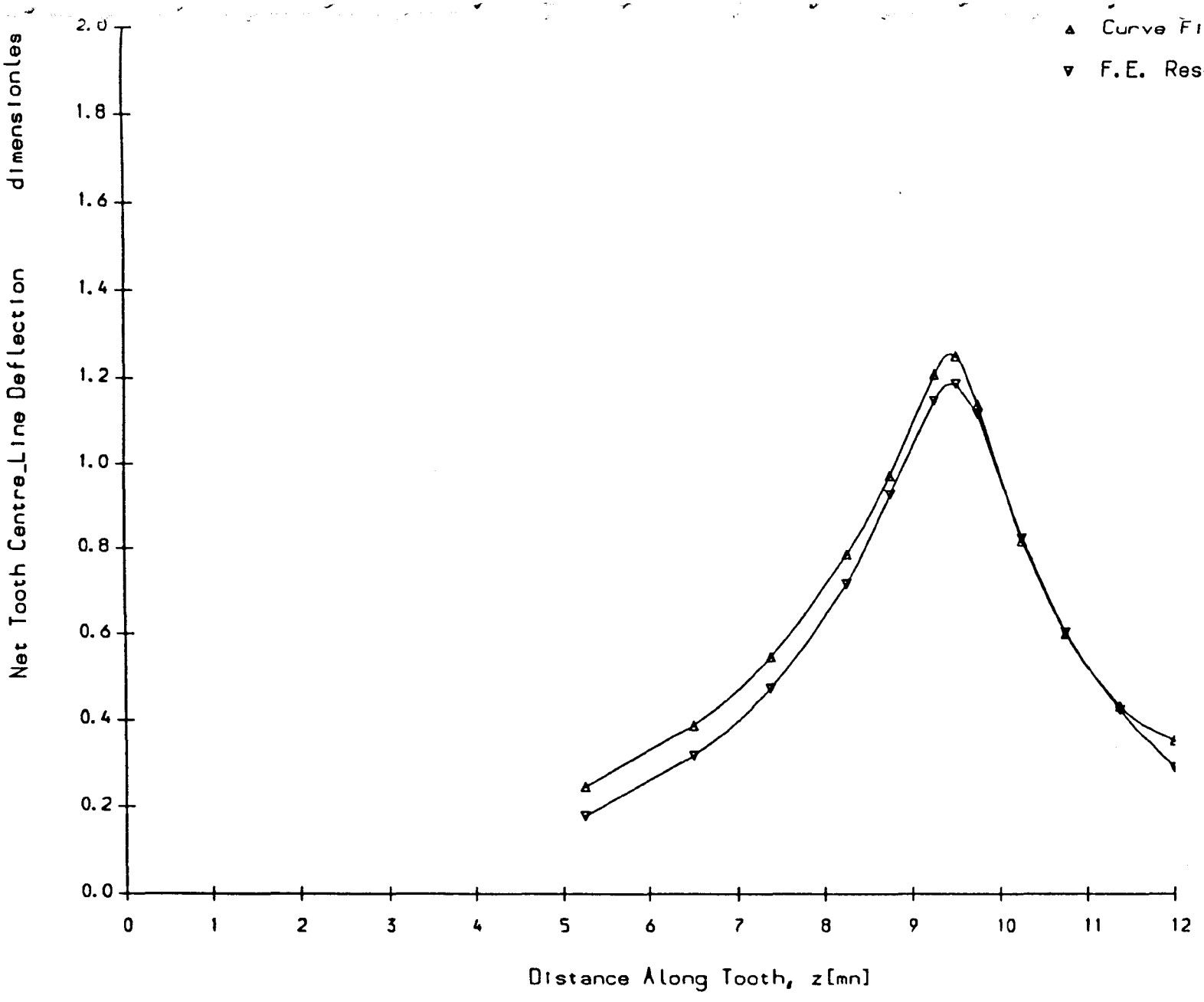

Fig. 2.62 Ktb for Loading at Ref Dia & zf=9.50mn, Z=40

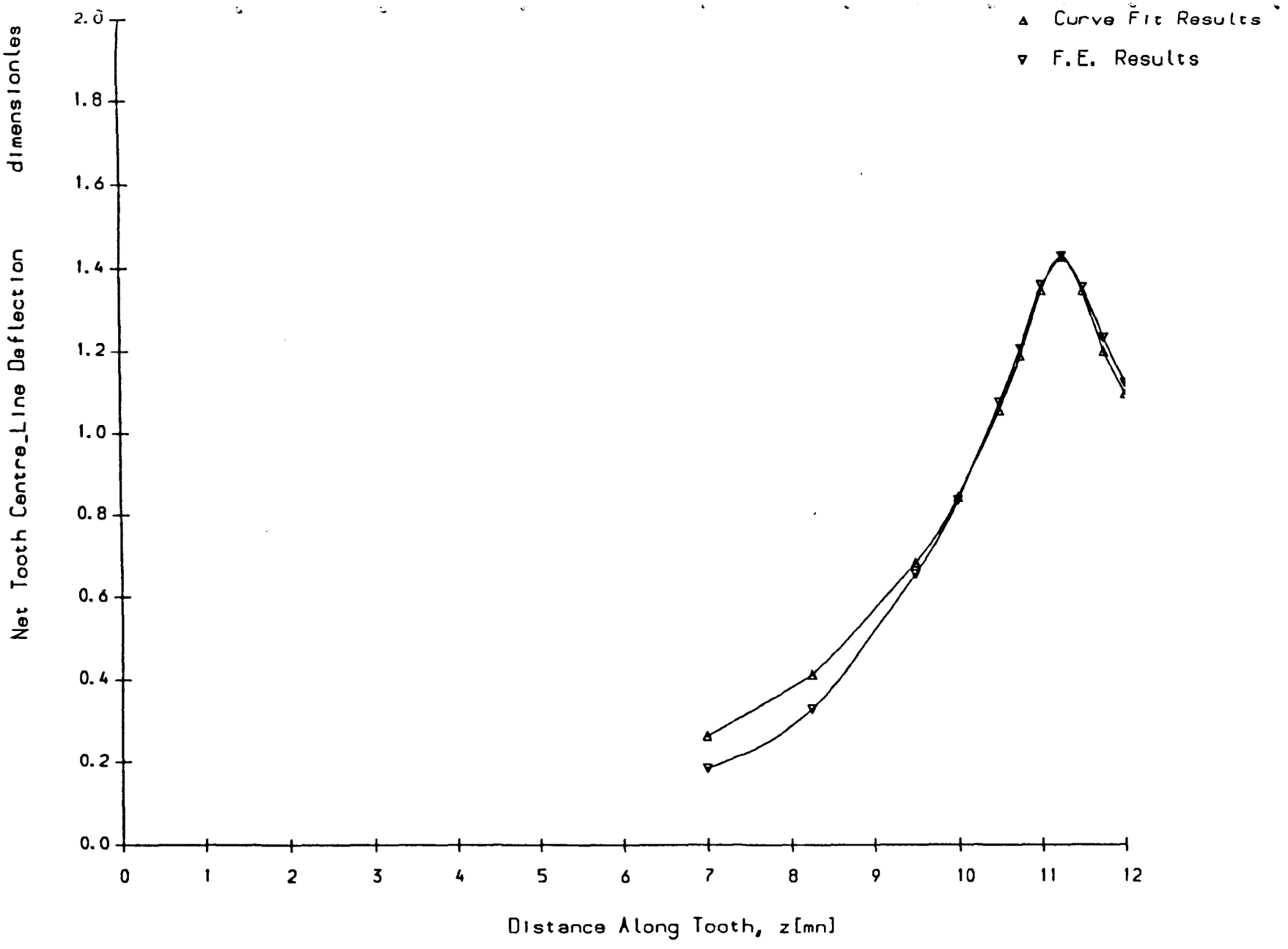

Fig. 2.68 Ktb for Loading at Ref Dia & zf=11.25mn, Z=40

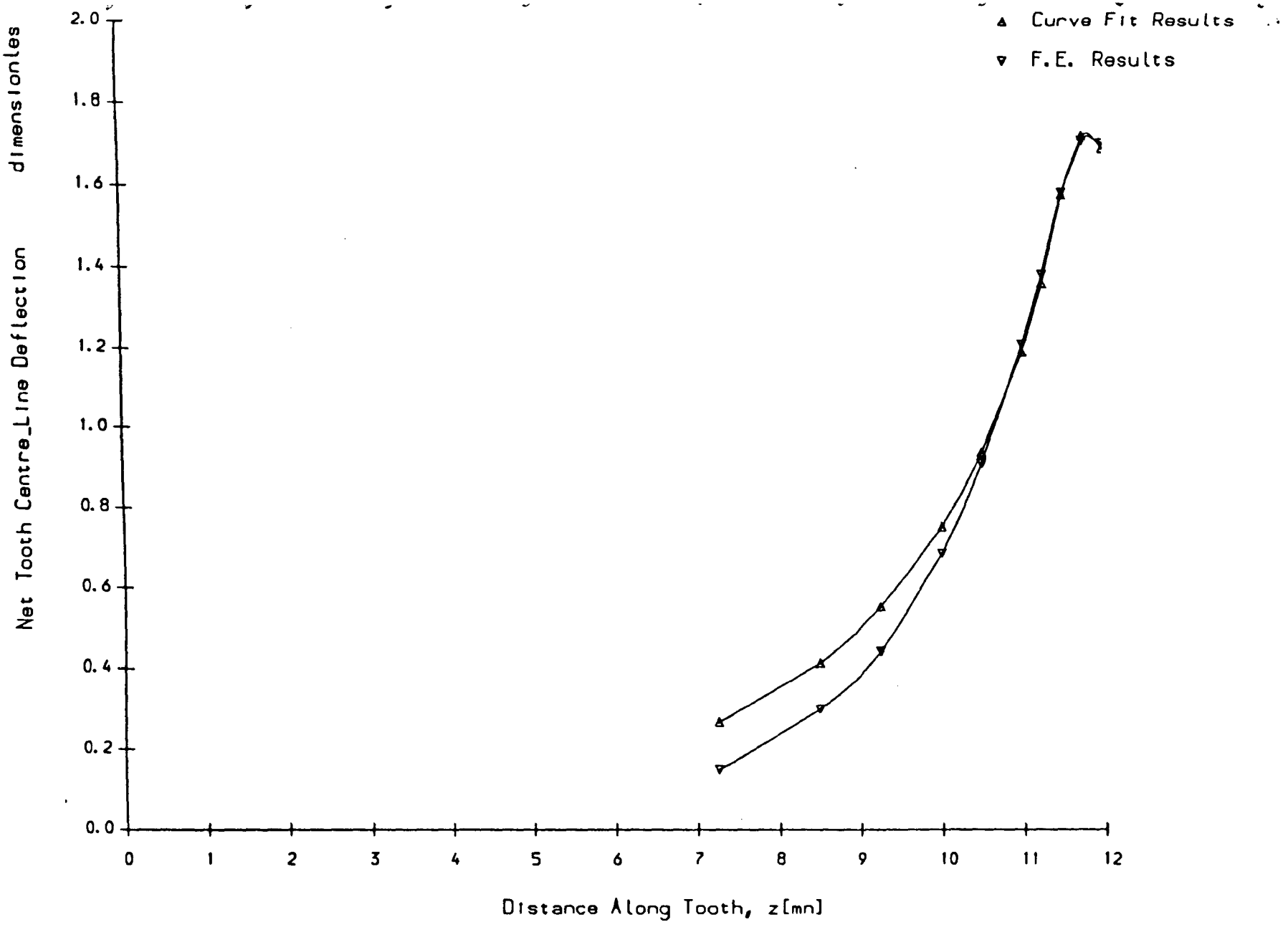

Fig. 2.64 Ktb for Loading at Ref Dia & zf=11.75mn, Z=40

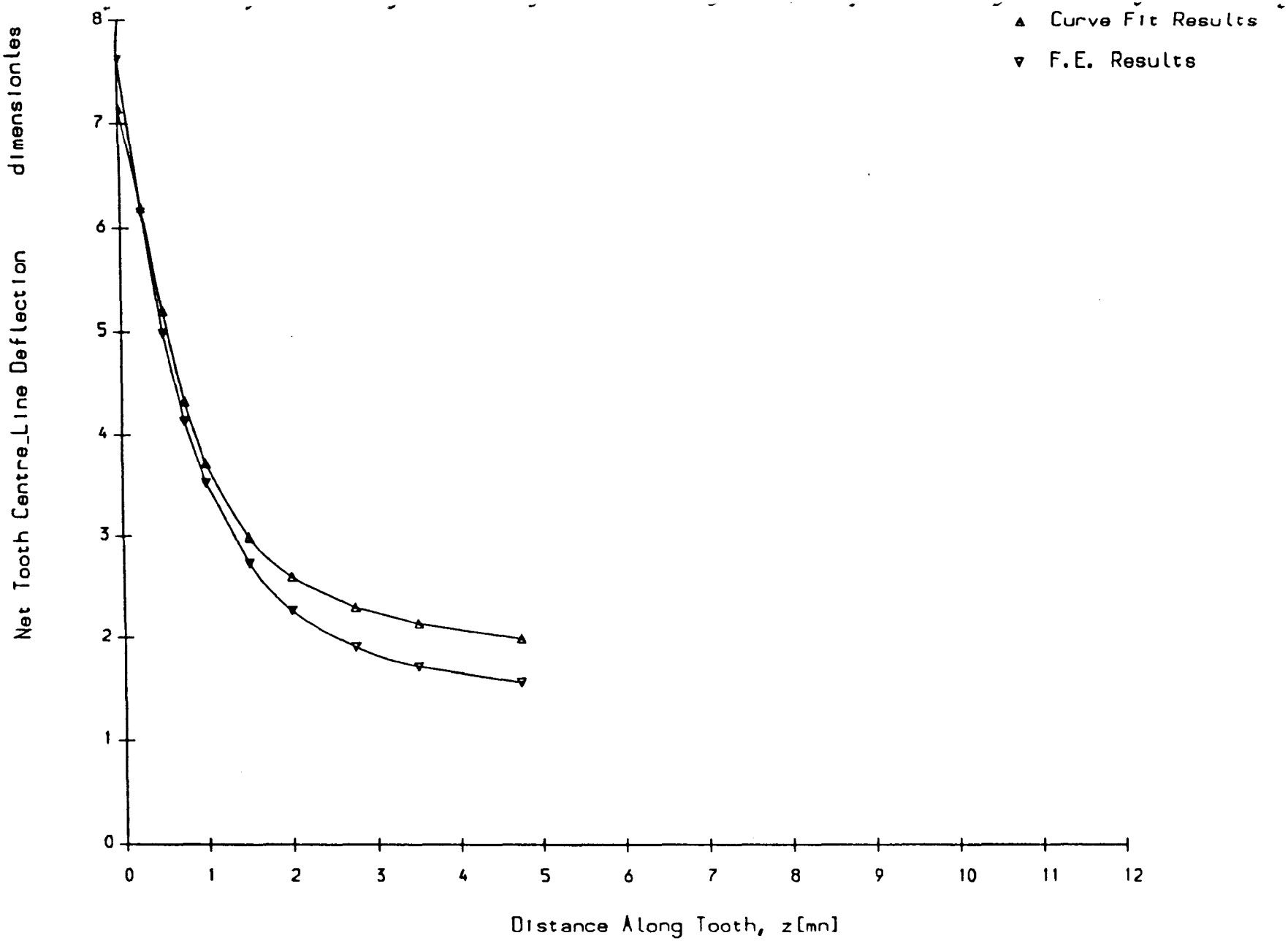

Fig. 2.55 Ktb for Loading at Ref Dia & zf=0.25mn, Z=100

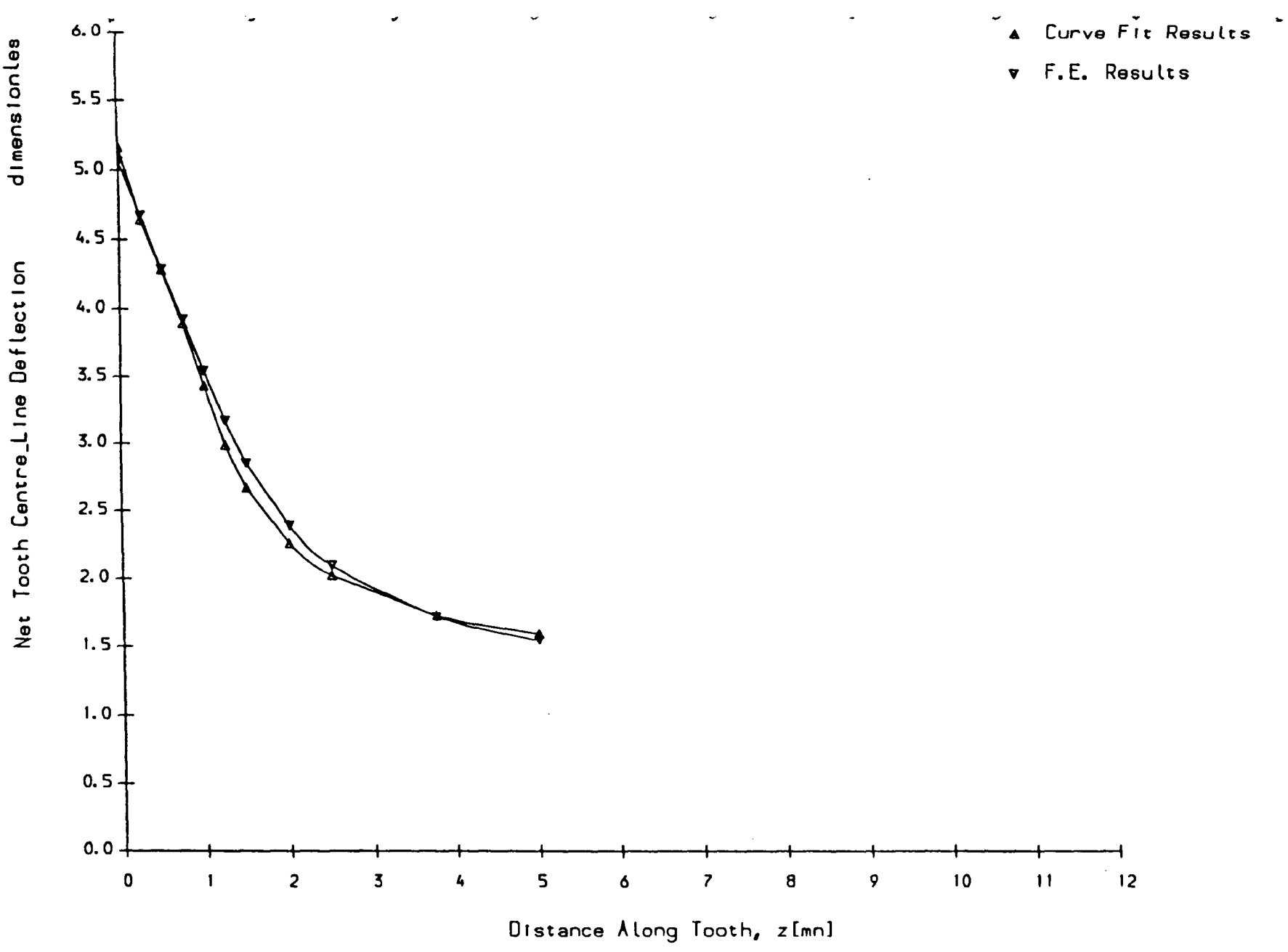

Fig. 2.66 Ktb for Loading at Ref Dia & zf-0.75mn, Z-100

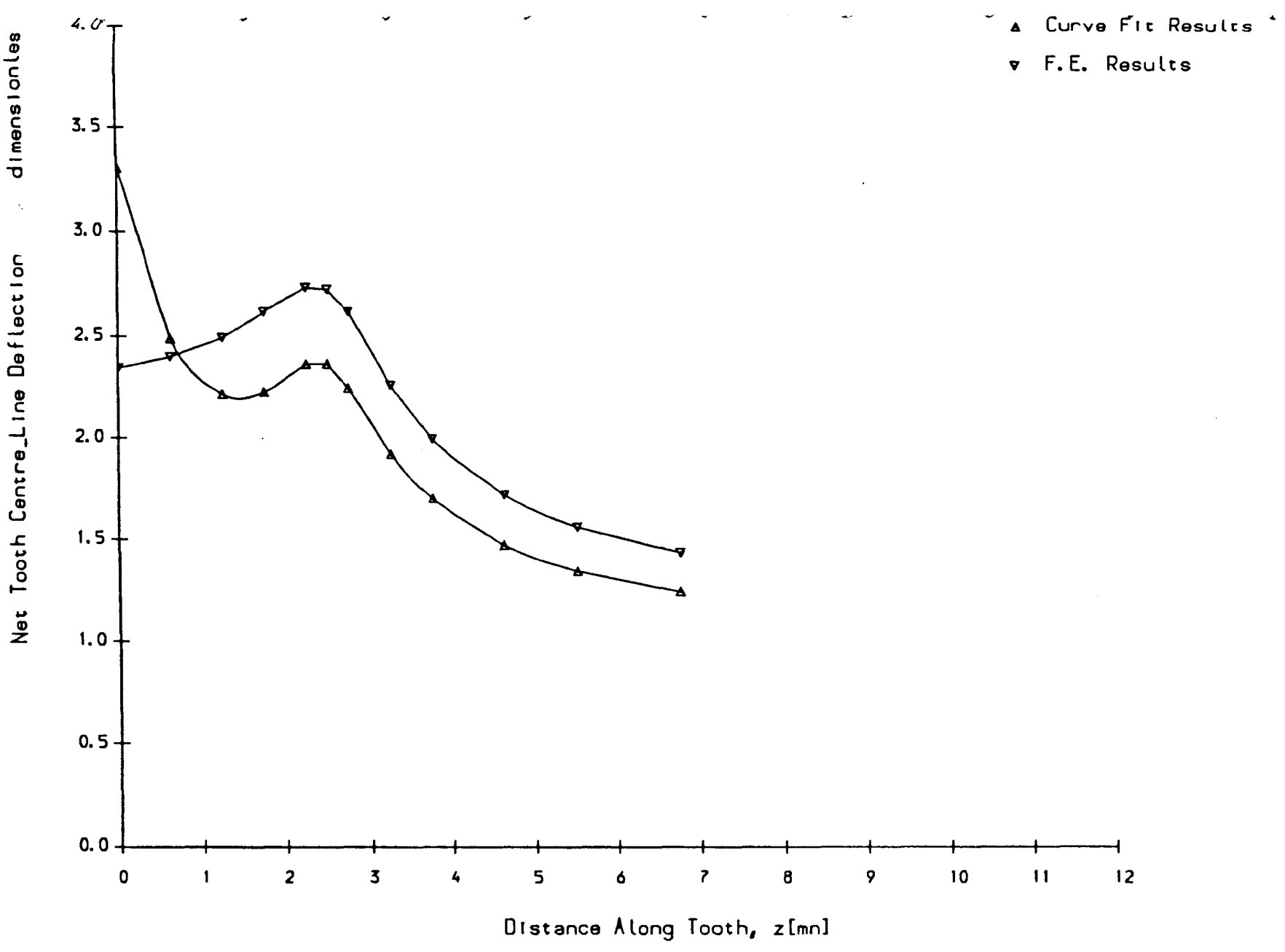

Fig. 2.57 Ktb for Loading at Ref Dia & zf=2.50mn, Z=100

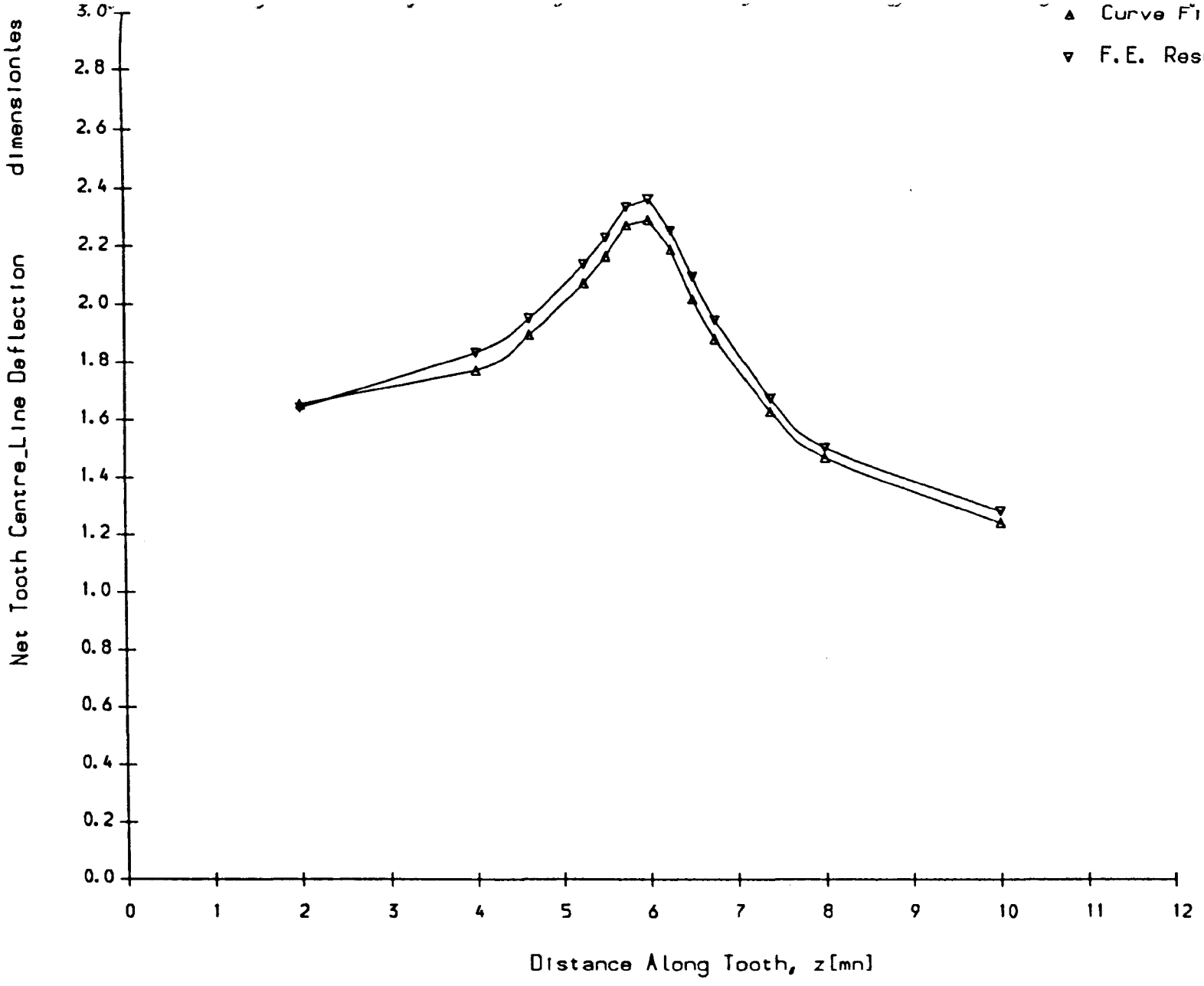

Fig. 2.58 Ktb for Loading at Ref Dia & zf=6.00mn, Z=100

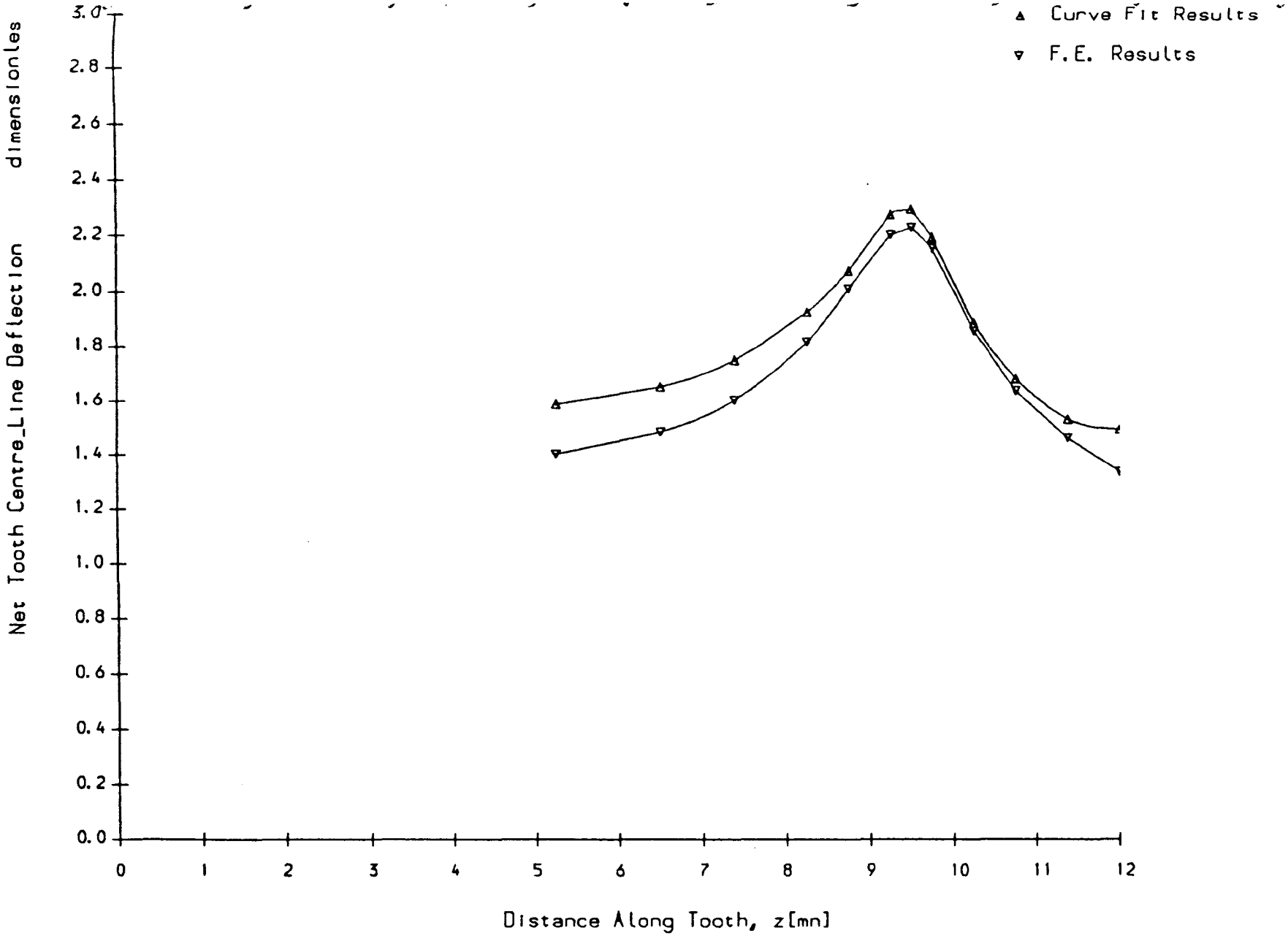

Fig. 2.69 Ktb for Loading at Ref Dia & zf=9.50mn, Z=100

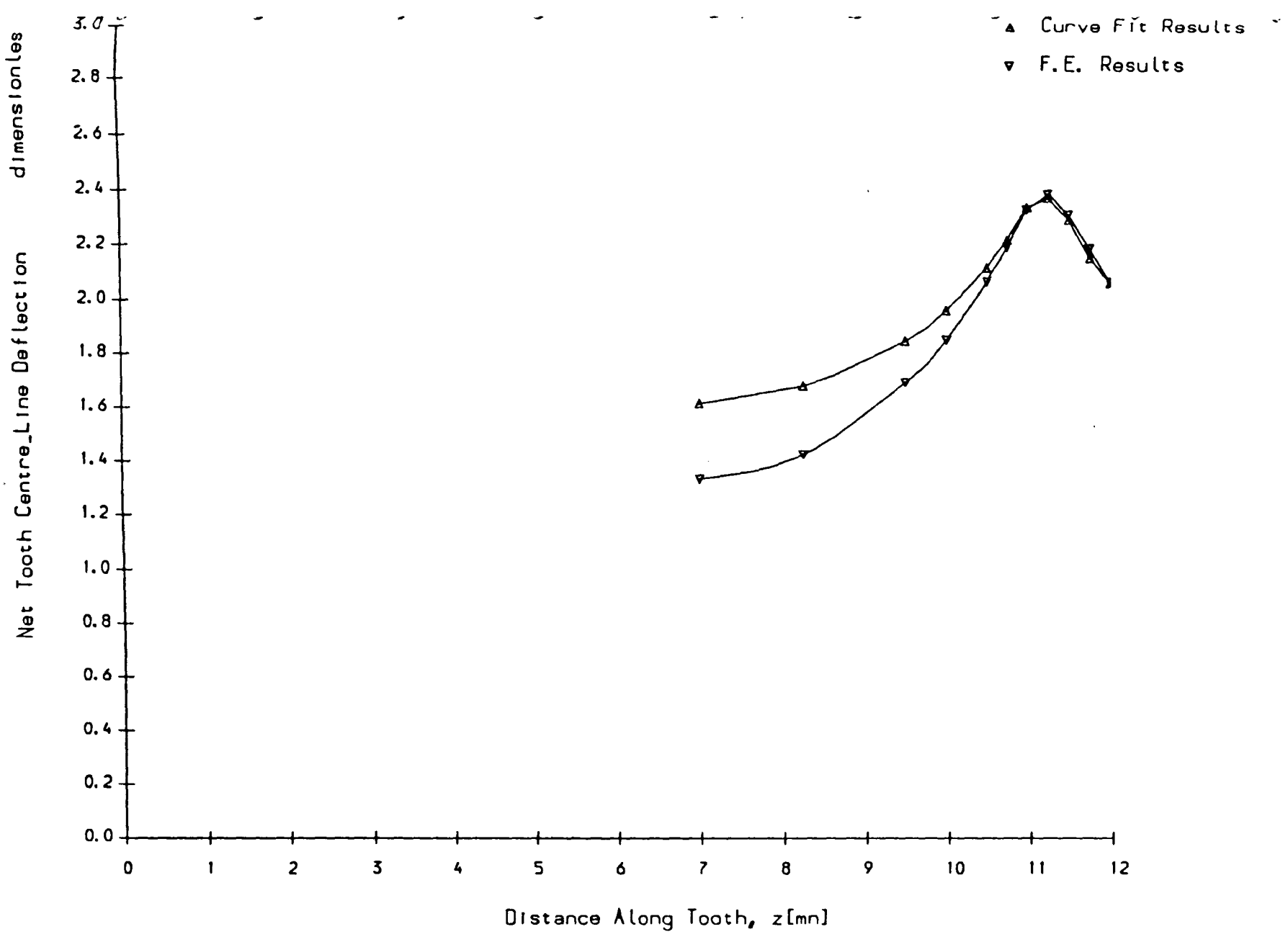

Fig. 2.60 Ktb for Loading at Ref Dia & zf=11.25mn, Z=100

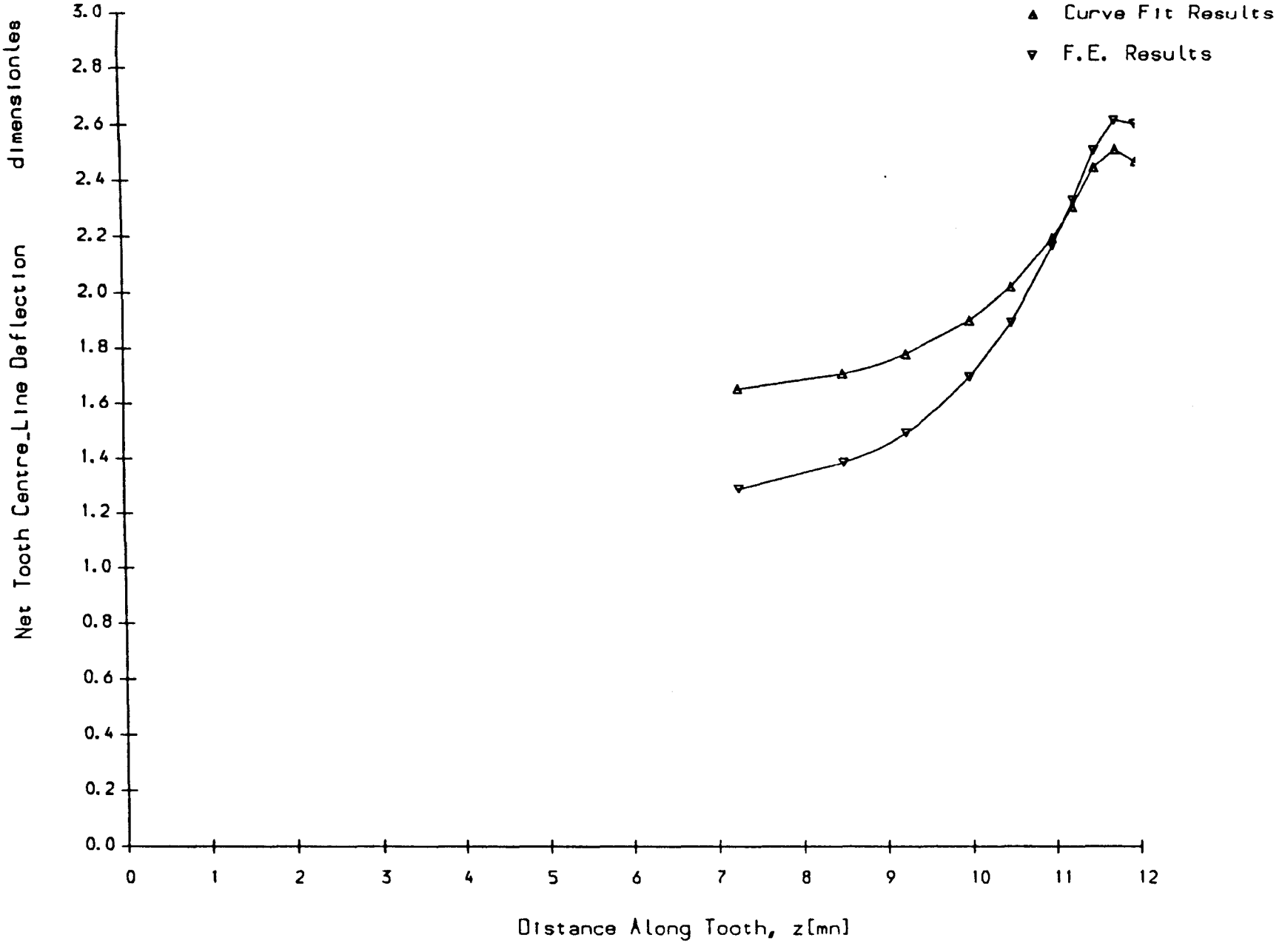

Fig. 2.61 Ktb for Loading at Ref Dia & zf-11.75mn, Z-100

the role of sharp and blunt ends.

2.6.3 Curve-Fitting of Adjacent Teeth Deflections

For gear teeth adjacent to the loaded tooth, the deformation is mainly a consequence of gear body rotation caused by the load on the loaded tooth. Again, Maxwell's reciprocal theorem (Eqn. 1.66) must be satisfied, so that a compliance fitting function symmetric in 'z' and 'z_f' is required as in equation 1.57.

For spur gears, Steward used Eqn. 1.63 which is clearly symmetric about the tooth mid-face. For helical gears, a similar but assymmetric function was devised in the present work and is given by

$$K_{tb.adj}(z_f,z) = C_{a1}+C_{a2}\cdot e^{-C_{a3}(z_f+z)} + C_{a4}\cdot e^{-C_{a5}\cdot(2b-(z_f+z))} + C_{a6}\cdot (z_f+z) \qquad 2.9$$

where for spur gears $C_{a2} = C_{a4}$, $C_{a3} = C_{a5}$ and $C_{a6} = 0$, so that Eqn. 2.9 reduces to Eqn. 1.63.

Functions both with and without the last term in equation 2.9 were tried. The results in both cases showed no significant difference, even for the largest gear (z = 100 teeth). As a result, C_{a6} was set to zero in the final curve-fitting analysis, with very satisfactory results. Figs. 2.62 and 2.63 show a comparison between the fitted curves and original F.E. results, for mid-face loading at reference diameter, for the 18, 40 and 100-tooth gears.

For spur gears of normal proportion the transverse contact ratio ϵ_α is less than 2, so that no more than two pairs of teeth are ever simultaneously in contact, and it only proves necessary to be able to calculate the deflection of the two teeth immediately adjacent to any given loaded tooth. On so-called 'high contact ratio' (HCR) spur gears, and on all helical gears with an overall transverse contact ratio $\epsilon_\alpha > 2$ however, it is possible for three or more tooth pairs to be simultaneously in mesh, (see Figs. 2.64 and 2.65).

This means that for complete contact analysis, the effect of loads applied to any particular tooth, on the deflection of adjacent teeth one, two or even more pitches away, must be considered. In view of the substantial gear body compliance component $K_{tb.adj}$ (especially on large gears), these deflections, which give rise to remote off-diagonal 'coupling' terms in the compliance matrix (see Eq. 1.70 and Fig. 2.65b) can not be ignored.

Fig. 2.62 Succeeding Tooth FE & Curve Fit Results

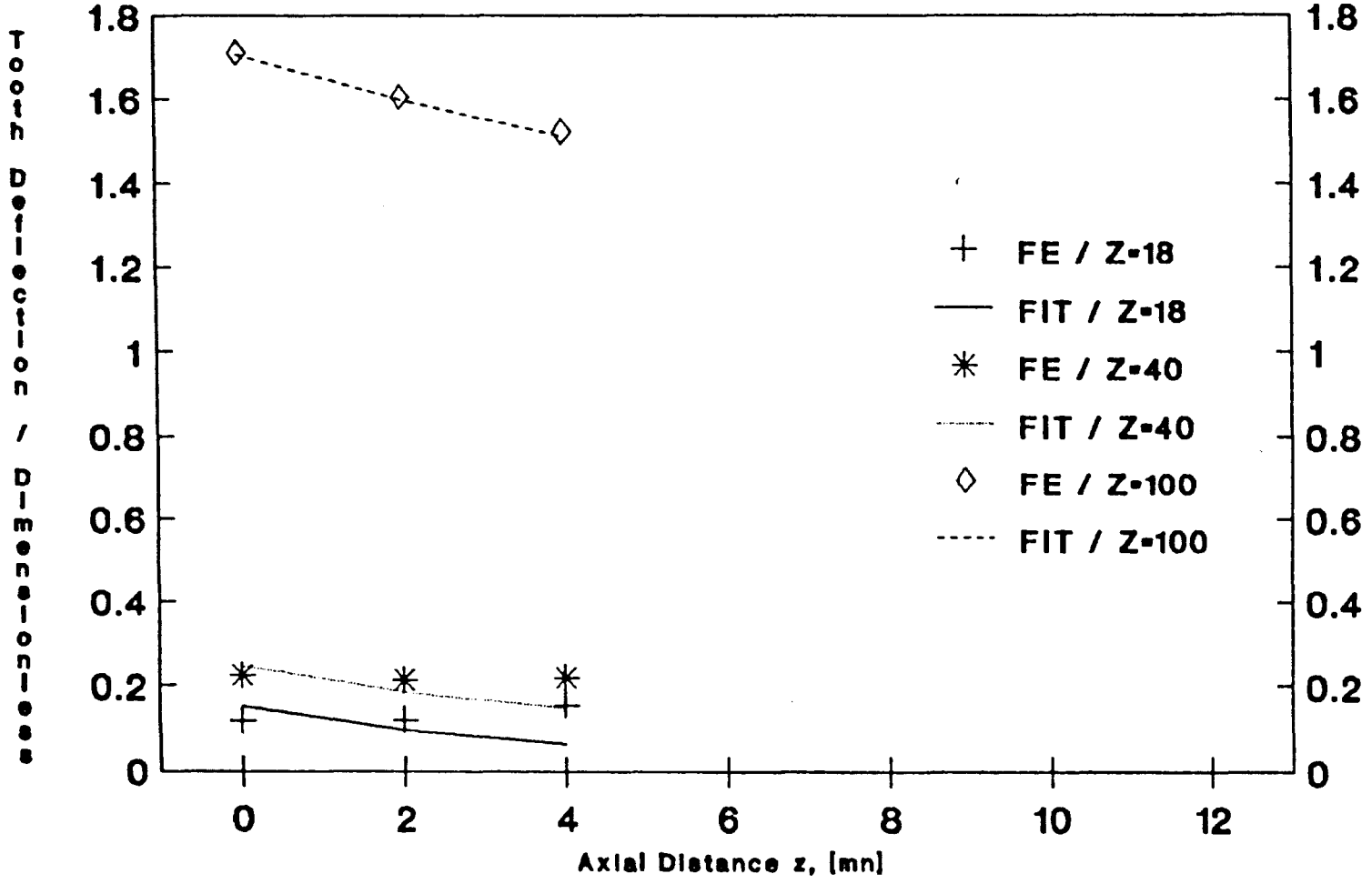

Loaded Tooth Force at Ref Dia & Mid_Face

Fig. 2.63 Preceeding Tooth FE & Curve Fit Results

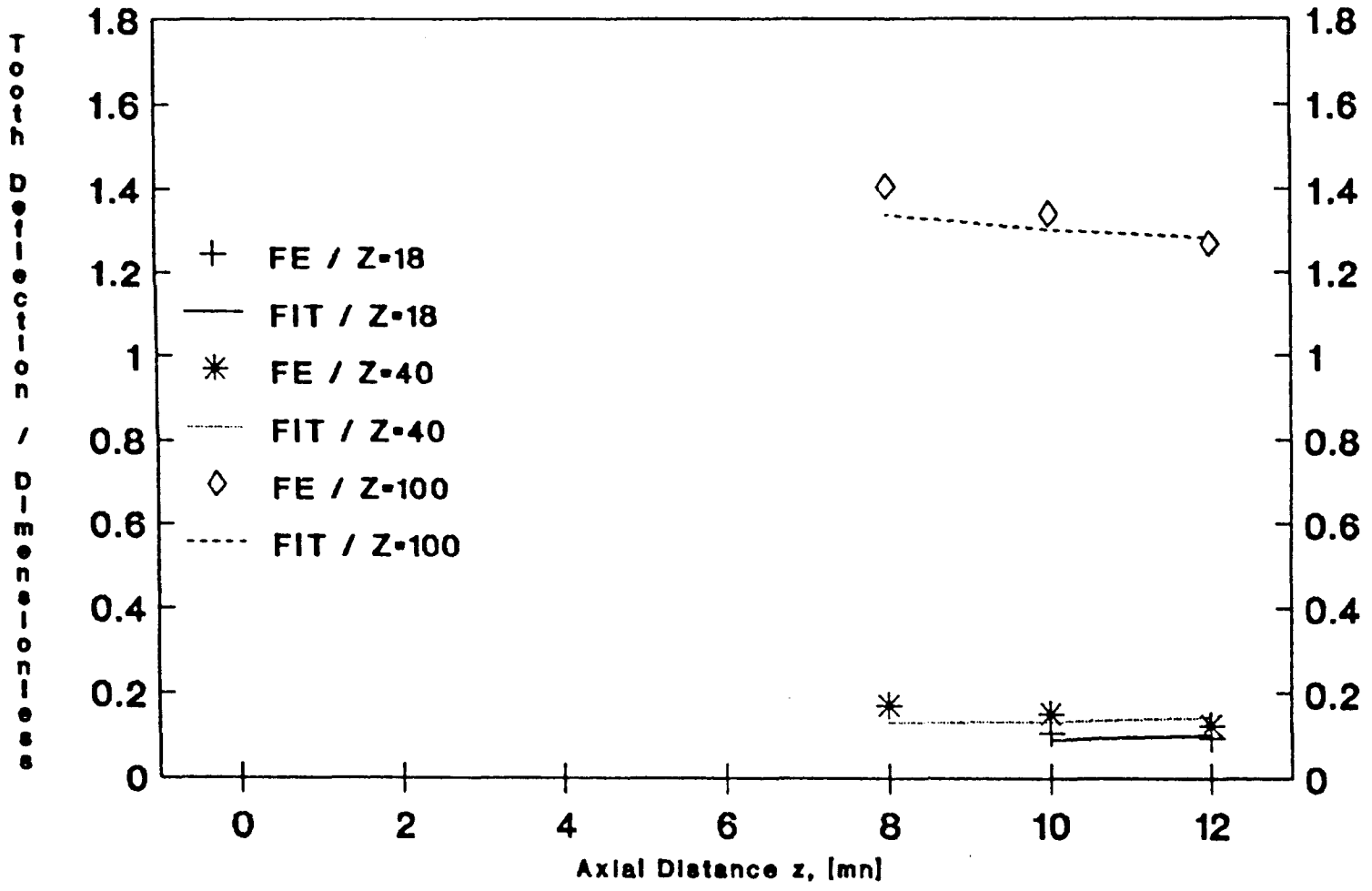

Loaded Tooth Force at Ref Dia & Mid_Face

Since for most helical gears $\epsilon_\alpha \simeq 1.6$ and $\epsilon_\gamma > 2$, these coupling terms relate to 'convection' effects across the face-width of the gear, rather than along the base tangents. On helical gears with high face contact ratio ϵ_β, and overall contact ratios ϵ_γ of order 5 or higher, the interacting points z and z_f (NB: on different teeth) may easily be 3 or 4 axial pitches apart (possibly 20 or more modules apart), so that the 'local' convective effects represented by the master curve fitting function $F(\bar{z},r_f)$ will have died away altogether.

On the gears modelled by F.E. analysis, no data on the compliance this far away from a loaded point is available, since the face-width was only 12 modules. However, it is clearly reasonable to assume that these remote deflections are wholly due to the gear body compliance.

To allow for this, the deflection of all non-loaded teeth other than the two adjacent teeth, has been assumed equal to the least calculated deflection of the corresponding adjacent tooth section, on the assumption that these too are mainly due to gear body compliance. For a more reliable analysis of very wide-faced gears, it will be necessary to check these assumptions by including more than three teeth in the F.E. model (c.f. Fig. 2.4) and extending the face-width modelled.

Since adjacent tooth deformations are not identical for helical gears, it also becomes necessary to modify the fit equation 2.9, when the loading is reversed, as in the case of the loaded tooth curve fitting equations. It transpires in this case that the terms $(z+z_f)$ in equation 2.70 should be replaced by $(b-(z+z_f))$.

2.7 Compatibility Condition

Steward used equation 1.64 to calculate the transmission error f_t for spur gears, using the condition for contact along the base tangent (in the transverse plane). Exactly the same equation was used for helical gears in the present work, but all the terms in the equation refer to quantities measured normal to the tooth flank in the normal plane.

2.8 Load Distribution Solution

Steward's solution procedure described in section 1.4.3.3, under the heading "Load Distribution Solution" was also adopted in the present work on helical gears, with some important modifications which are explained below.

As shown in Fig. 2.64, helical gear contact lines unlike those on spur

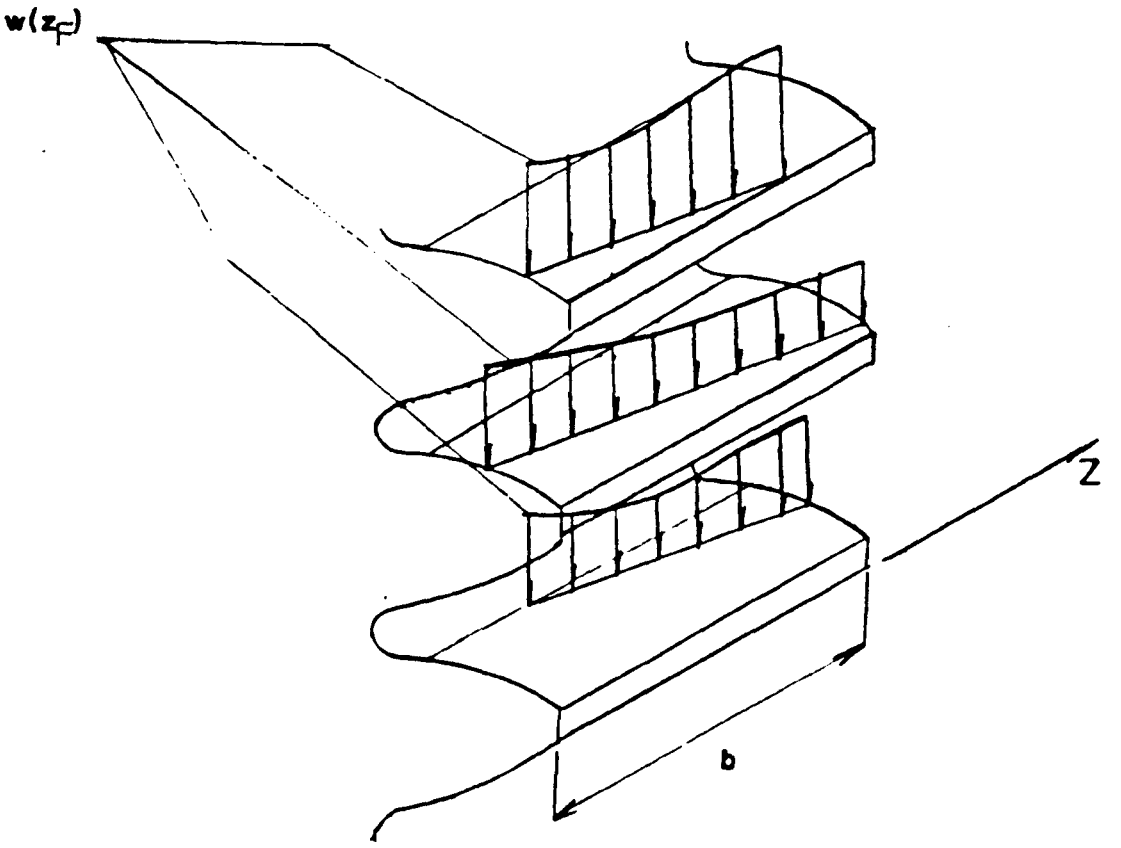

Fig. 2.64 Load Distribution Along Simultaneous Contact Lines

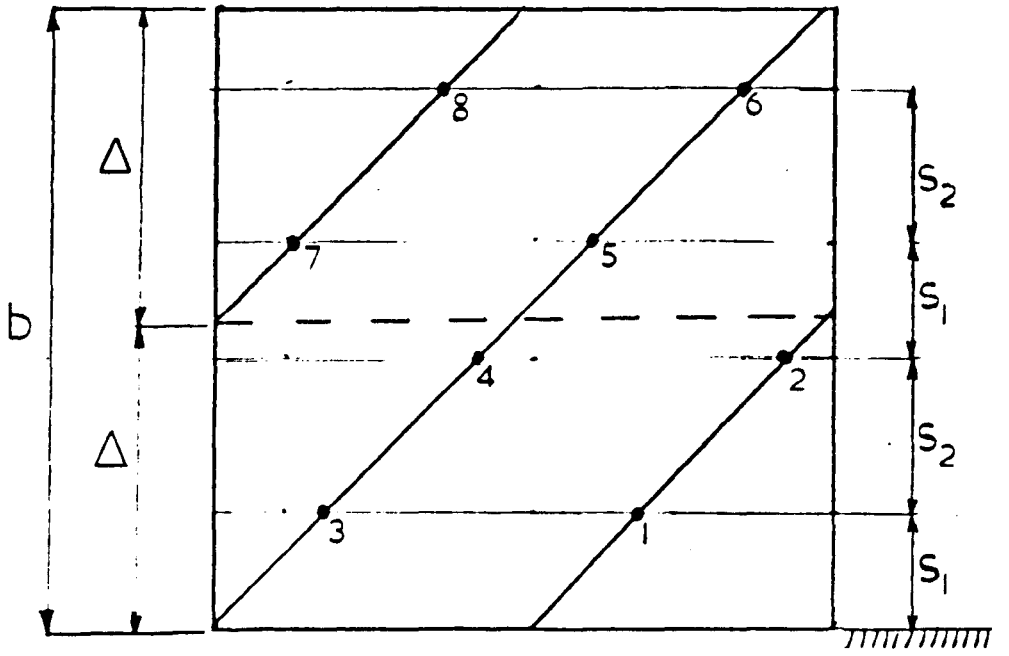

s1 & s2 are the Gauss spacings
# of Gauss intervals m=2
size of Gauss interval Δ = b/2

Fig. 2.65a Plane of Action Shown for a Particular Case with 3 Contact Lines & 8 Gauss Points

$$
\begin{bmatrix}
K_{11}^{tb}+\frac{2}{\Delta'}K_1^{tc} & K_{12}^{tb} & K_{13}^{tb} & K_{14}^{tb} & K_{15}^{tb} & K_{16}^{tb} & K_{17}^{tb} & K_{18}^{tb} & \frac{-2}{\Delta'} \\
K_{21}^{tb} & K_{22}^{tb}+\frac{2}{\Delta'}K_2^{tc} & K_{23}^{tb} & K_{24}^{tb} & K_{25}^{tb} & K_{26}^{tb} & K_{27}^{tb} & K_{28}^{tb} & \frac{-2}{\Delta'} \\
K_{31}^{tb} & K_{32}^{tb} & K_{33}^{tb}+\frac{2}{\Delta'}K_3^{tc} & K_{34}^{tb} & K_{35}^{tb} & K_{36}^{tb} & K_{37}^{tb} & K_{38}^{tb} & \frac{-2}{\Delta'} \\
K_{41}^{tb} & K_{42}^{tb} & K_{43}^{tb} & K_{44}^{tb}+\frac{2}{\Delta'}K_4^{tc} & K_{45}^{tb} & K_{46}^{tb} & K_{47}^{tb} & K_{48}^{tb} & \frac{-2}{\Delta'} \\
K_{51}^{tb} & K_{52}^{tb} & K_{53}^{tb} & K_{54}^{tb} & K_{55}^{tb}+\frac{2}{\Delta'}K_5^{tc} & K_{56}^{tb} & K_{57}^{tb} & K_{58}^{tb} & \frac{-2}{\Delta'} \\
K_{61}^{tb} & K_{62}^{tb} & K_{63}^{tb} & K_{64}^{tb} & K_{65}^{tb} & K_{66}^{tb}+\frac{2}{\Delta'}K_6^{tc} & K_{67}^{tb} & K_{68}^{tb} & \frac{-2}{\Delta'} \\
K_{71}^{tb} & K_{72}^{tb} & K_{73}^{tb} & K_{74}^{tb} & K_{75}^{tb} & K_{76}^{tb} & K_{77}^{tb}+\frac{2}{\Delta'}K_7^{tc} & K_{78}^{tb} & \frac{-2}{\Delta'} \\
K_{81}^{tb} & K_{82}^{tb} & K_{83}^{tb} & K_{84}^{tb} & K_{85}^{tb} & K_{86}^{tb} & K_{87}^{tb} & K_{88}^{tb}+\frac{2}{\Delta'}K_8^{tc} & \frac{-2}{\Delta'} \\
1 & 1 & 1 & 1 & 1 & 1 & 1 & 1 & 0
\end{bmatrix}
\times
\begin{bmatrix} w_1 \\ w_2 \\ w_3 \\ w_4 \\ w_5 \\ w_6 \\ w_7 \\ w_8 \\ \\ ft \end{bmatrix}
= \frac{2}{\Delta'} \times
\begin{bmatrix} \delta_1 \\ \delta_2 \\ \delta_3 \\ \delta_4 \\ \delta_5 \\ \delta_6 \\ \delta_7 \\ \delta_8 \\ \\ F \end{bmatrix}
$$

Fig.2.65b Matrix Solution for Helical Gear Load Distribution (simple example)

gears do not necessarily extend along the whole face-width, so that equation 1.65 must be modified to give

$$\delta_{tb}(z) = \sum_{k=1}^{N} \int_{z_F^{(k)}}^{z_L^{(k)}} K_{tb}^{(k)}(z,z_f) \cdot w^{(k)}(z_f) \cdot dz_f/\cos\beta_b \qquad 2.10$$

where 'N' is the number of simultaneous contact lines. Recall that $\delta_{tb}(z)$ is calculated in the normal plane, normal to the tooth flank, and that z_L and z_F are the limits of contact line k as shown in Fig. 2.1, and integration is along the contact line length (thus including the factor $\cos\beta_b$.

For helical gears, only the component of the total load (F) in the transverse plane contributes to the torque, so that equation 1.67 must be modified to give

$$F = \frac{T}{(d_{b/2}) \cdot \cos\beta_b} = \sum_{k=1}^{N} \int_{z_F^{(k)}}^{z_L^{(k)}} w^{(k)}(z_f) \cdot dz_f/\cos\beta_b \qquad 2.11$$

The load $w(z_f).dz_f$ is measured normal to the contact line and not along the base tangent in the transverse plane as in Vedmar's and Simon's work[5,43].

Equation 1.68 for the localised contact deflection remains unchanged, and substituting for δ_{tb} and δ_{tc} from Eqn. 2.10 and 1.68 into Eqn. 1.64 gives the analogue of Eqn. 1.69 as

$$f_t = \sum_{k=1}^{N} \int_{z_F^{(k)}}^{z_L^{(k)}} \frac{K_{tb}^{(k)}(z,z_f).w^{(k)}(z_f).dz_f + K_{tc}(z_f).w(z_f) + \delta_s(z) - \delta_e(z) + c_n(z)}{\cos\beta_b} \qquad 2.12$$

Equations 2.11 and 2.12 are a pair of coupled integral equations whose solution yields the unknown load distribution $w(z_f)$ and the transmission error f_t. To solve these equations, the integrals are replaced by numerical approximations, based on (n-1) values $w_{\tilde{i}}$ (i.e. $w(z_{\tilde{i}})$) at points $z_{\tilde{i}}$ along the simultaneous contact lines.

Following Hyashi[31], Steward[30] and Zablonski[20], 2-point Gauss integration was used over equal intervals Δ given by

$$\Delta = b/m$$

and $$\Delta' = b/(\cos\beta_b . m)$$

where m is the number of Gauss intervals across the whole face width as shown in Fig. 2.65a for a particular case (m=2 giving 8 Gauss points). Eqn.2.11 thus becomes

$$F = \frac{T}{(d_{b/2}) . \cos\beta_b} = \frac{\Delta'}{2} . \sum_{j=1}^{n-1} w(j) \qquad 2.13$$

and for the $\tilde{i}$th point ($z_{\tilde{i}}$), equation 2.12 becomes

$$f_t = \frac{\Delta'}{2} \sum_{j=1}^{n-1} K_{tb}(i,j).w(j) + K_{tc}(i).w(i) + \delta_s(i) - \delta_e(i) + c_n(i) \qquad 2.14$$

Combining equations 2.13 and 2.14, the matrix equation presented in Fig. 2.65b is obtained (for the example shown in Fig. 2.65a). The terms in the 2x2 upper and lower diagonal submatrices are the off-diagonal 'coupling' terms caused by deflections of the 'next-to-adjacent' tooth referred to in section 2.6. Steward assumed these were zero, but as explained in section 2.6, calculated non-zero values are necessary for the analysis of helical gears.

The matrix equation (Fig. 2.65b) was solved using a Gauss elimination procedure given by Atkinson[48]. Since $K_{tc}(i)$ depends on w(i), and must be set to zero if w(i) is negative, the iterative procedure adopted by Steward[30] was again used, in which initial values of $K_{tc}(i)$ were calculated for an assumed (uniform) distribution $w_0(i)$, and progressively modified as improved values of w(i) emerged from the Gauss solutions.

Replacement of this rather slow process by a Gauss-Siedel iteration process, or one similar to that used by Vedmar was originally planned, but not carried through due to lack of time.

2.9 Contact and Bending Stresses

Referring to section 1.4.3.3 under the heading of 'Contact and Bending Stresses', the same analysis applies to helical gears and will not be repeated here. A diagram showing the contact point radius of curvature $\rho_{\tilde{j}}$ is shown in Fig. 2.1, since Fig. 1.1 applies only to spur gears as it is in the transverse plane. The value of $\rho_{\tilde{j}}$ is given by

$$\rho_j = [r_j^2 - r_b^2]^{\frac{1}{2}} / \cos \beta_b \qquad 2.15$$

2.10 Mesh Stiffness c_γ

As explained in section 1.2.4.2, the gearing standards are based on a 2-D elastic meshing model using a 'single tooth' stiffness c' derived from Winter and Podlesnik's work[14]. For helical gears the value of c' used in the model is that of the equivalent spur gears at their pitch point (when there is single tooth pair contact). The overall mesh stiffness $c\gamma$ used to calculate for example, system natural frequencies, K_V, $K_{H\alpha}$, $K_{H\beta}$, etc., is the mean stiffness (averaged over the meshing cycle) and is given empirically by equation 1.29.

There is, in fact, no period of 'single tooth pair contact' during meshing of real helical gears with $\epsilon_\gamma > 2$, and for the 3-D elastic mesh model developed in this chapter, the concept of 'equivalent spur gears' is unnecessary, so that not even an 'equivalent' single tooth contact region can be defined. The notation of a single tooth stiffness c' is thus irrelevant and it is consequently impossible to relate values of c' given by equation 1.28, to any of the results generated by the 3-D mesh model for helical gears, even though Steward[30] was able to make such a comparison in his work on spur gears, since for spur gears $\epsilon_\alpha < 2$ and single tooth pair contact does occur.

It is, however, possible to calculate the overall mean mesh stiffness c_γ using the 3-D model. The 'instantaneous' stiffness c_γ' in the base tangent plane can be calculated from

$$c'_\gamma = (F/b)/f_t \qquad 2.16a$$

where F and f_t are both normal to the contact line. However, the standard's define c' and therefore c_γ in the transverse plane (section 1.2.4.1) and for comparison purposes Eqn. 2.16a becomes

$$c'_{\gamma_t} = \frac{F.\cos\beta_b}{f_t/\cos\beta_b} = \frac{F/b}{f_t} \cdot \cos^2\beta_b \qquad 2.16b$$

By running the load distribution analysis program through a complete mesh cycle in phase increments of 0.10 base pitches or less, instantaneous

values of f_t are obtained from which the average value f_{tavg} can be calculated. This yields a mean value c_γ comparable with that given by the standards:

$$c_\gamma = \frac{F/b}{f_{tavg}} \qquad 2.17a$$

or

$$c_{\gamma_t} = \frac{F/b}{f_{tavg}} \cdot \cos^2\beta_b \qquad 2.17b$$

CHAPTER 3

THE BEHAVIOUR OF PERFECT GEARS IN MESH AND COMPARISON WITH PUBLISHED RESULTS

3.1 Introduction

In this chapter, the results obtained in the present work for gear tooth compliance K_{tb}, overall mesh stiffness c_γ, load distribution w, and the corresponding contact stress σ_H, are all compared with the results obtained by the gear rating standards[2,3,4], Vedmar[5] and Simon[43].

In addition, the effects of number of teeth Z, gear ratio U, helix angle β and gear facewidth b on K_{tb}, c_γ, w and σ_H are studied.

3.2 Gear Tooth Compliance : Comparison with Published Results

3.2.1 Introduction

As explained in Chapter 1, the author, Vedmar[5] and Simon[43] all used basically similar F.E. models to determine the tooth bending (and shear) compliance. All three sources fitted their results by algebraic approximating functions, and the results are compared in this section, (section 3.2).

To facilitate this comparison, Vedmar's[5] and Simon's[43] methods have been implemented in two micro-computer PRO-PASCAL programs which calculate the compliance of any helical gear tooth according to equations 1.37, 1.38 and 1.39 (Vedmar), and equation 1.74 (Simon). Vedmar's tabulated coefficients in equations 1.38 and 1.39 have been interpolated (or extrapolated) using cubic spline functions, so that values for any number of teeth or helix angle can be obtained.

3.2.2 Comparison with Vedmar's Results

Vedmar's[5] equations are of very similar form to the author's equations 1.57, 2.6 and 2.5, except for the differences pointed out in section 1.4.3.3 (under the heading F.E. Model and Bending Deformation).

Before making any comparisons, it is, in principal, necessary to correct Vedmar's[5] results to allow for the smaller depth ($0.5m_n$ below the tooth flank), at which his deflections are calculated. However, referring to section 2.4, a detailed analysis shows that the difference in

contact compliance between the author's (using the tooth centre-line as reference depth) and Vedmar's[5] results is negligible, so no corrections to Vedmar's results are, in fact, needed. It is worth noting that Steward[30] calculated much larger corrections but his values seem to be incorrect.

Comparison of the functions $G(z,r_f)$ [Eqn.2.6] and $\psi(\zeta,\eta)$ [Eqn.1.38] is facilitated if only the tooth centre-line deflections, under the point of load application are considered, by setting $z = z_f$ ($\zeta=\zeta_F$). From equation 1.57 we have

$$K_{tb}(z_f,z_f,r_f) = G(z_f) \cdot F(0,r_f) \qquad 3.1$$

and similarly from equation 1.37

$$\alpha(\zeta_F,\eta_F) = \psi(\zeta_F,\eta_F) \cdot \Gamma(0,\eta.\eta_F) \qquad 3.2$$

Noting that Γ in equation 3.2 is equal to 1.0 for all values of η and η_F, and that F in equation 3.1 is also equal to 1.0 for all r_f, then the influence functions in equations 3.1 and 3.2 reduce to the "end effect" or "non-master curve" function $G(z_f)$ in the present work or Vedmar's $\psi(\zeta_F,\eta_F)$. These functions should be nearly identical.

$G(z_f)$ and $\psi(\zeta_F,\eta_F)$ are compared in Figs. 3.1, 3.3 and 3.5 for $\beta = 0^\circ$, and in Figs. 3.2, 3.4 and 3.6 for $\beta = 30^\circ$, for the 18, 40 and 100-tooth gears respectively. Note that since Vedmar's coefficients were only tabulated for $\beta = 0$, 10 and 20°, it was necessary to extrapolate for $\beta = 30^\circ$ using the cubic spline fits previously mentioned.

The spur gear results show excellent agreement for 18 and 40 teeth (Figs. 3.1 and 3.3), although the "end effect" predicted in the present work appears to be slightly less localised than Vedmar's[5]. For 100 teeth, however, the deflections predicted by the author are nearly 1.6 times those predicted by Vedmar in the central region, although only about 1.2 times at the tooth ends. The additional deflection at the ends relative to the central region, is, however, nearly the same on both curves, as for the smaller gears with 18 and 40 teeth. The discrepancy for the 100-tooth gear can therefore be completely explained by the effect of the larger gear body compliance. As shown in Fig. 3.5, this effectively adds a roughly constant deflection of about 0.7 units to the deflection of each point across the gear. If this were subtracted, the two curves would be in close agreement. Since as shown in section 1.4.3.2, Vedmar's F.E. model fails to include the proper gear body deflections, this discrepancy between the two sets of results is

Fig. 3.1 End Effect Function G(z) at Ref Dia Load, Beta=0 Deg, Z=18 Teeth

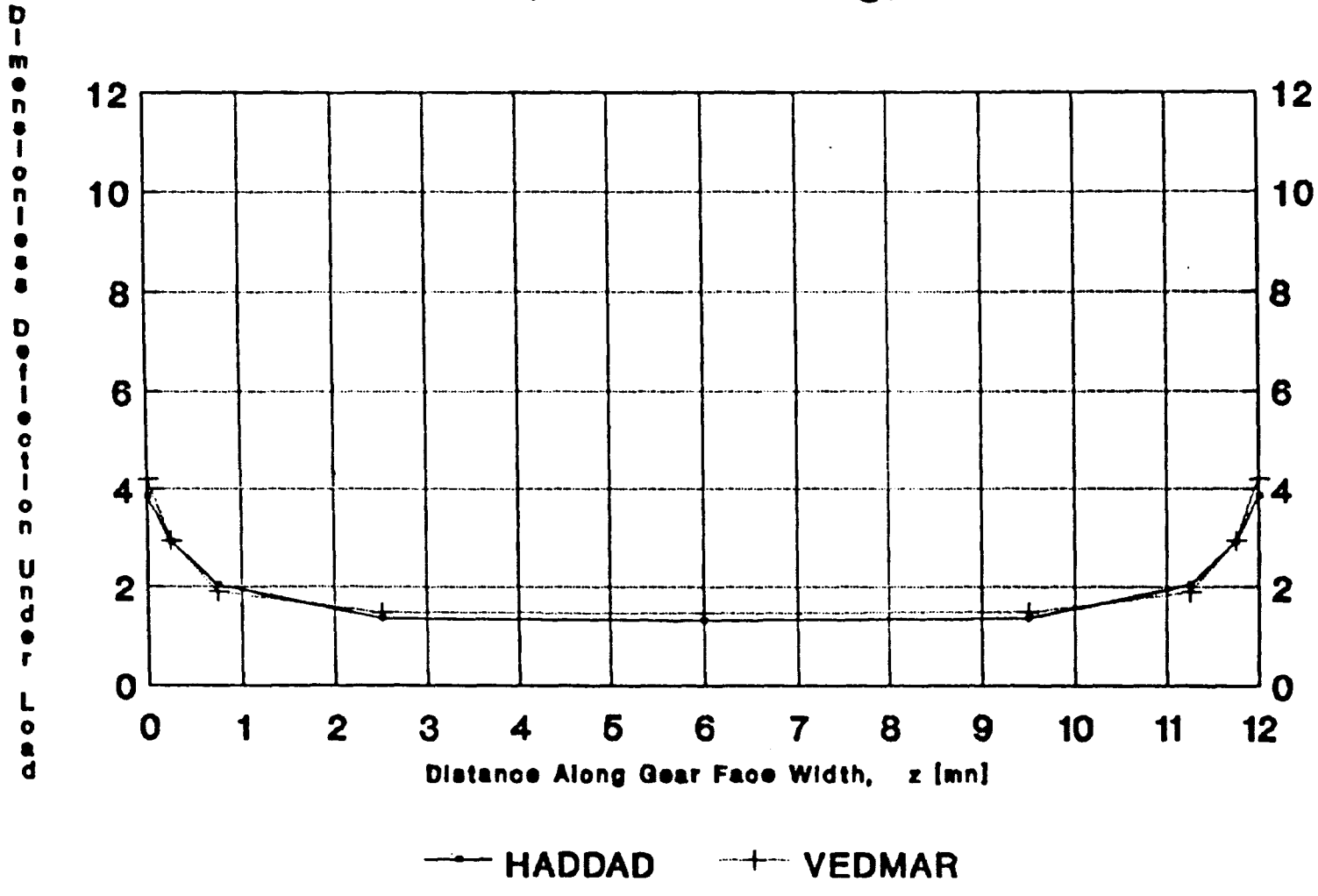

Fig. 3.2 End Effect Function G(z) at Ref Dia Load, Beta=30 Deg, Z=18 Teeth

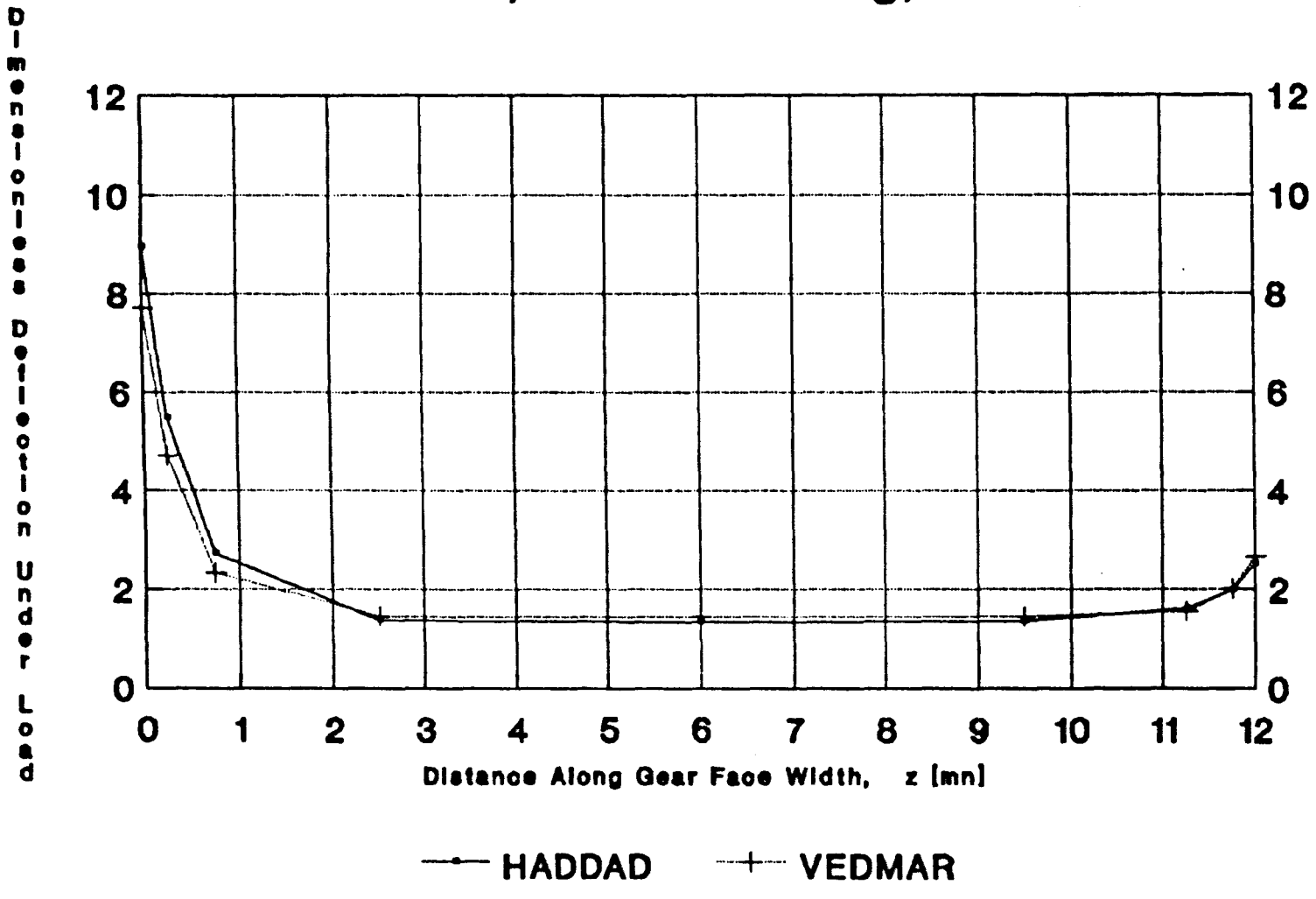

Fig. 3.3 End Effect Function G(z) at Ref Dia Load, Beta=0 Deg, Z=40 Teeth

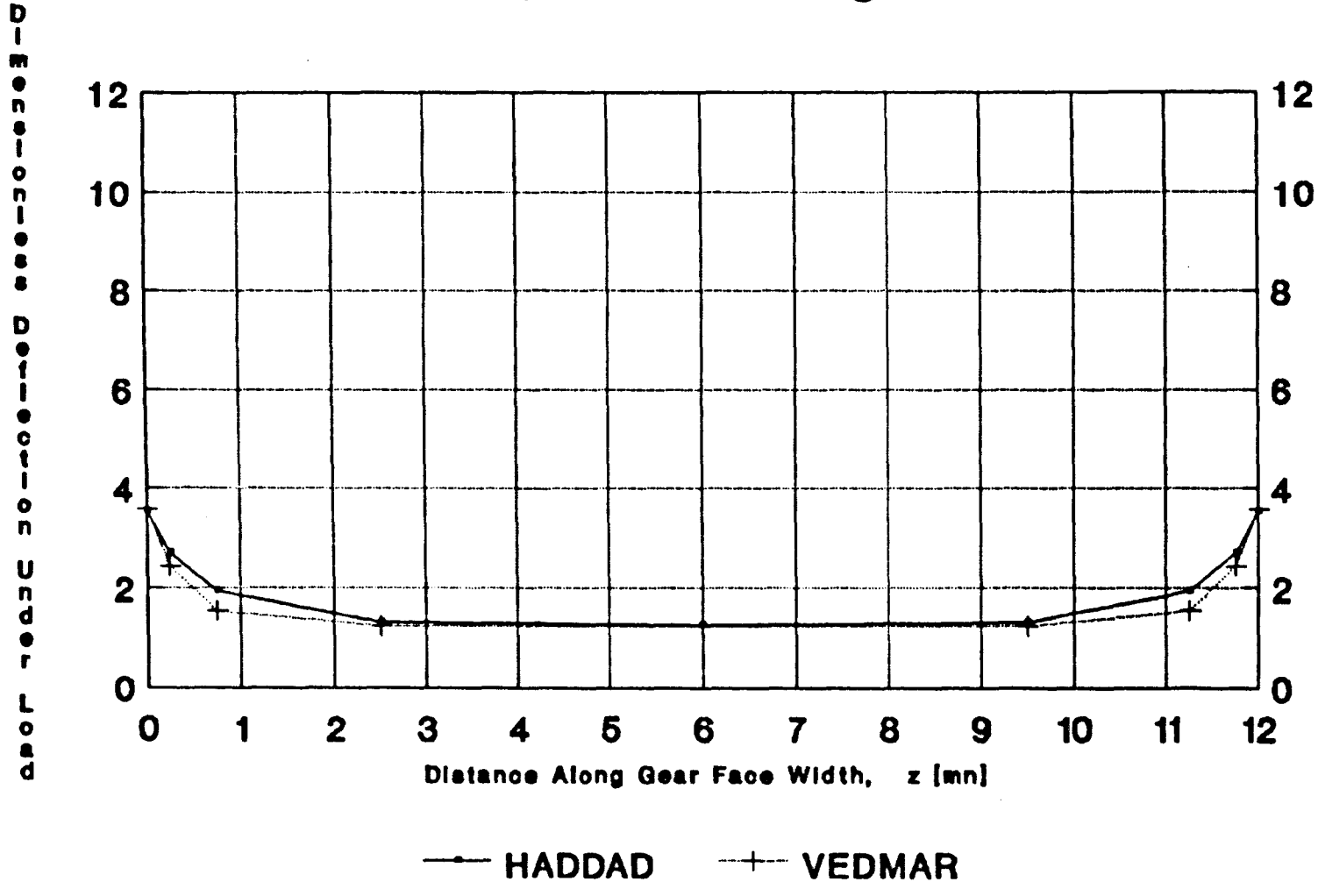

Fig. 3.4 End Effect Function G(z) at Ref Dia Load, Beta=30 Deg, Z=40 Teeth

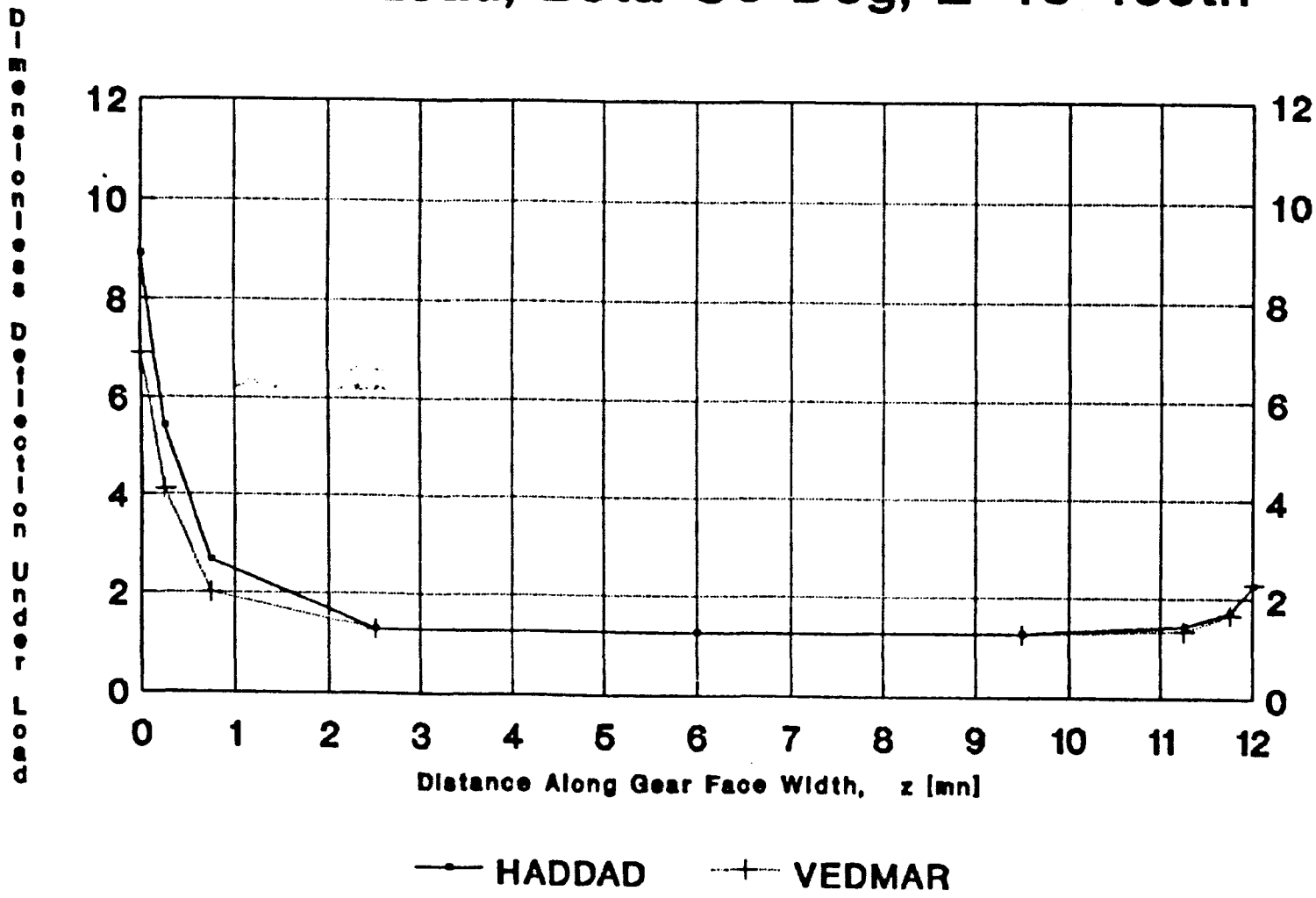

Fig. 3.5 End Effect Function G(z) at Ref Dia Load, Beta=0 Deg, Z=100 Teeth

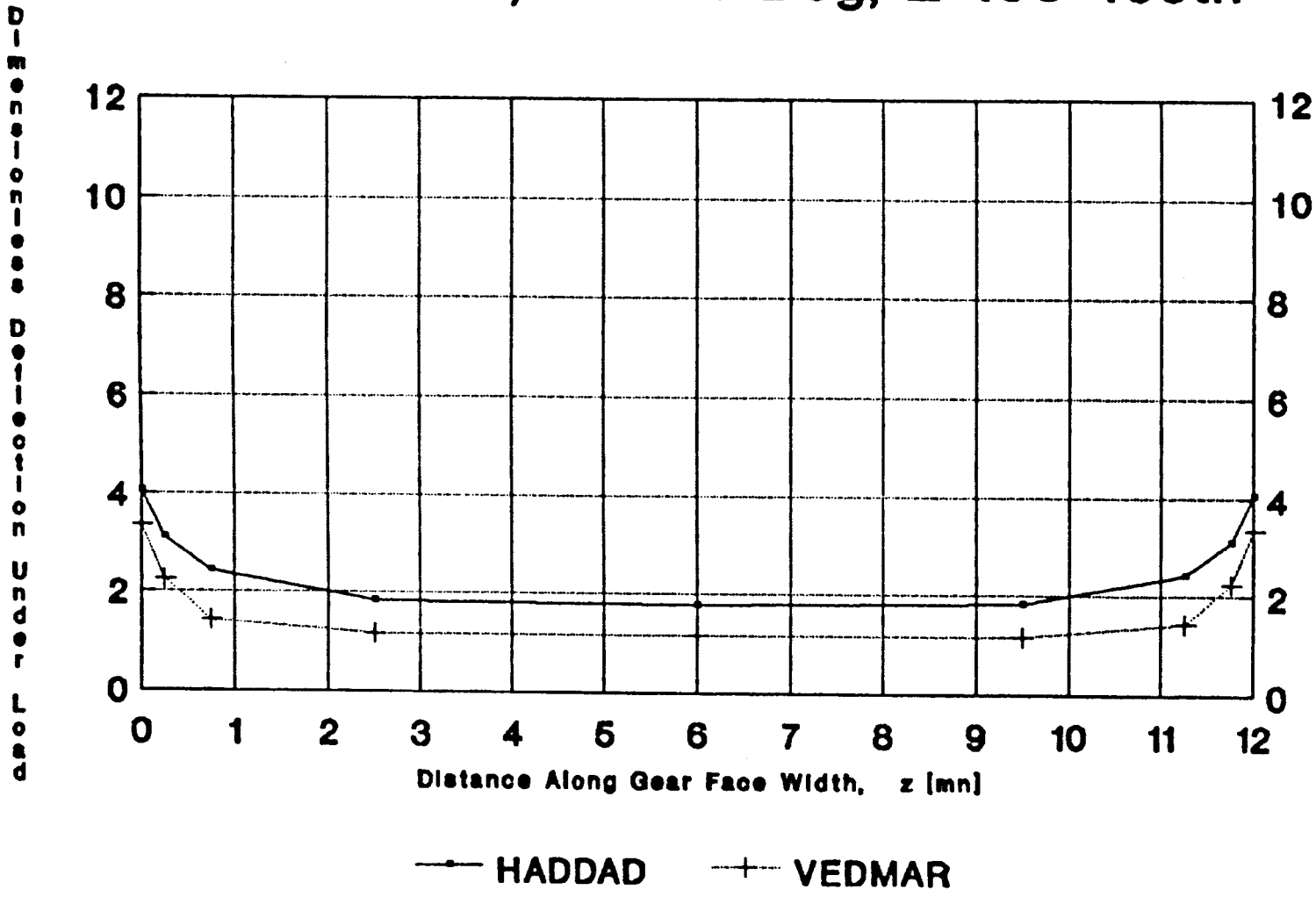

Fig. 3.6 End Effect Function G(z) at Ref Dia Load, Beta=30 Deg, Z=100 Teeth

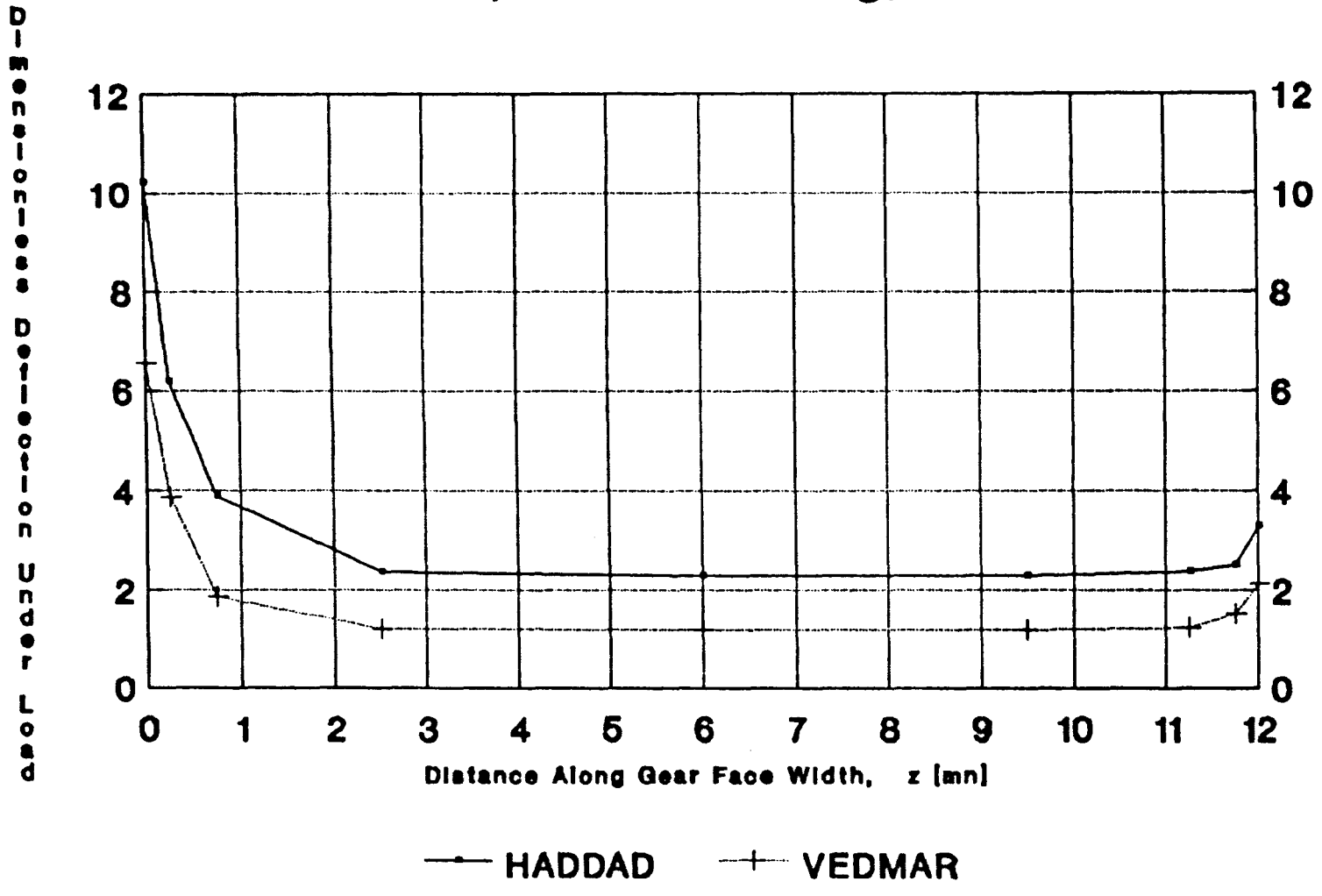

inevitable.

A very similar pattern of agreement is shown in Figs. 3.2, 3.4 and 3.6 for helical gears. For 18 and 40 teeth (Figs. 3.2 and 3.4) where gear body deflections are small, agreement between the author's and Vedmar's results is again excellent, although at the "sharp" end of the teeth (Fig. 3.7), where the compliance is greatest, Vedmar's compliance tends to be smaller than the author's. On the 100-tooth gear (Fig. 3.6) this difference is again apparent but is combined, as in the case of the 100-tooth spur gear, with an additional gear body deflection of about 1.1 units (see also relevant part of section 2.5). This is clearly larger than the gear body deformation of the 100 tooth spur gear due to the larger helical gear diameter.

One possible explanation for the greater discrepancy at the sharp end is shown in Fig. 3.7. Vedmar's deflection for a load applied at point p_{fs} is that of the point p_{Vs} 0.5mn below the tooth surface in the transverse plane. As explained at the beginning of section 2.5, the author's deflection is for the point p_{Hs} in the same normal plane as p_{fs}. So at the sharp end of the tooth, point p_{Hs} is about 0.165mn nearer to the end of the tooth (at reference diameter loading) than the point p_{Vs}, and will thus show higher deflections. Shifting Vedmar's curve about 0.165mn to the right in Figs. 3.2 and 3.4 brings Vedmar's curve into very good agreement with the Author's.

At the "blunt" end (Fig. 3.7), the situation is reversed since the author's point p_{Hb} is further from the tooth end than Vedmar's point p_{Vb}. In this case, however, the end effect is anyway too small for any discrepancy to be noticeable.

An alternative possibility is that Vedmar appears to have loaded his F.E. model in the transverse plane (see section 1.4.3.2). This would reduce his compliance values even more at the sharp end when compared with the author's.

To compare the author's function $F(\bar{z},r_f)$ with Vedmar's corresponding function $\Gamma(|\zeta-\zeta_F|,\eta,\eta_F)$, the effect of a load applied at mid-face ($z_f = \zeta_F = 6.0m_n$) is considered. The deflections are then given by the author's equation 1.57 and Vedmar's[5] corresponding equation 1.37.

Since the functions G and ψ in these equations (given by equations 2.6 and 1.39respectively) are both constant at points well away from the tooth ends (refer to equation 1.62), the curves of K_{tb} and α will only reflect the form of the functions F and Γ.

The results of this comparison for loading at the reference

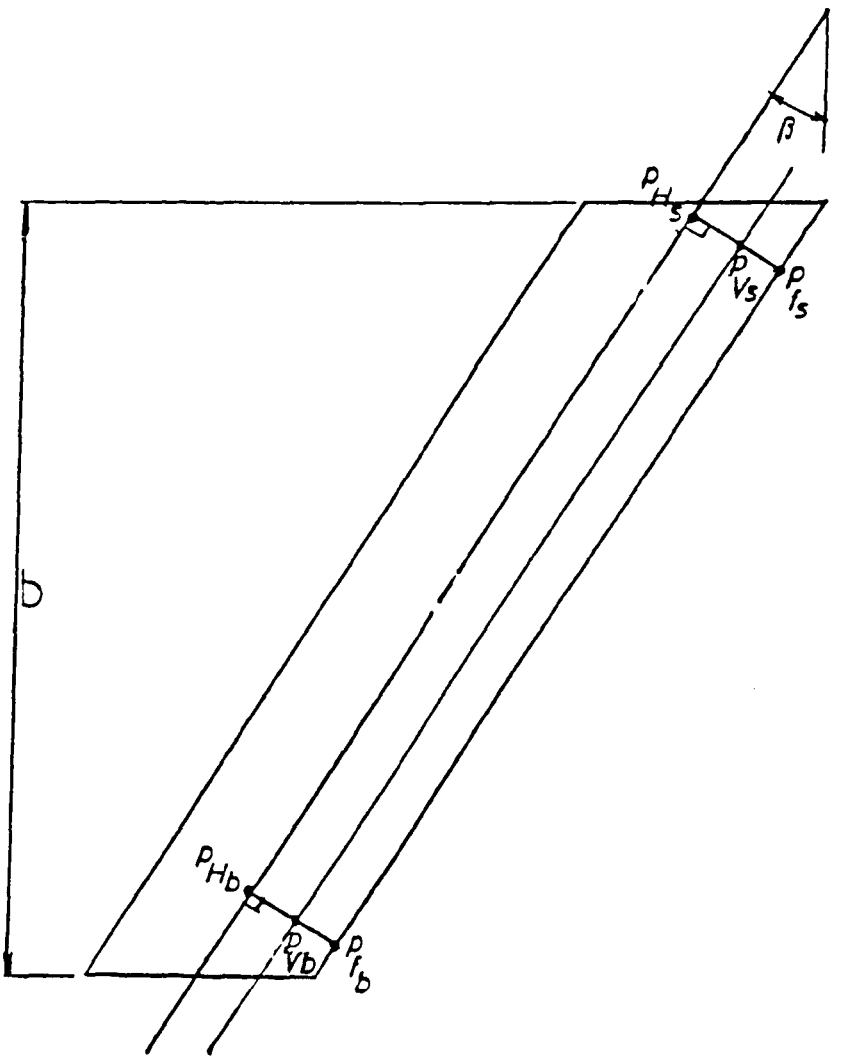

KEY:

f _ loaded surface point
s _ sharp end of tooth
b _ blunt end of tooth
H _ Haddad's centre_line pt.
V _ Vedmar's pt.

Fig. 3.7 Location of Deflected Points on Tooth Centre_Line According to Haddad & Vedmar

diameter are shown in Figs. 3.8 - 3.10 for gears with 18, 40 and 100 teeth, with $\beta = 0^{\circ}$ and 30°. Results have only been plotted for the range $2m_n \leq z \leq 10m_n$ to eliminate the end effects caused by the functions G and ψ. Spur gear results are symmetric about the centre of the gear facewidth as expected, whereas, in both cases, those for the helical gears are tilted as described in section 2.6.2. The "widths" of the master curves are also substantially the same for the author's and Vedmar's results, although Vedmar's show evidence in every case of a slightly sharper peak at the centre (point of load application). Steward[30] attributed this to Vedmar's[5] inclusion of more of the highly localised contact deflection in his compliance values, due to the different datum depth of $0.5m_n$ used, but, as shown in section 2.4, the discrepancy caused by this effect is actually only about 0.02 units and thus quite negligible.

For both spur and helical gears the effect of the increasing gear body deflection included in the author's results, is also apparent. This is negligible (about 0.1) for the 18-tooth gears, increasing to about 0.20 for the 40-tooth gears, and to about 0.80 and 1.30 units for the 100-tooth spur and helical gears respectively. If these (nearly constant) deflections were subtracted from the author's results, much better agreement would be obtained between the author's and Vedmar's curves (except at the loaded points, as discussed above).

Although Figs. 3.1 - 3.6 and 3.8 - 3.10 do reveal indirectly how the tooth deflections vary with the number of teeth, it is interesting to plot the deflections as a direct function of the number of teeth Z. The effect of the helix angle may also be displayed directly by plotting the results for the spur gears alongside those of the 30° helical gears. This has been done in Fig. 3.11 for tooth deflections directly under the load, at reference diameter loading, as an example.

As expected, the author's results are larger for larger gears due to gear body deformations not modelled by Vedmar, converging to nearly the same values as the number of teeth decreases. The interesting fact, however, is the crossing of the author's and Vedmar's curves at around Z = 40 teeth, beyond which the author's deflections become smaller than Vedmar's. This can not be explained by residual contact deflections caused by Vedmar's smaller datum depth, since this effect has already been shown to be negligible. Another possible explanation for this phenomenon is that Vedmar seems to have evaluated his deflections along the base tangent line, (i.e. in the transverse plane). Converting these values to the equivalent deflections along the load-line

Fig. 3.8 Tooth Deflection For Loading at Mid_Face & Reference Diameter, Z=18

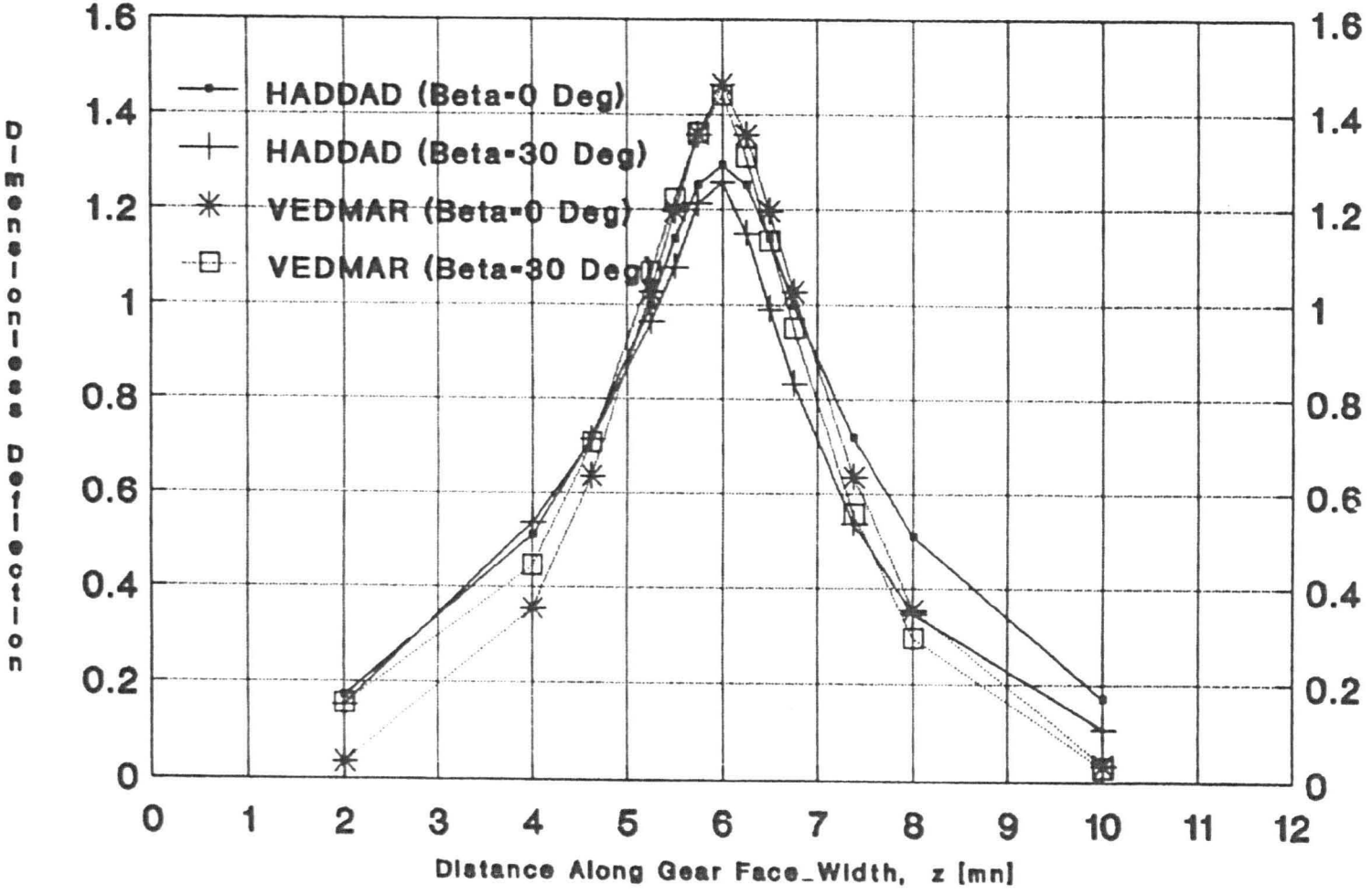

Fig. 3.9 Tooth Deflection For Loading at Mid_Face & Reference Diameter, Z=40

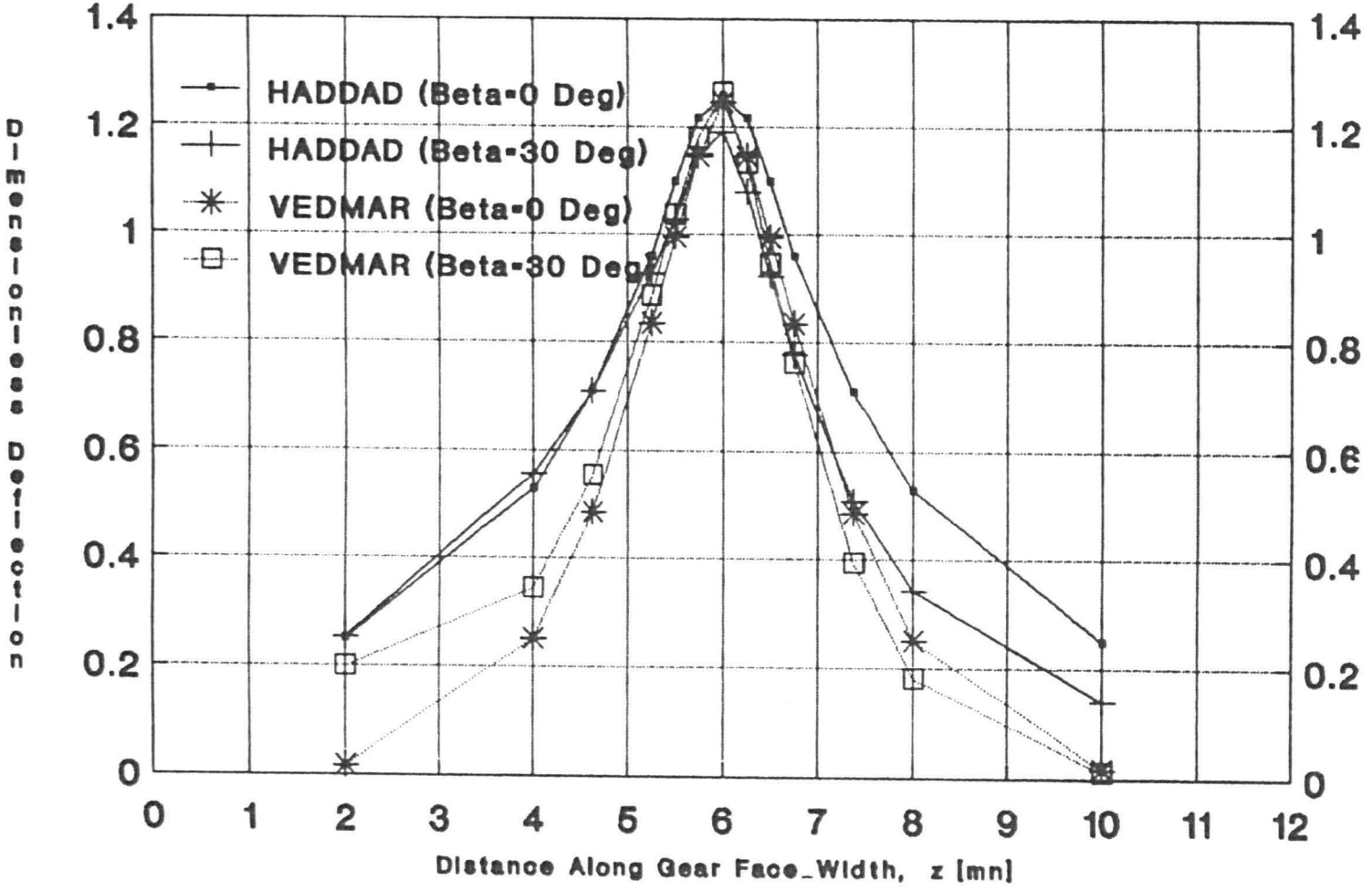

Fig.3.10 Tooth Deflection For Loading at Mid_Face & Reference Diameter, Z=100

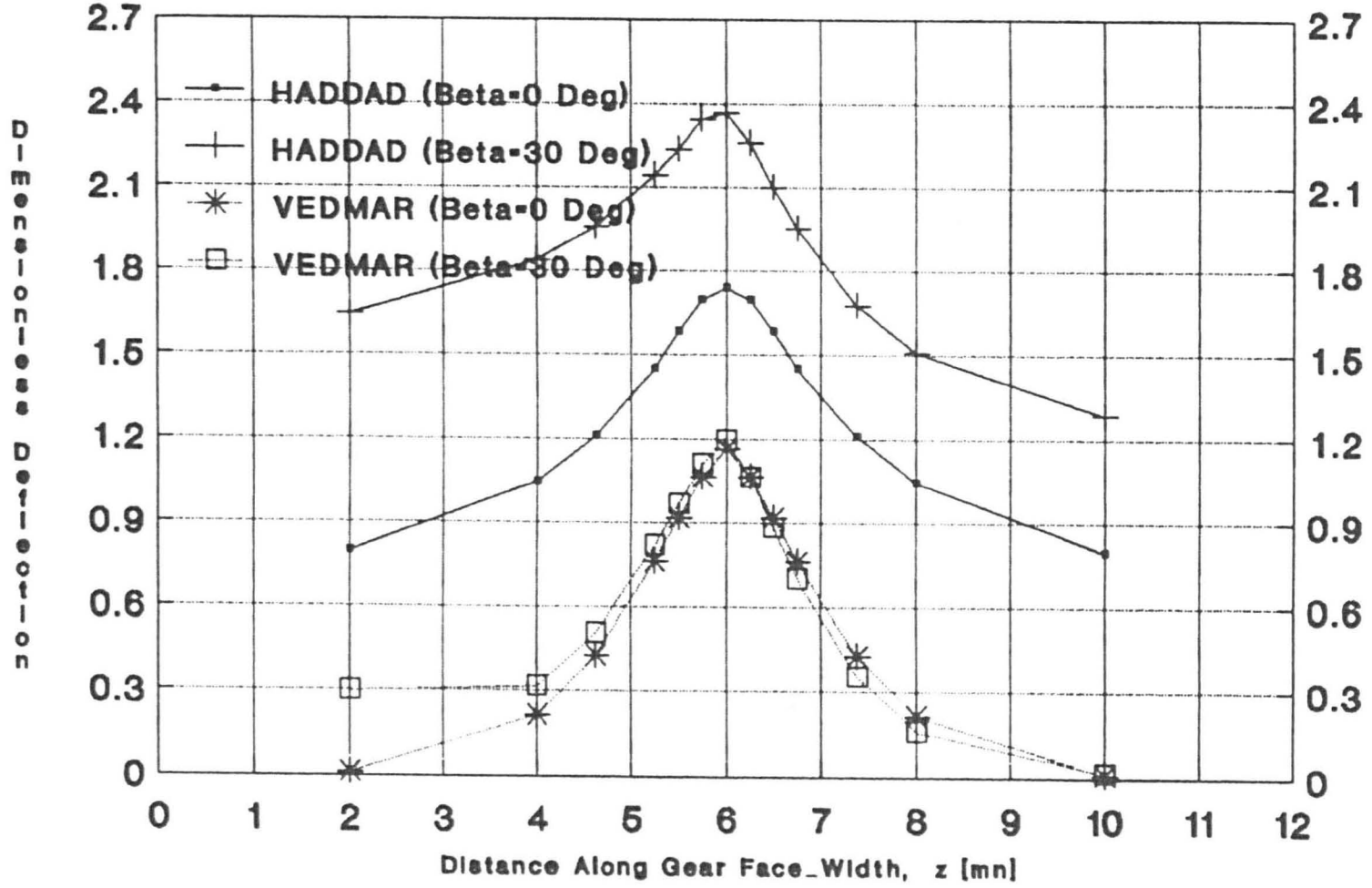

Fig.3.11 Tooth Deflection Under Load For Mid_Face & Reference Diameter Loading

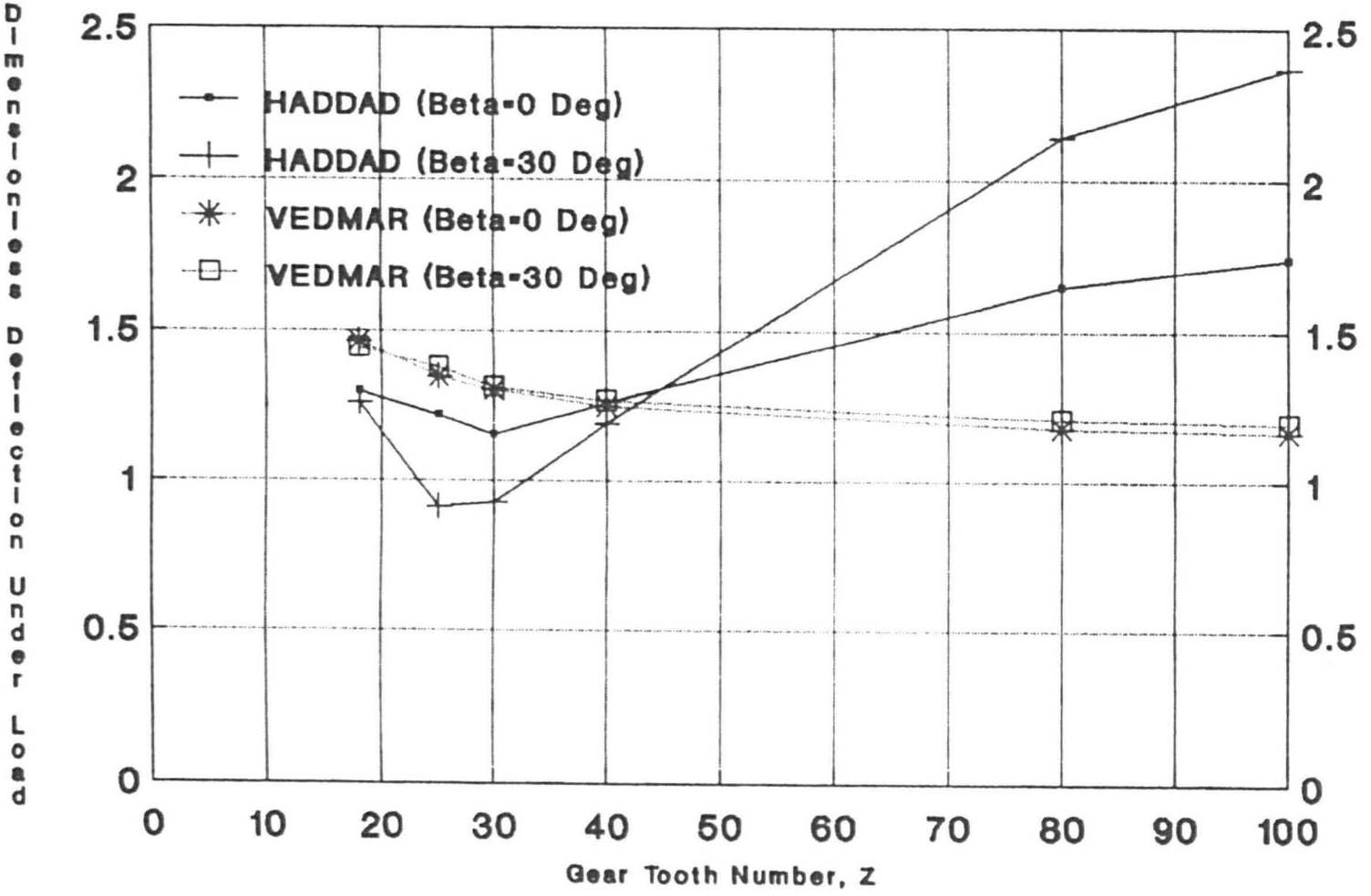

(in the normal plane) introduces an additional factor $\cos\beta_b$ which could bring Vedmar's curve for the 30° helix gears slightly below the author's for smaller values of Z. This theory however, does not explain Vedmar's larger deflections for the small spur gears, where the correction would have no effect. This explanation is thus unreliable. The discrepancy however, may be explained by Vedmar's inadequate FE coarse mesh, (see Fig. 1.10).

Another observation is that Vedmar's 0° and 30° gears exhibit nearly identical curves. This is clearly contrary to the explanation above based on the factor $\cos\beta_b$, since if this theory were true, the curves for the helical gears should differ significantly (by a factor $1/\cos\beta_b$). The same observation also confirms that Vedmar did exclude gear body deformations since his spur and helical gear results are much closer together than the author's, in which the gear body deformations of the helical gears are much greater than those of the spur gears.

It is, however, important to remember that Vedmar's 30° helical gear results were obtained by linear extrapolation of his coefficients for β = 0, 10 and 20°, as explained above. Even though the error so introduced is not expected to be very significant, there is a possibility that the β = 30° "Vedmar" curves plotted are, in fact, unrepresentative of his theory.

3.2.3 Comparison with Simon's Results

Comparison of the author's results with compliances obtained from Simon's equation (1.74) showed wide discrepancies. Simon's deflections are unreasonably large for small values of Z (4 times as large as Vedmar's and the author's deflections for Z = 18, and twice as large for Z = 40), similar to those obtained by Vedmar and the author for large values of Z (Z = 100), and approaching zero for very large gears (rack teeth). This variation is physically unreasonable.

Examination of equation 1.74 shows that Simon assumes the compliance to be inversely proportional to Z, even though there is no logical reason why it should be. An essential feature of any good empirical relationship is that it should give physically reasonable results for limiting values of each parameter. Simon's equations do not satisfy this requirement, and can thus only be valid for a very limited (and undefined) range of Z values.

A possible reason for Simon's unlikely results may be the presence of misprints in the published equations (Eq. 1.74). A different form of these equations was actually given in an earlier publication. Several

attempts were accordingly made to contact Simon personally, to check that his published equations were correct, and to establish the logic underlying them. These attempts met with no success, however, and as a consequence, Simon's results have not been plotted against the author's for comparison.

3.3 Overall Mesh Stiffness : Comparison with Published Results

3.3.1 Introduction

The definitions of the overall mesh stiffness c_γ and single tooth stiffness c' are, for both spur and helical gears, based on the 2-D "thin-slice" model used in the gear rating standards. (See section 1.2.4). As explained in section 2.10, however, only the overall mesh stiffness c_γ has any meaning in the author's 3-D meshing model for helical gears, so only values of c_γ calculated from equations 1.29 and 2.17 have been plotted below for comparison.

Recall, however, that c' and c_γ are both defined by the standards only (i.e. in the transverse plane), so that Eq. 2.17(b) for spur gears must be used to obtain comparable values from the 3-D model of helical gears. However, the term c_γ must be defined not in the transverse plane, but in the normal plane, along the load line direction, and Eqn.2.17a was used to estimate c_γ from the author's 3-D model. The information presented by Vedmar[5] is insufficient to allow calculation of c_γ, but since his contact deformation equation yields nearly identical results with the author's, and his tooth bending (and shear) deflections were shown (see section 3.2.2) to be in very good agreement with the author's, Vedmar's c_γ values will be nearly identical with the author's for perfect gears, and need not be presented for comparison purposes. As mentioned in section 3.2.3, Simon's compliance results were highly illogical, and so, his c_γ values will not be used for comparison purposes. Consequently, only the results for c_γ as calculated by the standards[2,3,4] are compared with the author's.

3.3.2 Comparison of c_γ with the ISO Formulae

Values of c_γ obtained from the author's equations 2.16a and the ISO equation 1.29 for standard helical gears with m_n = 10mm, β = 30°, b = 120mm and $z_1:z_2$ = 18:18, 18:54 and 18:100, at a specific load F/b = 100 N/mm are plotted in Figure 3.12 for a number of phases during a complete cylce of engagement. ISO values are the same at all phases of mesh since the overall mesh stiffness c_γ is based on the maximum single tooth stiffness c' at the pitch point (section 1.2.4).

Fig. 3.12 Instantaneous Mesh Stiffness
Beta=30Deg b=120mm mn=10mm

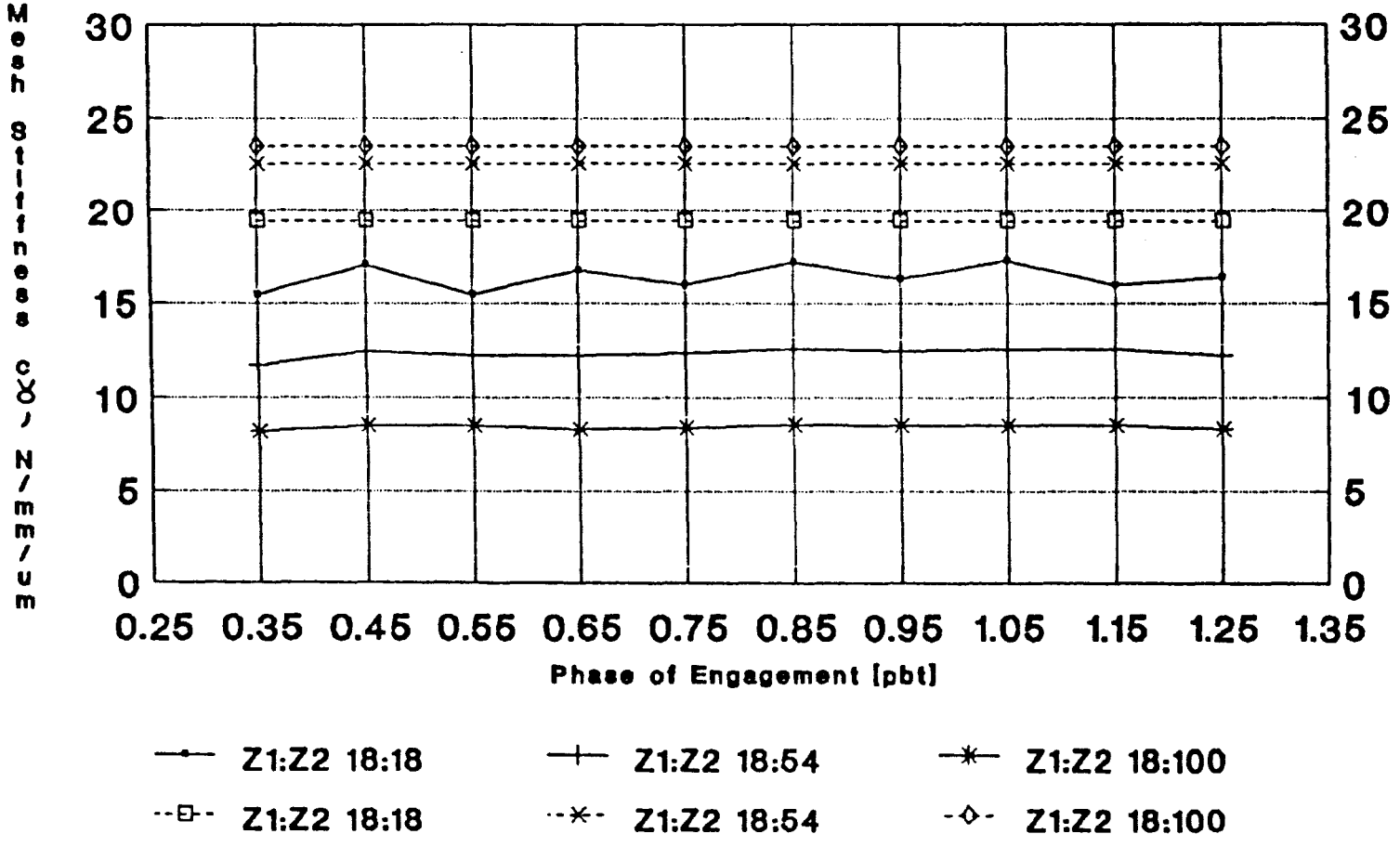

HADDAD solid line / ISO dashed line

From Figure 3.12 for the 18:18 mesh, the instantaneous mesh stiffness c'_γ (equation 2.16a) varies from about 15 to 18 N/(mm.μm). Equation 1.29 predicts a mean value of about 19.75 N/(mm/μm) which is in substantial agreement with the author's results. For the 18:54 and 18:100 mesh, the ISO equation predicts higher mean mesh stiffness values than the 18:18 mesh as shown in Figure 3.12. This is partly due to the increase in ϵ_α from 1.278 for the 18:18 mesh, to 1.353 and 1.377 for the 18:54 mesh and 18:100 mesh respectively, but mainly due to the higher values of the single tooth stiffness c' given by equation 1.24. The author's 3-D model, on the other hand, predicts a reduced mesh stiffness, for these ratios, due to the increasing influence of gear body compliance on the 54 and 100 tooth gear wheels. For the 18:54 mesh, the ISO mesh stiffness is, on average, about 1.8 times that given by the author's mesh model, and about 2.8 times for the 18:100 mesh. For completeness, the instantaneous transmission error values f_t are also plotted in Figure 3.13.

If, instead, relative stiffnesses are calculated from the author's model, by subtracting the gear body compliance terms (Steward[30]), there is then much closer agreement between the ISO value of c_γ, and those given by the 3-D model. The ISO[4] prediction that the 18:100 mesh is stiffest is also confirmed. This has been done in Figure 3.14, where the curves are in much better agreement than those in Figure 3.12 for the 18:100 mesh.

It is worthwhile mentioning at this point that if equation 2.16b were used instead of equation 2.16a to calculate c'_γ (see section 2.10), then the differences between the ISO and the author's results would be significantly greater.

The cyclic variations of c'_γ and f_t shown in Figures 3.12 and 3.13 respectively are significantly greater for the 18:18 mesh than for the other two meshes shown. This can be traced to the associated variations of ϵ_α and hence ϵ_γ which are as shown in Table 3.1. As Z_2 increases, the average number of teeth in contact increases, tending to produce a smoother stiffness wave form. $\epsilon_{\alpha 0}$ and $\epsilon_{\gamma 0}$ are the ratios for the extended plane of mesh shown in Figure 2.1.

Another interesting effect to examine, is that of the gear ratio $U(Z_2/Z_1)$ on the overall mesh stiffness c_γ. Figure 3.15 shows this effect according to the author's equation 2.17a and the ISO equation 1.29. As explained earlier, the author's curves show reduced stiffness for the larger gears, since the increased tooth "cantilever" stiffness on larger gears is offset by the large gear body deformations, which reduce

Fig. 3.13 Instantaneous Transmission Error, Beta=30Deg b=120mm mn=10mm

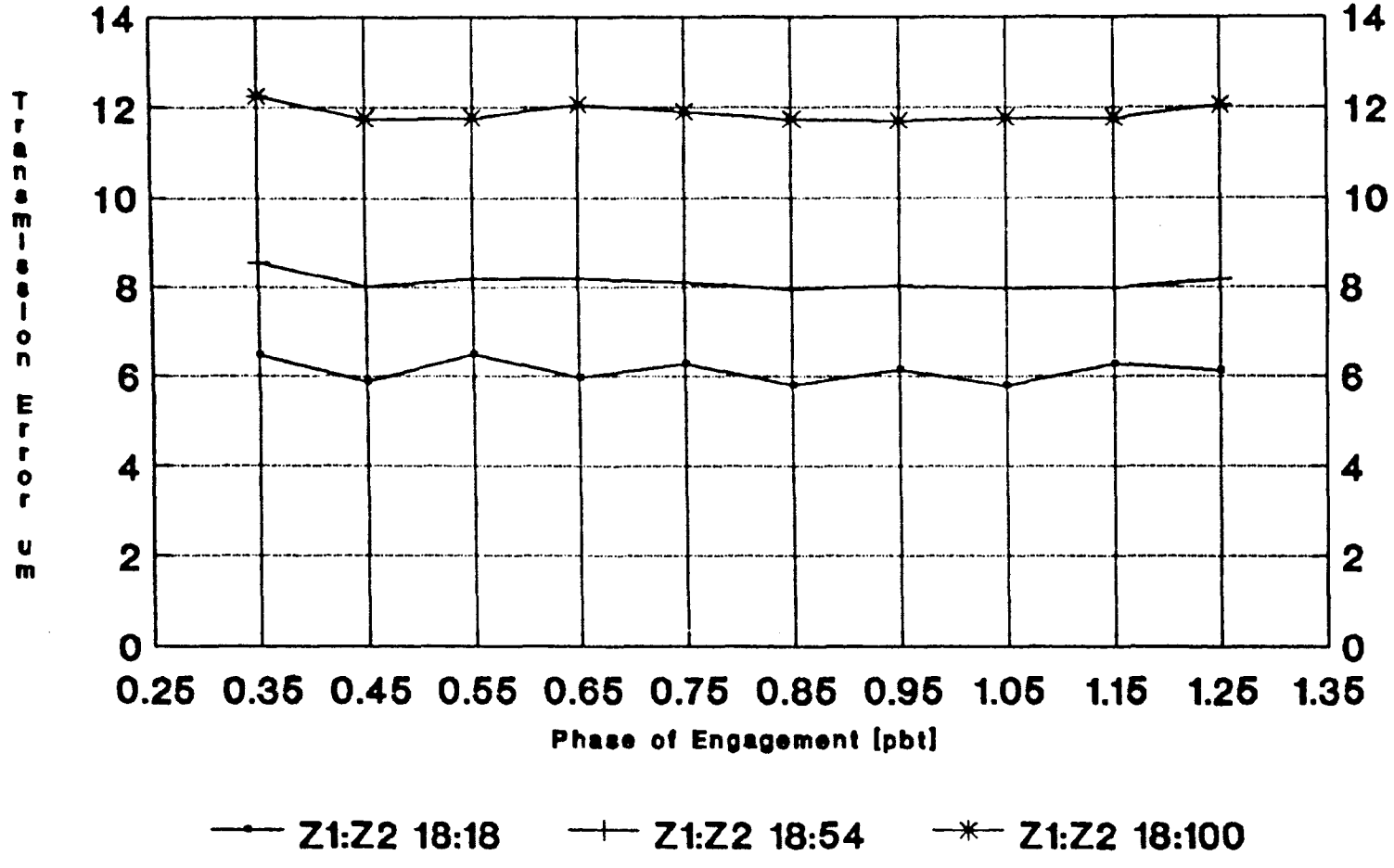

Fig. 3.14 Instantaneous Relative Mesh Stiffness, Beta=30Deg b=120mm mn=10mm

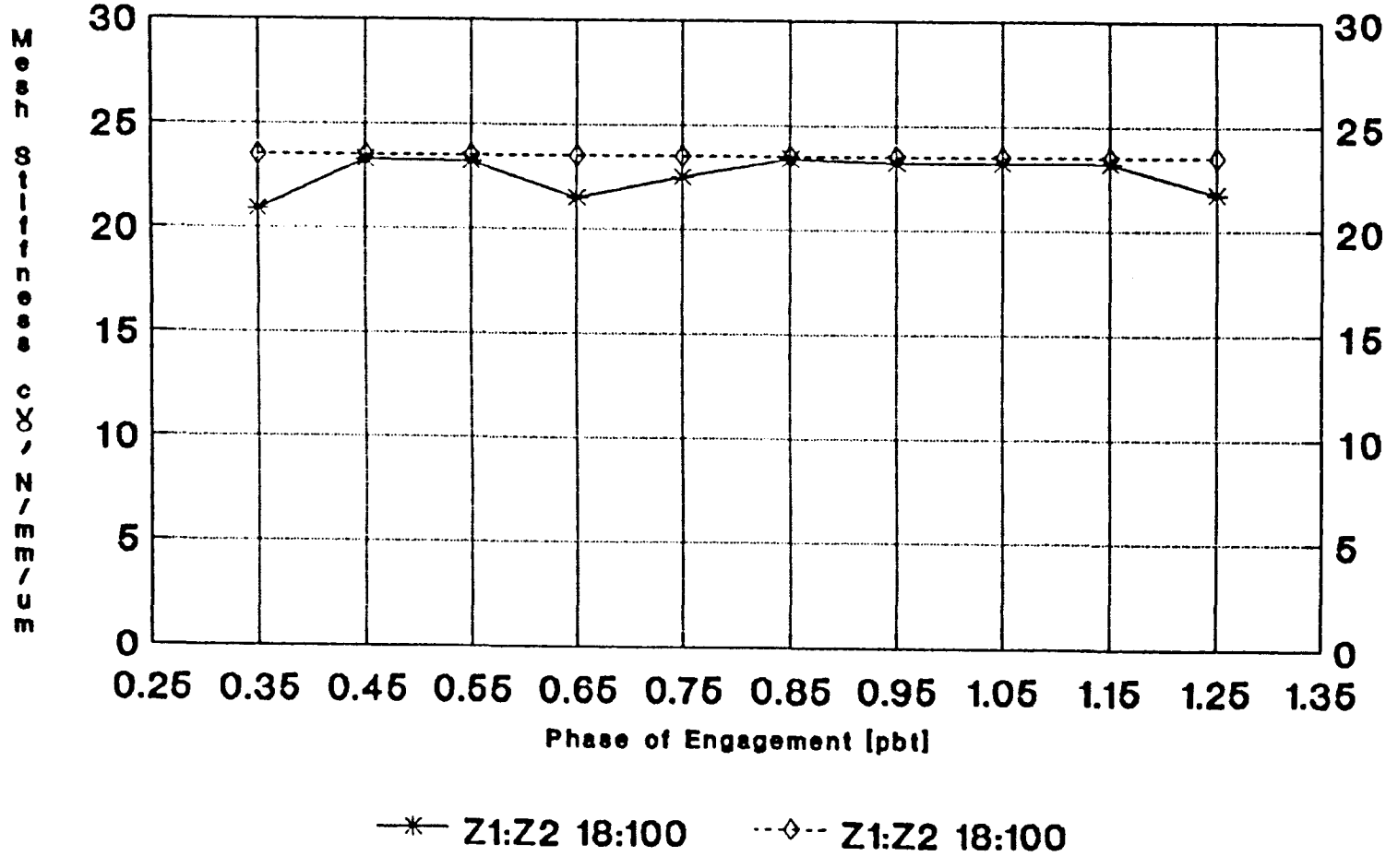

HADDAD solid line / ISO dashed line

Z1:Z2	ε_{α}	ε_{α_c}	ε_{β}	ε_{γ}	ε_{γ_o}
18:18	1.278	1.978	1.910	3.188	3.888
18:54	1.353	2.053	1.910	3.263	3.963
18:100	1.377	2.077	1.910	3.287	3.987
Beta=30 Deg b=120 mm mn=10 mm					

Table 3.1 Variation of Transverse Contact Ratio

Fig. 3.15 Overall Mesh Stiffness & Gear Ratio, Beta=30Deg b=120mm mn=10mm

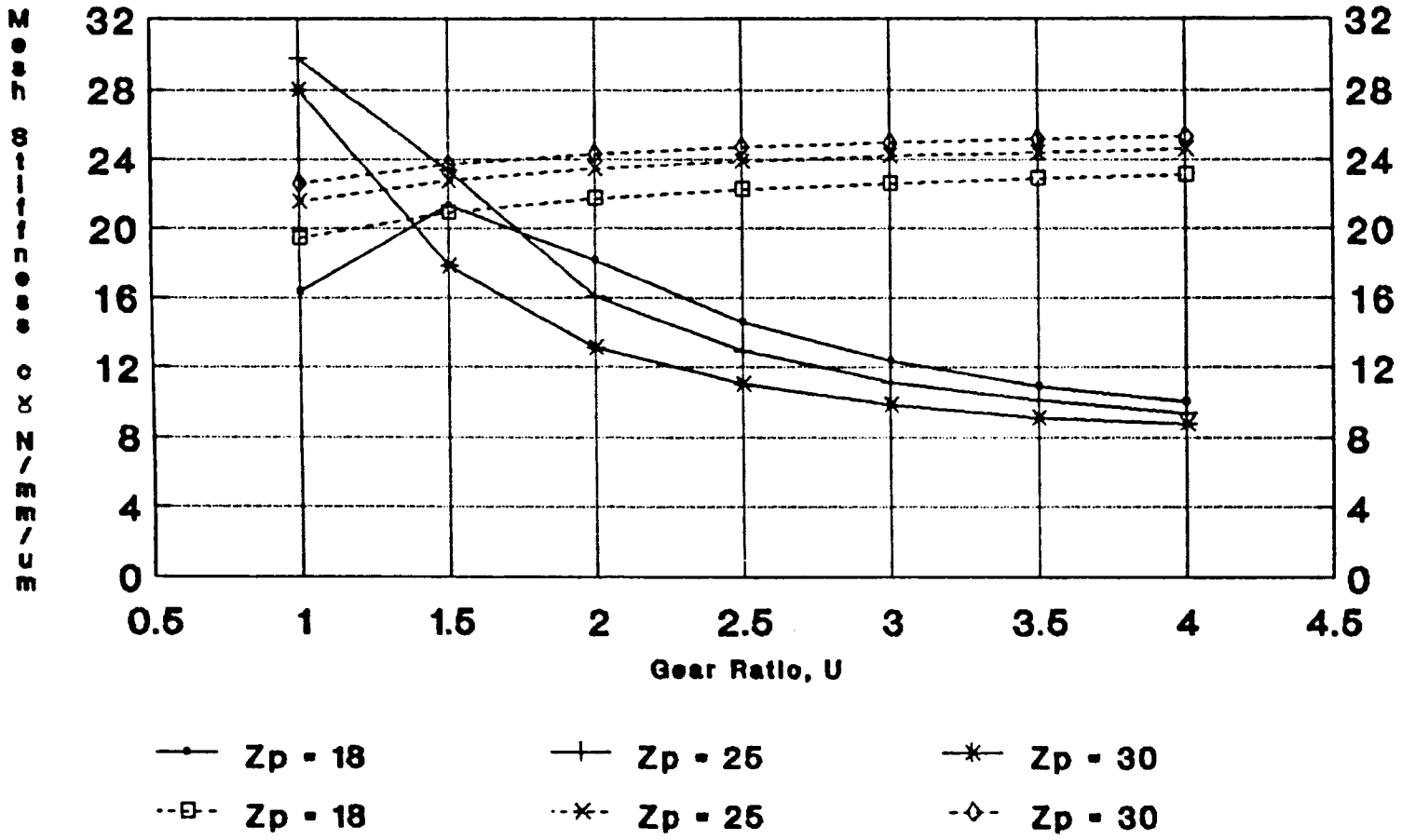

HADDAD solid Line / ISO dashed line

the overall mesh stiffness. The curves based on ISO formulae, however, show increasing stiffnesses for larger size wheels since the effect of gear body compliance is not accounted for.

It is interesting to consider the "hump" in the author's zp=18 curve, which is not evident in the other two curves. At very low values of Z_1 and Z_2 (U=1), gear body deformations are negligible (0.10 to 0.12 units), but tooth "cantilever" deformations are relatively large due to the reduced root section. As a result, the mesh stiffness c_γ is relatively small. As U increases to about 1.5, gear body deformations are still negligible (0.10 to 0.12 units), but the wheel teeth become slightly stiffer giving a slightly larger c_γ as shown. Beyond that point, gear body deformations become significant, offsetting the increased tooth cantilever stiffness for larger gears, and so c_γ becomes smaller again.

This effect might also have been observed in the other two solid curves if values of U less than 1 had been used in order to give very small values of Z_2.

The variation of c_γ with $Z_1(=Z_2)$ for U=1 has also been plotted in Fig.3.16 for completeness, and exhibits the same trend as the curves plotted in Figure 3.15. Steward[30] shows similar results for spur gears.

Finally, the effect of gear face width b on c_γ is studied. For facewidth ratios b_0 $(=b/m_n)$ of 2, 4, 4.5, 6, 8, 10 and $12m_n$, ten meshes were analysed at equal phase increments through a complete mesh cycle, and the average value of c_γ calculated from equation 2.17a. The values obtained are plotted against b_0 in Figure 3.17, which shows that c_γ decreases gradually with increasing facewidth ratio b_0.

The function $G(z,r_f)$ of equation 2.6 does not change significantly with a variation of b_0 between $2m_n$ and $12m_n$. However, the function $F(z,r_f)$ of equation 2.5 decreases progressively with decreasing values of b_0, resulting in smaller tooth compliance values in equation 1.57, for narrower gears at the same value of $\bar{z}$. This results in a drop in the transmission error f_t of equation 1.64, and consequently a rise in the mesh stiffness c_γ of equation 2.17a as shown in Figure 3.17. These results must, however, be viewed with caution, since for $b_0 \leqslant 5$ the two end-effect functions in $G(z,r_f)$ "overlap", and there is no FE data available to support the simple superposition implied by Equation 1.57.

Fig. 3.16 Overall Mesh Stiffness & Z
Beta=30Deg b=120mm mn=10mm U=1

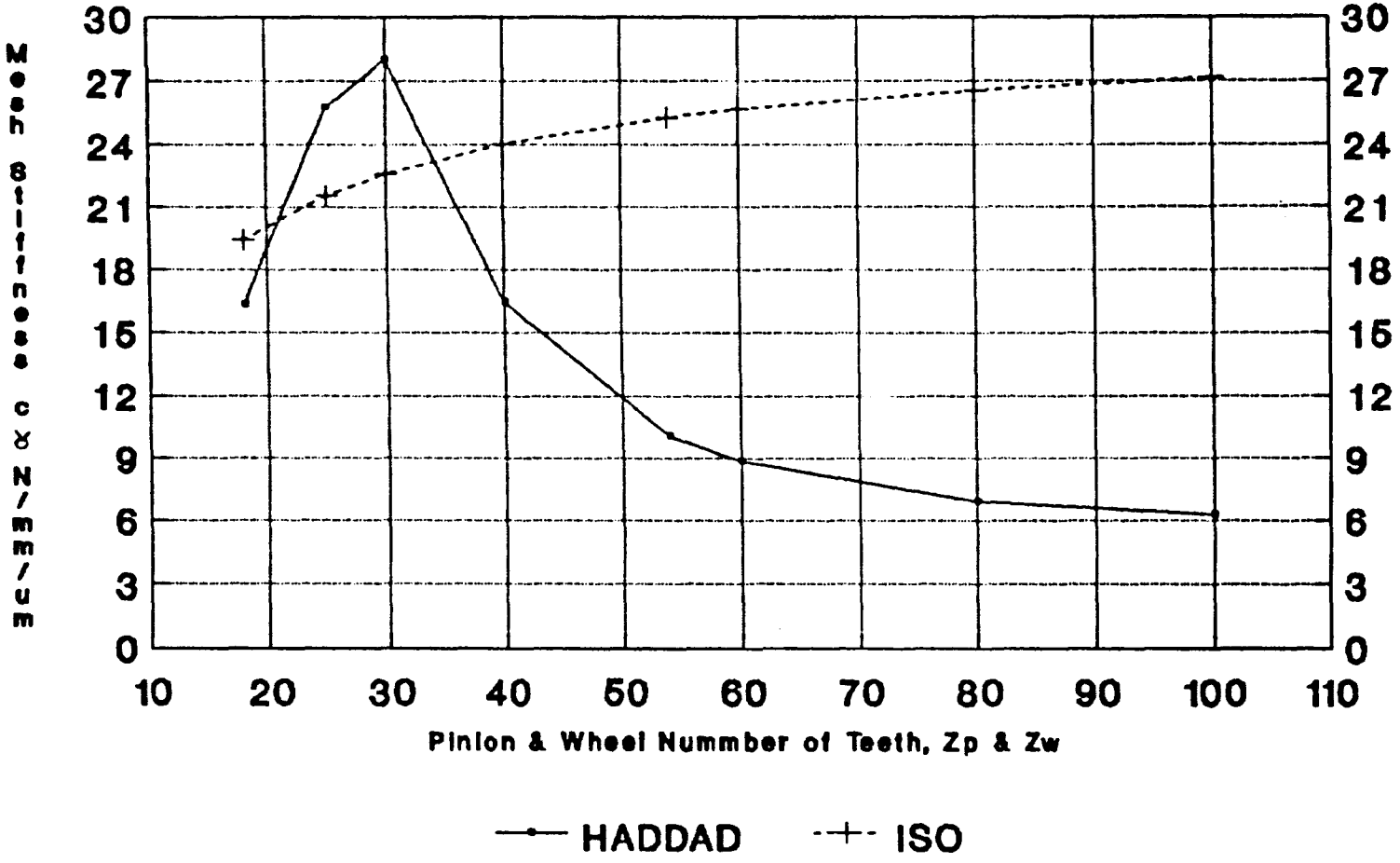

Fig. 3.17 Overall Mesh Stiffness & b0
Beta=30Deg mn=10mm Z1=18 Z2=54

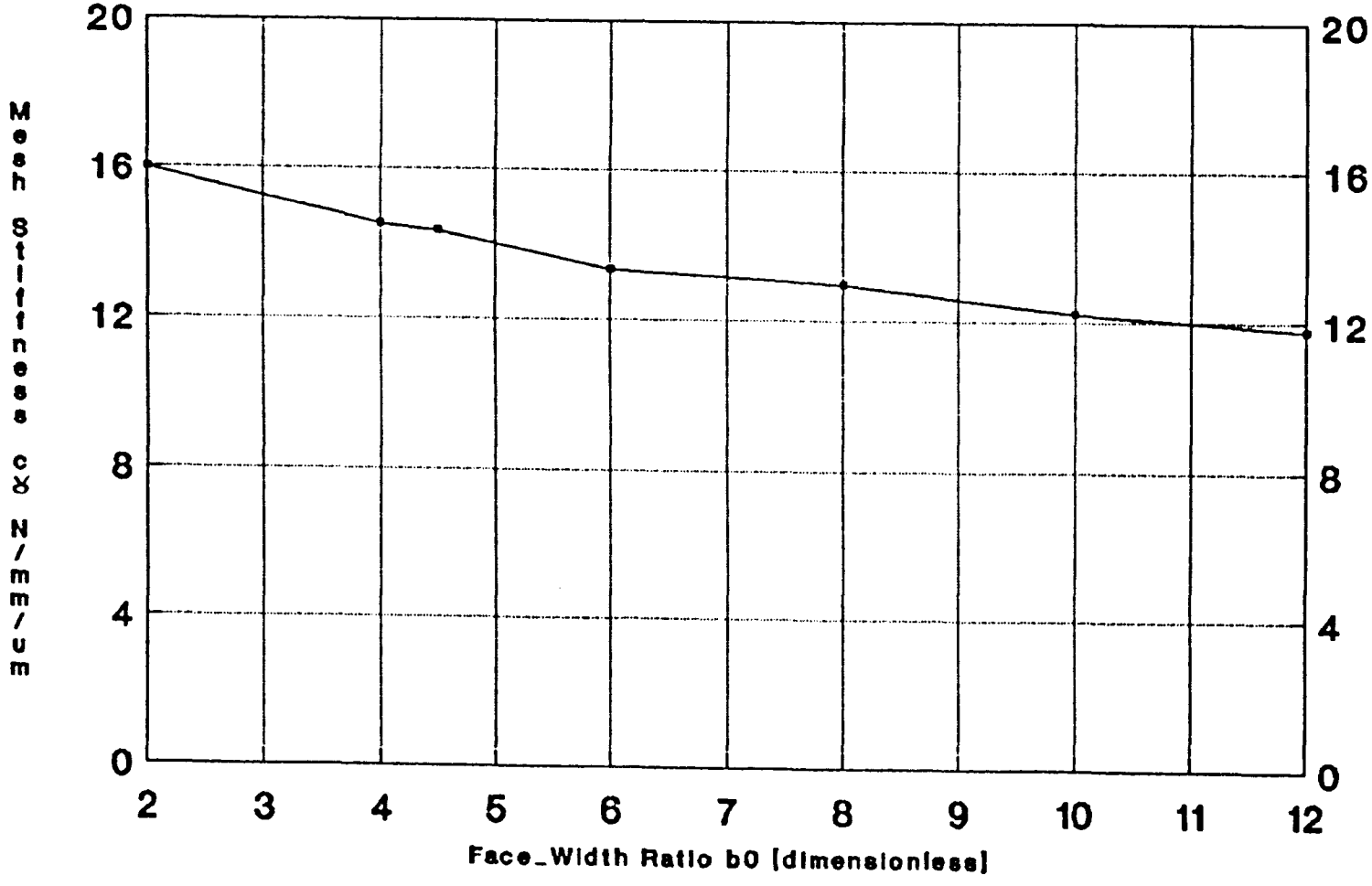

3.4 Contact Loads and Stresses

The main purpose of the program described in section 2.1 is to calculate the contact load and contact stress distributions across simultaneous contact lines of engaged helical gear teeth. The results for the load distribution so obtained are presented in figures 3.18, 3.19 and 3.20, where the non-dimensional load intensity w is plotted against axial location along the contact line for a standard gear pair with b = 120mm, mn = 10mm, Z_1 = 18, Z_2 = 72 and β = 0°, 15° and 30° respectively. The total normal load used in each case is 12000 N (100 N/mm), which gives typical safety factors for good quality carburised gears. Figures 3.18a and 3.18b show the load distribution for a spur gear mesh. Phase 1 represents the start of mesh (line A_0A_0' in figure 2.1), and phase 10 represents the end of mesh (line B_0B_0' in figure 2.1). Phases 5 and 6 give single tooth pair contact. Figure 3.18c shows Vedmar's[5] results for a very similar spur gear (Z_1:Z_2 = 20:80) with a rather narrower facewidth.

The close qualitative agreement between the author's and Vedmar's[5] set of results is self evident. Particularly important features of both are:

1. Peak load intensity is in the single tooth pair contact region as expected.
2. Load is not uniform across the facewidth, with peak values at about $2.0m_n$ from the teeth ends, varying from about 1.06 to 1.11 times the loads at mid-facewidth of the teeth ($z = 6.0m_n$), and minimum values at the teeth ends, varying from about 0.88 to 0.96 times the loads at mid-face (average to 0.92). At the tooth ends, deformation is plane stress, and at mid-face deformation is approximately plane strain, and since the total deformation must be the same at each section, the ratio of the load at the ends to that at mid-face is expected to be

$$1-\upsilon^2 = 1-0.3^2 = 0.91$$

which is close to the average ratio of 0.92 obtained from figure 3.18.

The cause of the load peaks at about $2.0m_n$ from the teeth ends is not clear. However, the differential equations for tooth deflection proposed by both Kagawa[24], using his "beam" model and Seager[34] using his deflection measurements are of the general form (refer to section 1.4.2 and figure 1.8)

Fig.3.18a Load Intensity Along a Single Contact Line Going Through Mesh (F=12kN)

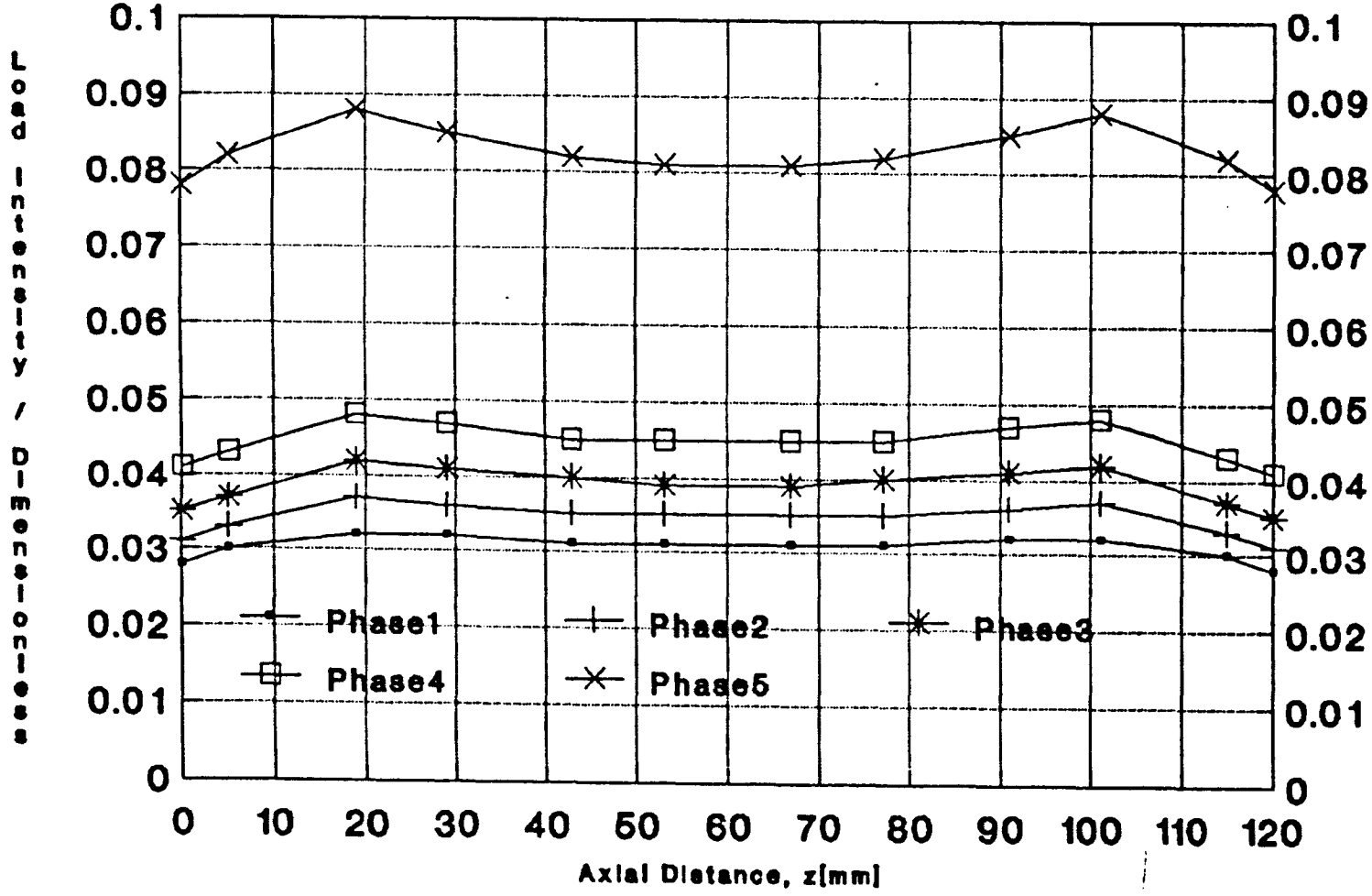

Beta=0 Deg b=120mm mn=10mm Z1=18 Z2=72

Fig.3.18b Load Intensity Along a Single Contact Line Going Through Mesh (F=12kN)

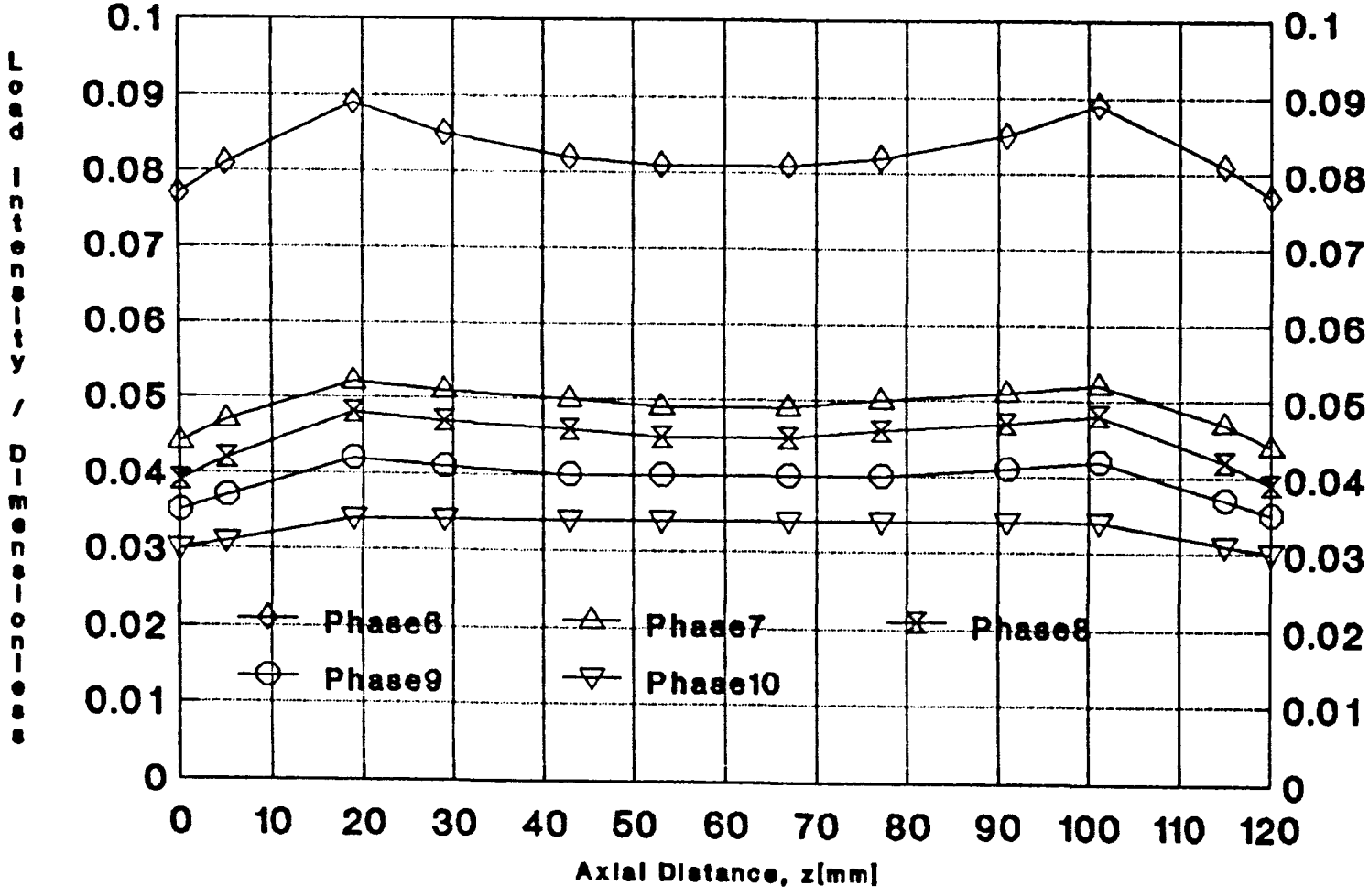

Beta=0Deg b=120mm mn=10mm Z1=18 Z2=72

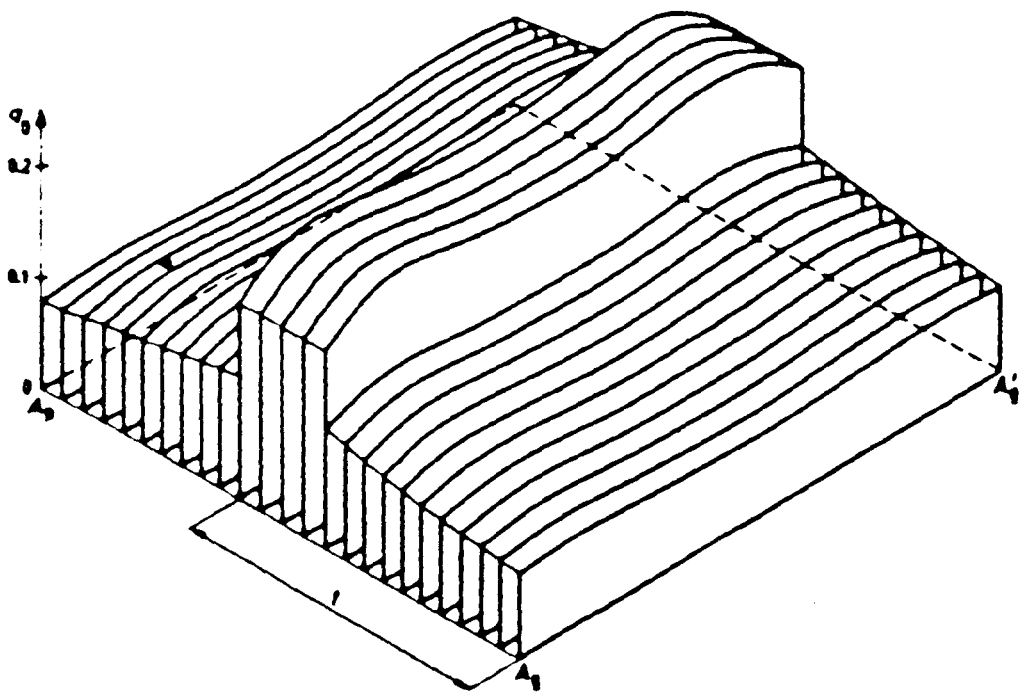

$z_p = 20$
$U = 4$
$\beta_n = 0$
$b_o = 5$

Fig. 3.18c Vedmar's Non_Dimensional Load Distribution

$$K \cdot \frac{d^4\omega_0}{dx^4} - k_2 \cdot \frac{d^2\omega_0}{dx^2} + k_1 \cdot \omega_0 = p_{(x)}$$

which yield a solution of the form

$$\omega_0 = e^{\lambda_1 x} \cdot (A.\cos\lambda_2 x + B.\sin\lambda_2 x) + e^{-\lambda_1 x} \cdot (C.\cos\lambda 2x + D.\sin\lambda_2 x) + w(x)$$

where

ω_0	-	is the beam defelction along the free edge
$P(x)$	-	is the load intensity at the free edge (figure 1.8)
K	-	is the flexural rigidity
k_1, k_2	-	see figure 1.8
λ_1, λ_2	-	are functions of poisson ratio υ, and dimension b (figure 1.8)
A,B,C,D	-	are arbitrary constants determined from the boundary conditions
w(x)	-	is a particular integral

Over a wide faced gear, the solution w(x) dominates behaviour at mid-face, while the two damped sinusoidal functions produce "end effects" very similar to those shown in figure 3.18, and similar to those seen in a beam of finite length resting on an elastic foundation. It thus seems likely that the load peaks near the tooth ends shown in figure 3.18, are inherent features of spur gear contact lines, and not the result of any shortcomings in the 3-D model.

Next, variations of the load distribution along one contact line on a helical gear as it passes through a complete mesh cycle is plotted. Figures 3.19 and 3.20 give the results for two helical gears with β = 15° and 30°. The module and facewidth chosen are those for which the actual FE data was obtained as described in section 2.5.

To compare the author's results with Vedmar's[5] load distributions, a gear with the same geometry as one of those analysed by Vedmar[5] was also analysed. The comparison is presented in figures 3.21 and 3.23.

In this case, the parameters b, m_n, Z(20 and 80) and β(=20°) were different from those for which the authors FE data was available. The module m_n has no efect on the stiffness data, and, as shown in figure 3.17, the factor (b/m_n) also has very little effect. As explained in section 2.6, it was necessary to interpolate the coefficients of equations 2.5 and 2.6 using a cubic spline fitting routine to obtain

results for Z = 20 and 80, while only linear interpolation between values at β = 0 and 30° was possible to give values at 20°. (These procedures for interpolating for Z and β are built into the mesh analysis software, as outlined in Appendix 2A.)

Because of hardware limitations, the analysis was performed using only 10 Gauss points per full-length contact line, giving a mean point spacing of about 1.1 modules. Values of the load intensity and stresses at the end points of each contact line (not Gauss points) were obtained from equation 1.70.

In figures 3.21 and 3.23, the author's results are plotted both with and without the factor M (equation 1.54). With M included, the increased contact compliance near and at tooth tip contact results in smaller load intensities there. Results with M are plotted as "solid" lines, those without (M = 1), as dotted lines which coincide with the solid lines except near and at the tooth tips. The "dashed" lines show Vedmar's[5] load distributions derived from his '3D' plots (figures 3.22, 3.24).

The letters a to j on figures 3.21 and 3.22, and the corresponding letters on figures 3.22 and 3.24 indicate the different contact lines (phases) analysed. Line 'a' is at the start of mesh, near A_g' in figures 3.22 and 3.24.

The author's and Vedmar's curves in figures 3.21 and 3.23 exhibit a number of quantitative and qualitative common features as follows:

1. Noticeable load peaks occur on the short contact lines, particularly on those lines near A_g' and A_p. Such load "spikes" have been observed by several authors[5,6,7] and can be explained by the "buttressing" effect of the adjacent unloaded positions of one of the teeth in these regions (section 1.2.1). In spite of the increased contact compliance near and at the tooth tips, accounted for by the factor M (equation 1.54) in the author's model, substantial load peaks are nevertheless still observed (solid curves in figures 3.21 and 3.23), and with M = 1 (as in Vedmar's theory), the peaks increase to become nearly identical to Vedmar's end load peaks.
2. On the full-width contact lines present in gears with small β (see figure 3.19 for β = 15°), the peak loads are neither at the pitch line nor at mid-face, as suggested by Merrit's[17] thin slice theory.

Fig. 3.19 Load Intensity Along a Single Contact Line Going Through Mesh (F=12kN)

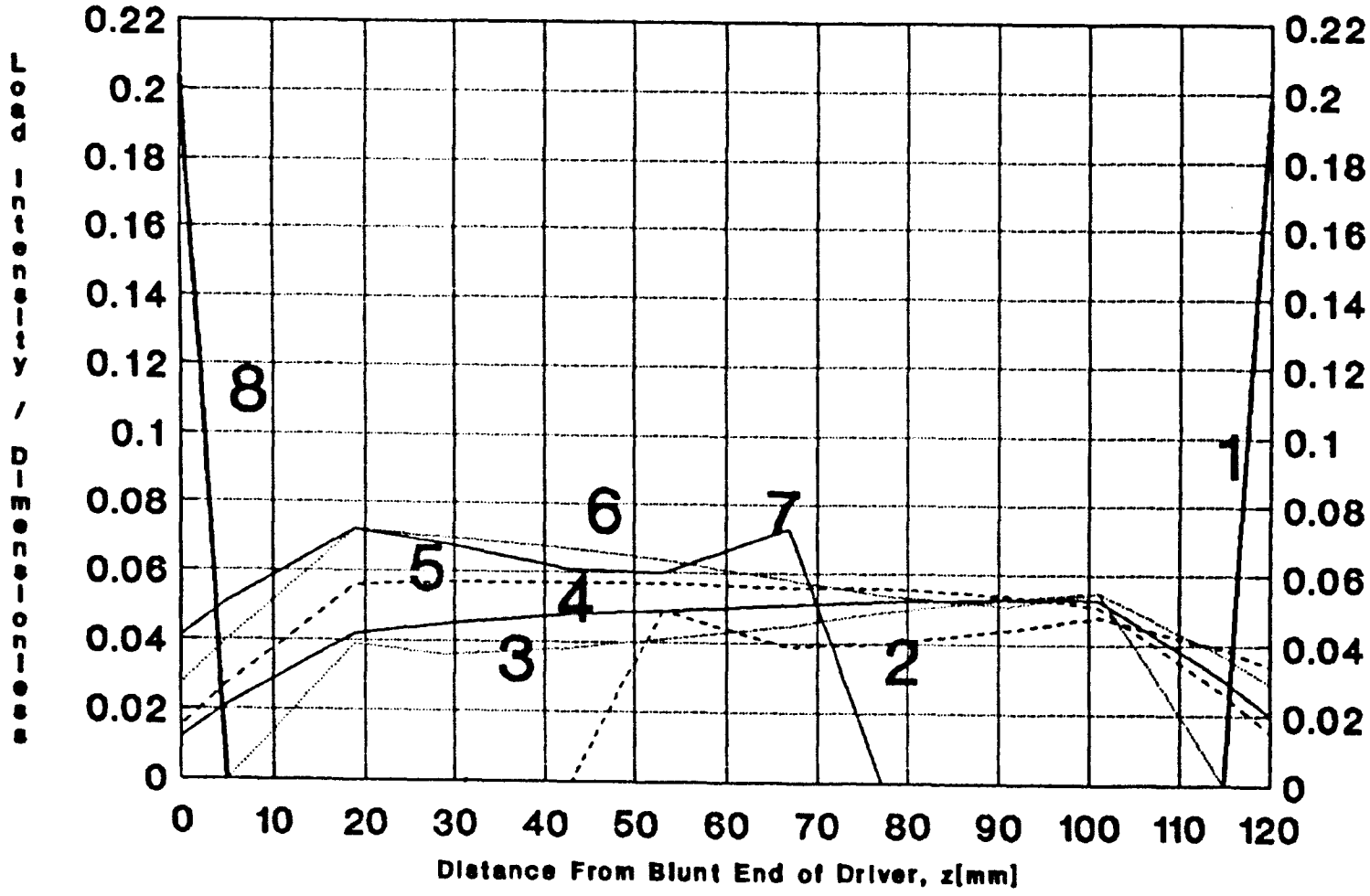

Beta=15Deg b=120mm mn=10mm Z1=18 Z2=72

Fig. 3.20 Load Intensity Along a Single Contact Line Going Through Mesh (F=12kN)

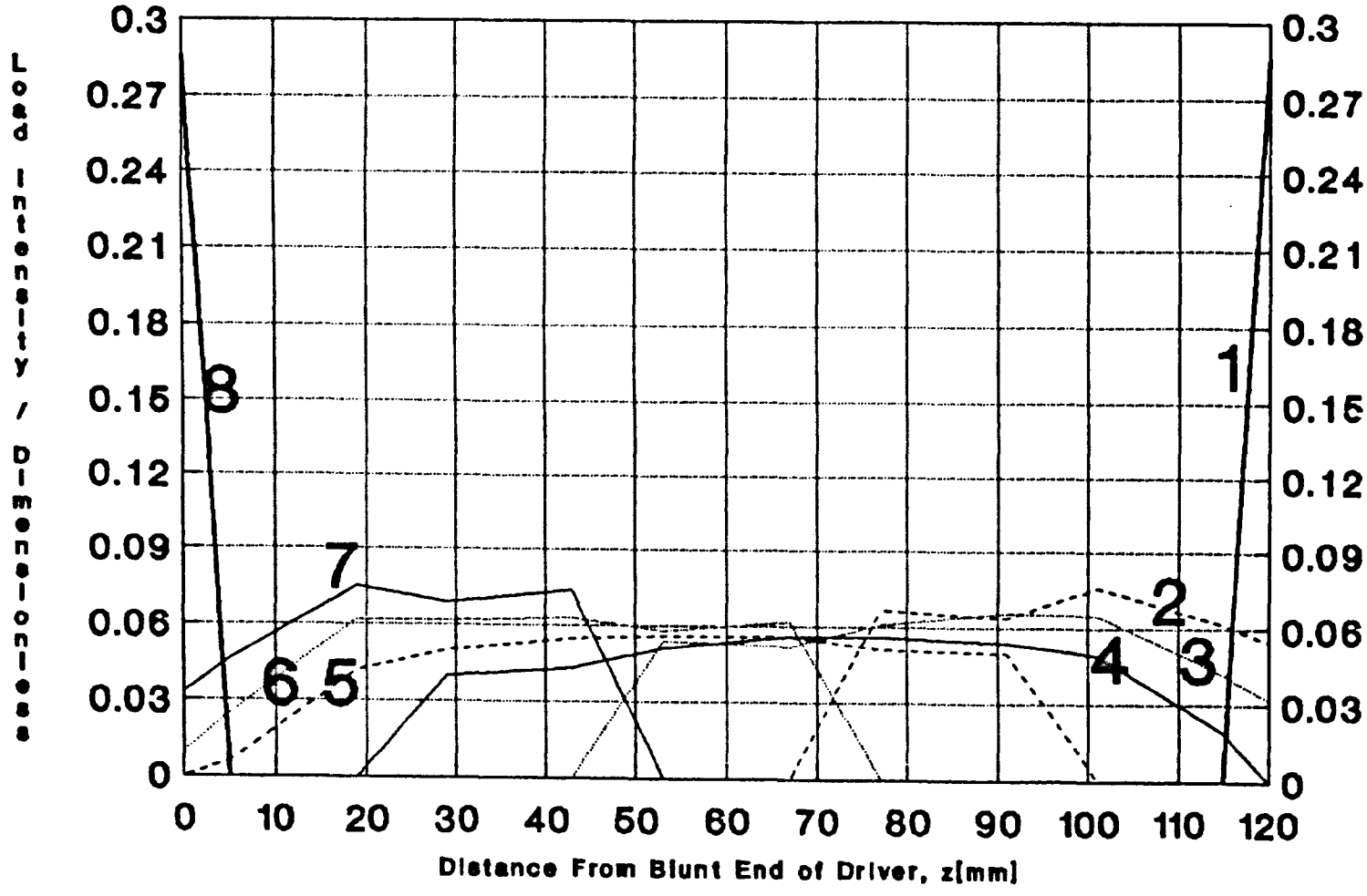

Beta=30Deg b=120mm mn=10mm Z1=18 Z2=72

Fig. 3.21 Load Distribution Along a Single Contact Line Going Through a Complete Mesh Cycle

(F=2.93kN Beta=20Deg b=30mm mn=6mm Zp=20 U=1)

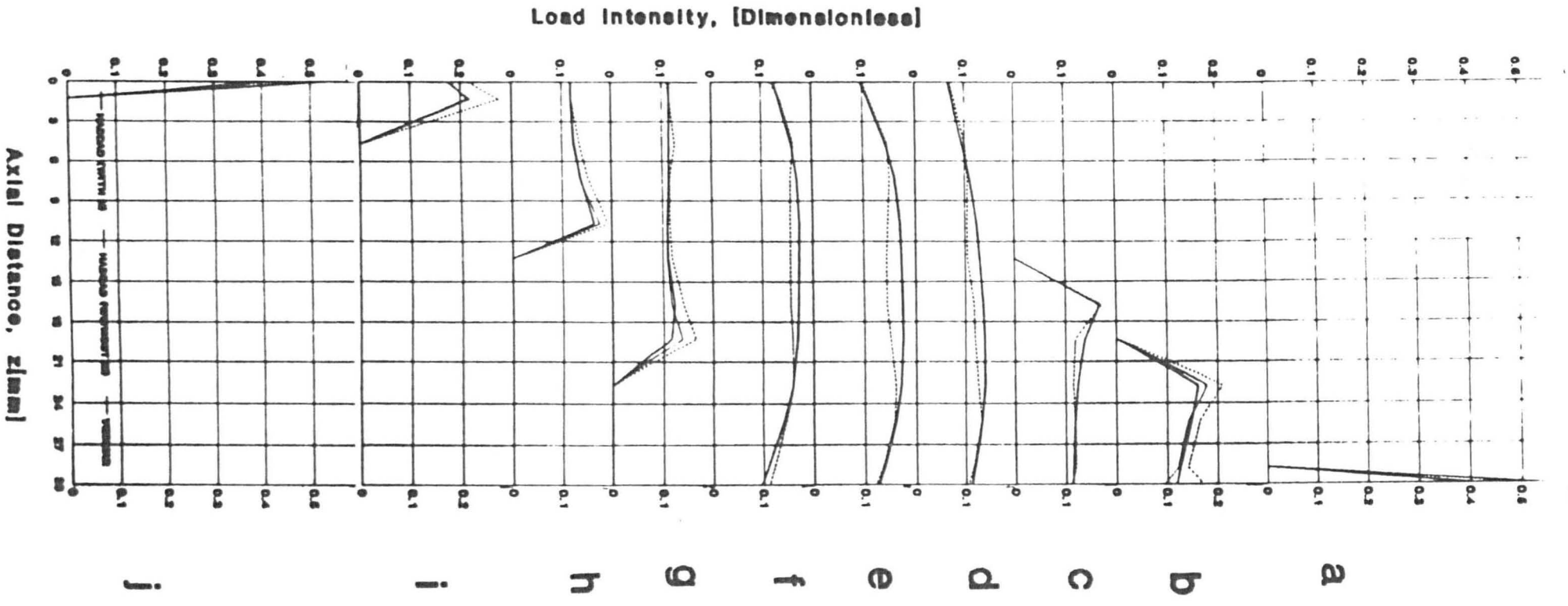

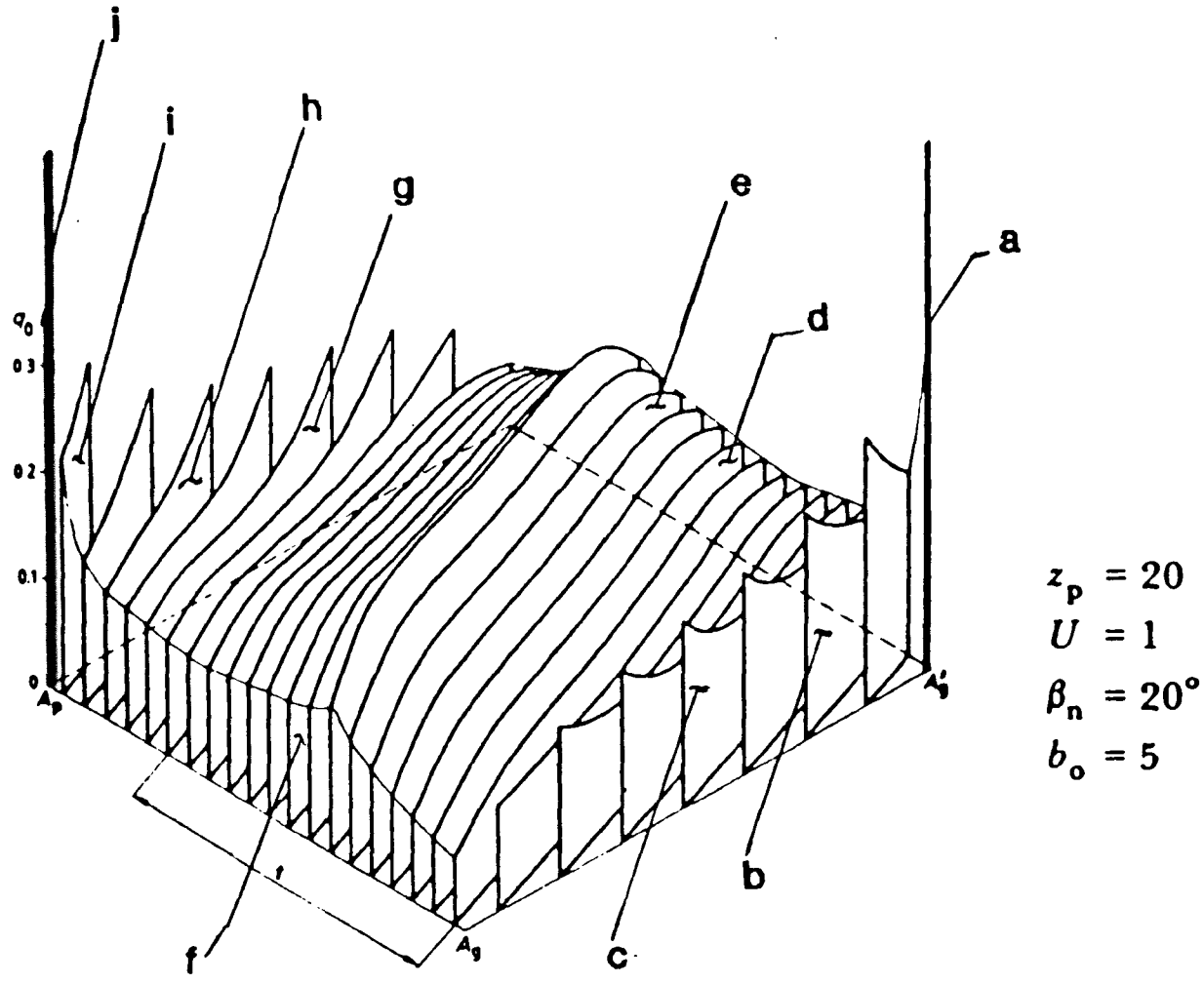

Fig. 3.22 Vedmar's Actual Non_Dimensional Load Distribution Chart (Refer to Fig. 3.21)

Fig. 3.23 Load Distribution Along a Single Contact Line Going Through a Complete Mesh Cycle

(F=3.61kN Beta=20Deg b=30mm mn=6mm Zp=20 U=4)

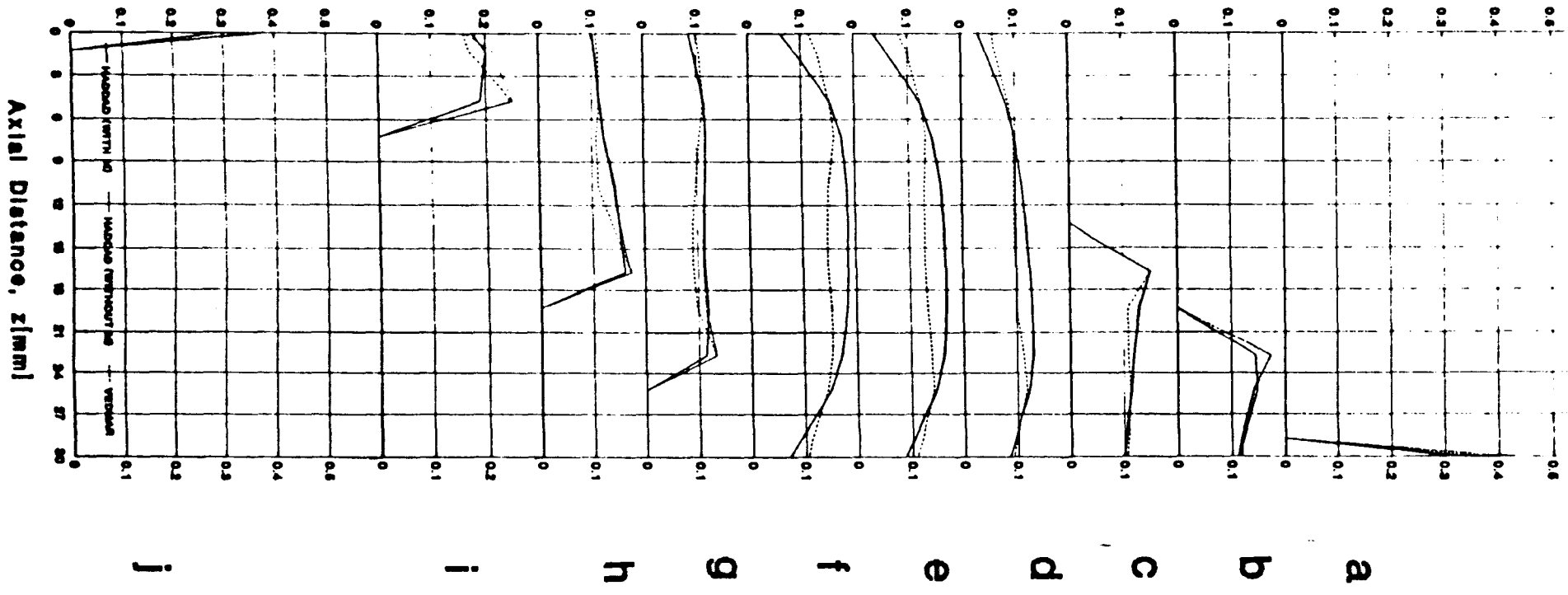

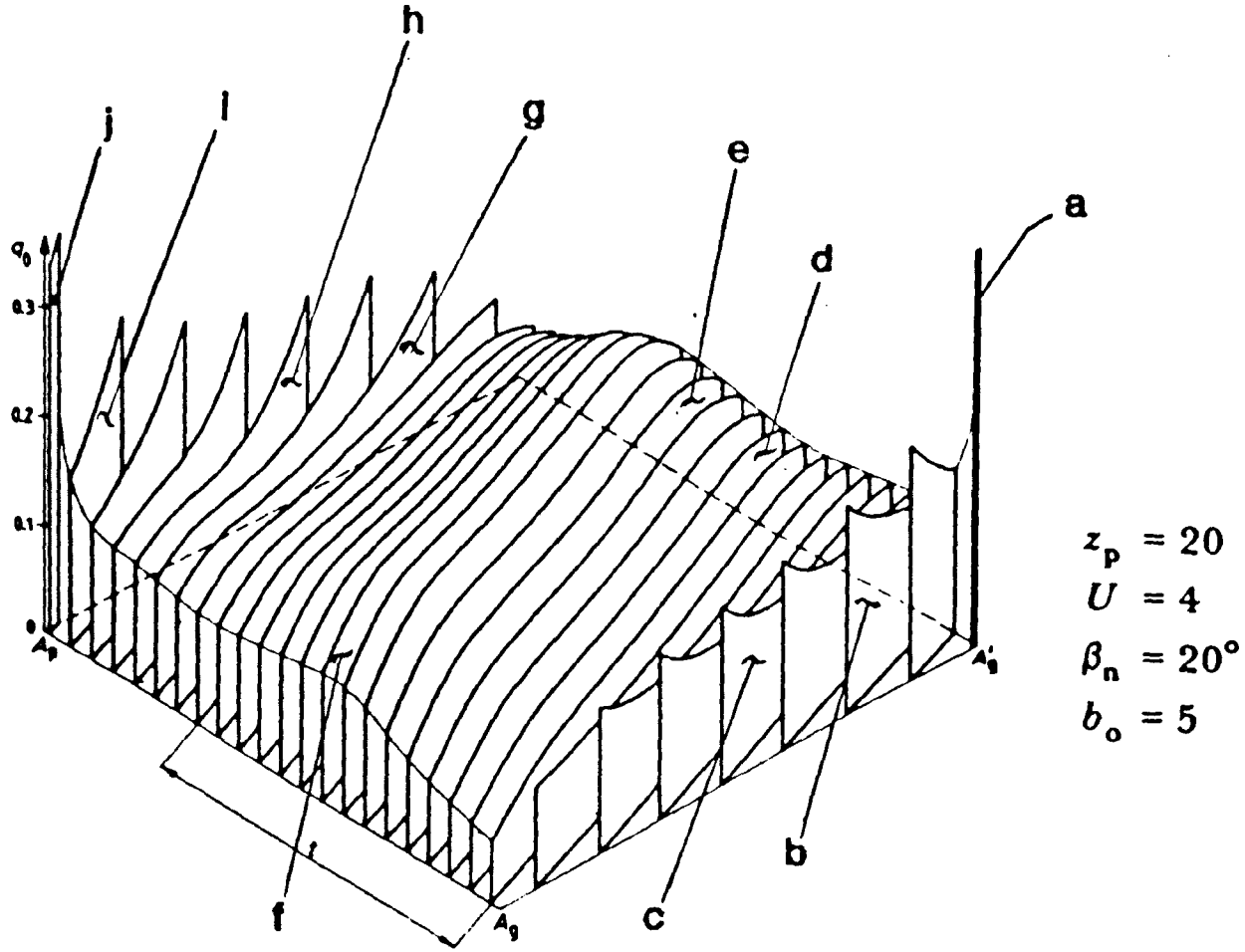

Fig. 3.24 Vedmar's Actual Non_Dimensional Load Distribution Chart (Refer to Fig. 3.23)

As with the spur gears of figure 3.18, the peak load intensity on these full contact lines tends to occur at about $2.0m_n$ from one end of the facewidth. In Vedmar's[5] work this also occurs for the 20° helix angle gears as shown by figures 3.21 to 3.24 (peaks at about $1.0m_n$ from one end for b = 30mm, m_n = 6mm). The author's curves for β = 20° (figures 3.21 and 3.23) are seen to behave in a similar fashion to the curves for β = 30° given in figure 3.20. Realling that the stiffness data for figures 3.21 and 3.23 required linear interpolation for β = 20°, it is clear that a "high helix angle solution" has been obtained for 20°. Vedmar's[5] stiffness coefficients for β = 0, 10 and 20° do not, however, show a linear variation with β, so that the linear interpolation used is probably not justifiable. In the absence of a third set of FE data to complement that for β = 0° and 30°, however, only linear interpolation was possible.

3. On the author's 30° helix angle gear, $\epsilon_\beta > 1$, and there are no full contact lines. Figure 3.20, and the solid curves of figures 3.21 and 3.23 given by the "high helix angle solution" for β = 20° show peak load intensities at mid-face, near the pitch circle as predicted by Merrit[17]. Sharp load "spikes" are again apparent at the ends of these contact lines.
4. The author's results for full (or nearly full) contact lines show lower load intensities at the tooth ends than Vedmar's. A possible reason for this is the effect of the adjacent tooth stiffness functions included in the author's analysis, but not in Vedmar's[5]. This is discussed further below.

Possible reasons for the discrepancies between the author's and Vedmar's results in figures 3.21 and 3.23 are:

1. Vedmar's[5] results were extracted by measuring his rather small diagrams (which were enlarged for figures 3.22 and 3.24). It is estimated that the errors in this process could be of order ±5%.
2. Vedmar did not allow for contact outside the theoretical phase of mesh as the author did (see sections 2.3 and 1.4.3.3), so that the limits of contact at corresponding phases of mesh could have been slightly different. However, for the cases chosen, the author's start and end of mesh do occur within the "theoretical" meshing limits, so that this argument does not apply.
3. The linear interpolation for β = 20° referred to above probably tends to over estimate the effect of β, since Vedmar's coefficients for β = 0°, 10° and 20° show non-linear variations. This will

tend to produce (for β = 20°) a "high helix angle" solution, giving load intensity maxima on the full contact lines at mid-face rather than near the ends as in the spur and "low helix angle" solutions of figures 3.18 and 3.19.

4. Vedmar has effectively ignored the adjacent tooth deflections by assuming that a tooth deflects only under its own loads. The author has, however, shown (see section 2.5) that adjacent tooth deflections are significant, and, further more, not uniform across the facewidth, particularly for large values of β, where the deflections increase rapidly near the ends of the teeth. This increased compliance in the author's model implies lower peak loads near, and at the ends of contact lines, as the figures show.

By comparing the author's results for β = 0°, 15° and 30° shown in figures 3.18a,b, 3.19 and 3.20 respectively a further insight is possible. Clearly, the end-of-contact load "spikes" evident in helical gears do not occur in spur gears, which have only full-length contact lines, and lead to a relatively uniform load distribution. Even for helical gears at corresponding phases of mesh in figures 3.19 and 3.20 the load distribution does not vary significantly except at and near the ends of contact, where the contact lines become shorter as β increases. This gives, in the limit, a near "point" contact (lines 1 and 8 of figure 3.19, for example) with large load intensity "spikes".

Once the contact load at any point has been determined, the corresponding contact stress can easily be calculated from equation 1.1. The radius of curvature at any contact point j is given by equation 2.15, and the equivalent relative radius of curvature ρ_{eff} by equation 1.2. This has minima at the start and end of mesh, where, as described above, the peak loads also occur. Thus the peak contact stresses also occur at these points.

The two peak load intensities at the start and end of mesh are usually of comparable magnitude as shown in figures 3.19 and 3.20, but ρ_{eff} is smaller at the start of mesh (on a speed reducing drive), thus producing larger peak contact stresses at this point. These peak contact load and stress values thus occur when nominal "point" contact is achieved on a very short contact line at the start of mesh. To find these values, a trial and error procedure was used, in which the phase of mesh was changed in small increments until the load/stress peak was found. For comparison, a contact line at an intermediate phase has been chosen. The phase used is the mean of the two phases at the start and end-of-mesh load spikes. This allows comparison of contact

loads and stresses on corresponding contact lines for three different relative facewidths (b_0 = 2, 6 and $12m_n$). Figures 3.25 and 3.26 show the resulting contact load and stress distribution respectively, along these intermediate contact lines.

Clearly, the wider faced gears tend to give smaller contact loads, and consequently smaller contact stresses. Since the same specific load was used in each case (F/b = 100 N/mm), the only possible explanation for this is the reduced overall mesh stiffness on the wider gears as demonstrated in figure 3.17 (see also section 3.5.2 on the relation between peak loads/stresses and mesh stiffness).

3.5 Peak Contact Loads and Stresses

3.5.1 Variation of Peak Contact Load and Peak Contact Stress in a Complete Mesh Cycle

The mesh analysis program calculates the contact load intensity and contact stress at the Gauss points and at the end points of each contact line (see section 2.8, and Appendix 4A) for successive phases of mesh. Plotting of the results as in figures 3.18c, 3.22 and 3.24 then shows the variation of load intensity (or stress) both across the facewidth and with varying phase of mesh. For design, however, the instantaneous peak load intensity (or contact stress) on a contact line, and the way these quantities vary through the mesh cycle, are of greatest importance.

Figure 3.27 shows the variation of the instantaneous peak contact load intensity and contact stress with phase for helical gear pairs with ratios $Z_1:Z_2$ = 18:18, 18:54 and 18:72. Contact of a particular tooth pair is followed from the start of contact (phase $\simeq 0.35p_{bt}$). Note that the peak contact load and peak contact stress do not necessarily occur at the same point on the contact length, since σ_H depends not only on w but also on ρ_{eff} (equation 1.2) which also varies across the facewidth (figure 2.1).

As shown in figure 3.18, the peak contact loads (and contact stresses) on spur gears occur in the region of single tooth pair contact near the pitch point, but for wide-faced helical gears (with $\epsilon\alpha>2$), the peak contact loads (and stresses) are substantially constant in these central regions of the mesh cycle. The maxima occur at the load "spikes" at the beginning and end of contact, where the load transmitted by the particular tooth pair is concentrated on a very short contact line as shown in figures 3.19

Fig. 3.25 Variation of Load Intensity Along a Contact Line Across Face_Width

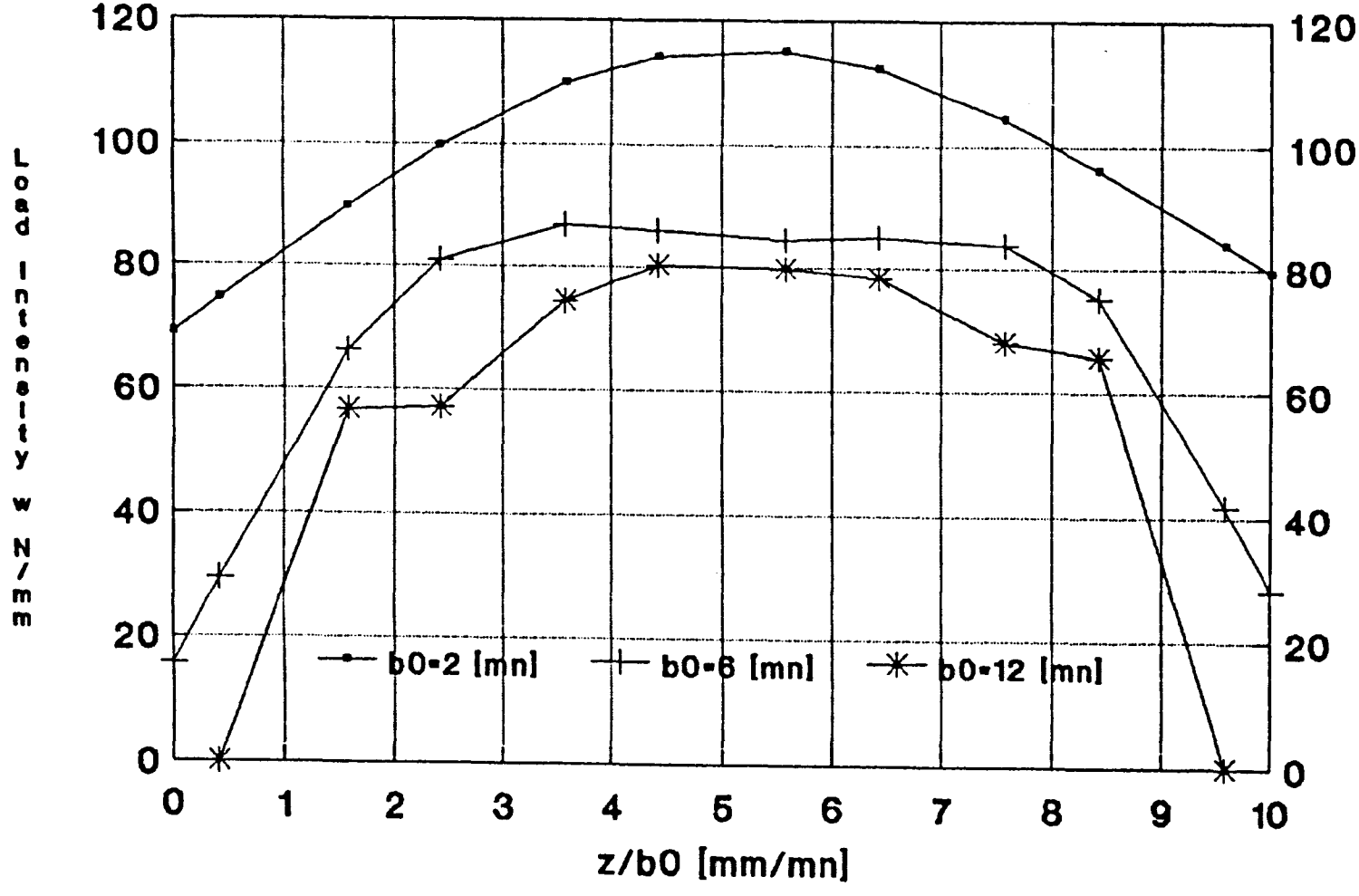

Beta=30 Degrees mn=10 mm Z1=18 Z2=64

Fig. 3.26 Variation of Contact Stress Along a Contact Line Across Face_Width

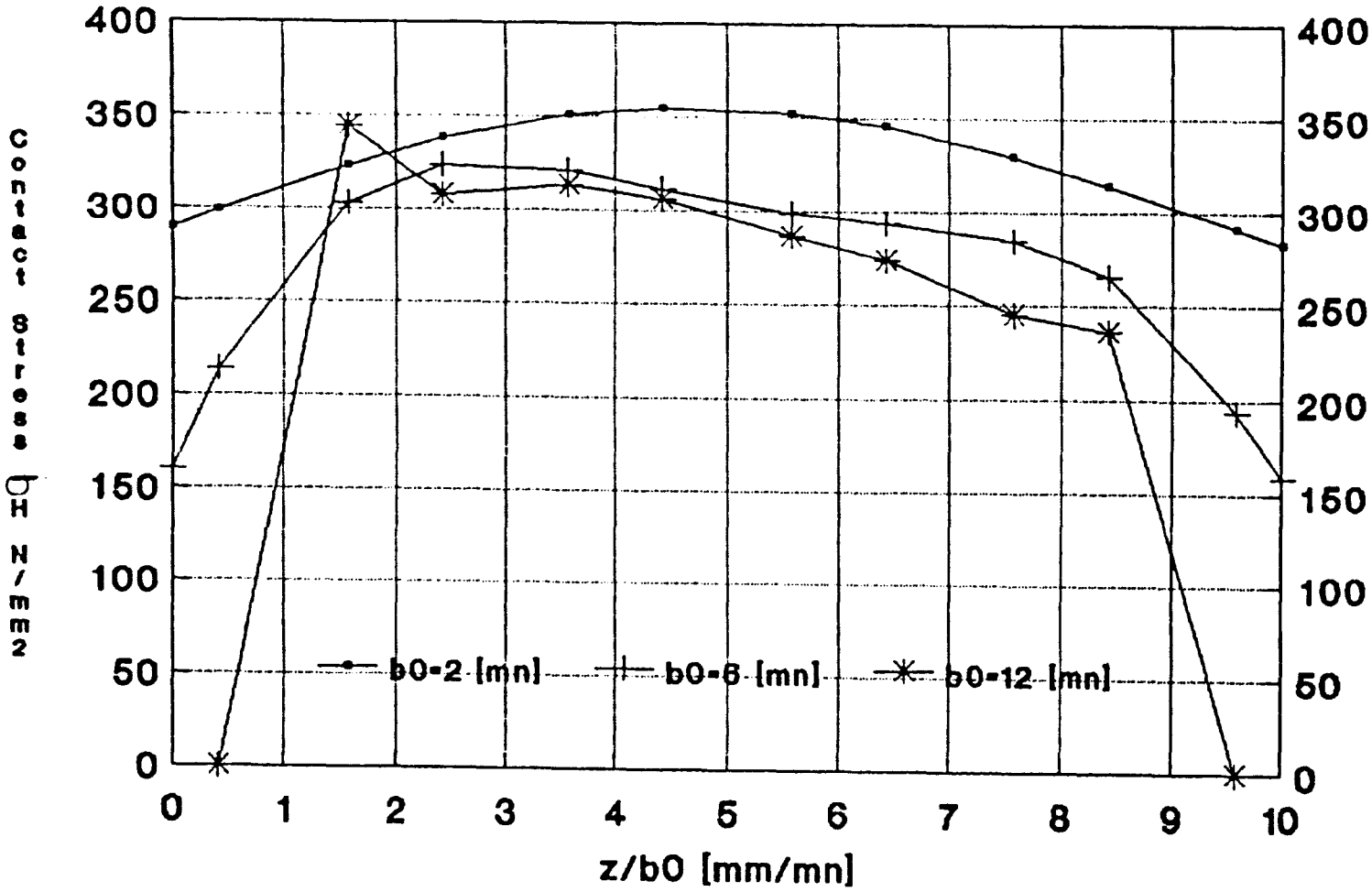

Beta=30 Degrees mn=10 mm Z1=18 Z2=54

Fig. 3.27 Peak Load & Contact Stress

Beta=30 Deg b=120mm mn=10mm

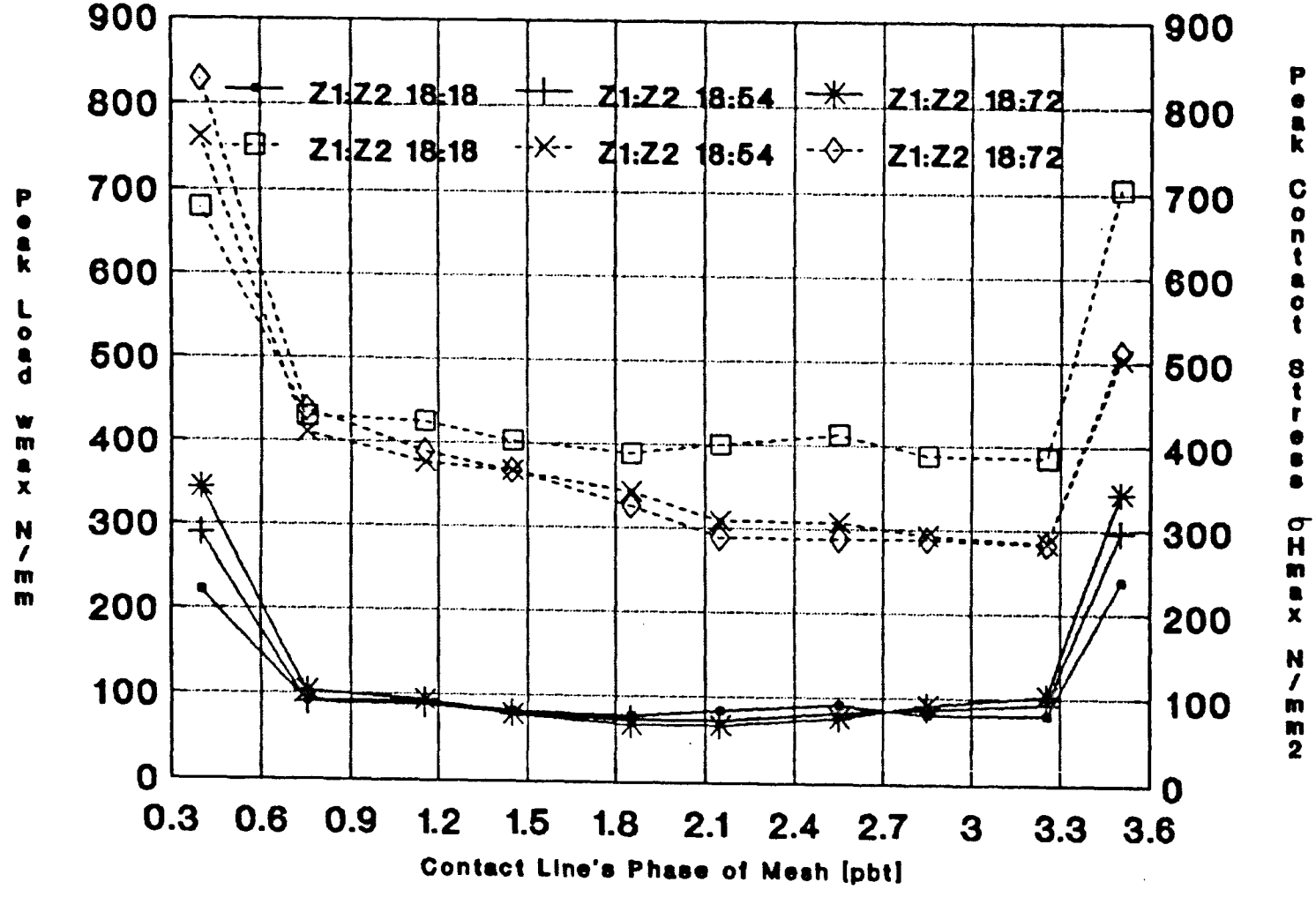

wmax solid line /σHmax dashed line

to 3.24. This gives virtually "point" contact at the instants when contact begins and ends.

For all 3 ratios of $Z_1:Z_2$ shown in figure 3.27, these peak load intensities at the beginning and end of contact are approximately equal. The curves of peak contact stress are however skewed due to variation of the effective relative radius of curvature ρ_{eff} through the mesh cycle. Only for the $Z_1:Z_2$ = 18:18 mesh, where ρ_{eff} varies symmetrically about the pitch point, are the contact stress peaks at the beginning and end of contact approximately equal. The curves for this mesh are not exactly symmetric about the pitch point. This is due to the fact that the "start" and "end" phase of mesh were found by trial and error and no attempt was made to make them correspond to one another geometrically, plus the fact that the phases shown are not mirror images of one another about the pitch point (not plotted). For $Z_1:Z_2>1$, the peak contact stress always occurs at the beginning of mesh where ρ_{eff} is minimum.

3.5.2 Variation of Peak Contact Load and Peak Contact Stress with U and Z_p

Fig. 3.27 only shows indirectly the effect of the gear ratio $U = Z_2/Z_1$ on the peak load and stress distributions. Here the effect of varying U is studied in detail.

As explained in section 2.5 (see figures 2.11 to 2.25) there are two main 'components' of tooth compliance: namely the "cantilever" compliance of the teeth themselves which is greatest on smaller gears, and the"gear body" compliance which is greatest on larger gears. The total compliance is the sum of these two component compliances, so that the mesh stiffness c_γ is also a function of those two factors as clearly explained in the part of section 3.3.2 which discusses figures 3.15 and 3.16.

Figure 3.28 shows how the non-dimensionalised load peaks vary with U. The peak loads seem to vary with U, in a fashion completely opposite to that in which c_γ varies with U (figure 3.15), increasing where c_γ decreases, and vice vera.

A possible explanation for this correspondence between the variations of c_γ and the peak load with U is as follows: the load peaks, (or "spikes") occur only at the start of mesh (new tooth pair coming into contact with near "point" loading) and at the end of mesh (old tooth pair almost losing contact, also with near

Fig. 3.28 Cycle's Peak Load
Beta=30Deg b=120mm mn=10mm

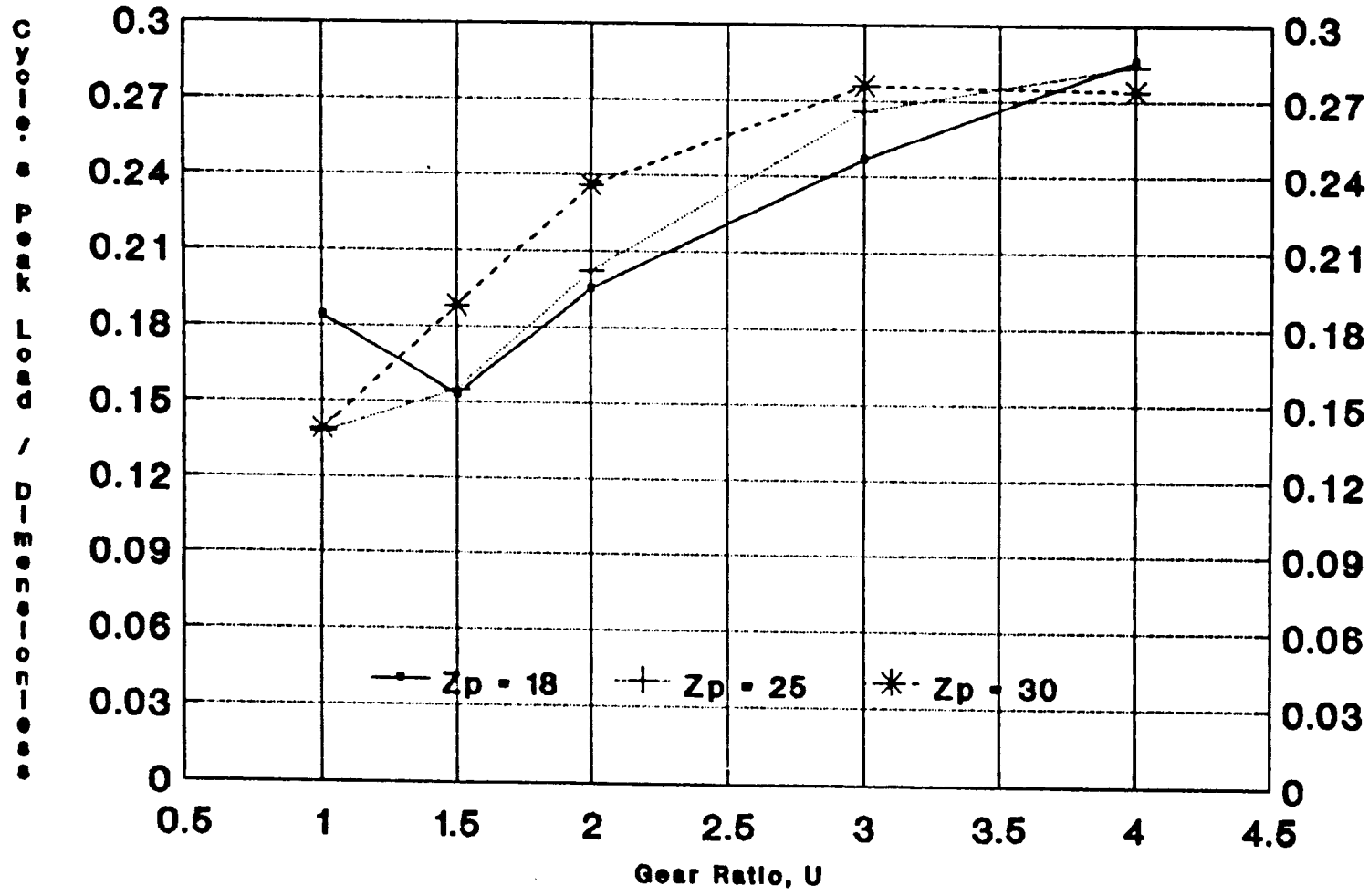

"point" loading). In the theoretically defined region of mesh (AA'B'B in figure 2.1), the tooth pairs at the start and end of mesh must deform by an amount equal to the transmission error f_t (equation 1.64 with $\delta_e = \delta_s = c_t = 0$). Since these tooth pairs carry a negligible amount of the total load F (since their contact lines are very short), f_t is hardly affected by them at these particular instances of mesh (as has been demonstrated from the numerical results). Thus equation 2.17a remains valid, and we can write

$$f_t = \delta_{tb} + \delta_{tc} = \delta_t = \frac{F/b}{c_\gamma} = \frac{w_{spike}}{c_{spike}} = w_n/c_n$$

where n refers to any phase of mesh, and c_{spike} is the single pair tooth stiffness at the start/end of contact where the spike occurs. Thus:

$$w_{spike} = f_t \cdot c_{spike} = \frac{F/b}{c_\gamma} \cdot c_{spike}$$

whence, non-dimensionalising, we obtain

$$[w_{spike}]_{dimensionless} = \frac{m_n}{F} \cdot \frac{F/b}{c_\gamma} \cdot c_{spike} = [m_n \cdot c_{spike}/b] \cdot \frac{1}{c_\gamma}$$

If the quantity inside the brackets is regarded as a constant, then clearly the peak load is inversely proportional to c_γ, which itself varies with U as in figure 3.15. This would explain the shape of Fig. 3.28. The factor c_{spike} is likely to be dominated by the contact and bending compliance of the pinion, loaded by a 'corner' point load. Since Z_p = constant, in Fig. 3.28, this can thus be expected to remain approximately constant, as assumed.

For large values of U, the curve for c_γ (Fig. 3.15) tends to level off. This same effect is also apparent in Fig. 3.28, particularly on the $Z_p = 30$ curve for which the values of Z_g are largest. Clearly for very large gears, ϵ_α becomes significantly larger. Consequently, the total contact length at any instant is larger, thus allowing for the load to be distributed more evenly along the simulatneous contact lines. Whence the shortest lines of contact at the start and end of mesh also will carry a smaller portion of the total load. The irregularity in the 18:18 mesh

(z_p=18,U=1) may be due to the fact that ϵ_α is very small, concentrating the load on a very short length of contact, and consequently giving a relatively large value for w_{spike}. The other two curves could exhibit the same irregularity for ratios U<1.

Figure 3.29 shows how the contact stress peaks vary with U. The contact stress has been plotted non-dimensionally by multiplying the actual stress by Vedmar's factor[5]:

$$\left[\frac{a^2.b.2.(1-\nu^2)}{T_p.E}\right]^{\frac{1}{2}}$$

where the symbols are defined in the nomenclature.

3.5.3 Comparison of Peak Contact Stress

Figures 3.30, 3.31 and 3.32 show the variation of peak contact stress (during a complete mesh cycle) as a function of U, for a 25-tooth pinion with β = 0°, 20° and 30° respectively. For comparison, values obtained by Vedmar[5], and others calculated using the ISO[4] equations, are also plotted.

For the spur gears (figure 3.30), the author's results are between 1.1% and 3.8% lower than Vedmar's[5]. The ISO analysis assumes a uniform load distribution across the face width (sections 1.2.2 and 1.2.3) which, as shown in Fig.3.18, does not occur in practice, even with perfect gears. The ISO analysis thus inevitably predicts a lower peak stress than the other two analyses. However, Figs. 3.18a and 3.18b show that the peak load intensity is actually only about 6% to 11% greater than the mean, leading to peak stresses about 3% to 5.4% greater than average, whereas the ISO values in Fig.3.30 are about 16% to 22% lower than those given by the author. Clearly, the assumption of uniform load across the face width of perfect gears in the ISO[4] standard, does not explain the extra 13% to 16.6% discrepancy in the peak contact stress.

The discrepancy above can be explained by the fact that the ISO equations calculate σ_H at the pitch point, whereas the author's model shows that the peak contact stress occurs nearer the innermost point of single tooth contact. This can be allowed for in the ISO analysis by means of a correction factor Z_β. If this factor is included in the ISO analysis, the dotted curve in

Fig. 3.29 Cycle's Peak Contact Stress
Beta=30Deg b=120mm mn=10mm

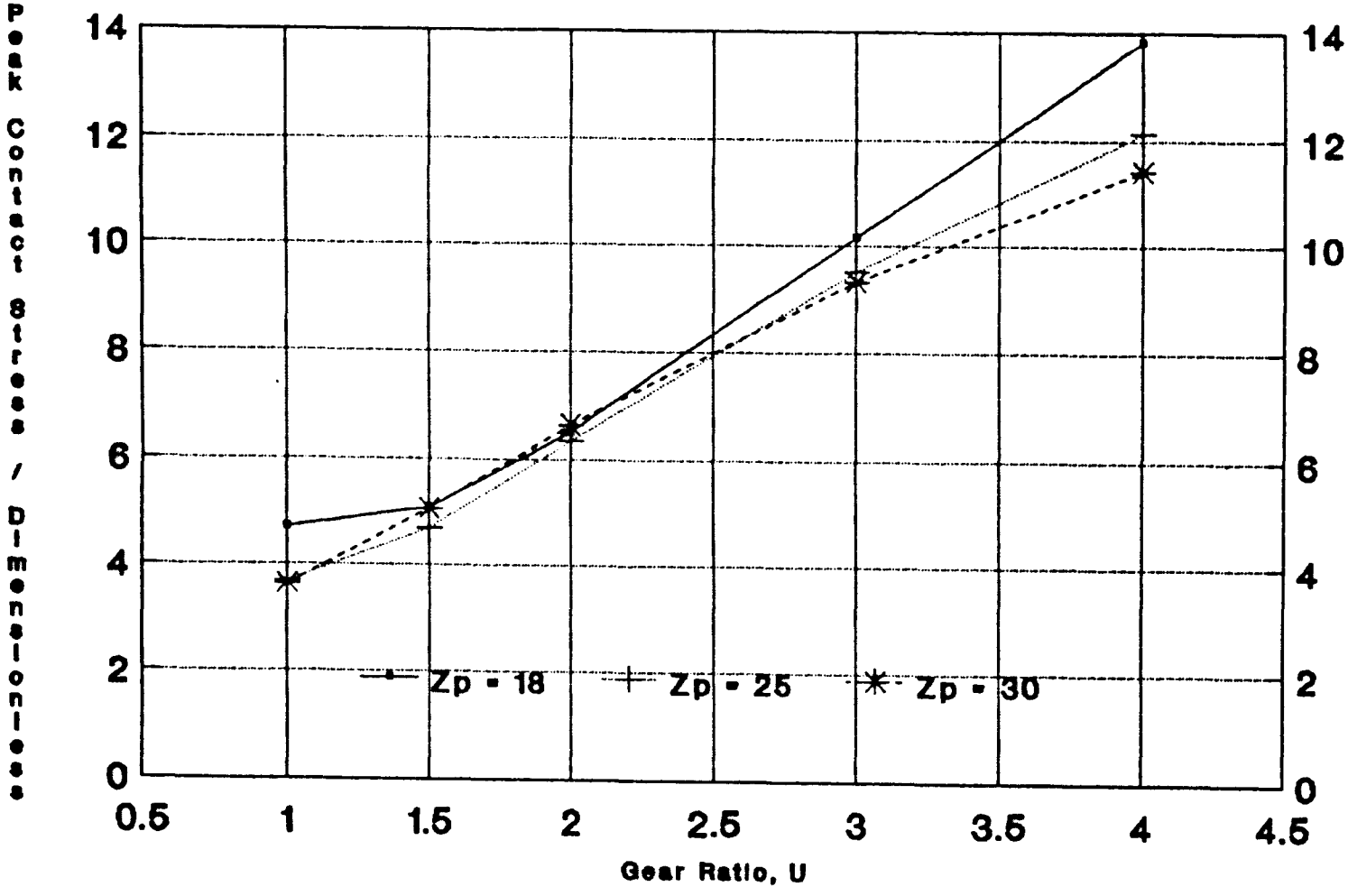

Fig. 3.30 Peak Contact Stress Comparison
Beta=0Deg b=54mm mn=6mm Zp=25

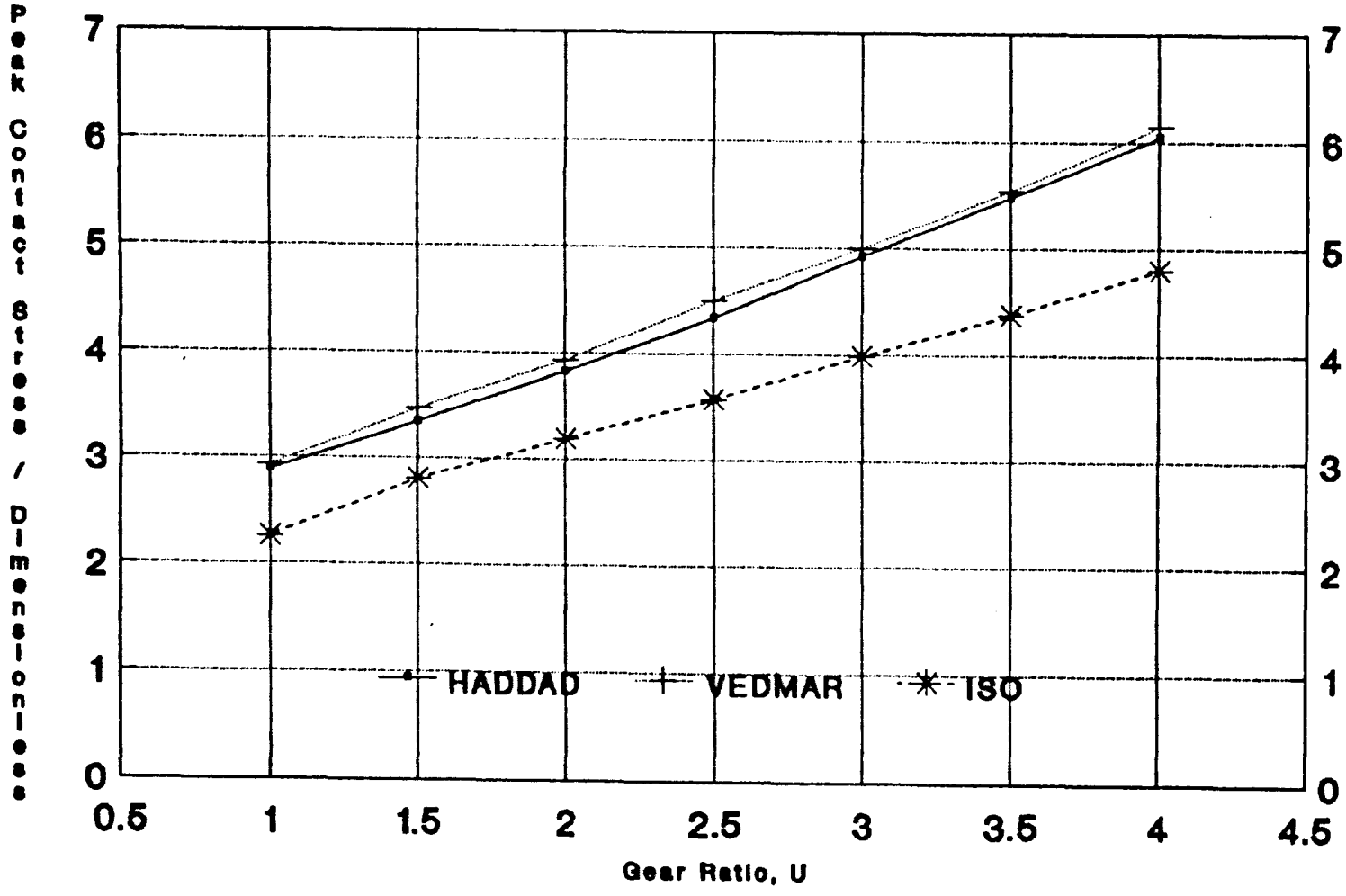

Fig.3.30 is obtained. This shows much improved agreement with the author's results.

The results for the two helical gears shown in Figs. 3.31 and 3.32 show much greater discrepancies between the author's and the other results. The author's peak stresses are roughly between 1.9 and 2.9 times those calculated using the ISO procedure, and differ from Vedmar's by up to 20%, with the greatest discrepancies for β=30°.

As described in section 1.2.2, ISO[4] treats helical gears as equivalent spur gears, and so again for perfect gears the load is assumed to be uniformly distributed across the face width. As shown in Figs. 3.18, 3.19 and 3.20 however, on helical gears the variations of load intensity during the meshing cycle are much more significant than those for spur gears, with peak loads up to 3 times greater than those arising on spur gears at the same nominal loading. With such high peak loads, the peak contact stresses on helical gears computed by Vedmar[5] and the author are inevitably much greater than those calculated using the ISO[4] 'equivalent spur gear' analysis, as shown.

In practice, the very high load and stress spikes predicted by both the author and Vedmar[5] will not occur. The teeth will usually be relieved at the tips and ends, or, if they were not, the tooth edges and corners will soon become rounded by real plastic deformation or wear, and will thus assume a modified profile with a small amount of effective tip and/or end relief. As will be shown in Chapter 4, this can be expected to reduce the peak contact stresses by a factor of about 2 to 2.5, bringing them much closer to those predicted by the ISO[4] procedure, particularly if the factor Z_β is again introduced, to give the stresses at the innermost point of single tooth contact on the virtual spur gear. Further discussion of the effects of tip and root relief, etc. is given in Chapter 4.

Vedmar's[5] values for the helical gears in Figs. 3.31 and 3.32 deviate substantially from the author's for the larger gear ratios, as shown, but not very significantly at low values of U. Possible reasons for these deviations are:

1. It was necessary to calculate contact stresses for the 30° helix angle gear by extrapolating Vedmar's published values

Fig. 3.31 Peak Contact Stress Comparison
Beta=20Deg b=54mm mn=6mm Zp=25

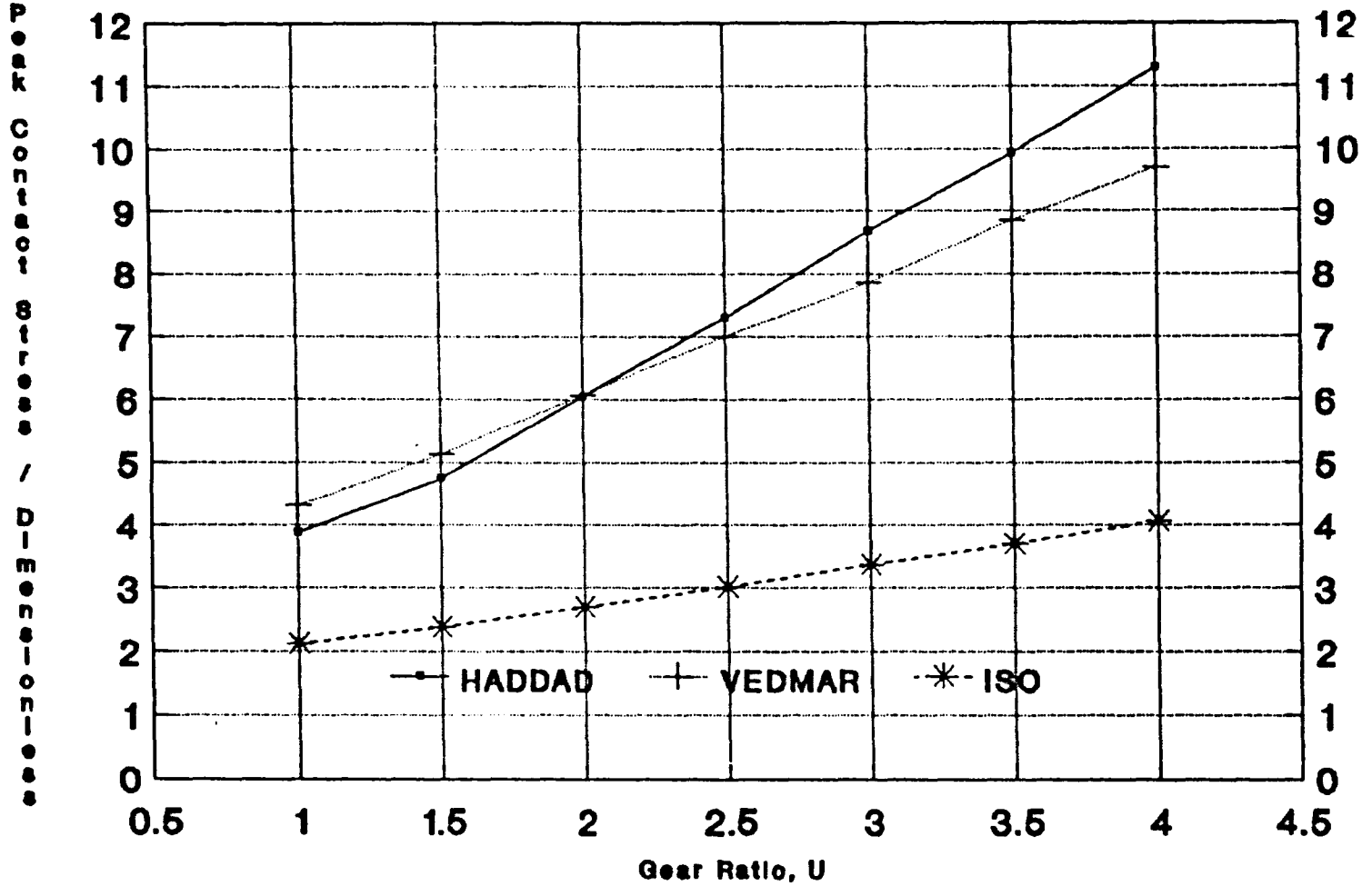

Fig. 3.32 Peak Contact Stress Comparison
Beta=30Deg b=54mm mn=6mm Zp=25

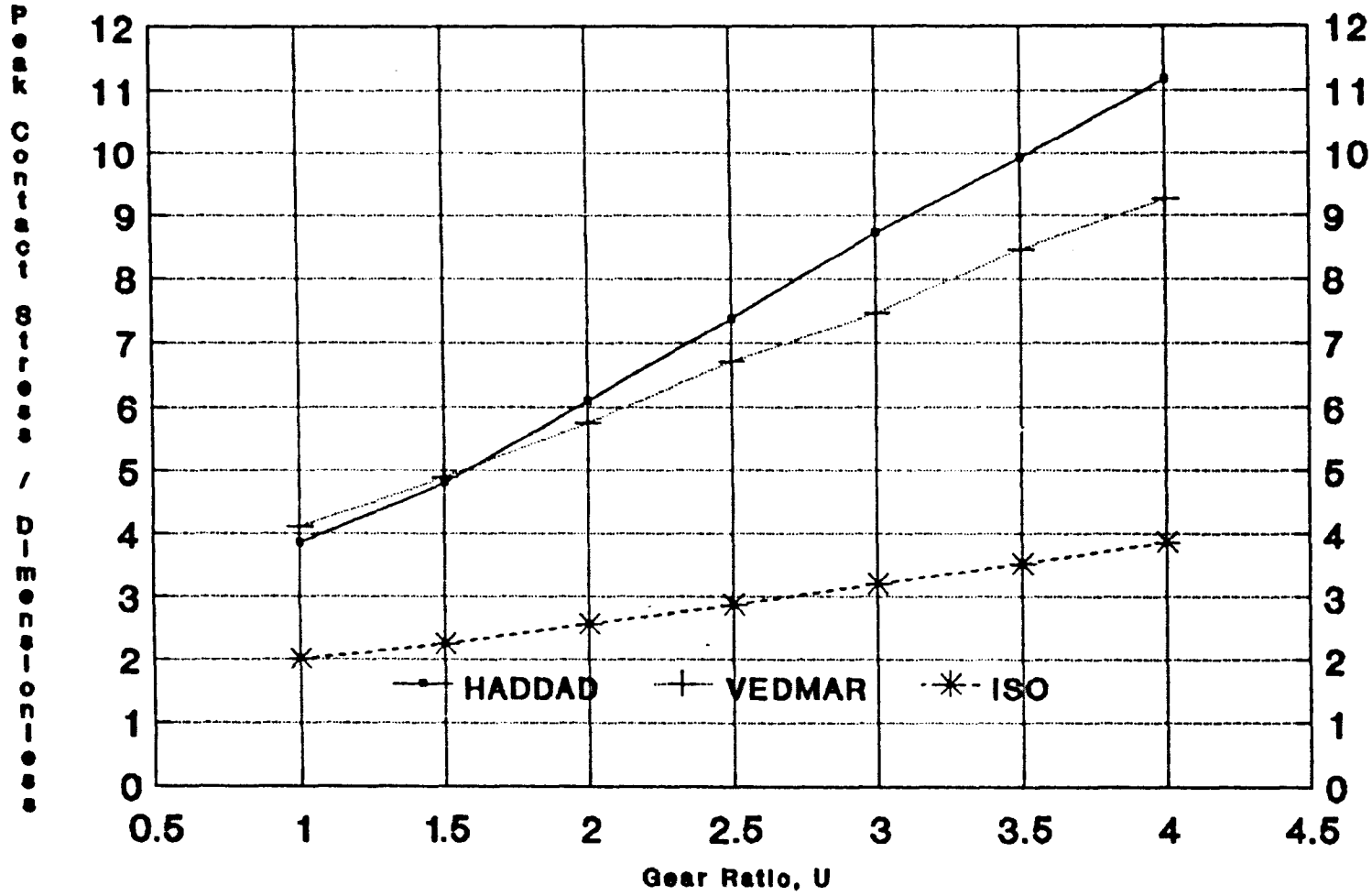

for β=0°, 10° and 20°. In a similar manner, it was necessary to interpolate the author's FE results for β=0° and 30° to obtain stiffness coefficients for the 20° gear. In both cases, as mentioned in Section 3.4, only linear extrapolation/interpolation was possible so that significant interpolation/extrapolation errors could have occurred.

2. As explained in Sections 3.2.2 and 1.4.3.2 Vedmar's FE model seems to ignore the possibility of axial deflections of the gear teeth under the influence of the axial component of the tooth load. This deflection (mainly gearbody deflection) will cause additional tipping of the teeth of large diameter gear wheels, tending to increase the depth of engagement at the leading end of the teeth, and so increasing tooth loads and contact stresses in this region where the peak loads (spikes) occur. Even if Vedmar[5] did, in fact, allow for the effect of axial tooth deflections (his monograph is not very clear on this point), the author's peak loads and contact stresses will still be generally larger since the "tipping" effect is mainly due to gear body deflection. This is negligible in Vedmar's[5] model since he did not model the whole gear. As a result, the "tipping effect" on the author's gears is more significant, particularly on large gears. One side 'tips' relative to the other by 0.34 units according to the author, and by 0.28 units according to Vedmar[5] in Fig. 3.10, making the author's "tipping effect" 1.2 times Vedmar's. From Fig.3.32, it is apparent that the author's peak stress is also about 1.2 times Vedmar's at U=4, even though the gear data in Figs. 3.10 and 3.32 are not exactly the same. This suggests that the higher stresses predicted by the author in this region are mainly associated with gear body deflections.

3. Vedmar has also neglected the adjacent tooth deformations. This must also cause corresponding discrepancies between the load distributions and contact stresses predicted by the two methods, although it is not possible to predict the precise effect without carrying out a detailed investigation (e.g. by running analyses with/without inclusion of the "adjacent tooth" deflections).

3.5.4 Variation of Peak Contact Stress with Helix Angle

To show the effect of the helix angle on the peak contact stress, the results from which Figs. 3.30, 3.31 and 3.32 were plotted, were used to plot Figs. 3.33, 3.34 and 3.35. In each figure, the values of peak stress for β=0°, 20° and 30° are plotted for only one of the three sources being compared.

Both the author's results and Vedmar's in Figs. 3.33 and 3.34 show the peak stresses on helical gears to be much greater than those found on spur gears. As explained earlier, this is to be expected since with increased helix angles, the contact lines are shorter, resulting in load peaks at the start and end of contact where the lines of contact are shortest (near point contact). For the spur gears, the contact lines are all of equal length, allowing for a much more even load distribution, with a peak near the pitch point, where single tooth pair contact occurs (Fig.3.18). Vedmar's results for β=30° seem to be slightly smaller than those for β=20°. This may possibly be due to the linear extrapolation for β=30° as discussed in Section 3.5.3.

The ISO results in Fig.3.35, show a completely opposite trend to the author's and Vedmar's, giving larger contact stress peaks for gears with smaller helix angles, with the largest peaks for β=0°. The trend of the ISO curves may be derived from Eqn. 1.5. For β=30°, Z_H is smaller than for spur gears by a factor of 0.89, Z_E is the same, Z_ϵ is smaller by a factor of 0.971 and Z_β is smaller by a factor of $\sqrt{\cos 30}$, leading to a total reduction in the peak contact stress in Eqn. 1.5 of 0.80, which matches the curves in Fig.3.35, where for β=30°, the values are about 0.80 times those for β=0°. For β=20°, Z_H is smaller by a factor of 0.922, Z_E is the same, Z_ϵ is smaller by a factor of 0.886 and Z_β is smaller by a factor of $\sqrt{\cos 20}$ leading to a total reduction in the peak contact stress in Eqn. 1.5 of about 0.80 again, which is agreeable with Fig.3.35.

This explains the trend of the ISO curves, but not the difference from the author's and Vedmar's curves, which may be explained by the fact that both the author and Vedmar plotted stress "spike" values, whereas ISO gives values at the pitch point (or IPSTC). As already pointed out, the agreement with ISO for spur gears (IPSTC values) is much better than for helical

Fig. 3.33 HADDAD'S Peak Contact Stress Comparison, b=54mm mn=6mm Zp=25

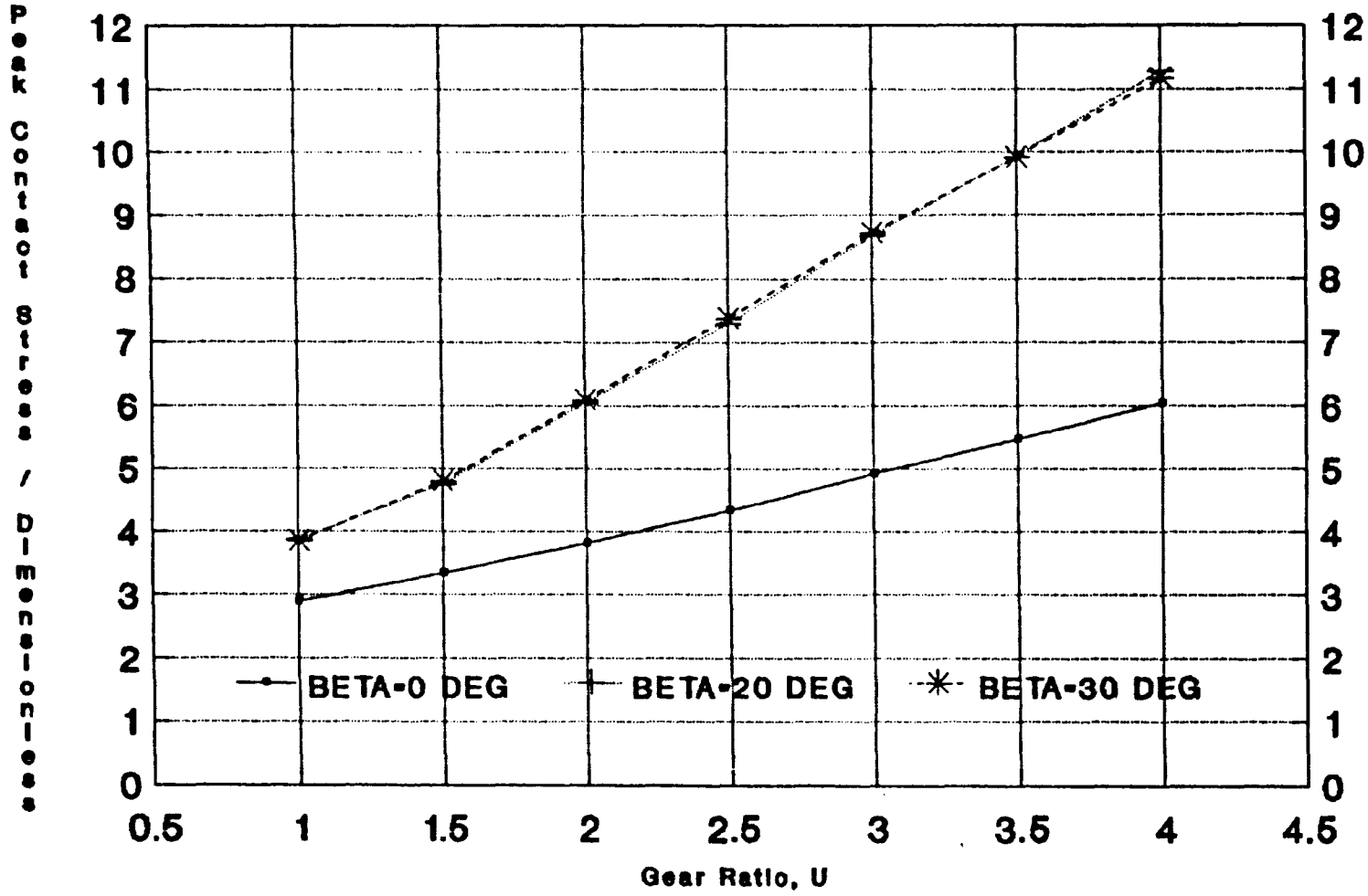

Fig. 3.34 VEDMAR'S Peak Contact Stress Comparison, b=54mm mn=6mm Zp=25

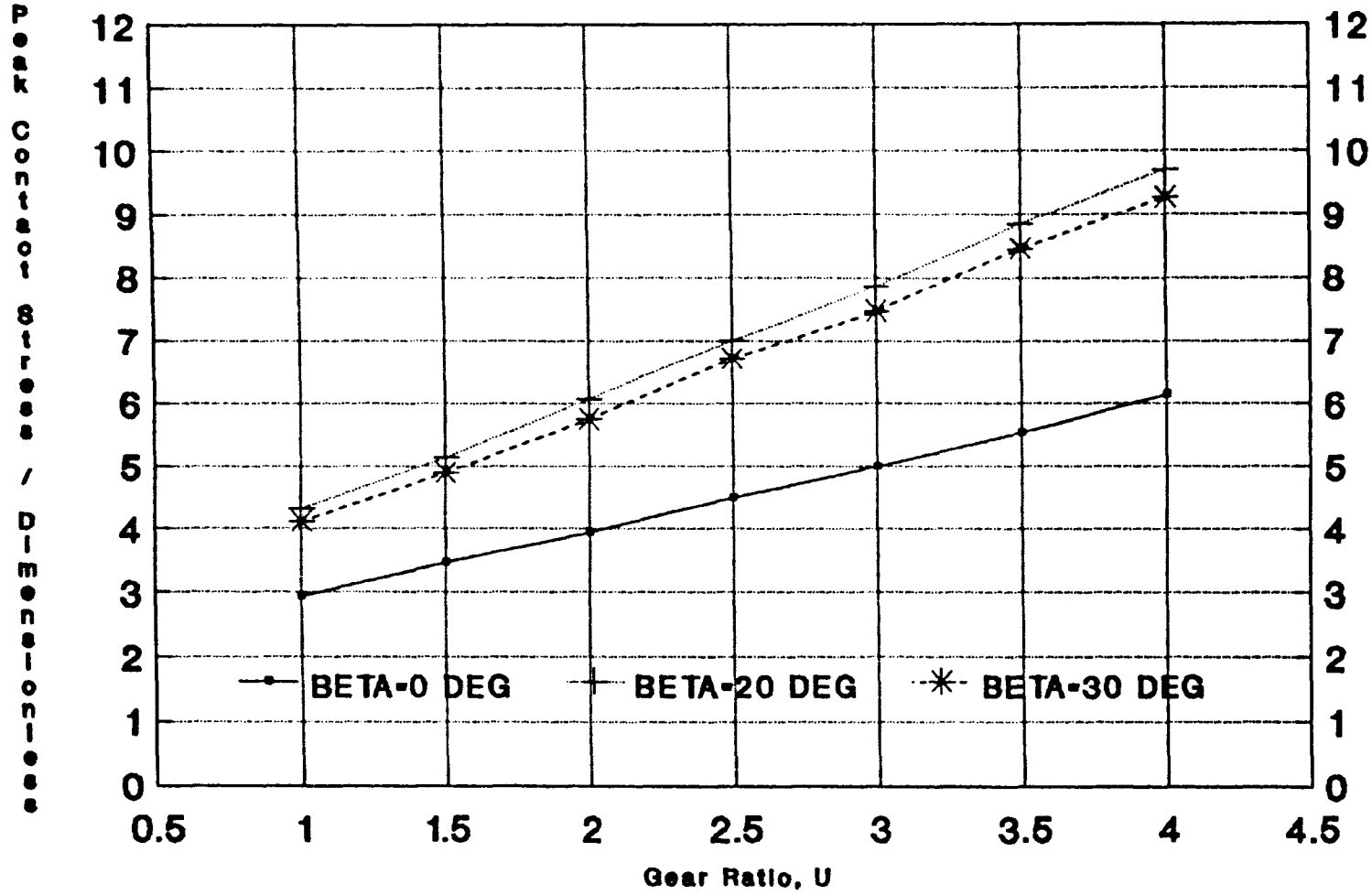

Fig. 3.35 ISO'S Peak Contact Stress Comparison, b=54mm mn=6mm Zp=25

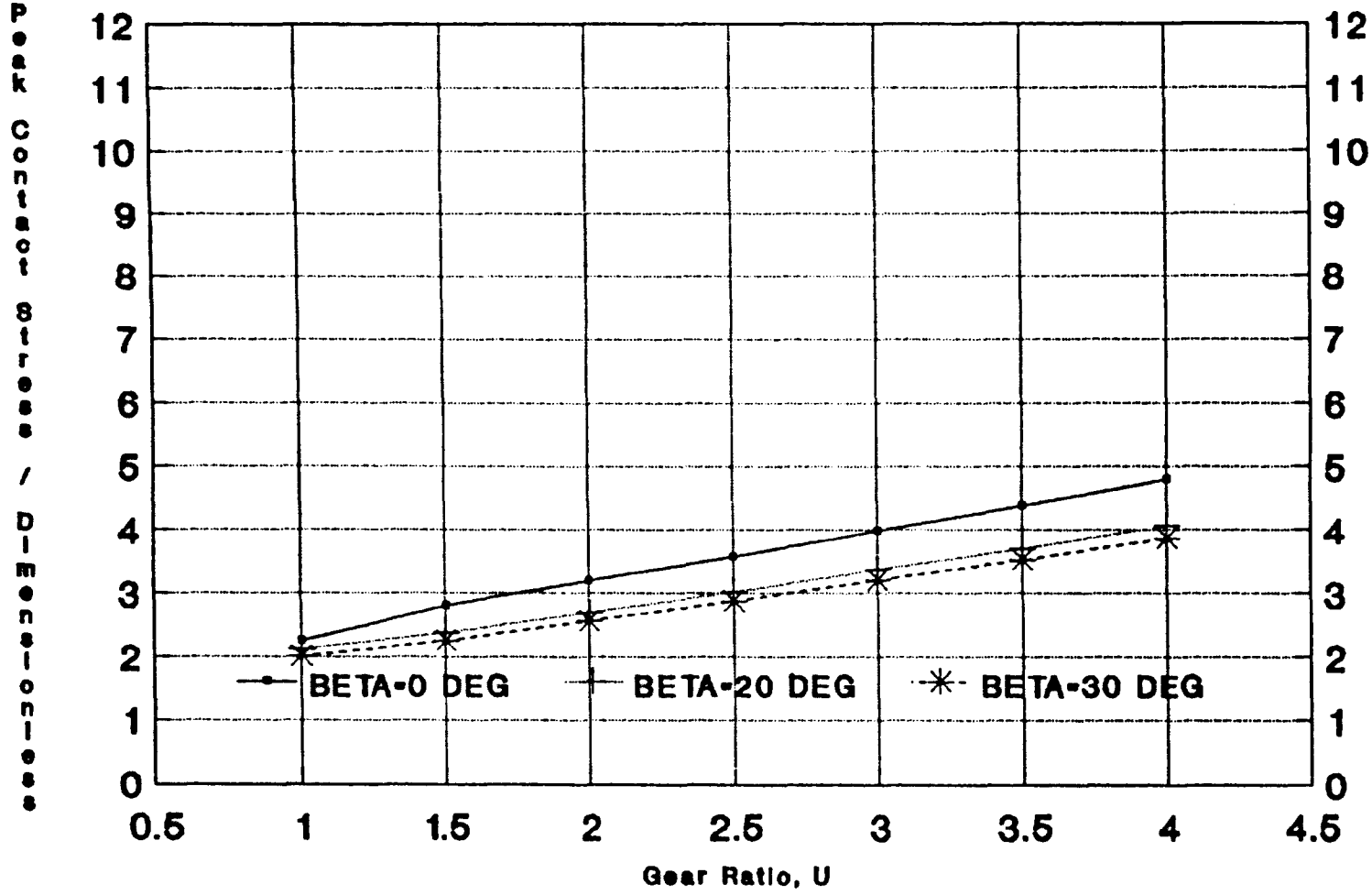

gears as can be seen from Figs. 3.33, 3.34 and 3.35, recalling that spur gears do not exhibit the "spike" effect.

CHAPTER 4

EFFECTS OF LEAD AND PROFILE AND PITCH DEVIATIONS ON CONTACT LINE LOAD DISTRIBUTION

4.1 Introduction

In the previous chapter, ideal gears with no errors or modifications were analysed, and the results compared with other published data. The effects on performance of parameters such as gear ratio U, number of teeth Z, face-width b, and helix angle β, were also discussed. In this chapter, to complement Chapter 3, the effects of various gear tooth errors and modifications are studied, for gears in which the parameters U, Z, b and β are fixed.

The work is reported under three main headings, covering:

1. gear tooth errors and modifications affecting the longitudinal load distribution factor, $K_{H\beta}$.
2. gear tooth errors and modifications affecting the transverse load distribution factor, $K_{H\alpha}$.
3. the combined effect of errors affecting both $K_{H\beta}$ and $K_{H\alpha}$.

The gear pair chosen for these studies has the parameters shown in Table 4.1.

			Pinion	Gear
Number of teeth		Z	18	54
Face-width	(mm)	b	120	120
Normal module	(mm)	m_n	10	
Ref. helix angle	(deg)	β	30 RH	30 LH
Normal pressure angle	(deg)	α_n	20	
Tool addendum	(m_n)	h_{a0}	1.25	1.25
Tool tip radius	(m_n)	r_{a0}	0.39	0.39
Crest rounding radius	(mm)	ρ_{an}	0	0
Addendum mod. factor	( )	x	0	0
Operating torque	(Nm)	T	1014.868	3044.604

Table 4.1 : Gear Pair Specifications

The torque chosen is based on a nominal load intensity of 100 N/mm for 'perfect' gears. This gives rise to peak contact stresses of up to 1000 N/mm^2 when certain tooth errors are introduced. Assuming case-hardened steel gears, this gives a factor of safety against pitting of typically 1.3.

Typical printouts from the load distribution program (HELICALDIST) described in Appendix 2A, are included in Appendix 4A.

4.2 Effect of Lead Errors and Lead Modifications on the Longitudinal Load Distribution Factor $K_{H\beta}$

4.2.1 Introduction

The results from this work are compared with those from the DUISO software package[45] which implements the latest revision of the draft ISO standard[4]. As explained in section 1.2.2, the effects of lead errors and modifications are taken into account by the factor $K_{H\beta}$ given by eqns. 1.11 to 1.13 (Fig. 1.3 is shown here again as Fig. 4.1 for convenience), which can be thought of as defining either the increase in load intensity w, or the increase in the peak contact stresses σ_H due to these effects (Eqns. 1.11 and 1.10 respectively).

In this work, the approach used is to calculate the load distribution by using the 'exact' three-dimensional mesh model rather than the approximate thin-slice theory of the standards. It thus becomes necessary to calculate, from the load/stress distributions, a factor $K_{H\beta}$ that is equivalent to that defined in the standards. This presents a number of problems, since according to the results discussed in Chapter 3, even a perfect gear set will not produce a constant load intensity across contact lines equivalent to the mean value w_m assumed in the standards. However, if the load distribution program is run for a sufficient number of phases to produce a load distribution chart for the perfect gear like these shown in Figs. 3.22 and 3.24, the instantaneous peak load intensity deduced from these can be taken as equivalent to w_m. If the analysis is then repeated for the same set of gears, but the desired error, or combination of errors is now introduced, the peak resulting instantaneous load intensity, derived in the same way, can be taken as equivalent to the quantity w_{max} defined in the standards. This yields a ratio (w_{max}/w_m) from which $K_{H\beta}$ could be calculated according to Eqn. 1.11. A further problem arises, however, since the standards model a helical gear as an equivalent spur gear, and assume that under the worst conditions, the whole load is carried by only a single pair of meshing teeth. This gives rise to peak contact stresses near the pitch circle, (or as discussed in Section 3.5.4

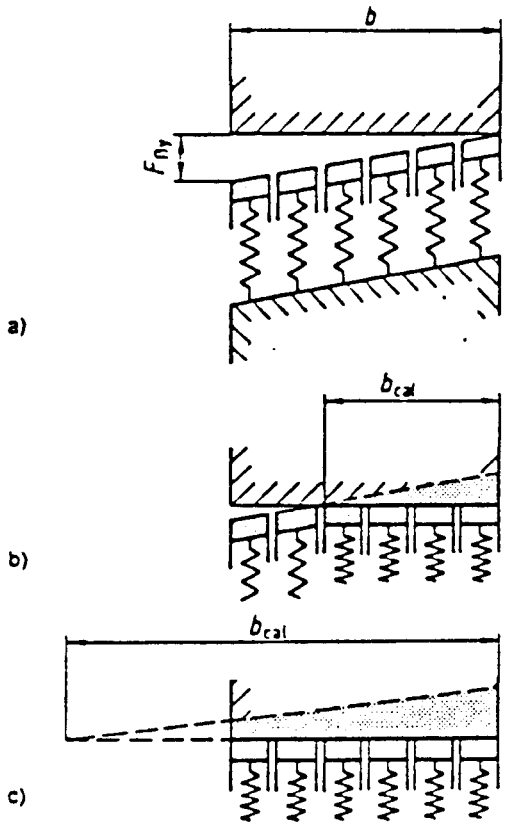

a) Without load

b) With light load and/or high mesh alignment error (large value of $F_{\beta y}$)

c) With heavy load and/or small mesh alignment error (small value of $F_{\beta y}$)

Fig.4.1 Distribution of longitudinal load with linear mesh misalignment (illustration of principle)

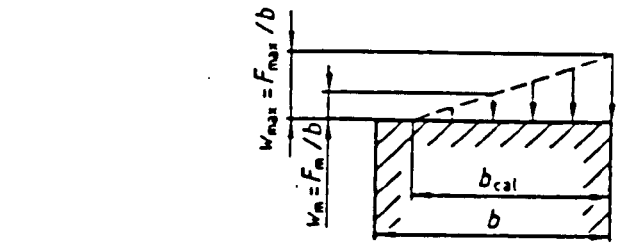

a) $w_{max} = \frac{F_{max}}{b} = \frac{2\,F_m}{b} \cdot \frac{b}{b_{cal}}$

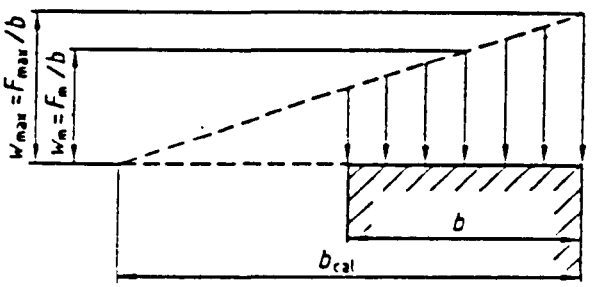

b) $w_{max} = \frac{F_{max}}{b} = \frac{F_m}{b} \cdot \frac{b_{cal}}{b_{cal} - \frac{b}{2}}$

a) Light load and/or large value of $F_{\beta y}$ $b_{cal}/b < 1$

b) Heavy load and/or small value of $F_{\beta y}$, $b_{cal}/b > 1$

Fig. 4.16 Calculation of the maximum line loading $(F/b)_{max}$ with linear distribution of the longitudinal loading.
$F_m = F_t \cdot K_A \cdot K_v$

at the innermost point of single tooth contact on the equivalent spur gears). According to this theory, the peak load intensity w_{max} and the peak contact stress σ_{Hmax} will thus occur at the same place, so that equations 1.10 and 1.11 yield identical values of $K_{H\beta}$ as can be seen from the contact stress equation 1.1.

As shown in Section 3.5.1 however, this does not actually occur. The peak loads occur near the start and end of contact due to the load spike effect as do also the peak contact stresses (Section 3.5.1). However, the peak load often occurs at the end of contact (stiffer pinion tip), while the peak contact stress occurs at the start of contact due to the changing radii of curvature, so that, in this case, different values of $K_{H\beta}$ are yielded by Eqns. 1.10 and 1.11. Just to complicate matters further, it should be pointed out that most gears are usually tip relieved (or run in), to reduce the load spike-effect, so that the peak contact loads and stresses will occur at some intermediate phases of mesh (see Figs. 3.21 to 3.24) when several tooth pairs may be in contact. Which value of w_{max} or σ_{Hmax} should then be used to calculate $K_{H\beta}$ then depends on how much tip correction is assumed and is even less clearly defined.

Essentially, six different equations for calculating $K_{H\beta}$ may be used. The subscript (0) refers in each case to values calculated on a perfect gear set, and the parameters without this subscipt refer to nominally identical "real" gears (with errors and/or modifications).

The six equations are:

$$K_{H\beta} = \left[\frac{w_{max}}{w_{max0}} \right]_{\substack{\text{For complete cycle} \\ \underline{\text{ignoring}} \text{ end spikes}}} \qquad 4.1$$

$$K_{H\beta} = \left[\frac{\sigma_{Hmax}}{\sigma_{Hmax0}} \right]^2_{\substack{\text{For complete cycle} \\ \underline{\text{ignoring}} \text{ end spikes}}} \qquad 4.2$$

$$K_{H\beta} = \left[\frac{(\sigma_H) \text{ At } w_{max} \text{ for complete cycle } \underline{\text{ignoring}} \text{ end spikes}}{(\sigma_{H0}) \text{ At } w_{max0} \text{ for complete cycle } \underline{\text{ignoring}} \text{ end spikes}} \right]^2 \qquad 4.3$$

$$K_{H\beta} = \left[\frac{w_{max}}{w_{max0}} \right]_{\substack{\text{For complete cycle} \\ \underline{\text{including}} \text{ end spikes}}} \qquad 4.4$$

$$K_{H\beta} = \left[\frac{\sigma_{Hmax}}{\sigma_{Hmax0}} \right]^2_{\substack{\text{For complete cycle} \\ \underline{\text{including}} \text{ end spikes}}} \qquad 4.5$$

$$K_{H\beta} = \left[\frac{(\sigma_H) \text{ At } w_{max} \text{ for complete cycle } \underline{\text{including}} \text{ end spikes}}{(\sigma_{H0}) \text{ At } w_{max0} \text{ for complete cycle } \underline{\text{including}} \text{ end spikes}} \right]^2 \qquad 4.6$$

Considering equations 4.1 and 4.4, it is clear from the previous discussions that there are no clear-cut definitions of w_m and w_{max} in this work which exactly conform with the definition of $K_{H\beta}$ in the standards.

In any case, the ultimate purpose of $K_{H\beta}$ is to assist in predicting pitting failures, for which the values of σ_{Hmax} given by Eqn. 1.6 are needed. It follows that there is no particular merit in using the expressions 4.1, 4.3, 4.4 or 4.6, all of which are based on values of w_{max} and w_{max0}. Eqn. 1.6 and the two equations 4.2 and 4.5 are thus the most logical basis for comparison with the standards and are used in the comparison presented below.

4.2.2 Effect of Mesh Misalignment on $K_{H\beta}$

Fig. 4.2 shows how the values of $K_{H\beta}$ calculated from Eqns. 4.2 and 4.5 vary with mesh misalignment $F_{\beta y}$, and compares these curves with the results obtained from Eqn. 1.6. The misalignment error $F_{\beta y}$ was introduced equally on the pinion teeth only in the load distribution program (HELICALDIST), and Fig. 4.3 shows how it tends to increase the peak contact loads and stresses at the start of mesh (where the peaks occur), and decrease them at the other end of the face, where the load spike can be completely eliminated.

Reversing the sign of $F_{\beta y}$ in the load distribution program will have the opposite effect (reducing or completely eliminating the spike effect at start of mesh and increasing it at end of mesh). In the standards, the sign of $F_{\beta y}$ is always assumed to be positive.

As to be expected, Fig. 4.2 shows a progressive increase in $K_{H\beta}$ with increasing misalignment error, due to the increased contact resulting from metal added on the loaded side of the tooth. All three curves follow a similar trend, however, the standards clearly overestimate $K_{H\beta}$ when compared with $K_{H\beta}$ of equations 4.2 and 4.5. This is to be expected, since as

Fig.4.2 Effect of Mesh Misalignment on Longitudinal Load Distribution Factor

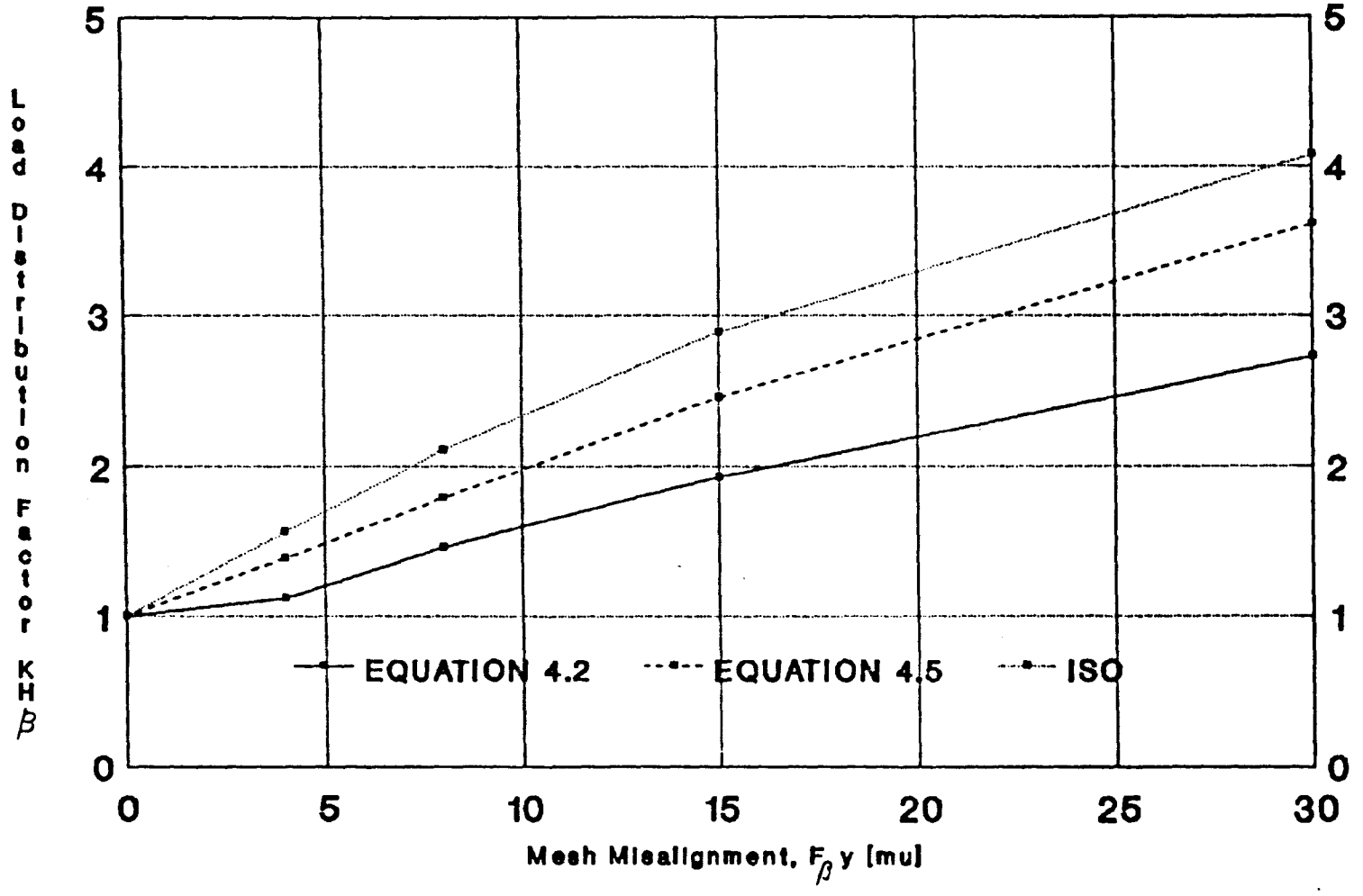

demonstrated in Section 3.3, the standards overestimate the mesh stiffness c_γ, implying higher peak contact loads and stresses, and in turn higher $K_{H\beta}$.

The same effect was observed by Steward[30] on spur gears, when his values of $K_{H\beta}$ were compared with those from the standard (Fig. 5.2 in reference 30). Steward recommended the use of c' in place of c_γ in the ISO formulae (Eqns. 1.12 and 1.13 for $K_{H\beta}$ as shown in Fig. 5.2 in Ref. 30). If this is done for the helical gears of Fig. 4.3, the modified ISO results lie very close to those given by Eqn. 4.3, indicating that Steward's modification would also be worthwhile for helical gears as well.

Equation 4.5 (spikes included) gives larger values of $K_{H\beta}$ than equation 4.2 (spikes ignored). This is to be expected since introducing errors causes the spikes at the tooth-ends to sharpen in greater proportion than the peaks at intermediate phases away from the end spikes. Since a designer must always base his analysis on the worst tooth loading conditions to be expected during the mesh cycle, the end load spikes which occur on helical gears which are not relieved in any way can not be ignored. In such cases, the values of $K_{H\beta}$ obtained from Eqn. 4.5 must be used. Where careful running in or deliberate tip relief can be guaranteed to eliminate the spike effects, however, the lower values of $K_{H\beta}$ given by Eqn. 4.2 (or, approximately, by the "modified" ISO formulae) can be used instead.

4.2.3 Effect of Face Crowning (Barrelling) and End Relief on $K_{H\beta}$

Fig. 4.4 shows the difference between face crowning, or barrelling, and end relief. Clearly, end relief is a form of localised face crowning, whose main purpose is to reduce the loads at the weaker end sections of the teeth, and will not be studied in this section.

Face crowning is a type of non-linear helix modification, used to compensate for the effect of random manufacturing errors, such as misalignment or helix angle errors. If introduced on a gear tooth with lead errors, moderate face crowning tends to reduce the load and contact stress peaks at the start or end of contact caused by the lead errors. However, it may either reduce or increase the load intensity at intermediate phases of mesh, depending on the amount of crowning introduced. This is discussed in the following section.

If introduced on a perfect gear, (without misalignment of any form), however, face crowning always increases the peak load intensity for the intermediate phases of a mesh cycle, and decreases the spikes at the start and end of the mesh cycle. This is demonstrated clearly in Fig. 4.5 which shows the effect of variable amounts of face crowning on $K_{H\beta}$ for an otherwise

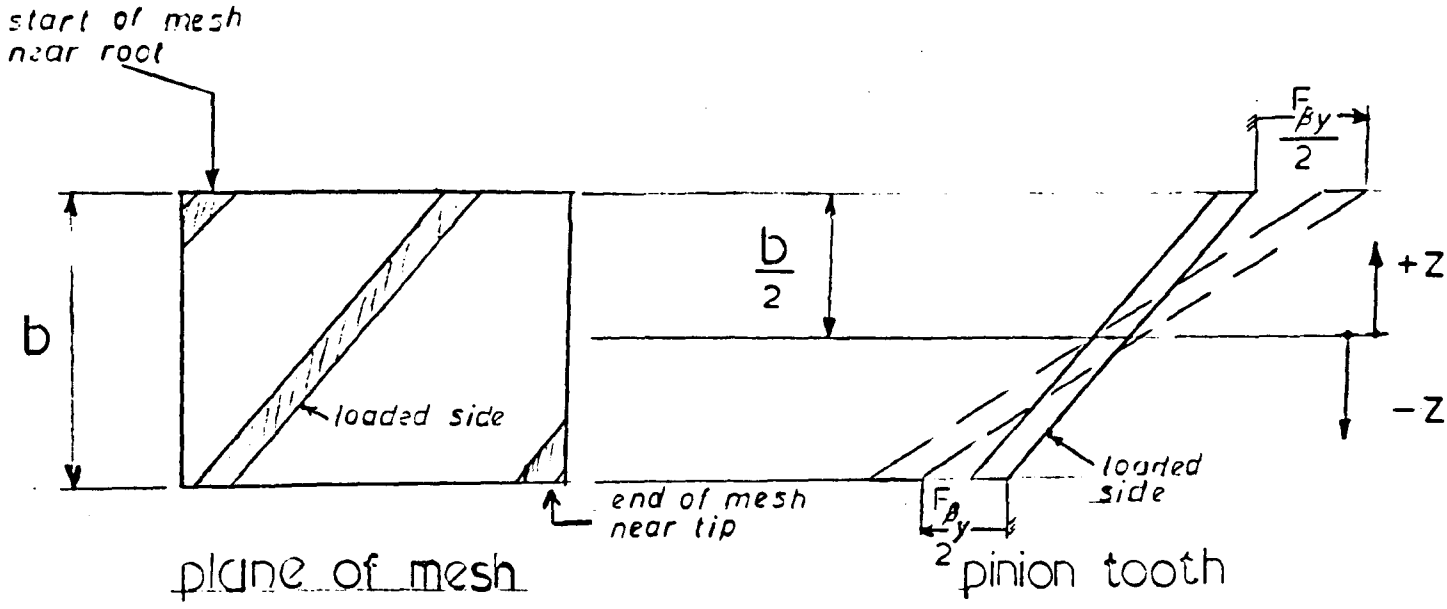

error varies as $\frac{F_{\beta y}/2}{b/2} \cdot z \cdot \cos \beta_b$

metal added in +z dir.

metal removed in -z dir.

FIG. 4.3. MESH MISALIGNMENT

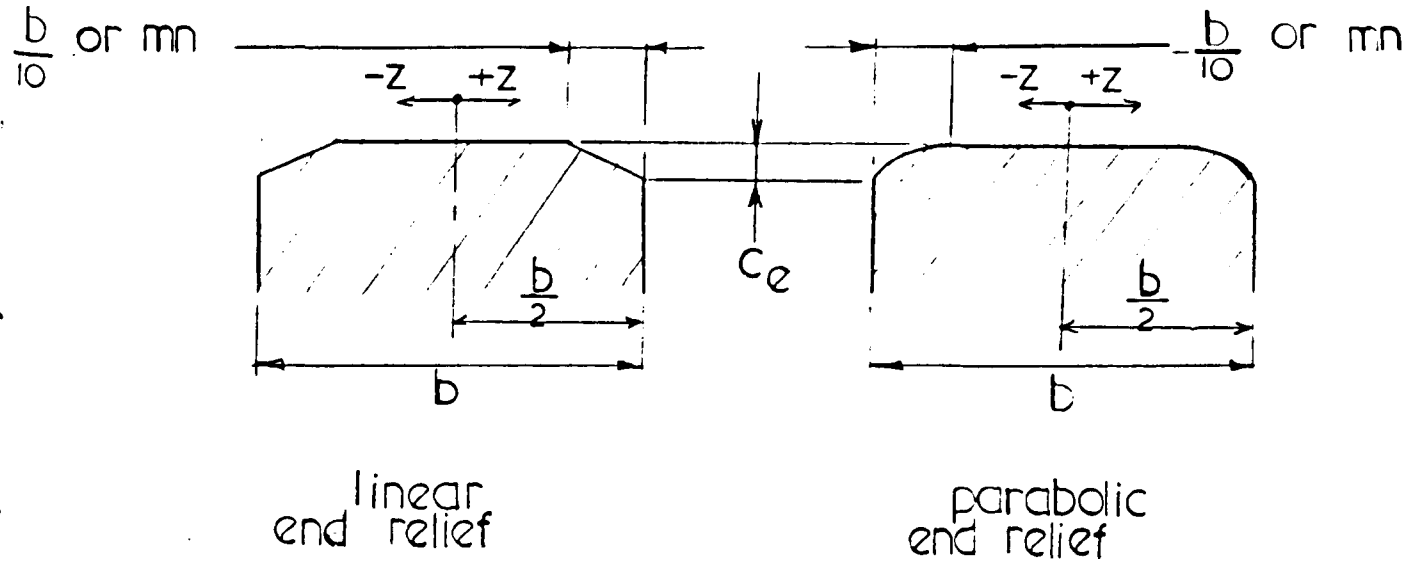

linear
end relief

parabolic
end relief

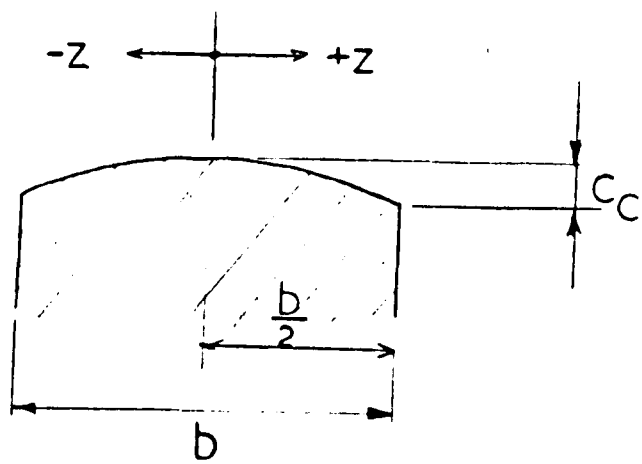

parabolic
face crowning.

crowning varies as $\frac{z \cdot z}{b/2 \cdot b/2} \cdot \cos \beta_b \cdot c_c$

FIG. 4.4 END RELIEF & CROWNING

Fig.4.5 Effect of Face Crowning on Longitudinal Load Distribution Factor KH_{β}

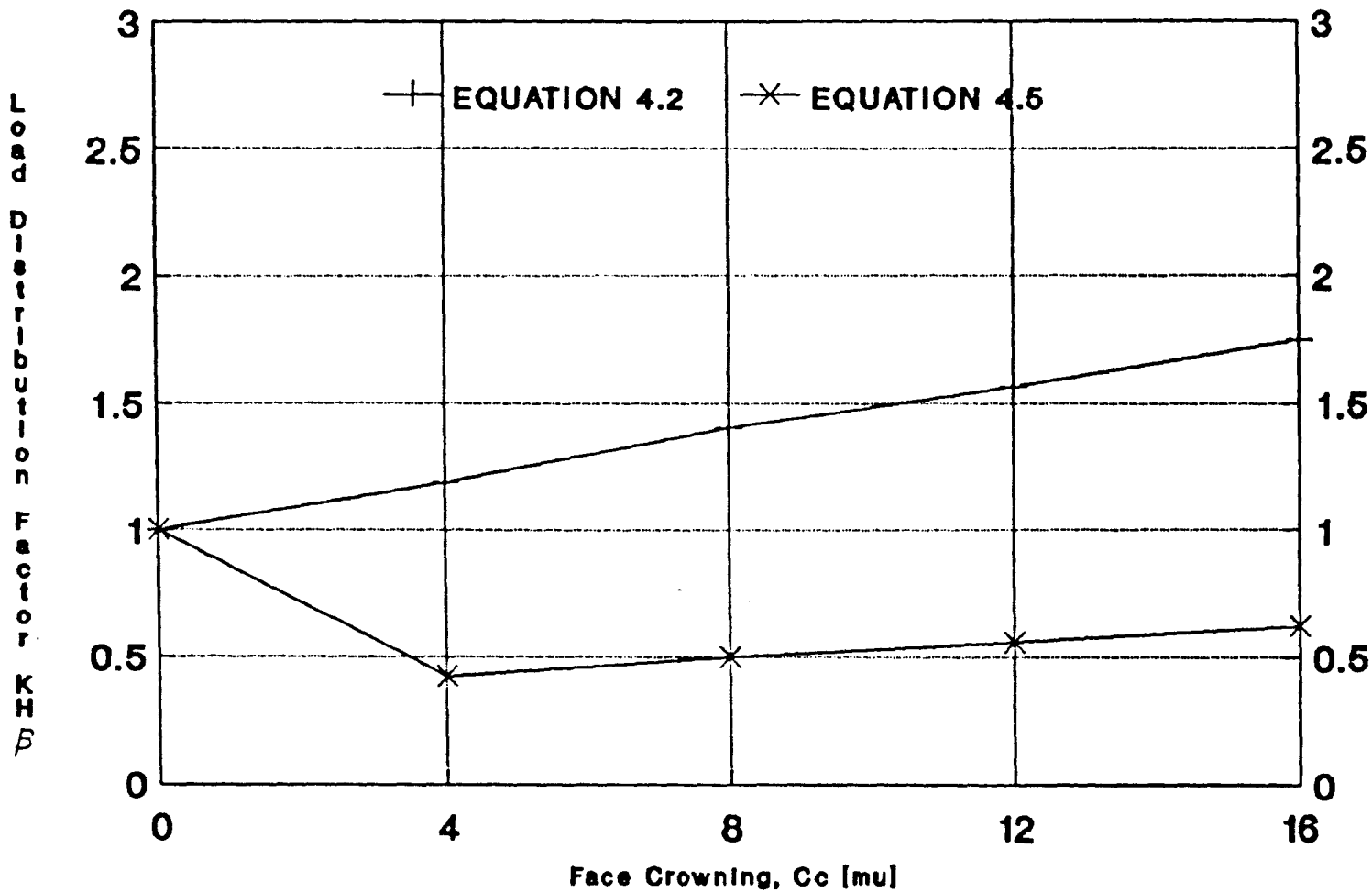

crowning introduced to perfect gear set

perfect gear set. Face crowning removes metal from the ends of the gear, thus reducing contact deformation at the start and end of mesh, so that the load spikes are reduced. On the other hand, the total load must remain constant, so loads at intermediate phases must increase.

Clearly, face crowning on a perfectly aligned gear is highly undesirable, but may be essential for a misaligned gear as shown in the following section.

The standards consider any form of lead error or lead modification as equivalent to a pure mesh misalignment $F_{\beta y}$. This is obviously completely untrue since as demonstrated by Figs. 4.2 and 4.5, the introduction of face crowning affects the load intensity in a completely different manner to misalignment. In any case, the crowning height may be positive as in Fig. 4.4 or negative, e.g. due to manufacturing errors or shaft bending. When this occurs, the effect is apposite to that due to conventional (positive) crowning. The load spikes tend to worsen, rapidly putting large loads on the first and last engaged teeth, while relieving the intermediate teeth from most of the load. This tends to give values of $K_{H\beta}$ from Eqn. 4.2 below 1.0, and values from equation 4.5 above 1.0. No plot of these results is presented due to space limitations.

4.2.4 Combined Effect of Mesh Misalignment and Face Crowning on $K_{H\beta}$

In the previous two sections, the effects of mesh misalignment and face crowning on $K_{H\beta}$ were studied individually. The results were both qualitatively and quantitatively as expected, and demonstrate that to assume that any type of lead error or modification may simply be treated as mesh misalignment error is fundamentally wrong. This point will now be taken further by studying the effect of face crowning, on the load distribution factor $K_{H\beta}$, of gears with various amounts of misalignment.

On each pinion tooth of the gear set studied, a constant mesh misalignment of 8μm was introduced in the form of a helix angle error $f_{H\beta}$ in such a way as to produce the worst peak loads and stresses, (see section 4.2.2). At the same time, face crowning was progressively introduced on each pinion tooth to give crowning heights of 0, 4, 8, 12 and 16 μm. The values of $K_{H\beta}$ obtained are plotted in Fig. 4.6.

The 8μm mesh misalignment causes an increase in $K_{H\beta}$ as shown earlier in Fig. 4.2, and discussed in section 4.2.2. Referring to Figs. 4.3 and 4.4, it is apparent that introducing face crowning tends to reduce the metal 'added' by the misalignment at the highly loaded end, while increasing the

Fig.4.6 Combined Effect of Cc & fH_β on Longitudinal Load Distribution Factor

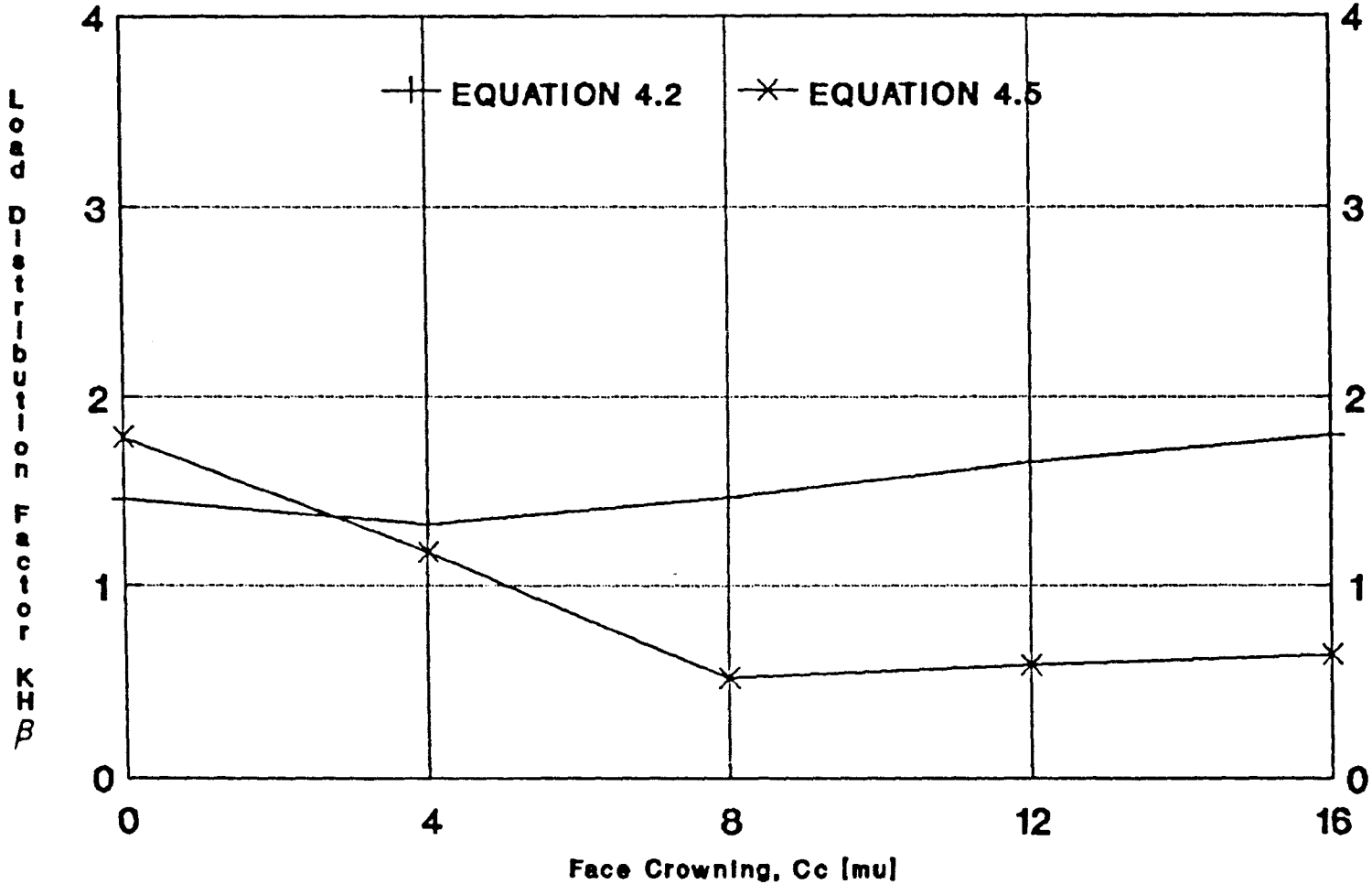

total misalignment fH_β=8um is included

loss of metal at the other end.

Consideration of equation 4.5 shows that when the spike effect is included, the mesh region of interest is that where metal is added (causing greater spikes). For small values of C_c, the elastic deflections in this region are reduced, giving lower spikes, and lower values of $K_{H\beta}$ as shown in Fig. 4.6. At values of $C_c \approx 0.5\ f_{H\beta} = 4\mu m$ (see Fig. 4.7), $K_{H\beta}$ is reduced to about 1.0, since at the end of the face-width the peak stresses occur, and the crowning then exactly cancels the error due to $f_{H\beta}$, as shown in Fig. 4.7, giving the same deflection that a perfect gear would have at that point. As C_c increases further, the spike effect at that end completely disappears but $K_{H\beta}$ eventually begins to increase again due to the reduced length of contact.

The values of $K_{H\beta}$ calculated using Eqn. 4.2, for points away from the load spikes at the tooth ends show a similar trend, although the initial reduction in $K_{H\beta}$ caused by the crowning reducing the elastic deflections at the ends of the teeth is less pronounced than that considered previously. An optimum occurs near $C_c \approx 0.5\ f_{H\beta}$, in agreement with Myer's[46] 2-D theory, which predicts minimum values of $K_{H\beta}$ for $C_c = 0.426\ f_{H\beta}$. Thereafter $K_{H\beta}$ again increases slowly with C_c, as the effective face-width is reduced by increasing loss of contact at the ends.

Face crowning of misaligned gears is clearly beneficial in moderate amounts, and Myers'[46] and Munro's[47] recommendations for the optimum amount of crowning are confirmed.

4.3 Effect of Pitch Errors, Profile Errors and Profile Modifications on the Transverse Load Distribution Factor $K_{H\alpha}$

4.3.1 Introduction

As explained in Section 1.2.2, the factor $K_{H\alpha}$, like $K_{H\beta}$, is defined in the standards [2,3,4] both as a ratio of load intensities (Eqn. 1.14) and as a ratio of contact stresses (Eqn. 1.9).

The same problems of defining an equivalent ratio from results obtained using the 3-D mesh model occur with $K_{H\alpha}$ as occurred with $K_{H\beta}$, so that there are, again, six possible definitions of $K_{H\alpha}$, analogous to Eqns. 4.1 - 4.6 for $K_{H\beta}$, viz:

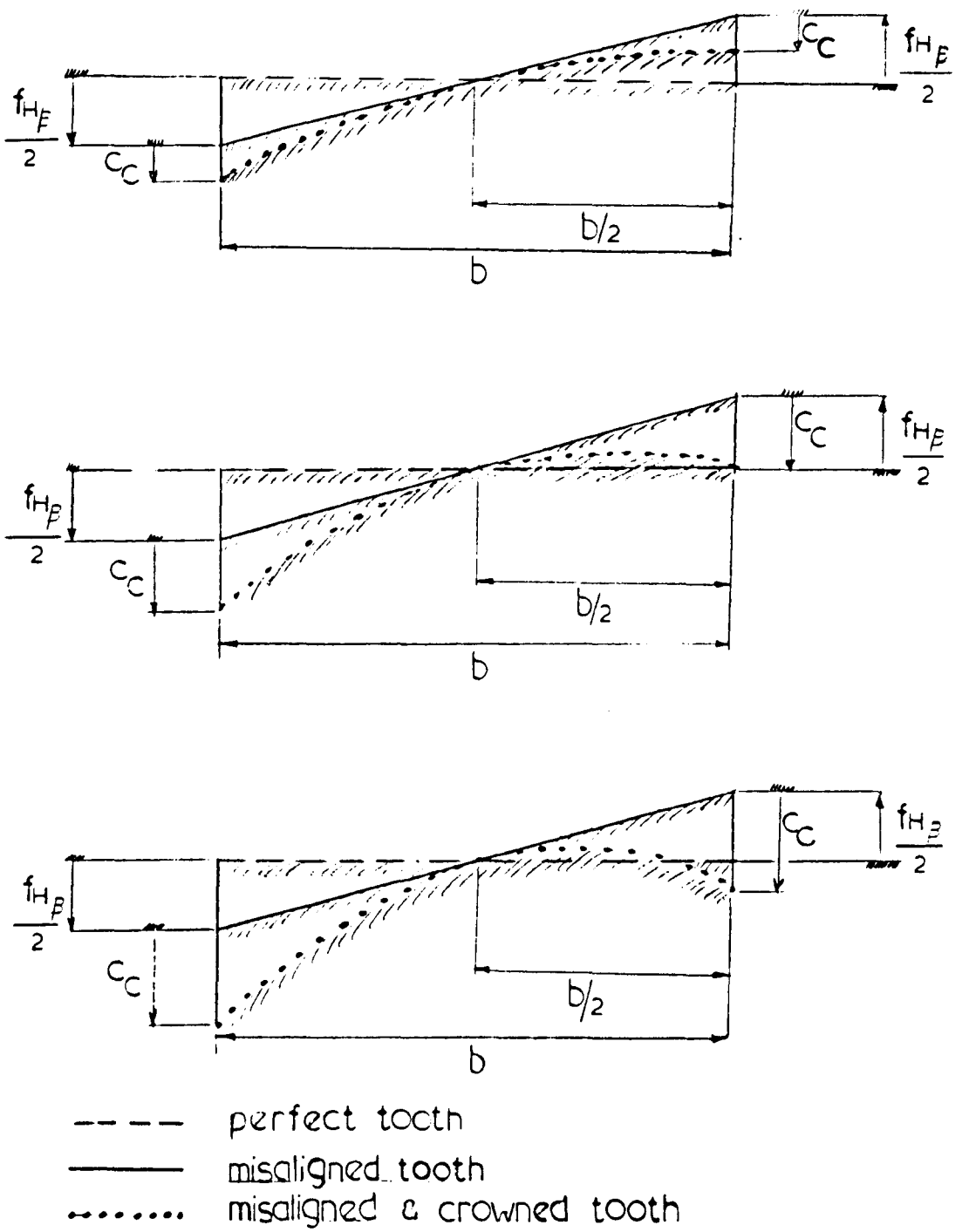

FIG.4.7 CROWNING OF MISALIGNED TEETH

$$K_{H\alpha} = \left[\frac{w_{max}}{w_{max0}} \right]_{\substack{\text{For complete cycle} \\ \underline{\text{ignoring}} \text{ end spikes}}} \qquad 4.7$$

$$K_{H\alpha} = \left[\frac{\sigma_{Hmax}}{\sigma_{Hmax0}} \right]^2_{\substack{\text{For complete cycle} \\ \underline{\text{ignoring}} \text{ end spikes}}} \qquad 4.8$$

$$K_{H\alpha} = \left[\frac{(\sigma_H) \text{ At } w_{max} \text{ for complete cycle } \underline{\text{ignoring}} \text{ end spikes}}{(\sigma_{H0}) \text{ At } w_{max0} \text{ for complete cycle } \underline{\text{ignoring}} \text{ end spikes}} \right]^2 \qquad 4.9$$

$$K_{H\alpha} = \left[\frac{w_{max}}{w_{max0}} \right]_{\substack{\text{For complete cycle} \\ \underline{\text{including}} \text{ end spikes}}} \qquad 4.10$$

$$K_{H\alpha} = \left[\frac{\sigma_{Hmax}}{\sigma_{Hmax0}} \right]^2_{\substack{\text{For complete cycle} \\ \underline{\text{including}} \text{ end spikes}}} \qquad 4.11$$

$$K_{H\alpha} = \left[\frac{(\sigma_H) \text{ At } w_{max} \text{ for complete cycle } \underline{\text{including}} \text{ end spikes}}{(\sigma_{H0}) \text{ At } w_{max0} \text{ for complete cycle } \underline{\text{including}} \text{ end spikes}} \right]^2 \qquad 4.12$$

As with $K_{H\beta}$, however, the logical choice is to use values based on a contact stress ratio, so that equations 4.8 (without spike effects) and 4.11 (with spike effects) are used in what follows.

4.3.2 Effect of Profile Errors on $K_{H\alpha}$

Fig. 4.8a shows the variation of $K_{H\alpha}$ with the profile angle error $f_{H\alpha}$ defined as shown in Fig. 4.8b.

The sign of $f_{H\alpha}$ in Fig. 4.8a was chosen in such a way as to maximise its effect on σ_{Hmax}. Metal was "added" in the region (near the pinion's root) where peak stresses occur on an error-free gear pair. However, a limited number of results were also obtained with the sign of $f_{H\alpha}$ reversed. These gave values of $K_{H\alpha}$ differing considerably from those plotted in Fig. 4.8a, since although the load spikes at the start and end of mesh are of very similar magnitude, the contact stresses are much larger at the start of

Fig.4.8a Effect of Profile Angle Error on Transverse Load Distribution Factor

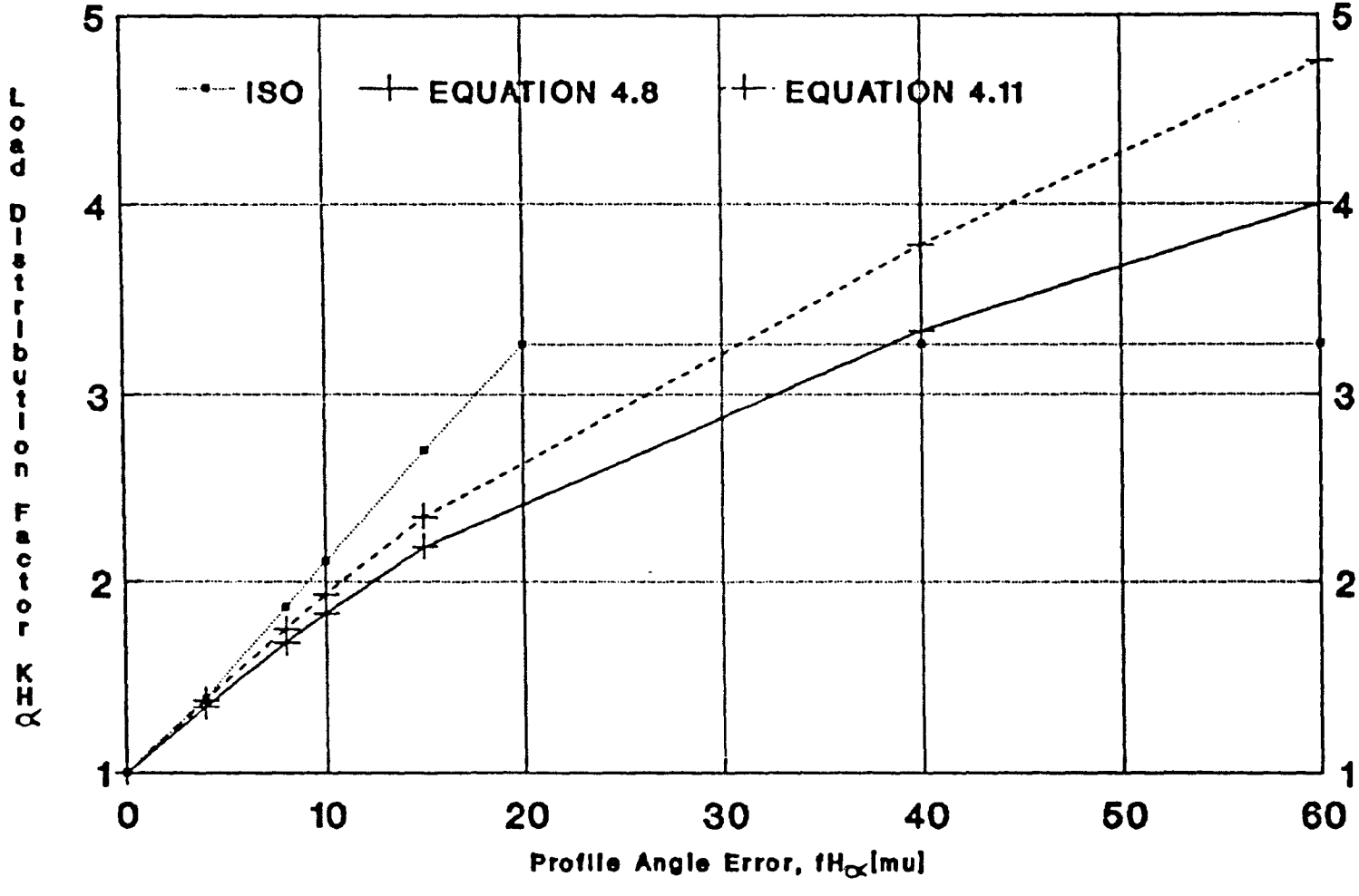

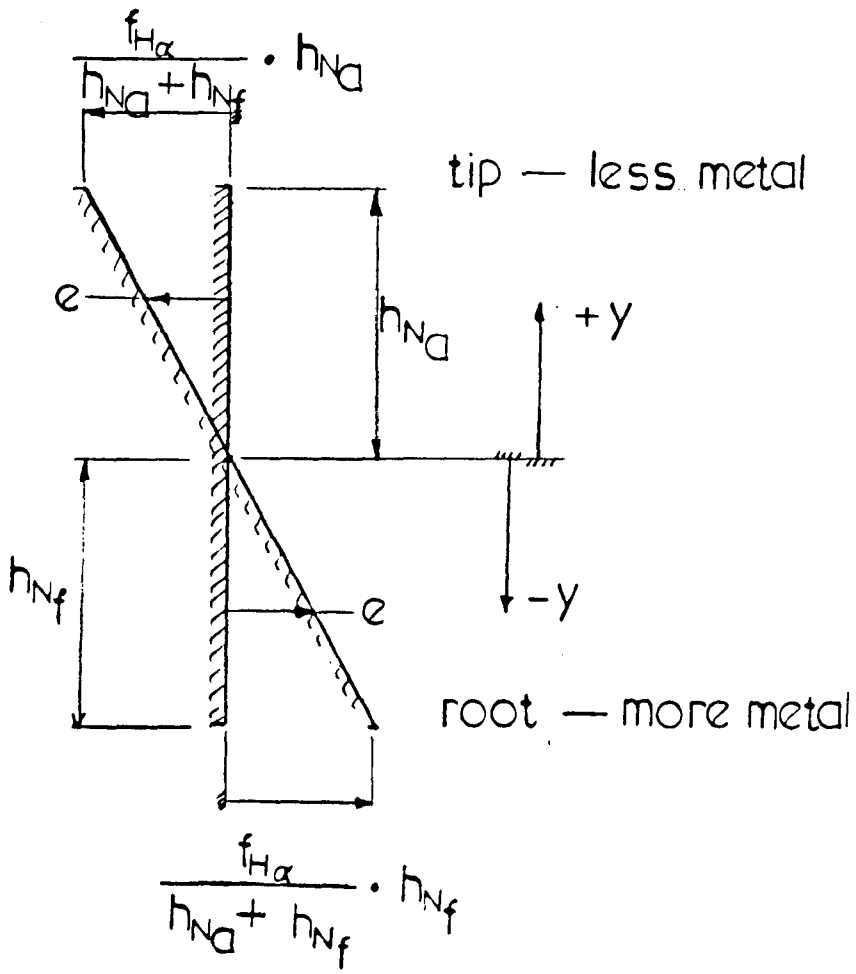

FIG.4.8b PROFILE ANGLE ERROR

mesh, resulting in larger values of $K_{H\alpha}$ based on Eqn. 4.11.

As explained in section 1.2.2, the value of $K_{H\alpha}$ calculated from Eqn. 1.15 has an upper limit of $\epsilon_\gamma/(\epsilon_\alpha.Z_\epsilon{}^2)$. This is shown in Fig. 4.8a by the horizontal line at $K_{H\alpha} \approx 3.26$. The standards thus predict that for errors $f_{H\alpha}$ greater than about 20μm, there is no further increase in σ_{Hmax}. The results from the 3-D model, however, show progressive increases in $K_{H\alpha}$ as $f_{H\alpha}$ increases, although at a reduced rate.

In the region $f_{H\alpha} < 20\mu m$ below the cut-off point, the ISO formula Eqn. 1.15 predicts values of $K_{H\alpha}$ that are up to 20% greater than those given by either of equations 4.8 and 4.11. As with $K_{H\beta}$, however, the agreement between the ISO predictions and those from the 3-D mesh model is much improved if c' is used instead of c_γ in Eqn. 1.15.

4.3.3 Effect of Tip/Root Relief and Profile Crowning on $K_{H\alpha}$

Tip and root relief are "straight-line" forms of profile crowning which is generally applied as a parabolic curve varying from zero correction at the reference (or pitch) circle, to peak values at tip and/or root, as shown in Fig. 4.12, which shows both tip relief and addendum profile crowning. Root relief and dedendum profile crowning are not shown, since introducintg tip-relief (or addendum crowning) on both mating gears is equivalent to introducintg both tip and root relief (or addendum and dedendum crowning) on only one of the mating gears. The results presented in this section were obtained by introducing tip relief or addendum crowning to both mating gears.

The purpose of introducing either of these corrections is to reduce or completly eliminate the load peaks at the start and end of contact which lead to premature scuffing or pitting failures. Using the definitions of $K_{H\alpha}$ presented in Eqns. 4.8 (ignoring spikes) and 4.11 (including spikes), results in Fig. 4.9a which shows how $K_{H\alpha}$ changes with varying amounts of tip relief. The starting point of the tip relief was based on the 'short relief' recommended by Munro[47], who recommends for this that the relief should start at a roll length of

$$\frac{\epsilon_\alpha - 1}{2} \cdot p_{bt} \qquad 4.13$$

This gives a height along the tooth profile for the gear set considered of about 2.5mm, corresponding to $h_{ay} = 7.5mm$ (Fig. 4.12).

When the end-spikes are ignored, Eqn. 4.8 shows a near linear, gradual increase in $K_{H\alpha}$ with increasing tip relief values C_{ay}. This is to be

expected, as the metal removal caused by the relief reduces the effective contact length, thus concentrating the load on fewer, shorter contact lines. Considering the effect of tip relief on the load spikes (Eqn. 4.11), one might expect that a progressive increase in tip relief would gradually reduce the end spikes until they were eventually completely eliminated. The results in Fig. 4.9a show, however, that this does not occur since $K_{H\alpha}$ starts to rise again beyond $C_{ay} \approx 6\mu m$.

There appear to be two mechanisms which combine to cause this behaviour. One is the 'expected' effect of C_{ay} in reducing the elastic deformation and hence the load spike at the tooth tip. This is essentially a 2-dimensional effect and is the only mechanism in operation in spur gears. However, an opposing, unexpected effect also appears to operate on helical gears causing an increase in $K_{H\alpha}$ for short relief heights as C_{ay} is increased above about $6\mu m$.

For very large values of C_{ay}, there will be no contact in the relieved region at all (the teeth are then effectively 'topped', with a reduced value of ϵ_α). Not only does this increase the <u>average</u> loading throughout the mesh (as indicated by the results based on Eqn. 4.8), but it will also give rise to a new 'shifted' buttressing effect caused by the sudden start of contact loading near h_{ay}. This buttressing will be even more effective than on the unrelieved gear, and will give rise to even greater load spikes, since the local tooth tip stiffness is now enhanced by the adjacent unloaded (relieved) tip section. It thus appears that on tip relieved helical gears the load peaks tend to just shift down the tooth to the start of the <u>actual</u> contact line, and, for large C_{ay}, intensify.

The general principle to be followed if this is to be prevented is to restrict C_{ay} to a value that still allows contact at the tooth tip, and vary the height of relief to achieve minimum values of σ_{Hmax} (or $K_{H\alpha}$). Fig. 4.10 shows the effect of varying h_{ay} for $C_{ay} = 4\mu m$.

The optimum height of relief is about 5 .. 6mm, nearly twice the 'short relief' suggested by Munro[47]. If the relief height extends below the reference circle, approaching Munro's 'long relief' value, $K_{H\alpha}$ again increases since tip relief over the full depth of the tooth tends to shift the whole length of the tooth pair profiles closer together, again allowing for contact near the tooth tips.

Time limitations precluded a systematic study of all possible combinations of C_{ay} and h_{ay}, but from the results presented, it is clear that to design tip relief for helical gears using rules (such as Munro's[47]) derived from 2-dimensional 'thin-slice' models or spur gear testing is quite unreliable.

In Fig. 4.9b, a plot is shown representing all possible ways of

Fig.4.9a Effect of Tip Relief on Transverse Load Distribution Factor

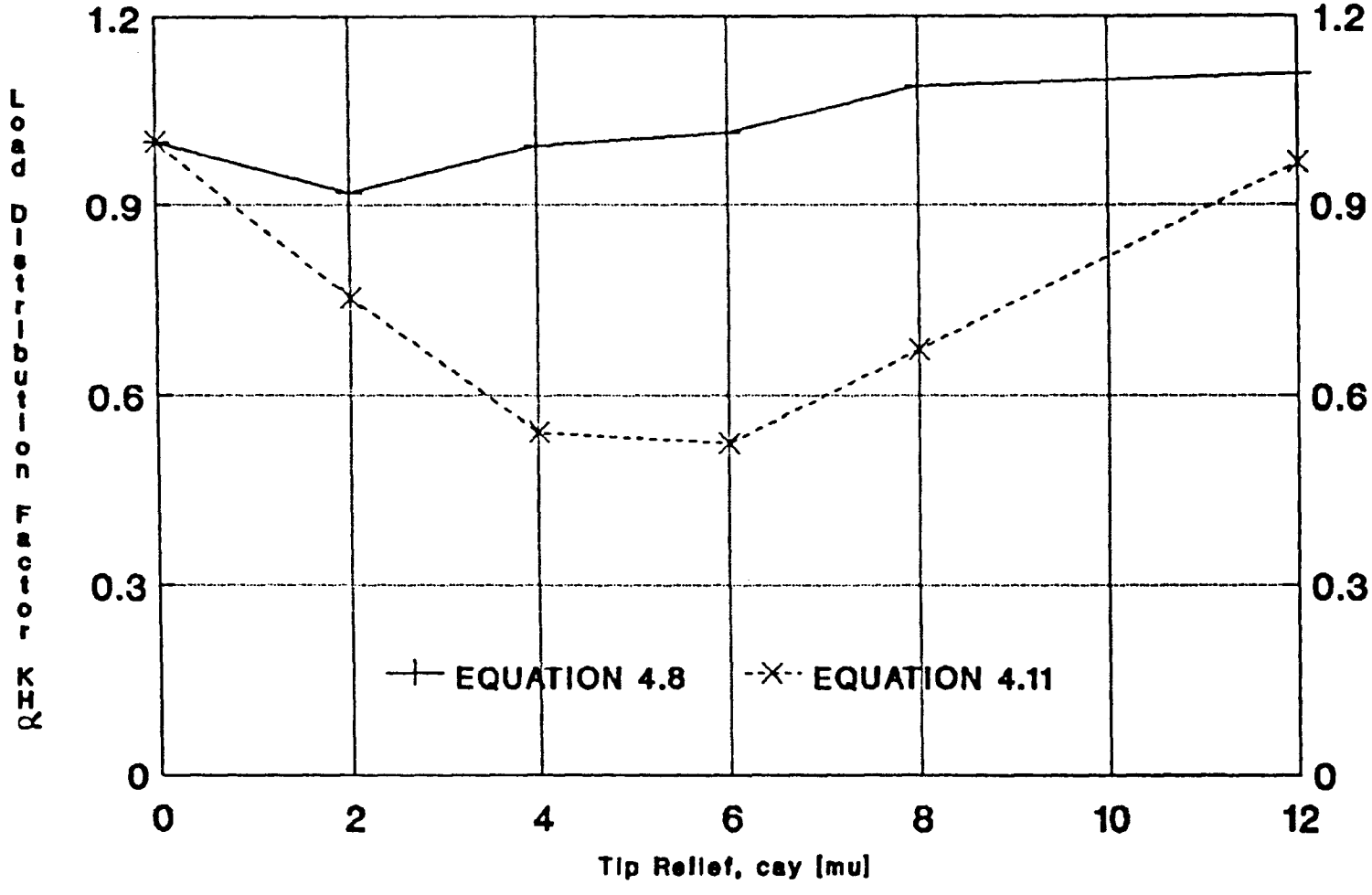

start of relief hay=7.5mm

Fig.4.9b Effect of Tip Relief on Transverse Load Distribution Factor

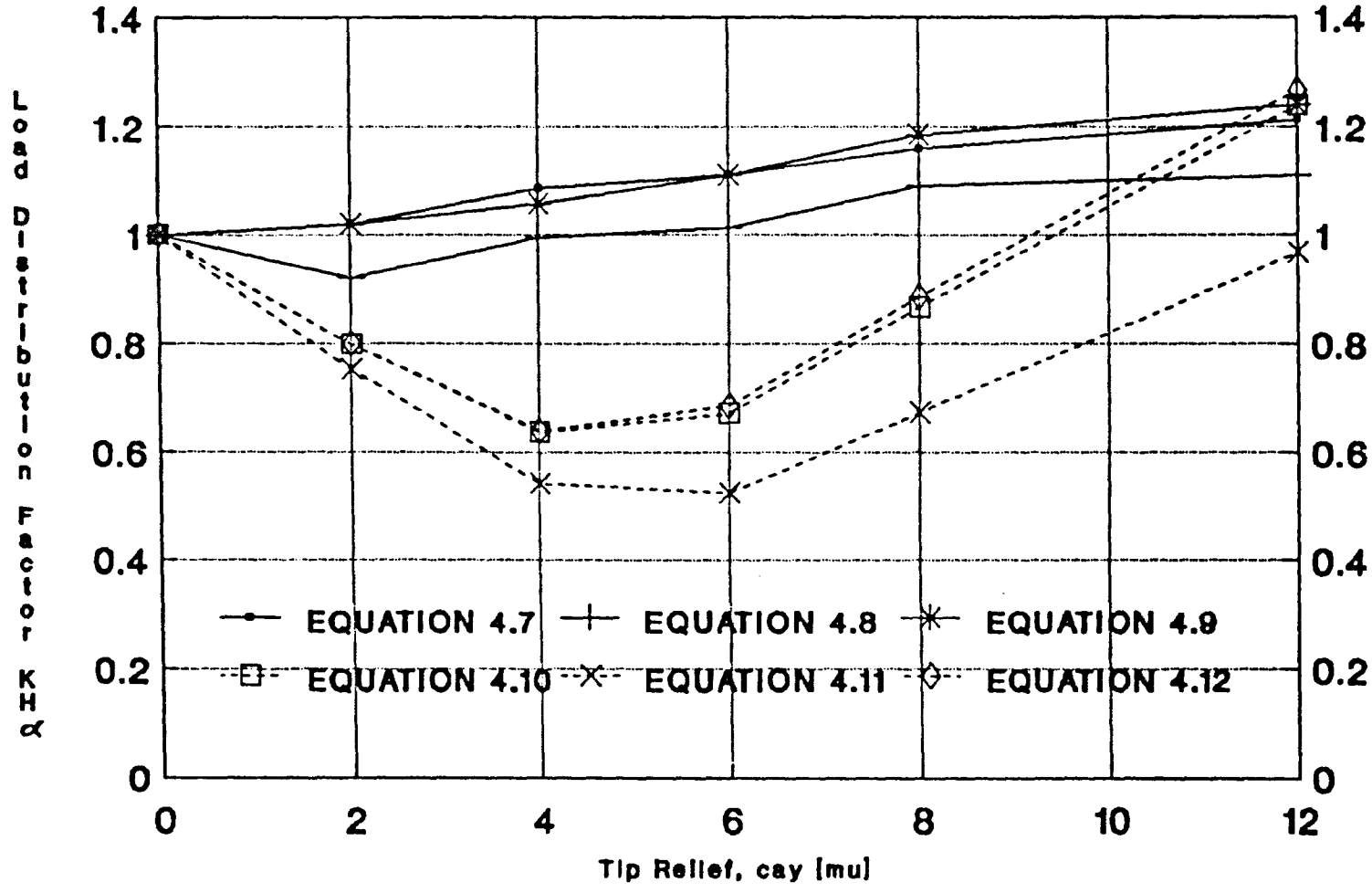

start of relief hay-7.5mm

Fig.4.10 Effect of height of Relief on Transverse Load Distribution Factor

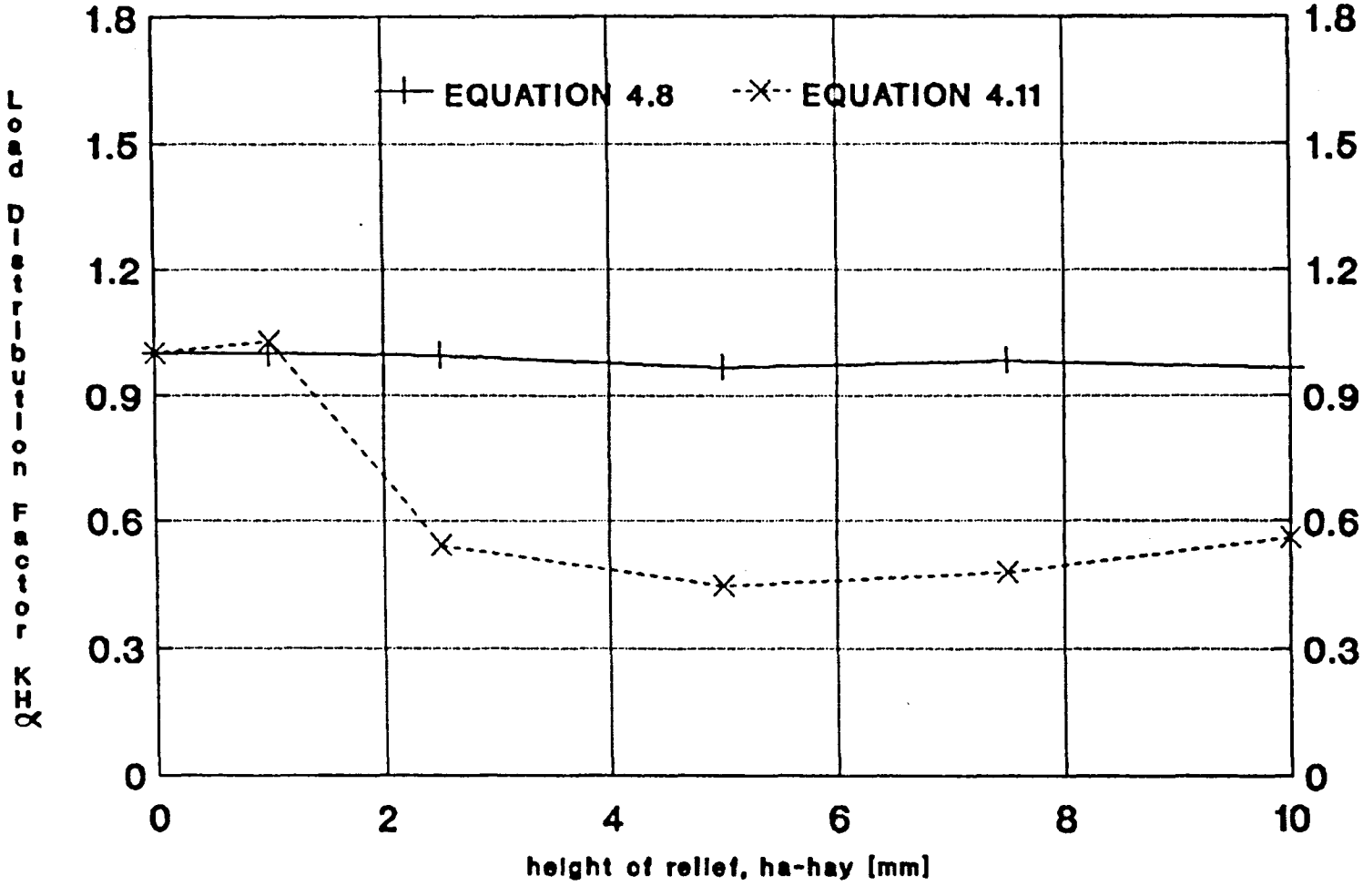

amount of relief oay-4um

calculating $K_{H\alpha}$ (Eqns. 4.7 to 4.12). Clearly equations 4.9 and 4.12 give very close results to those from equations 4.7 and 4.10 respectively. This is true since the peak loads for the perfect and the relieved gears, occur at the same, or nearly the same phases of mesh, and therefore at nearly equal radii of curvature thus resulting in nearly the same values for $K_{H\alpha}$ regardless of whether peak loads or the corresponding stresses are used. The same phenomenon occurred for face crowning effect on $K_{H\beta}$ in Section 4.2.3.

A comparison of Figs. 4.12a and 4.12b shows that the effect of profile crowning should be very similar to that of the same amount of tip relief at a height h_{ay} of about $0.33m_n$ ($h_a - h_{ay} \simeq 0.67m_n = 6.7$mm on the gears studied as explained in more detail later on in this section). This proves to be so. Fig. 4.11 shows the effect of variable profile crowning on $K_{H\alpha}$ (calculated from Eqns. 4.8 and 4.11). For an amount of crowning of 4μm, the values are virtually identical to those given in Fig. 4.10 for $h_a - h_{ay} = 6.7$mm.

The wide minimum in Fig. 4.11 from a crowning amount of 4 to 10μm thus suggests that the amount of tip relief would not be critical in this region either, provided the optimum height of relief is used.

The general impression gained from Figs. 4.9 - 4.11 is that profile crowning is generally preferable to tip relief as a method of controlling peak contact stresses. However, as pointed out by Munro, other factors such as the transmission error waveform (which affects noise performance) and the ease with which the correction can be produced will influence the choice.

In order to make a direct comparison between the effect of $C_{\alpha a}$ and C_{ay} on $K_{H\alpha}$, the proper height of relief ($h_a - h_{ay}$) must be used. For tip relief, the volume of metal removed is

$$1/2 \cdot C_{ay} \cdot (h_a - h_{ay}) \qquad \text{(see Fig. 4.12a)}$$

and for profile crowning, the volume of metal removed is

$$1/3 \cdot C_{\alpha a} \cdot h_a \qquad \text{(see Fig. 4.12b)}$$

where equating both values when $C_{ay} = C_{\alpha a}$ yields

$$h_a - h_{ay} = 2/3 \cdot h_a$$

and for the gears used, this reduces to

$$h_a - h_{ay} = 2/3 \cdot 10 = 6.7\text{mm}$$

Therefore, a run is made for various amounts of tip relief with a height of relief of 6.7mm, and the results are plotted alongside those obtained for profile crowning in Fig. 4.13 using equations 4.8 (ignoring spikes) and 4.11 (including spikes). Clearly, the curves follow a similar trend for tip relief and crowning, and the actual values are quite close as shown.

Fig. 4.11 Effect of Profile Crowning on Transverse Load Distribution Factor

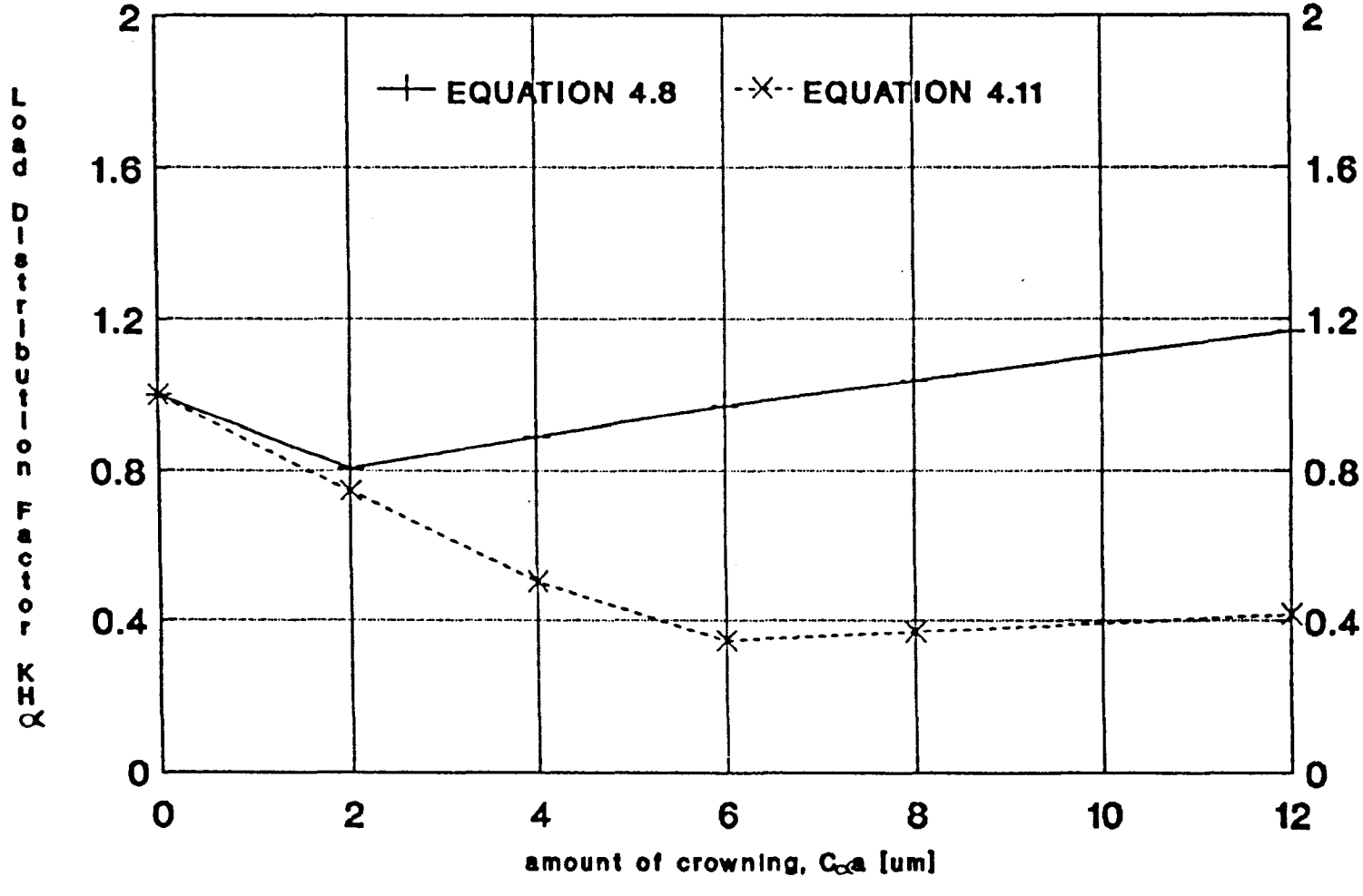

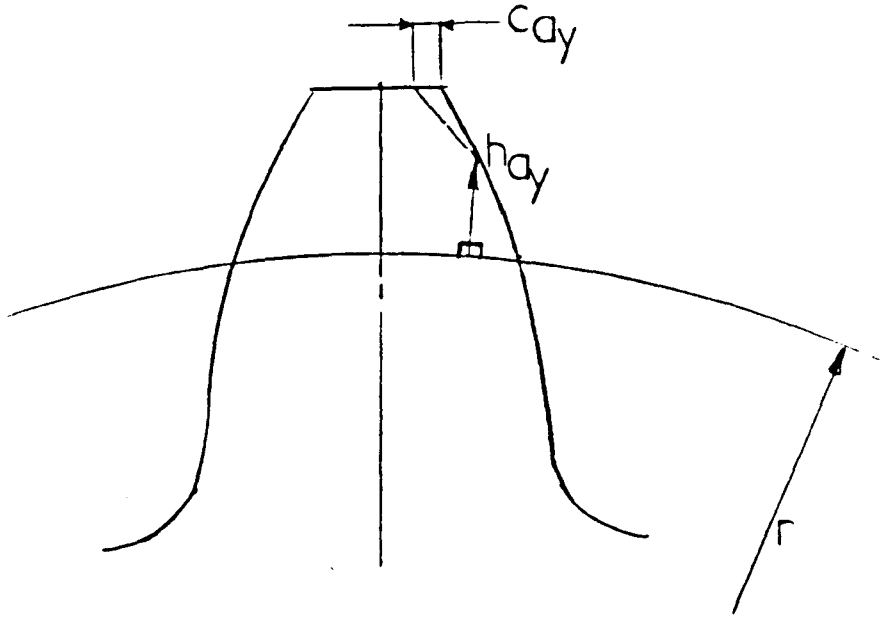

a— tip relief

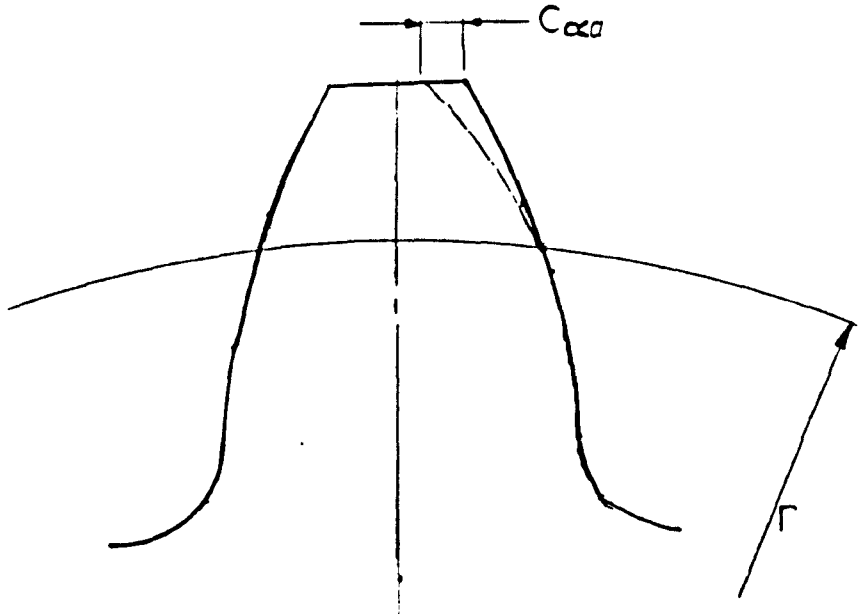

b— profile crowning

FIG.4.12 TIP RELIEF & PROFILE CROWNING

Fig.4.13 Comparison of Effect of Tip Relief & Profile Crowning on KH_{α}

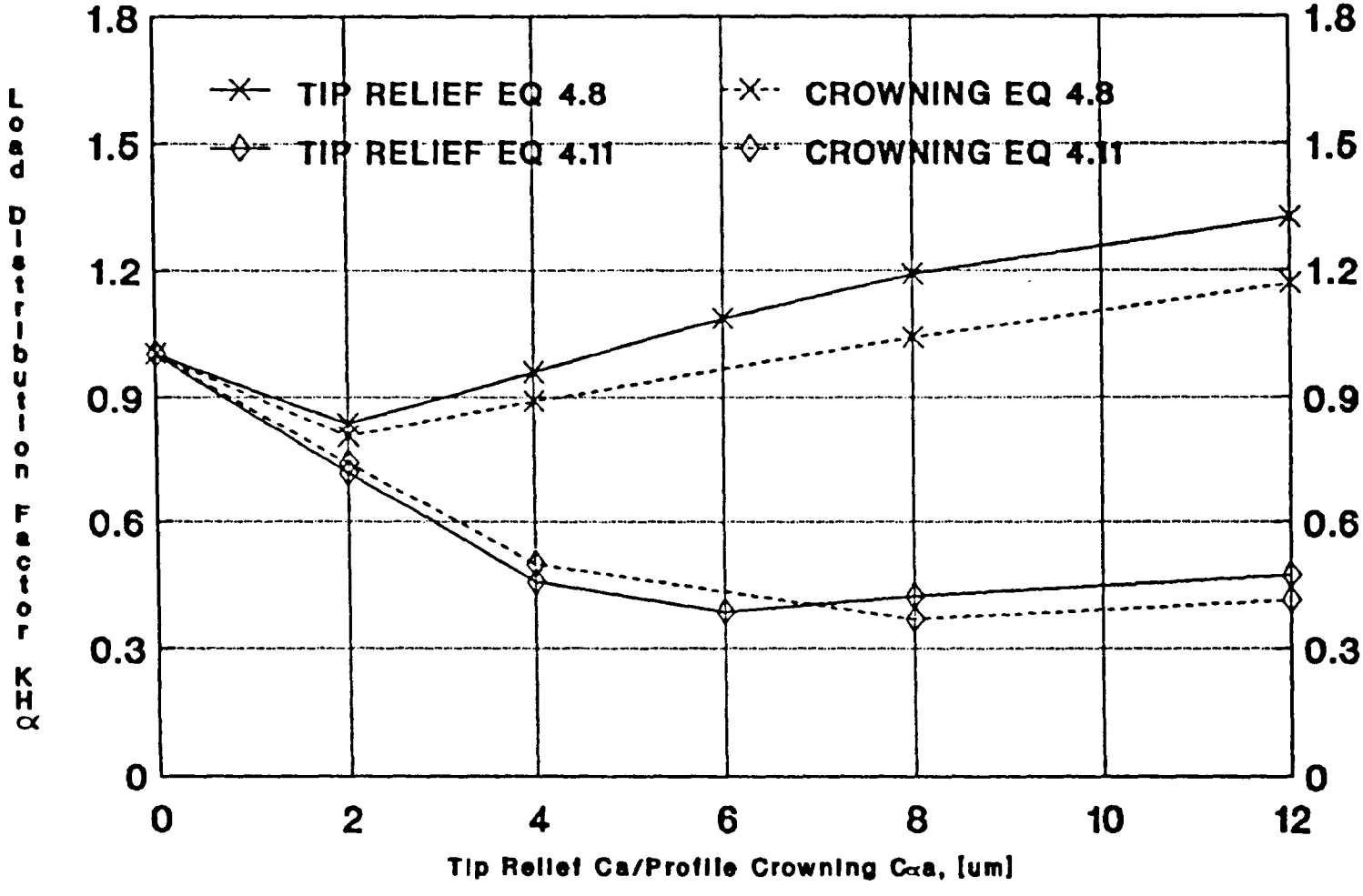

start of relief hay=3.3mm

4.3.4 Combined Effect of Profile Angle Error and Profile Crowning on $K_{H\alpha}$

In sections 4.3.2 and 4.3.3, the effects on $K_{H\alpha}$ of profile angle error $f_{H\alpha}$ and profile crowning were studied independently. In this section the advantages of introducing profile crowning on a gear with a profile angle error are studied. Fig. 4.14 shows the geometry of the tooth forms studied.

Addendum profile crowning of 2, 4, 6, 8, 12, 16 and 20μm was introduced on both mating gears, and the pinion was also given a profile angle error $f_{H\alpha}$ of 8μm as shown in Fig. 4.14. There was no profile angle error on the wheel. The effect of these deviations on $K_{H\alpha}$, calculated by equations 4.8 and 4.11, is shown in Fig. 4.15(a). Notice the great similarity in the trend of these curves when compared to Fig. 4.6 of section 4.2.4 on the combined effects of lead error and face crowning. The shapes of the curves can be explained by arguments analogous to those presented in Section 4.2.4, which will not be repeated here.

The optimum amount of crowning appears to be about 12μm in this case, equal to 1.5 times the profile angle error $f_{H\alpha}$ (c.f. optimum face crowning of about $f_{H\beta}$ in Section 4.2.4). However, crowning of about 8μm is desirable <u>without</u> $f_{H\alpha}$ (Fig. 4.11); an <u>additional</u> 4μm is thus needed to offset the effect of $f_{H\alpha}$.

Also shown in Fig. 4.15(b) are values of $K_{H\alpha}$ (derived from Eqn. 4.11) for a separate profile angle error $f_{H\alpha}$ = 8μm, and profile crowning $C_{\alpha a}$ <u>only</u>, taken from Figs. 4.8 and 4.11 respectively. The figure shows clearly that the two 'errors' interact, and can not be considered as independent effects. It is also worth noting that the ISO standard[4] treats <u>all</u> deviations from involute form as profile form errors f_f, all of which are assumed to have the same effect regardless of their 'shape' as discussed in Section 1.2.2. The results shown in Fig. 4.15 show that this is far from true.

4.3.5 Effect of Pitch Errors on $K_{H\alpha}$

Adjacent base pitch error f_{pb} for a particular pitch is defined as the difference between the actual transverse base pitch and the nominal value p_{bt} (= $\pi d_b/Z$). On a gear with Z teeth, there are Z adjacent base pitch errors for the Z right hand flanks, and Z base pitch errors for the Z left hand flanks.

The cumulative pitch error F_{pbk} is the deviation of the actual pitch span over k individual pitches, from its nominal value $k.p_{bt}$, and is the algebraic sum of the k adjacent base pitch errors in the span:

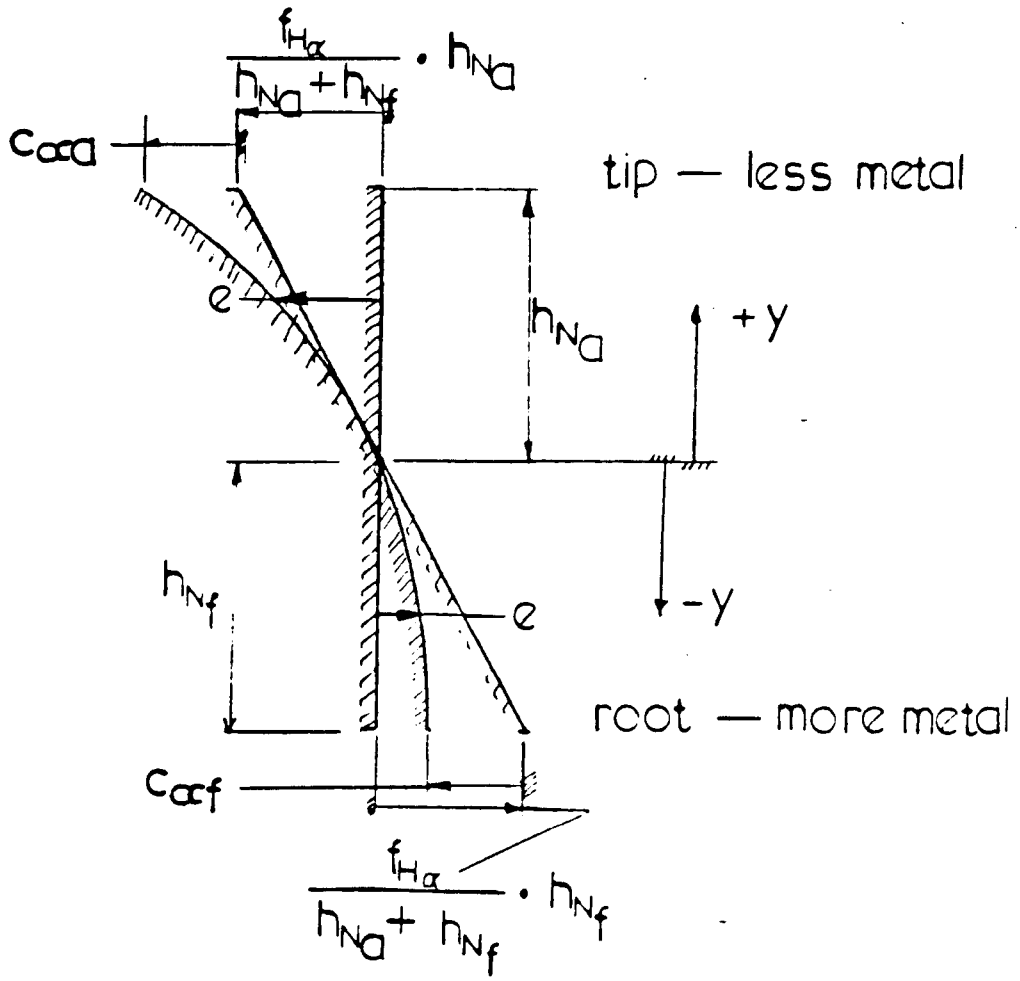

FIG.4.14 PROFILE ANGLE ERROR

Fig.4.15a Combined Effect of Profile Angle Error and Profile Crowning on KH_{α}

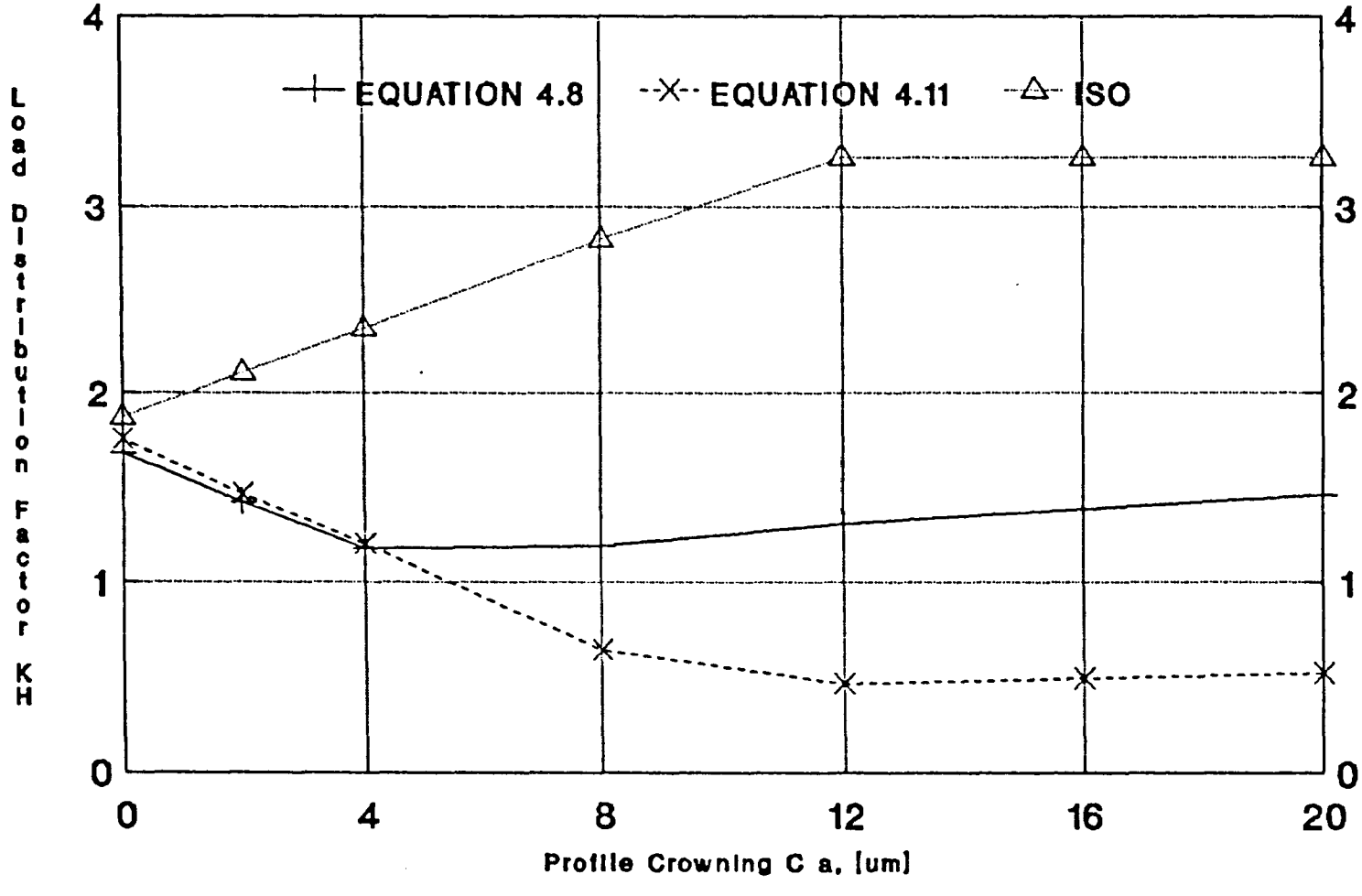

Profile Angle Error fH_{α} 8um

Fig.4.15b Effect of fH_{α}, $C_{\alpha}a$, fH_{α} & $C_{\alpha}a$ Combined on KH_{α}(Results of Eq.4.11)

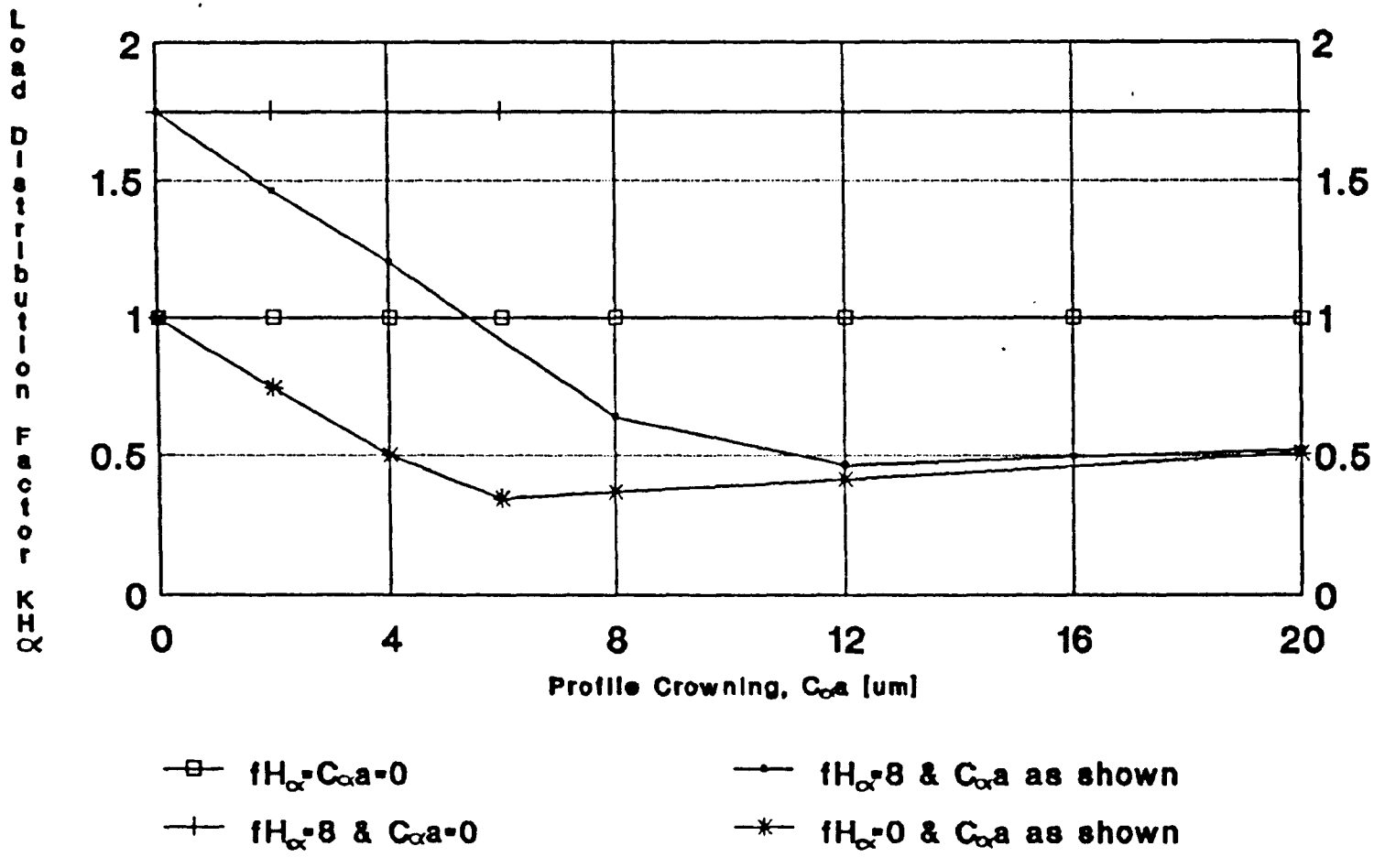

fH_{α} is in [um]

$$F_{pbk} = \sum_{k} f_{pb} \qquad 4.14$$

Fig. 4.16 shows the corresponding adjacent and cumulative pitch errors f_p and F_{pk} (measured around the reference circle rather than the base circle), where

$$f_p = \frac{f_{pb}}{\cos \alpha_t} \quad \text{and} \quad F_{pk} = \frac{F_{pbk}}{\cos \alpha_t}$$

The standards BS/ISO/DIN[2,3,4] use an equivalent spur gear to analyse a helical gear, as mentioned in a number of places in this work. The expression (Eqn. 1.15) for $K_{H\alpha}$ given in the ISO[4] standard is based on a simple "load sharing" model of the effect of a single base pitch error p_{bt} on the loading of the equivalent spur gears. Since, in such a model, only at most two tooth pairs are in contact, only a single pitch error need be considered.

On the helical gears considered here, up to four tooth pairs can be in contact at once, and, as shown in Fig. 4.16, it is quite possible for all these four pitches to have consecutive adjacent pitch errors of similar magnitude f_{pb} and sign, giving a possible cumulative error over these four teeth of $3f_{pb}$. It would thus be quite unrealistic to consider the effect of only a single pitch error on one tooth (i.e. on one pitch).

In the results presented below, positive cumulative pitch errors of f_{pb}, $2f_{pb}$, $3f_{pb}$, etc. were thus applied to successive pinion teeth in the mesh. Values of f_{pb} of 2, 4, 6, 8, and 10μm were considered. The wheel was left error free. The values of $K_{H\alpha}$ obtained are shown in Fig. 4.17 compared with those calculated from the ISO[4] equation 1.15. To clarify what happens, values of $K_{II\alpha}$ calculated from equations 4.8 and 4.11 are studied.

As can be seen, the results are most interesting. To begin with, the introduction of the pitch errors to the load distribution program, in the manner discussed earlier, causes the total load to be dumped on less teeth than the error-free gear, and furthermore, on less contact points. For the gear-set used, the general picture reveals that during the initial phases of mesh of a particular tooth pair (maximum of four tooth pairs in mesh at any one instant), the first two are totally relieved of the load, the third carries comparable loads and stresses to those of the error-free gear. The last engaged tooth pair carries the biggest loads and stresses, taking on its portion plus that portion which was supposed to be carried by the first two pairs.

As mesh proceeds, the first tooth pair still carries no loads or

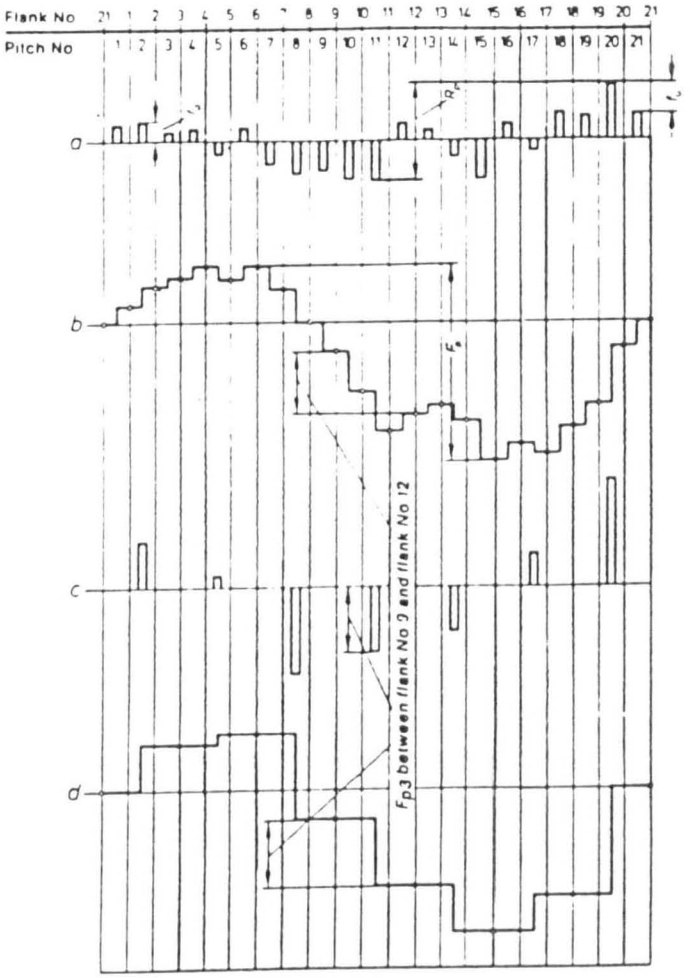

a) adjacent pitch errors f_p shown as vertical blocks between the flank numbers

   R_p range of pitch errors

   f_u difference between adjacent pitches (in this case between pitches Nos 20 and 21, i.e. on flank No 20)

b) cumulative circular pitch errors referred to flank No 21, shown as a stepped-line diagram

   F_p cumulative pitch error

c) cumulative circular pitch errors over a sector of $k = 3$ individual pitches each time, shown as vertical blocks in mid-span

d) cumulative pitch-span deviations calculated from the span deviations of figure *c*, referred to flank No 21, shown as a stepped-line diagram (with correspondingly large step width)

Figure 416 Graphical representation of circular pitch deviations (example: $z = 21$)

Fig.4.17 Effect of Pitch Errors on Transverse Load Distribution Factor KH_{α}

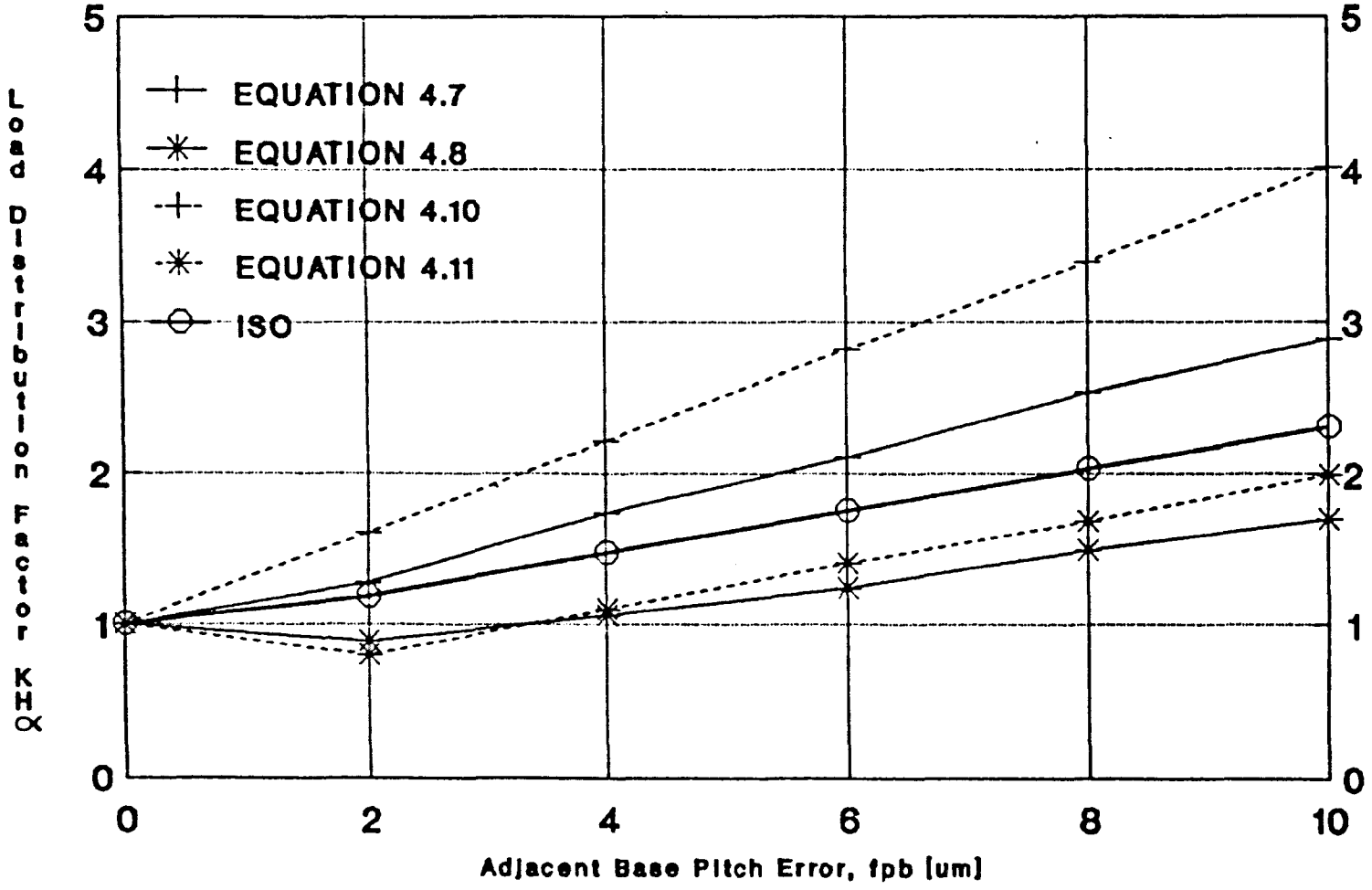

equal fpb on each pinion tooth

stresses, the second tooth pair however receives a very small portion of the total load which keeps increasing during the mesh cycle. The third tooth pair also starts receiving increased loads and stresses. On the fourth tooth pair, the contact length starts to converge to single point contact, explaining why the second and third tooth pairs start receiving higher loads dumped onto them from the reduced contact length on number four. At the same time, the point contact on four causes a huge load and corresponding stress (spike effect).

Due to the interesting results obtained using equations 4.7 and 4.10, these curves were plotted alongside the curves from equations 4.8 and 4.11 as shown in Fig. 4.17.

With or without the spike effect, equations 4.7 and 4.10 give quite large values of $K_{H\alpha}$, caused by the reduced contact on the last engaged tooth pair, even before approaching point contact which gives rise to spikes. These values are much larger than those predicted by the standards. This is to be expected, as the standards assume the total load is carried by a single tooth pair, but is still spread out along the whole face-width of the equivalent spur gear. This tends to give less peak loads even near the pitch point, or the inner point of single tooth contact.

Equations 4.9 and 4.12 were also plotted (not shown) and give nearly identical results to those of equations 4.7 and 4.10 respectively. This is not surprising since the peaks for the gear with pitch errors and for the perfect gear, generally occur on the same engaged tooth at nearly the same axial location, and nearly the same phase of mesh. This means that the relative radii of curvature are nearly fixed. By referring to equation 1.1 for the contact stress, the near identical results are easily explained.

Considering equations 4.8 and 4.11, the values of $K_{H\alpha}$ are quite small. Recall from the above discussion that peak loads and contact stresses occur on the last engaged pair of teeth of a gear-set with pitch errors. On the perfect gear-set however, the peak stresses may be on other engaged teeth than the last, and this is actually the case. These peak stresses are comparable to those obtained from the gear-set with errors, thus giving relatively low $K_{H\alpha}$ values. If in equation 4.8 (spikes ignored), the peak stress on the last engaged tooth were used instead (this will not be the actual cycle's peak value) comparable results to those obtained from equations 4.7 and 4.9 result. This also applies very well to equation 4.11 (spikes considered).

The larger than 1.0 values of $K_{H\alpha}$ obtained using equation 4.11 reflect the high load concentration on the last tooth pair, even before the

As in previous cases, the ISO formula (Eqn. 1.15) overestimates the effect of the pitch errors on σ_{Hmax}, and is again slightly improved if c' is substituted for c_γ. Before making such a change, however, it would be wise to investigate the effect of positive pitch errors on the gear wheel, (or of negative pitch errors on the pinion). These would both cause progressive concentration of tooth loads at the beginning of the mesh cycle, where the effective flank curvature is greatest, and could thus lead to even higher values of $K_{H\alpha}$ than those given in Fig. 4.17 by Eqn. 4.11.

4.4 Combined Effect of Lead and Profile Errors on Overall Load Distribution Factor K_H

In sections 4.2 and 4.3, the effects on the load distribution along helical gear contact lines of lead errors/modifications and profile errors/modifications were studied independently. In this section, the combined effect of simultaneous lead and profile errors/modifications on the overall load distribution factor K_H is studied.

According to the BS/ISO/DIN standards[2,3,4] the factor $K_{H\beta}$ given by Eqns. 1.12 and 1.13 is totally unaffected by the introduction of profile errors. However, $K_{H\alpha}$, given by Eqn. 1.15, is affected by the presence of lead errors or modifications, since the load F_{tH} used in Eqns. 1.15 is already modified by the factor $K_{H\beta}$, as shown in Section 1.2.2. $K_{H\alpha}$ is thus, in this sense a 'combined' factor, so that the overall load distribution factor is given by

$$(K_H)_{combined} = K_{H\beta} \cdot (K_{H\alpha})_{combined} \qquad 4.15(a)$$

which represents ISO.

For comparison, the values of K_H obtained by multiplying the values of $K_{H\beta}$ and $K_{H\alpha}$ obtained independently in sections 4.2 and 4.3 have also been calculated, giving

$$(K_H)_{separate} = K_{H\beta} \cdot (K_{H\alpha})_{separate} \qquad 4.15(b)$$

where equation 4.15(b) does not represent ISO.

The factor K_H has also been determined directly using the 3-D mesh model by introducing simultaneous lead and profile errors/modifications.

Referring to equation 1.6, and by setting both K_A and K_V to unity.

$$\sigma_H = \sigma_{H0} \cdot [K_{H\alpha} \cdot K_{H\beta}]^{\frac{1}{2}} \qquad 4.16$$

whence

$$K_H = K_{H\alpha} \cdot K_{H\beta} = (\sigma H/\sigma_{H0})^2 \qquad 4.17$$

For comparison with the standards[2,3,4], equation 4.17 seems to be most suitable. However, as with $K_{H\alpha}$ and $K_{H\beta}$ themselves, there are again six alternative ways to calculate K_H as follows:

$$[K_H]_{combined} = \left[\frac{w_{max}}{w_{max0}} \right]_{\substack{\text{For complete cycle} \\ \underline{\text{ignoring}} \text{ end spikes}}} \qquad 4.18$$

$$[K_H]_{combined} = \left[\frac{\sigma_{Hmax}}{\sigma_{Hmax0}} \right]^2_{\substack{\text{For complete cycle} \\ \underline{\text{ignoring}} \text{ end spikes}}} \qquad 4.19$$

$$[K_H]_{combined} = \left[\frac{(\sigma_H) \text{ At } w_{max} \text{ for complete cycle } \underline{\text{ignoring}} \text{ end spikes}}{(\sigma_{H0}) \text{ At } w_{max0} \text{ for complete cycle } \underline{\text{ignoring}} \text{ end spikes}} \right]^2 \qquad 4.20$$

$$[K_H]_{combined} = \left[\frac{w_{max}}{w_{max0}} \right]_{\substack{\text{For complete cycle} \\ \underline{\text{including}} \text{ end spikes}}} \qquad 4.21$$

$$[K_H]_{combined} = \left[\frac{\sigma_{Hmax}}{\sigma_{Hmax0}} \right]^2_{\substack{\text{For complete cycle} \\ \underline{\text{including}} \text{ end spikes}}} \qquad 4.22$$

$$[K_H]_{combined} = \left[\frac{(\sigma_H) \text{ At } w_{max} \text{ for complete cycle } \underline{\text{including}} \text{ end spikes}}{(\sigma_{H0}) \text{ At } w_{max0} \text{ for complete cycle } \underline{\text{including}} \text{ end spikes}} \right]^2 \qquad 4.23$$

Values of K_H derived from equations 4.18 to 4.23 have therefore been compared with equations 4.15(a) with emphasis on equation 4.19, which is most nearly equivalent to equation 4.17 derived from the standards.

The factor K_H has also been determined using the independently calculated values of $K_{H\beta}$ and $K_{H\alpha}$ using expressions:

$$(K_H)_{separate} = (K_{H\beta})_{eqn.4.1} \cdot (K_{H\alpha})_{eqn.4.7} \quad 4.24$$

$$(K_H)_{separate} = (K_{H\beta})_{eqn.4.2} \cdot (K_{H\alpha})_{eqn.4.8} \quad 4.25$$

$$(K_H)_{separate} = (K_{H\beta})_{eqn.4.3} \cdot (K_{H\alpha})_{eqn.4.9} \quad 4.26$$

$$(K_H)_{separate} = (K_{H\beta})_{eqn.4.4} \cdot (K_{H\alpha})_{eqn.4.10} \quad 4.27$$

$$(K_H)_{separate} = (K_{H\beta})_{eqn.4.5} \cdot (K_{H\alpha})_{eqn.4.11} \quad 4.28$$

$$(K_H)_{separate} = (K_{H\beta})_{eqn.4.6} \cdot (K_{H\alpha})_{eqn.4.12} \quad 4.29$$

In each of the graphs shown below, K_H as calculated by equations 4.15(a) and 4.15(b), has been compared with K_H obtained from equations 4.18, 4.19, 4.21 and 4.22 and equations 4.24, 4.25, 4.27 and 4.28.

In Figs. 4.18 to 4.21, the mesh misalignment is maintained at a fixed value ($F_{\beta y}$ = 8μm), while the profile angle error $f_{H\alpha}$ is varied from 0 to 15 μm. Figs. 4.22 to 4.25 are analogous to Figs. 4.18 to 4.21 respectively, but this time the profile angle error is maintained at a fixed value ($f_{H\alpha}$ = 8μm), while the mesh misalignment $F_{\beta y}$ is varied from 0 to 15 μm.

The figures show that whether $F_{\beta y}$ is fixed and $f_{H\alpha}$ is varied, or $f_{H\alpha}$ is fixed and $F_{\beta y}$ is varied, the results are strikingly similar for the range of errors studied. Equations 4.21, 4.22, 4.27 and 4.28 which take the end-spike-effect into account should not really be used as a basis for comparison with the standards in which the spike effect is ignored, although Eqn. 4.22 does give the best estimate of the effective value of K_H.

As with the individual factors, the ISO/DIN values of K_H given by Eqn. 4.17 would be slightly closer to the effective values predicted by Eqn. 4.22 if c_γ were replaced by c' in equations 1.12, 1.13 and 1.15.

As previously indicated, equations 4.19 and 4.25 are the best basis for comparison with the standards, although equations 4.18 and 4.24 also give similar results. In both cases, the values of K_H are significantly lower than

Fig.4.18 Effect of Profile & Lead Errors on KH (Spikes Ignored)

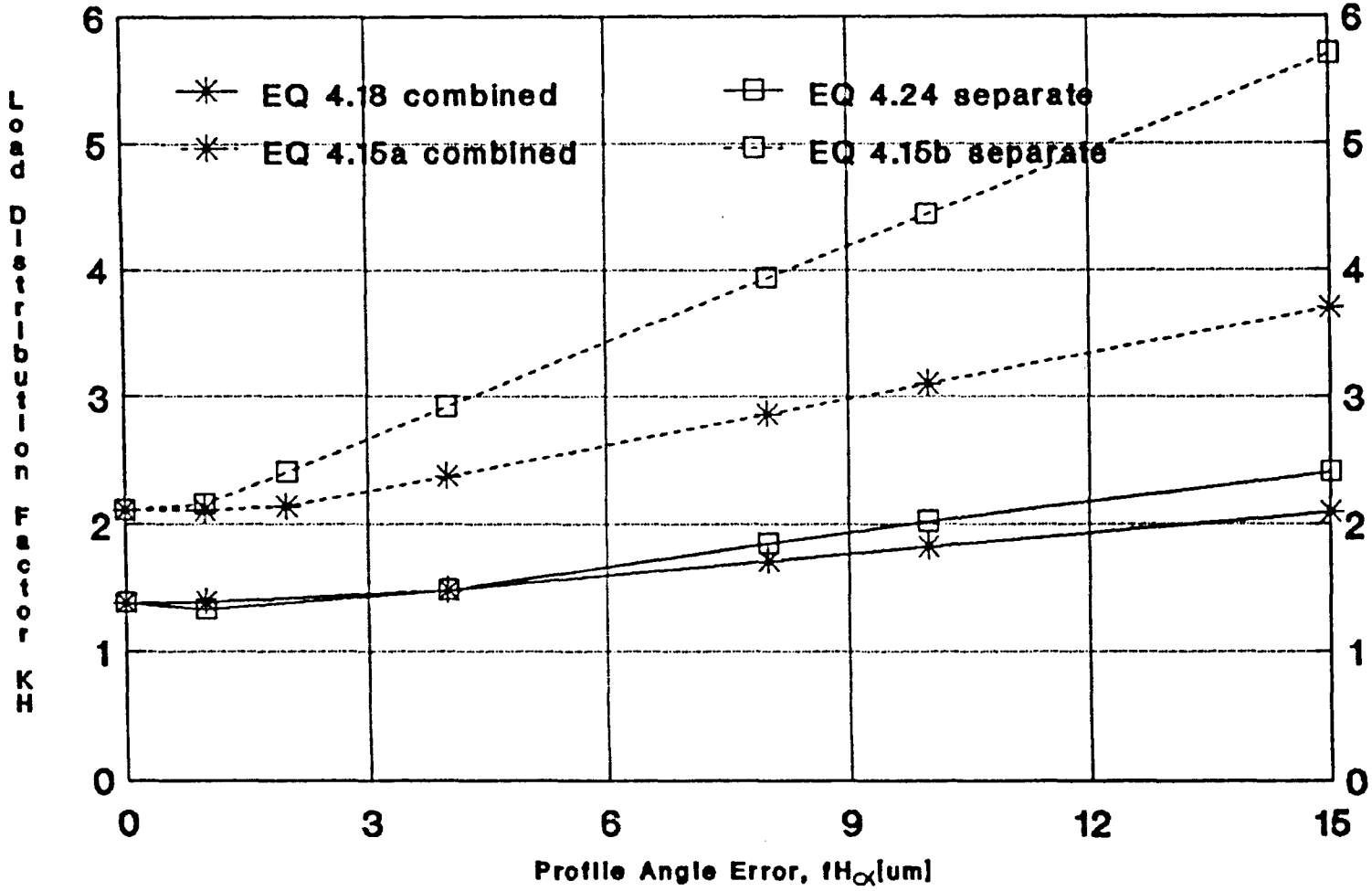

mesh misalignment $F_{\beta}y$ = 8 [um]

Fig.4.19 Effect of Profile & Lead Errors on KH (Spikes Ignored)

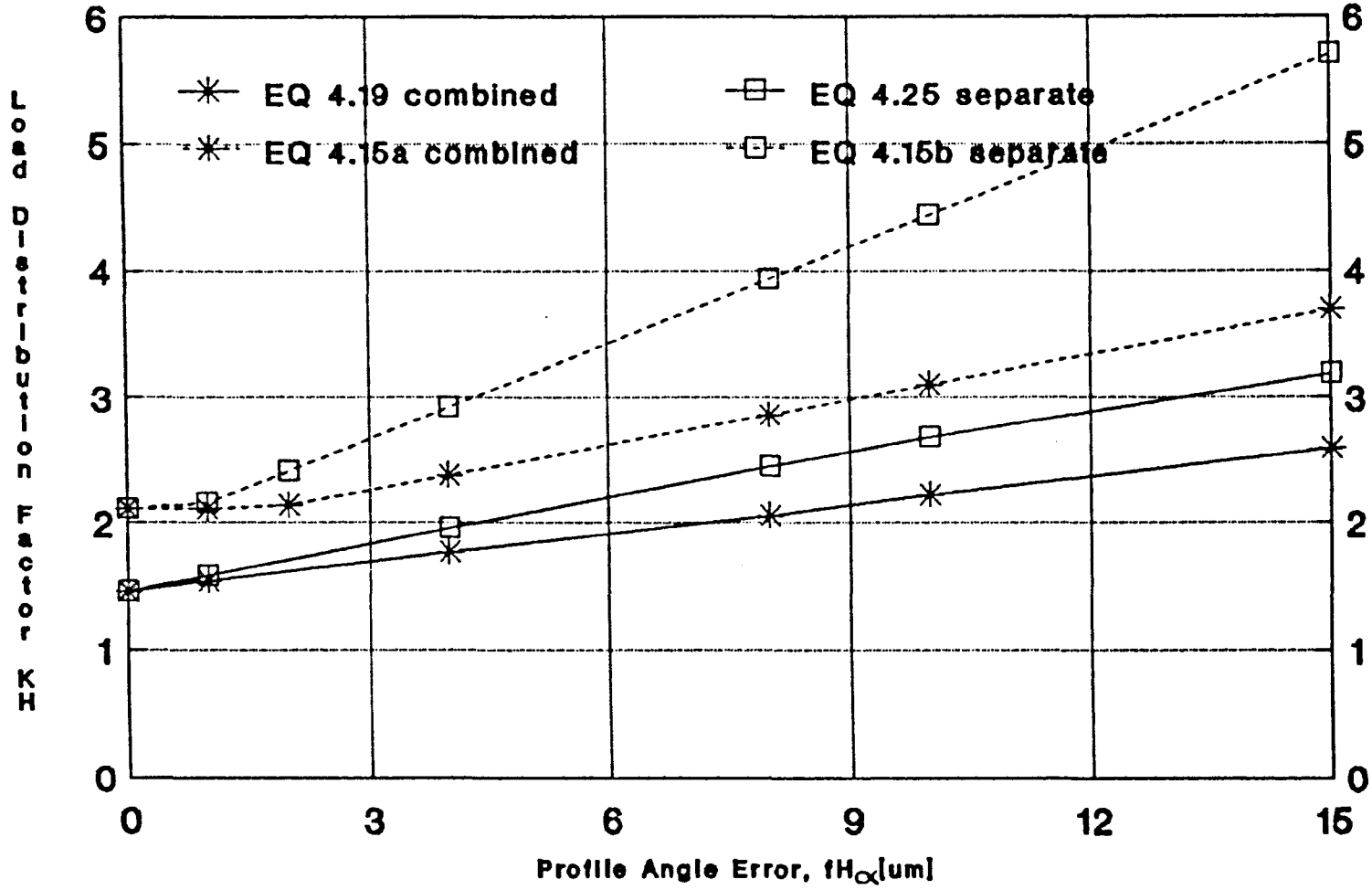

mesh misalignment $F_{\beta}y$ = 8 [um]

Fig.4.20 Effect of Profile & Lead Errors on KH (Spikes Considered)

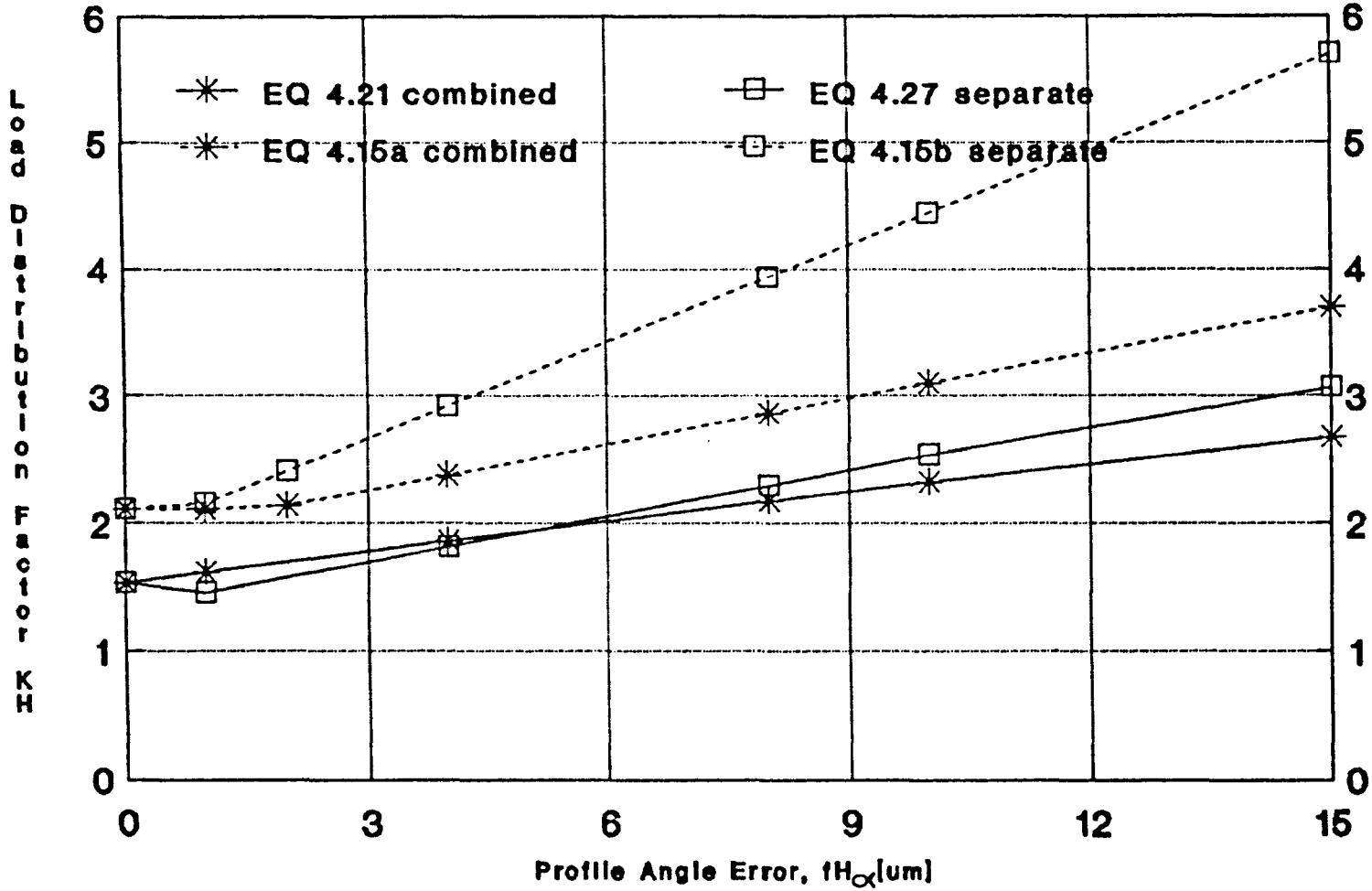

mesh misalignment $F_\beta y$ = 8 [um]

Fig.4.21 Effect of Profile & Lead Errors on KH (Spikes Considered)

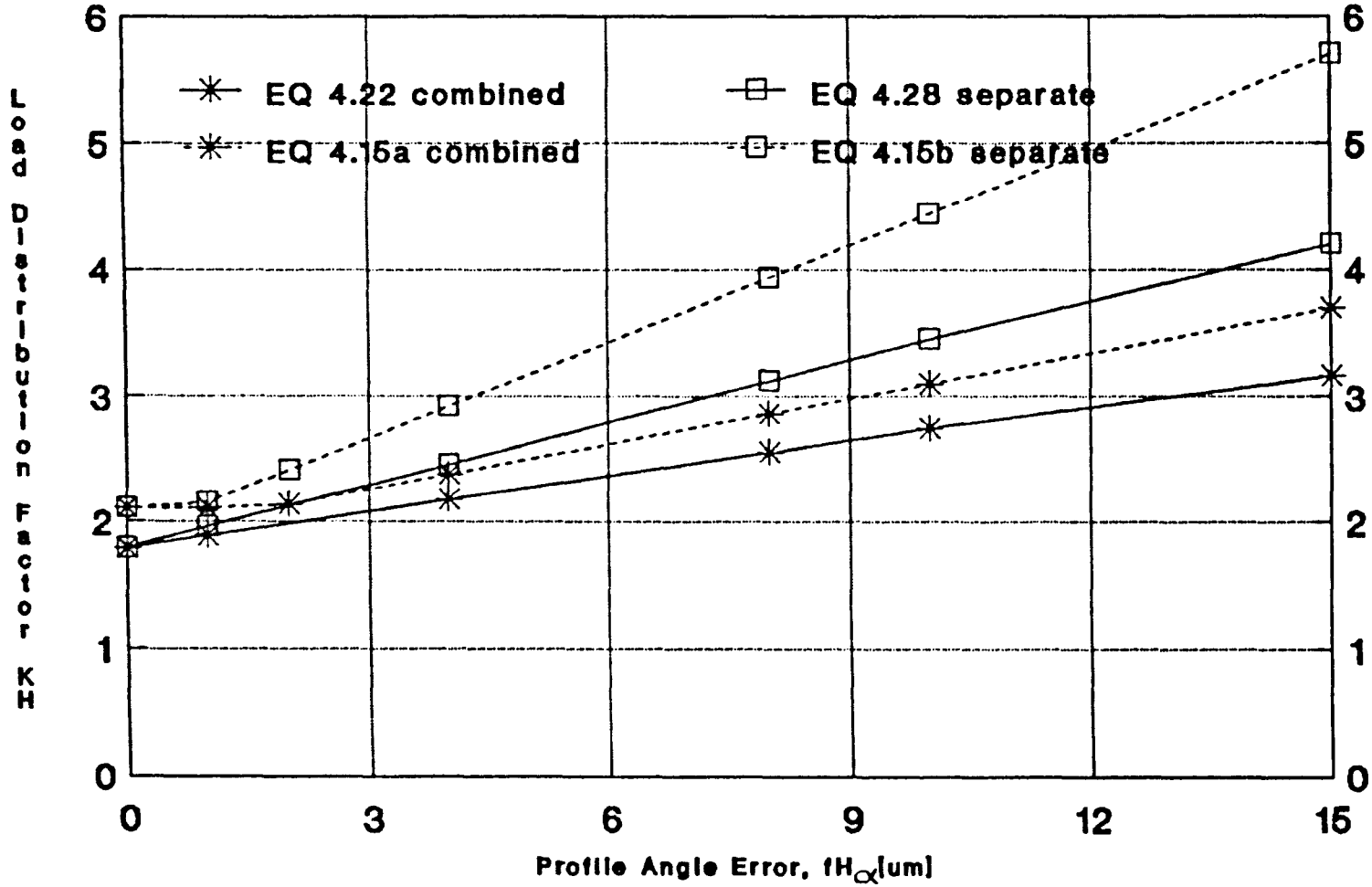

mesh misalignment $F_{\beta}y$ = 8 [um]

Fig.4.22 Effect of Profile & Lead Errors on KH (Spikes Ignored)

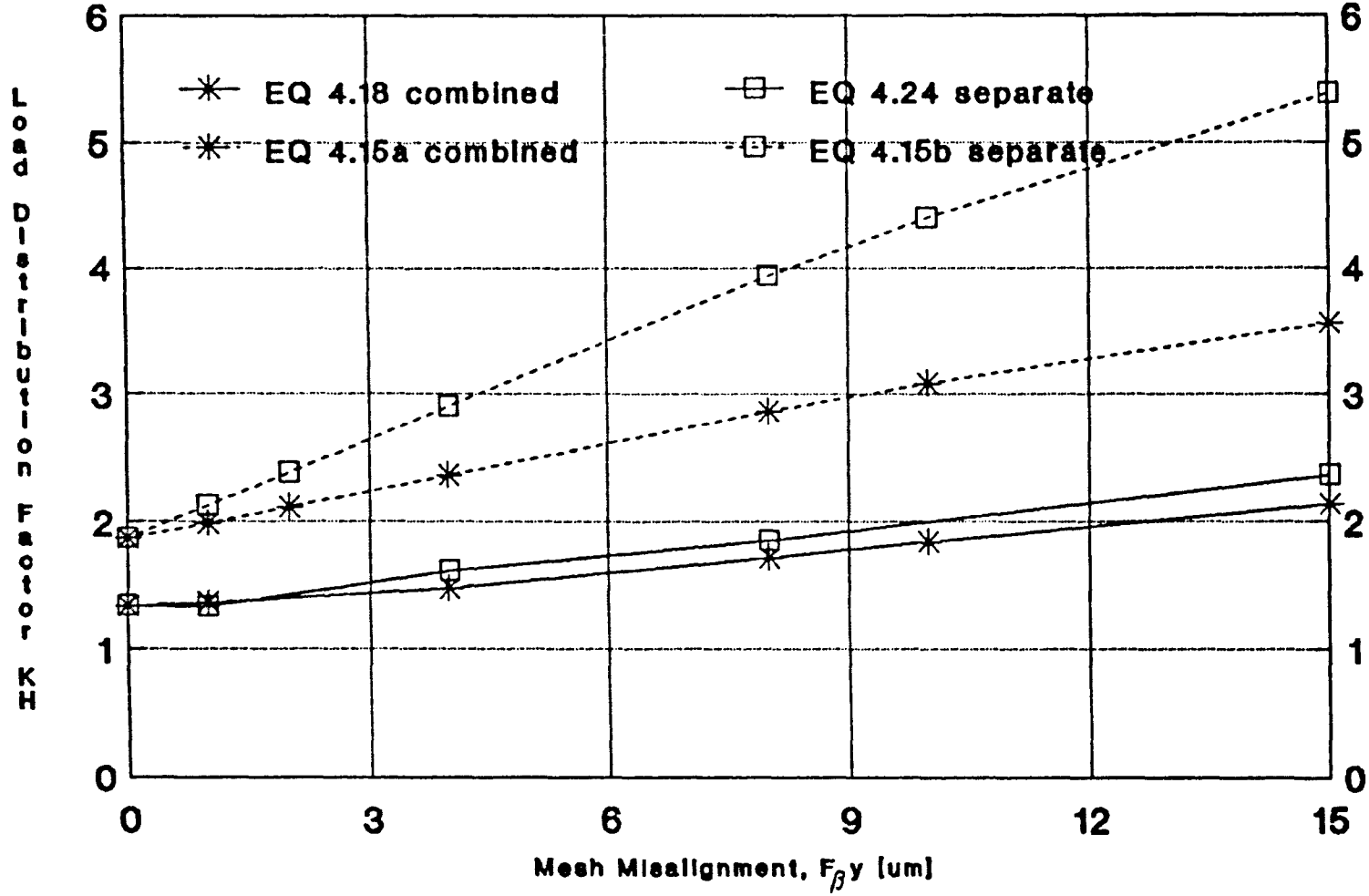

profile angle error fH_{α}= 8 [um]

Fig.4.23 Effect of Profile & Lead Errors on KH (Spikes Ignored)

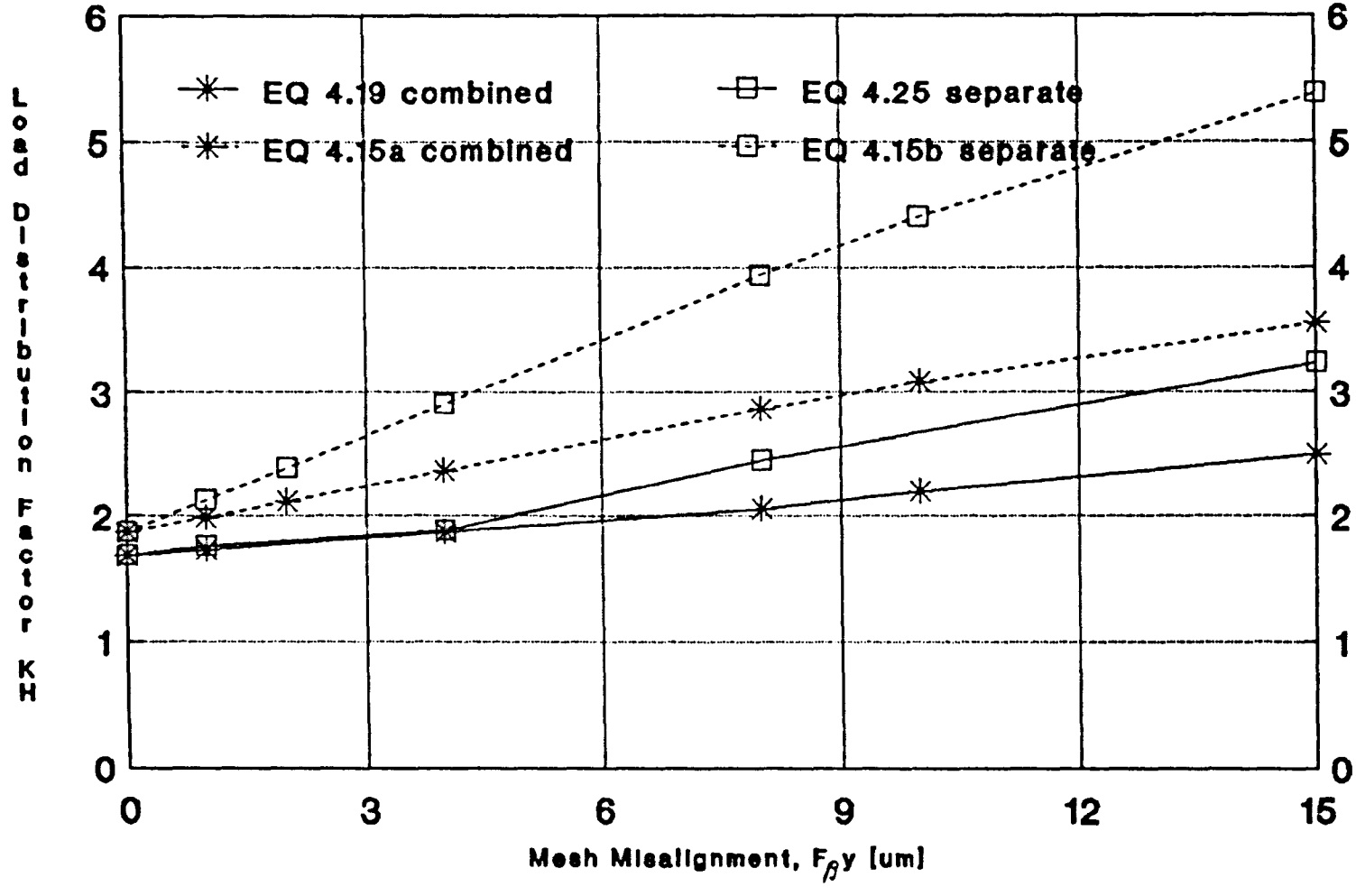

profile angle error fH_{α} = 8 [um]

Fig.4.24 Effect of Profile & Lead Errors on KH (Spikes Considered)

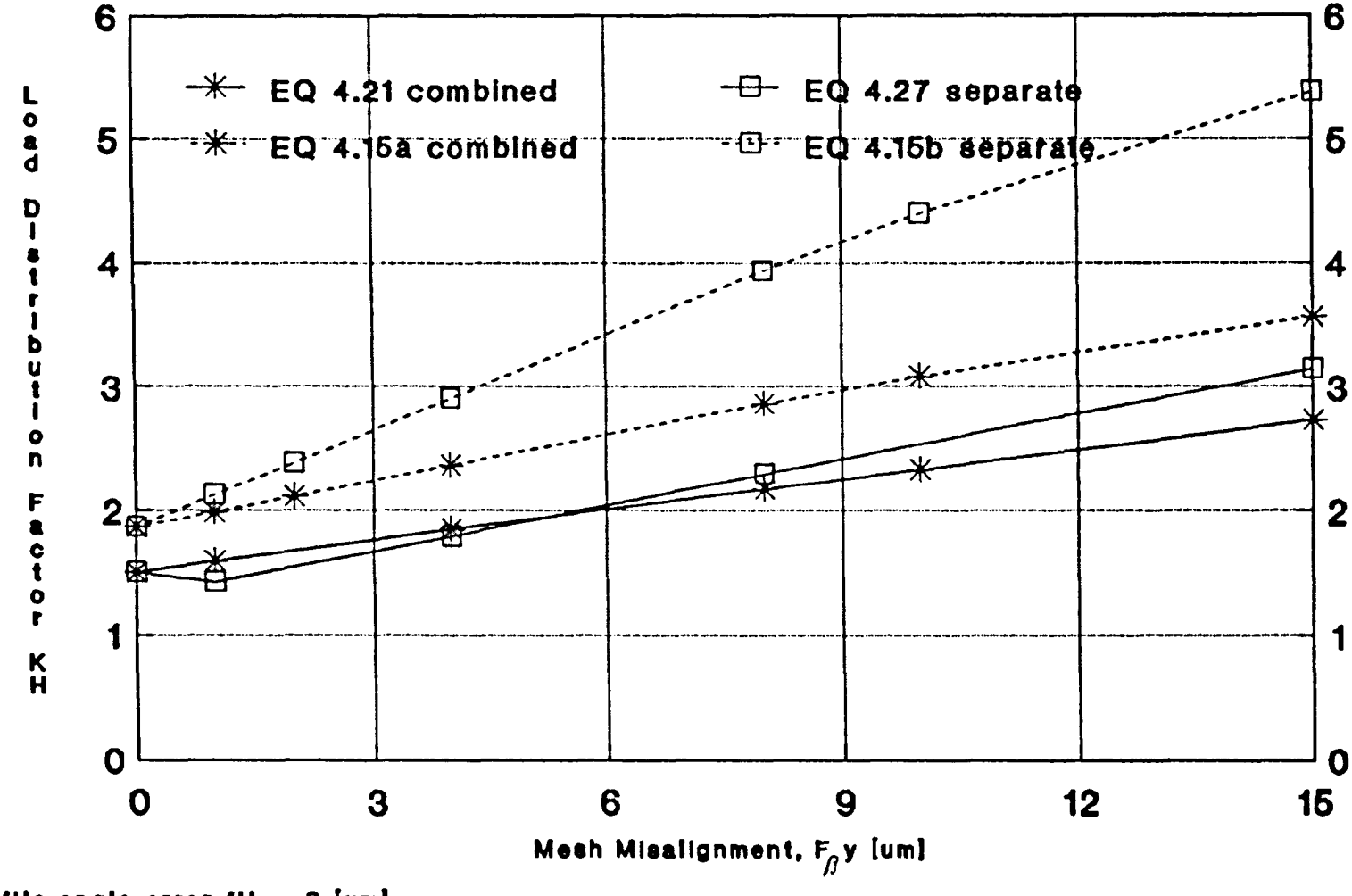

profile angle error fH_{α}= 8 [um]

Fig.4.25 Effect of Profile & Lead Errors on KH (Spikes Considered)

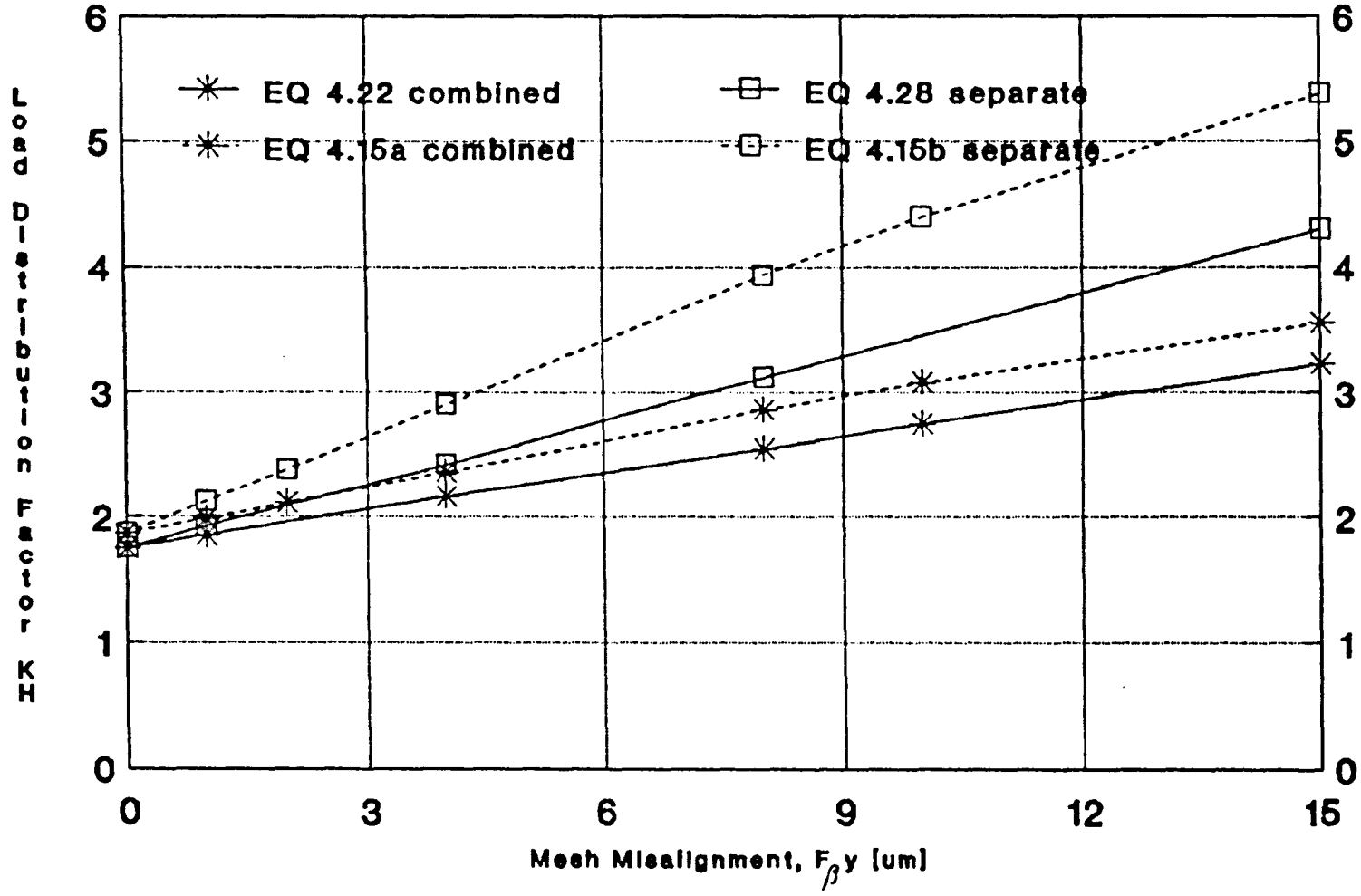

those given by the standards which, as already explained, overestimate the effective tooth stiffness, leading to higher peak loads and stresses, and therefore larger K_H values.

In every case $K_{Hcombined}$ is significantly less than $K_{Hseparate}$ as expected. Clearly $K_{H\alpha}$ does depend on the lead deviations as assumed, thus giving the differences in the results of equations 4.15(a) and 4.15(b). Obviously, the effect of $K_{H\beta}$ is to increase F_{tH} so that $K_{H\alpha}$ is reduced, (see p.11). Consequently as $K_{H\alpha}$ is changed, and assuming that the overall factor K_H is the product of $K_{H\alpha}$ and $K_{H\beta}$, then clearly $K_{Hcombined}$ will be smaller than $K_{Hseparate}$. $K_{Hseparate}$ values were presented only for comparison purposes, and should not be confused with the proper $K_{Hcombined}$ values.

From the above discussion, the plots of interest presented in Figs. 4.18 to 4.25 are those resulting from Eqn. 4.15(a) representing the European standards, which are to be compared with Eqns. 4.18 and 4.19 representing this work. Also of major interest, but not to be compared with the standards, are Eqns. 4.21 and 4.22. These two equations are the analogues of Eqns. 4.18 and 4.19, but account for the end spikes which should be the basis for design, as they represent the worst loading and contact stress.

As expected, the results from the load distribution program show that when end-spikes are accounted for (Eqns. 4.21 and 4.22), the resulting K_H values are larger than those when the end-spikes are ignored (Eqns. 4.18 and 4.19). As explained in Sections 4.2.2 and 4.3.2, introducing lead and/or profile errors sharpens the spikes in proportions greater than the sharpening of the peak loads away from spikes. This of course leads to higher K_H values with spikes considered.

CHAPTER 5

EXPERIMENTAL INVESTIGATION OF THE LOAD DISTRIBUTION IN MESHING HELICAL GEARS

5.1 Objectives

The objectives of the experimental work were:

1. To test helical gears of known geometry under known loads and mounting conditions.
2. To determine the load distribution across the contact lines of the meshing teeth by measuring tooth root strains, for comparison with theoretical values.
3. To measure the instantaneous transmission error f_t, for comparison with the theoretical predicted values.

5.2 Experimental Test Rig

5.2.1 Introduction

The test rig was based on a modified back-to-back gear tester. This existing rig was chosen after a rigorous study and preliminary design of a new test rig using some large naval gears proved to be economically and practically unfeasible. Figs. 5.1 and 5.2 show the test rig used, and Fig.5.3 shows a section through it before modification and installation of the instrumentation.

The most basic components of the original design (see Fig.5.3) were the helical slave gears (1 and 2) and supporting shafts (3 and 4) and bearings (5, 6, 7 and 8), the spur test gears (9 and 10), the torsion bar (11) by which the spur pinion (9) is driven via a spline, and finally the mechanical torque-up assembly (12) by which the torsion bar is wound up.

The back-to-back rig was used for the experimental work with the role of the slave and test gears reversed so that the helical gears were treated as the test gears, and slowly rotated through mesh under a torque 'locked-in' by the torquing device. Additional equipment was designed and installed in the rig to allow measurement of transmission error and continuous monitoring of the shaft misalignment in both planes during the mesh cycle. Since the gears rotated less than one

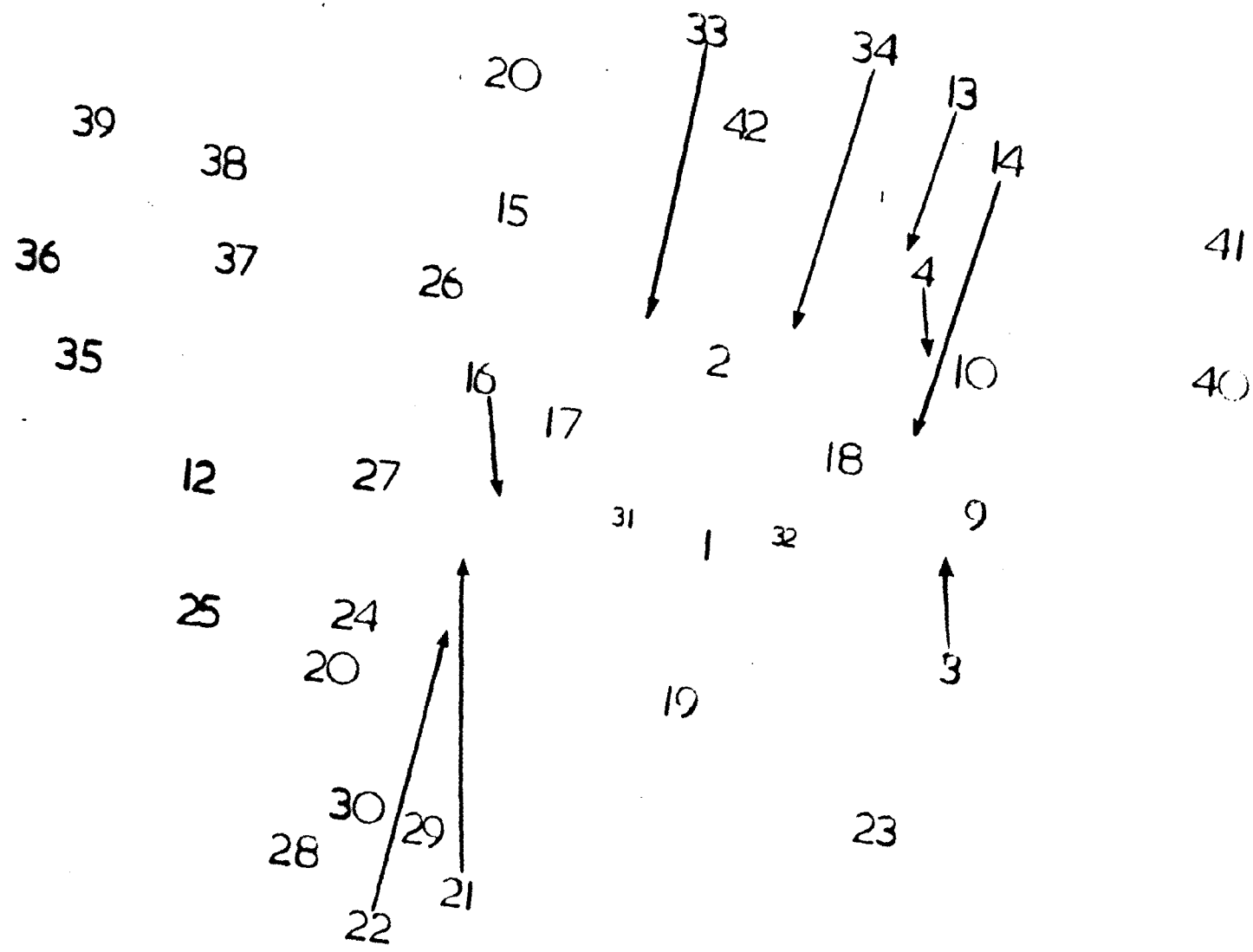

Fig.5.1 Gear Rig Assembly (view 1)

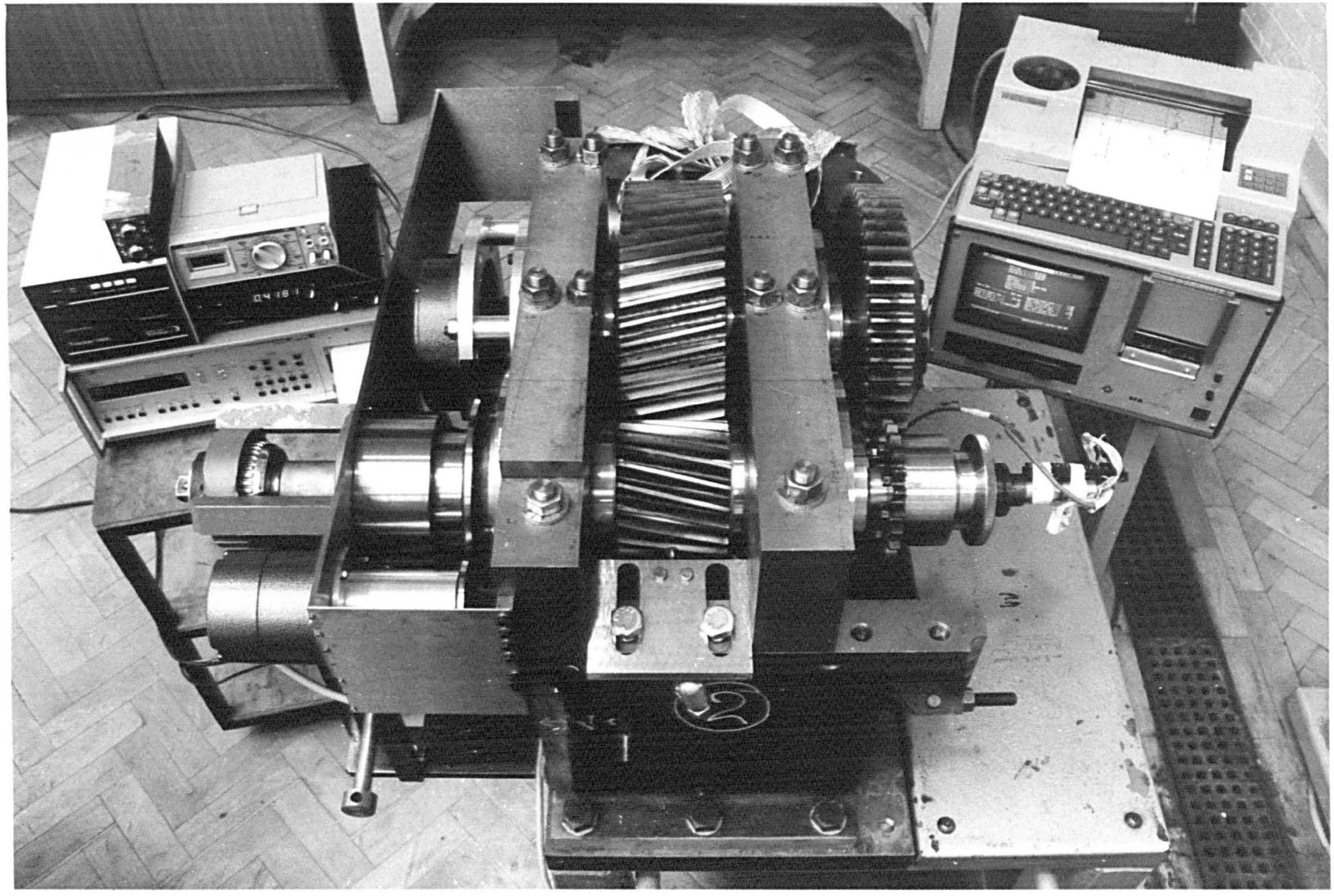

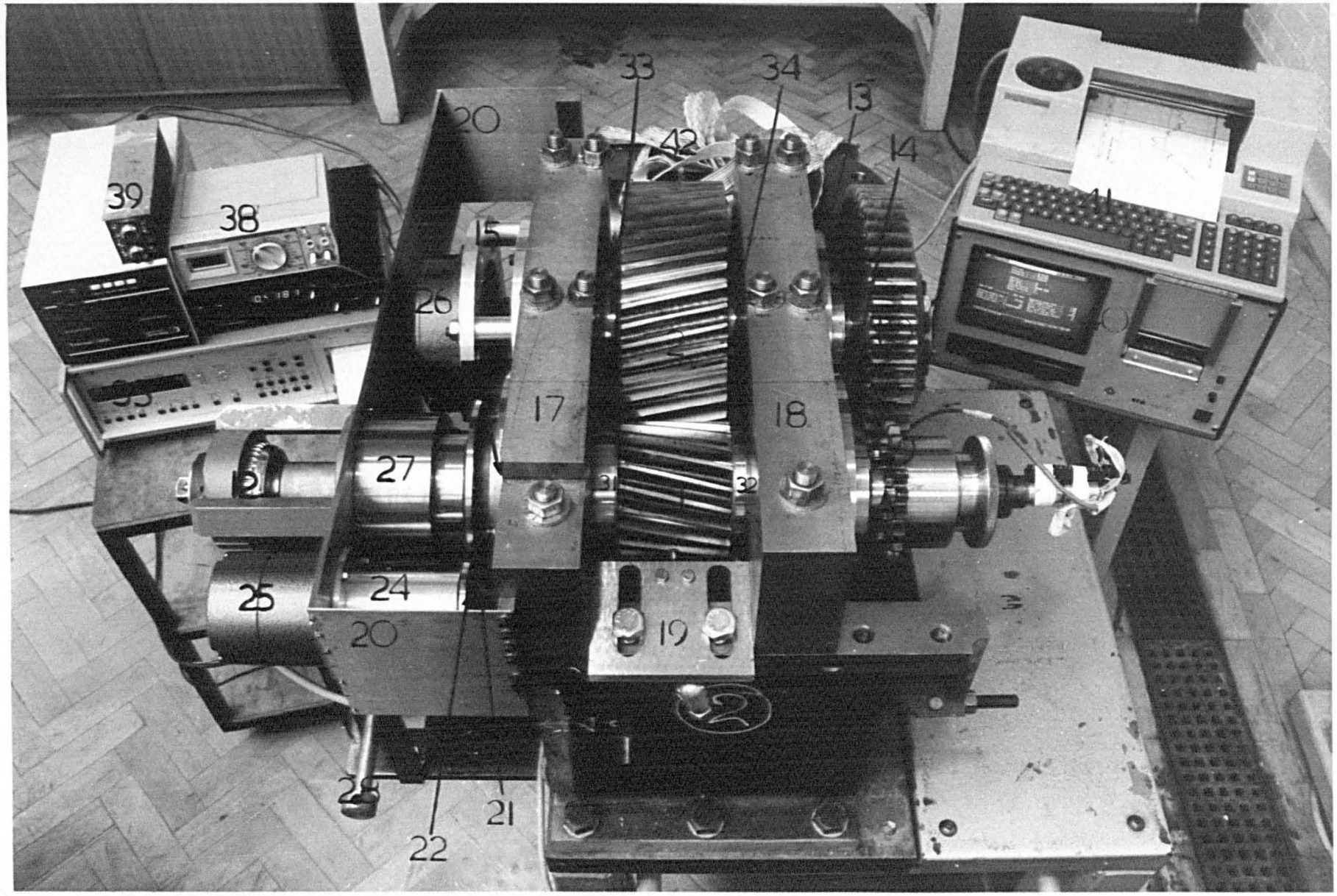

Fig.5.1 Gear Rig Assembly (view 1)

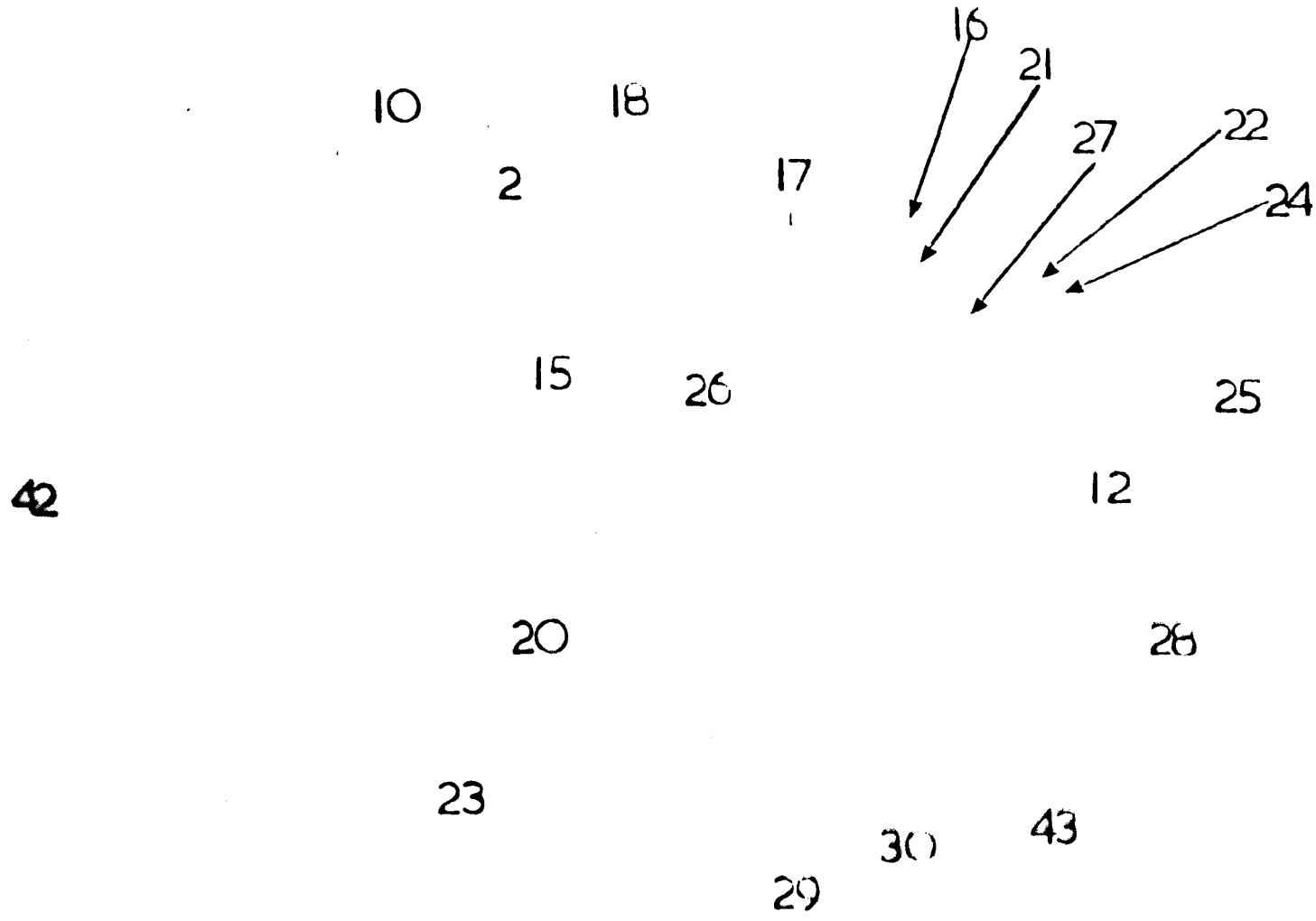

Fig.5.2 Gear Rig Assembly (view 2)

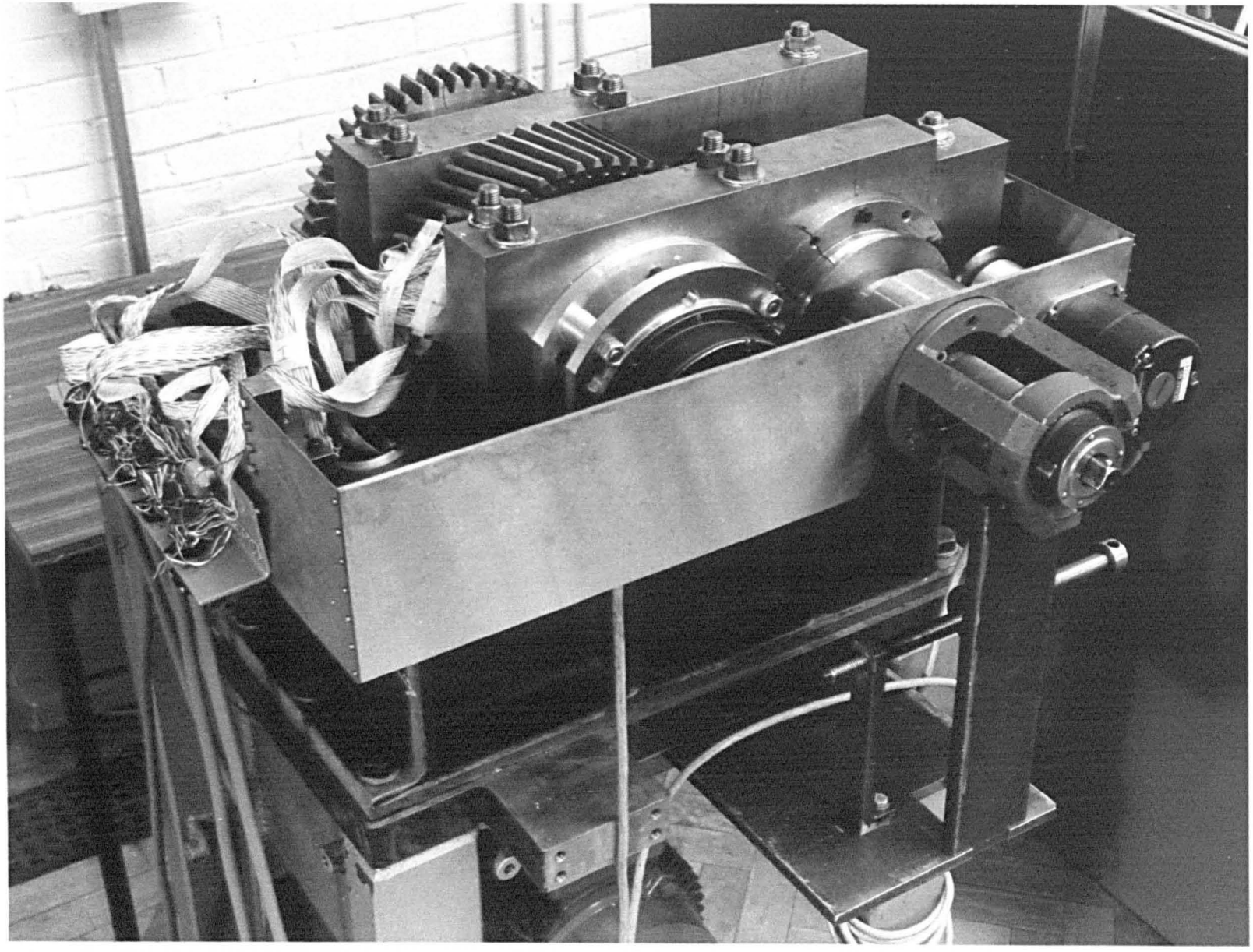

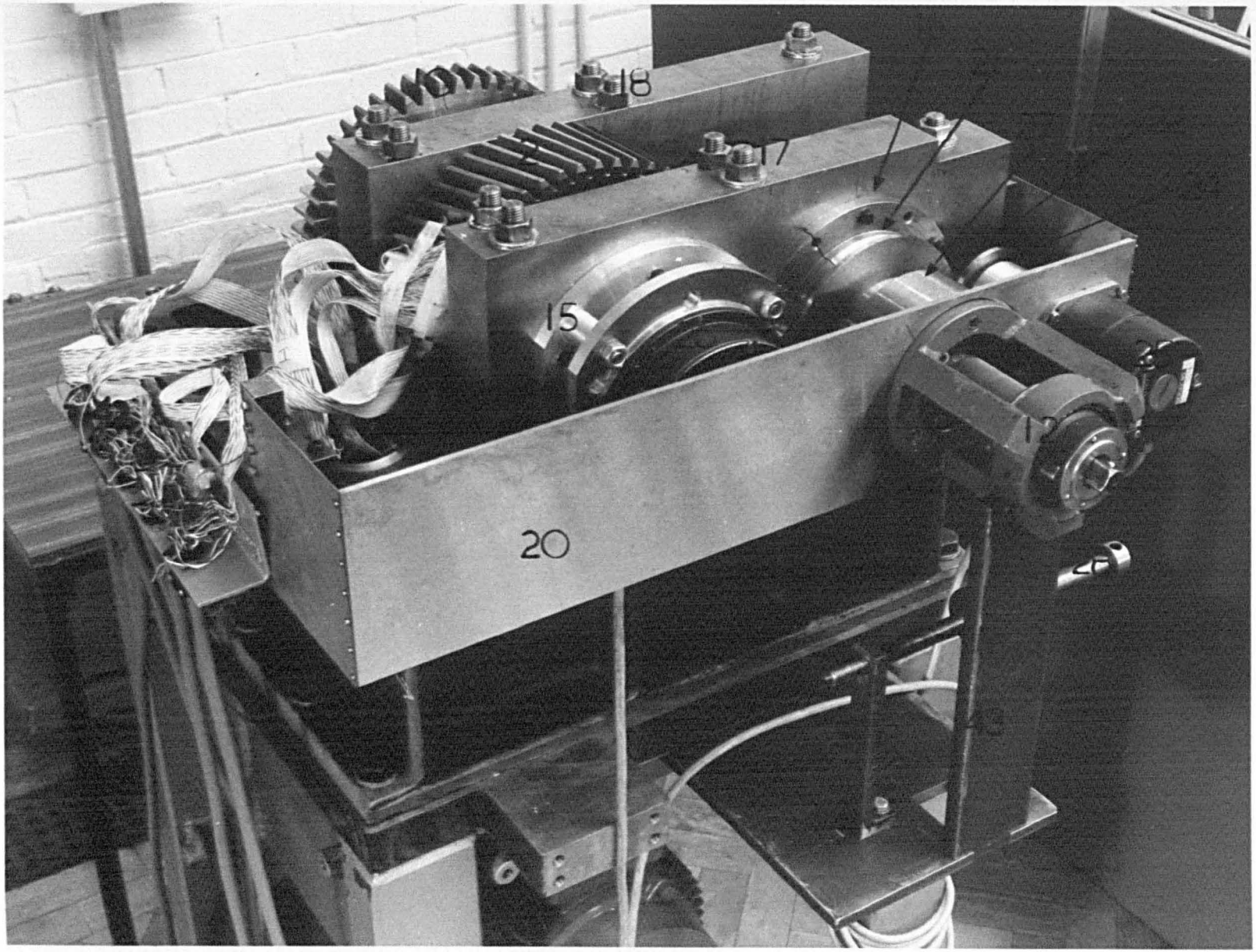

Fig.5.2 Gear Rig Assembly (view 2)

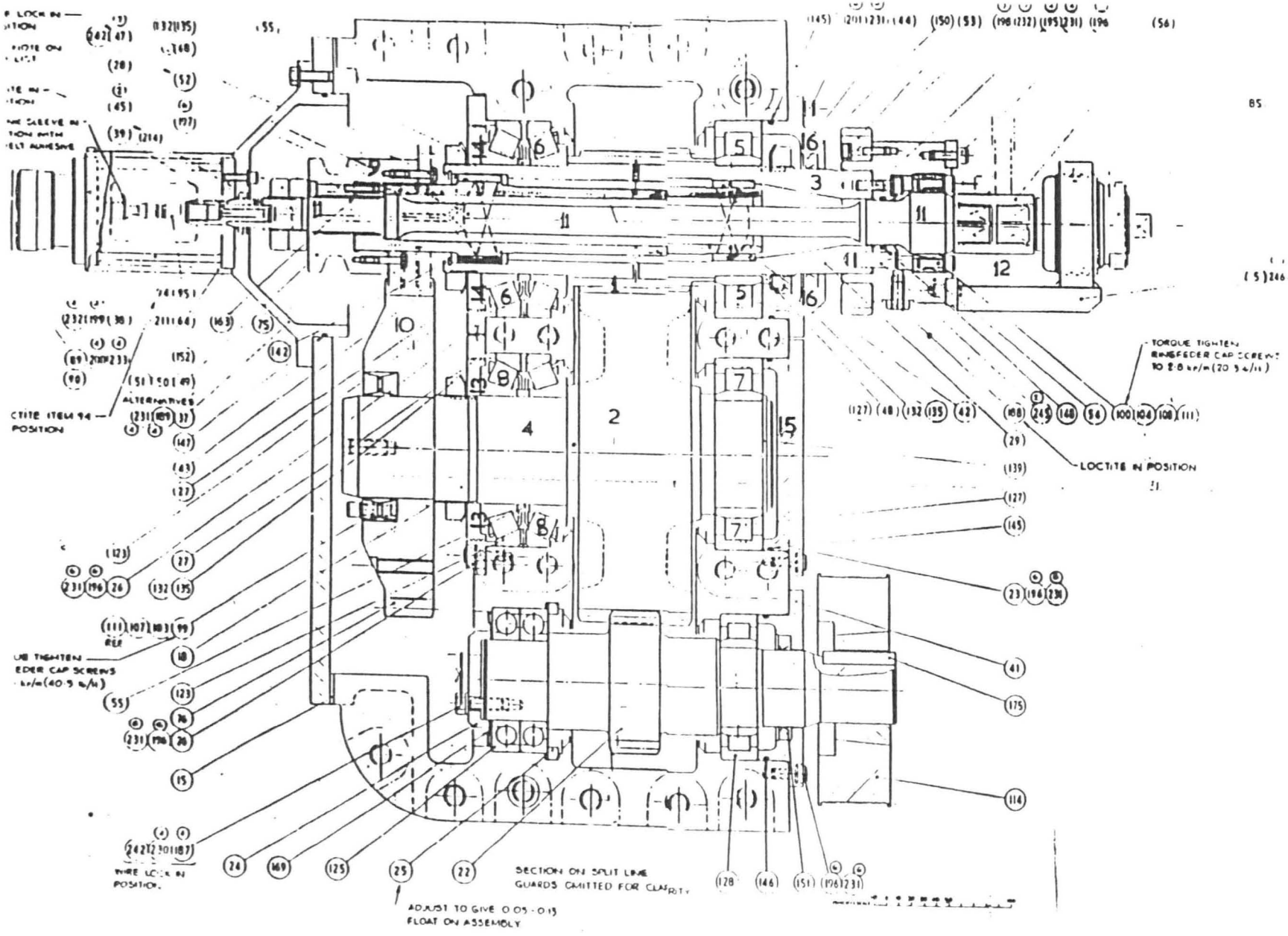

Fig.5.3 Existing Design Assembly

revolution during each test, elaborate slip rings were not needed and the strain gauges could be connected via flexible leads.

5.2.2 Basic Components and their Functions

5.2.2.1 Test Gears and Reference Rings

The test gear specifications are given in Table 5.1 below, and the detail drawings for the original pinion and wheel are shown in Figs. 5.4 and 5.5 respectively. These figures do not show the ground radial reference surfaces on the two circular rings which were fitted against the pinion and wheel shaft shoulders on both sides of the gear facewidth. These rings can be seen in Fig. 5.1. Their function is to allow monitoring of shaft misalignment, as described in Section 5.5.3.2 below.

The gears were measured for profile, lead and pitch errors on all teeth, and the results for both wheel and pinion are presented. First, consider the wheel errors. These were measured on the Gleason GMS430 at positions given by the tooth face grid shown in Fig.5.6. Only the results for the teeth which were engaged during the tests are shown in Tables 5A.1 and 5A.2 of Appendix 5A.

	Pinion	Wheel
Z	21	54
m_n(mm)	5	
b(mm)	90	90
x_n(-)	0	0
k(-)	0	0
$r_{a0}(m_n)$	0.39	0.39
$h_{a0}(m_n)$	1.40	1.40
$\alpha_n(^\circ)$	20	
$\beta(^\circ)$	12 RH	12 LH
a(mm)	191.689	
Backlash at Nominal Centre Distance "a"(μm)	200-280	
Backlack Allowance (μm)	100	100

Table 5.1 Test Gear Specifications

The wheel was mounted between centres during measurement, and radial runout, measured on the two reference bands (rings), was as given in Table 5A.3. Peak values of about 10μm and 18μm were recorded, which must be allowed for in evaluating the involute and lead errors given in Tables 5A.1 and 5A.2 (See Chapter 6).

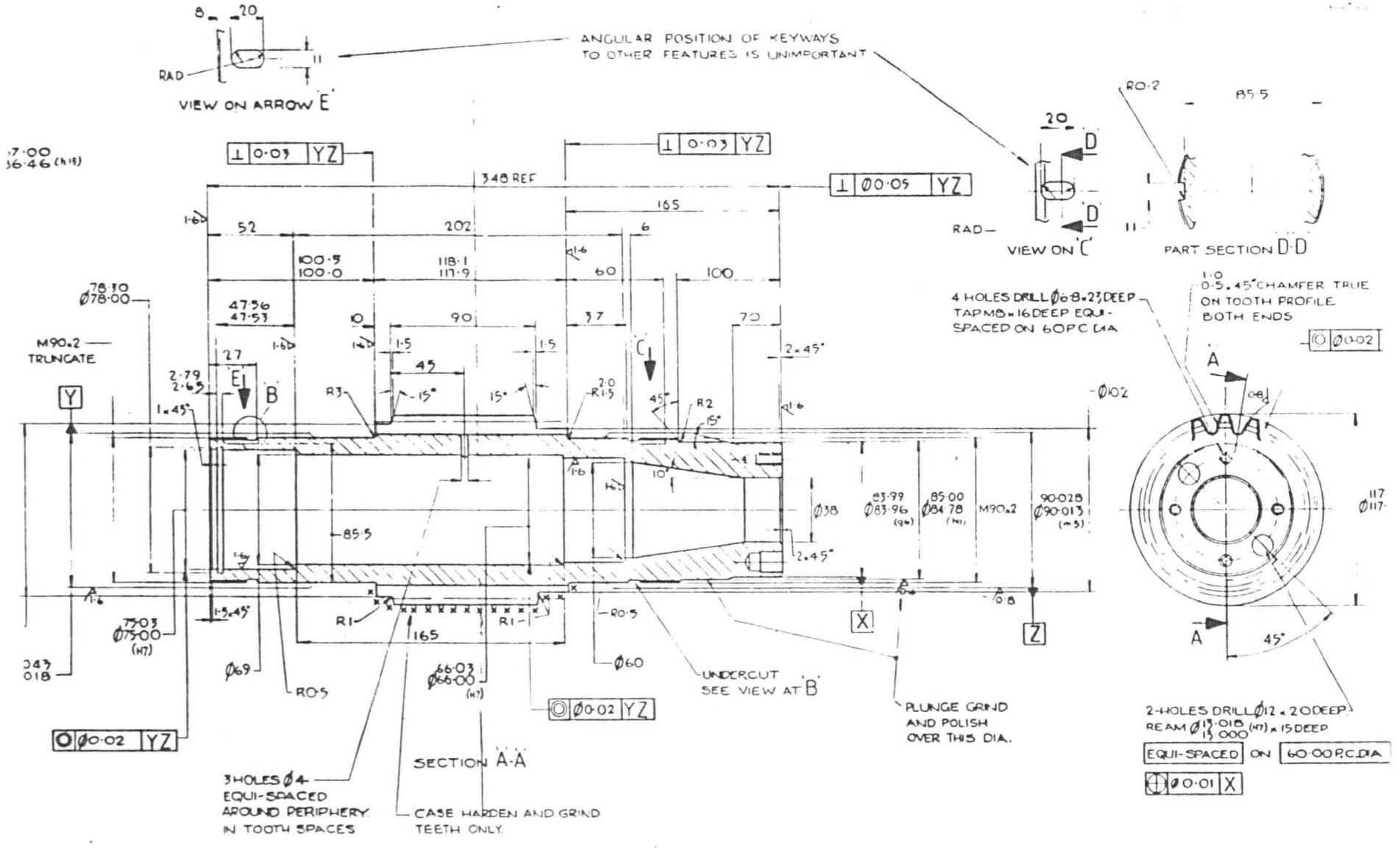

Fig.5.4 Test Pinion

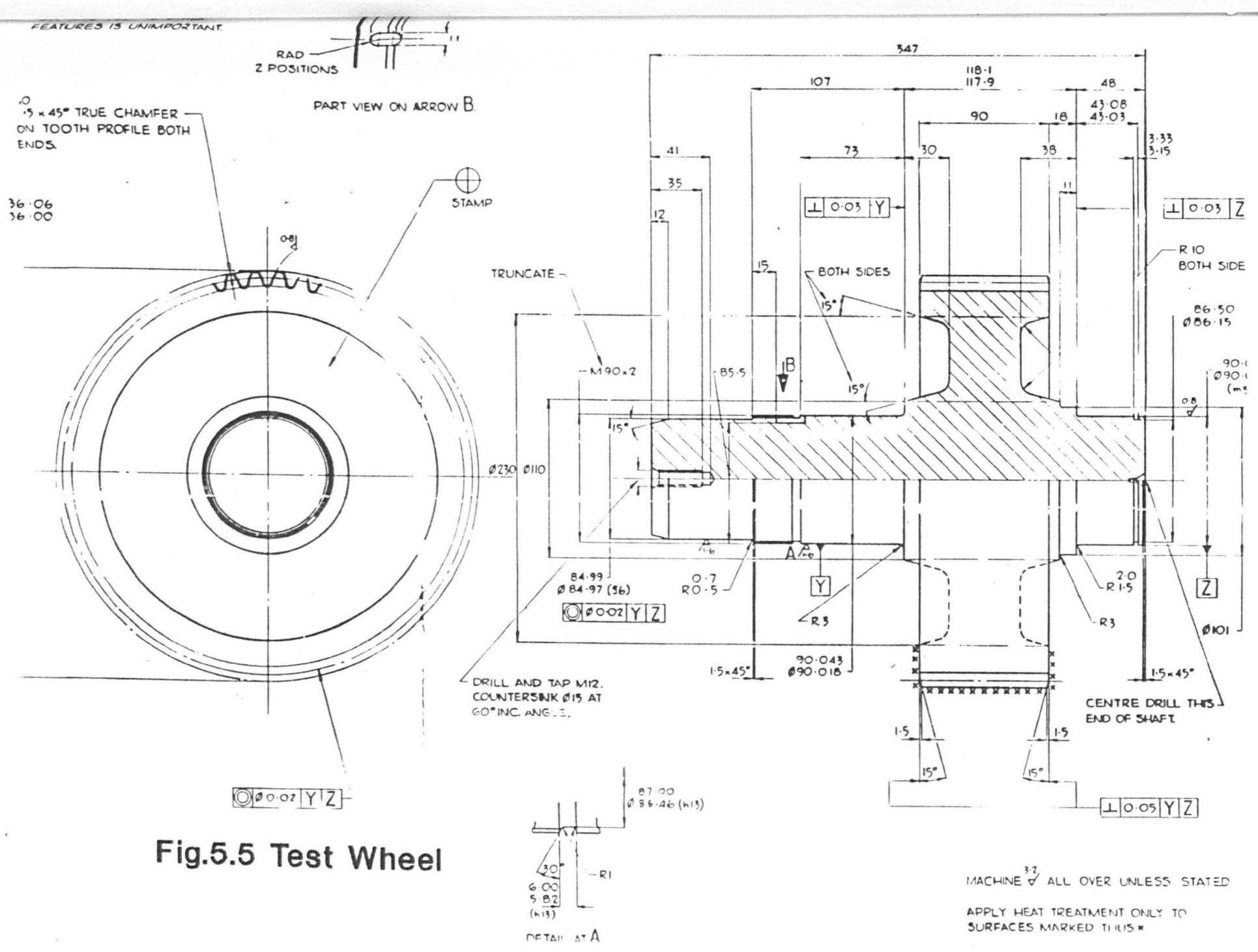

Fig.5.5 Test Wheel

The wheel teeth are marked 1 to 54 in a clockwise fashion on the face of the wheel adjacent to the short shaft (torque-up end), and in Table 5A.3, the tooth number for both rings is that adjacent to where the runout was measured. This means that the angular position for a certain tooth number is slightly different for the two rings. The teeth chosen are 9, 10, 11 and 12.

Next, consider the pinion tooth errors. These were measured on the manual Höfler 630 at the positions corresponding to the tooth face grid shown in Fig.5.7. Again, results for only the teeth that were in mesh with the wheel teeth 9, 10, 11 and 12 are included in the tables of errors 5A.4 and 5A.5. The teeth chosen are 4, 5, 6 and 7, numbered in a clockwise fashion when viewed from the torqued end of the wheel when both gears are mounted. The meshing pairs were thus teeth 9 and 7, 10 and 6, 11 and 5, and 12 and 4.

Radial runout readings on the pinion during the profile and lead error measurements are listed in Table 5A.6. As pitch measurements on the Höfler EFRS630 require a different set-up than that for profile and lead measurements, a new set of runout readings were taken before measuring the pitch errors as shown in Table 5A.7. Note that the pinion runout readings in Table 5A.6 and 5A.7 are generally greater than the wheel runout readings in Table 5A.3. This is expected, since the pinion shaft is hollow and had to be centred on the Hofler 630 by trial and error. All runout readings are averages over two or three revolutions.

Pitch measurements on the wheel were taken at all nine grid points in Fig.5.6, but on the pinion (using the Maag ES421 pitch checker on the Höfler machine) pitch was only measured at points 2, 5 and 8 of Fig. 5.7. However the readings taken are sufficient since, as anticipated, and clearly demonstrated in Table 5A.2, the pitch errors at each axial location do not vary significantly in the radial direction.

5.2.2.2 Wheel Teeth Strain Gauging

Since the load distribution along a contact line is common to both meshing teeth, it is sufficient to strain gauge the teeth of one of the meshing gears only. Thus, only the teeth of the wheel that were simultanteously engaged were strain-gauged as shown in Figs. 5.1 and 5.2 The maximum number of engaged teeth at any instant was determined (from the load distribution program 'HELICALDIST') to be 4, and the teeth chosen for the meshing tests were 9, 10, 11 and 12. This included the 'misaligned' tooth number 11 (see Table 5A.1).

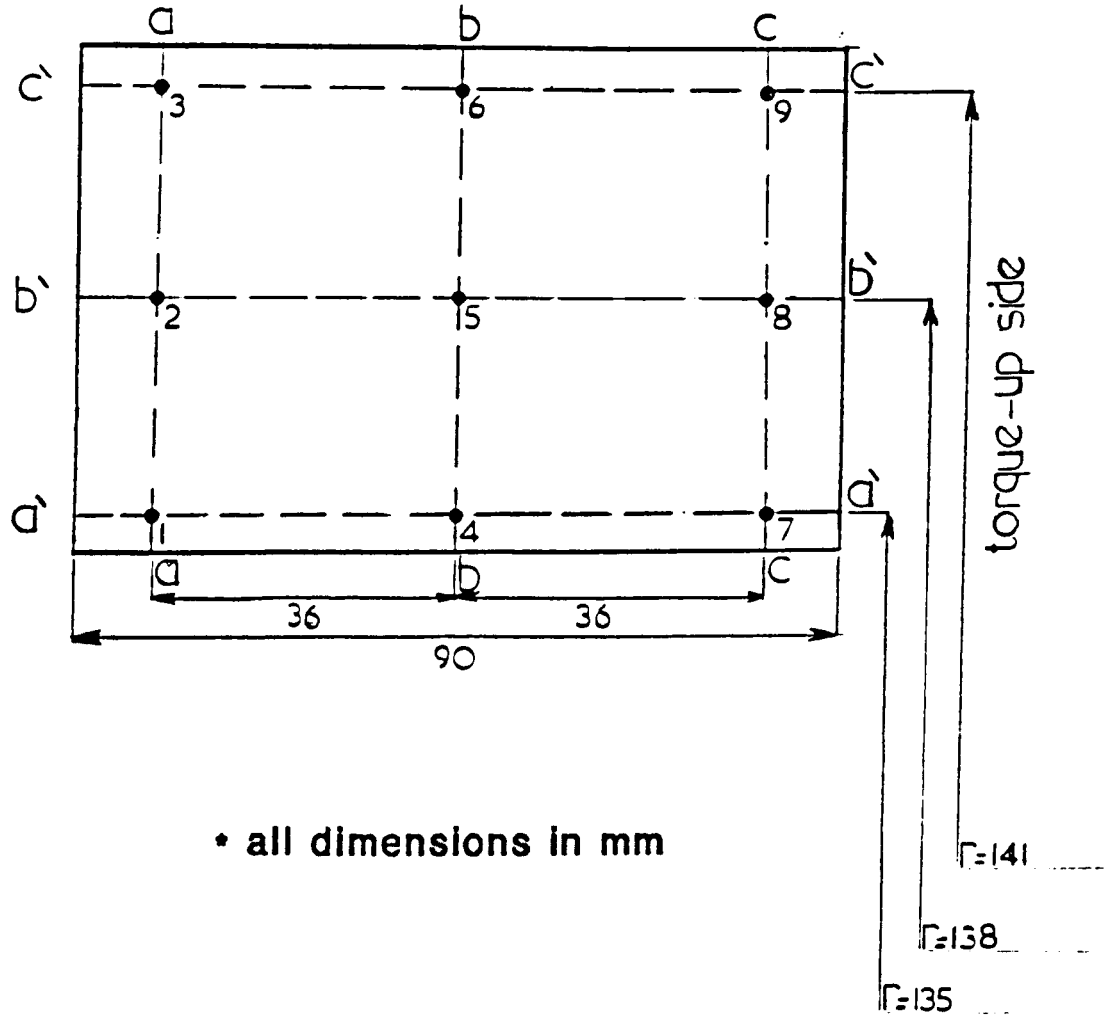

Fig.5.6 Wheel Tooth Error Grid

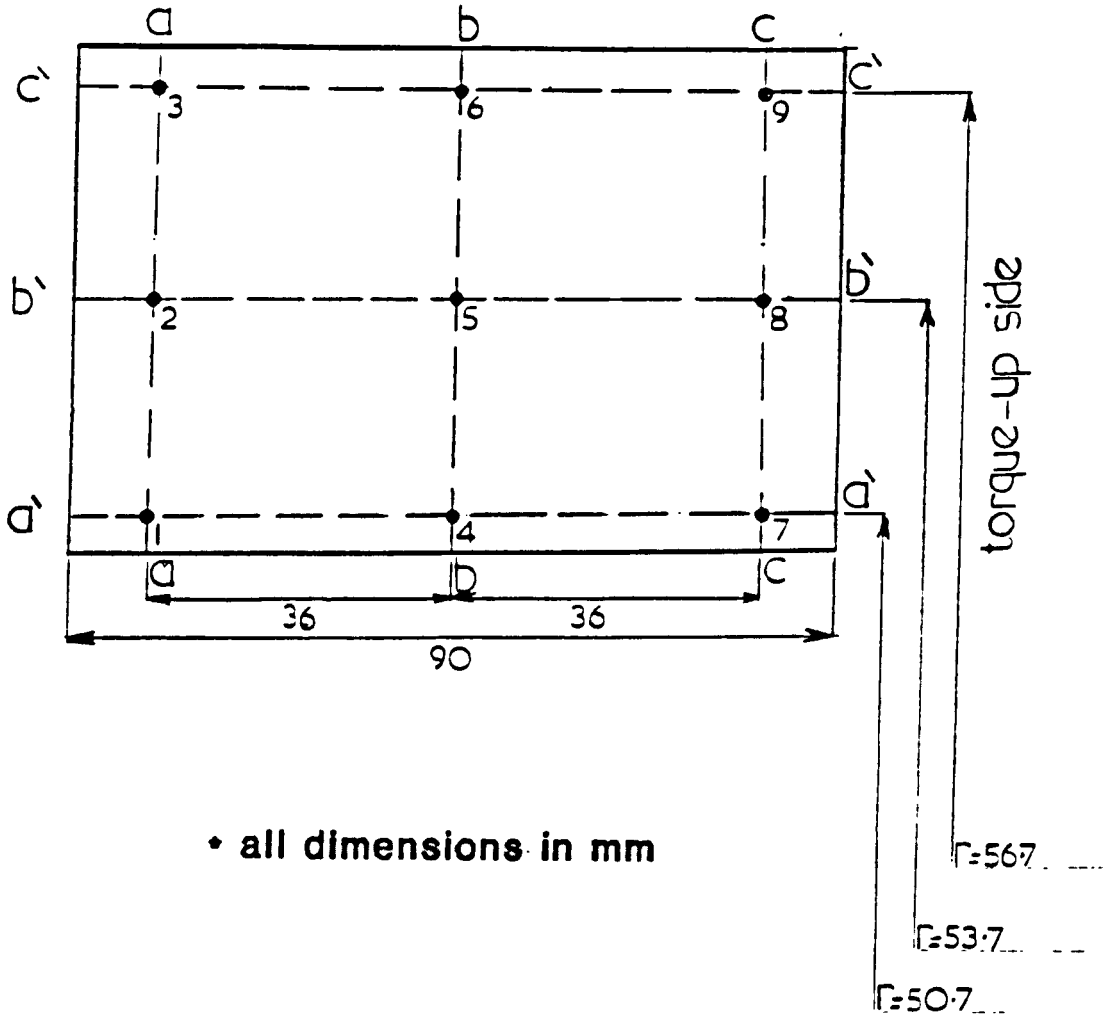

Fig.5.7 Pinion Tooth Error Grid

It would have been best to also strain-gauge the pinion teeth as well, to provide a cross-check on the measured load distribution. However, due to the high cost of the gauges used, the difficulty of installing the tiny gauges, and the lack of space for the extra wiring needed, the pinion teeth were not strain-gauged. For the same reasons, only four wheel teeth were strain-gauged. However, this is not a major limitation since measurements at any phase of mesh are sufficient for comparison with the theoretical results.

The gauges were placed as accurately as possible at the 30° tangent points to produce peak tensile strains (see Section 1.2.3 and Fig.1.4). Table 5.2 gives details of the strain gauges used.

Manufacturer		BLH Electronics
Type		FAE-02W-35-S6
Gauge Factor		1.88 ±1%
Resistance	(Ω)	350.0 ± 0.5
Gauge Length	(mm)	0.51
Carrier Material		Polyimide
Gauge Thickness	(mm)	0.038
Min. safe bending radius	(mm)	1.58
Temp. Range	(°C)	73 to 204
Temp. Compensation	(°C)	196 to 204 (mild steel)
Sensing Element		Foil Gauge
Type of Alloy		Constanton (400)
Tab or Grid Arrangement		Wide Grid

Table 5.2 Wheel Teeth Strain Gauge Specifications

The gauges were positioned at the 12 Gauss points used in "HELICALDIST" when obtaining the theoretical results as shown in Fig. 5.8.

The bottom right diagram in Fig.5.9 shows the strain gauge connection diagram made up of a chain of 10 gauges (0,1,2...9) and a single compensating gauge[51]. On the wheel, each of the four gauged teeth has 12 strain gauges giving a total of 48. Therefore, five chains were made, four having 10 gauges each and the fifth with only 8 gauges. Starting with tooth 9, ten gauges form one chain, the second chain is formed by the remaining two gauges on tooth 9 and eight of the gauges on tooth 10. The third chain is the sum of the remaining

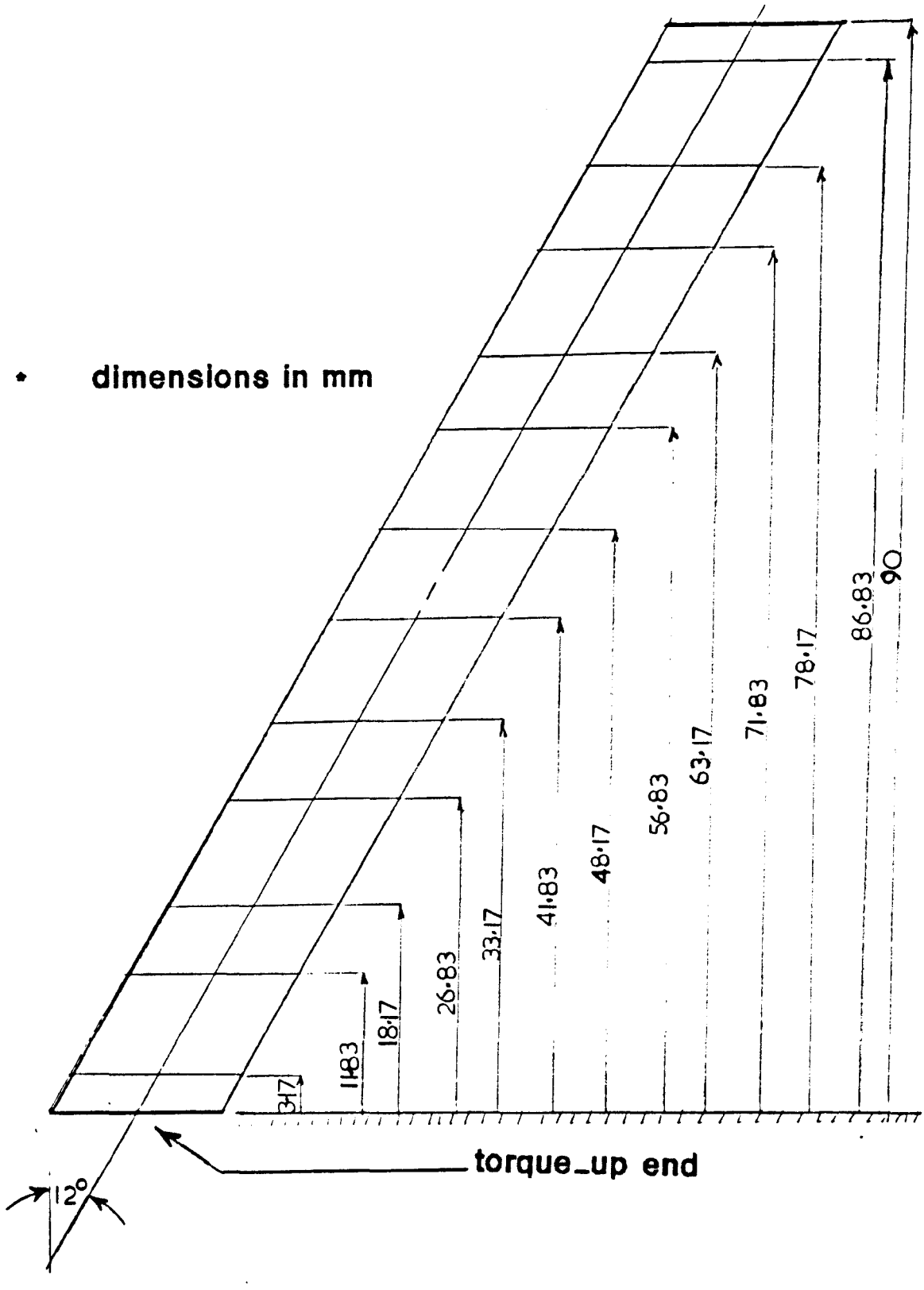

Fig.5.8a Wheel Teeth Strain Gauge Locations

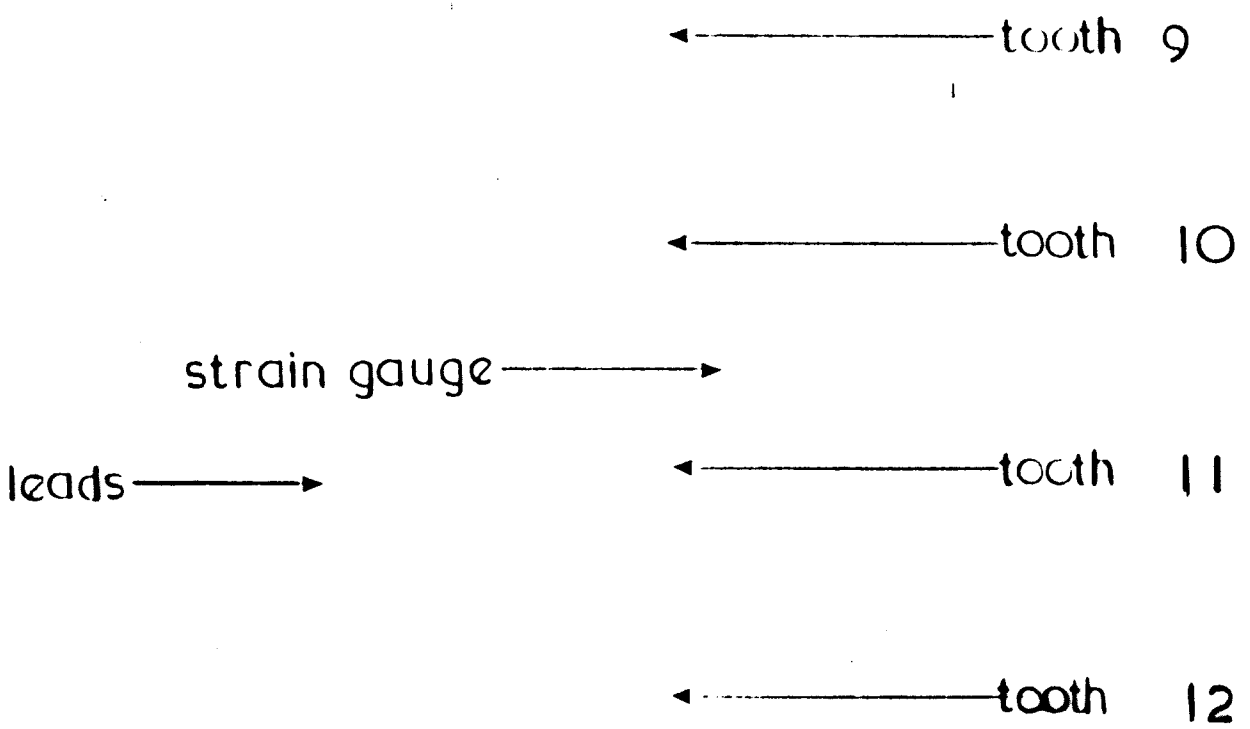

Fig.5.8b Wheel Teeth Strain Gauges

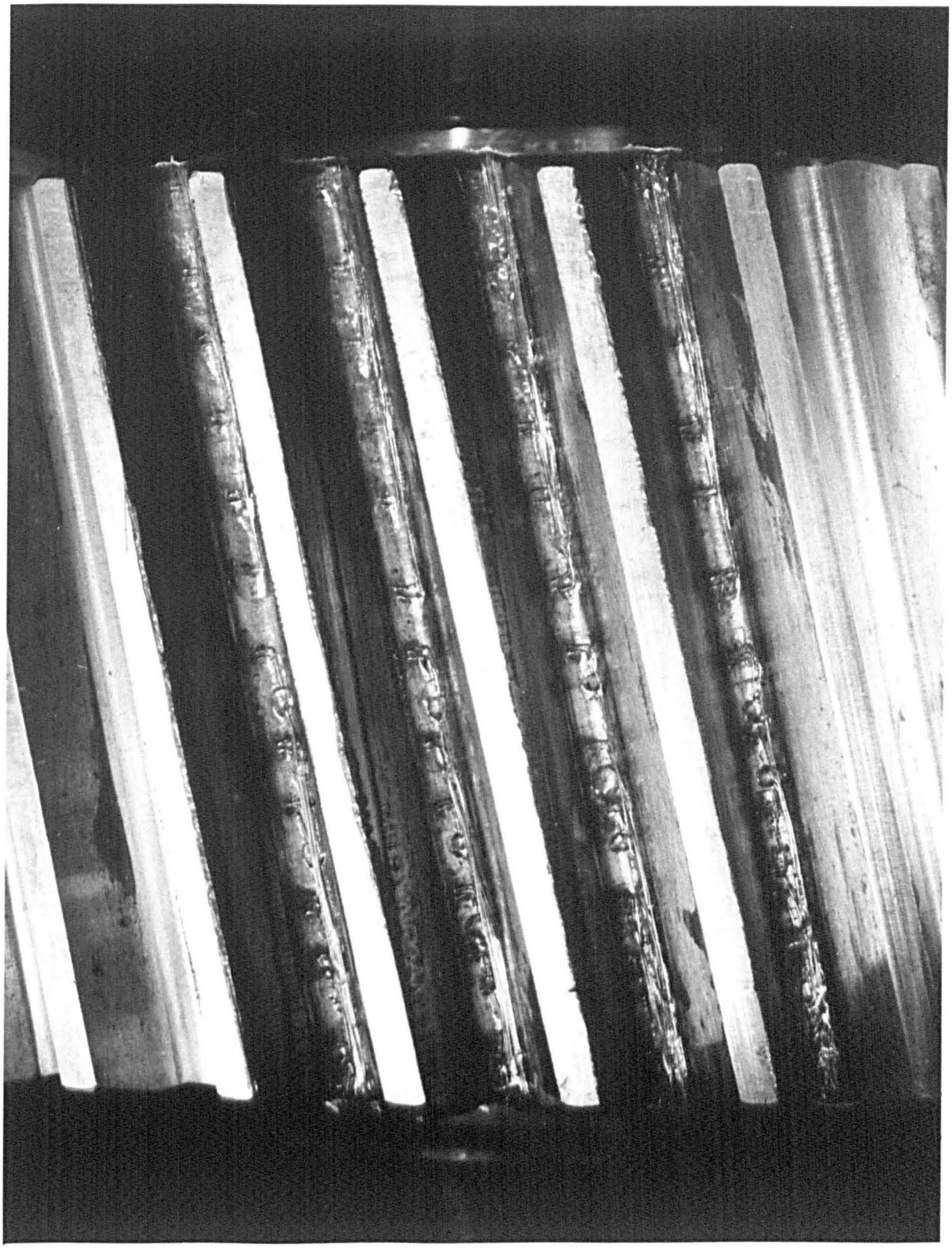

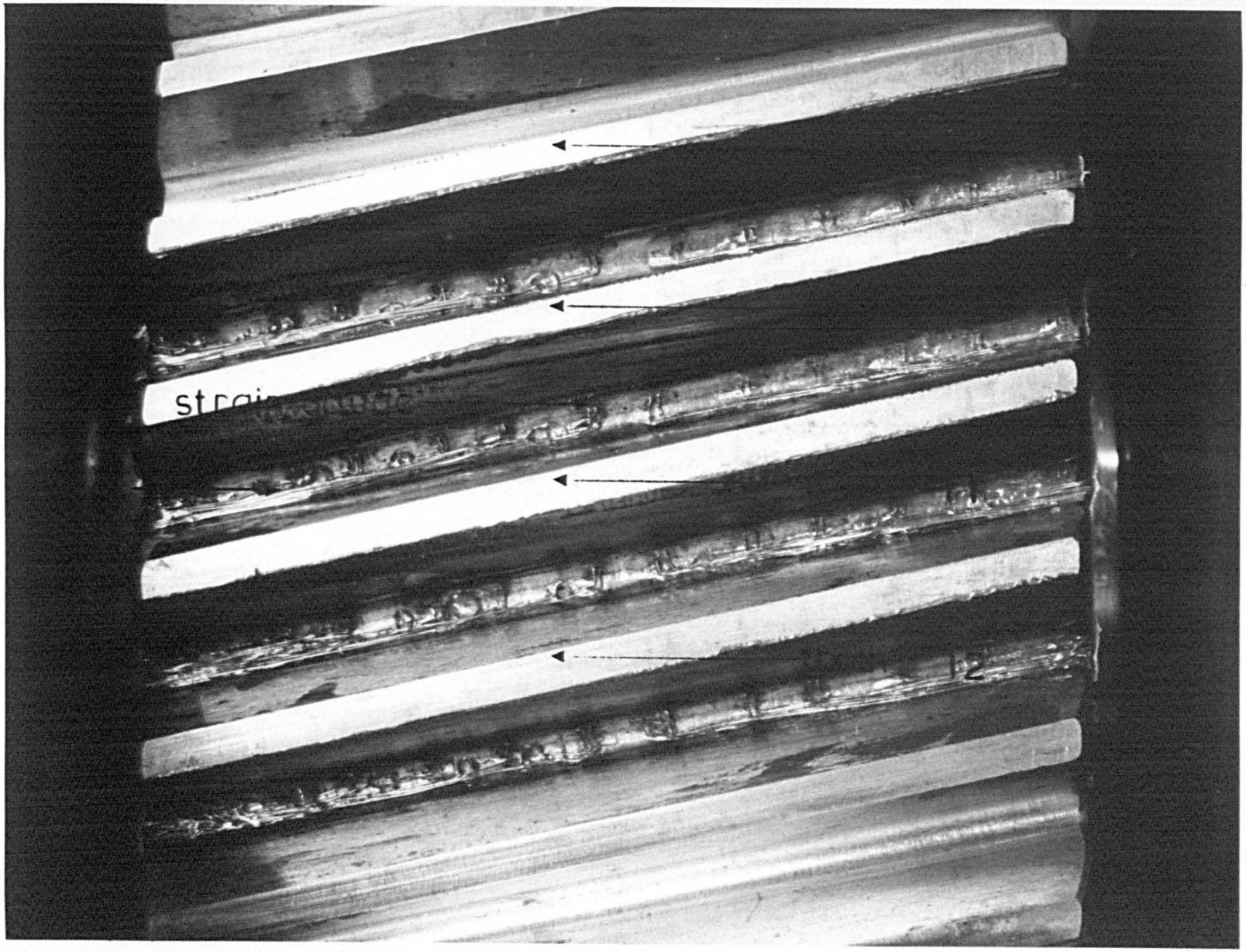

Fig.5.8b Wheel Teeth Strain Gauges

Scanning block UMH 3209

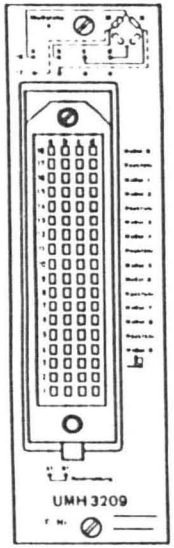

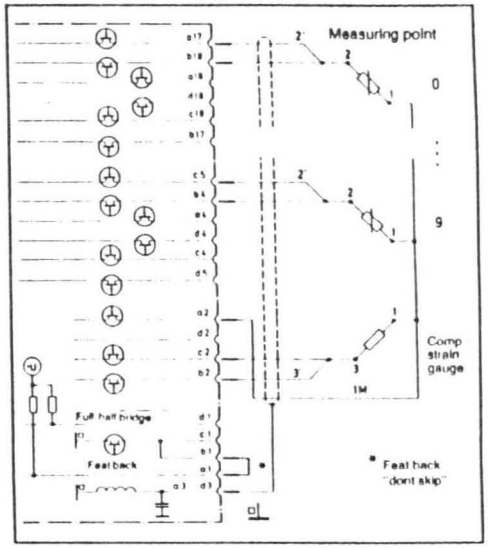

Selections on the printed circuit board

S 23		off
S 22		off
S 21		on

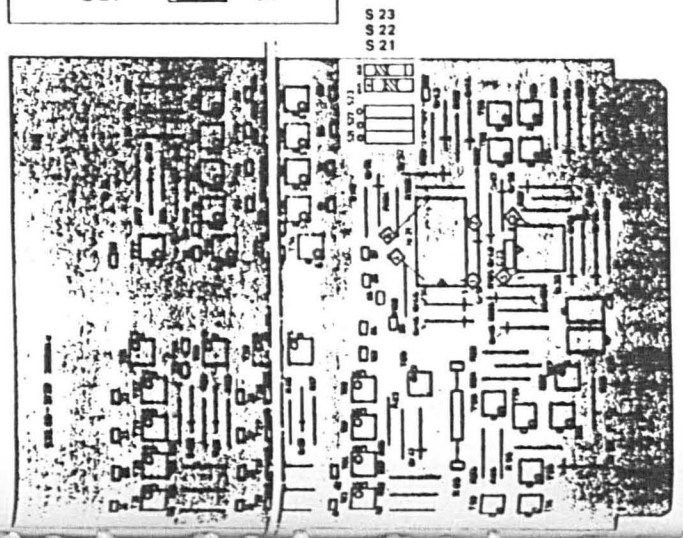

Programming the instrument

UPM 40

Bridge type	€
gauge factor	*selectable strain gauge*
Indication	*max. 20000*
Resolution	*1 d ≙ 1 µm/m*

UPM 60

Amplifier type/Bridge excitation voltage	DC/5 V; 225 Hz/5 V/0.5 V
Bridge type	€
gauge factor	selectable strain gauge
Indication, max	*40000 (DC), 20000 (225 Hz)*
Resolution Basic setting	*1 d ≙ 1 µm/m*

Cable-lead description

Measuring point	Transducer-connections 1	2	2'	3	3'
0		b 18 bl 22	a 17 nf 21		
1		b 16 rs 20	c 17 nf 19		
2		b 15 gr 18	a 14 nf 17		
3		b 13 ge 16	c 14 nf 15		
4		b 12 gn 14	a 11 nf 13		
5		b 10 br 12	c 11 nf 11		
6		b 9 ws 10	a 8 nf 9		
7		b 7 sw 8	c 8 nf 7		
8		b 6 gn 6	a 5 nf 5		
9		b 4 br 4	c 5 nf 3		
	1M			3	3'
comp.-strain gauge	a 2 ws 1			c 2 rt 24	b 2 nf 23
Shield	a 3				
RM	a 1 ——— b 1				

bl = blue, br = brown, ge = yellow, gn = green, gr = grey, rs = pink, rt = red, ws = white

Method of connecting 72-pole plug

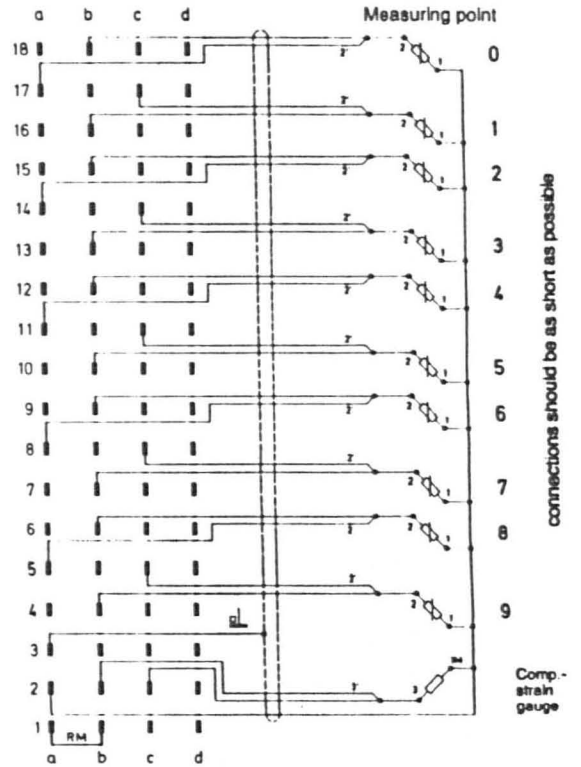

The extended Kreuzer circuit does not work with this version.

Cable cross-section

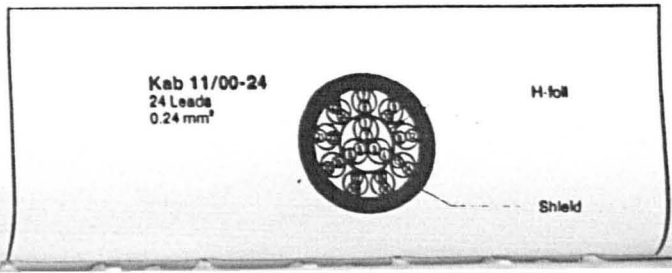

Fig.5.9 Wheel Teeth Strain_Gauge Connection Diagram

four gauges on tooth 10, and six of the gauges on tooth 11. The fourth chain is the sum of the remaining six gauges on tooth 11, and four of the gauges on tooth 12 whose remaining eight gauges form the fifth and last chain. The compensating gauge is common to all five chains since it is activated only by the individual activation of each gauge.

The gauges were connected to a HBM UPM60 data logger which can process and display the readings from up to 60 measuring points (Fig.5.10).

For calibration of the gauges refer to section 5.5.2, and for the determination of the experimental load distribution from measured gauge strains refer to section 5.5.3.

5.2.2.3 Torque Measurement

The torsion bar (Fig.5.3 and Fig.5.11a) used to wind up the helical wheel against the fixed helical pinion to develop the required loading torque was also used as a torque measuring device.

Near the middle of the bar, two identical strain-gauge bridges were positioned to measure the torque applied to the bar. One bridge acts as a back-up for the other, or both may be used simultaneously if needed. By calibrating the torsion bar, output signals from the bridge induced by torsional wind-up can be converted into units of torque as discussed in detail in section 5.4.

These strain gauge bridges were originally intended to measure the torque applied to the spur gear pinion (Fig.5.3) during back-to-back testing, so that small corrections are needed (for bearing/mesh friction, etc.) to convert the results to obtain the helical pinion torque required for these tests.

5.2.2.4 Torsion Bar Calibration Accessories

Torsion bar calibration (see Section 5.4) is done before mounting the wheel and other components inside the rig. Therefore a method was devised to load the torsion bar at its splined end, while locking it at its squared end. A 1 meter long arm (Fig.5.15a) was designed to be fitted at the bar's splined end. The arm is loaded at its free end to induce torsion in the bar. A locking arm (Fig.5.15b) and a base plate (Fig.5.2 and 5.11b) were designed to restrain the bar's squared end from rotation.

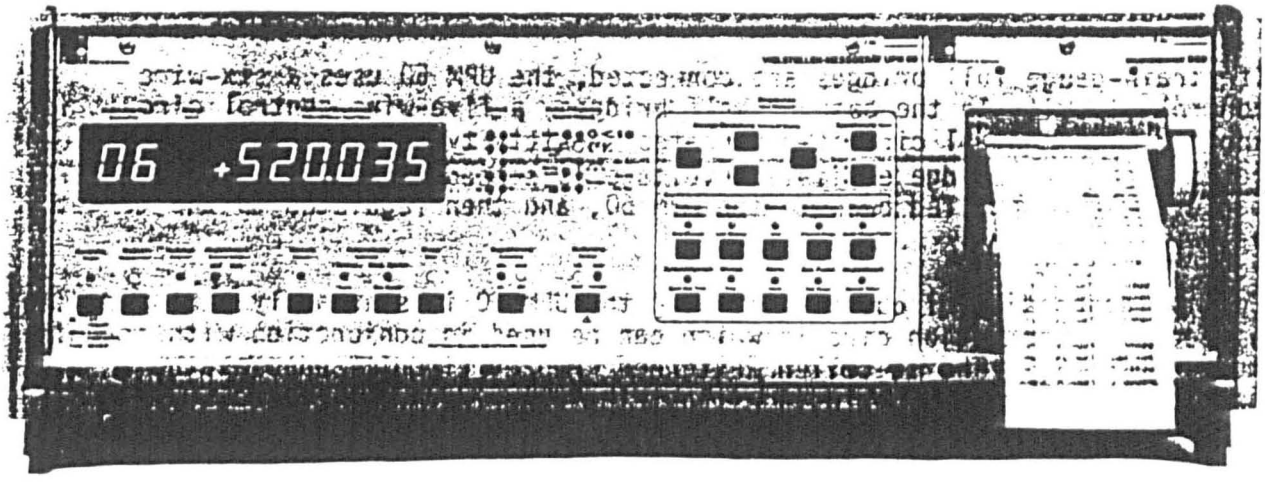

Fig.5.10 Multipoint Measuring Instrument UPM60

5.2.2.5 Modifications to Main Bearing Caps

Figure 5.3 shows the bearing types and arrangements used. Since the meshing gear teeth had to be accessible at all times during the experiments, the original upper housing, which makes the gears inaccessible, was replaced by individual bearing caps designed to suit the existing bearings as shown in Figs. 5.1 and 5.2. The existing bearing covers (retainers) shown in Fig.5.3 (parts 13, 14 and 16) were not altered, however retainer 15 was altered to function as both a bearing retainer and a support frame for encoder ROD 800 as shown in Figs. 5.1 and 5.2.

5.2.2.6 Transmission Error Measurement

To measure transmission error, a pair of Heidenhain incremental angular encoders were coupled to the projecting ends of the pinion and wheel shafts. Their outputs were monitored by using either the matching Heidenhain VRZ counters, or a Klingelnberg PEW 02 transmission-error measuring system which automatically processed the signals to give a direct readout of transmission error.

On the wheel shaft, the ROD 800 encoder was coupled directly to the shaft end using a Heidenhain type K01 coupling, and a carefully aligned aluminium mounting frame for the encoder body (Fig.5.1).

Because of the need for access to the end of the pinion shaft for torque setting, the ROD 270 encoder for pinion rotation could not be directly coupled in this way, and was driven via a precision friction disc mounted on the pinion shaft (Fig.5.1).

The ROD 270 was itself mounted on a "spring table" assembly supported, as shown in Fig. 5.2, on two leaf springs so that it could only move horizontally, perpendicularly to the shafts. The table was pre-loaded to act as a tension spring to maintain contact between the friction disks, which were designed to give a step-up ratio of 2:1 to increase the effective angular resolution of the encoder.

This arrangement suffers from the disadvantage that it is sensitive not only to rotation of the pinion (as required) but also to lateral motion of the pinion shaft (caused, e.g. by bearing deflections or shaft deflections). It was thus also necessary to monitor the lateral motion of the driving disk (on the pinion shaft) relative to the spring table upon which the ROD 270 is mounted. Coupled with readings of disk runout, this allowed the appropriate corrections for lateral motion to be made if necessary (See section 5.7).

5.2.2.7 Torque Setting

Torque is set into the system by twisting the projecting squared end of the torsion bar relative to the helical pinion shaft, by locking the pinion shaft against rotation (Fig.5.2), and rotating the end of the torsion bar using a splined torque multiplying unit and a lever with weights. The pinion shaft and torsion bar are then clamped together by tightening the screws on the ringfeder assembly, when the lever system and rotation lock can be removed.

After some initial problems, this system worked reasonably well, although it proved difficult to set particular exact values of torque. (Torque varied slightly as the gears were turned anyway, see section 5.5.2).

5.2.2.8 Driving Screw Assembly

The driving assembly (see Fig.5.11b) consists of a driving fine-pitch screw, driving clamp, guiding clamps, and the same base plate used for calibrating the torsion bar as discussed earlier in section 5.2.2.4. It is used for driving the gears through a range of phases of mesh by driving the screw, which drives the driving clamp that is clamped onto the squared end of the torsion bar. This arrangement is used during calibration of the strain gauges (section 5.5.2) and during the actual tests (section 5.5.3).

5.2.2.9 Measurement of Shaft Misalignment

Two jigs were designed for measuring the positions of the pinion and wheel shafts relative to one another in the vertical and horizontal planes, as shown in Fig.5.12. Both relied on the radial reference bands on the two shafts to determine the position of the shaft centres.

For measurements in the vertical direction, the jig (Fig.5.12(a)) is placed on the bands (rings) at a particular instant of mesh and positioned by means of the locating pins which contact the rings on the inner side as shown. Since the rings are (nominally) all the same diameter, the four points of contact should lie in a plane. The jig has 3 flat machined and ground contact faces, and, in place of the fourth, a vertical probe set (on a reference surface table) to read zero when all four contacts are co-planar.

Non-zero readings at any instant, coupled with knowledge of the actual ring diameters and radial runout at the contact points, allow the shaft misalignment in the vertical plane to be determined.

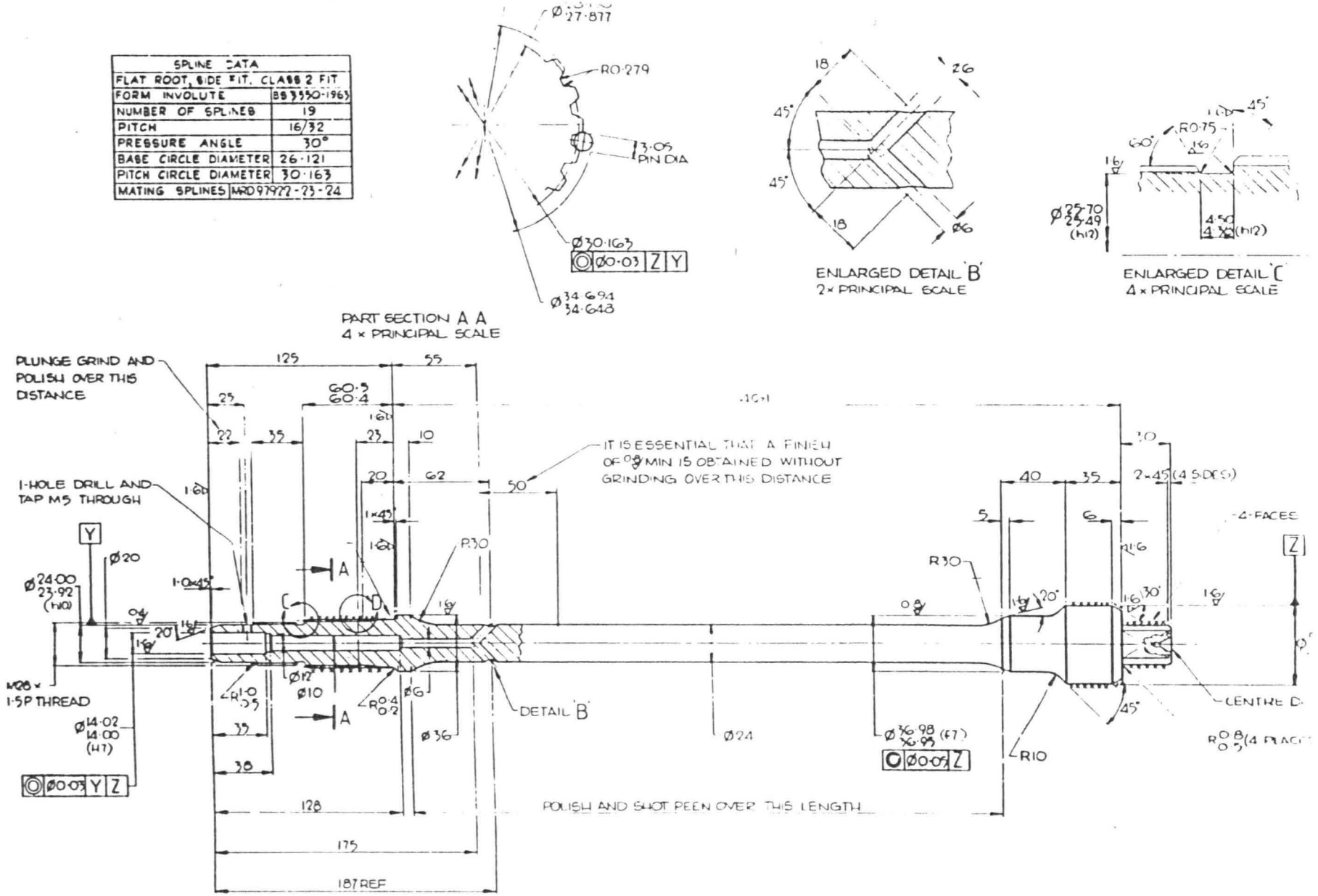

Fig.5.11a Torsion Bar

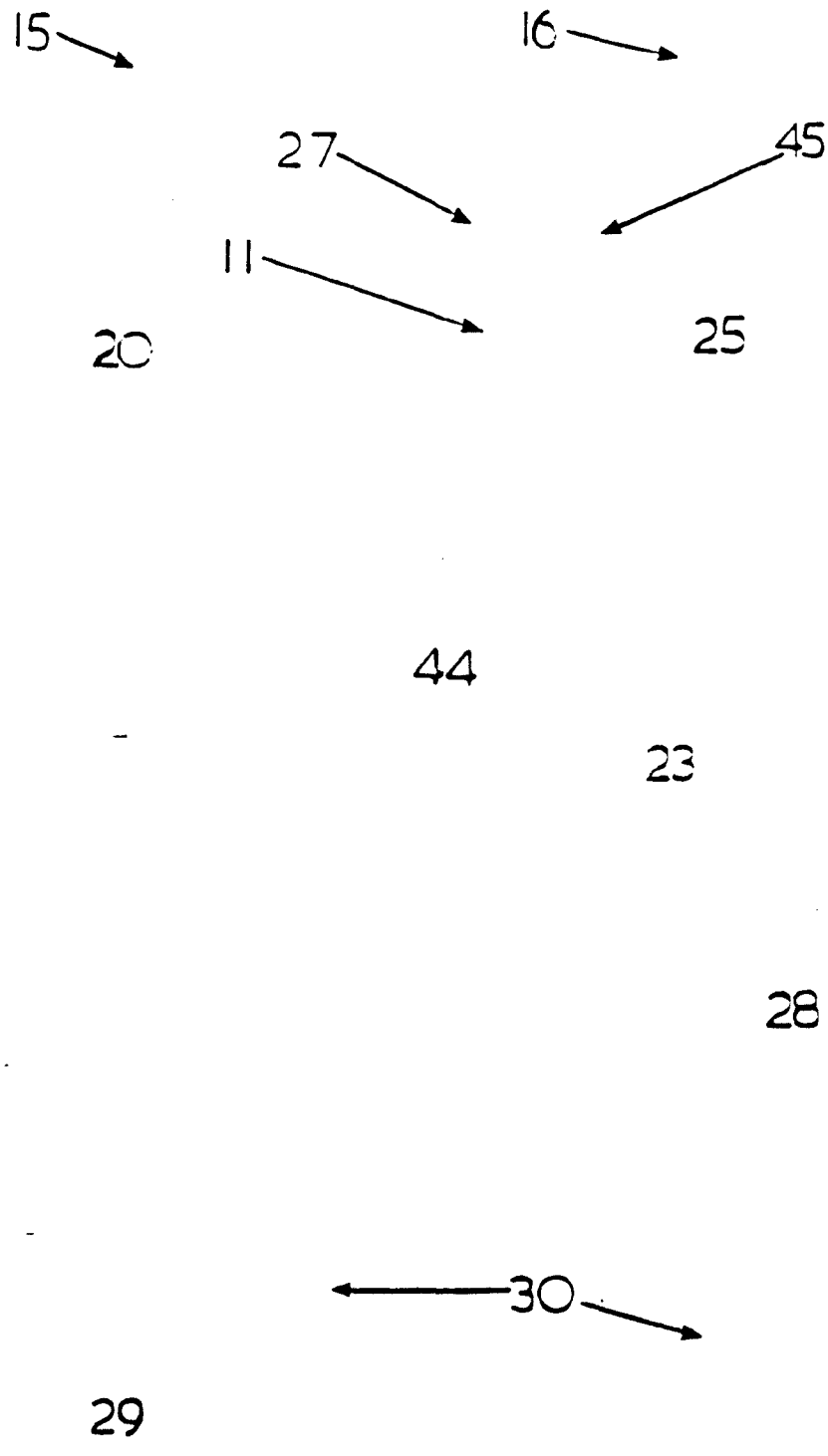

Fig.6.11b Driving Screw Assembly

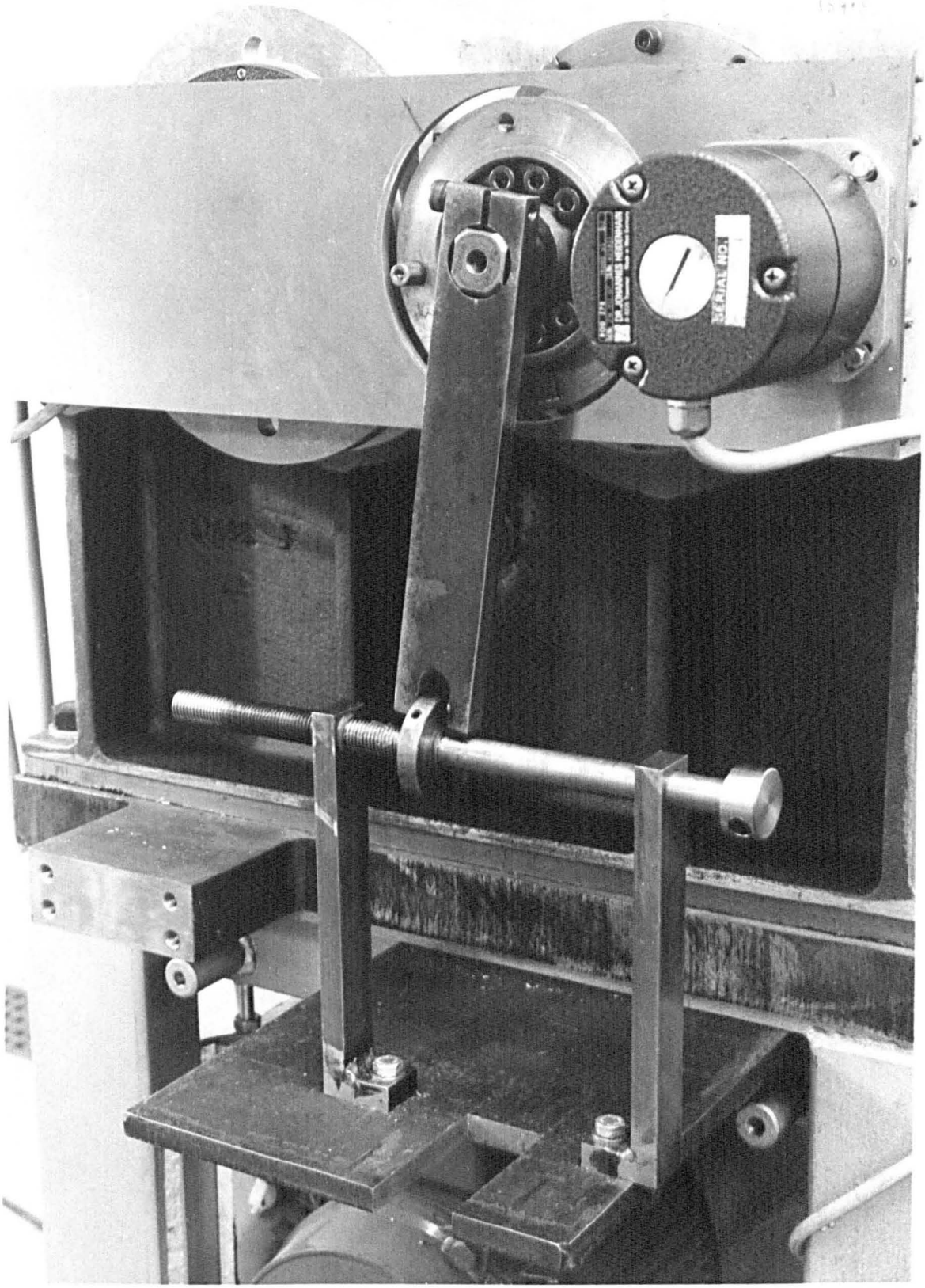

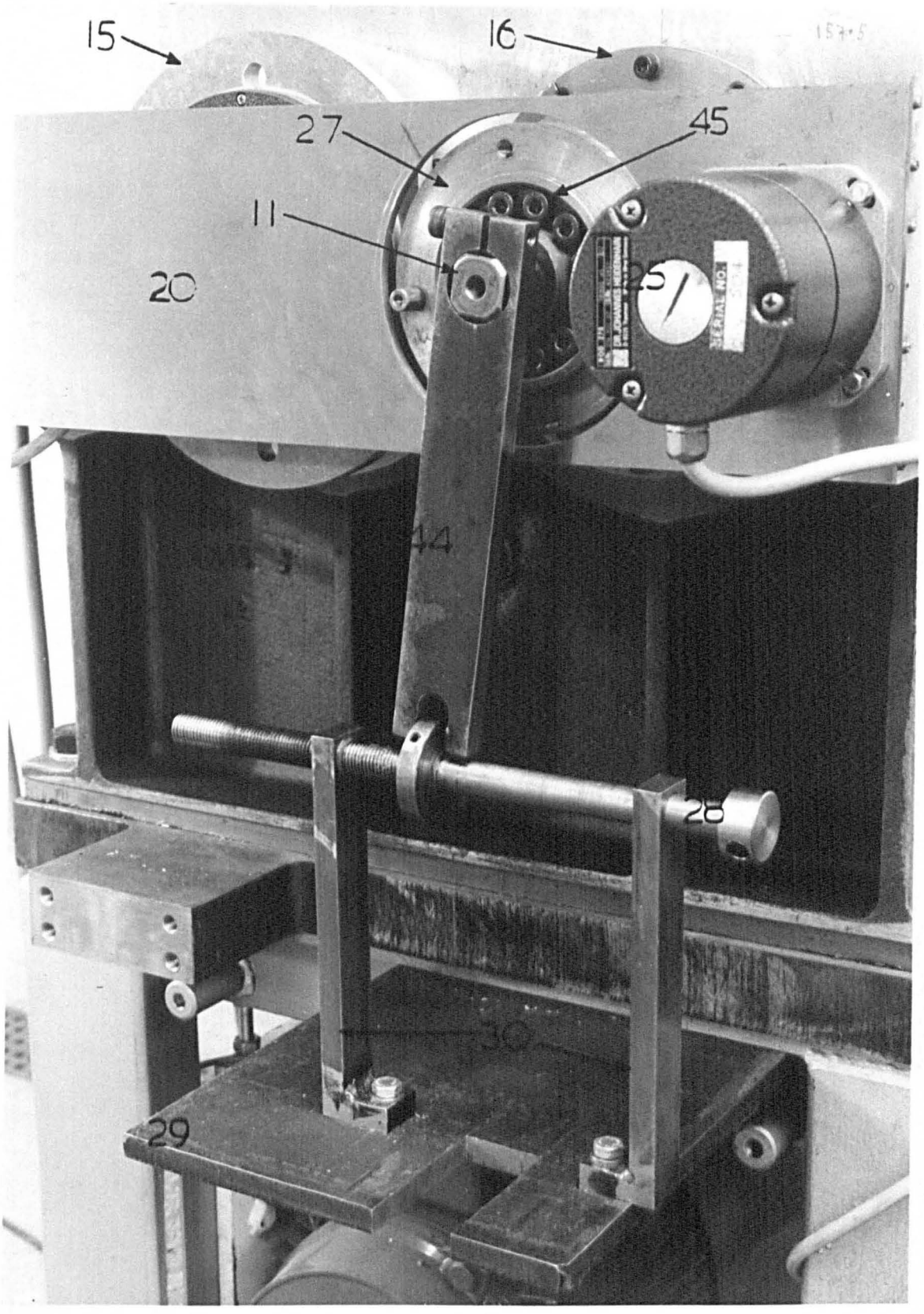

Fig.5.11b Driving Screw Assembly

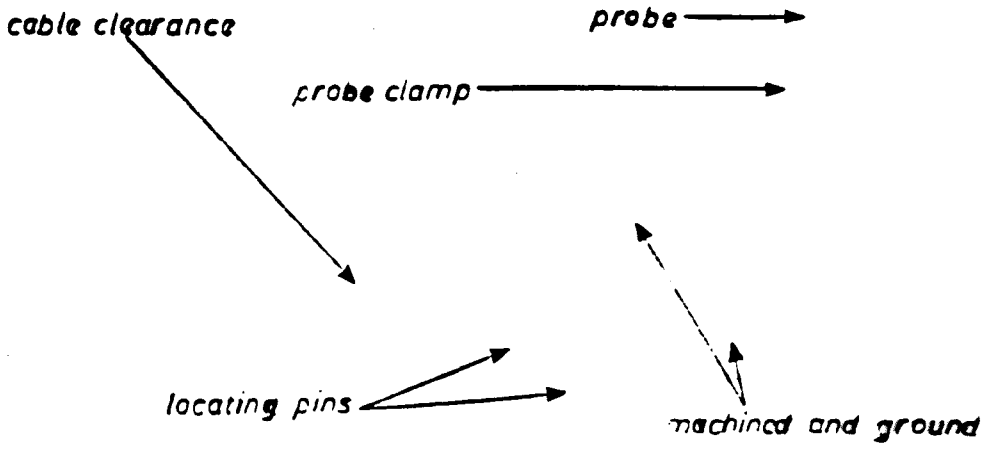

Fig.5.12a Shaft Vertical Misalignment Measurement Jig

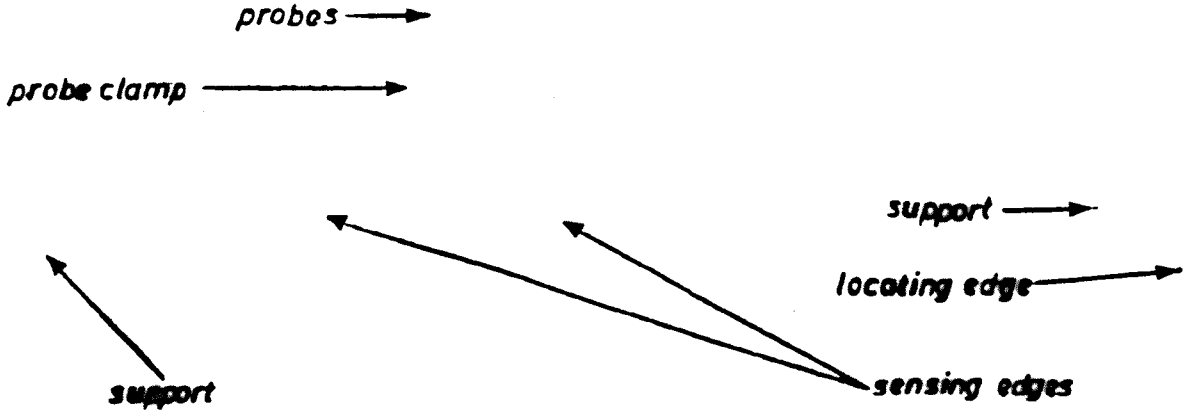

Fig.5.12b Shaft Horizontal Misalignment Measurement Jig

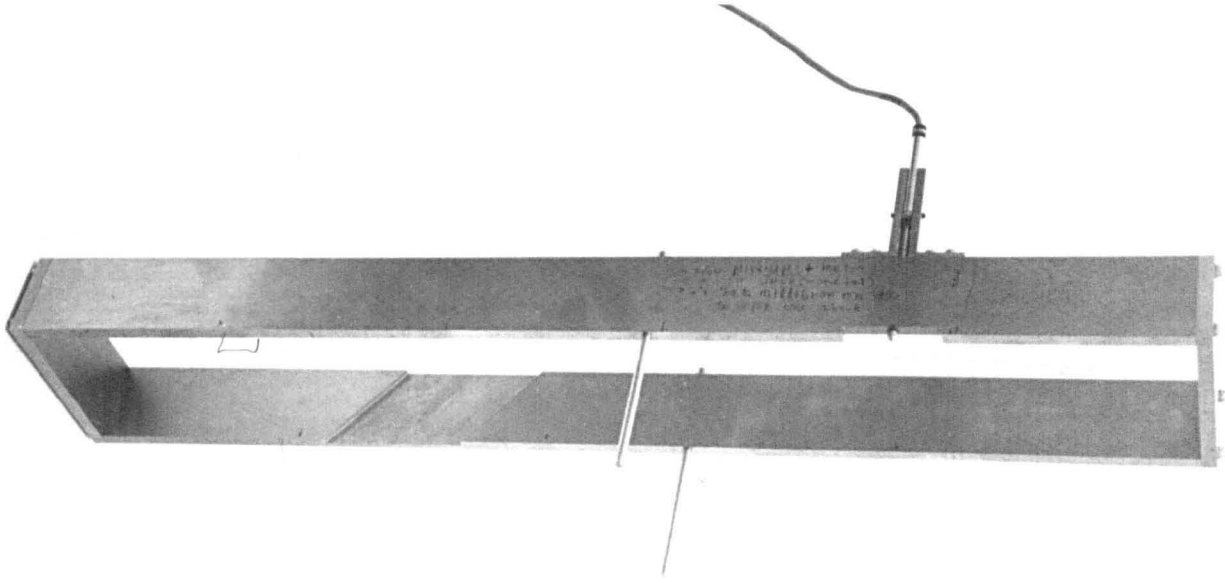

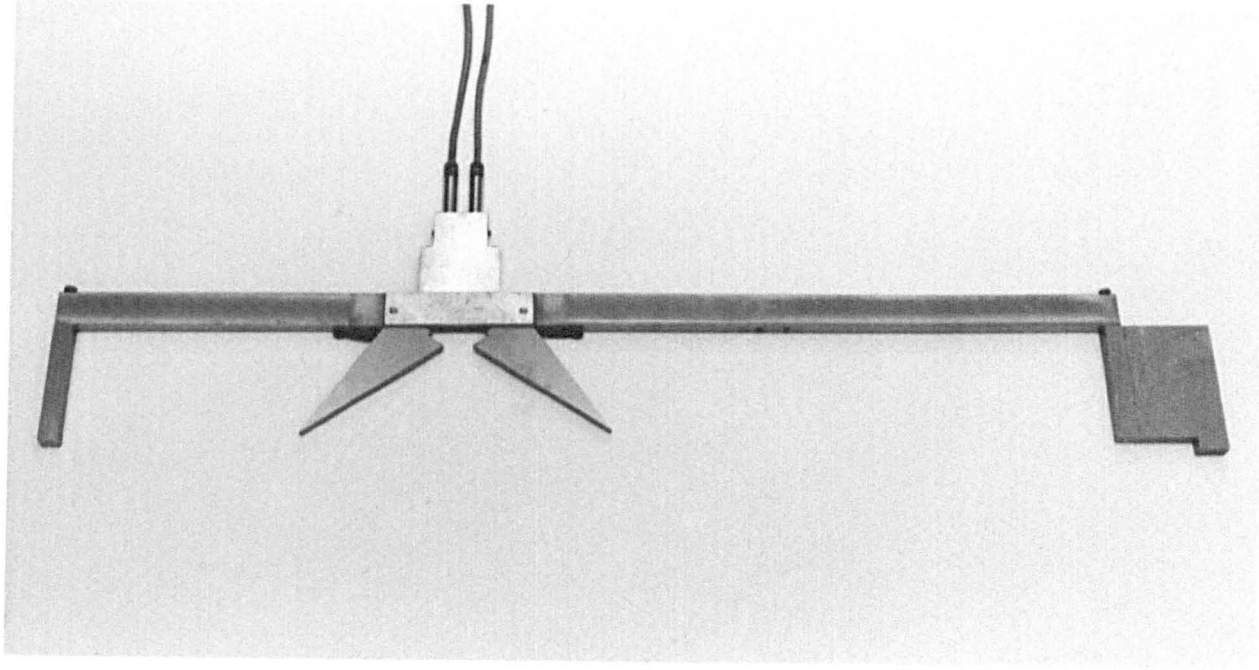

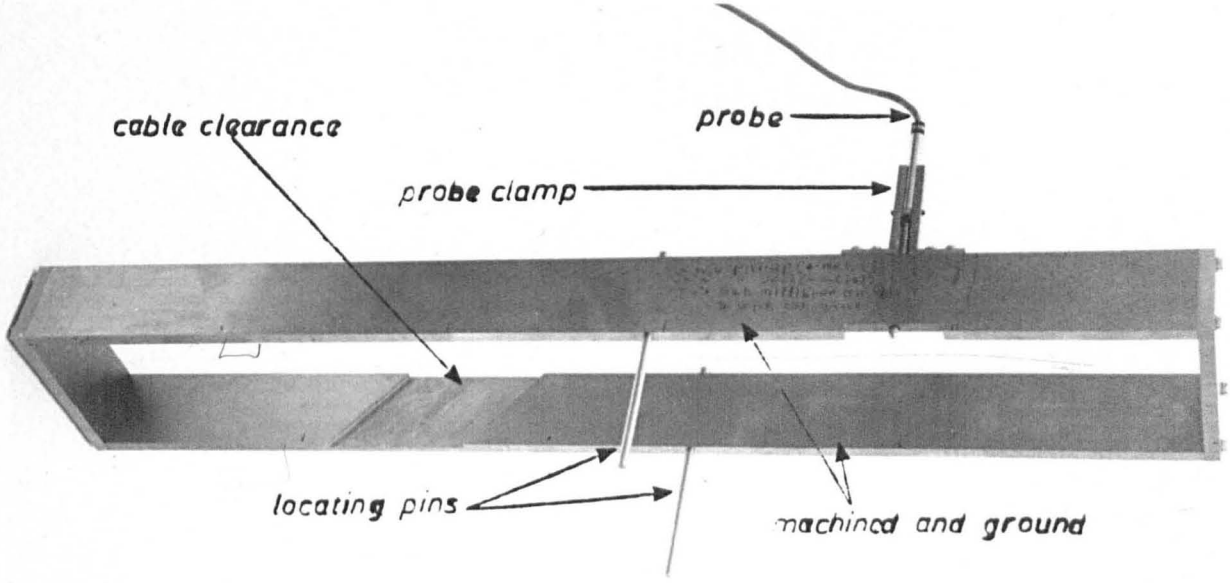

Fig.5.12a Shaft Vertical Misalignment Measurement Jig

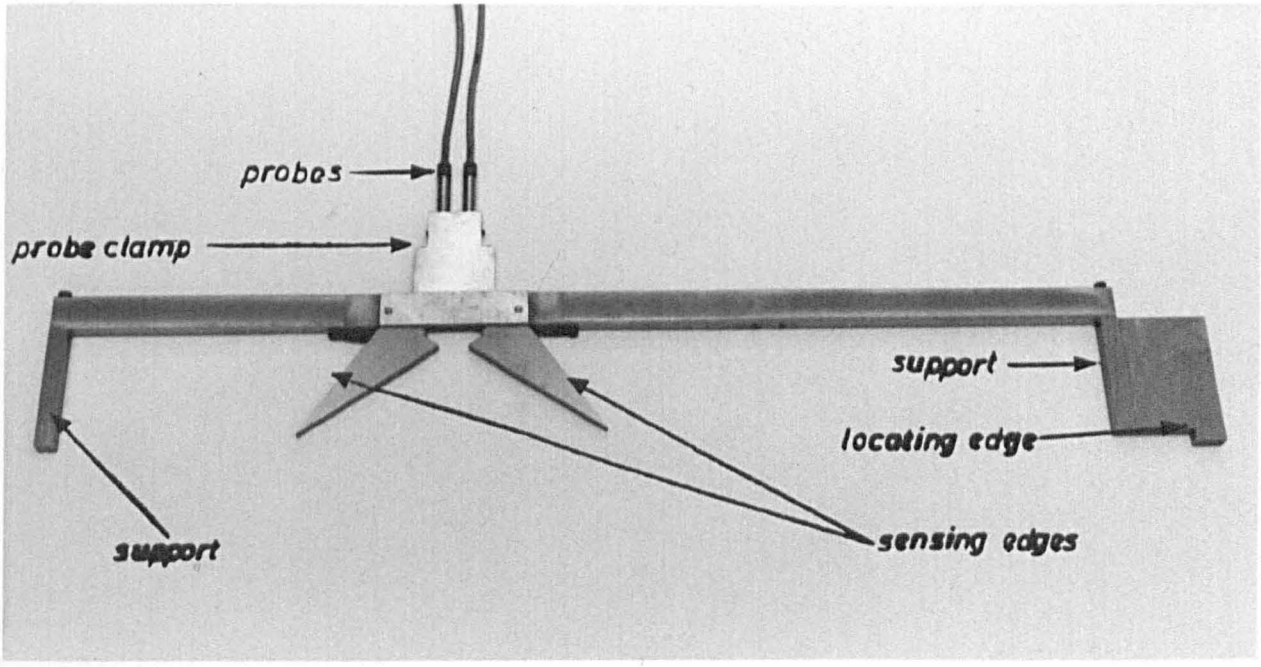

Fig.5.12b Shaft Horizontal Misalignment Measurement Jig

For measurements in the horizontal direction, the second jig (Fig.5.12(b)) is placed at each end of the gearbox in turn, in contact with only two of the rings (one on each shaft) in each position. It is located by the stepped end plate which makes contact with the outer edge of the gearbox. The triangular bell cranks are spring-loaded into contact with the inner surfaces of the two rings, and the (vertical) probes are set to read the sum of the inward displacements of the two contact points (x the lever ratio of 28/73.5, see Fig.5.25). They thus measure any change in centre distance (when corrected for runout and actual ring diameters). Further details in section 5.5.3.2.

5.3 Load Limitations

During testing, the load applied must not exceed the design load of any of the four gears in mesh. The replaceable spur gears are considerably weaker than the helical gears, and so the design load of the spur gears must not be exceeded. The gears were analysed using the DUISO software[45].

Figure 5.13 shows the output for the spur gears giving a factor of safety of 1.15 and 1.70 for contact and bending stresses respectively for the pinion (smaller than the wheel's factors) when a torque of 800Nm is applied for 1000 pinion revolutions. This is taken as the limiting value that must not be exceeded during the experiments.

Figure 5.14 shows the output for the helical gears. This is included for comparison and, as expected, the corresponding factors of safety are much higher than for the spur gears and are 2.21 and 6.24 for pinion contact and bending stress respectively, for the same loading at 800Nm.

Splines, keys, pins, the torsion bar and other components of the rig subjected to loading, are all designed to accommodate the gear design loads. Note that the gears will be loaded statically, and so the load application and dynamic factors K_A and K_V respectively are 1.0 in Figs. 5.13 and 5.14. Also an arbitrary low speed of 10 r.p.m. was chosen for the pinion. The errors input for Fig.5.14 were based on the pair of teeth in mesh which have the worst combined measured errors (tooth 11 on the wheel with tooth 5 on the pinion).

5.4 Calibration of the Torsion Bar

The torsion bar strain-gauge bridge was calibrated by locking the bar at the helical pinion end as previously described (locking arm of Fig.5.15b) and applying a known torque at the other through a 1m long

```
* DUISO * Design Unit Newcastle Univ* Wheel :Case Hardening Steel   HV700
**1000*****891004********************* Pitting permitted?     NO
Disk: DATA     File: FIG5.13 31 Aug 89 Lube. viscosity nu40/nu50   168/100
                                       Load cycles       NL  1.00E3    3.99E2
[ comment here up to <<< 40 character  Application fac   KA        1.000
---------------------------------------Dynamic factor    Kv        1.000
                                       Power             P         0.84      kW
Number of teeth  z        21      54   Torque            T   800.0   2057.1 Nm
Normal module    mn          5.000     Tang.force        Ft      15233.1      N
Transv. module   mt          5.000     R.P.M             n      10.0      3.9
Gear ratio       i           2.571     Peripheral vel    v          0.055   m/s
Closed centres   a         191.689     Sliding vel.      vg    0.011    0.020 "
Ref.   centres   a0        191.689     Reduced mass      mred       0.030 kg/mm
Facewidth        b    10.000   20.000   Reference speed   N          0.001
Ref. circle dia  d   105.000  270.000   Singl.stiffness   c'        18.16N/mm/mu
Base circle dia  db   98.668  253.717   Mesh stiffness    cgamma   24.74      "
Pitch circ. dia  dw  107.372  276.098   DIN quality   5
Tip diameter     da  114.329  288.470   Base pitch err.   fpb       15.600    mum
Root diameter    df   91.000  265.141   Run-in allowce.   ypb        1.170     "
Tooth depth      H    11.664   11.664   Form error        ff        10.500     "
Ref.pr.ang.Norm  alphan   20.0000       Run-in allowce.   yff        0.787     "
Ref.pr.ang.Tran  alphat   20.0000       Tip relief        cay        2.085     "
Wkg.pr.ang.Norm  alphatn  23.2288       Errors:Shaft      fsh          -       "
Wkg.pr.ang.Tran  alphatw  23.2288              Bearings    fbe          0.0     "
Ref. helix ang.  beta        0.0               Casing      fca          0.0     "
Base helix ang.  betab       0.0               Manufac.    fma        5.742     "
Addend.mod.fac.  x       0.0  0.91413              Total   fbetax    45.000     "
Sum of mod.facs  x12       0.91413     Run-in allowce.   ybeta      6.000     "

Base tang.lgth.  zzw  -38.372  117.613  Tool tip rad/mn   roa0     0.400   0.400
 over no. teeth  zs       3        8     " tooth add/mn   ha0      1.400   1.400
Transv.cont.rat  epsalpha  1.483        protubce.angle    apro       -       -
Face cont.ratio  epsbeta     0.0        protuberance/mn   pro        -       -
Total cont.rat.  epsgamma  1.483        protubce.ht./mn   hk         -       -
-----------------------TOOTH FLANK-------------------------------TOOTH ROOT---
Longt.load dist  KHbeta     1.316       Longt.load dist   KFbeta     1.081
Trans.load dist  KHalpha    1.000       Trans.load dist   KFalpha    1.000

Zone factor      ZH         2.297       Form factor       YF       1.912   1.190
Elasticity fac.  ZE       189.812       Notch parameter   qs       1.556   3.044
Cont.ratio fac.  Zepsilon   0.916       Stress corr.fac   YS       1.661   2.338
Helix angle fac  Zbeta      1.000       Helix angle fac   Ybeta      1.000
Life factor      ZN     1.600   1.600   Life factor       YNT      2.500   2.500
Lubrication fac  ZL     1.000   1.000   Sensitivity fac   YdrelT   0.851   1.149
Roughness fac.   ZR     1.000   1.000   Surf.cond. fac.   YRrelT   1.000   1.000
Speed factor     ZV     1.000   1.000   Size factor       YX       1.000   1.000
Matl.mating fac  ZW     1.000   1.000   Root chord lgth   sFn/mn   1.976   2.445
Size factor      ZX     1.000   1.000   Bending mom.arm    hF/mn   1.246   1.225
Single cont.fac  ZB         1.000       Root radius       roF/mn   0.635   0.402
---------------CONTACT STRESS(N/mm2)-----------------BENDING STRESS(N/mm2)
Endurance limit  sigHlim 1475.0 1475.0  Endurance limit   sigFlim  417.5   417.5
Permiss. stress  sigHp   2360.0 2360.0  Permiss. stress   sigFp   1775.8  2397.7

Basic contact "  sigH0     1793.1       Basic root   "    sigF0    967.9   424.1
Contact stress   sigH      2057.6       Tooth root   "    sigF    1046.6   458.6


SAFETY FACTOR    SH       1.15   1.15   SAFETY FACTOR     SF       1.70    5.23
```

Fig.5.13 DUISO Rough Estimate of Spur Gear Load Capacity

```
********************************** Pinion:Case Hardening Steel   HV700
* DUISO * Design Unit Newcastle Univ* Wheel :Case Hardening Steel   HV700
**1000****891004********************* Pitting permitted?     NO
Disk: DATA    File: FIG5.14 31 Aug 89 Lube. viscosity nu40/nu50  168/100
                                      Load cycles      NL  1.00E3   3.89E2
[ comment here up to <<< 40 character Application fac  KA        1.000
---------------------------------------Dynamic factor  Kv        1.001
                                       Power           P         0.84      kW
Number of teeth  z        21      54   Torque          T   800.0   2057.1 Nm
Normal module    mn          5.000     Tang.force      Ft      14905.1      N
Transv. module   mt          5.112     R.P.M           n      10.0     3.9
Gear ratio       i           2.571     Peripheral vel  v          0.056   m/s
Closed centres   a         191.689     Sliding vel.    vg    0.017   0.019 "
Ref.   centres   a0        191.689     Reduced mass    mred      0.032 kg/mm
Facewidth        b      90.000  90.000 Reference speed N         0.001
Ref. circle dia  d     107.346 276.032 Singl.stiffness c'       17.06N/mm/mu
Base circle dia  db    100.607 258.702 Mesh stiffness  cgamma   24.97     "
Pitch circ. dia  dw    107.346 276.032 DIN quality   5
Tip diameter     da    117.346 286.032 Base pitch err. fpb       15.600   mum
Root diameter    df     93.346 262.032 Run-in allowce. ypb        1.170    "
Tooth depth      H      12.000  12.000 Form error       ff       10.500    "
Ref.pr.ang.Norm  alphan    20.0000     Run-in allowce. yff        0.787    "
Ref.pr.ang.Tran  alphat    20.4103     Tip relief      cay        2.085    "
Wkg.pr.ang.Norm  alphatn   20.0000     Errors:Shaft    fsh          -      "
Wkg.pr.ang.Tran  alphatw   20.4103            Bearings fbe          0.0    "
Ref. helix ang.  beta      12.0000            Casing   fca          0.0    "
Base helix ang.  betab     11.2665            Manufac. fma        7.811    "
Addend.mod.fac.  x          0.0     0.0           Total fbetax    45.000    "
Sum of mod.facs  x12              0.0      Run-in allowce. ybeta     6.000    "

Base tang.lgth.  zzw   38.468  99.972 Tool tip rad/mn roa0    0.400   0.400
 over no. teeth  zs         3       7  " tooth add/mn  ha0     1.400   1.400
Transv.cont.rat  epsalpha   1.618     protubce.angle  apro       -       -
Face cont.ratio  epsbeta    1.191     protuberance/mn pro        -       -
Total cont.rat.  epsgamma   2.810     protubce.ht./mn hk         -       -
----------------------TOOTH FLANK----------------------------TOOTH ROOT---
Longt.load dist  KHbeta     3.428     Longt.load dist KFbeta     2.916
Trans.load dist  KHalpha    1.188     Trans.load dist KFalpha    1.188

Zone factor      ZH         2.450     Form factor     YF      1.649  1.365
Elasticity fac.  ZE       189.812     Notch parameter qs      1.585  2.025
Cont.ratio fac.  Zepsilon   0.786     Stress corr.fac YS      1.737  1.954
Helix angle fac  Zbeta      0.989     Helix angle fac Ybeta     0.900
Life factor      ZN     1.600  1.600  Life factor     YNT     2.500  2.500
Lubrication fac  ZL     1.000  1.000  Sensitivity fac YdrelT  0.884  0.980
Roughness fac.   ZR     1.000  1.000  Surf.cond. fac. YRrelT  1.000  1.000
Speed factor     ZV     1.000  1.000  Size factor     YX      1.000  1.000
Matl.mating fac  ZW     1.000  1.000  Root chord lgth sFn/mn  2.000  2.256
Size factor      ZX     1.000  1.000  Bending mom.arm  hF/mn  1.085  1.155
Single cont.fac  ZB         1.000     Root radius     roF/mn  0.631  0.557
---------------CONTACT STRESS(N/mm2)-----------------BENDING STRESS(N/mm2)
Endurance limit sigHlim1475.0 1475.0 Endurance limit sigFlim 417.5  417.5
Permiss. stress sigHp  2360.0 2360.0 Permiss. stress sigFp  1845.5 2045.0

Basic contact "  sigH0     529.2     Basic root   "  sigF0    85.3   79.5
Contact stress   sigH     1068.2     Tooth root   "  sigF    295.8  275.5


SAFETY FACTOR    SH       2.21  2.21 SAFETY FACTOR    SF      6.24   7.42
```

Fig.5.14 DUISO Rough Estimate of Helical Gear Load Capacity

horizontal lever (Fig.5.15a) bolted in place of the spur pinion and loaded with weights. The output from the bridge was monitored using a Fylde amplifier and an Avometer (Figs.5.1).

During calibration, the lever was progressively loaded to 839.5 Nm (giving a torque slightly greater than the maximum test torque of 800 Nm), and progressively unloaded. During this calibration, only the pinion shaft was mounted in the rig. Thus no meshing friction or main bearing friction was involved.

The loading and unloading readings agreed to within 0.17%, and repeating the experiment gave results which agreed with the original readings to within 0.25%.

These results were compared with the theoretical output from a full-bridge circuit (Fig.5.17), given by

$$V_o = V_i . \epsilon . G_F . K_g \qquad 5.1$$

$$\epsilon = \frac{8T}{\pi d^3 G}$$

G_F = gauge factor (2.09)

K_g = amplifier gain (200)

with $d = 24.0\text{mm}$, $V_i = 2.5\text{V}$, $G = 82 \times 10^9\ \text{N/m}^2$

this gives

$$V_o = 0.002348 \ . \ T \qquad 5.2$$

with T in Nm, and V_o in V.

The experimental results, and those given by Eq.5.2 are compared in Fig.5.16. They agree within 2%, well within the tolerance of factors such as V_i, G_F and K_g. This verifies the absence of frictional effects.

Fig.5.15a Torsion Bar 1_Meter Loading Arm

Fig.5.15b Torsion Bar Locking Arm

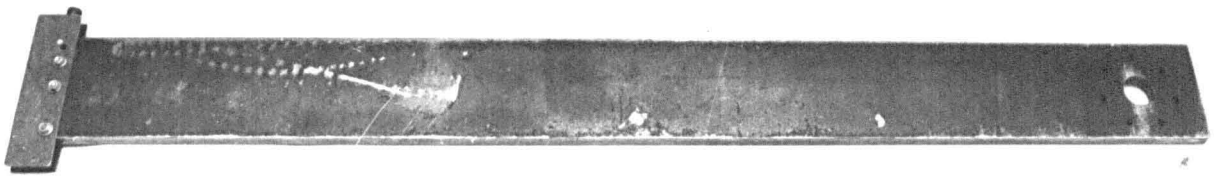

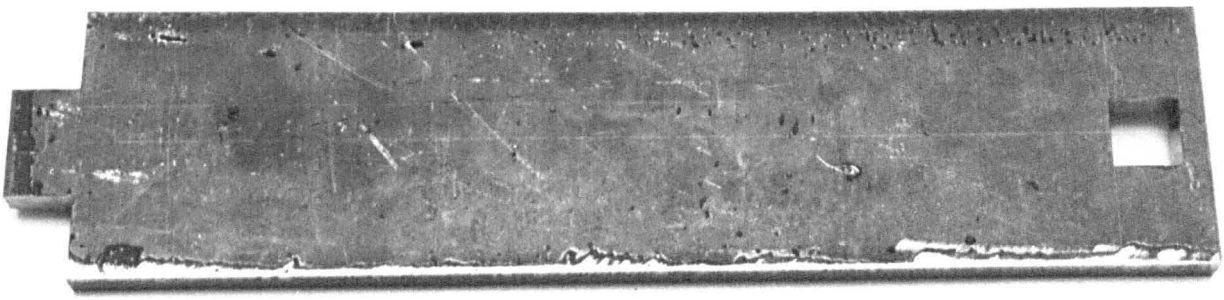

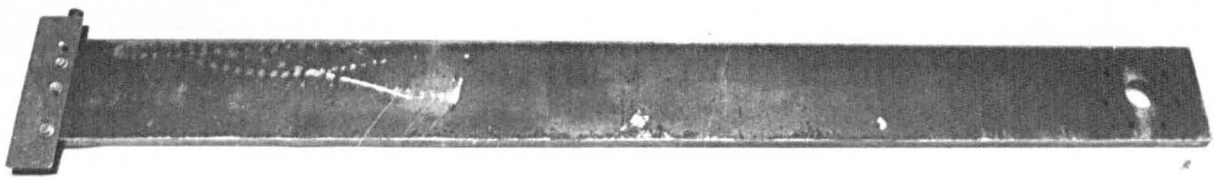

Fig.5.15a Torsion Bar 1_Meter Loading Arm

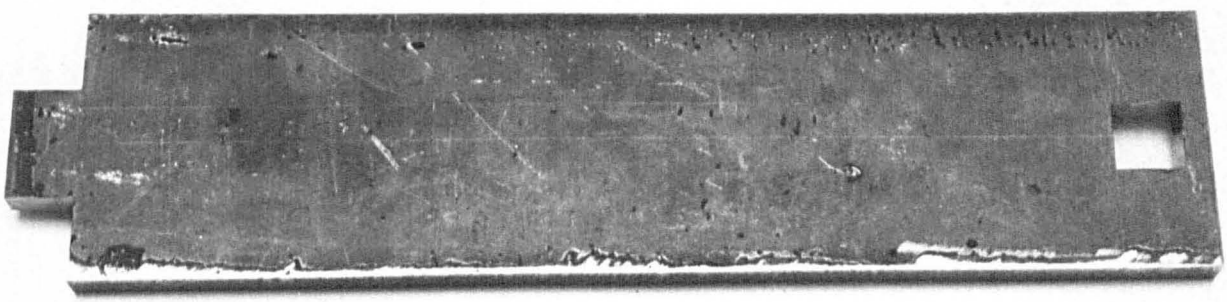

Fig.5.15b Torsion Bar Locking Arm

Fig. 5.16 Torsion Bar Calibration (GF=2.09 Vi=2.5V GAIN=200 ds=24mm)

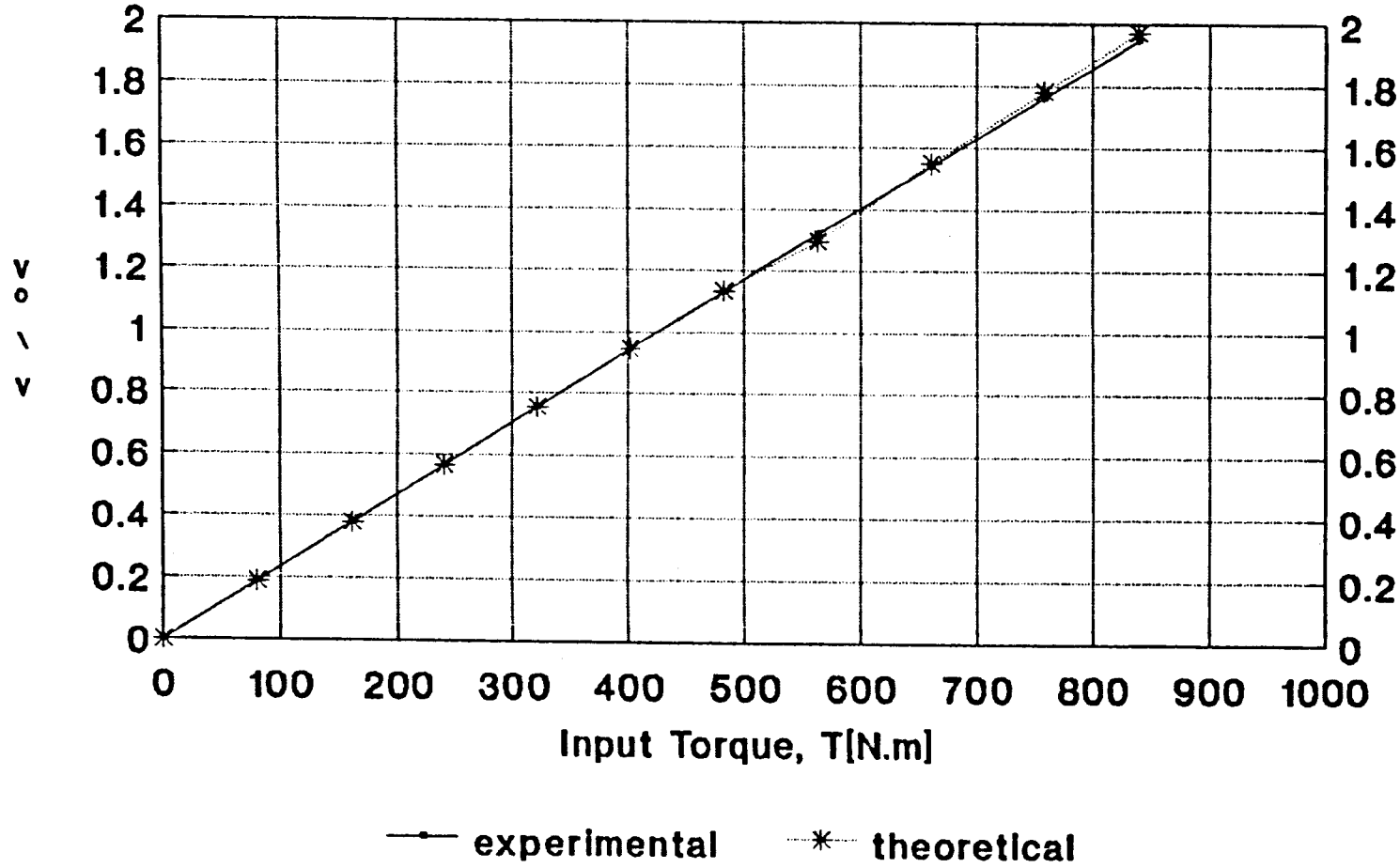

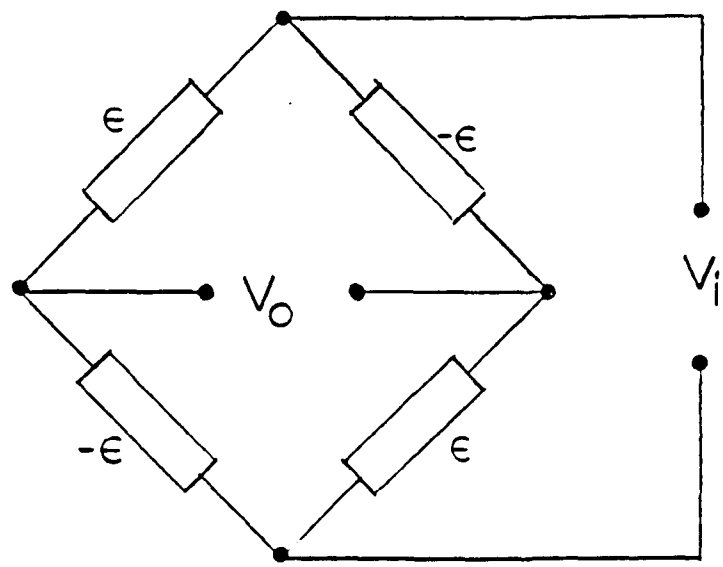

Fig.5.17 Torsion Bar Strain_Gauge Full Bridge

5.5 Calibration of Tooth Root Strain Gauges and Experimental Load Distribution

5.5.1 Introduction

During any phase of mesh of a pair of helical gears, there are two or more pairs of teeth in mesh. From section 2.8 and Fig. 2.65a the number of Gauss points in the theoretical solution is given by

$$n = b'/(\Delta'/2) \qquad 5.3$$

where

$$b' = b/\cos\beta_b \qquad 5.4$$

The strain gauges measure the tooth root strains "e_i" at sections corresponding to each of the "n" Gauss points used in the theoretical solution, (as well as at the other points which may be out of the mesh region at that particular phase of mesh).

Since the gear is a linear elastic solid, the contributions of each Gauss load "F_j^*" to each tooth root strain "e_i" can be superposed, so that we can write

$$\{e_i\} = [a_{ij}] \times \frac{\Delta'}{2} \{F_j^*\} \qquad 5.5$$

where
- i = is the number of rows ($1 \leqslant i \leqslant n$)
- j = is the number of columns ($1 \leqslant j \leqslant n$)
- $\{F_j^*\}$ – is a column vector of Gauss loads intensities
- $\{e_i\}$ – is a column vector of strain gauge readings
- $[a_{ij}]$ – is a matrix of the influence factors (to be determined as discussed in section 5.5.2)

The values of "e_i" can be obtained directly from the strain gauge readings logged by the UPM60 in (μm) when the gears are loaded and meshed at the required phases as discussed in section 5.5.3. However, to calculate the load intensities "F_j^*", the influence factors "a_{ij}" must first be determined. This is the objective of the calibration discussed in detail below. Once the values of "a_{ij}" are obtained, the matrix equation 5.5 may readily be solved for $\{F_j^*\}$ by inverting the matrix $[a_{ij}]$ to give

$$\{F_j^*\} = [a_{ij}]^{-1} \times \frac{2}{\Delta'} \{e_i\} \qquad 5.6$$

5.5.2 Point Loading and Calibration Procedure

In order to apply point loads at the individual Gauss-point locations, along the simultaneous lines of contact at a given phase of mesh, a method was devised in which thin strips of brass shim were inserted between the meshing teeth at the required Gauss locations. The dimensions of the shim strip were chosen such that an approximate point load was obtained upon meshing, while at the same time making sure that contact did not take place at any other point other than that where the shim was inserted.

First consider the choice of shim width at the maximum test load of 800 Nm (section 5.3), the total normal load is 16216 N, giving a mean normal, specific load of 180.2 N/mm on the helical gears.

In view of the "width" of the master influence curve of e.g. Figs. 2.38 to 2.40, a "point" load can be reasonably considered as one with a width of (say) $0.5m_n$ or less. For this reason, a shim width of 2mm ($= 0.4m_n$) was chosen, so that the calibrating "point" loads were applied over a nominally rectangular "Hertzian" contact patch as shown in Fig.5.18(b).

From Fig.5.14, the effective Hertzian contact pressure at the mean normal specific load of 180 N/mm is 529 N/mm^2. The presence of the more elastic (brass) shim will reduce this, and it seems likely that some local yielding of the shim will also occur, so there is clearly no danger of overloading the tooth flanks, which can withstand Hertzian stresses of up to 2360 N/mm^2 as shown.

As shown in Fig.5.19, the specific load intensity on the helical gears can be increased by a factor of over 16x before the nominal Hertzian stresses in these gears approach the failure limit. However, such loads tend to damage the weaker material shim, particularly at the tip of the tooth where the shim is sharply curved, and for this reason, the calibration loads were limited to 5x the nominal value (i.e. 5 x 180.2 N/mm x 2mm = 1802N giving a specific load of 180.2 N/mm on the spur pinion and 1802/2 = 901 N/mm on the helical gears).

Next, consider the choice of shim thickness which is affected by gear tooth errors and the backlash allowance. The shim must be thick enough to separate the other contact points, so that contact occurs on the loaded flank only at the point where the shim is inserted. On the other hand, the shim must not be too thick in order to avoid contact on the 'unloaded' tooth flank. A comprehensive analysis was carried

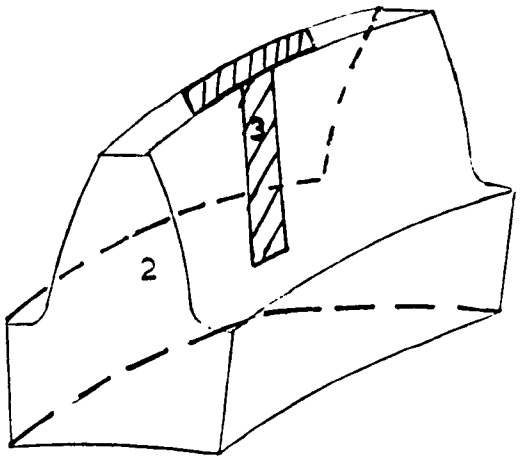

a) 2_mm shim strip in transverse plane glued to top land

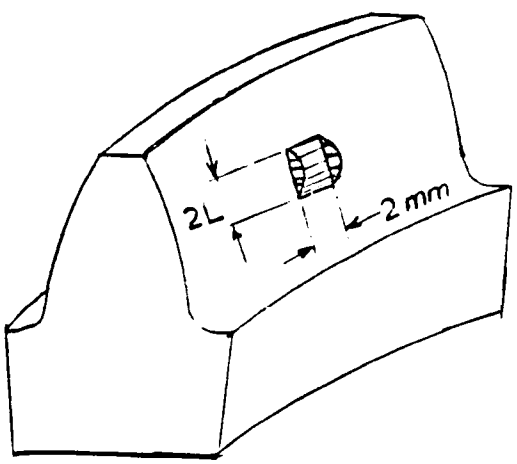

b) Hertzian load distribution along contact patch

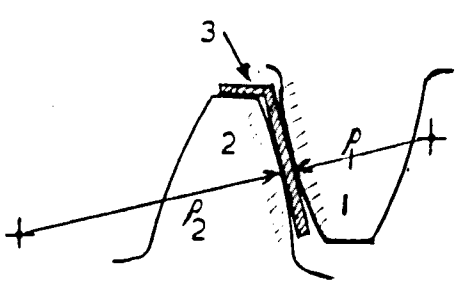

c) radii of curvature in normal plane

Fig.5.18

```
**********************************  Pinion:Case Hardening Steel  HV700
* DUISO * Design Unit Newcastle Univ*  Wheel :Case Hardening Steel  HV700
**1000****891004**********************  Pitting permitted?     NO
Disk: DATA    File: FIG5.19  2 Sep 89  Lube. viscosity nu40/nu50   168/100
                                       Load cycles      NL   1.00E3    3.89E2
{ comment here up to <<< 40 character  Application fac  KA        1.000
----------------------------------------  Dynamic factor   Kv        1.000
                                       Power            P        13.45      kW
Number of teeth  z        21       54  Torque           T12848.0  33037.7  Nm
Normal module    mn          5.000     Tang.force       Ft     239376.0       N
Transv. module   mt          5.112     R.P.M            n      10.0      3.9
Gear ratio       i           2.571     Peripheral vel   v          0.056   m/s
Closed centres   a         191.689     Sliding vel.     vg    0.017   0.019  "
Ref.   centres   a0        191.689     Reduced mass     mred       0.032 kg/mm
Facewidth        b      90.000   90.000  Reference speed N          0.001
Ref. circle dia  d     107.346  276.032  Singl.stiffness c'        17.06N/mm/mu
Base circle dia  db    100.607  258.702  Mesh stiffness  cgamma    24.97     "
Pitch circ. dia  dw    107.346  276.032  DIN quality   5
Tip diameter     da    117.346  286.032  Base pitch err. fpb       15.600    mum
Root diameter    df     93.346  262.032  Run-in allowce. ypb        1.170     "
Tooth depth      H      12.000   12.000  Form error      ff        10.500    "
Ref.pr.ang.Norm  alphan    20.0000       Run-in allowce. yff        0.787     "
Ref.pr.ang.Tran  alphat    20.4103       Tip relief      cav        2.085     "
Wkg.pr.ang.Norm  alphatn   20.0000       Errors:Shaft    fsh          -       "
Wkg.pr.ang.Tran  alphatw   20.4103              Bearings  fbe         0.0      "
Ref. helix ang.  beta      12.0000              Casing    fca         0.0      "
Base helix ang.  betab     11.2665              Manufac.  fma         7.811    "
Addend.mod.fac.  x       0.0      0.0                 Total  fbetax  45.000    "
Sum of mod.facs  x12           0.0       Run-in allowce. ybeta      6.000     "

Base tang.lgth.  zzw   38.468   99.972  Tool tip rad/mn  roa0    0.400   0.400
 over no. teeth  zs        3        7     " tooth add/mn  ha0     1.400   1.400
Transv.cont.rat  epsalpha  1.618        protubce.angle   apro      -       -
Face cont.ratio  epsbeta   1.191        protuberance/mn  pro       -       -
Total cont.rat.  epsgamma  2.810        protubce.ht./mn  hk        -       -
-----------------------TOOTH FLANK-----------------------------TOOTH ROOT---
Longt.load dist  KHbeta     1.183       Longt.load dist  KFbeta     1.157
Trans.load dist  KHalpha    1.000       Trans.load dist  KFalpha    1.000

Zone factor      ZH         2.450       Form factor      YF      1.649   1.365
Elasticity fac.  ZE       189.812       Notch parameter  qs      1.585   2.025
Cont.ratio fac.  Zepsilon   0.786       Stress corr.fac  YS      1.737   1.954
Helix angle fac  Zbeta      0.989       Helix angle fac  Ybeta      0.700
Life factor      ZN      1.600   1.600  Life factor      YNT     2.500   2.500
Lubrication fac  ZL      1.000   1.000  Sensitivity fac  YdrelT  0.984   0.980
Roughness fac.   ZR      1.000   1.000  Surf.cond. fac.  YRrelT  1.000   1.000
Speed factor     ZV      1.000   1.000  Size factor      YX      1.000   1.000
Matl.mating fac  ZW      1.000   1.000  Root chord lgth  sFn/mn  2.000   2.256
Size factor      ZX      1.000   1.000  Bending mom.arm   hF/mn  1.085   1.155
Single cont.fac  ZB          1.000      Root radius      roF/mn  0.631   0.557
---------------CONTACT STRESS(N/mm2)-----------------BENDING STRESS(N/mm2)
Endurance limit  sigHlim 1475.0 1475.0  Endurance limit  sigFlim  417.5   417.5
Permiss. stress  sigHp   2360.0 2360.0  Permiss. stress  sigFp   1845.5 2045.0

Basic contact "  sigH0     2120.6       Basic root   "   sigF0   1370.6 1276.4
Contact stress   sigH      2306.6       Tooth root   "   sigF    1586.2 1477.2


SAFETY FACTOR    SH       1.02   1.02   SAFETY FACTOR    SF       1.16   1.38
```

Fig.5.19 Effect on Fig.5.14 Result When Load is 16x Larger

out which accounts for the combined backlash and total meshing tooth-pair errors. All possible combinations of positive and negative errors combined with the minimum backlash were studied and the final conclusion was that the shim must fall in the range

$$89\ \mu m < t < 145\ \mu m$$

where t is the shim thickness. A nominal thickness of 127 μm (0.005") was chosen.

Simple analysis showed that the elastic compression of the shim under the expected test loads was negligible (<1.5μm).

The shim was made T-shaped in order to enable it to be glued to the tooth top land with the 2mm "active" strip projecting freely down the flank in the transverse plane of the gear (Fig.5.18(a)).

The intention was to study the contact loading at three phases of mesh, so that values for the coefficients "a_{ij}" of Eq.5.5 were required at these three phases. Before describing the calibration tests, it is thus appropriate to explain how the phase of mesh defined in the theory was related to the angular position of the test gears.

As discussed earlier, the pairs of teeth to be meshed are (pinion/wheel) 5/11, 6/10 and 7/9, so the pair 5/11 was arbitrarily chosen as the "reference pair" for the purpose of inputting phase in "HELICALDIST".

To minimize the angular rotation required during a test (to avoid damaging the wires), pinion tooth 16 was chosen as the "datum" tooth, to which all angular positions were referred. To set this tooth at its zero position, the setting jig shown in Figs.5.20 and 5.23 was used. This places the datum ball at mid-face width (z=45mm) with its centre on the line of centres of the gears (see Fig.5.1), while the ball is pushed between tooth 16 and tooth 17 as far as possible. The gears were very lightly loaded to overcome the backlash and bring the meshing teeth together during this process.

Fig.5.20 shows the transverse section passing through mid-face of the gears (z=45mm). Therefore, at z=90mm, the angle "$180-23\pi/Z_1$" becomes

$$180 - \left[\frac{23.\pi}{Z_1} - \frac{\tan\beta\ .\ 45}{r_1}\ .\ \frac{180}{\pi}\right]$$

and with $\beta = 12^{\circ}$, $Z_1 = 21$ teeth and $r_1 = 53.673$mm this angle is 6.9323° measured CCW from reference position 2 in Fig.5.20.

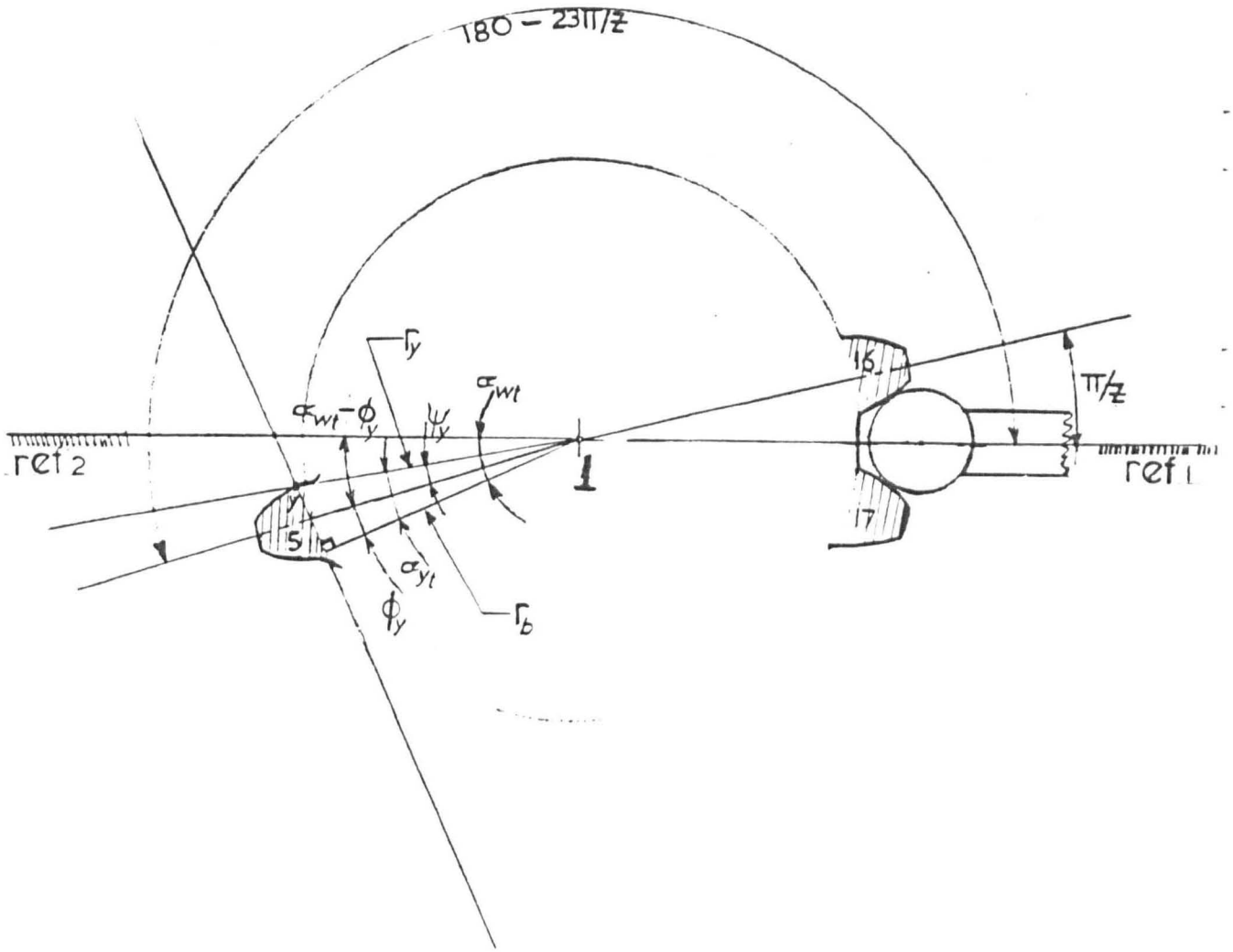

Fig.5.20 Transverse Section Through Pinion Mid_Face Showing Zero Datum Position

Hence this is the "zero" position for the gears and the counter connected to the wheel-shaft encoder is set to zero at this point, (see section 5.2.2.6).

Referring to section 2.3 and Fig.2.1, the phase $\varphi_{z0}(5/11)$ input in "HELICALDIST" is used to calculate angles "α_{yt1}" and "φ_{y1}" shown in Fig.5.20, where

$$(\alpha_{yt1})_{z=90mm} = \tan^{-1}\left[\varphi_{z0}\cdot P_{bt} - TE + \epsilon_\beta \cdot P_{bt}\right]/(d_{b/2}) \qquad 5.7$$

$$(\varphi_{y1})_{z=90mm} = \left[\alpha_{yt1}\right]_{z=90mm} - \left[\Psi + inv(\alpha_t) - inv(\alpha_{yt})_{z=90mm}\right] \qquad 5.8$$

The angle through which the pinion must be rotated in the rig to correlate with the input phase "φ_{z0}" in "HELICALDIST" is then given by (see Fig.5.20).

$$(phase)_{RIG} = (\varphi_{y1})_{z=90mm} - \alpha_{wt} \qquad 5.9$$

where if the result is positive, the pinion must be rotated clockwise from reference position 2 in Fig. 5.20. But recalling from the previous paragraph that the reference tooth pair (5/11) is 6.9323° counterclockwise from reference position 2 in Fig.5.20 (−6.9323°), at the zero datum position of the gears discussed earlier, then Eqn.5.9 must be corrected to become

$$(phase)_{RIG} = (\varphi_{y1})_{z=90mm} - \alpha_{wt} + 6.9323 \qquad 5.10$$

where again positive is clockwise from reference position 2 in Fig.5.20.

The three experimental phases chosen as inputs to "HELICALDIST" are φ_{z0} = 0.5626147, 0.7752294 and 0.9878441 p_{bt}. From Eqns.5.7, 5.8 and 5.10 the corresponding pinion rotations on the rig are −8.3743°, −4.7292° and −1.0827° respectively all measured counterclockwise from the zero datum position. Since the ROD 800 encoder on the wheel shaft is used to measure phase however, the corresponding wheel rotations from reference position 2 are 3.25667°, 1.83913° and 0.42105° respectively (clockwise rotation of wheel from the "zero datum" position determined by tooth 16 of the pinion).

The phases as stated above are correct during the actual meshing of the gears. However, for point loading during the calibration procedure, the effect of the shim thickness (t=0.127mm) must be accounted for. Referring to Fig.5.21 the shim causes earlier contact of the wheel tooth given by (t/r_b) where "t" is the shim thickness along the base tangent. Since we are interested in the correct positions of the contact lines on the wheel (which is strain gauged) during calibration, it means that the wheel angular position is determined by the contacting surfaces with or without the shim inserted (contact plane fixed in space). However, since the pinion is used for the zero datum position as shown in Fig.5.20, and recalling that angular position is measured using the counter attached to the wheel shaft, it is obvious that no correction to this angular measure is required. The correction for "t" is anyway so small that it makes no difference and is calculated as

$$\frac{t}{r_{b2}} \cdot \frac{180}{\pi} = \frac{0.127}{129.35} \cdot \frac{180}{\pi} = 0.056^{\circ}$$

Calibration was carried out at each of the three phases listed above, with the results shown (including the calculated contact radii) in Figs. 5.22a, 5.22b and 5.22c.

In each case, every one of the Gauss points was individually and independently calibrated using the sequence listed below:

1. The gears were meshed at an initial torque of around 22.2 Nm which corresponds to a total normal load of 450.0N. This was quite safe to use as it is only a quarter of the maximum permissible load of 1802N calculated previously. This load however did not remain constant as the gears rotated due to the presence of the shim. In some cases it almost doubled.

2. The gauged teeth were then brought totally out of mesh by rotating the wheel counterclockwise in Fig.5.20, and a piece of shim was glued onto the top land at the desired Gauss location along the face width, such that the projecting part of the shim lay in the transverse plane (Fig.5.18(a)).

3. The area where the point load was to be applied was then lightly smeared with a graphite based grease. This was done to reduce

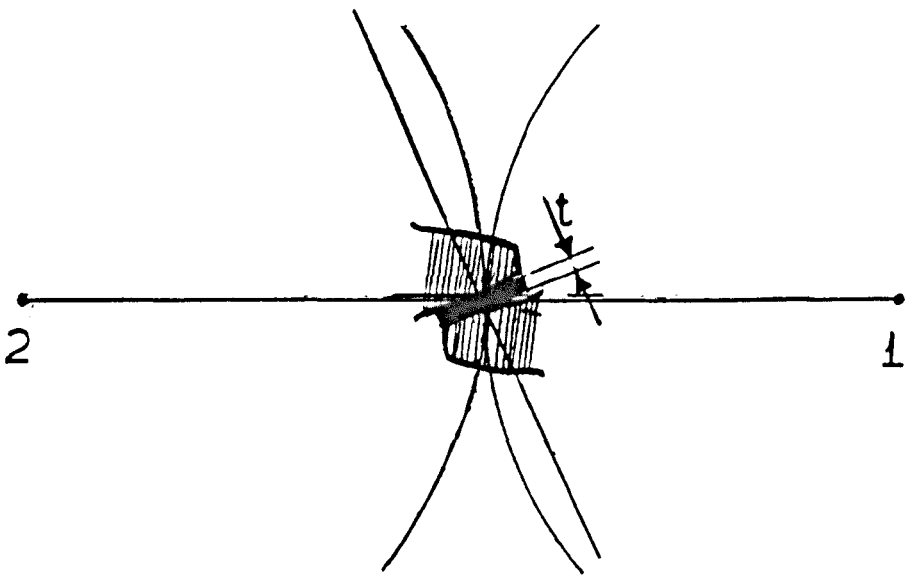

Fig.5.21 Early Contact Induced by Shim

Gauss pt.	ry [mm]
1	136.9560
2	136.3990
3	136.0035
4	135.4805
5	135.1105
6	134.6220
7	134.6340
8	142.6120
9	141.8940
10	141.3795
11	140.6920
12	140.2000
13	139.5440
14	139.0750
15	138.4505
16	138.0050
17	137.4135
18	136.9925
19	136.4340
20	143.0160
21	142.6585
22	141.9395

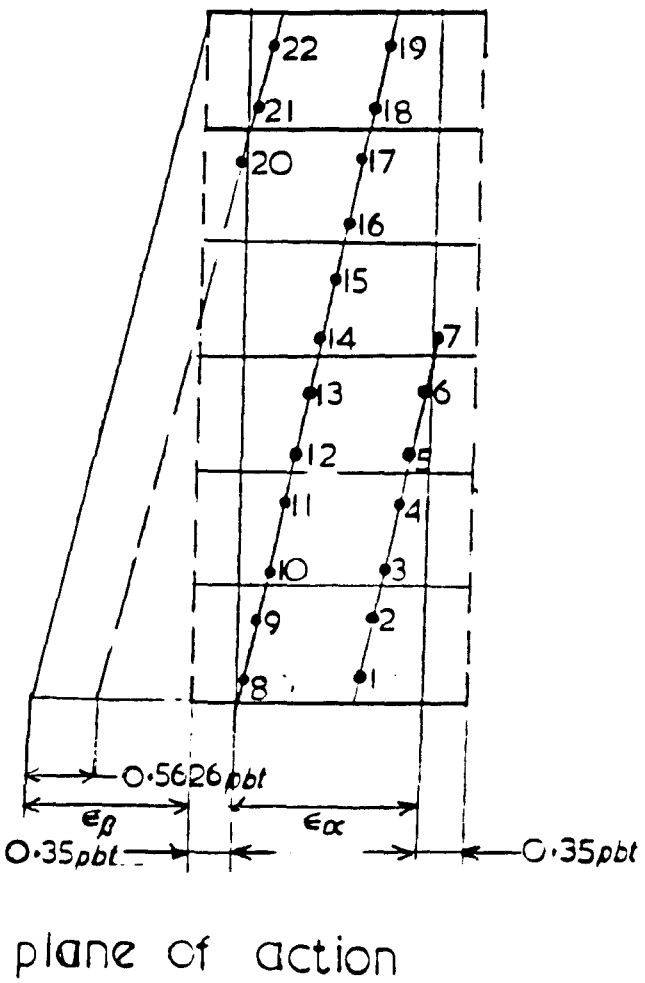

Fig.5.22a Phase 1 Point Loading Data

Gauss pt.	ry [mm]
1	135.9385
2	135.4180
3	135.0495
4	134.5635
5	134.7025
6	141.2945
7	140.6090
8	140.1185
9	139.4645
10	138.9975
11	138.3750
12	137.9315
13	137.3420
14	136.9230
15	136.3665
16	135.9720
17	135.4505
18	143.0160
19	142.5690
20	141.8525
21	141.3385
22	140.6520

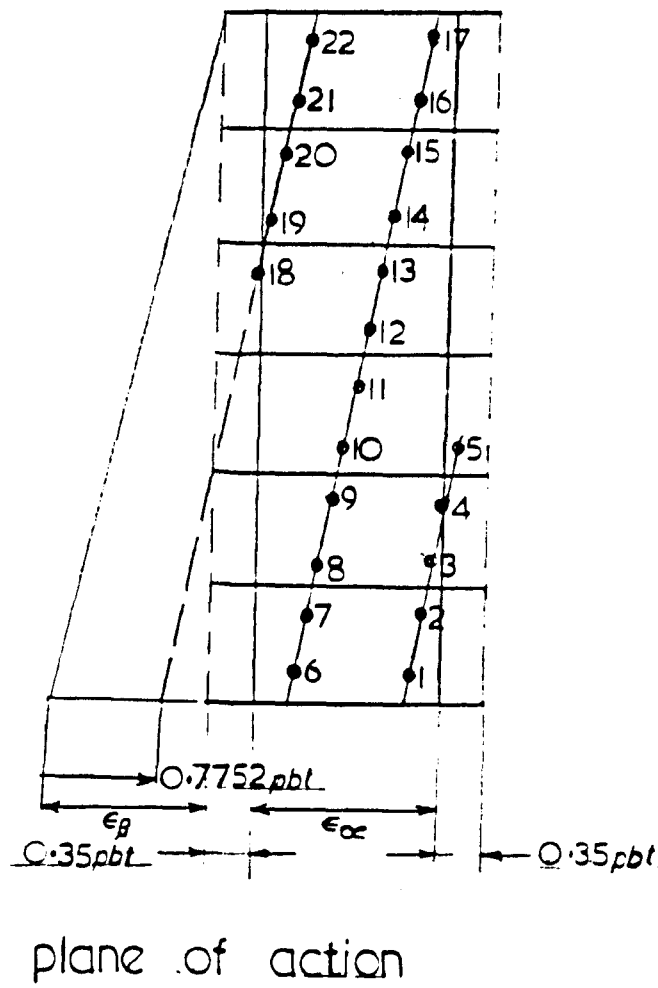

Fig.5.22b Phase 2 Point Loading Data

Gauss pt.	ry [mm]
1	134.9885
2	134.5055
3	134.7720
4	140.0375
5	139.3855
6	138.9200
7	138.3000
8	137.8580
9	137.2710
10	136.8535
11	136.3000
12	135.9070
13	135.3875
14	135.0200
15	134.5355
16	143.0145
17	142.4800
18	141.7655
19	141.2535
20	140.5690
21	140.0795
22	139.4265

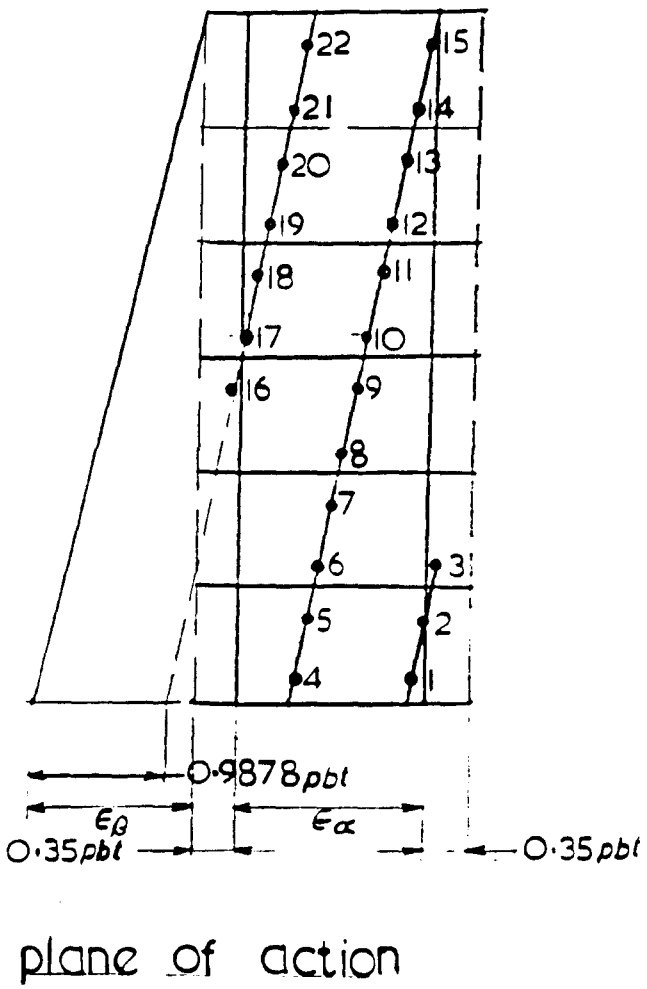

Fig.5.22c Phase 3 Point Loading Data

the effects of friction which were, in any case, quite small. Tests were made with and without a lubricant and the results were in agreement to within 5%.

4. The zero datum jig (see Fig.5.23) was then used to locate the datum position of the gears as previously described, and the ROD 800 readout set to zero.

5. The strain gauge bridges were then balanced and the residual balance values recorded.

6. Immediately after balancing the bridges, the wheel was rotated progressively clockwise (as viewed in Fig.5.20) through phases 3, 2 and 1 in turn, starting with the lowest angle phase 3. At each phase the gauge readings were logged by the UPM60, and the output voltage from the torque bridge circuit was recorded from the Avometer (see Section 5.5).

7. The gauged teeth were then brought completely out of mesh on the other side by rotating the wheel further in the clockwise direction beyond phase 1, at which point the gauges should again be balanced.

8. The residual strain gauge readings were again logged to identify any zero drift (it was generally less than ±2 microstrain).

9. The strain gauges were then re-balanced as in step 5, and the balance values again logged.

10. Step 6 was then repeated but with the wheel this time rotating counterclockwise (as viewed in Fig.5.20) through phases 1, 2 and 3 in turn, starting this time with the largest angle phase 1. During these readings relative motion of the two gears, and any friction effects in the mesh are reversed relative to those in step 6.

11. As in step 7, the gauged teeth were next brought completely out of mesh by further rotating the wheel in the counterclockwise direction beyond phase 3.

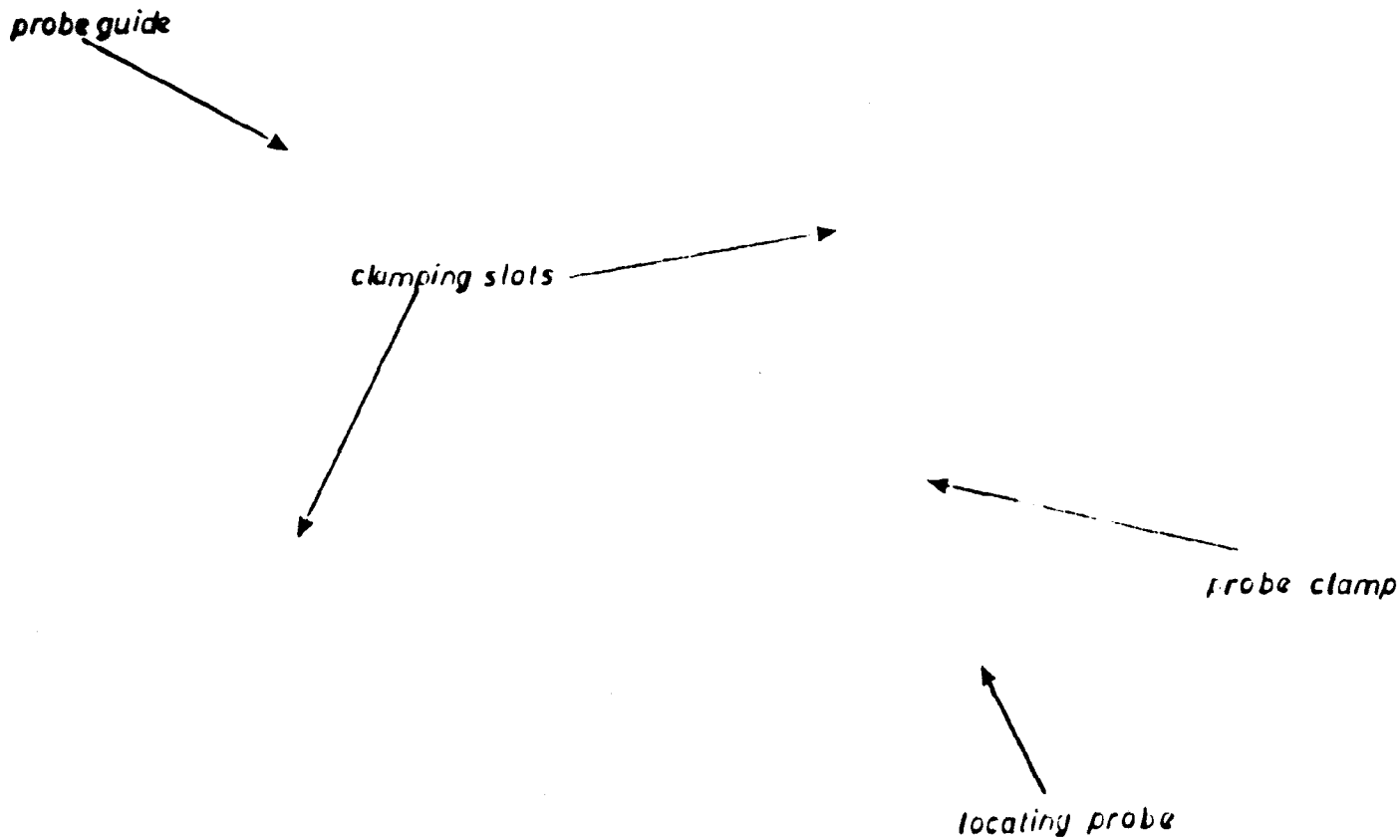

Fig.5.23 Zero Datum Jig

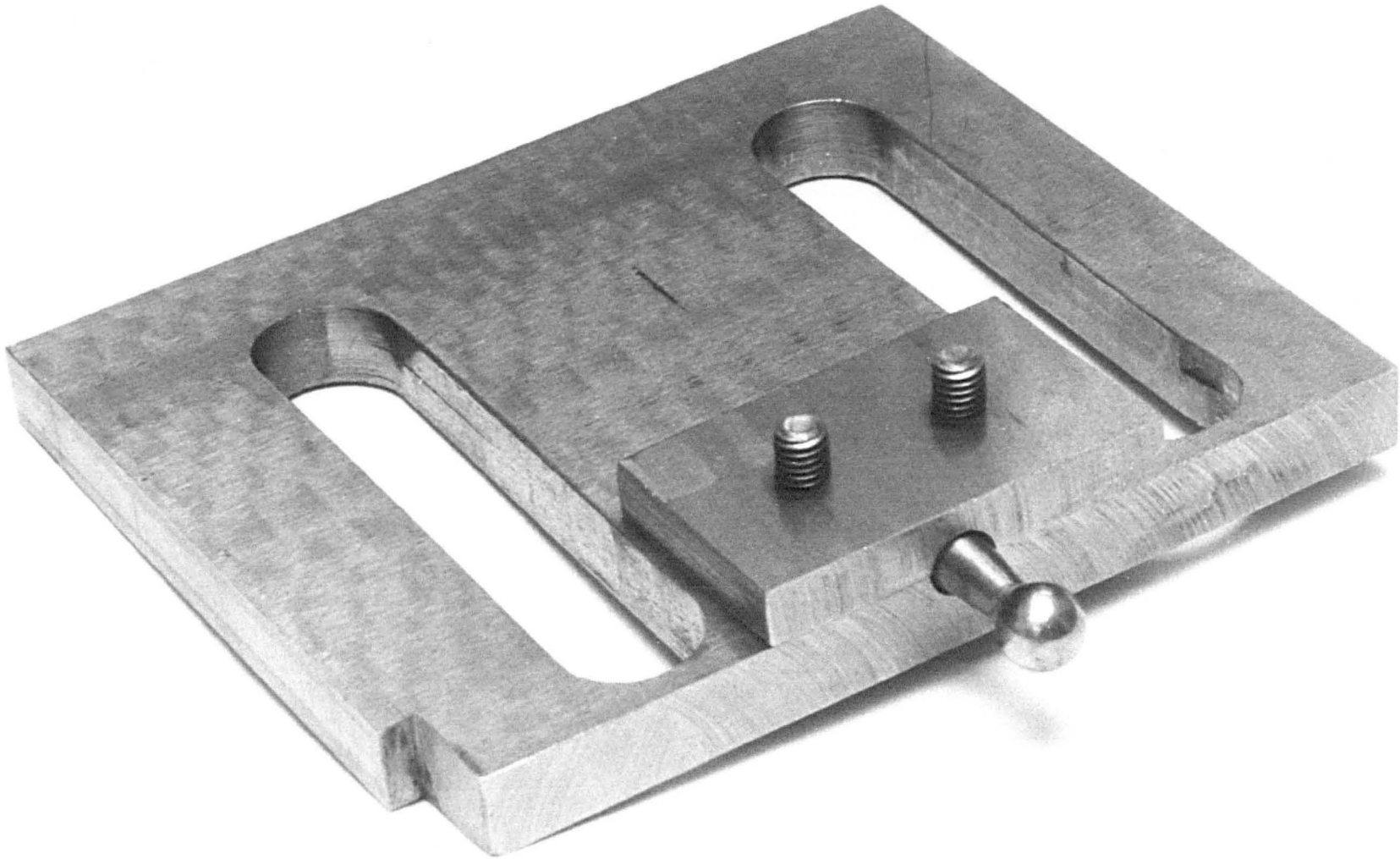

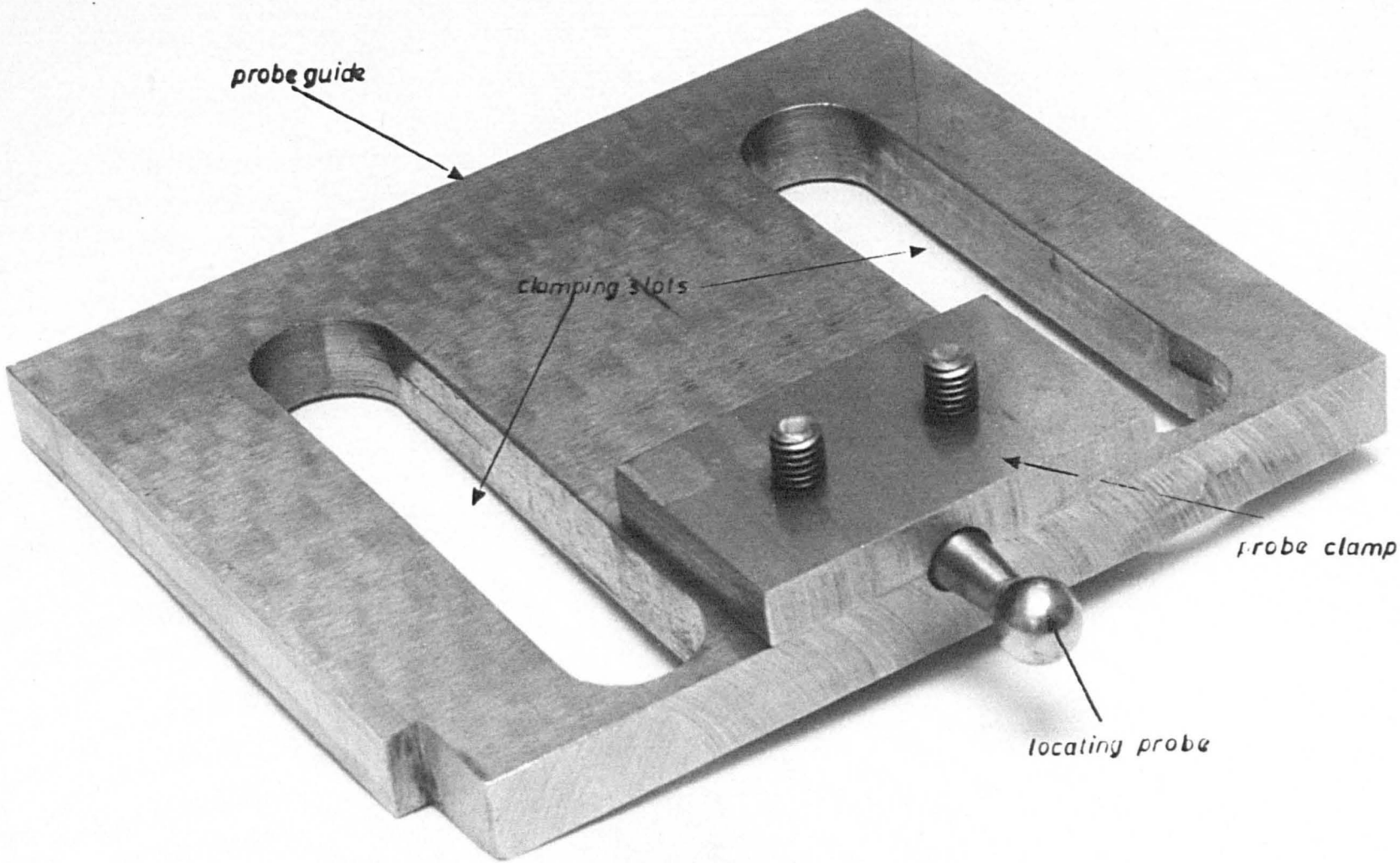

Fig.5.23 Zero Datum Jig

12. The residual strain gauge readings were again logged to check the drift, if any, since the readings taken in step 9 above (generally less than ±1 microstrain).

Steps 2 to 12 were repeated for each position of the shim (i.e. once for each of the 'active' Gauss points).

The results obtained by this process were used to determine the coefficients "a_{ij}" in Eqn. 5.6 (see section 5.5)

As shown in Fig.5.16, the relationship between torque and output voltage from the torsion bar bridge circuit is linear, so that the applied loads F_j will also be proportional to the bridge output voltage.

From the calibration curve of Fig.5.16, a torque of 425Nm gives an output of 1V, from which it can be shown that at any instant

$$(F_{cal})_j = 8620.7\ (V_o)_j \qquad 5.11$$

where $(V_o)_j$ is the instantaneous output from the torque bridge when $(F_{cal})_j$ is applied. This fluctuates slightly as the gears rotate due to varying effects of friction and the tooth errors at the different contact points.

For each load point "j", two values of the calibration strain "ϵ_{ij}" were measured at each gauge "i": one during clockwise rotation (step 7 above), and one during counterclockwise rotation (step 11). These strain values were estimated by subtracting from the logged values the mean of the zero balance residuals logged immediately before and after the test (in steps 5 and 8 for clockwise rotation, and steps 8 and 12 for counterclockwise rotation).

Since the calibration load $(F_{cal})_j$ given by Eqn. 5.11 was, in general, different for the clockwise and counterclockwise calibrations due to friction reversal, the mean calibration strain "ϵ_{ij}" was calculated from

$$(\epsilon_{ij})_{mean} = \left[(\epsilon_{ij})_{ccw} + \frac{(V_o)_{jccw}}{(V_o)_{jcw}} \cdot (\epsilon_{ij})_{cw}\right] / 2 \qquad 5.12$$

whence, the corresponding mean calibration coefficients a_{ij} (Eqn.5.6)

were obtained from

$$a_{ij} = [\epsilon_{ij}]_{mean} / (F_{cal})_j \qquad 5.13$$

where $(F_{cal})_j$ is the point load for the ccw case.

The mean coefficient matrices $[a_{ij}]$ obtained in this way for the three test phases of mesh are given in Appendix 5B. Comparison with Figs. 5.22(a)-(c) shows that each load $(F_{cal})_j$ causes significant strains only on the loaded tooth and only at points within a distance of about 5 .. 6 modules from the loaded point. (see master influence curve of Figs. 2.38 ..2.40.) This result is thus generally in accordance with Jaramillo's[28] conclusion (from plate theory) that the distribution of bending moments (and hence, stresses) along the tooth root is similar to the axial variation of tooth deflections, (Figs. 2.11 .. 2.25).

5.5.3 Experimental Load Distribution

5.5.3.1 Measuring Procedure

As shown in section 5.5.1, to find the load distribution solution from equation 5.6 requires a knowledge of the strains $\{e_i\}$ and the coefficient matrix $[a_{ij}]$. The matrix $[a_{ij}]$ was obtained from the calibration tests described above: here, the measurement of $\{e_i\}$ during the meshing tests is described.

Almost the same procedure was used to determine $\{e_i\}$ as was described for the point loading calibration tests (steps 1 to 12 inclusive), with the exception that no shim was inserted between the teeth. The three angular positions of the wheel, for the three different phases of mesh 1, 2 and 3 were those determined in section 5.6.2: viz. 3.25667°, 1.83913° and 0.42105° respectively, and correspond to input phases in the program "HELICALDIST" of 0.5626147. 0.7752294 and 0.9878441 (p_{bt}). As for point loading, graphite grease was again used on all engaged teeth and the strain gauge readings "e_i" obtained for both cw and ccw rotations of the wheel were averaged in a similar way to give

$$(e_i)_{mean} = \left[(e_i)_{ccw} + \frac{(V_o)_{ccw}}{(V_o)_{cw}} \cdot (e_i)_{cw} \right] /2 \qquad 5.14$$

The mean values $(e_i)_{mean}$ from Eqn. 5.14, and the mean values of the "a_{ij}" given by Eqn. 5.13 were then used in Eqn. 5.6 to calculate the experimental Gauss loads "F_j*" at each point along the simultaneous

contact lines and hence the local load intensity. These results are discussed in Chapter 6.

5.5.3.2 Shaft Misalignment in the Rig

Since the purpose of the experimental work described in this chapter was to verify the theoretical load distributions predicted by the program "HELICALDIST", it is essential to modify the measured gear tooth errors tabulated in Appendix 5A to account for the different instantaneous positions of the shafts in the rig, relative to those on the Gleason and Höfler machines when the tooth errors were measured (see section 5.2.2.1). To go one step further, the eccentricity and roundness errors of the ground rings (section 5.2.2.1), which are used to measure the position of the shafts in the rig may also be accounted for, adding a further modification to the tooth errors of Appendix 5A. Without these corrections, the errors input to the program would not correctly represent the actual meshing conditions during the tests.

Although these two effects are expected to be insignificant, the analysis using "HELICALDIST" will be more comprehensive and accurate once the tooth errors have been modified before being input to the program, thus reducing the uncertainty factor. Consequently, additional measurements must be taken during the actual tests to locate the shafts in the rig relative to the theoretical position (no shaft misalignments). Once the true shaft positions have been determined, the tooth errors tabulated in Appendix 5A (measured relative to the Gleason/Höfler axis) may be corrected for the axes in the rig.

The misalignment measuring devices and their method of use have already been described in section 5.2.2.9. In this section, the analysis of the measured misalignment is discussed.

First, consider shaft misalignments in the vertical direction (normal to the line of centres of the gears). Referring to Fig. 5.24, and recalling (section 5.2.2.9) that the probe is located over the pinion ring near the torque-up end (see Fig. 5.12a), then any deflection of the probe upwards (positive reading) tends to bring the teeth close together and should be treated as metal addition in program "HELICALDIST". Downward deflections of the probe (negative reading) tend to separate the teeth and are treated as negative metal in "HELICALDIST". The probe deflections "δ_v" must now be transformed into the "transverse" plane of action along the base tangent to give

$$\delta_{vt} = \delta_v \cdot \cos \alpha_t \qquad 5.15$$

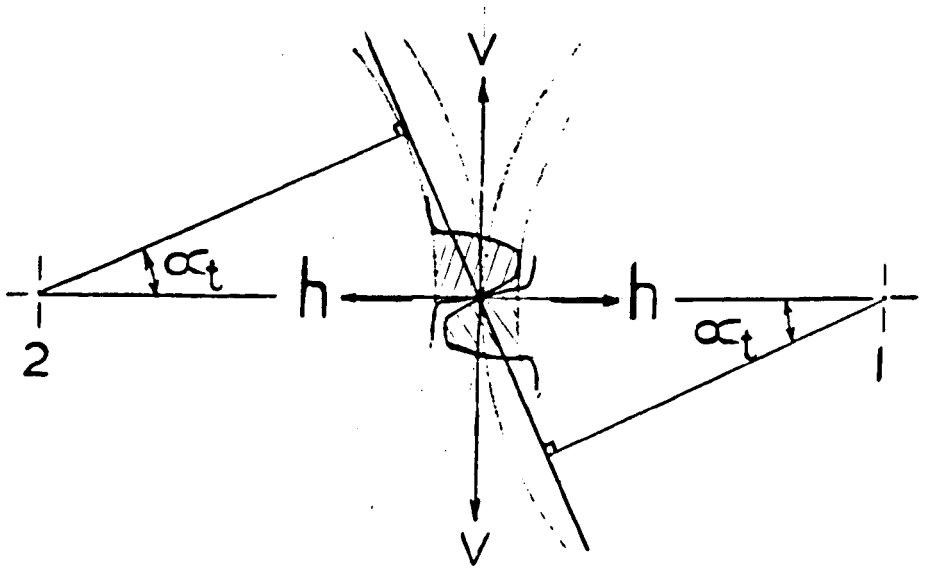

Fig.5.24 Transverse Section Through Gears Showing Vertical & Horizontal Directions & Loaded Side of Tooth

The angular misalignment is given by,

$$\theta_{vt} = \delta_{vt}/\ell \qquad 5.16$$

where ℓ is the distance between the rings at opposite ends of one shaft. Since the measuring device is in contact with the other three rings, the value given by equation 5.15 may be considered as the relative misalignment of the pinion shaft to the wheel shaft. Note that the zero position of the probe was determined by sitting the square table with ground surfaces on a parallel surface.

Next, consider shaft misalignments in the horizontal direction (along the line of centres of the gears). Contrary to the case of vertical misalignment, the zero position of the probes is not crucial in the case of horizontal misalignments since we are only interested in the difference of the difference in the two probe readings at both ends of the shafts. However, for convenience, the zero position was located by setting the two triangular bell cranks (Fig. 5.12b) such that the distance between them is equal to the nominal distance between the shaft centres (when unloaded) less the sum of the nominal theoretical radii of the two rings at each end.

The convention used for positive or negative readings is clearly shown in Fig. 5.25 where the actual horizontal misalignments are given by multiplying the probe readings by 2.625 (73.5/28). Again positive readings bring the shafts together and are thus treated as positive metal in "HELICALDIST", whereas negative readings tend to separate the shafts and are thus treated as negative metal in "HELICALDIST".

Considering the torque-up side of the shafts, then

$$\delta_{h1} = 2.625 \cdot (\delta_{A1}+\delta_{B1}) \qquad 5.17$$

whereas at the opposite side of the shafts

$$\delta_{h2} = 2.625 \cdot (\delta_{A2}+\delta_{B2}) \qquad 5.18$$

where δ_A and δ_B are the two probe readings (see Fig. 5.12b), and the resultant is

$$\delta_h = \delta_{h1} - \delta_{h2} \qquad 5.19$$

where equations 5.17 to 5.19 are algebric sums based on the convention

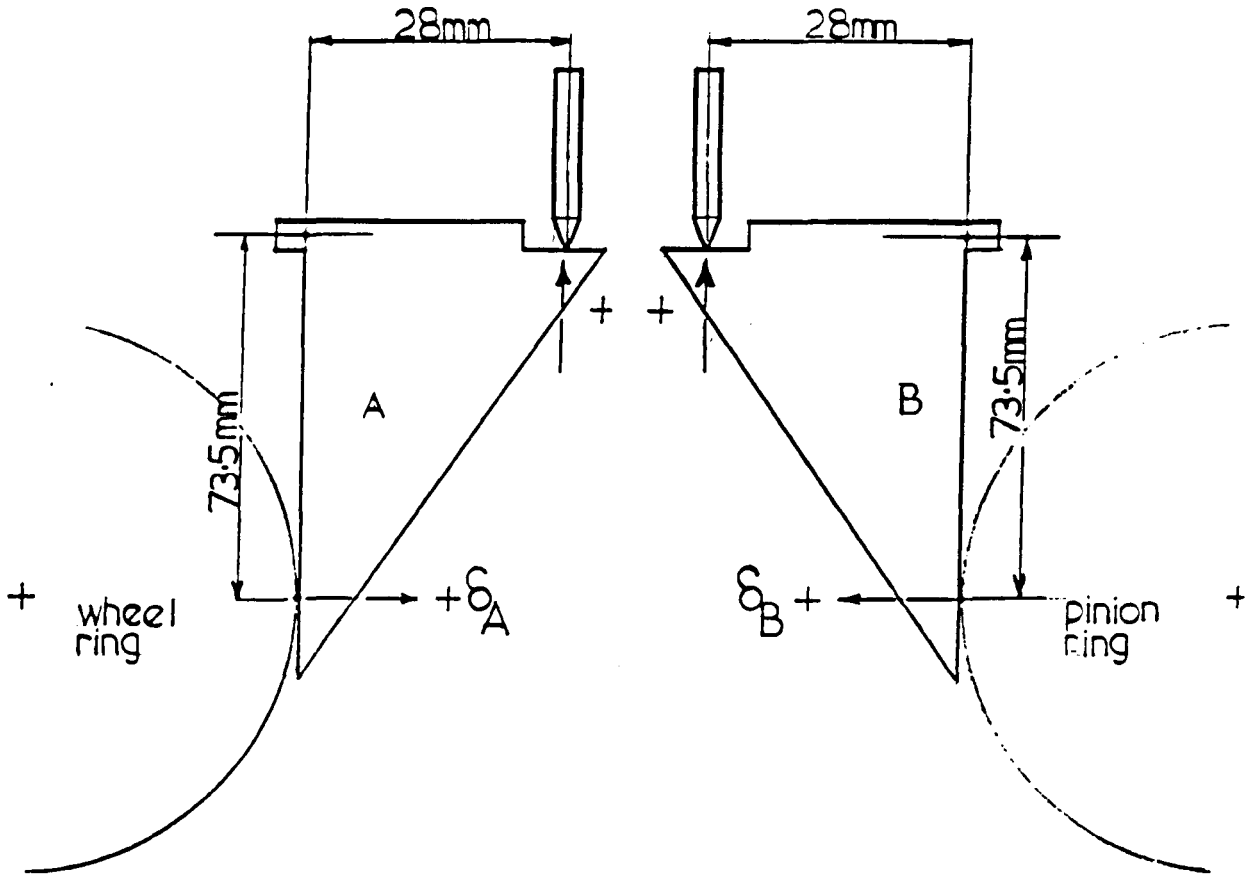

Fig.5.25 Convention Used in the Measurement of Horizontal Misalignments

described in Fig. 5.25. If the resultant is negative it means the shafts tend to separate (negative metal in "HELICALDIST"), and if it is positive it means the shafts tend to move closer together (positive metal in "HELICALDIST"). To transform the resultant horizontal misalignment "δ_h" into the "transverse" plane of action along the base tangent we have

$$\delta_{ht} = \delta_h \cdot \sin \alpha_t \qquad 5.20$$

and the angular misalignment is given by

$$\theta_{ht} = \delta_{ht}/\ell \qquad 5.21$$

where ℓ is as defined earlier.

Finally, the overall misalignment in the transverse plane along the base tangent is the algebric sum of θ_{vt} and θ_{ht}

$$\theta_t = \theta_{vt} + \theta_{ht} \qquad 5.22$$

which must be determined for each of the three test phases of mesh and then added algebraically to <u>one</u> of the meshing gear's tooth alignment errors $f_{H\beta}$ (conveniently added to the pinion tooth errors), since the value of "θ_t" is a relative misalignment of one of the shafts to the other. Before this final step however, "θ_t" must further be corrected since it was derived by assuming that the shaft rings are concentric and perfectly round. This however is not the case and the ring errors must be accounted for (see first two paragraphs of this section).

In order to account for ring errors, the following equation will be used (refer to Fig. 5.26) to determine the actual roundness errors "Δr_i" of the rings at any point "i",

$$\Delta r_i = \Delta r_{im} - \Delta \bar{r} - e \cdot \cos(\theta_i - \varphi) \qquad 5.23$$

where

Δr_{im} - actual (measured) runout reading of the rings at point "i" (tables 5A.3 and 5A.6).

$\Delta \bar{r}$ - is the (arbitrary) mean of the measured runout readings of the rings "Δr_{im}" taken on the Gleason/Höfler (tables 5A.3,

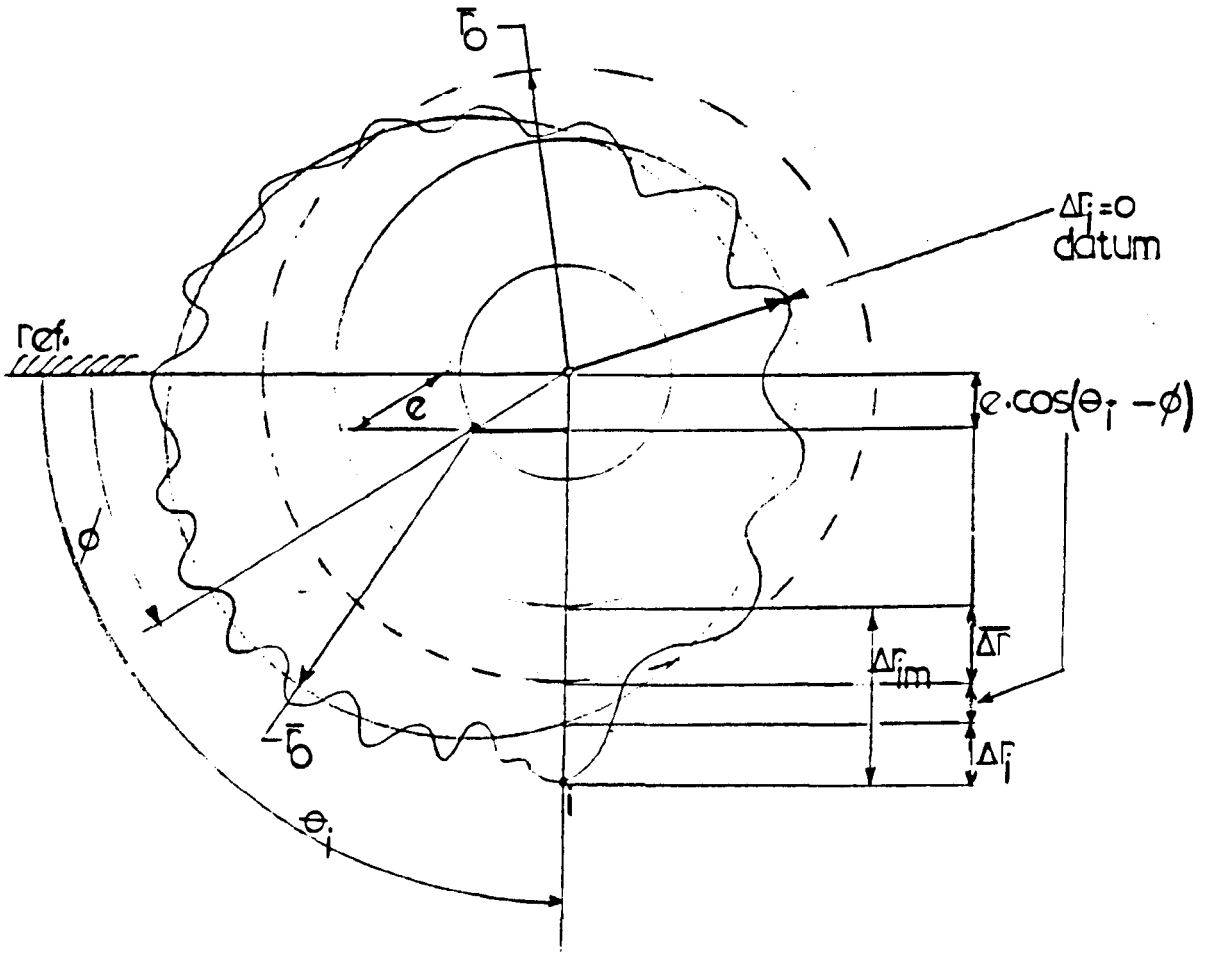

Fig.5.26 Ground Ring Eccentricity and Radial Run_Out

5A.6 and 5C.1).

e – is the eccentricity of the mean (best fit) circle in direction φ (Fig. 5.25).

$(\theta_i - \varphi)$ – is the angle between point "i" and the point where maximum eccentricity "e" occurs on the ring surface (see Appendix 5C).

By plotting the runout readings listed in Appendix 5A, the best fit circle corresponding to sine wave variations of "Δr_{im}" was easily deduced "by eye". Almost identical results were obtained from one set of data with much greater effort by "Fourier analysis". In any case "e" and "$\theta_i - \varphi$" could be obtained and "Δr_i" is calculable from equation 5.23.

The results are tabulated in Appendix 5C for points "i" corresponding to the four contact points of the alignment jig with the rings at the three mesh phases tested.

Similar values of Δr_i (agreeing to within $\pm 2\mu m$, in spite of additional variations caused by run-out/eccentricity of the rig bearings) were obtained by analysing the runout readings of Tables 5a.8 and 5a.9.

Finally, the vertical and horizontal misalignments may be corrected for, and equation 5.22 may now be modified as

$$(\theta_t)_{mod} = \theta_{vt} - [(\delta_{vrB1} - \delta_{vrB2}) - (\delta_{vrA1} - \delta_{vrA2})].\cos(\alpha_t)/\ell + \theta_{ht} - [(\delta_{hrB1} - \delta_{hrB2}) + (\delta_{hrA1} - \delta_{hrA2})].\sin(\alpha_t)/\ell \qquad 5.24$$

where

$$\delta r = \bar{r}_o + \Delta r_i - r_{th} \qquad 5.25$$

and

$\bar{r}_o$ – mean <u>measured</u> radius of a ring given by

$$\left[\frac{1}{N} \cdot \sum_{1}^{N} [d_{meas}/2]\right]$$

where the comparator of Fig. 5.27 was used to measure the diameters (see Appendix 5C).

r_{th} – is the theoretical (intended) radius of a ring (note that this is constant and cancels out in equation 5.24 and has a value of 60.5mm for each ring).

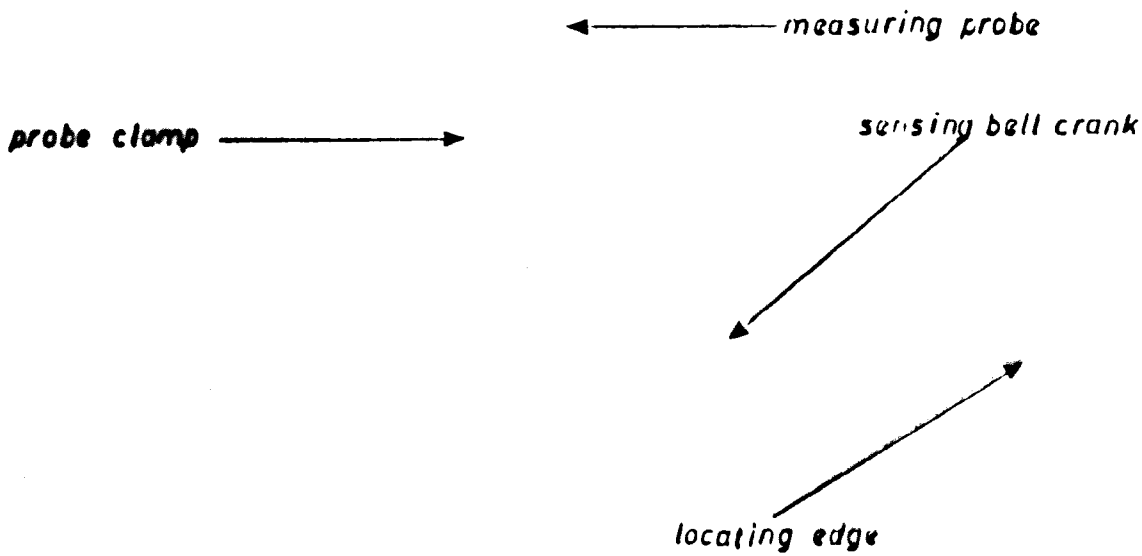

Fig.5.27 Comparator for Measurement of Reference Band Dia.

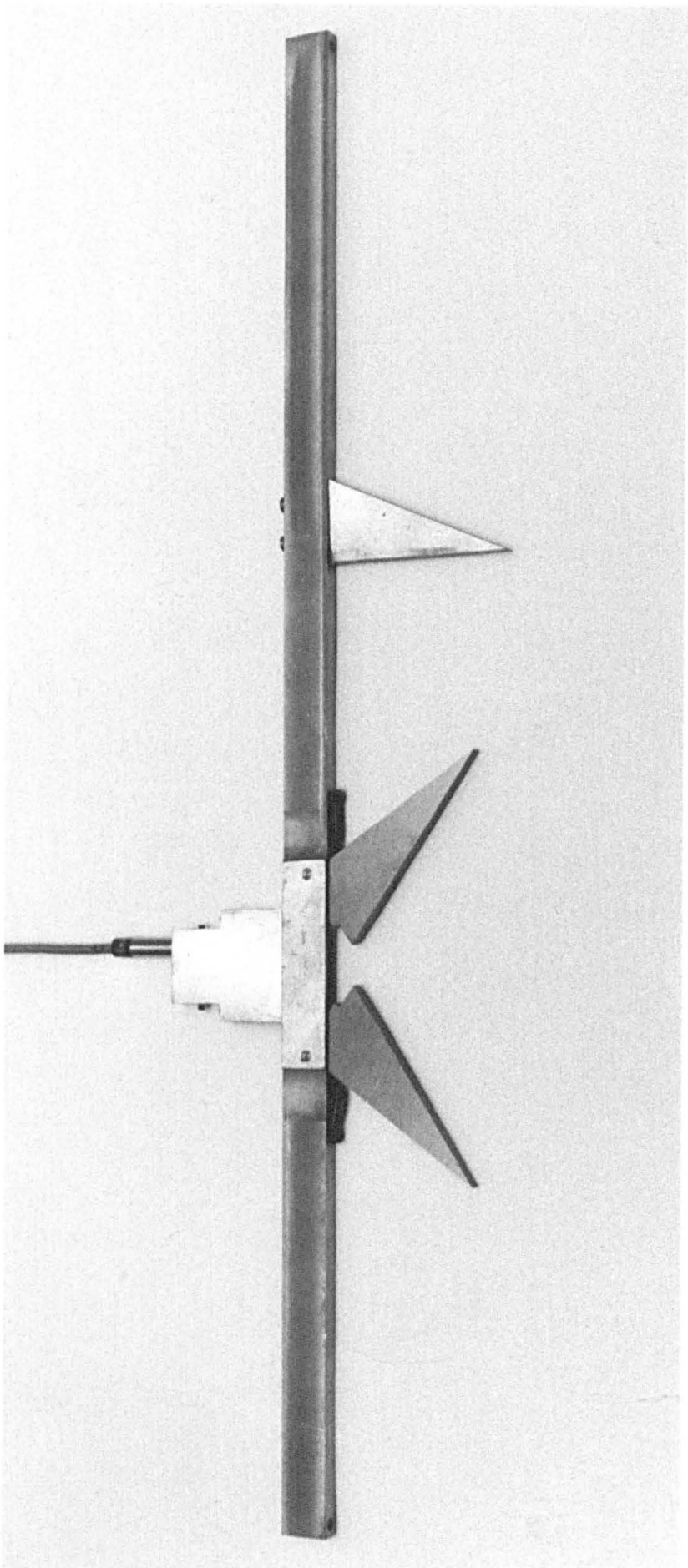

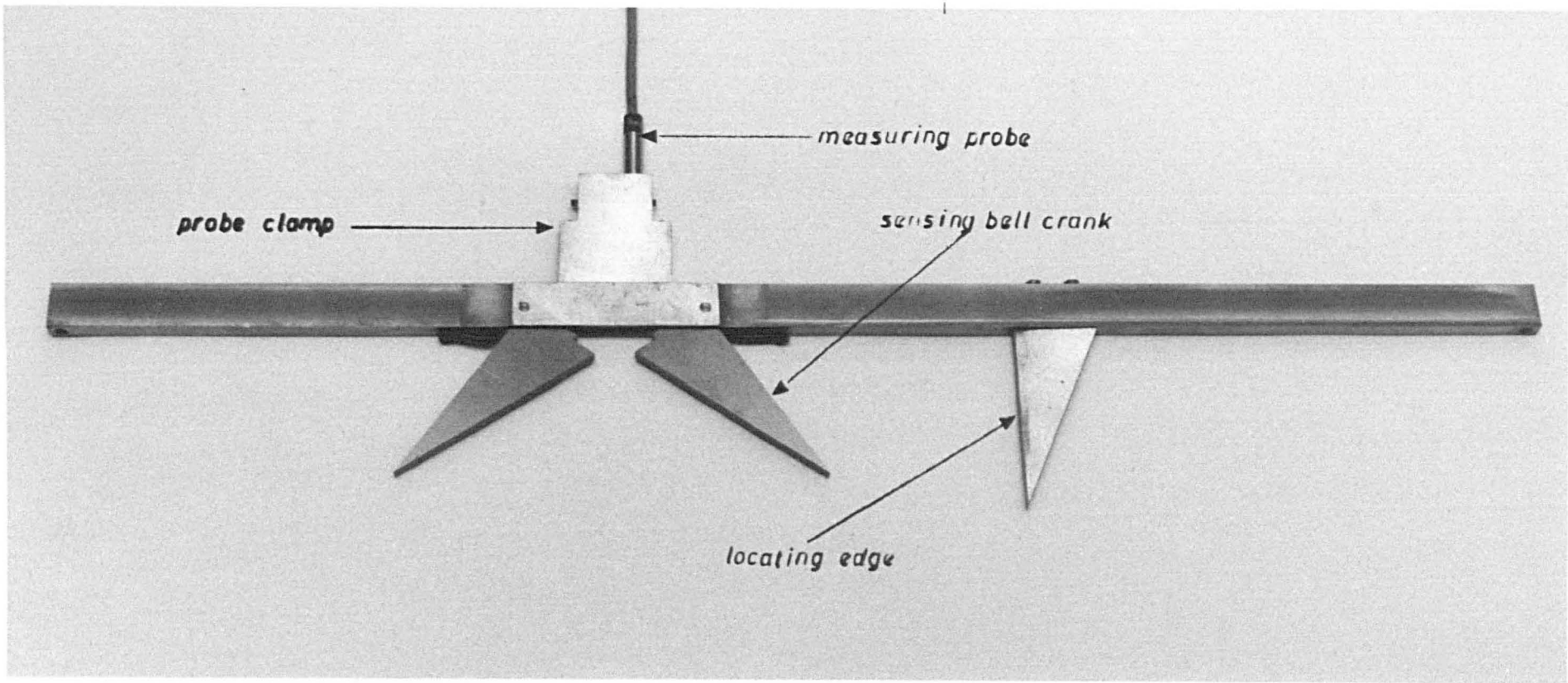

Fig.5.27 Comparator for Measurement of Reference Band Dia.

Δr_i - as given by equation 5.23.

ℓ - as defined in equations 5.16 and 5.21.

Using equation 5.25, "δr" for each of the four rings is calculated and may be positive or negative, and the sign obtained is entered unaltered in equation 5.24 (algebric sum) where subscripts

1 - refers to rings at torque-up end

2 - refers to rings at other end

A - refers to wheel rings

B - refers to pinion rings

v - refers to vertical errors

h - refers to horizontal errors.

Appendix 5C calculates the actual values of $(\theta_t)_{mod}$ for each of the three test phases, which must be added algebraically to the engaged teeth measured average misalignments (table 6A.2) as determined by the Gleason/Höfler, and analysed in section 6.2.2. Table 5C.1 is a listing of "$\Delta\bar{r}$", "Δr_{im}", "e" and "$|\theta_i - \varphi|$", and table 5C.2 is a listing of "Δr_i", "δr" and "θ_t". Note that in equation 5.24, "δr" is transformed into an angular measure in the transverse plane along the base tangent line and the values "θ_t" are as calculated in Appendix 5C. $(\theta_t)_{mod}$ is then calculated from the results given in table 5C.2.

Note that all modifications due to misalignments and ring imperfections were defined in the transverse plane along the base tangent since the measured tooth errors were also obtained in that direction on the Gleason/Höfler. Program "HELICALDIST" transforms all these errors into the normal plane, normal to the tooth flank as shown in equation 6.1.

The experimental load distribution results are presented in chapter 6 along with the theoretical results, and will not be plotted here to avoid repetition.

5.6 Transmission Error Measurements

The transmission error f_t was measured experimentally by means of the "Klingelnberg PEW02" apparatus shown in Fig. 5.1, which transforms the relative rotations of the pinion and wheel shafts into a displacement at the pitch point, by using the output signals from the wheel encoder (sine wave from ROD 800) and the pinion encoder (square wave from ROD 270).

Upon inputting the proper gear and encoder specifications, the built-in micro-computer program calculates the transmission errors throughout the specified test cycle at each angular position of the test gears and plots them

out. With the gears very lightly loaded (just to bring the teeth in contact), and taking the datum position shown in Fig. 5.20 as an arbitrary zero position, the transmission error is plotted as shown in Fig. 5.28(a) with the three test phases 1, 2 and 3 as shown (the fine curve is the "filtered" signal showing only the low frequency variations). Since this is at near zero load, the plot only shows the effect of the gear tooth errors and misalignments, but not the effect of gear and shaft deformations. The curve plotted, however, does not represent absolute values of the transmission error since the zero datum position selected does not necessarily represent zero transmission error. Therefore the plot is only a measure of the variation (relative to the zero datum position at the start of the test) in the transmission error during the test cycle. Unfortunately, a separate "VRZ" counter capable of decoding the pulses from the "ROD 270" encoder was not available, so absolute rotations could only be measured on the wheel.

The same test described above was made under full-load (526.5 Nm), and the results are shown in the plot of Fig. 5.28(b). This test however fails to show the additional transmission error caused by shaft and gear deformation, it does on the other hand show the change in the pattern of "f_t", caused by these deformations. More details on this are discussed in section 6.5. The test phases 1, 2 and 3 in Fig. 5.28 in terms of revolutions of the "wheel" are 0.00905, 0.00511 and 0.00117 rev. respectively.

One method to determine the transmission error due to loading was to load-up the gear to maximum load and to record the angular displacement on the counter attached to encoder ROD 800 on the wheel (no counter was available for ROD 270). During loading, the locking arm and plate (Fig. 5.11b) restrained the pinion hollow shaft from rotation, however, these are elastic components and do tend to deform under load. To determine the amount of this deformation, the loads were slowly removed, after the ringfeder was tightened to hold in the torque, and so the applied load now acted only upon the arm and plate. Upon unloading, the counter reading dropped by a certain amount which was substracted from the first reading, thus giving the true relative rotation of the shafts, as measured by ROD 800 at the end of the wheel shaft.

Referring to Fig. 6.1 and realising that wheel shaft rotations are minimal across the facewidth, this represents the relative rotations of the two shafts at gear mid-face, which may be converted into displacement at the pitch radius. The first reading gave 0.1400° and the second reading gave a drop of 0.1199 and so, the relative shaft rotation is 0.0201. Converting this into displacement at the pitch radius gives (this rotation does not include the effects of tooth errors/misalignments),

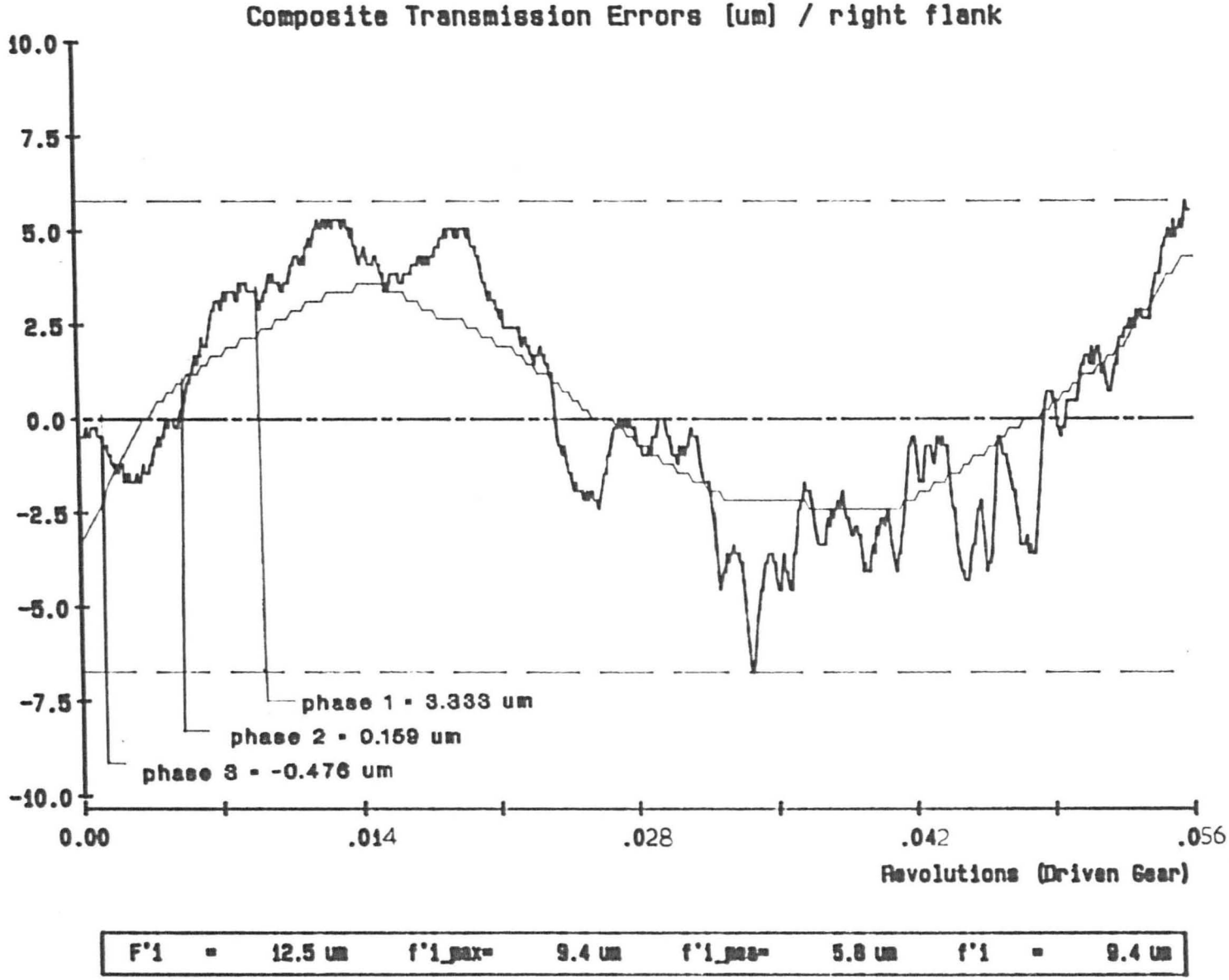

Fig.5.28a Transmission Error Measurement (no_load)

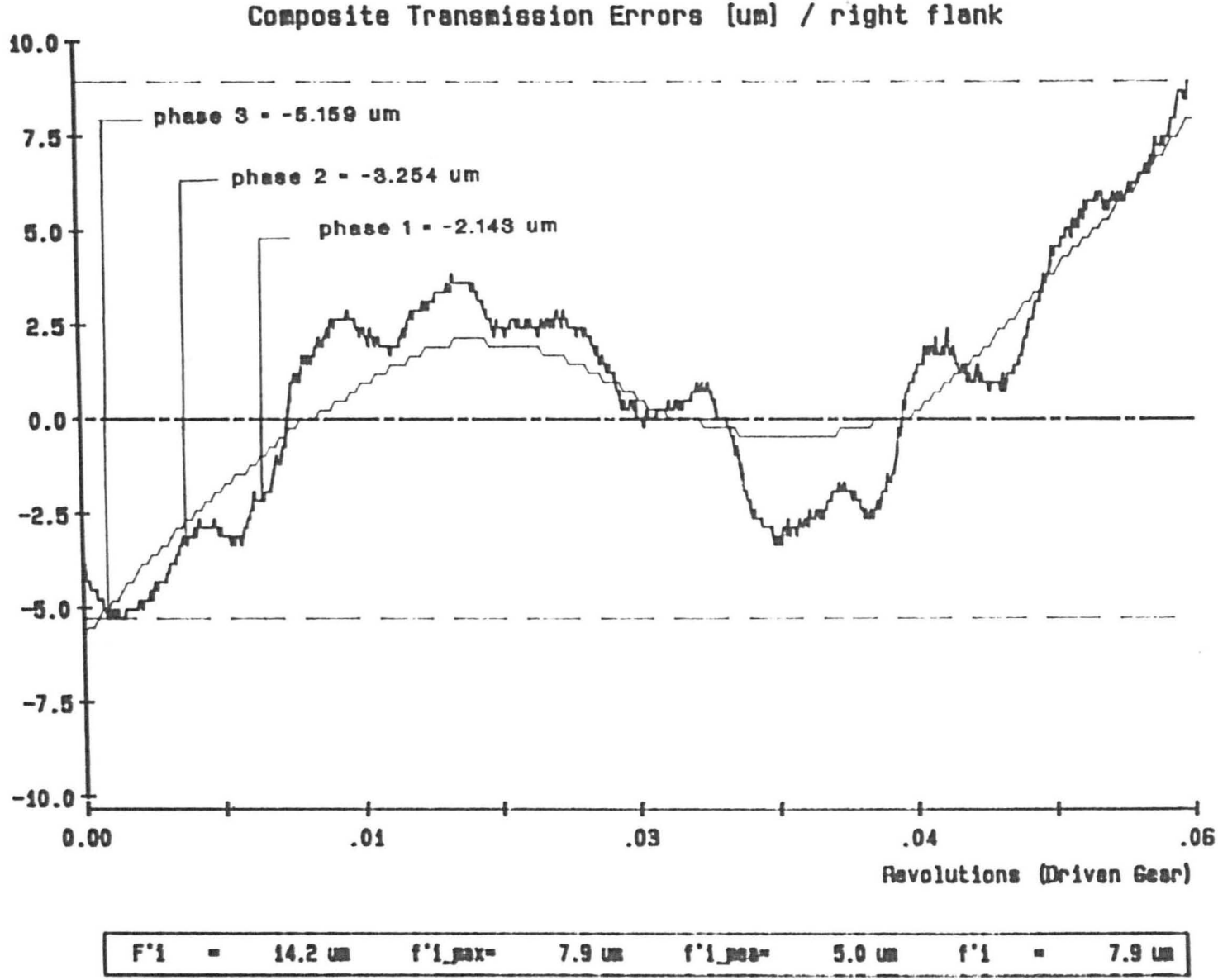

Fig.5.28b Transmission Error Measurement (full_load)

$$\left[0.0201^{\circ} \times \frac{\pi}{180}\right] \times 138.0\text{mm} = 0.0484\text{mm} = 48.4\mu\text{m}$$

where the wheel pitch radius is 138.0mm. Further comments on this point are presented in Chapter 6.

Although a direct comparison of transmission error with theoretical results is not possible, the pattern of variation in transmission error may be compared, and this is done in Chapter 6, where the theoretical transmission error for the three test phases is obtained from programme "HELICALDIST".

5.7 Probable Sources of Error

Experimental errors are unavoidable and may be due to many factors, which will be discussed in this section.

Gear tooth errors although mesured on highly sophisticated machines (Gleason/Höfler) are expected to produce results with an error of no more or less than $\mp 2\mu$m. The eccentricity of the axis of rotation and ring roundness errors were accounted for in detail in section 5.5.3.2.

The jig for measuring vertical misalignment (Fig. 5.12a) accounts for "relative" positions of the reference rings in the rig, and since all surfaces were machined and ground to the same degree of accuracy, errors are expected to be comparable at each contacting point thus cancelling out one another in the final reading. Four sets of readings yielded a repeatability to within $\pm 0.9\mu$m ($\pm 3\%$).

Similarly, the errors in the readings at the four positions of the rings in the rig, using the horizontal misalignment measuring jig (Fig. 5.12b), are comparable and cancel out upon taking differences in readings. The repeatability however was not very good amounting to $\pm 48\mu$m ($\pm 12\%$). Nevertheless, this has no effect on the final results since complimentary readings varied by comparable amounts, which cancel out upon taking differences (Fig. 5.24).

The comparator used for measuring reference ring diameter (Fig. 5.27) is a modification of the horizontal misalignment measuring jig (Fig. 5.12b), and the same analyses on error and repeatablity applies. However, as indicated by equations 5.24 and 5.25, these errors cancel out since they are comparable. As shown in Appendix 5C, the averaged measured diameters of the rings were within -0.03mm (-0.025%) of the intended nominal diameter of 121.0mm. Since on all four rings, the measurements were within -0.0291, -0.0288, -0.0275, and -0.0287mm of the nominal diameter, these results show

good consistancy possibly verifying the validity of the measurements.

As discussed in section 5.5.2, frictional effects play an important role. This is caused by bearing friction, mesh friction, etc.... To quantify the effect of mesh friction, readings with a lubricating grease to minimise friction were taken. Considering a typical case during the point loading procedure, the strain readings "ϵ" for opposing directions of motion varied from 56.0 μstrain to 58.35 μstrain. Considering a typical case during the actual meshing tests, the strain readings "e" for opposing direction of motion with the use of a lubricant were 67 μstrain and 83 μstrain. To reduce these frictional effects, equations 5.12 and 5.14 were used. This procedure however only accounts for mesh friction. The output torque as recorded by the Avometer must be corrected for bearing and other frictional losses. To quantify this error, a 1m long arm with weights was used to apply the load, and the Avometer reading was taken. The actual torque applied (weight in N x arm length in m) was then used to find the voltage output from Fig. 5.16 (which as discussed in section 5.4 is practically free of frictional effects). This voltage exceeded that given by the Avometer reading by mostly 3%, rendering any torque corrections unnecessary.

The location of the strain gauges at the 30° tangent line at the tooth root is accomplished with a jig which is made of a sticky tape. This tape acquires the form of the tooth flank and the gauge positions may easily be marked on it. The tape may then be rolled down the flank thus locating the gauge positions axially (Fig. 5.8) and radially. Slip gauges locate gauge positions very accurately on the tape, but the gauges have to be then glued to the root, and that is where human error comes in. Some gauges were observed to be at least ±1mm off their proper locations.

A similar problem arises when attempting to locate the shim (during point load calibration) to coincide with the axial position of a gauge. Again a jig was devised by locating the axial positions of the gauges on a sticky tape (using slip gauges) which when fixed to the tooth top land gives a good indication of where the shim must be. However, the shim was glued into position by eye, and that was estimated to throw it off position by at least ±1mm. A further complication arose during point loading the sections near the tooth ends. This obviously required one of the ends of the T-shaped shim which sits on the top land of the tooth to be cut-off. As a result, the shim seemed to be significantly dislocated during point loading. This may explain the large discrepancies between experimental and theoretical results at the tooth ends as explained in section 6.4

The zero datum jig (Fig. 5.23) was designed so as to locate the probe centre at tooth mid-face and along the line of centres of the gears (Fig.

5.20). As shown in Fig. 5.1, the guides for the jig are the parallel bearing cap inside surfaces and the flat casing surface on which the jig rests. All these surfaces are machined but not ground. The misalignment along the bearing caps (jig's length) was measured to be about 200μm. Also the jig's width was made 200μm smaller than the nominal gap between the guiding caps. It is also estimated that the surface of the casing on which the jig rests is misaligned by roughly 200μm. From geometric considerations, the worst possible combination of these misalignments, was found to result in an angular position error of only a fraction of the angular rotation needed to produce any significant change in strain readings. It was demonstrated that an angular rotation of up to 0.1° (larger than any angular error) hardly caused any change in strain readings. The repeatability of the jig was better than 0.001° also.

Drift on the Fylde amplifier and Avometer was observed only during the first 20 minutes of turning the power on, after which a "constant" value of torque reading in volts was maintained for the rest of the testing period.

Drift was also observed on the UPM60, and seemed to progress over long periods of time, but at a very slow rate. As discussed in section 5.5, the tests were made within one minute of zero balancing to reduce the amount of drift, and the balance values were recorded again after the test was completed. Typically, the amount of drift from start to finish of a test was about 2 to 3 μstrain. To overcome this effect, the mean of the zero balance residual before and after a test were subtracted from the actual strain readings (section 5.5.2). Typical peak strains during meshing tests were up to 800μstrain and during point loading they were up to 90μstrain.

Electrical noise was completely eliminated by using the screen shown in the circuitry diagram of Fig. 5.9.

For transmission error measurements as well as phase location, encoder errors should be looked at. First, consider ROD 800 (Figs. 5.1 and 5.2) with coupling K01. K01 is expected to give a kinematic error of transfer of ±1 angular second (consisting of a radial runout λ = 100μm, and an angular error α = 0.09° which results in 78.5μm over the whole length of coupling, see Fig. 5.29). In the worst case, the resultant error of transfer is a misalignment of 178.5μm.

The misalignment of the adaptor fixed on the wheel shaft to which the K01 and ROD 800 are coupled is measured to be within ±10μm (adjusting screws can further improve this value). Therefore, in the worst case the total error of transfer is less than 200μm (178.5+10), whereas the permissible values of λ and α are ±300μm and ±0.5° respectively, each in itself being larger than the combined worst error of 200μm. Clearly the additional 10μm

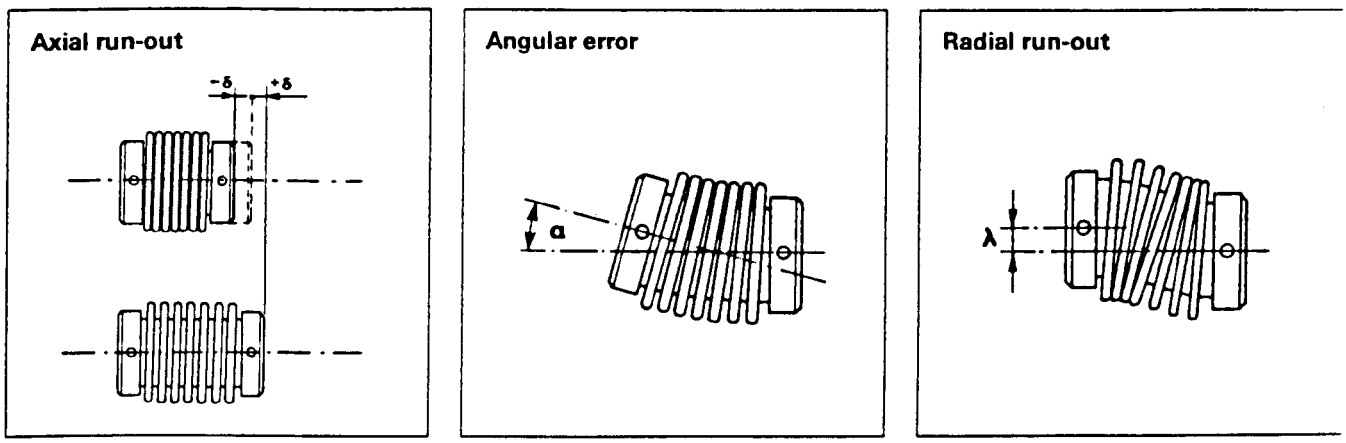

Fig.5.29 Encoder Coupling Error and Run_Out

(±10μm) adaptor misalignment has a negligible effect on the already tiny error of ±1 angular second. The ROD 800 itself is highly accurate with a fine angular resolution of 0.0001°.

Another source of error affecting the output from ROD 800 is the relative deformations of shaft to gear casing. This was checked by resting the measuring probe on the bearing cap (part of the casing) and checking the readings of the probe (which is made to contact the adaptor vertically/ horizontally) before and after loading. The difference in probe readings before and after loading was less than 3μm, surely an insignificant error.

Considering encoder ROD 270 (Fig. 5.1 and 5.2), it is indirectly driven by the large friction drive press fitted onto the helical pinion shaft, and contacting the smaller friction wheel coupled to ROD 270. Coupling type K03 connects ROD 270 to the small friction wheel. It is less accurate than type K01, giving a kinematic error of transfer ±2 angular seconds.

A source of error which might influence output from ROD 270 is the radial runout on both friction drives. The mean runouts on the small and large drives were measured to be 2.25 and 2.05μm respectively, giving a total mean runout in the worst case of 4.30μm. From geometric considerations, such runout values have no significant effect on encoder transmission.

Another source of error is as before the relative deformation of shaft to casing. Again probe readings in the vertical and horizontal direction were less than 2μm as in the case of encoder ROD 800 (an insignificant misalignment compared with the total K01 alignment error of 278.5μm which gives ±2 angular seconds error).

Bearing runout errors may also contribute to errors in encoder output. However, upon comparison of radial runout readings in Appendix 5A measured on the Gleason/Höfler, with those measured inside the rig, the wheel shaft bearings show negligible bearing runout. Pinion Shaft bearings show a runout of up to 15μm, which as shown earlier hardly affects encoder readings.

So far, only the possibility of experimental errors has been investigated. As discussed in section 6.4, the theoretical results may be in error as a result of filtering out the misalignment and profile errors (the wave form was ignored by taking the best fit line through the error curve along the tooth facewidth/tooth height). The magnitudes of the wave forms can be inspected from the tables in Appendix 5A ($f_{\beta f}$ and f_f). It is shown in section 6.4 that discrepancies in the load intensity of ±10N/mm result from using filtered errors in program "HELICALDIST".

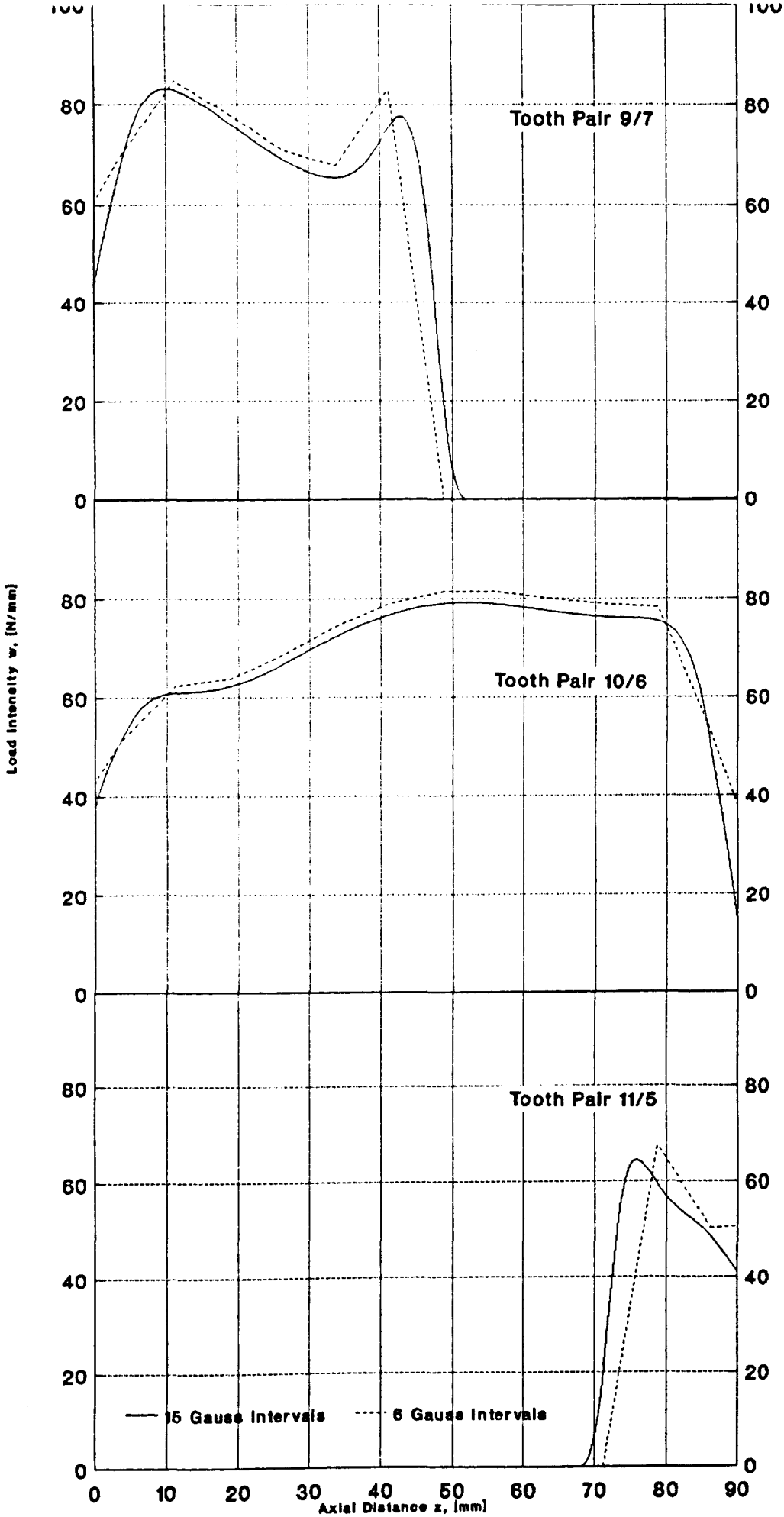

Fig.5.30 Effect of Number of Gauss Intervals on load Distribution Solution

Another possible source of error in the theoretical results is that the Gauss interval of integration used was too big (see section 6.4). Very recently, more advanced computing facilities allowed for the use of much smaller Gauss intervals in "HELICALDIST". Fig. 5.30 compares the results for two pairs of meshing perfect gears using 6 and 15 Gauss intervals. The figure however does not show any major discrepancies between the two sets of results.

******

CHAPTER 6

COMPARISON OF THEORETICAL AND EXPERIMENTAL RESULTS

6.1 Introduction

Before a direct comparison between the experimental results and those obtained from program "HELICALDIST" is possible, two further steps are needed. First, the measured gear tooth errors tabulated in Appendix 5A (in the transverse plane) must be approximated by analytical expressions as in Eqn.6.1. Secondly, the shaft deflections must be calculated, since, as explained in section 2.5, they were excluded from the gear compliance functions "K_{tb}" of Eqn.2.14.

6.2 Analytical Approximation to Measured Gear Tooth Errors

6.2.1 Form of Error Equation

Program "HELICALDIST" incorporates an equation for calculating the errors "δ_e" appearing in Eqn.2.14. From Figs.4.16, 4.3, 4.8(b), 4.4, 4.14 and 4.12, the error equation takes the form (see comments below)

$$\delta_e = \cos(\beta_b).[F_p.\cos(\alpha_t) - f_{H\beta}.z/b + f_{H\alpha}.y/(h_{Na}+h_{Nf}) + f_{yz}.y.z/(b.(h_{Na}+h_{Nf})) - c_c.z.z/b^2 - c_\alpha.y.y/h_N^2 - c_e.(z-b_e)/(b/2-b_e) - c_y.(y-h_y)/(h-h_y)] \quad 6.1a$$

where

- y – is the radial distance from the reference circle to the contact point.
- h_y – is the radial distance from the reference circle to the start of tip/root relief (c_{ay}/c_{fy}).
- z – is the axial distance from mid-face of the tooth to the contact point (see Figs.5.6 and 5.7).
- b_e – is the axial distance from mid-face of the tooth to the start of end relief (c_e) as can be seen in Fig.4.4.
- f_{yz} – is the "twist" error associated with variations of "$f_{H\beta}$" radially up the tooth flank, or variations of "$f_{H\alpha}$" axially across the tooth flank.

The following must be applied to Eqn.6.1a:

1) In the sixth term:

if $y > 0$ then $c_\alpha = c_{\alpha a}$ and $h_N = h_{Na}$ (Fig.4.14)

if $y < 0$ then $c_\alpha = c_{\alpha f}$ and $h_N = h_{Nf}$ (Fig.4.14)

2) In the seventh term:

if $z > 0$ then $b_e > 0$

if $z < 0$ then $b_e < 0$ and b/2 is replaced by -b/2.

3) In the eighth term:

if $y > 0$ then $c_y = c_{ay}$ and $h_y = h_{ay}$ (Fig.4.12) and $h = h_a$

if $y < 0$ then $c_y = c_{fy}$ and $h_y = h_{fy}$ (not shown in Fig.4.12) and $h = -h_f$.

The factor $\cos(\alpha_t)$ in the first term of Eqn.6.1a transforms circular cumulative pitch error (F_p) into the base tangent direction. All the terms need to be multiplied by $\cos(\beta_b)$ as shown since "δ_e" in Eqn.2.14 is the error in the normal plane normal to the tooth flank, whereas the errors $f_{H\alpha}$, $f_{H\beta}$, F_p, etc.... are all defined and measured in the transverse plane.

The error equation in "HELICALDIST" can also actually account for tooth errors due to pitting or wear craters, but this has not been shown in Eqn.6.1a.

Since the tooth errors were measured over test ranges a little smaller than "b" or "$h_{Na} + h_{Nf}$", and realizing that the Gleason/Höfler give "$f_{H\beta}$" and "$f_{H\alpha}$" based on the test ranges, it becomes necessary to replace "b" and "$h_{Na} + h_{Nf}$" in Eqn.6.1a by the test ranges "ℓ_1" and "ℓ_2" respectively.

6.2.2 Analysis of Measured Gear Tooth Errors

As shown in Figs.5.6 and 5.7 and Appendix 5A, the tooth errors were measured at nine points (F_p), on three radial sections ($f_{H\beta}$), and on three axial sections ($f_{H\alpha}$). The error measurements revealed no tip or root relief, no profile or face crowning and no end relief so that only the first four terms of Eqn.6.1a need be considered ($c_c = c_\alpha = c_e = c_y = 0$). Eqn.6.1a thus reduces to

$$\delta_e = \cos(\beta_b).[F_p.\cos(\alpha_t) - f_{H\beta}.z/\ell_1 + f_{H\alpha}.y/\ell_2 + f_{yz}.y.z/(\ell_1.\ell_2)]$$

6.1b

Considering Figs.5.6 and 5.7, pitch errors were measured at all nine grid points (y=0, $\pm y_1$ and z=0, $\pm z_1$), so it follows from Eqn.6.1b that the best estimate of "F_p" is obtained by averaging the nine measured values (see Table 6A.1 for results obtained).

Similar considerations show that the values of "$f_{H\alpha}$" and "$f_{H\beta}$" used in Eqn.6.1b should be the mean, in each case, of the three measured values on each flank (see Tables 6A.2 and 6A.3).

The twist coefficient "f_{yz}" can be determined from the variations of either "$f_{H\beta}$" or "$f_{H\alpha}$", and is given by (see Figs.5.6 and 5.7)

$$(f_{yz})_1 = [(f_{H\alpha})_{aa} - (f_{H\alpha})_{cc}] \qquad 6.2a$$

or

$$(f_{yz})_2 = [(f_{H\beta})_{a'a'} - (f_{H\beta})_{c'c'}] \qquad 6.2b$$

The mean of these two values was used in the analysis (see Table 6A.4).

In all cases, the measured errors used in Eqn.6.1 were <u>first</u> modified, as explained in section 5.5.3.2, to allow for the misalignment $(\theta_t)_{mod}$ of the two shafts in the test rig, (also see Appendix 5C).

The misalignment $(\theta_t)_{mod}$ is added to the already <u>averaged</u> misalignment errors $(f_{H\beta})_{avg}/\ell_1$, and the results are listed in Table 6A.5 as $(f_{H\beta})_{mod}$ where, as mentioned earlier, the modification was only made to the pinion tooth misalignments.

6.3 <u>Shaft Deformations</u>

As explained in section 6.1, the stiffness coefficients used in program "HELICALDIST" do not include the effect of shaft deformations. However provisions were made in the program to allow for input of shaft deformations. The main advantage in this is that the FE results from which the stiffness coefficients were derived are based on a specific shaft support arrangement (sec.2.5), so that removing the FE shaft deformations enables the entry of different theoretically-determined values for any type of support arrangement.

Referring to Fig.6.1a, it is evident that both shafts are subjected to the effect of tooth loads on the slave spur gears. The spur gear wheel is directly overhung on the wheel shaft, and the spur pinion is supported on needle bearings inside the hollow pinion shaft and so, effectively also overhung on the pinion shaft. In both cases, the effect of the additional loads can be calculated by superposing the bending/shear deflections due to the spur gear tooth loads, on those already calculated in Appendix 2C caused by the helical gear loads.

The generalized bending moment and shear force diagrams for the

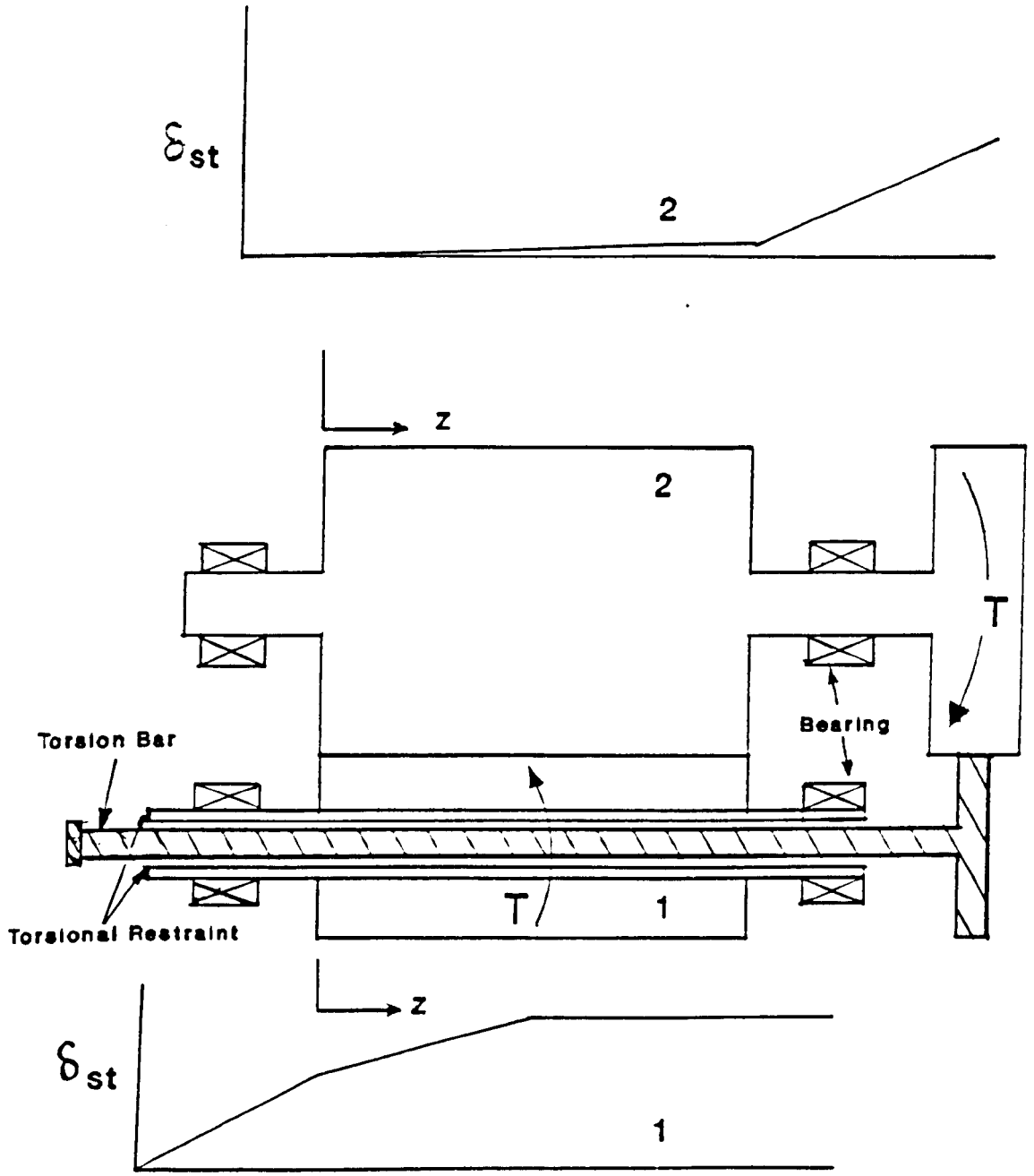

Fig.6.1a Cross_Section Showing Shaft Orientation & Torsional Restraints in Rig

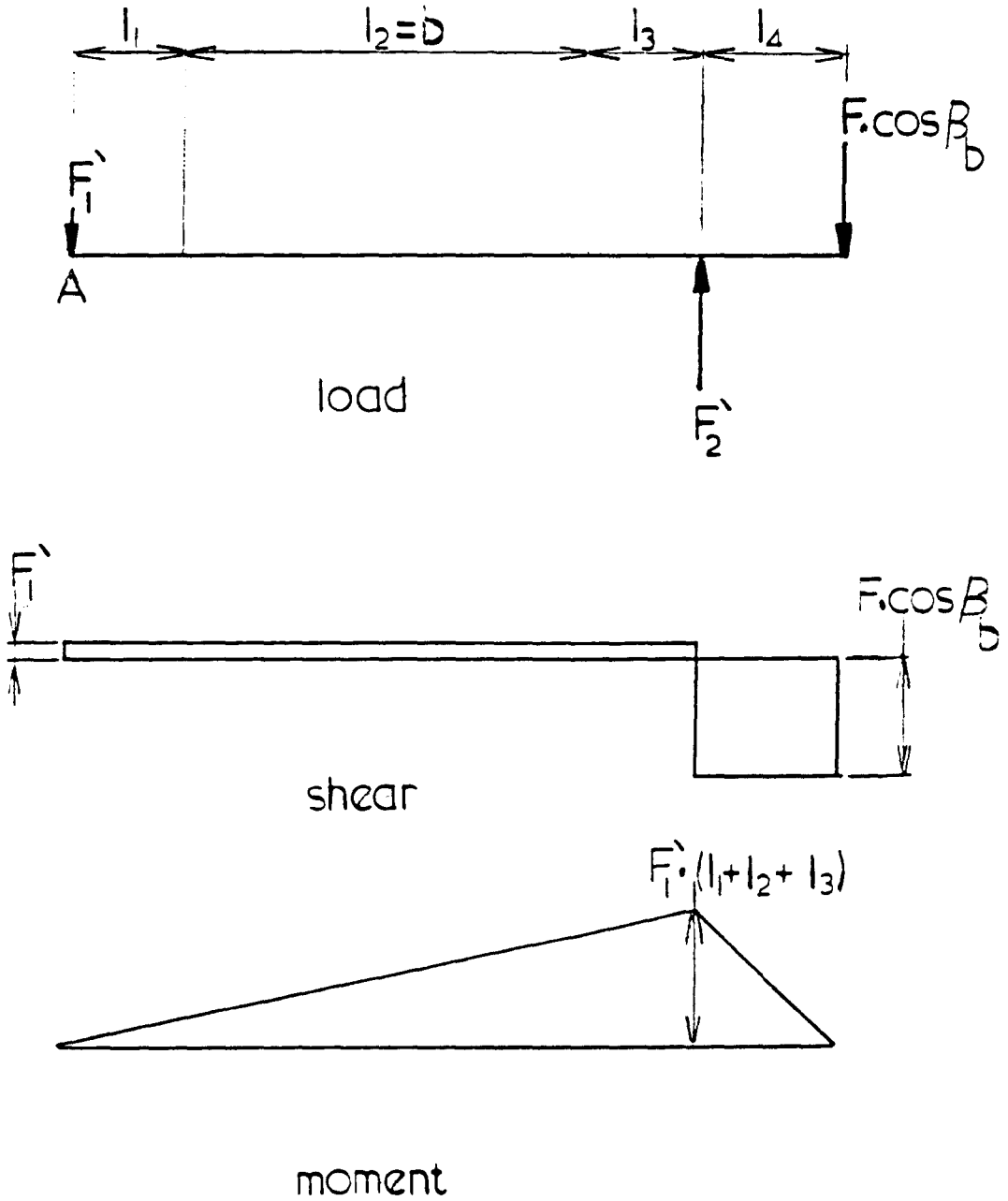

Fig.6.1b Load, Moment & Shear Force Diagram of Overhung Load

overhung spur gear loading (wheel or pinion) are as shown in Fig.6.1b. The shear force in the section of interest is small, so shear deflections were in this case ignored. The bending deflection δ'_{sb} at point "z" where $0<z<b$ is given by the exact same expression given in Eqn. 2C.24 of Appendix 2C, however, F_1, F_2 and θ_A are replaced by F_1', F_2' and θ_A'. F_1' and F_2' are determined from Fig. 6.1a to be

$$F_1' = F_2' - F \cdot \cos\beta_b \qquad 6.3a$$

$$F_2' = \frac{F.\cos(\beta_b)}{(1-\ell_{4/\ell})} \qquad 6.3b$$

where $\ell = \ell_1+\ell_2+\ell_3+\ell_4$ and F is the total normal load acting on the helical gears. From basic theory, the slope θ'_A was derived and is given by

$$\theta'_A = -\frac{F_1'}{E.I_1.(\ell_1+\ell_2)}\left(\ell_1.\ell_3^2/2+\ell_2.\ell_3^2/2+\ell_1^2.\ell_2/2+\ell_1^2.\ell_3/2+\ell_1^3/6\right)$$

$$-\frac{F_1'}{E.I_2.(\ell_1+\ell_2)}\left(\ell_1.\ell_2^2/2+\ell_1.\ell_2.\ell_3+\ell_2^2.\ell_3/2+\ell_2^3/6\right) \qquad 6.3c$$

where I_1 and I_2 are as defined in Appendix 2C with the proper modification to I_2 in the case of the hollow pinion shaft. The corresponding slope θ'_{sb} was ignored for the same reasons discussed in Appendix 2C.

δ'_{sb} is in the plane of action of the spur gears. To resolve it normally to the tooth flanks of the helical gears, the relative inclination of the two base tangent planes of action must be considered. This gives

$$(\delta'_{sb})_n = \delta'_{sb} \cdot \cos(\beta_b) \cdot \cos(\alpha_t + \alpha'_t) \qquad 6.4$$

where α_t and α'_t are the transverse pressure angles of the helical and spur gears respectively.

The equations in Appendix 2C (modified to allow for the hollow helical pinion shaft), coupled with the additional bending deformations due to the overhung spur gears as described above, were incorporated in a micro-computer program and the results are listed in Appendix 6B. These shaft deformations were input as values of "δ_s" (Eqn.2.14) in the program "HELICALDIST".

6.4 Theoretical and Experimental Load Distribution Results

Theoretical load distributions were obtained from "HELICALDIST" for

the test gears specified in Table 5.1 using the error and shaft deflection results obtained in section 6.3. A mean test torque of 526.5 Nm was used.

Experimental load distributions were derived from the experimental strain readings "e_i" (tabulated in Appendix 5B) using the calibration coefficients "a_{ij}" (also tabulated in Appendix 5B) determined in Chapter 5, by solving the matrix equation 5.6.

Figures 6.2, 6.3 and 6.4 show a comparison of the theoretical and experimental load distribution results for test phases 1, 2 and 3 respectively. The load distributions along each of the three simultaneous contact lines were plotted separately at each of the test phases as shown.

The figures show that the theoretical and experimental load distributions are generally in good agreement.

On tooth pair 9/7 for all three test phases, the theoretical and experimental results are in relatively very good agreement, although the loads are in all cases low and within the experimental error band (see section 5.7).

On tooth pair 10/6, the agreement is generally good except for the end points in phases 1 and 2 where theory predicts much smaller load intensities than those deduced from experiment. As discussed in section 5.7, greater experimental errors are likely at the tooth ends, and since phase 3 does not seem to exhibit these discrepancies, it may be that these end of tooth differences are the result of the experimental errors discussed in section 5.7.

Tooth pair 10/6 also exhibits another discrepancy in all three test cases (but mostly test cases 1 and 2) where the difference between the theoretical and experimental results in clearly cyclic, changing sign at alternate Gauss points. This again must be an experimental effect, since as shown in section 5.7, Fig.5.30, altering the number and spacing of the Gauss points had a negligible effect on the theoretical results for the test gears, while the Gauss points themselves have no physical significance so far as the actual behaviour of the gears is concerned.

Cyclic variations of the calibration coefficients "a_{ij}" in alternate rows or columns of the matrix is evident from the results tabulated in Appendix 5B, but can easily be attributed to the alternately long–short pitch of the Gauss point axial locations at which the strain gauges were located (see Fig.5.8). These cyclic errors have not, so far, been explained. It is worth noting, however, that if alternate experimental points are averaged and the results plotted at mid positions (to eliminate the unexplained cyclic error) the resultant curves will be in excellent agreement with the theory, except as previously noted, at the tooth ends.

On the highly misaligned tooth pair 11/5, the sharply peaked curves also show excellent agreement except, as for the other tooth pairs, at the tooth

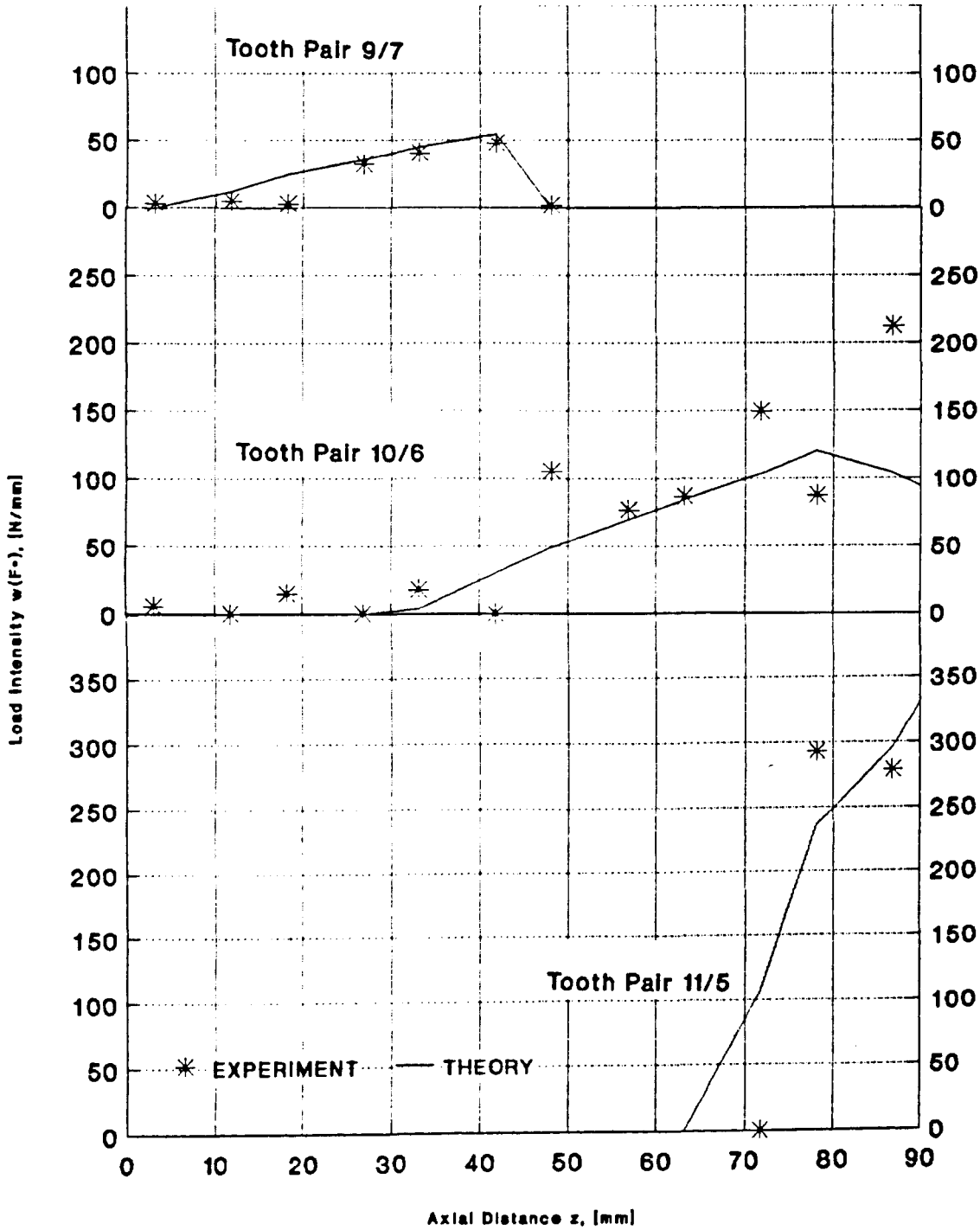

Fig.6.2 Phase 1 Load Distribution Along the Contact Lines of Simultaneously Engaged Tooth_Pairs

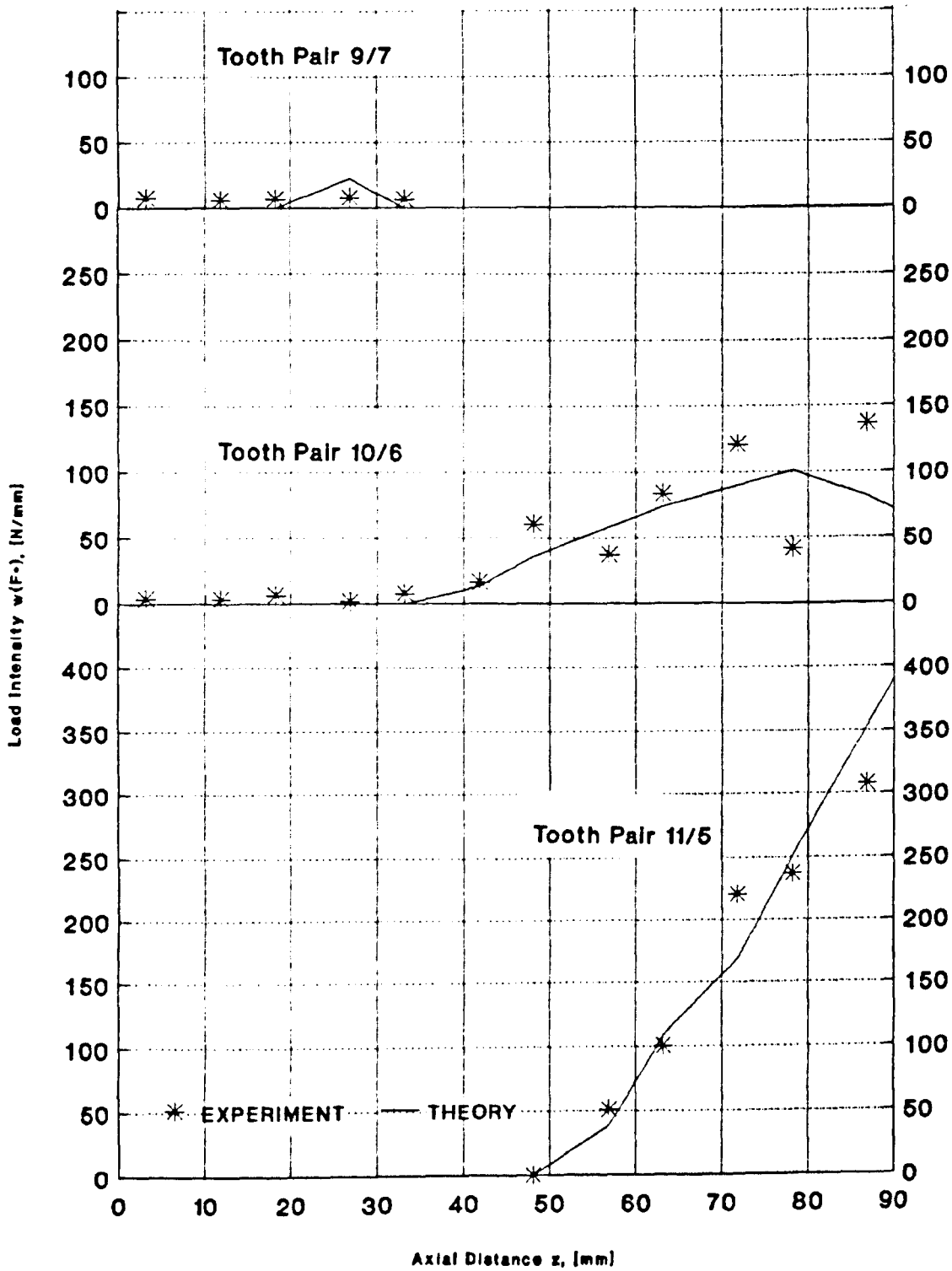

Fig.6.3 Phase 2 Load Distribution Along the Contact Lines of Simultaneously Engaged Tooth_Pairs

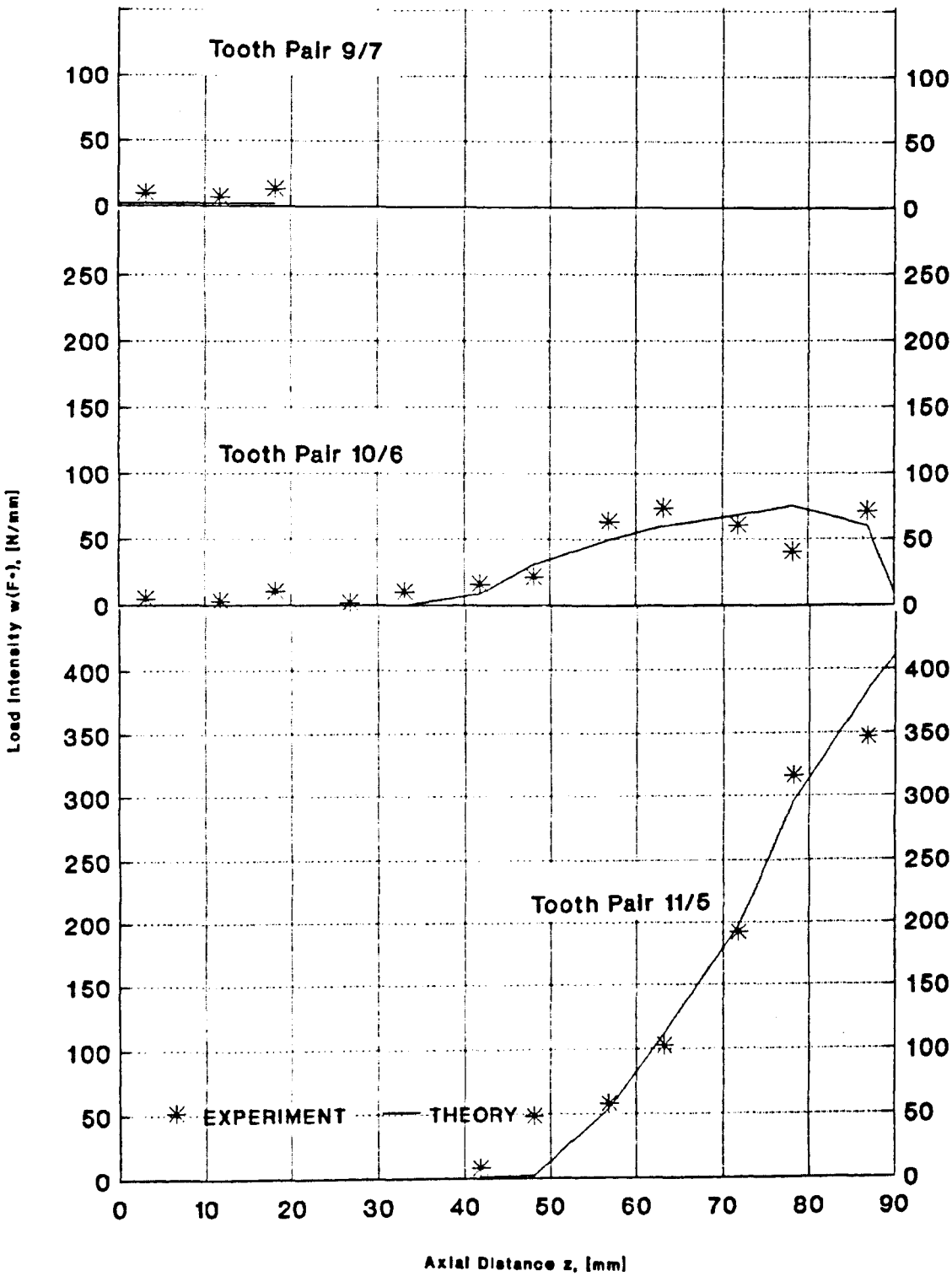

Fig.6.4 Phase 3 Load Distribution Along the Contact Lines of Simultaneously Engaged Tooth_Pairs

ends. Possibly, the unexplained periodic error contributes to the overall experimental error at this point, but it is here far less evident than on tooth pair 10/6.

Another possible cause of the discrepancies is that Eqn.6.1 inadequately models the actual tooth flank errors as mentioned earlier in section 5.7. However, a comparison of the actual measured errors at a few points across the face width, with those obtained using Eqn.6.1 showed no obvious systematic or cyclic component, and peak discrepancies only caused differences of order ±10 N/mm in the load intensity.

Another possibility that remains is that the gear measurements failed to identify positive tooth flank errors localized (say) at the corners of the teeth. These could cause higher theoretical values at the ends of the 10/6 and 11/5 contact lines, for example. It would be worthwhile to carry out some contact line tests along the nine contact lines involved (using the Höfler tester) to check this when the test rig is next dismantled, but this has not, so far, been possible.

As a final check on the overall accuracy of the results, the total normal tooth load was estimated by adding all the experimentally-determined Gauss loads, and comparing the result with the values calculated from the measured torques. For test phase 1, the experimentally determined load was 3.5% larger than the calculated one, for test phase 2, it was 5.5% larger and for test phase 3 it was 6.0% larger, clearly indicating good agreement.

In all, upon obtaining the percentage differences between the theoretical and experimental values in Figs. 6.2, 6.3 and 6.4 (except at the few odd points), it was found that for phase 1, the average difference for all three contact lines of most points plotted showed that the theoretical results were 0.59% greater than the experimental ones, for phase 2, they were 3.34% smaller and for phase 3 they were 1.53% smaller.

6.5 Theoretical and Experimental Transmission Error

As was shown in section 5.6, the experimental transmission error curves of Fig.5.28 do not represent a true measure of the transmission error "f_t", but the variations of "f_t" during mesh. Table 6.1 lists the theoretical transmission errors obtained from program "HELICALDIST" alongside the experimental transmission errors for the three test phases. The results for no-load and full-load (526.5 Nm) are tabulated, and in the case of the theoretical results, values of "f_t" with zero shaft deflections are also included in brackets (to show the effect of shaft deflections on "f_t").

To facilitate graphical comparison of variations of "f_t", a constant has

PHASE	ft [um]			
	EXP no load	THEORY no load	EXP full load	THEORY (no δ_s) full load
1	3.333	-22.868	-2.143	25.460(5.387)
2	0.159	-24.648	-3.254	23.867(3.581)
3	-0.476	-25.783	-5.159	22.755(2.183)

Table 6.1 Theoretical and Experimental Transmission Errors

Fig.6.5 Theoretical vs Experimental Transmission Error

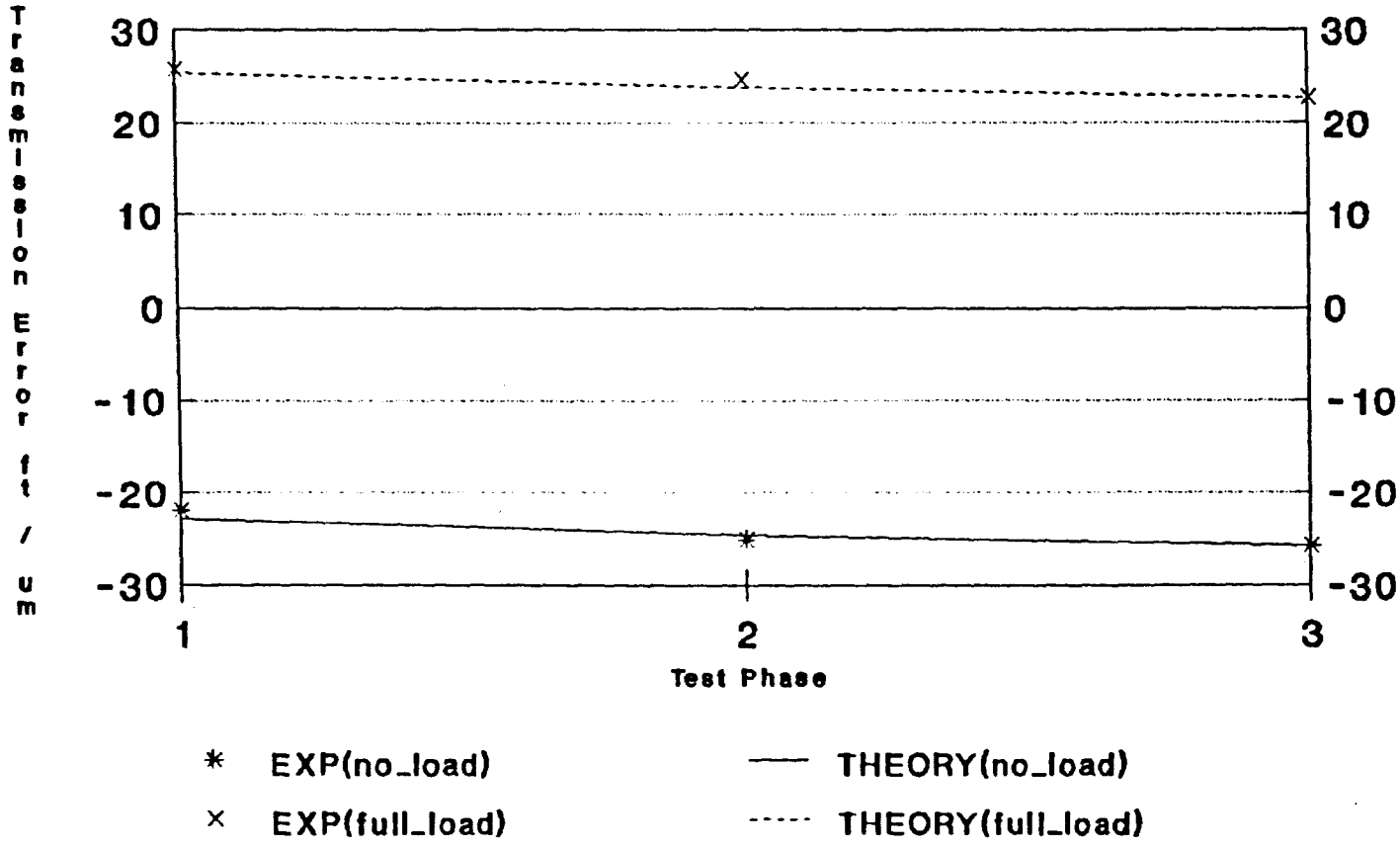

been added to the experimental results to make them coincide with the theoretical values of "f_t" at phase 3. This phase was arbitrarily chosen as the reference since it exhibits the smallest algebraic value of "f_t". The constant for the no-load case is thus (-25.783 - (-0.476)) = -25.307μm. Similarly, the constant for the full load case is (22.755 - (-5.159)) = 27.914μm.

Fig. 6.5 shows a comparison of the 'corrected' experimental and theoretical transmission error obtained in this way for phases 1 to 3. Any cyclic errors of the encoders which measure "f_t" will have almost identical effects on all three phases (since the three phases are not far apart), and therefore will not alter appreciably the form of the transmission error curves.

In view of the possible errors in measuring "f_t" (see Sec.5.7), the agreement between the measured and theoretical variations in "f_t" shown in Fig.6.5 (maximum discrepancy $\pm 1\mu$m) is as expected very good, despite the fact that the curves of Fig.5.28 (especially that for no load) exhibit a substantial amount of high-frequency 'noise' (probably associated with runout/roundness errors in the bearings, friction effects, local (short-wavelength) tooth form errors not effectively modelled by Eqn.6.1).

It would thus have been better to average the values of f_t over several revolutions before making comparisons with the theory. However, with the experimental rig used, this was not possible.

Finally, refer to the end of section 5.6 where an experimental value for the transmission error, only due to loading (no tooth errors or misalignments) was calculated to be 48.40μm. Comparing this value with the difference between columns 2 and 4 in table 6.1 shows excellent agreement, where the mean difference for cases 1, 2 and 3 in the table is 48.46μm (the individual differences for cases 1, 2 and 3 respectively are 48.328, 48.515 and 48.538μm).

CHAPTER 7

CONCLUSION

7.1 Main Achievements

The aim of this work was to determine the load and stress distributions, and the transmission error in wide-faced helical gear teeth. To achieve this, the following was done:

1. A 3-D FE elastic gear model satisfying all the requirements for a good 3-D model (Sec. 1.4) was developed (see Sec. 2.5 ... 2.6).
2. The FE results in step 1 above were incorporated into a micro-computer software package, developed by the author for the analysis of load and stress distributions, and transmission error (see Sec. 2.6 ... 2.10).
3. The load and stress distributions thus obtained, were then compared with other published data (see Sec. 3.1 ... 3.4).
4. The effect of different parameters such as Z, U, b and β, on the load and stress distribution results was studied (see Sec. 3.5).
5. The load distribution factors $K_{H\alpha}$ and $K_{H\beta}$ predicted by the program were compared with other published data (see Chapter 4).
6. An experimental rig was developed to determine the actual load distribution and transmission error in helical gears of known geometry, mounting and meshing conditions. The results were then compared with the theoretical results obtained from the 3-D model (see Chapter 5 and Chapter 6).

7.2 Main Conclusions

The objectives listed in Section 1.5 were successfully achieved as shown in section 7.1 above, and to this end, the following main conclusions were drawn:

1. The FE gear-tooth compliance results agreed well with other reliable published data.
2. Gear body compliance was shown to be significant in larger gears. This explains why the mesh stiffness values obtained differed from those given by ISO.
3. The load and stress distributions obtained agreed well with Vedmar's[5] published data, showing peaks (spikes) at and near the ends of contact lines, attributed to the so called "buttressing" effect.
4. The load distribution factors $K_{H\alpha}$ and $K_{H\beta}$ were shown to be considerably smaller than those obtained by ISO[4]. This was mainly

explained by overestimation of the mesh stiffness in the ISO analysis used to calculate the load distribution factors.

5. The experimentally-determined load distribution results agreed well with those obtained theoretically. The cyclic variations of the former relative to the latter on the full contact lengths (Figs. 6.2 .. 6.4), could only be explained by random errors in the experimental results. Discrepancies between experiment and theory at the ends of contact lines could be partially attributed to inadequate measurement of gear tooth errors, which may have resulted in erroneous end-of-contact theoretical load distributions.
6. Experimental transmission errors for the three test phases considered were not absolute values. However, upon adding a constant to them, they agreed very well with the theoretical results at the corresponding phases. Nevertheless, since the test phases were not far apart, this method may not be very reliable and the small variations observed were actually within the measurement error.

7.3 Suggestions for an Improved 3-D Model

In this section, suggestions for future research, to further improve the 3-D gear model used in this work are presented. To this end, the following improvements are recommended:

1. FE modelling of the "further" adjacent teeth (i.e. at least the second tooth from the loaded one on either side) should be carried out. In this work, these teeth were assumed to have the minimum compliance of the corresponding "directly" adjacent teeth (see Sec. 2.6.3).
2. With the advances in computer hardware, increased processing power could allow a much finer FE mesh to be used around the loading point. This would permit correct FE modelling of the gear tooth contact compliance, which could then replace the approximate 2-D Hertzian contact compliance. Although this does not greatly improve the accuracy of the results as shown by Steward[30], it does greatly reduce the amount of work invloved in interpreting the FE results.
3. Another advantage to be gained from increased computing power, is the ability to use much smaller intervals of integration to solve the equilibrium and compatability equations (Eqns. 2.13 and 2.14 respectively), thus improving the accuracy of the results. This has recently been done (see Fig. 5.30).
4. The Gauss elimination used to solve equations 2.13 and 2.14, may be replaced by a faster, more efficient method, such as a Gauss-Seidel or similar iterative procedure in which the contact non-linearities can be

more conveniently accomodated.

5. The shaft deformation δ_s in equation 2.14 was based on theoretical calculations, by assuming that a concentrated load acted at gear mid-face. Although this was shown to be a reasonable assumption, a better approach would be to calculate δ_s at each integration point in terms of the unknown loads w_j. The term δ_s could then be included in the influence coefficient terms K_{tb} in equation 2.14.

6. Errors in transmission error measurements could be reduced by eliminating the friction wheels (items 21 and 22 in Fig. 5.1), which are a major source of measuring errors. Instead, the encoder could be directly coupled to the pinion shaft by means of an offset arm, which rotates with the pinion shaft. This set-up is possible since rotations during the tests are restricted to less than 90°. Also, with such a set-up, the more accurate encoder ROD 800 (see item 26) may replace ROD 270 (item 25). This would greatly increase the accuracy of FE measurement.

7. The transmission error measurements could also be taken in a totally different manner, in order to obtain absolute rather than relative values. This may be done by connecting encoder ROD 270 to a compatible counter, similar to the VRZ counter connected to ROD 800 (Fig. 5.1). Differences in the readings from both counters would then give the absolute transmission error.

8. The accuracy of the measured load distributions could usefully be confirmed by instrumenting <u>one</u> of the pinion teeth with strain gauges. The instrumented tooth could be meshed, in turn, with each of the instrumented wheel gear teeth to provide a cross-check on the load intensity along each contact line.

REFERENCES

1. AGMA 218.1, "The Rating of Spur and Helical Gears", Dec.1982.
2. BS436, "Spur and Helical Gears",
   Part 2, "Basic Rack Form, Modules and Accuracy (1 to 50 metric module)".
   Part 3, "Method for Calculation of Contact and Root Bending Stress Limitations for Metallic Involute Gears", 1986.
3. DIN 3960, "Concepts and Parameters Associated with Cylindrical Gears and Cylindrical Gear Pairs with Involute Teeth", July 1980.
   DIN 3961, "Accuracy of Cylindrical Gears: General Bases", Aug. 1978.
   DIN 3962, "Accuracy of Cylindrical Gears: Tolerances and Individual Errors", Aug. 1978.
   DIN 3990, "Calculation of Load Capacity of Helical Gears",
   Part 1, "Introduction and General Influence Factors", Dec. 1987.
   Part 2, "Calculation of Pitting Resistance", Dec. 1987.
   Part 3, "Calculation of Tooth Strength", Jan.1986.
4. a) ISO/DS6336, "Spur and Helical Gear Analysis", 1983.
   b) ISO/DP6336, "Gear Loading", Parts I,II,III and IV, July 1980.
5. Vedmar, L., "On the Design of External Involute Helical Gears", Machine Elements Division, Lund Technical University, Lund, Sweden, 1981.
6. Hayashi, K., Umezawa, K., Kajiyama, T., and Uchibori, R., "Analysis of Loading in Cylindrical Gears", JSME Semi-International Symposium, Tokyo 1967, pp.181-188.
7. Trbojevic, M.D., "Load Distribution on Helical Gear Teeth", The Engineer, Vol.204, No.5298, 1957, pp.187-190, and No.5290, 1957, pp.222-224.
8. Hertz, H., "Gessamelte Werke", Vol.l, Leipzig, 1895.
9. Hirt, M.C.O., "Stresses in Spur Gear Teeth and Their Strength as Influenced by Fillet Radius". (English Translation of PhD Thesis by John Maddock, published by AGMA, 1976).
10. Cardou, A., and Tordion, G.V., "Calculation of Spur Gear Flexibility by the Complex Potential Method", Transactions of the ASME, Vol.107, March 1985, pp.38-42.
11. Lewis, F.M., "Load Distribution of Reduction Gears", Journal of Applied Mechanics, June 1945, pp.A87-A90.
12. Dolan, T.J., and Broghammer, E.L., "A Photoelastic Study in Gear Tooth Fillets", University of Illinois Engineering Experiment Station, Bulletin No.335, 1942.
13. Heywood, R.B., "Tensile Fillet Stresses in Loaded Projections", Transactions - Institution of Mechanical Engineers, 1948.

14. Winter, H., and Podlesnik, B., Research work quoted in BS436 draft and DIN3990 Part 1 (full reference not given).
15. Weber, C., and Banaschek, K., Research work quoted in BS436 draft and DIN3990 Part 1 (full reference not given).
16. Brossmann, U., "The Effect of Tooth Root Radius and Helix Angle on the Loading and Strength of Helical Gears", (in German), PhD Dissertation, T.U. Munchen, 1979.
17. Merrit, H.E., "Gears", Pitman, London, 1942.
18. Weber, C., "The Deformation of Loaded Gears and the Effect on Their Load Carrying Capacity", Part 1, D.S.I.R., London, Sponsored Research (Germany), Report No.3., 1949.
19. Weber, C., and Banaschek, K., "The Deformation of Loaded Gears and the Effect on Their Load Carrying Capacity", Part 5, D.S.I.R., London, Sponsored Research (Germany), Report No. 6, 1950.
20. Zablonski, K.I., "Load Distribution on Gear Drive Contact Lines", Russian Engineering Journal, Vol.8, 1969, pp.26-31.
21. Wilcox, L. and Coleman, W., "Application of Finite Elements to the Analysis of Gear Tooth Stresses", ASME Journal of Engineering for Industry, Vol.95, 1973, pp.1139-1148.
22. Chabert, G., Dang, Tran, T., and Mathis, R., "An Evaluation of Stresses and Deflections of Spur Gear Teeth Under Strain", ASME Journal of Engineering for Industry, Vol.96, 1974, pp.85-93.
23. Schmidt, G., "Berechnung der Walzpressung Schragverzahnter stirnrader unter Berucksichtigung der Lastverteilung", PhD Dissertation, T.U. Munchen, 1973.
24. Kagawa, T., "Deflection and Moment Due to a Concentrated Edge Load on a Cantilever Plate of Finite Length", Proceedings of the 11th Japan National Congress for Applied Mechanics, 1961.
25. Terauchi, Y., and Nagamura, K., "Study on Deflection of Spur Gear Teeth, 1st Report - Calculation of Tooth Deflection by Two-Dimensional Elastic Theory", Bulletin of the JSME, Vol.23, No.184, Oct. 1980, pp.1682-1688.
26. Terauchi, Y., and Nagamura, K., "Study on Deflection of Spur Gear Teeth, 2nd Report - Calculation of Tooth Deflection for Spur Gears with Various Tooth Profiles", Bulletin of the JSME, Vol.24, No.188, Feb.1981, pp.447-452.
27. Terauchi, Y., and Nagamura, K., "On Tooth Deflection Calculation and Profile Modification of Spur Gear Teeth", International Symposium on Gearing and Power Transmission, Tokyo 1981, pp.159-164.
28. Jaramillo, T.J., "Deflections and Moments Due to a Concentrated Load on a Cantilever Plate of Infinite Length", Journal of Applied Mechanics, Vol.17, March 1950, pp.67-72.

29. Wellauer, E.J., and Seireg, A., "Bending Strength of Gear Teeth by Cantilever Plate Theory", Trans. ASME, Ser. B, 82, 1960, pp.213-222.
30. Steward, J.H., "Elastic Analysis of Load Distribution in Wide-Faced Helical Gears", PhD Dissertation, University of Newcastle upon Tyne, Newcastle upon Tyne, U.K. 1988.
31. Hayashi, K., "Load Distribution on the Contact Lines of Helical Gear Teeth", (Part 1 - Fundamental Concept), Bulletin of JSME, Vol.6, No.22, 1963, pp.336-343.
32. Fredholm, Work on integral equations quoted in Reference 30 (full reference not given).
33. Hayashi, K., and Sayama, T., "Load Distribution on the Contact Line of Helical Gear Teeth", (Part 2 - Gears of Large Tooth Width), Bulletin of JSME, Vol.6, No.22, 1963, pp.344-353.
34. Seager, D.L., "Tooth Loading and Static Behaviour of Helical Gears", Trans. ASLE, Vol.13, No.1, 1970, pp.66-77.
35. Umezawa, K., "Deflections and Moments Due to a Concentrated Load on a Rack-Shaped Cantilever Plate with Finite Width for Gears", Bulletin of the JSME, Vol.15, No.79, 1972, pp.116-130.
36. Umezawa, K., "The Meshing Test on Helical Gears under Load Transmission", Bulletin of the JSME, Vol.15, No.90, 1972, pp.1632-1639.
37. Umezawa, K., "The Meshing Test on Helical Gears under Load Transmission", (2nd Report - The Approximate Formula for Bending-Moment Distribution of Gear Tooth), Bulletin of the JSME, Vol.16, No.92, Feb. 1973, pp.407-413.
38. Inoue, K., and Tobe, T., "Longitudinal Load Distribution of Helical Gears", International Symposium on Gearing and Power Transmission, Tokyo 1981, pp.165-170.
39. Tobe, T., and Inoue, K., "Longitudinal Load Distribution Factor of Helical Gears", Journal of Mechanisms, Transmission, and Automation in Design, Transactions of the ASME, Vol.107, March 1985, pp.17-23.
40. Weber, C., and Banaschek, K., "Schriftenreihe Antriebstechnik", Ht 11. Friedr. Vieweg and Sohn, Braunschweig, 1953.
41. Buckingham, E., "Analytical Mechanics of Gears", McGraw-Hill, New York 1949.
42. Maxwell, Discussion of the reciprocal theorem quoted in reference 30 (full reference not given).
43. Simon, V., "Load and Stress Distributions in Spur and Helical Gears", Journal of Mechanisms, Transmissions, and Automation in Design, Transactions of the ASME, Vol.110, June 1988, pp.197-202.

44. Tobe, T., and Inoue, K., "Longitudinal Load Distribution Factor for Straddle- and Overhang-Mounted Spur Gears", Third International Power Transmissions and Gearing Conference, San Francisco 1980, Paper No. DET-45.
45. Computer Software Package - DUISO, "Spur and Helical Gear Analysis", (Implements ISO/DS6336 Standard Given in Reference 4), Design Unit - University of Newcastle upon Tyne, Newcastle, U.K., Aug. 1989.
46. Myers, E.J., "The Effect of Face Crowning on Load Distribution of Gear Teeth", Unpublished Report, Design Unit - University of Newcastle upon Tyne, D.U.902/MGR17, April 1988.
47. Munro, R.G., "Profile and Lead Correction", A Report for the British Gear Association, Dec. 1988.
48. Atkinson, L.V., "Pascal Programming", Wiley, 1983.
49. PAFEC, "Data Preparation User Manual Level 5.1", PAFEC Ltd., Strelley, Nottingham 1984.
50. BLH Strain Gauges and Accessories, Catalogue No. 211, Jan. 1990.
51. Hottinger, Baldwin, and Messtechnik, "HBM Operating Manual for Multipoint Measuring Instrument UPM60".

APPENDIX 1A

F.E. MESH GEAR TEETH CO-ORDINATES

In this Appendix, methods are given for the calculation of:

a) loaded and adjacent tooth involute profile co-ordinates x, y and z

b) loaded and adjacent tooth trochoidal fillet co-ordinates x_f, y_f and z_f

c) loaded tooth centre-line co-ordinates x_c, y_c and z_c

d) remaining internal co-ordinates of the F.E. mesh.

The required data for profile generation is:

number of teeth	:	Z
normal module	:	m_n
normal pressure angle	:	α_n
helix angle	:	β
addendum modification coefficient	:	x_n
tool addendum	:	h_{a0}
tool tip radius	:	r_{a0}
trochoidal fillet angle	:	λ (see Fig. 1A.3)

a) Loaded and adjacent tooth involute profile co-ordinates

These co-ordinates for the corner and mid-side nodes of the F.E. mesh are calculated using a micro-computer program (INVBUCK) developed for involute gear teeth with no undercutting. The radii (r_y) at any two corner nodes are input, and the following may be calculated for each value of r_y ($r_{if} \leq r_y \leq r_a$):

reference radius : $r = Z.m_n/(2.\cos(\beta))$ 1A.1

transverse pressure angle : $\alpha_t = \tan^{-1}[\tan(\alpha_n)/\cos(\beta)]$ 1A.2

base radius : $r_b = r.\cos(\alpha_t)$ 1A.3

addendum radius : $r_a = \frac{m_n}{2}.\left[\frac{Z}{\cos(\beta)} + 2.x_n + 2\right]$ 1A.4

tooth thickness in transverse plane at reference radius : $s_t = m_n.\left[\frac{\pi}{2.\cos(\beta)} + 2.x_n.\tan[\alpha_t]\right]$ 1A.5

pressure angle at r_y : $\alpha_{yt} = \cos^{-1}[r_b/r_y]$ 1A.6

tooth thickness half angle at r_y : $\psi_y = \frac{s_t}{2.r} + \text{inv}[\alpha_t] - \text{inv}[\alpha_{yt}]$ 1A.7

rectangular co-ordinates : $x = r_y.\sin(\psi_y)$; $y = r_y.\cos(\psi_y)$ 1A.8

Thus the involute profile co-ordinates may be determined for the two corner nodes on the involute. The F.E. package (PAFEC) requires the mid-side node co-ordinates as well, otherwise, PAFEC assumes straight lines between corner nodes, thus producing an inaccurate tooth profile. Therefore, the two corner node co-ordinates obtained above are used to iterate successively for the corresponding mid-side node co-ordinate as shown in the flowchart of program INVBUCK in Fig. 1A.1, (see also Fig. 1A.2).

The co-ordinates of the involute profile for the two directly adjacent teeth may next be calculated from simple geometric considerations, by making use of the co-ordinates obtained thus far for the loaded tooth. The co-ordinates need only be obtained at an arbitrary transverse section, (the reference section). The co-ordinates for the other F.E. mesh sections are automatically obtained by PAFEC, once the proper axial positions of the different sections with respect to the reference section are input to the PAFEC data files. The reference section was conveniently chosen at one end of the gear face (see Fig. 2.7, z=0), with the line of centres of the gears coinciding with the tooth centre-line, and representing the y-axis. Clearly this axis-system makes the two adjacent teeth symmetrical with respect to the y-axis at the reference section.

b) Loaded and Adjacent Tooth Trochoidal Fillet Co-ordinates

The trochoidal fillet co-ordinates were obtained using Vedmar's equations.[5] Referring to Figs. 1A.2 and 1A.3, values for the angle λ representing any two corner nodes on the trochoidal fillet are input, and the following may be calculated for each value of λ, where $\alpha_t \leq \lambda < 90^\circ$:

$$\lambda_n = \tan^{-1}[\tan(\lambda) \cdot \cos(\beta)] \quad \text{1A.9}$$

$$\varphi_1 = \frac{2}{Z}\left[\frac{\pi}{4} + h_{a0} \cdot \tan\alpha_n + r_{a0}\frac{1-\sin(\alpha_n)}{\cos(\alpha_n)}\right] \quad \text{1A.10}$$

$$\varphi = \frac{2.\cos^2(\beta)}{Z.\tan(\lambda_n)}[h_{a0} - x_n - r_{a0}(1+\sin(\lambda_n).\tan^2\beta)] \quad \text{1A.11}$$

The rectangular fillet co-ordinates for the two corner nodes corresponding to the two values of 'λ' input may thus be obtained as:

$$x_f = \frac{Z}{2} \cdot \frac{1}{\cos(\beta)} \cdot \sin(\varphi_1 + \varphi) - \frac{h_{a0} - x_n - r_{a0}(1-\sin\lambda_n)}{\sin\lambda} \cdot \cos(\varphi_1 + \varphi - \lambda) \qquad 1A.12$$

$$y_f = \frac{Z}{2} \cdot \frac{1}{\cos(\beta)} \cdot \cos(\varphi_1 + \varphi) + \frac{h_{a0} - x_n - r_{a0}(1-\sin\lambda n)}{\sin\lambda} \cdot \sin(\varphi_1 + \varphi - \lambda) \qquad 1A.13$$

$$r_f = \left[x_f^2 + y_f^2 \right]^{\frac{1}{2}} \qquad 1A.14$$

From the two sets of values of x_f and y_f thus obtained for the two corner nodes, an iteration scheme similar to that used in Fig. 1A.1 above is devised to solve for the trochoidal fillet mid-side node co-ordinates. Fig. 1A.4 shows the flowchart of the micro-computer program developed (FILVED) for carrying out the above calculation.

Again, the trochoidal co-ordinates for the adjacent teeth are obtained from simple geometric considerations, using the trochoidal co-ordinates of the loaded tooth obtained from program FILVED.

The standards [2,3,4] have established that peak root stresses occur near the 30° tangent line for a range of equivalent spur gears as shown in Fig. 1.4. For an actual helical gear, the peak stress will also be near the 30° tangent line in the normal plane, which, if converted into the transverse plane, will yield a slightly larger angle as demonstrated in Fig. 1A.5. For a helical gear with $\beta = 30°$, this angle is 33.7° as shown below,

$$ang_t = \tan^{-1}\left[\frac{\tan(ang_n)}{\cos(\beta)}\right] = \tan^{-1}\left[\frac{\tan 30}{\cos 30}\right] = 33.69°$$

Therefore, when constructing the finite element mesh for the gear tooth, a node is required at the 33.69° tangent line. That way, the stress at that location may be obtained directly from the F.E. results without the need to interpolate. The micro-computer program FILTAN2 calculates the 33.69° tangent line trochoidal fillet point by iteration, as the flowchart in Fig. 1A.6 clearly shows. The iteration progresses from an initial value assumed for λ, by successively iterating until the angle $(\lambda - \varphi - \varphi_1)$ converges to 33.69°. The

value of λ obtained thus is then used in program FILVED to calculate the co-ordinates at the tangent line.

c) Loaded Tooth Centre-line Co-ordinates

The adjacent teeth can have a very coarse mesh compared to the loaded tooth. This is justified since the adjacent teeth deformations are mainly due to gear body deformation. As they are not directly loaded, adjacent teeth will have no contact deflections, and the F.E. surface deflections may be used to define the tooth compliance instead of the centre-line deflections (see section 2.5). As mentioned earlier in part (a) of this Appendix, when using PAFEC the F.E. mesh needs to be developed only for the reference slice at z = 0 (see Fig. 2.7). PAFEC automatically models the rest of the gear once the proper axial positions of the remaining F.E. mesh gear sections in the transverse plane are input. To simplify interpolation of the F.E. results for tooth centre-line deflections directly under the normal load (discussed in more detail later on in Appendix 2B), the F.E. mesh was constructed in such a way as to allow the normal at the loaded point to intercept the tooth's central surface at an element boundary. This was accomplished by calculating the co-ordinates of these interception points for each radial loading position, and then projecting these points onto the reference section at z = 0 (see Fig. 2.7) to give

$$x_{c0} = 0; \quad y_{c0} = r_c; \quad z_{c0} = 0 \qquad \text{1A.15}$$

where the subcript (0) refers to the reference section. These points for all radial loading positions (5 in this work) are then taken as the F.E. mesh tooth centre-line nodes at the reference section. Again, PAFEC automatically calculates the corresponding points for the other sections.

At any axial loading position z_f, with five radial loading positions, five corner nodes were thus located on the tooth centre-line at the reference section.

At any point 'p' along a contact line, a 'hypothetical' load 'F' normal to the tooth flank at point 'p' is assumed. Referring to Fig. 1A.7, the components of 'F' in the global x, y and z directions are first obtained.

$$\gamma = \tan(\beta)/r \qquad \text{1A.16}$$

$$\gamma_{zp} = \gamma \times z_p \qquad 1A.17$$

$$\psi = \frac{\pi + 4 \cdot x_n \cdot \tan(\alpha_n)}{2.Z} \quad \text{(see Fig.2A.8)} \qquad 1A.18$$

$$\alpha_{pt} = \cos^{-1}[d_b/d_p] \qquad 1A.19$$

$$\alpha_{pn} = \tan^{-1}[\tan(\alpha_{pt}) \cdot \cos(\beta_p)] \qquad 1A.20$$

$$\psi_p = \psi + \text{inv}(\alpha_t) - \text{inv}(\alpha_{pt}) \qquad 1A.21$$

$$\beta_p = \tan^{-1}[\tan\beta \cdot {}^{d}p/d] \qquad 1A.22$$

$$F_x'' = -F \cdot \cos(\alpha_{pn}) \cdot \cos(\beta_p) \qquad 1A.23$$

$$F_y'' = -F \cdot \sin(\alpha_{pn}) \qquad 1A.24$$

$$F_z'' = -F \cdot \cos(\alpha_{pn}) \cdot \sin(\beta_p) \qquad 1A.25$$

$$F_x = F_x'' \cdot \cos(\gamma_{zp}-\psi_p) - F_y'' \cdot \sin(\gamma_{zp}-\psi_p) \qquad 1A.26$$

$$F_y = F_x'' \cdot \sin(\gamma_{zp}-\psi_p) + F_y'' \cdot \cos(\gamma_{zp}-\psi_p) \qquad 1A.27$$

$$F_z = F_z'' \qquad 1A.28$$

Equations 1A.23 to 1A.28 above apply to a right hand cartesian co-ordinate system loaded as shown in Fig. 1A.7. Next, by considering the points 'p' and 'c', since both lie on the normal to the tooth flank, one at the flank surface and the other at the tooth central surface, the co-ordinates of point 'c' may be determined easily from the co-ordinates of point 'p'. The co-ordinates of 'p' in turn are obtained from the <u>given</u> co-ordinates of point 'f' (the actual loaded point). By referring to Figs. 1A.8 and 1A.9 and considering Fig. 1A.8 first, the contact line is first projected onto a plane perpenducular to a line passing through the contact line at the pitch radius (plane A'B'C'D') where

$$\tan\delta_t = \ell \cdot \tan(\beta_b) \cdot \cos(\alpha_t)/\ell$$

$$= \tan(\beta_b) \cdot \cos(\alpha_t) \qquad 1A.29$$

$$= \tan(\beta) \cdot \cos(\alpha_t) \cdot \cos(\alpha_t)$$

Similarly, projecting the contact line onto a plane perpendicular to a line passing through the contact line at the loaded point 'f' gives

$$\delta_t = \tan^{-1}[\tan(\beta_f) \cdot \cos(\alpha_{ft}) \cdot \cos(\alpha_{ft})] \qquad 1A.30$$

Next, by considering the same Fig. 1A.8, the contact line is projected onto a plane perpendicular to plane A'B'C'D'(plane A'D'DA) to give

$$\tan \delta_s = \ell \cdot \tan(\beta_b) \cdot \sin(\alpha_t)/\ell$$

$$= \tan(\beta_b) \cdot \sin(\alpha_t) \qquad 1A.31$$

$$= \tan(\beta) \cdot \cos(\alpha_t) \cdot \sin(\alpha_t)$$

Applying this result to the loaded point 'f' along the contact line as before, we have

$$\delta_s = \tan^{-1}[\tan(\beta_f) \cdot \cos(\alpha_{ft}) \cdot \sin(\alpha_{ft})] \qquad 1A.32$$

where

$$\beta_f = \tan^{-1}[\tan(\beta) \cdot {}^{d_f}/_{d}] \qquad 1A.33$$

and

$$\alpha_{ft} = \cos^{-1}[{}^{d_b}/_{d_f}] \qquad 1A.34$$

We now proceed to calculate the co-ordinates of the point 'p'. Referring to Fig. 1A.9 we have

$$\psi_f = \psi + \text{inv}((\alpha_t) - \text{inv}(\alpha_{ft}) \qquad 1A.35$$

$$\gamma_{zf} = \gamma \times z_f \qquad 1A.36$$

$$x_f'' = x_f \cdot \cos(\psi_f - \gamma_{zf}) - y_f \cdot \sin(\psi_f - \gamma_{zf}) \qquad 1A.37$$

$$y_f'' = x_f \cdot \sin(\psi_f - \gamma_{zf}) + y_f \cdot \cos(\psi_f - \gamma_{zf}) \qquad 1A.38$$

$$z_f'' = z_f \qquad 1A.39$$

$$x_p'' = x_f'' - (z_p - z_f) \cdot \tan(\delta_t) \qquad 1A.40$$

$$y_p'' = y_f'' - (z_p - z_f) \cdot \tan(\delta_s) \qquad 1A.41$$

$$z_p'' = z_p \text{ (input parameter)} \qquad 1A.42$$

$$x_p = x_p''. \cos(\psi_p - \gamma_{zp}) + y_p'' \cdot \sin(\psi_p - \gamma_{zp}) \qquad 1A.43$$

$$y_p = -x_p''. \sin(\psi_p - \gamma_{zp}) + y_p''. \cos(\psi_p - \gamma_{zp}) \qquad 1A.44$$

Now, sufficient information is available in order to calculate the co-ordinates of point 'c' with

$$x_c = x_p + k.F_x \qquad 1A.45$$

$$y_c = y_p + k.F_y \qquad 1A.46$$

$$z_c = z_p + k.F_z \qquad 1A.47$$

where the factor k may be obtained by an iterative procedure. Referring to Fig. 1A.10a we have

$$\tan(ang) = x_c/y_c \qquad 1A.48$$

$$\tan(ang) = \frac{x_p + k.F_x}{y_p + k.F_y} \qquad 1A.49$$

Referring to Fig. 1A.10b we have

$$\tan(ang) = z_c \cdot \gamma \qquad 1A.50$$

$$\tan(ang) = (z_p + k.F_z).\gamma \qquad 1A.51$$

An iterative procedure included in the micro-computer program HGDEFN4, iterating for k through a convergence process of equations 1A.49 and 1A.51, by starting with an initial estimate of k, which in this case is reasonably taken as the value for a spur gear (where $x_c = 0$). Therefore, from equation 1A.45, the initial estimate of k was taken as

$$k = \left| x_p / F_x \right| \qquad 1A.52$$

d) Remaining Internal Co-ordinates of the F.E. Mesh

These were readily calculated from simple geometric considerations, and depend on the choice of the F.E. mesh element type and size.

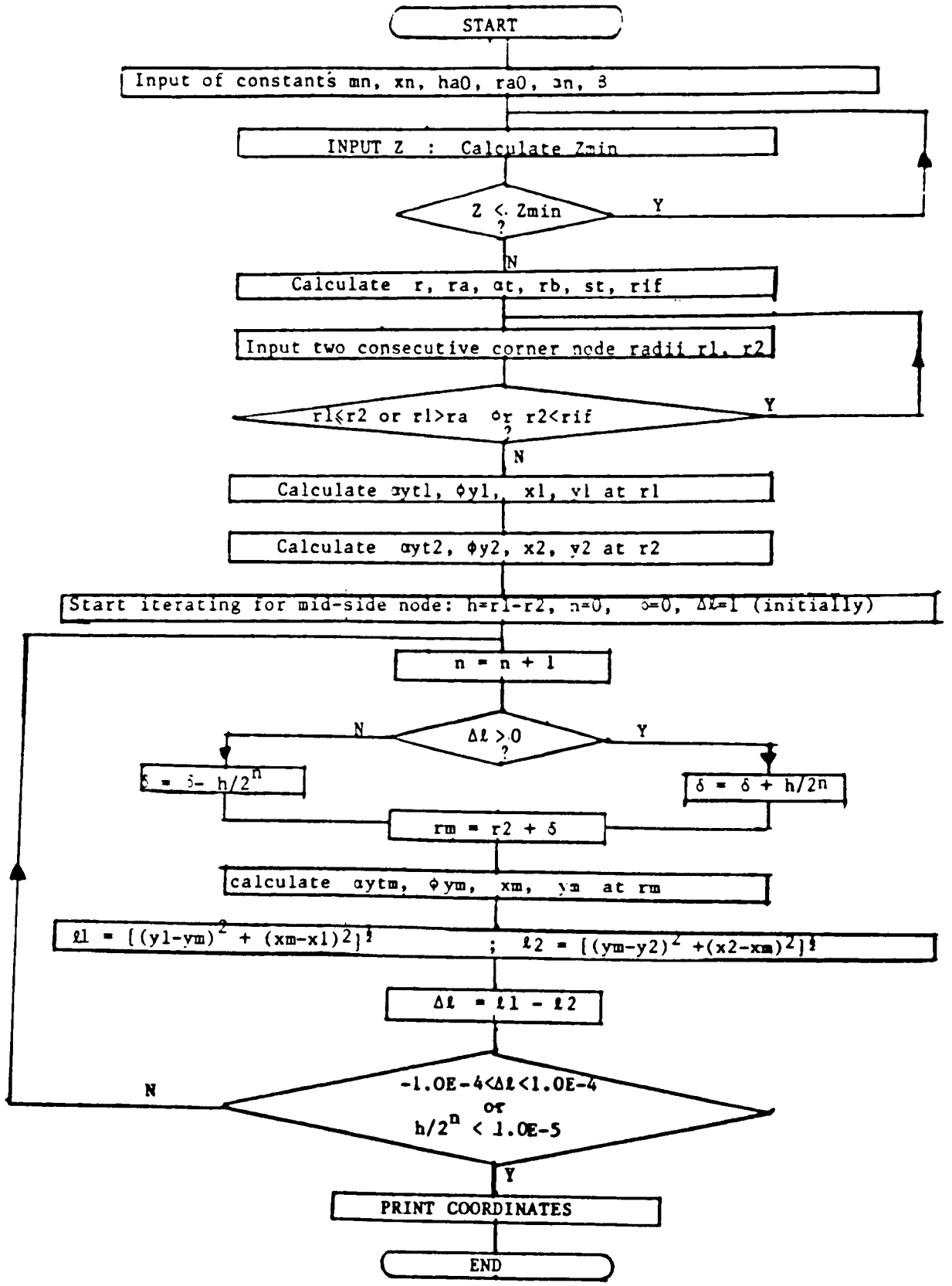

Fig.1A.1 Involute Corner and Mid-side Node Coordinates

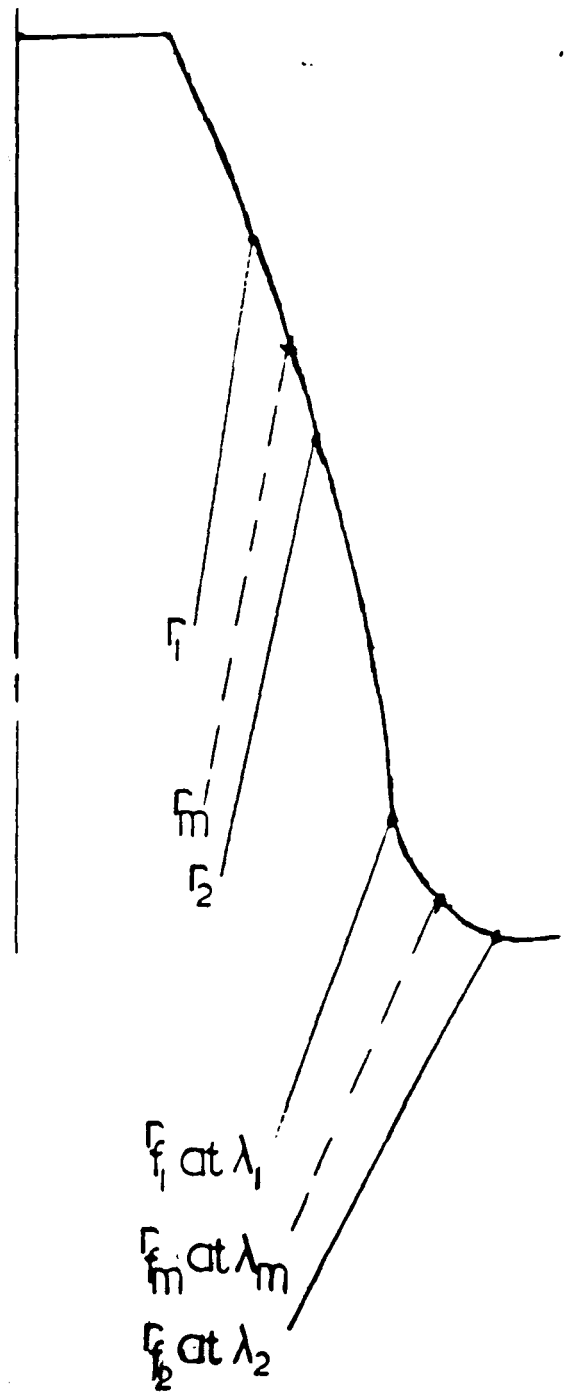

Fig. 1A.2 Involute & Trocholdal Mid_Side Node Coordinates

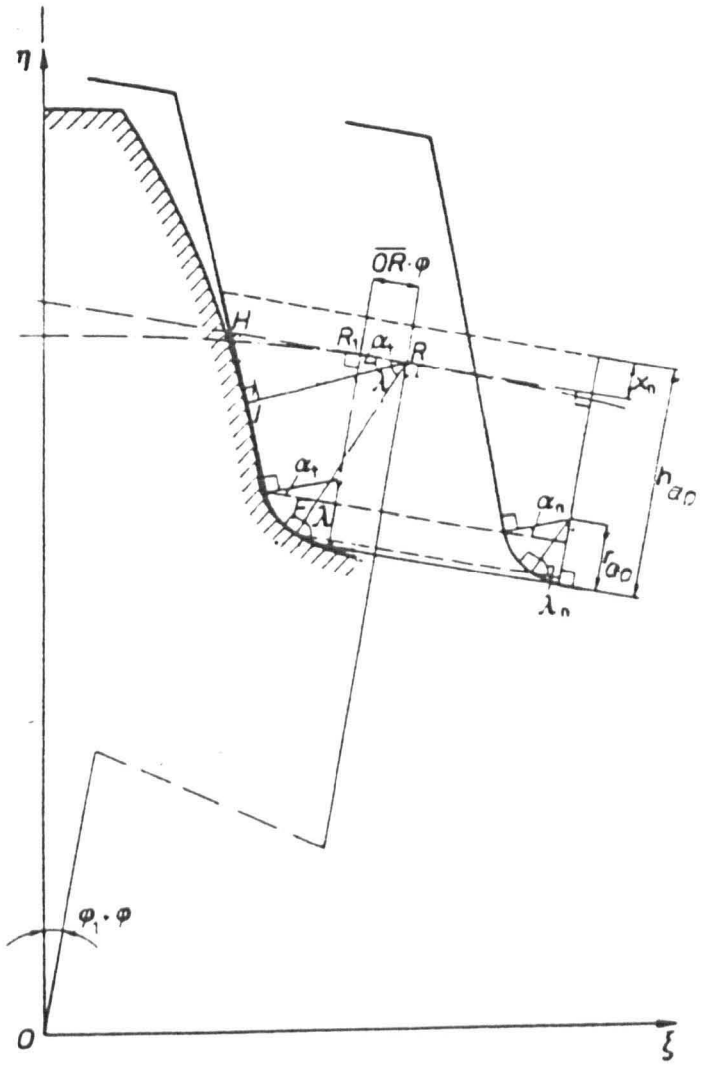

Fig. 1A.3 Gear Tooth Generated by a Rack Tool

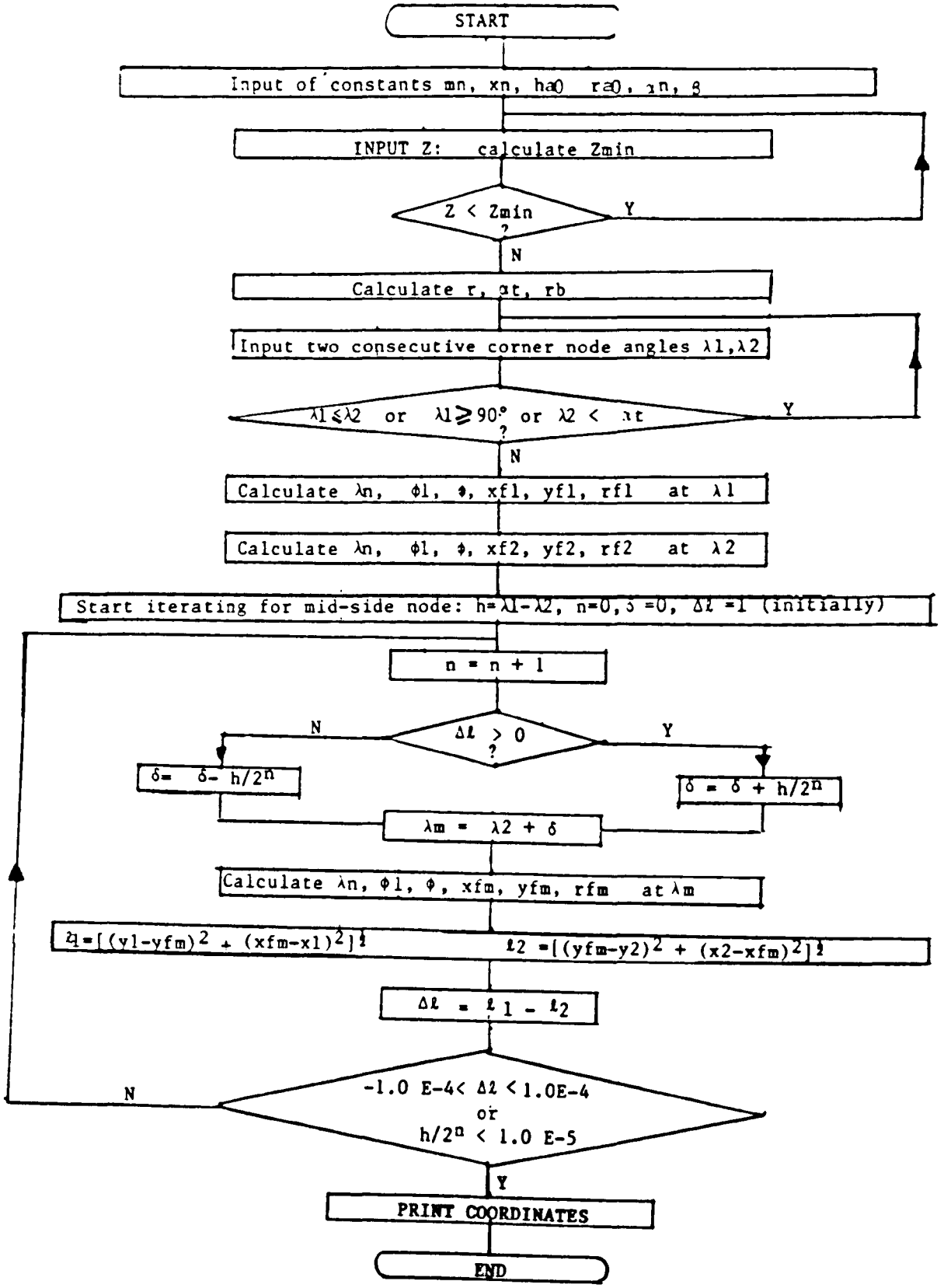

Fig.1A.4 Trochoidal Fillet Corner and Mid-side Node Coordinates

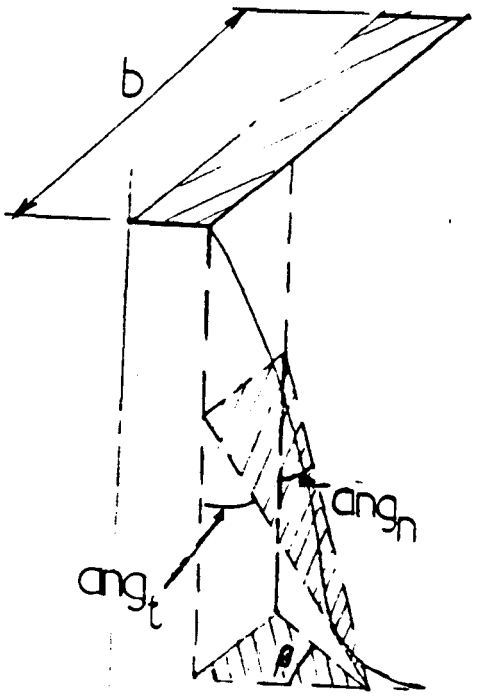

Fig.1A.5 Point of Tangency at Tooth Root Peak Bending Stress

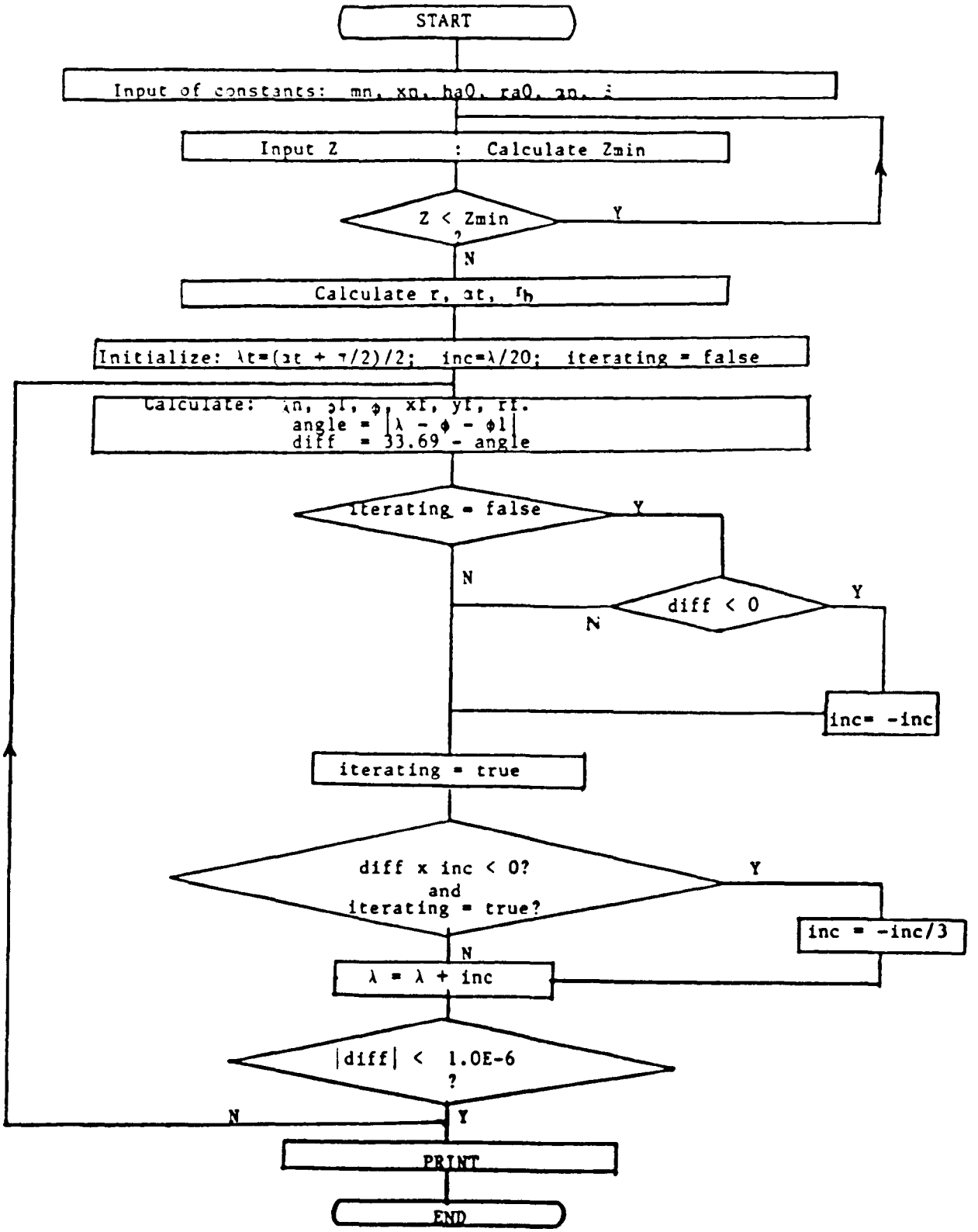

Fig. 1A.6 Trochoidal Fillet Corner Node Coordinates

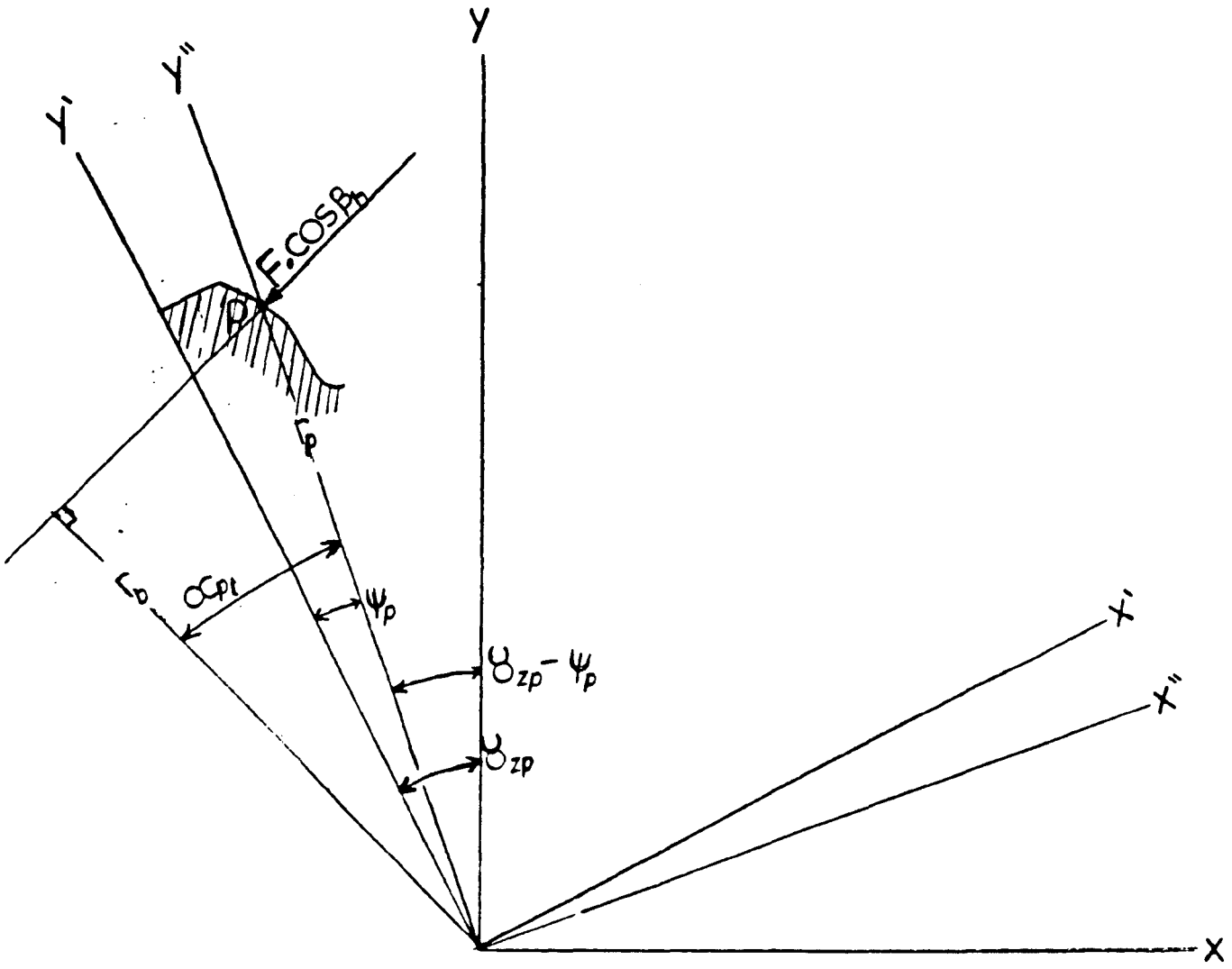

Fig.1A.7 Componenets of Force F in Global Directions x y z

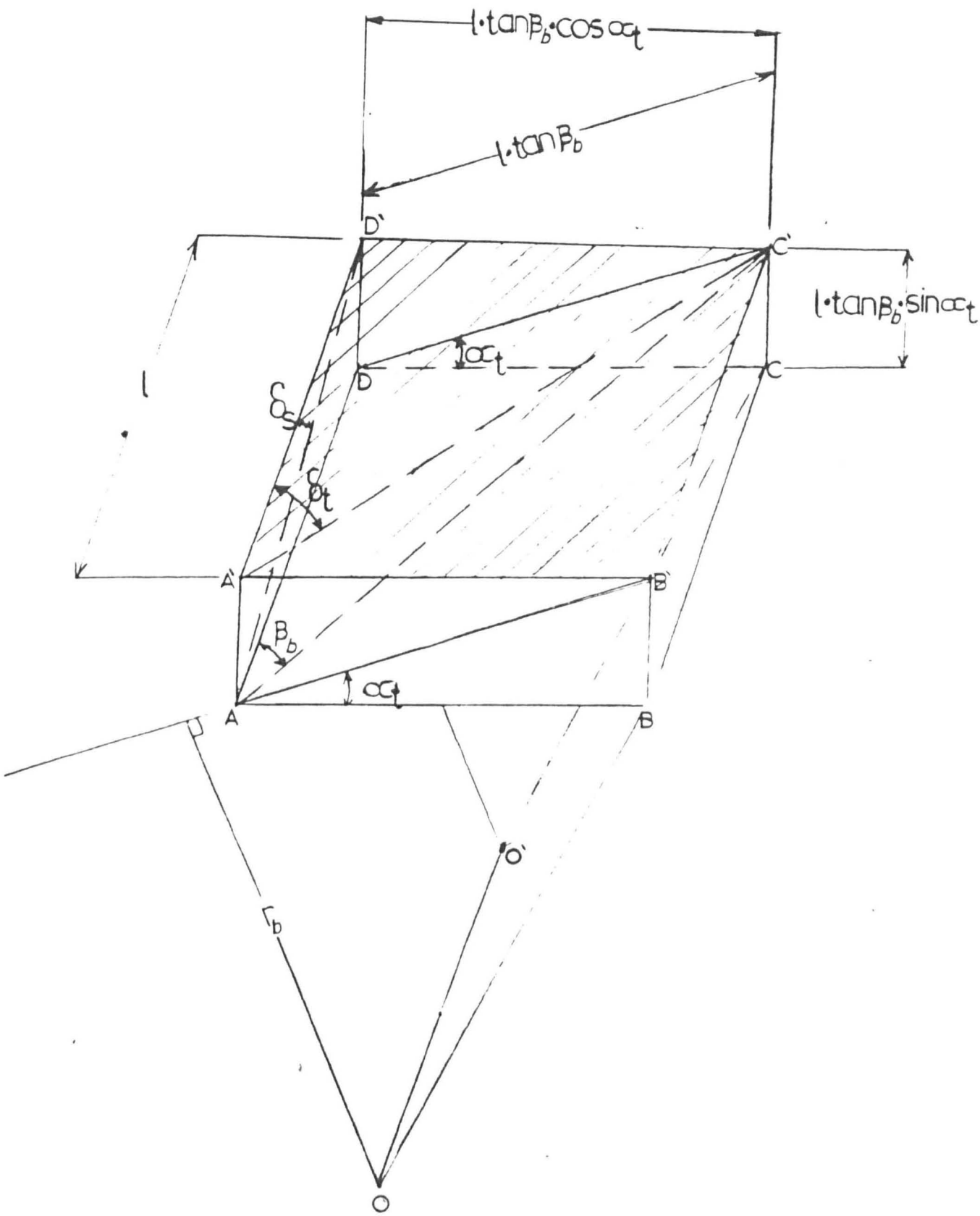

Fig. 1A.8 Contact Line Projections

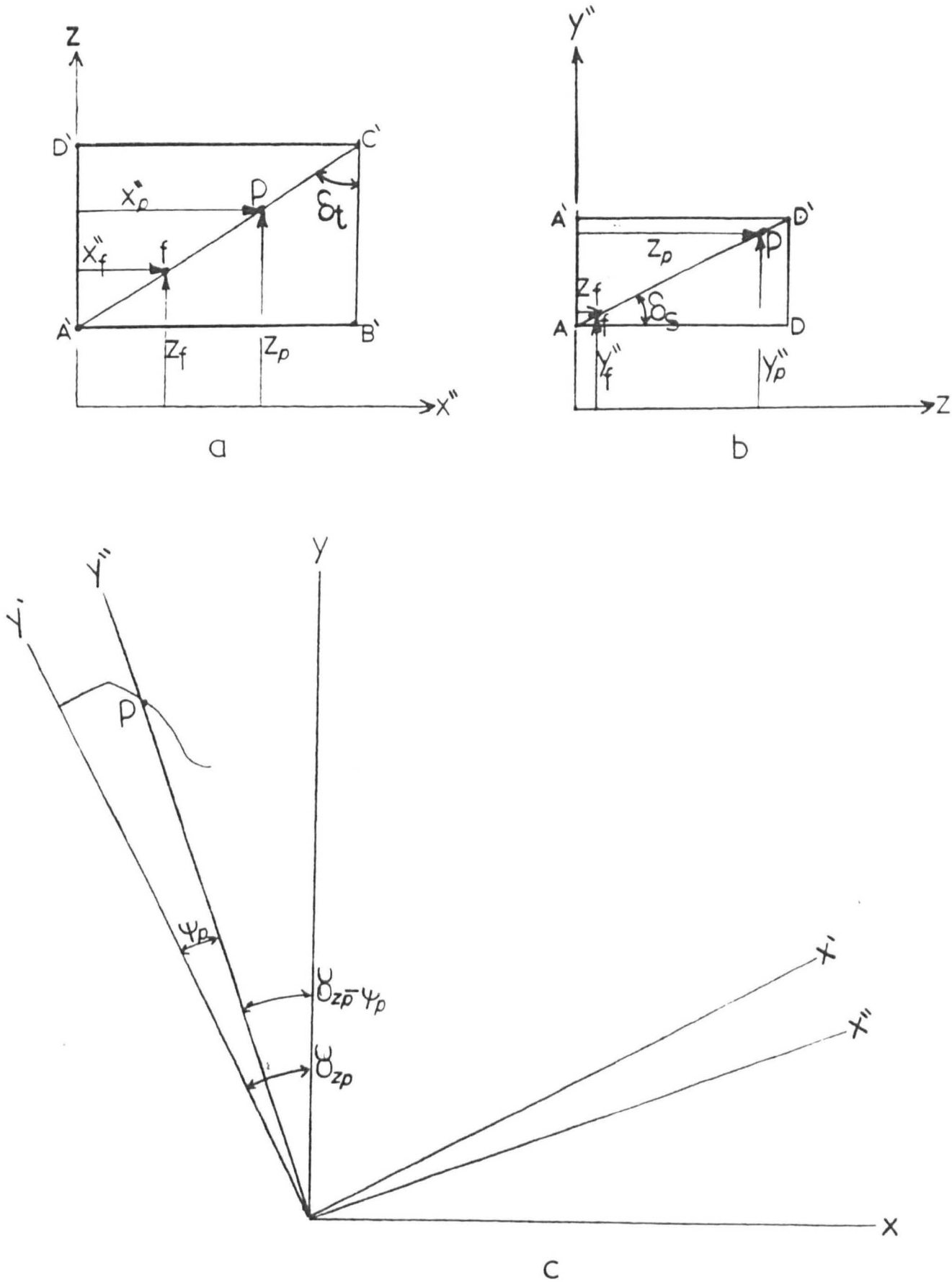

Fig. 1A.9 Determination of the Coordinates of Point "p" From the Known Coordinates of Point "f"

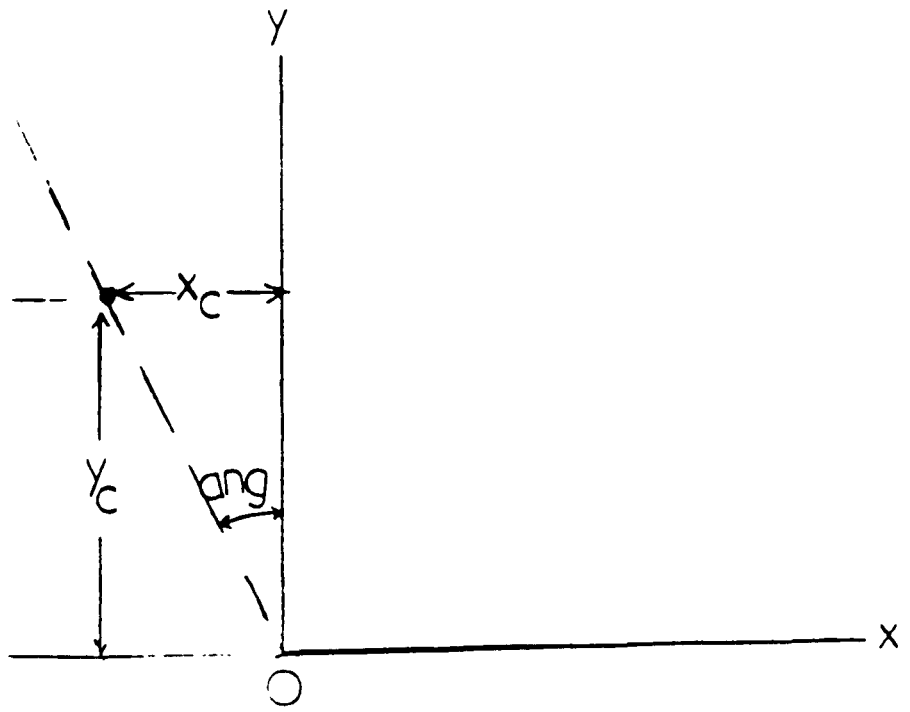

a) Transverse Section Through Point "c"

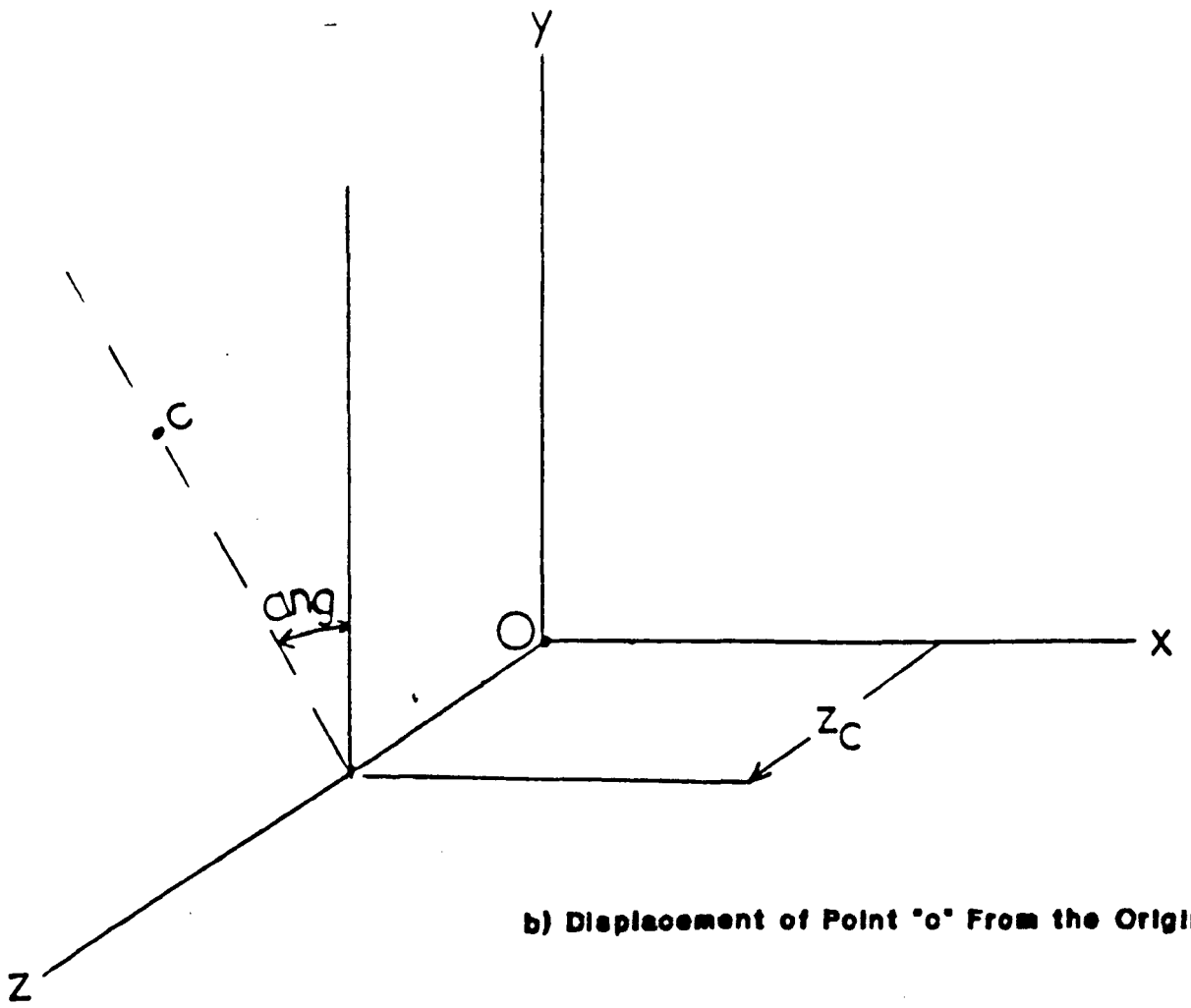

b) Displacement of Point "o" From the Origin

Fig. 1A.10 Determination of the Factor "k"

APPENDIX 2A

PROGRAM HELICALDIST FOR THE ELASTIC ANALYSIS OF HELICAL GEARS

Programme HELICALDIST determines the load distribution, the contact stress, the transmission error, and the load distribution factor in any pair of meshing helical gears. The elastic equations used are set out in Chapter 2.

Fig. 2A.1 reveals the menu heirarcy, and Fig.2A.2 briefly explains the main commands. The maximum possible number of teeth that may be simultaneously engaged at a given phase of mesh is calculated in PROCEDURE GEOMETRY as MaxTeeth (N_{max}). This is defined as the next integer greater than the sum of ϵ_β and $\epsilon_{\alpha 0}$, shown in Figure 2.1. Thus

$$\text{MaxTeeth} = \text{ROUND}\ [\text{TRUNC}(\epsilon_\beta + \epsilon_{\alpha 0}) + 1] \qquad 2A.1$$

The reference tooth number is taken as MaxTeeth, and is the tooth that specifies the phase of mesh. Up to (MaxTeeth-1) teeth on either side of the reference tooth may be in mesh at any one instant or phase of mesh. In other words (2 MaxTeeth-1) teeth must be checked for engagement at any one instant. This process is carried out in PROCEDURES PHASE and CLEARANCE with the respective flowcharts shown in Figures 2A.4 and 2A.5.

The theoretically defined phase of mesh is within points A and B in Fig.2.1. However tooth engagement is also checked outside these limits within points Ao and Bo in order to account for the elastic deflections of mating gear teeth as well as the various tooth pitch, lead and profile errors, tip/root/end relief, corrections, etc. (see Chapter 4), which may cause contact outside the theoretically defined limits applicable to a perfect gear. The new limits Ao and Bo were chosen by setting AoA and BoB equal to 0.35 times the transverse base pitch p_{bt} (see section 2.3). This value seems more than adequate when considering typical tooth profile errors and corrections, and other gear imperfections which may expand the theoretical range of mesh.

Gear error data files are created, manipulated, and assigned to each of the '2MaxTeeth-1' teeth using PROCEDURES MAKE and SELECT. These files are permanently stored on disk and may be listed or destroyed using PROCEDURES LIST and KILL respectively.

The PROCEDURE ETOOTH uses the error data files to calculate the resulting tooth errors at each of the "Gauss" and "end" points of contact. Error data files include pitch errors, lead errors, profile errors, tooth twist, face crowning

(barrelling), profile crowning and tip/root/end relief. The problem of wear craters can also be tackled by treating them as a profile error.

The PROCEDURE CALCMAT generates the tooth bending compliance matrix (excluding load dependent contact compliance). The bending compliance values are calculated in PROCEDURE BENDIC for the loaded tooth using the equations at Section 2.6.2. The two directly adjacent teeth bending compliance values are calculated in PROCEDURE ABENDIC using the equations of Section 2.6.3. Fig. 2A.6 accurately describes the process of generating the complete bending compliance matrix "totk" (see Figure 2.65b also).

The PROCEDURE LOADDIST adds to the bending compliance matrix generated in PROCEDURE CALCMAT the estimated tooth contact compliance, thus forming an estimated complete matrix "$totk_c$" including contact effects. The estimated matrix thus formed is then directly solved using PROCEDURE MATSOLVE, (which solves the matrix equation $[totk_c]x[Gloads]=[totdefn]$ for the vector [Gloads], see Fig.2A.3), for the Gauss point loads along the contact lines of the engaged teeth, based on the estimated compliance matrix. The process described is repeated iteratively until the estimated Gauss point loads and the calculated ones converge. Each time, a new compliance matrix is formed.

Considering the end loads, initial estimates are first made, from which new values are recalculated using equation 1.70. Again an iterative solution is used until convergence of the estimated and recalculated end loads occurs.

The contact deflections are calculated using PROCEDURE CONDEFN which makes use of equations 1.2, 1.31 and 1.34a. PROCEDURE CONSIGMA calculates the contact or Hertzian stress as calculated in equation 1.1, where w is the Gauss point (or end point) contact load.

The flowchart of Figure 2A.7 describes in detail the process of obtaining the load distribution along the contact lines of engaged teeth, the contact deflection and the contact stress. The analysis for both the Gauss points and the end points is included in the figure. The tooth error at each Gauss (or end) point is also calculated, and the transmission error "f_t" at any instant of mesh is determined.

To conclude Appendix 2A, the determination of the contact diameters and clearances outside the theoretically defined phase of mesh (ABB'A' in Figure 2.1) will be discussed for the start of contact (PROC. STARTCLR). A similar analysis applies for the end of contact (PROC. ENDCLR). Referring to Figures 2A.8, 2A.9, 2A.10 and 2.1:

$$\psi_p = [\pi + 4.x_{np}\tan(\alpha_n)]/[2.Z_p] \quad .. \quad .. \quad 2A.2$$

$$\psi_{yp} = \psi_p + \text{inv}(\alpha_t) - \text{inv}(\alpha_{ypt}) \quad .. \quad .. \quad 2A.3$$

$$\alpha_{ypt} = \tan^{-1}[(\varphi_z \cdot p_{bt} - TE)/r_{bp}] \quad .. \quad .. \quad 2A.4$$

$$\varphi_{yp} = \alpha_{ypt} - \psi_{yp} \quad .. \quad .. \quad .. \quad 2A.5$$

$$\omega_{yp} = \alpha_{\omega t} - \varphi_{yp} \quad .. \quad .. \quad .. \quad 2A.6$$

$$\omega_{yg} = \omega_{Ag} - (\varphi_{yp}-\varphi_{sp}).Zp/Zg \quad .. \quad ... \quad 2A.7$$

$$\theta_{yg} = \omega_{yg} + \lambda_{Ag} \quad .. \quad .. \quad .. \quad 2A.8$$

$$x = (dag/2).\sin(\theta_{yg}) \quad .. \quad .. \quad .. \quad 2A.9$$

$$y_g = (dag/2).\cos(\theta_{yg}) \quad .. \quad .. \quad .. \quad 2A.10$$

$$y_p = a_w - y_g \quad .. \quad .. \quad .. \quad 2A.11$$

$$(d_{yp})est = 2.[x^2 + y_p^2]^{\frac{1}{2}} \quad .. \quad .. \quad .. \quad 2A.12$$

$$(\theta_{yp})est = \tan^{-1}[x/y_p] \quad .. \quad .. \quad .. \quad 2A.13$$

$$\theta_e = \cos^{-1}[d_{bp}/(d_{yp})est] \quad .. \quad .. \quad .. \quad 2A.14$$

$$\theta_n = (\theta_{yp})est + \theta_e - \omega_{yp} \quad .. \quad .. \quad .. \quad 2A.15$$

The flowchart of Fig. 2A.11 describes how an iterative solution is carried out to calculate the actual pinion contact diameter (d_{ypc}). Clearly the start of contact gear diameter is equal to the gear tip diameter. On the other hand, Procedure ENDCLR calculates the gear contact diameter (d_{ygc}) iteratively, where the end of contact pinion diameter is equal to the pinion tip diameter. Next the start/end

clearance is calculated. For STARTCLR the clearance along the load-line direction is:

$$c_{nc} = \tfrac{1}{2}[(d_{yp})^2_{est} - d^2_{bp}]^{1/2} - [d^2_{ypc} - d^2_{bp}]^{1/2} * \cos(\beta_b) \qquad 2A.16$$

and for ENDCLR:

$$c_{nc} = \tfrac{1}{2}[d_{yg})^2_{est} - d^2_{bg}]^{1/2} - [d^2_{ygc} - d^2_{bg}]^{1/2} * \cos(\beta_b) \qquad 2A.17$$

where $(d_{yp})_{est}$ and $(d_{yg})_{est}$ are the initial estimates for pinion and gear (Eqn.2A.12) respectively, and d_{ypc} and d_{ygc} are the actual contact diameters determined interatively as shown for d_{ypc} at the start of mesh in Figure 2A.11.

******

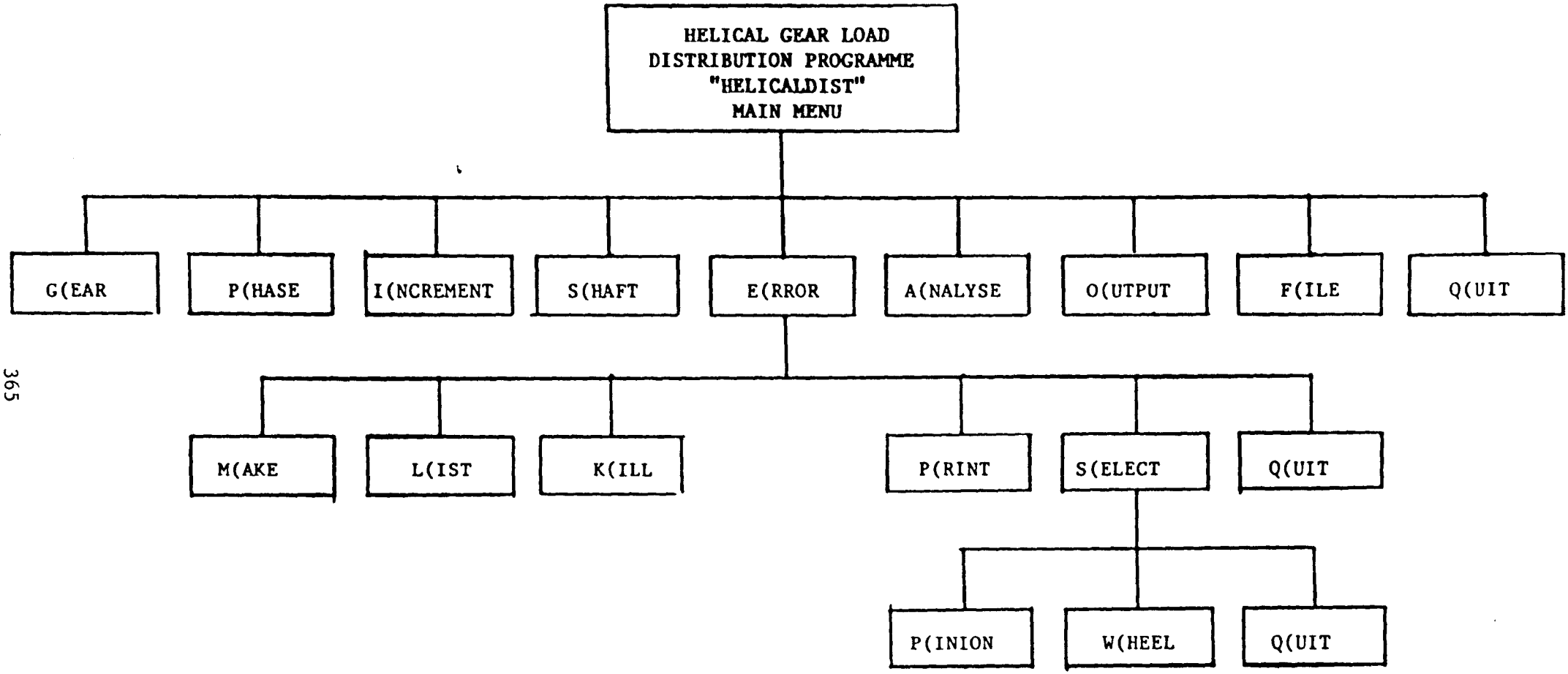

Fig.2A.1 Menu Heirarchy for Program HELICALDIST

G(EAR : Prompts for gear geometry independent of phase of mesh.

P(HASE : Prompts for the phase of mesh and uses PROCEDURE CLEARANCE to determine which of the (2MaxTeeth-1) teeth are potentially engaged. It also determines the number of teeth engaged "numzcon", the matrix order "mat-ord", the number of the first and last engaged teeth "firs-tooth" and last-tooth", the total number of Gauss and end points "numptsT" and "numptTE" respectively.

I(NCREMENT: If more than a single reference tooth phase is to be analysed, I(NCREMENT is used instead of P(HASE and allows for any number of reference tooth phases to be input at one time. Then for each phase input, PROCEDURES PHASE and ANALYSE are automatically called to analyse the gear without the need to prompt for either P(HASE or A(NALYSE in the main menu. In other words, only P(HASE or I(NCREMENT may be used at one time depending on the number of phases to be analysed. I(NCREMENT allows for the analysis to be "clicked" through any number of desired phases.

S(HAFT : Prompts for the shaft total deflections due to bending, torsion and shear, at the Gauss integration points. The deflections input must be in the components normal to the tooth flank.

E(RROR : Prompts for the error data files menu for handling gear tooth errors and corrections or modifications.

- M(AKE : creates a new error data file
- L(IST : lists an existing error data file on the screen
- K(ILL : destroys an existing error data file
- P(RINT : outputs a hard copy listing of an existing error data file.

S(ELECT : Assigns any of the existing error data files to any of the engaged teeth already determined in PROCEDURE PHASE.

- P(INION : prompts for pinion tooth numbers 1 to 2MaxTeeth-1 and assigns to each tooth the desired error data file prepared in M(ake.

(Fig.2A.2.....)

W(HEEL : prompts for wheel tooth numbers 1 to (2MaxTeeth-1) and assigns to each engaged tooth the desired error data file prepared in M(ake.

Q(UIT : returns to the E(RROR menu.

Q(UIT : Returns to the main menu.

A(NALYSE : Each phase of mesh entered is analysed and the load distribution, contact deflection, contact stress and total error at each Gauss and end point is calculated. The transmission error for each phase of mesh is also determined.

O(UTPUT : The results are output to the console, and then to the printer if so desired.

F(ILE : The results are stored to a filename on hard disk.

Q(UIT : Exits the program.

Fig.2A.2 Brief Description of the Main Menu Commands of Programme HELICALDIST

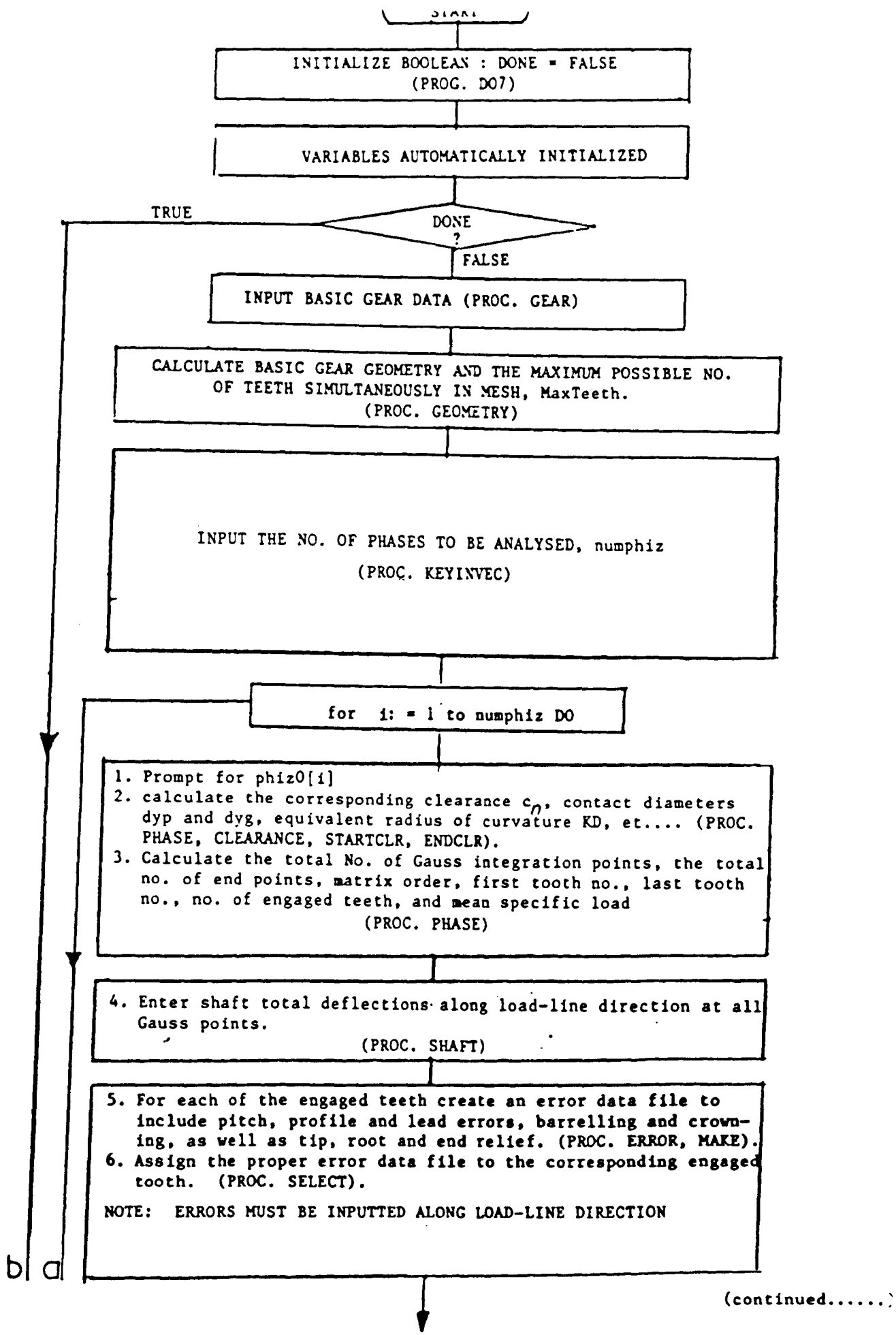
START
INITIALIZE BOOLEAN : DONE = FALSE
(PROG. DO7)
VARIABLES AUTOMATICALLY INITIALIZED
TRUE
DONE ?
FALSE
INPUT BASIC GEAR DATA (PROC. GEAR)
CALCULATE BASIC GEAR GEOMETRY AND THE MAXIMUM POSSIBLE NO. OF TEETH SIMULTANEOUSLY IN MESH, MaxTeeth.
(PROC. GEOMETRY)
INPUT THE NO. OF PHASES TO BE ANALYSED, numphiz
(PROC. KEYINVEC)
for i: = 1 to numphiz DO
1. Prompt for phiz0[i]
2. calculate the corresponding clearance c_n, contact diameters dyp and dyg, equivalent radius of curvature KD, et.... (PROC. PHASE, CLEARANCE, STARTCLR, ENDCLR).
3. Calculate the total No. of Gauss integration points, the total no. of end points, matrix order, first tooth no., last tooth no., no. of engaged teeth, and mean specific load
(PROC. PHASE)
4. Enter shaft total deflections along load-line direction at all Gauss points.
(PROC. SHAFT)
5. For each of the engaged teeth create an error data file to include pitch, profile and lead errors, barrelling and crowning, as well as tip, root and end relief. (PROC. ERROR, MAKE).
6. Assign the proper error data file to the corresponding engaged tooth. (PROC. SELECT).
NOTE: ERRORS MUST BE INPUTTED ALONG LOAD-LINE DIRECTION
b
a
(continued.....)

7. Using the curve fitting coefficients of the FE, bending deflection results for the five radial loading positions used in the FE analysis, and knowing that all the Gauss points on all the contact lines fall somewhere on or within these radial positions, the curve fitting coefficients for the Gauss points are interpolated for (PROC. CUBICSPLINE, TRIDIAG AND FUNC.NATSPLINE).
8. Solve for the bending influence function "totk" at each Gauss point (FUNC.BENDIC for the loaded tooth, and FUNC.ABENDIC for the adjacent teeth).

(PROC. CALCMAT)

9. Initial estimates of the loads at each of the Gauss points are made.
10. The corresponding contact deformations at the Gauss points are then calculated.
11. The contact deformations are then added to the diagonal terms of "totk" to form the matrix "totkc".
12. Next the vector totdefn[i] at each Gauss point "i" is formed by adding together the total shaft deflection, the calculated tooth error (PROC.ETOOTH), and the calculated clearance c_n at every Gauss point (all components along load-line direction)

    [totkc] x [Gloads] = [totdefn] .
13. Next the "Gloads" are solved for directly using (PROCEDURE MATSOLVE).
14. The "Gloads" obtained in step 13 are used as the new estimates in step 9 and the process is repeated over and over until the Gloads in step 14 and the estimates used in step 9 converge, thus solving for the Gauss points loads.
15. Using the "Gloads", calculate the corresponding contact deflections at the Gauss points (PROC. CONDEFN).

(PROC. LOADDIST)

b a

(continued.....)

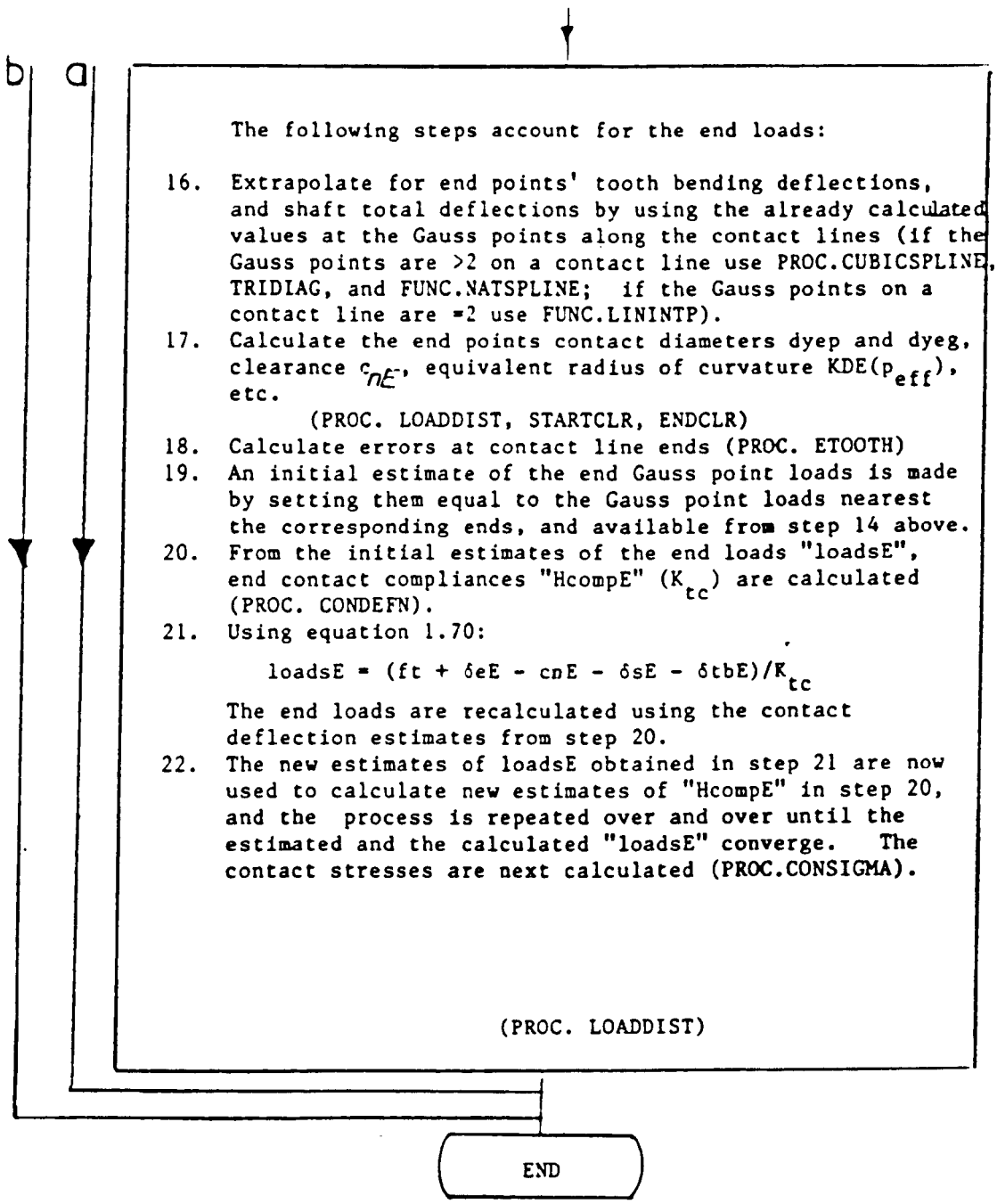

Fig.2A.3 Generalized Flowchart for Programme HELICALDIST.

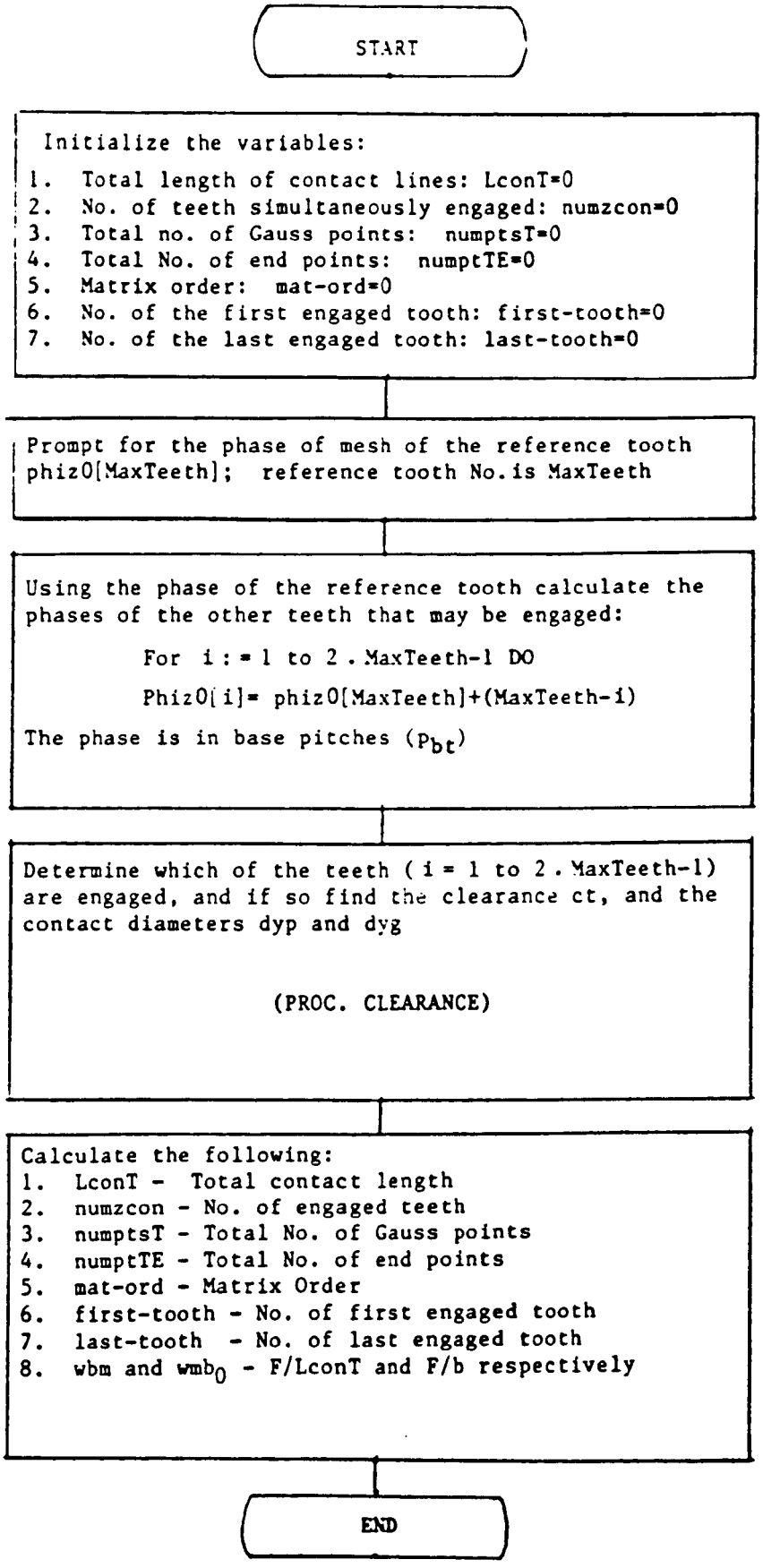

Fig. 2A.4 Flowchart for Procedure Phase in Programme HELICALDIST

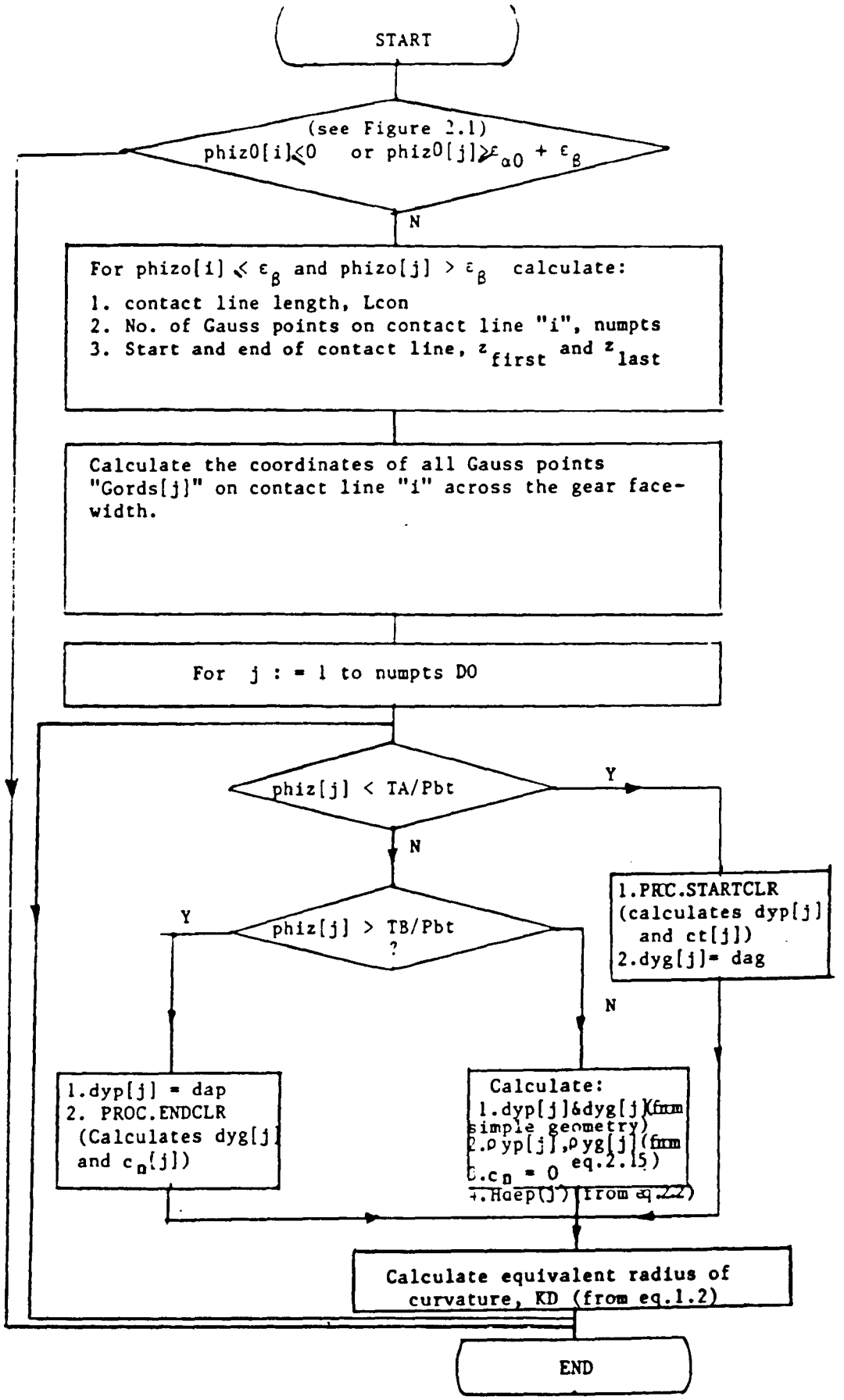

Fig. 2A.5 Flowchart for Procedure CLEARANCE in Programme HELICALDIST

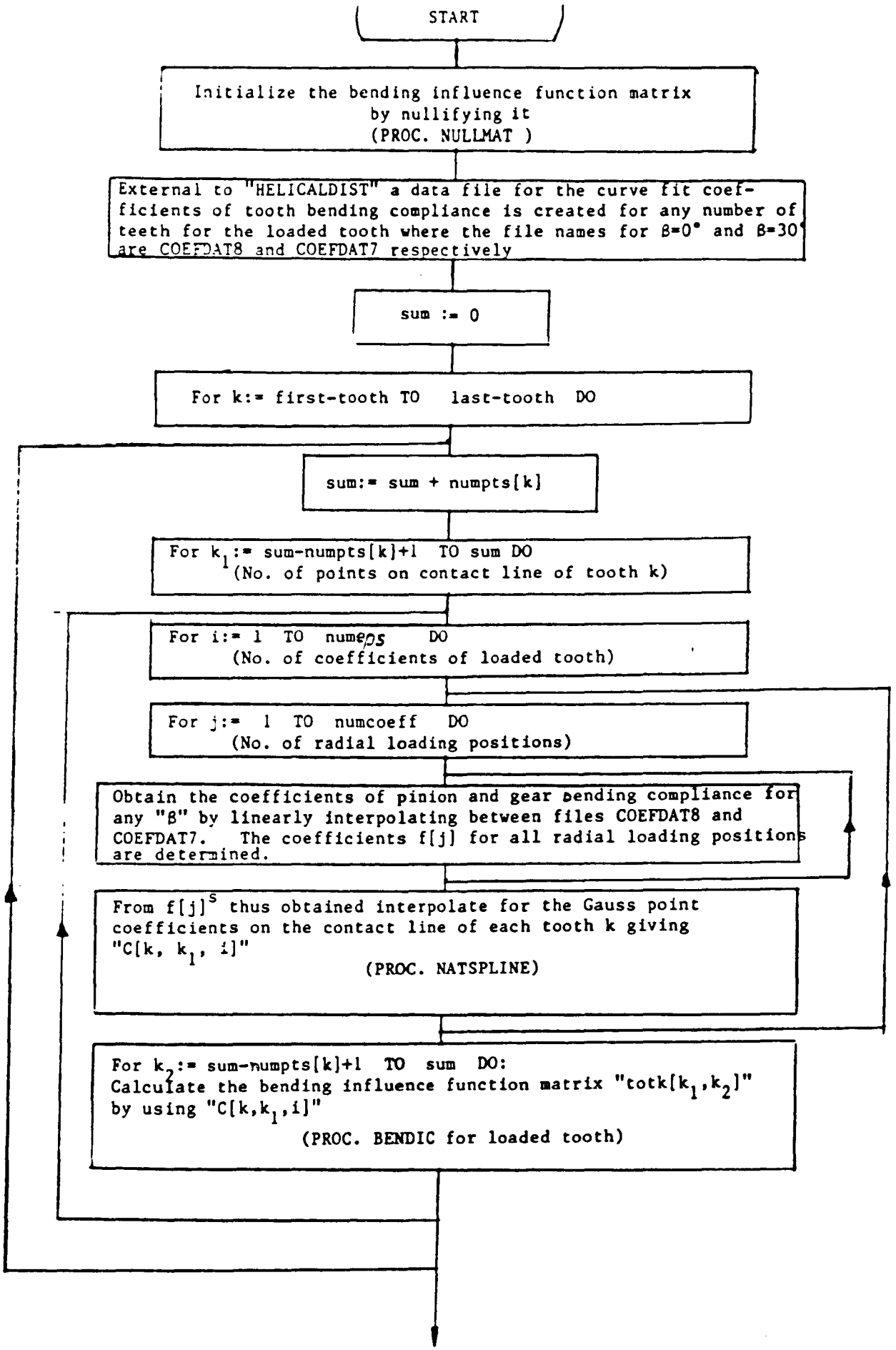
START
Initialize the bending influence function matrix by nullifying it (PROC. NULLMAT)
External to "HELICALDIST" a data file for the curve fit coefficients of tooth bending compliance is created for any number of teeth for the loaded tooth where the file names for β=0° and β=30° are COEFDAT8 and COEFDAT7 respectively
sum := 0
For k:= first-tooth TO last-tooth DO
sum:= sum + numpts[k]
For k1:= sum-numpts[k]+1 TO sum DO (No. of points on contact line of tooth k)
For i:= 1 TO numpts DO (No. of coefficients of loaded tooth)
For j:= 1 TO numcoeff DO (No. of radial loading positions)
Obtain the coefficients of pinion and gear bending compliance for any "β" by linearly interpolating between files COEFDAT8 and COEFDAT7. The coefficients f[j] for all radial loading positions are determined.
From f[j]s thus obtained interpolate for the Gauss point coefficients on the contact line of each tooth k giving "C[k, k1, i]" (PROC. NATSPLINE)
For k2:= sum-numpts[k]+1 TO sum DO:
Calculate the bending influence function matrix "totk[k1,k2]" by using "C[k,k1,i]"
(PROC. BENDIC for loaded tooth)

(continued.....)

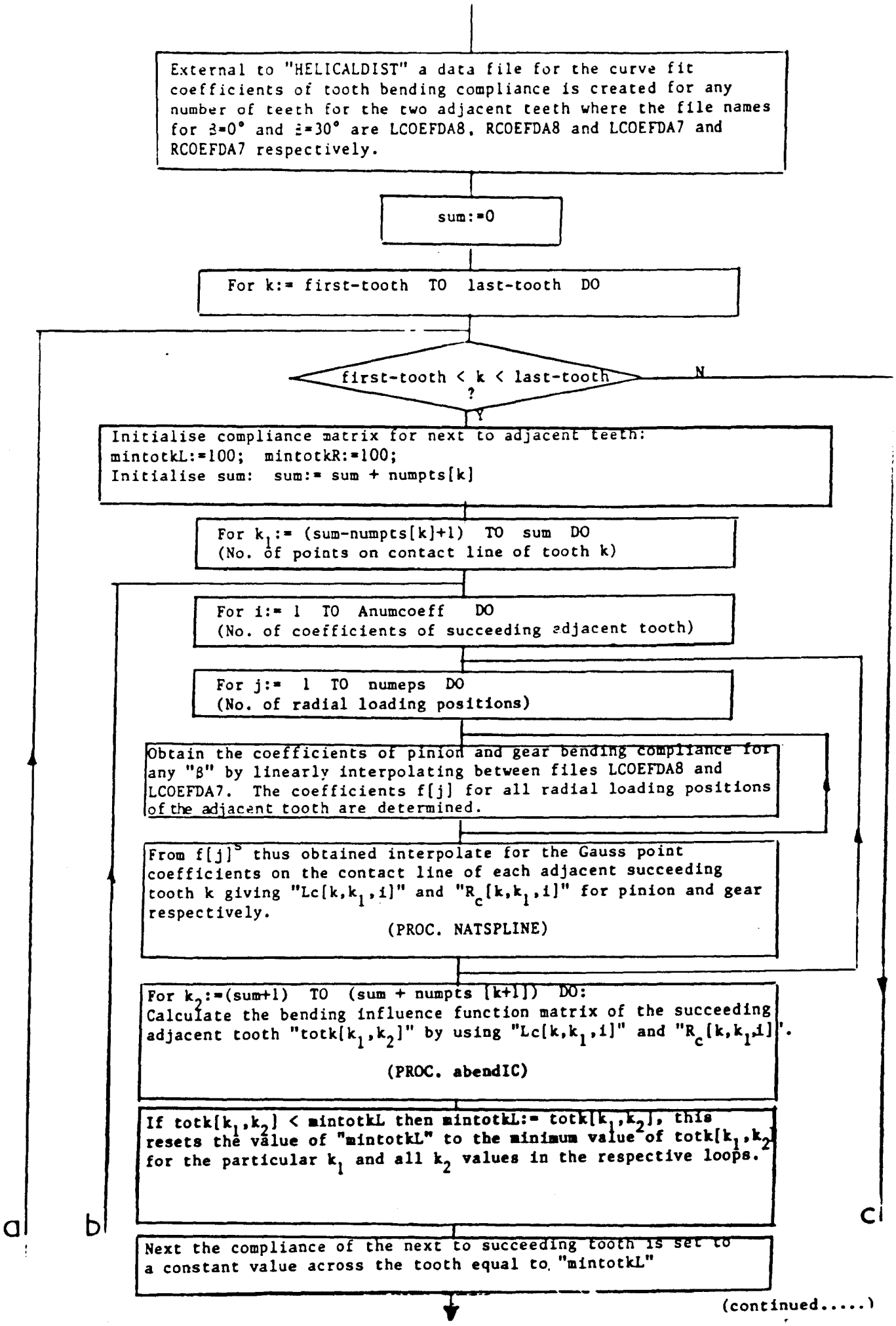
External to "HELICALDIST" a data file for the curve fit coefficients of tooth bending compliance is created for any number of teeth for the two adjacent teeth where the file names for β=0° and β=30° are LCOEFDA8, RCOEFDA8 and LCOEFDA7 and RCOEFDA7 respectively.
sum:=0
For k:= first-tooth TO last-tooth DO
first-tooth < k < last-tooth ?
N
Y
Initialise compliance matrix for next to adjacent teeth:
mintotkL:=100; mintotkR:=100;
Initialise sum: sum:= sum + numpts[k]
For k1:= (sum-numpts[k]+1) TO sum DO
(No. of points on contact line of tooth k)
For i:= 1 TO Anumcoeff DO
(No. of coefficients of succeeding adjacent tooth)
For j:= 1 TO numeps DO
(No. of radial loading positions)
Obtain the coefficients of pinion and gear bending compliance for any "β" by linearly interpolating between files LCOEFDA8 and LCOEFDA7. The coefficients f[j] for all radial loading positions of the adjacent tooth are determined.
From f[j]s thus obtained interpolate for the Gauss point coefficients on the contact line of each adjacent succeeding tooth k giving "Lc[k,k1,i]" and "Rc[k,k1,i]" for pinion and gear respectively.
(PROC. NATSPLINE)
For k2:=(sum+1) TO (sum + numpts [k+1]) DO:
Calculate the bending influence function matrix of the succeeding adjacent tooth "totk[k1,k2]" by using "Lc[k,k1,i]" and "Rc[k,k1,i]".
(PROC. abendIC)
If totk[k1,k2] < mintotkL then mintotkL:= totk[k1,k2], this resets the value of "mintotkL" to the minimum value of totk[k1,k2] for the particular k1 and all k2 values in the respective loops.
a
b
c
Next the compliance of the next to succeeding tooth is set to a constant value across the tooth equal to "mintotkL"
(continued.....)

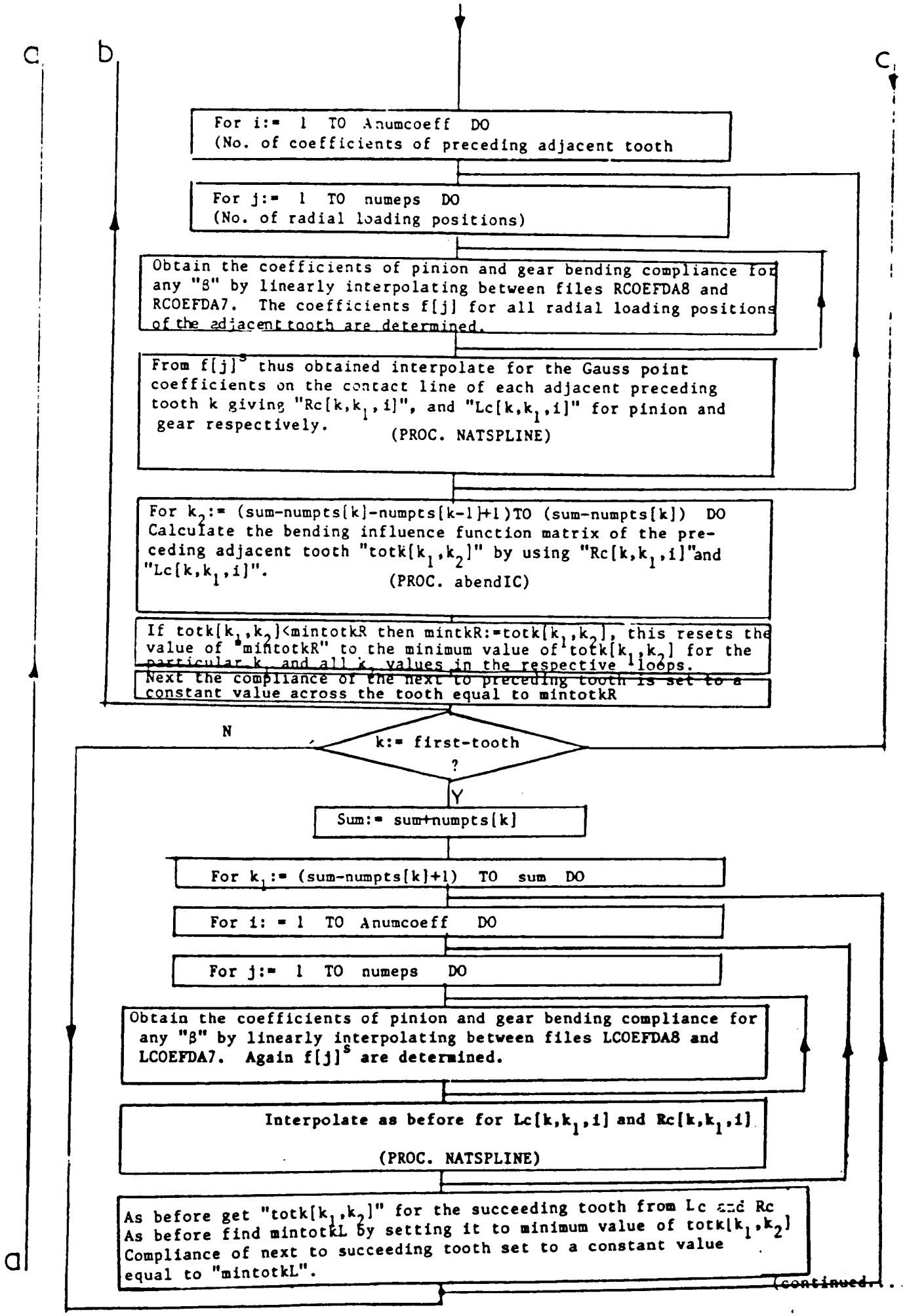
a
b
c
c
For i:= 1 TO Anumcoeff DO
(No. of coefficients of preceding adjacent tooth
For j:= 1 TO numeps DO
(No. of radial loading positions)
Obtain the coefficients of pinion and gear bending compliance for any "β" by linearly interpolating between files RCOEFDA8 and RCOEFDA7. The coefficients f[j] for all radial loading positions of the adjacent tooth are determined.
From f[j]^s thus obtained interpolate for the Gauss point coefficients on the contact line of each adjacent preceding tooth k giving "Rc[k,k1,i]", and "Lc[k,k1,i]" for pinion and gear respectively.
(PROC. NATSPLINE)
For k2:= (sum-numpts[k]-numpts[k-1]+1)TO (sum-numpts[k]) DO
Calculate the bending influence function matrix of the preceding adjacent tooth "totk[k1,k2]" by using "Rc[k,k1,i]"and "Lc[k,k1,i]".
(PROC. abendIC)
If totk[k1,k2]<mintotkR then mintkR:=totk[k1,k2], this resets the value of "mintotkR" to the minimum value of totk[k1,k2] for the particular k1 and all k2 values in the respective loops.
Next the compliance of the next to preceding tooth is set to a constant value across the tooth equal to mintotkR
N
k:= first-tooth
?
Y
Sum:= sum+numpts[k]
For k1:= (sum-numpts[k]+1) TO sum DO
For i: = 1 TO Anumcoeff DO
For j:= 1 TO numeps DO
Obtain the coefficients of pinion and gear bending compliance for any "β" by linearly interpolating between files LCOEFDA8 and LCOEFDA7. Again f[j]^s are determined.
Interpolate as before for Lc[k,k1,i] and Rc[k,k1,i]
(PROC. NATSPLINE)
As before get "totk[k1,k2]" for the succeeding tooth from Lc and Rc
As before find mintotkL by setting it to minimum value of totk[k1,k2]
Compliance of next to succeeding tooth set to a constant value equal to "mintotkL".
(continued...

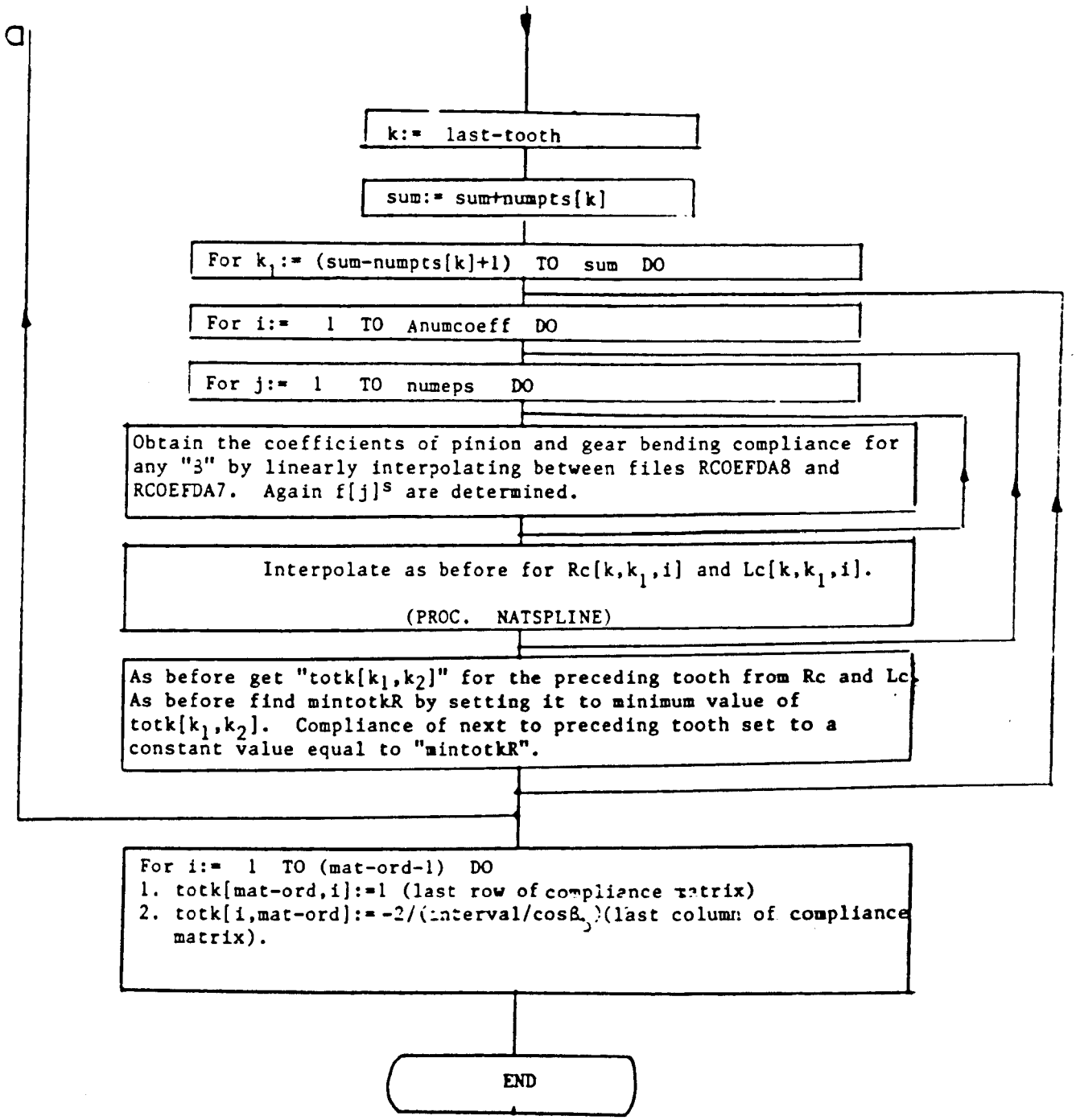

Fig.2A.6 Flowchart for Procedure CALCMAT in Programme HELICALDIST

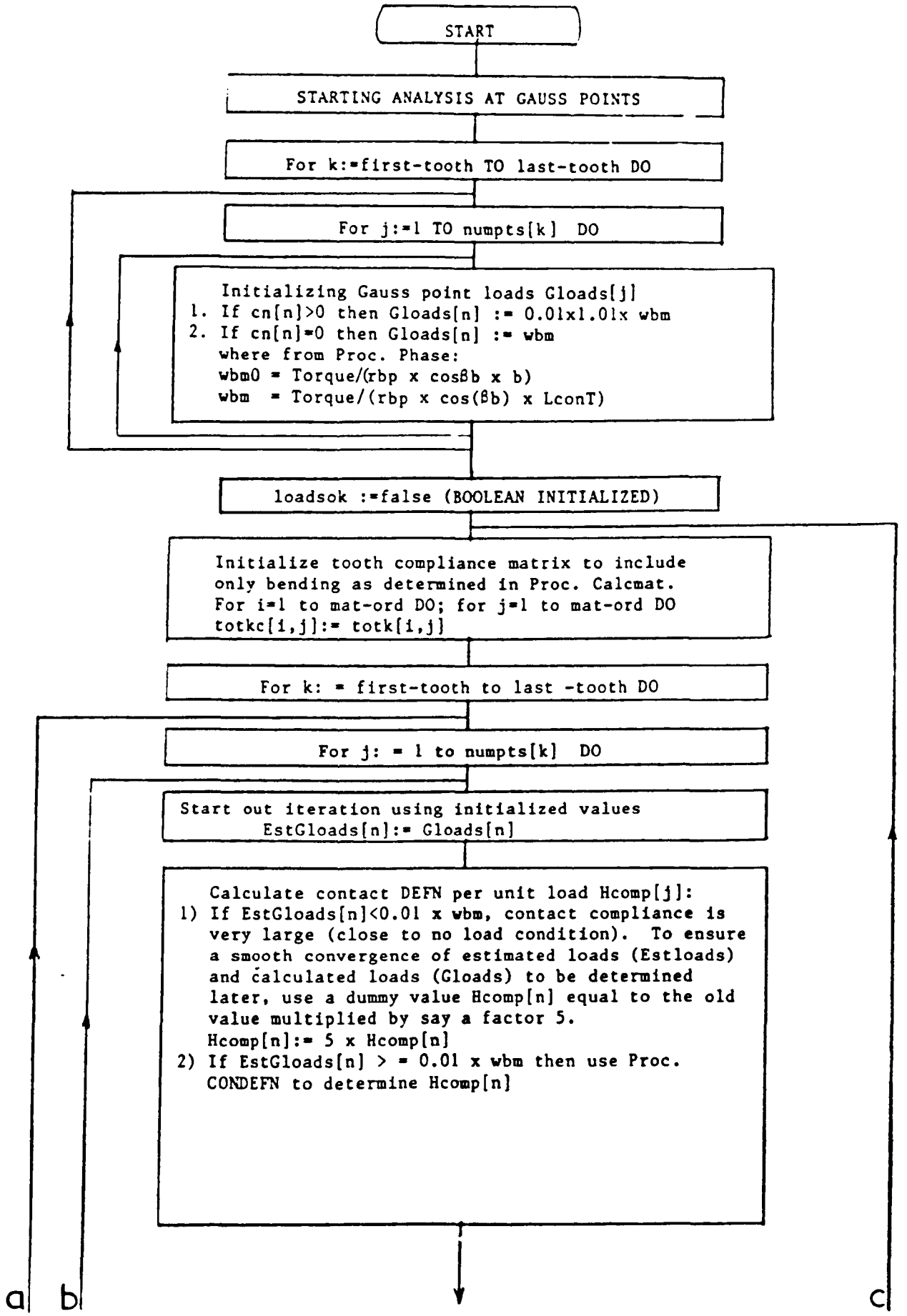
START
STARTING ANALYSIS AT GAUSS POINTS
For k:=first-tooth TO last-tooth DO
For j:=1 TO numpts[k] DO
Initializing Gauss point loads Gloads[j]
1. If cn[n]>0 then Gloads[n] := 0.01x1.01x wbm
2. If cn[n]=0 then Gloads[n] := wbm
where from Proc. Phase:
wbm0 = Torque/(rbp x cosβb x b)
wbm = Torque/(rbp x cos(βb) x LconT)
loadsok :=false (BOOLEAN INITIALIZED)
Initialize tooth compliance matrix to include only bending as determined in Proc. Calcmat.
For i=1 to mat-ord DO; for j=1 to mat-ord DO
totkc[i,j]:= totk[i,j]
For k: = first-tooth to last -tooth DO
For j: = 1 to numpts[k] DO
Start out iteration using initialized values
EstGloads[n]:= Gloads[n]
Calculate contact DEFN per unit load Hcomp[j]:
1) If EstGloads[n]<0.01 x wbm, contact compliance is very large (close to no load condition). To ensure a smooth convergence of estimated loads (Estloads) and calculated loads (Gloads) to be determined later, use a dummy value Hcomp[n] equal to the old value multiplied by say a factor 5.
Hcomp[n]:= 5 x Hcomp[n]
2) If EstGloads[n] > = 0.01 x wbm then use Proc. CONDEFN to determine Hcomp[n]
a
b
c

(continued.....)

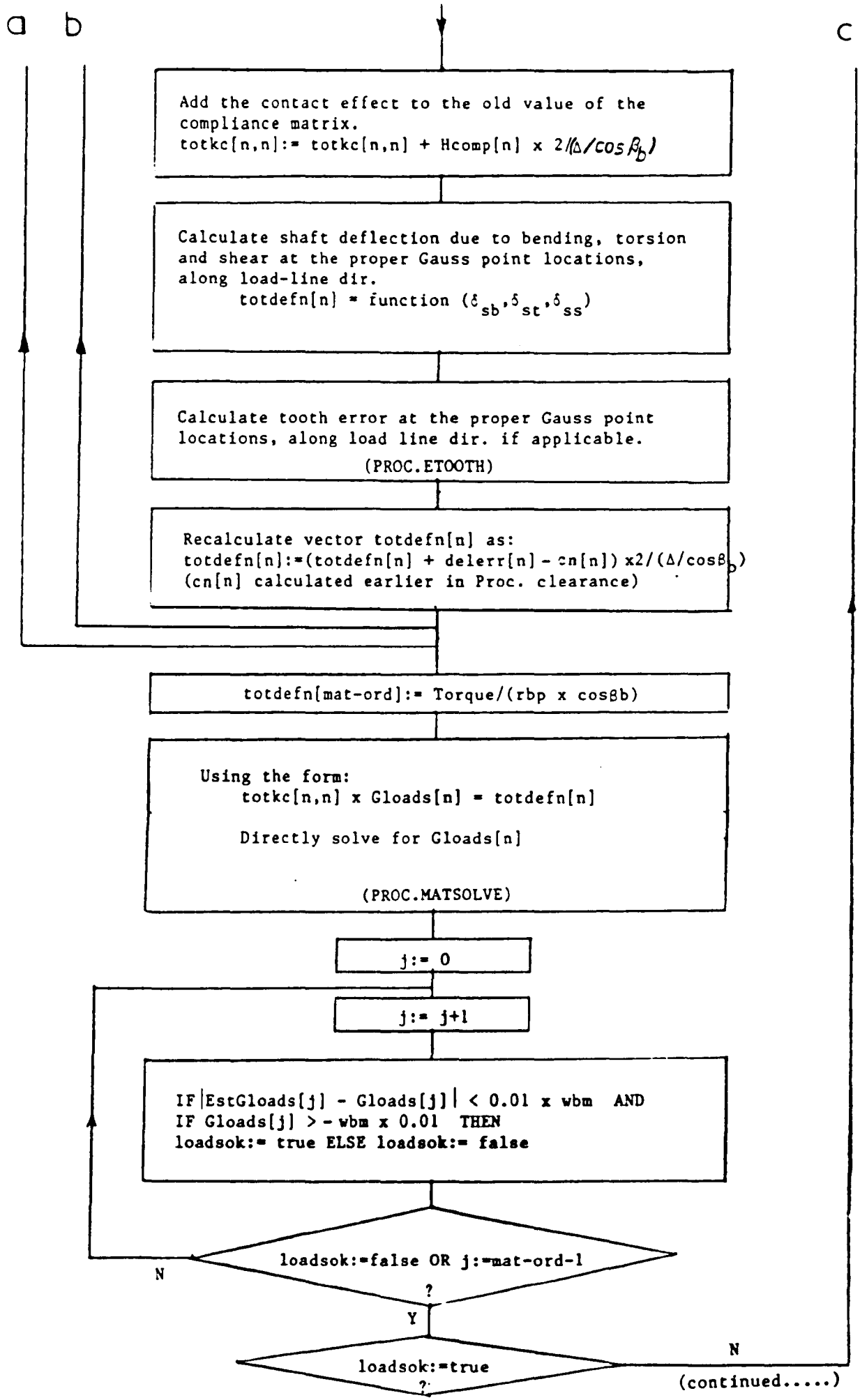
a
b
c
Add the contact effect to the old value of the compliance matrix.
totkc[n,n]:= totkc[n,n] + Hcomp[n] x 2/(Δ/cosβb)
Calculate shaft deflection due to bending, torsion and shear at the proper Gauss point locations, along load-line dir.
totdefn[n] = function (δsb, δst, δss)
Calculate tooth error at the proper Gauss point locations, along load line dir. if applicable.
(PROC.ETOOTH)
Recalculate vector totdefn[n] as:
totdefn[n]:=(totdefn[n] + delerr[n] - cn[n]) x2/(Δ/cosβb)
(cn[n] calculated earlier in Proc. clearance)
totdefn[mat-ord]:= Torque/(rbp x cosβb)
Using the form:
totkc[n,n] x Gloads[n] = totdefn[n]
Directly solve for Gloads[n]
(PROC.MATSOLVE)
j:= 0
j:= j+1
IF |EstGloads[j] - Gloads[j]| < 0.01 x wbm AND
IF Gloads[j] > - wbm x 0.01 THEN
loadsok:= true ELSE loadsok:= false
loadsok:=false OR j:=mat-ord-1
?
N
Y
loadsok:=true
?
N
(continued.....)

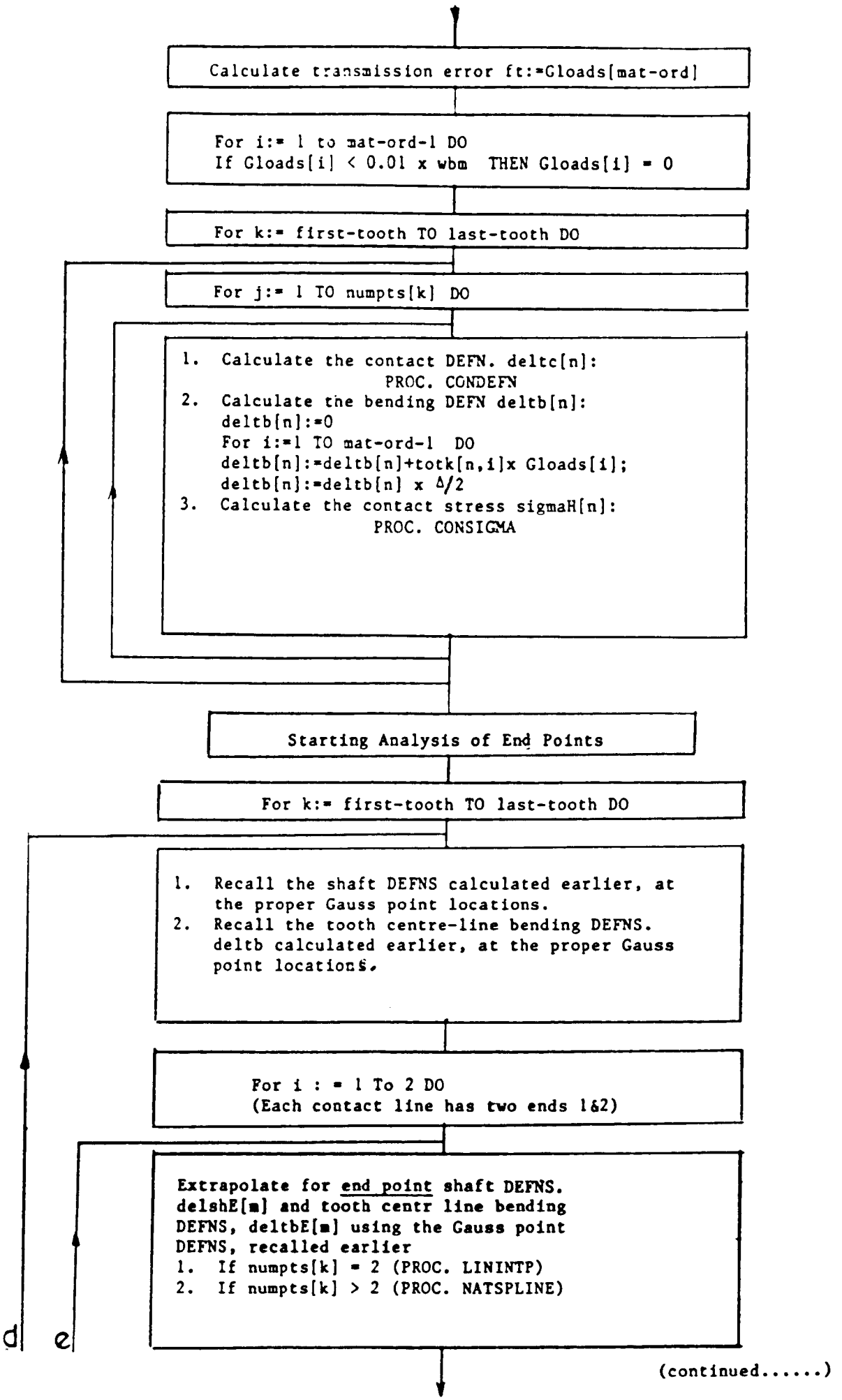
Calculate transmission error ft:=Gloads[mat-ord]
For i:= 1 to mat-ord-1 DO
If Gloads[i] < 0.01 x wbm THEN Gloads[i] = 0
For k:= first-tooth TO last-tooth DO
For j:= 1 TO numpts[k] DO
1. Calculate the contact DEFN. deltc[n]:
PROC. CONDEFN
2. Calculate the bending DEFN deltb[n]:
deltb[n]:=0
For i:=1 TO mat-ord-1 DO
deltb[n]:=deltb[n]+totk[n,i]x Gloads[i];
deltb[n]:=deltb[n] x Δ/2
3. Calculate the contact stress sigmaH[n]:
PROC. CONSIGMA
Starting Analysis of End Points
For k:= first-tooth TO last-tooth DO
1. Recall the shaft DEFNS calculated earlier, at the proper Gauss point locations.
2. Recall the tooth centre-line bending DEFNS. deltb calculated earlier, at the proper Gauss point locations.
For i : = 1 To 2 DO
(Each contact line has two ends 1&2)
Extrapolate for end point shaft DEFNS. delshE[m] and tooth centr line bending DEFNS, deltbE[m] using the Gauss point DEFNS, recalled earlier
1. If numpts[k] = 2 (PROC. LININTP)
2. If numpts[k] > 2 (PROC. NATSPLINE)
d
e
(continued.....)

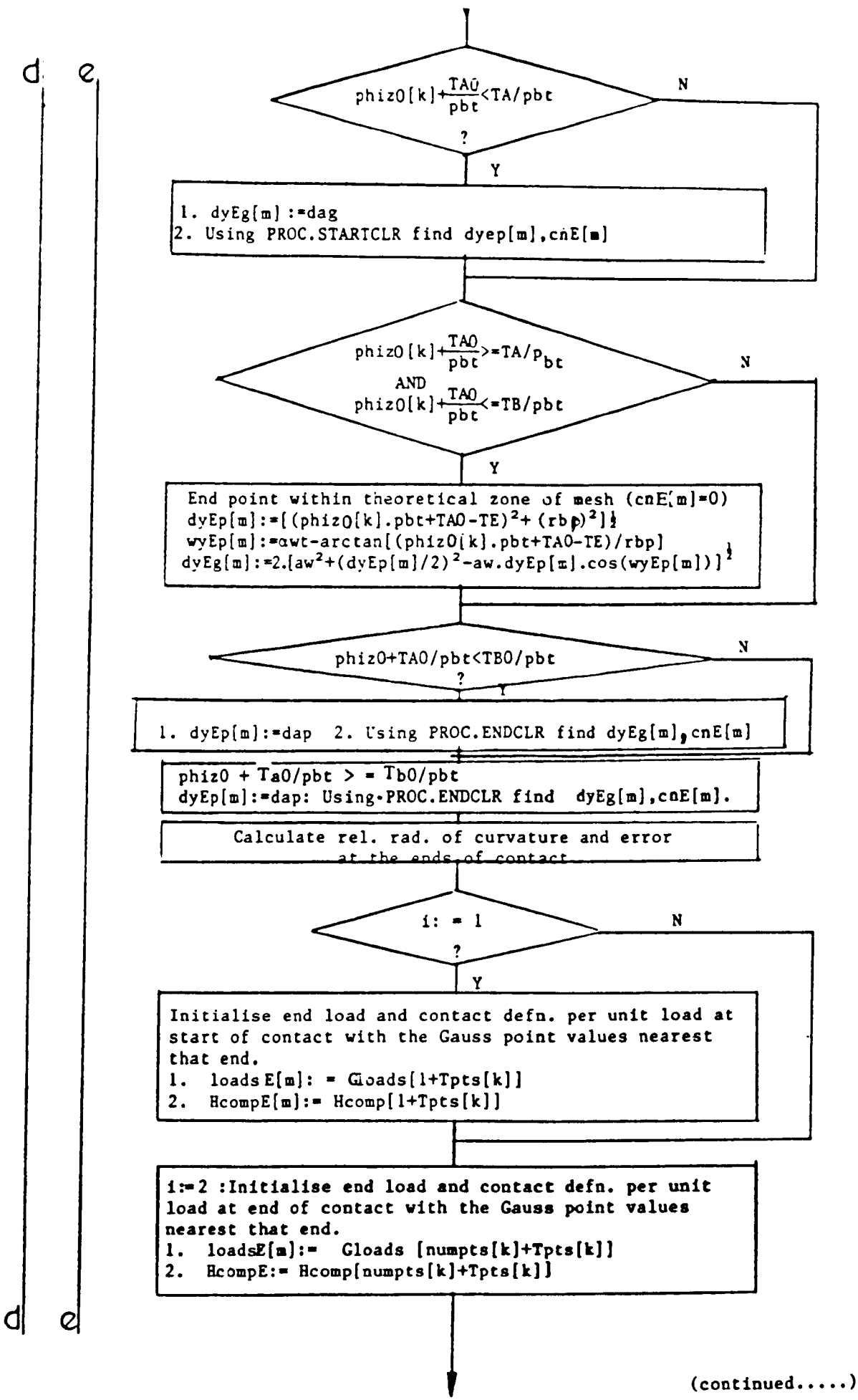
d
e
phiz0[k]+TA0/pbt<TA/pbt
?
N
Y
1. dyEg[m] :=dag
2. Using PROC.STARTCLR find dyep[m],cnE[m]
phiz0[k]+TA0/pbt>=TA/pbt
AND
phiz0[k]+TA0/pbt<=TB/pbt
N
Y
End point within theoretical zone of mesh (cnE[m]=0)
dyEp[m]:=[(phiz0[k].pbt+TA0-TE)^2+(rbp)^2]^½
wyEp[m]:=αwt-arctan[(phiz0[k].pbt+TA0-TE)/rbp]
dyEg[m]:=2.[aw^2+(dyEp[m]/2)^2-aw.dyEp[m].cos(wyEp[m])]^½
phiz0+TA0/pbt<TB0/pbt
?
N
Y
1. dyEp[m]:=dap 2. Using PROC.ENDCLR find dyEg[m],cnE[m]
phiz0 + Ta0/pbt > = Tb0/pbt
dyEp[m]:=dap: Using PROC.ENDCLR find dyEg[m],cnE[m].
Calculate rel. rad. of curvature and error at the ends of contact
i: = 1
?
N
Y
Initialise end load and contact defn. per unit load at start of contact with the Gauss point values nearest that end.
1. loadsE[m]: = Gloads[1+Tpts[k]]
2. HcompE[m]:= Hcomp[1+Tpts[k]]
i:=2 :Initialise end load and contact defn. per unit load at end of contact with the Gauss point values nearest that end.
1. loadsE[m]:= Gloads [numpts[k]+Tpts[k]]
2. HcompE:= Hcomp[numpts[k]+Tpts[k]]
d
e

(continued.....)

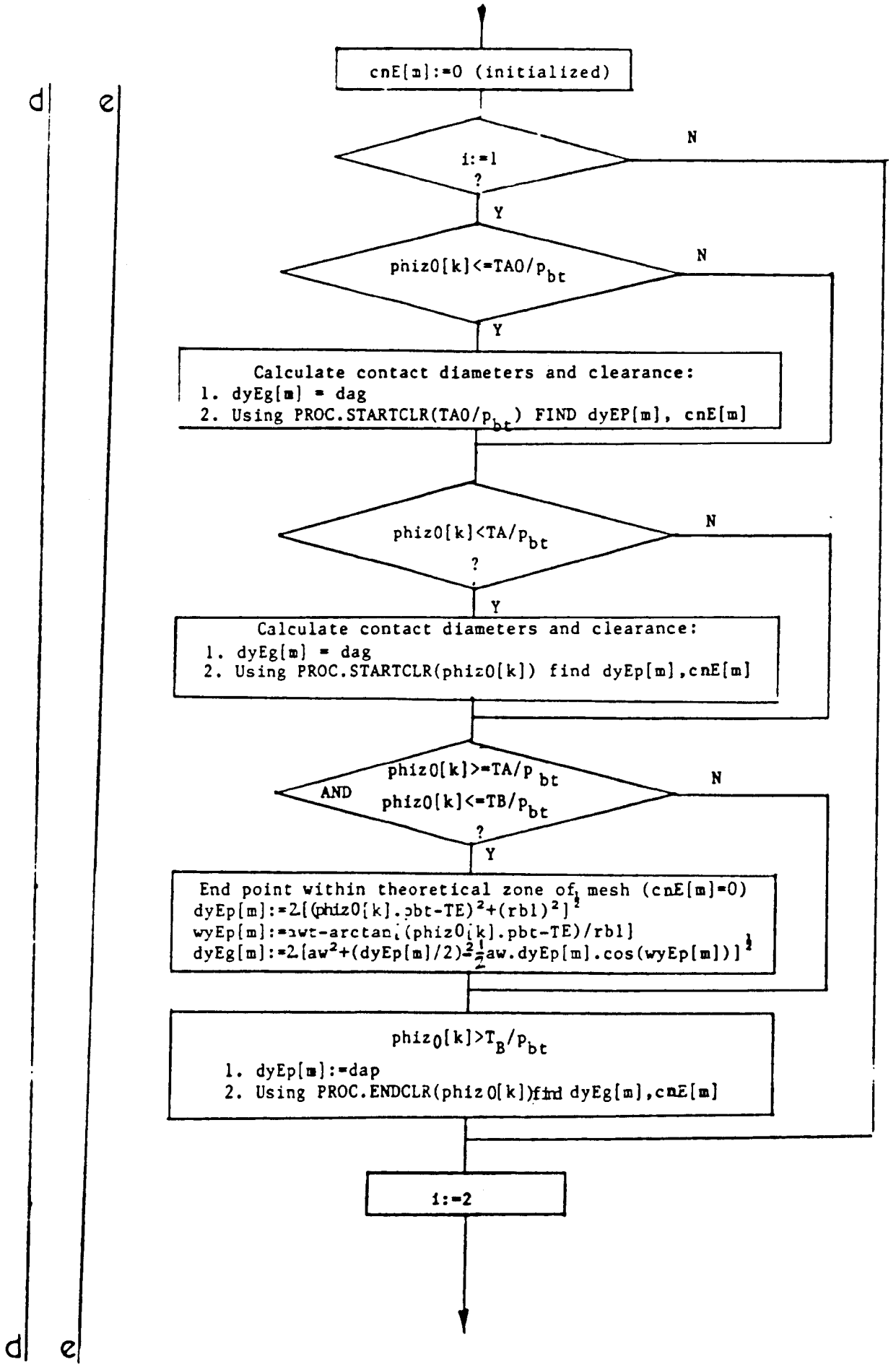
d
e
cnE[m]:=0 (initialized)
i:=1
?
N
Y
phiz0[k]<=TA0/p bt
N
Y
Calculate contact diameters and clearance:
1. dyEg[m] = dag
2. Using PROC.STARTCLR(TA0/p bt) FIND dyEP[m], cnE[m]
phiz0[k]<TA/p bt
?
N
Y
Calculate contact diameters and clearance:
1. dyEg[m] = dag
2. Using PROC.STARTCLR(phiz0[k]) find dyEp[m],cnE[m]
phiz0[k]>=TA/p bt
AND
phiz0[k]<=TB/p bt
?
N
Y
End point within theoretical zone of mesh (cnE[m]=0)
dyEp[m]:=2.[(phiz0[k].pbt-TE)^2+(rb1)^2]^½
wyEp[m]:=awt-arctan(phiz0[k].pbt-TE)/rb1]
dyEg[m]:=2.[aw^2+(dyEp[m]/2)^2-aw.dyEp[m].cos(wyEp[m])]^½
phiz0[k]>T B/p bt
1. dyEp[m]:=dap
2. Using PROC.ENDCLR(phiz0[k]) find dyEg[m],cnE[m]
i:=2
d
e

(continued.....)

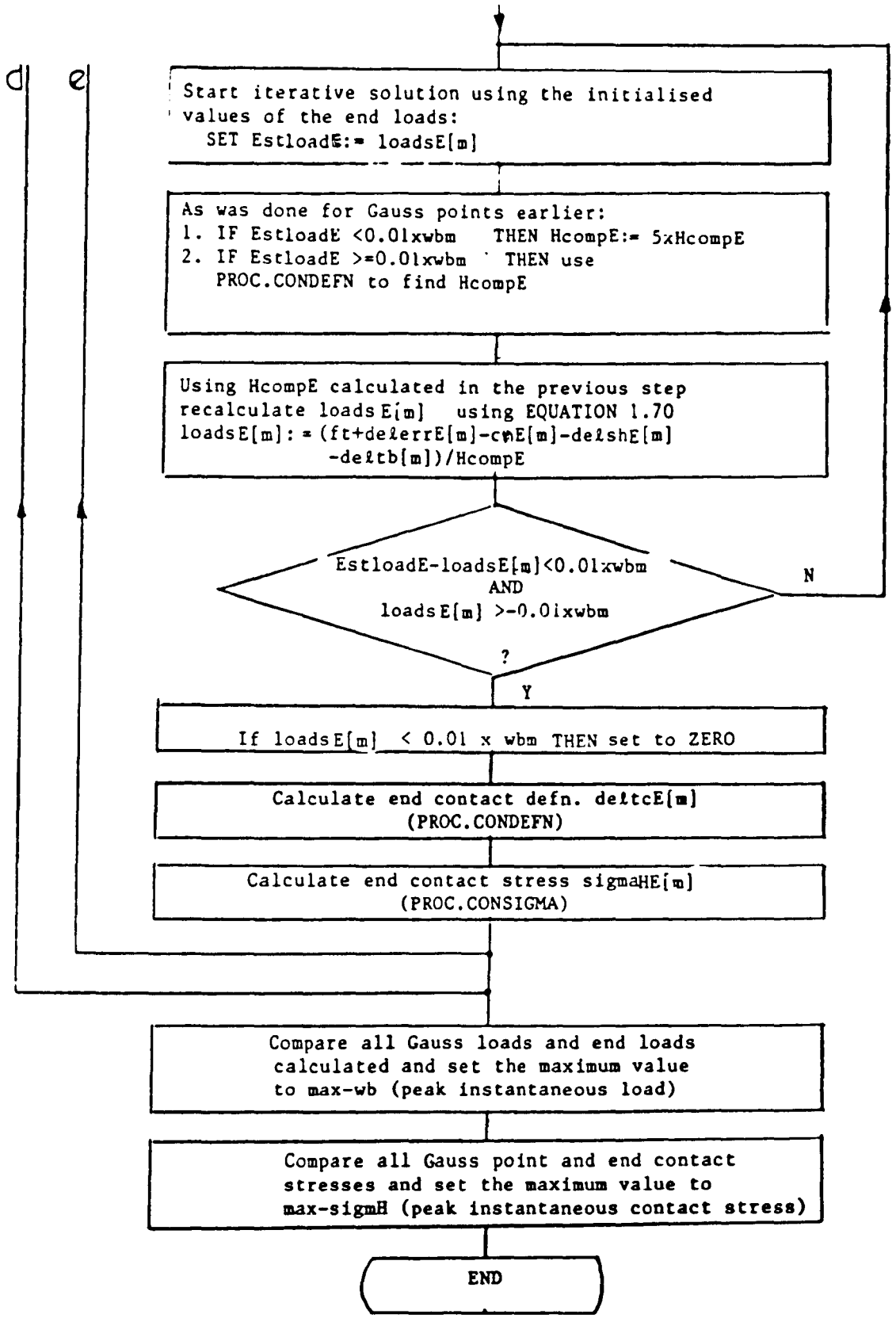
d
e
Start iterative solution using the initialised values of the end loads:
SET EstloadE:= loadsE[m]
As was done for Gauss points earlier:
1. IF EstloadE <0.01xwbm THEN HcompE:= 5xHcompE
2. IF EstloadE >=0.01xwbm THEN use PROC.CONDEFN to find HcompE
Using HcompE calculated in the previous step recalculate loadsE[m] using EQUATION 1.70
loadsE[m]:=(ft+delerrE[m]-cmE[m]-delshE[m] -deltb[m])/HcompE
EstloadE-loadsE[m]<0.01xwbm AND loadsE[m] >-0.01xwbm
?
N
Y
If loadsE[m] < 0.01 x wbm THEN set to ZERO
Calculate end contact defn. deltcE[m] (PROC.CONDEFN)
Calculate end contact stress sigmaHE[m] (PROC.CONSIGMA)
Compare all Gauss loads and end loads calculated and set the maximum value to max-wb (peak instantaneous load)
Compare all Gauss point and end contact stresses and set the maximum value to max-sigmH (peak instantaneous contact stress)
END

(continued.....)

KEY: Tpts[k] - total number of Gauss points on all contact lines between first-tooth and k^{th} tooth not including the k^{th} tooth points:

Tpts[k] = numptsT - numpts[k]

TptsE[k] - total number of end points on all contact lines between first-tooth and k^{th} tooth not including the k^{th} tooth points

TptsE[k] = numptsTE - 2

n = j + Tpts[k]

m = i + TptsE[k]

Δ = interval of Gauss integration chosen arbitrarily depending on accuracy of integration needed, and on computer limitations, and is the face width divided by the number of intervals chosen

Figure 2A.7 Flowchart for Procedure LOADDIST in Programme HELICALDIST

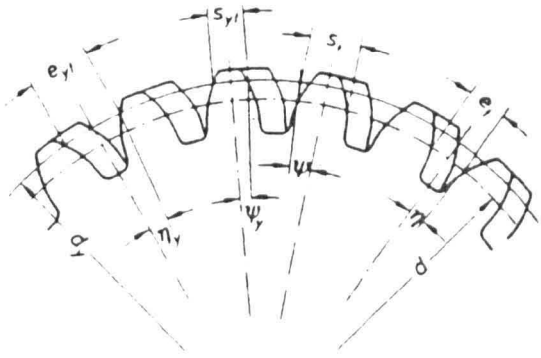

Fig. 2A.8 Helical gear: tooth thicknesses, spacewidths and their half angles

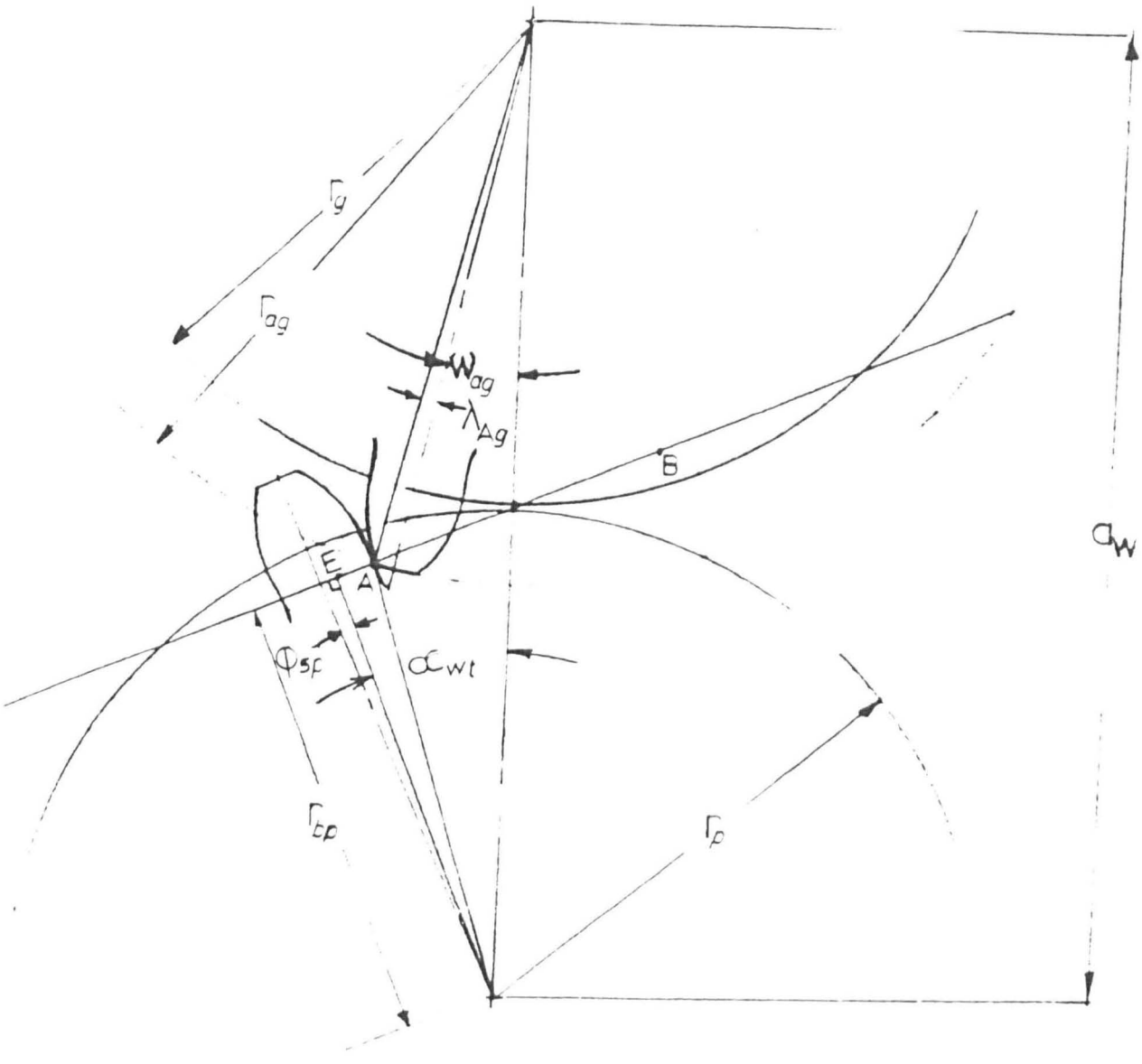

Fig. 2A.9 Contact at the Start of the Theoretically Defined Phase of Mesh

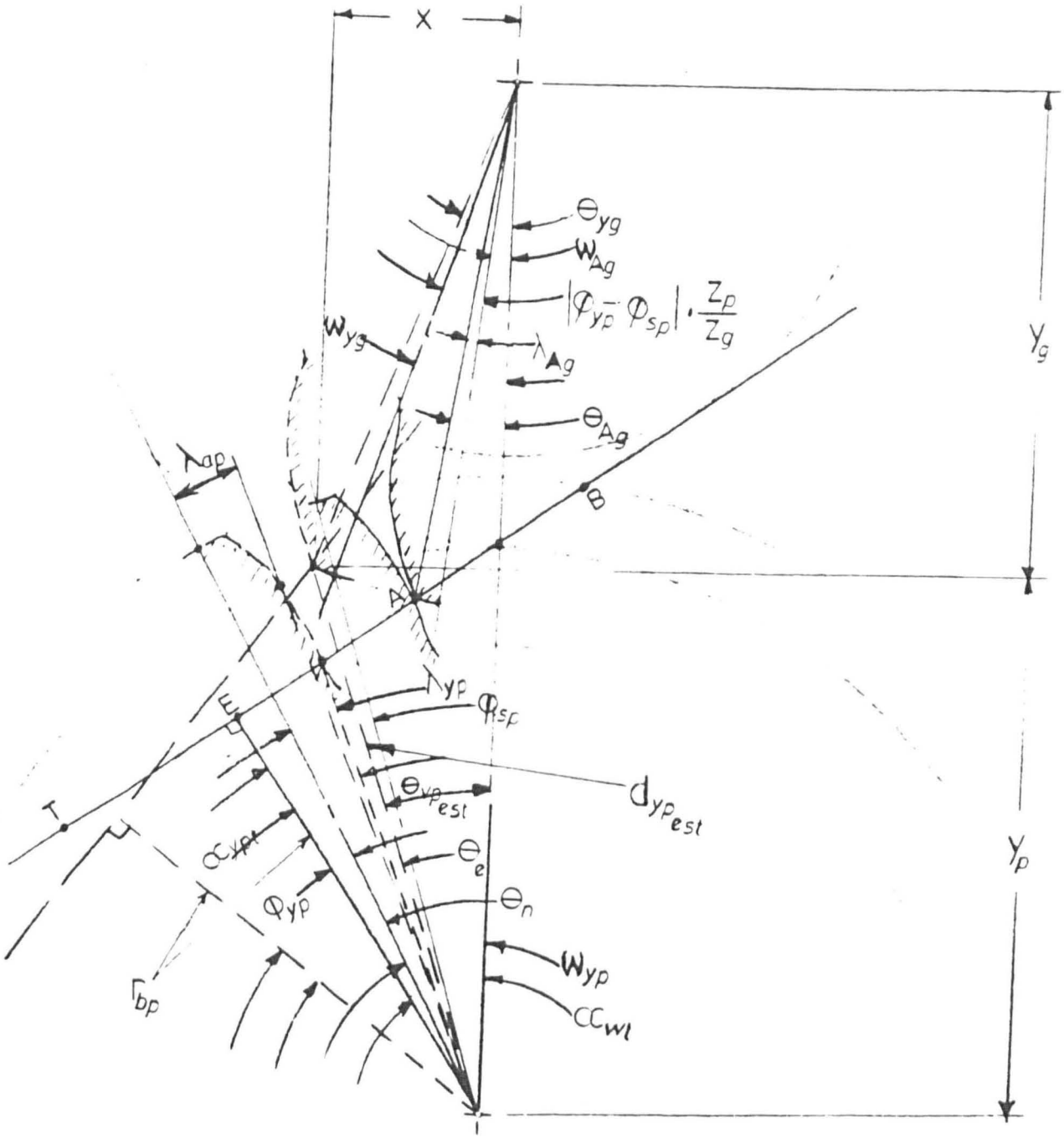

Fig. 2A.10 Contact Geometry Just Outside the Start of the Theoretically Defined Phase of Mesh

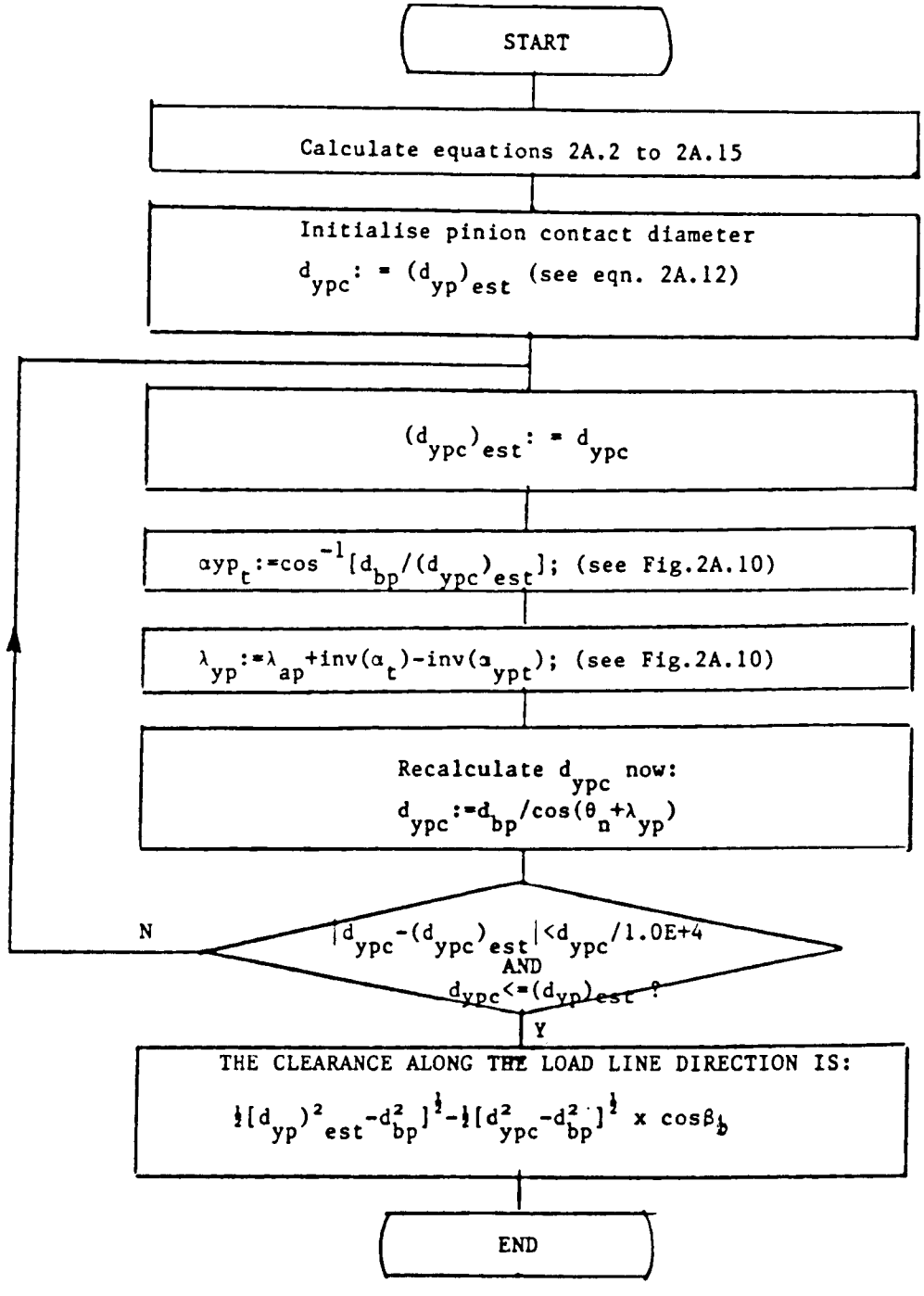

Figure 2A.11 Flow Chart for Procedure STARTCLR in Program HELICALDIST

APPENDIX 2B

INTERPRETING LOADED AND ADJACENT TEETH FE DEFLECTIONS

a) Interpretation of FE Loaded Tooth Centre-line Deflections

The micro-computer program "HGDEFN4" interpolates for any surface point "p" or "f" (see Figure 2.7) along any contact line across the face of a loaded tooth using the FE nodal deflections. It also interpolates for the tooth centreline points "c", obtained by extending the normals to a contact line at any point "p" or "f" to intercept the tooth central surface (see Figure 2.7 and the subsequent discussion).

As discussed in part (c) of Appendix 1A, and the part of section 2.5 corresponding to Figure 2.7, the interpolation for the deflections at "c" corresponding to the loaded points "f" is straightforward since the point "c" falls in this case on the boundary of the FE mesh elements, see Figure 2B.1a. Therefore, the two corner nodes n_1, n_2 and one mid-side node n_3, are used to quadratically interpolate for point "C" (quadratic extrapolation is used if "c" falls outside n_1 or n_2).

Considering any other point "p" (other than the loaded point "f") along a contact line (Figure 2.7), then the corresponding point "c" is the interception of the normal at point "p" with the central plane as shown in Figure 2B.1b. In this case, the interpolation procedure is much more complex. Referring to Figures 2B.1c and 2B.1b, where all deflections are calculated in the direction of the normal to point "p", we have:

u_{al} - linearly interpolated deflection of point "a" using nodes n_1,n_2.

u_{bl} - linearly interpolated deflection of point "b" using nodes n_4,n_5.

u_{dl} - linearly interpolated deflection of point "d" using nodes n_1,n_4.

u_{el} - linearly interpolated deflection of point "e" using nodes n_2,n_5.

u_{aq} - quadratically interpolated deflection of point "a" using nodes n_1, n_2, n_3.

u_{bq} - quadratically interpolated deflection of point "b" using nodes n_4, n_5, n_6.

u_{dq} - quadratically interpolated deflection of point "d" using nodes n_1, n_4, n_7.

u_{eq} - quadratically interpolated deflection of point "e" using nodes n_2, n_5, n_8.

u_{cll1} - linearly interpolated deflection of point "c" using u_{al} and u_{bl}.

u_{cll2} - linearly interpolated deflection of point "c" using u_{dl} and u_{el}.

u_{clq1} - linearly interpolated deflection of point "c" using u_{aq} and u_{bq}.
u_{clq2} - linearly interpolated deflection of point "c" using u_{dq} and u_{eq}

Referring to Figure 2B.1c, we have:

$$u_{cll1} = u_{cll2} = u_{cll} \qquad 2B.1$$

$$\Delta u_{c1} = u_{clq1} - u_{cll1} \qquad 2B.2$$

$$\Delta u_{c2} = u_{clq2} - u_{cll2} \qquad 2B.3$$

Note that in the example shown in Figure 2B.1c, u_{clq} is greater than u_{cll}, however, this situation may be reversed (depending on the values of the deflections of the mid-side nodes), thus reversing the signs of Δu_{c1} and Δu_{c2}. Therefore the overall deflection of point "c" is estimated by a quasi-quadratic interpolation method and is given as

$$u_c = u_{cll} \pm |\Delta u_{c1} - \Delta u_{c2}| \qquad 2B.4a$$

or expressed in another form

$$u_c = u_{cll} \pm |u_{clq1} - u_{clq2}| \qquad 2B.4b$$

For points "p" on a contact line away from the point of loading, the contact deformation diminishes quickly, thus for these points, the deflection may be interpolated for at the flank surface and not at the central surface in an identical fashion to that described above. This was done in order to compare deflections at the surface away from the loading point, with those at their corresponding locations at the tooth central surface. Table 2B.1 shows the results for the 40 tooth gear loaded at $z=0.25m_n$ from the gear end, and at the tooth tip. Clearly, as the distance from the loading point increases, the surface and centre-line deflections converge. In the present work however, all deflections were taken at the tooth central surface (points "c") for the loaded tooth, and at the tooth flank for the adjacent teeth, where there is no contact deformation.

b) Interpolating for Adjacent Teeth Surface Points p_r and p_ℓ Corresponding to Surface Points p on a Contact Line of the Loaded Tooth.

From Figures 1A.7 and 2.8 the following relations may be obtained:

$$\alpha = \alpha_{pt} + \gamma_{zp} - \psi_p \qquad 2B.5$$

$$x_{p\ell} = x_p - pp_\ell . \cos(\alpha) \qquad 2B.6$$

$$y_{p\ell} = y_p - pp_\ell . \sin(\alpha) \qquad 2B.7$$

$$x_{pr} = x_p + pp_r . \cos(\alpha) \qquad 2B.8$$

$$y_{pr} = y_p + pp_r . \sin(\alpha) \qquad 2B.9$$

$$pp_\ell = pp_r = p_{bt} = p_t . \cos(\alpha_t) = \pi m_n . \frac{\cos\alpha t}{\cos\beta} \qquad 2B.10$$

$$z_{p\ell} = z_{pr} = z_p \qquad 2B.11$$

Clearly, by looking at equation 2B.11 and Figure 2B.2, the interpolation for the deflections of points "p_r" and "p_ℓ" by using the FE deflections at the corner and mid-nodes, could be greatly simplified by choosing "p_r" and "p_ℓ" at the corner sections. Thus as shown in Figure 2B.2a, cubic interpolation for points p_ℓ and p_r may be carried out using the two corner and one mide-side nodes. If more points are needed, z_p values at mid-side sections may be chosen as shown in Figure 2B.2b. The interpolation is more complex than the previous case and becomes similar to the interpolation procedure discussed in part (a) of this Appendix for the central surface points of the loaded tooth (quasi-quadratic interpolation). However, quite a few steps in this case are no longer needed since points "a" and "b" now coincide with the mid-side nodes (compare with Figure 2B.1b), and need not be interpolated for at all in the process. The micro-computer program "HGDEFNADJ" does the interpolation for the adjacent teeth.

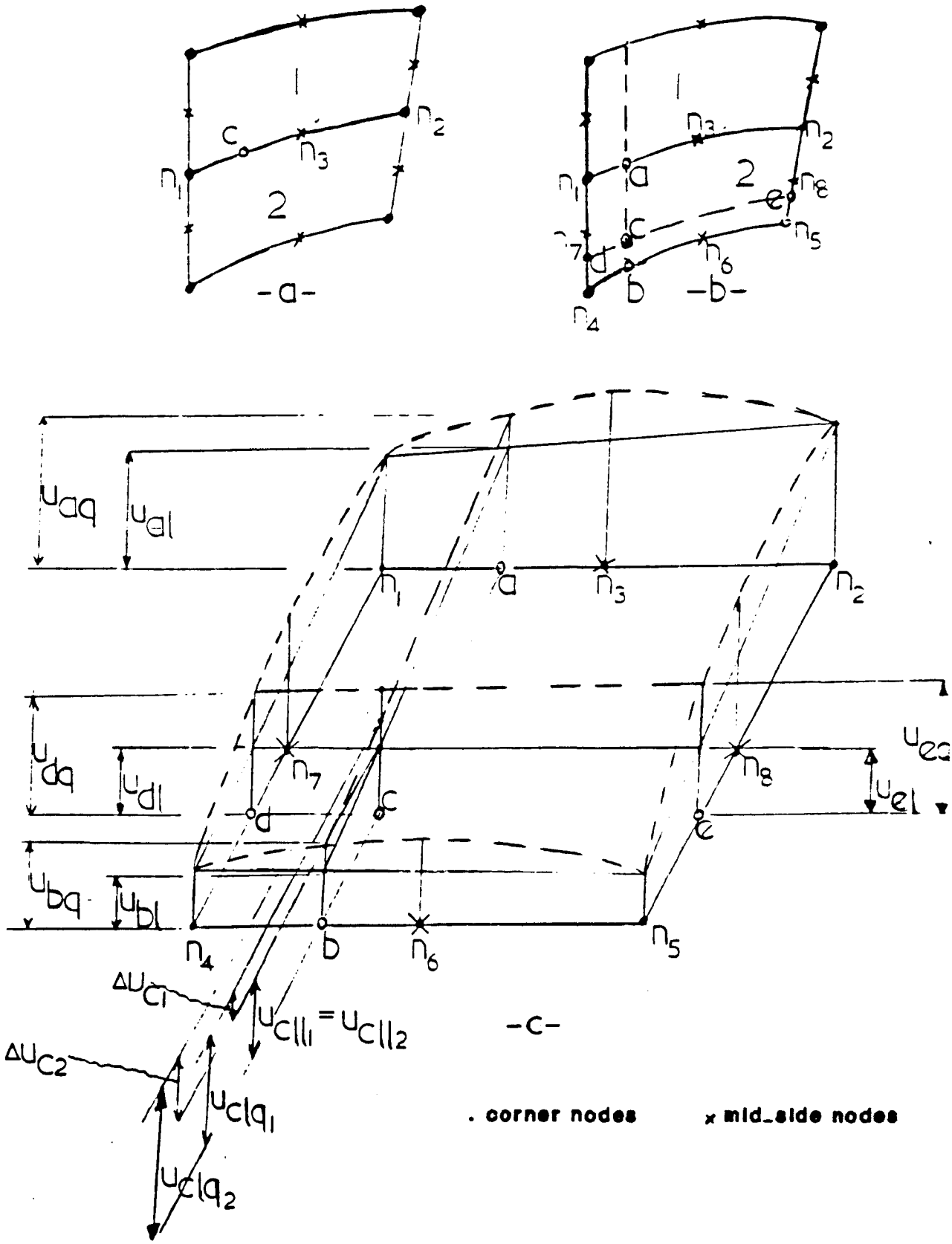

Fig. 2B.1 Interpolating for the Deflection of Point "c" Using Corner & Mid_Side Nodes

zp [mn]	unp [mm/N]*E06	unc [mm/N]*E06	unc-unp [mm/N]*E06	error [%]
0.25	9.031	6.898	-2.162	-31.50
0.50	5.408	4.991	-0.417	-8.40
0.75	3.000	2.914	-0.086	-2.95
2.50	1.323	1.281	-0.042	-3.28
4.00	0.521	0.498	-0.023	-4.61
6.50	0.276	0.270	-0.006	-2.22
9.50	0.234	0.232	-0.002	-0.86

zp _ distance of point "p" from the sharp end of the gear
unp _ deflection of point "p" normally to the tooth flank
unc _ deflection of point "c" along the normal to tooth flank

% error = (unc-unp)*100/unc

Table 2B.1 Comparison of Tooth Surface & Corresponding Tooth Centre_Line Deflections for the 40_Tooth Gear Loaded at 0.25[mn] From the Sharp End

. corner nodes x mid_side nodes

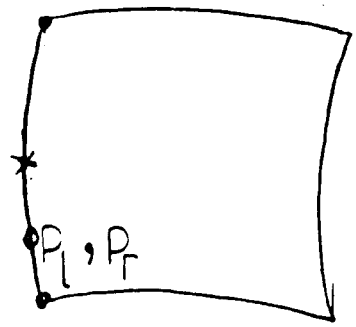

a) face of an element on tooth flank
(choose corner sections)

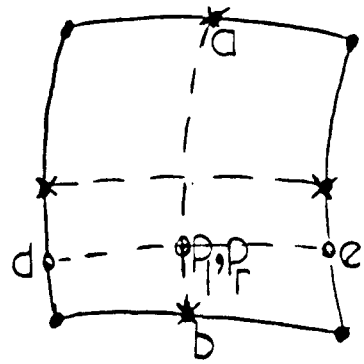

b) face of an element on tooth flank
(choose mid_side sections)

Fig. 2B.2 Interpolating for Adjacent Teeth Deflections at "pl" & "pr"

APPENDIX 2C

CALCULATION OF GEAR SHAFT DEFLECTIONS

The shaft is simply supported at one end, and torsionally and axially restrained at the other, and supports a helical gear (see section 2.5). The components of shaft deflection are due to torsion, shear and bending. Deflections are calculated by assuming that the resultant tooth load "F" acts at mid-face and through the pitch point, however, to generalize the equations, the load is taken at any point (z_F, r_f) as shown in Figure 2C.1. This assumption simplifies the analysis and is justified, since as in Steward's work[30], the shaft deflections are assumed to be independent of the actual load distribution.

a) Shaft Torsional Deflection

Torsional deflection results only from the component of the total load in the transverse plane ($F.\cos\beta_b$). Referrring to Figure 2C.1:

$$T = F \cdot \cos(\beta_b) \cdot r_b \qquad 2C.1$$

For $z<z_f$ the torsional deflection in the transverse plane is

$$\delta_{st} = \frac{T.r_b}{G} \cdot \left[\frac{\ell_1}{J_1} + \frac{z}{J_2}\right] \qquad 2C.2$$

and for $z \geq z_f$, the torsional deflection attains a constant value of

$$\delta_{st} = \frac{T.r_b}{G} \cdot \left[\frac{\ell_1}{J_1} + \frac{z_f}{J_2}\right] \qquad 2C.3$$

where

d_1 - shaft diameter

d_2 - gear tooth root diameter (since Steward[30] showed that the torsional rigidity of the gear can best be estimated by assuming its effective diameter to be the root diameter).

$$J_1 = \pi(d_1)^4/32 \qquad 2C.4$$

$$J_2 = \pi(d_2)^4/32 \qquad 2C.5$$

We are however interested in the torsional deflection component in the direction of F (normal to the tooth flank)

$$\delta_{stn} = \delta_{st} \cdot \cos\beta_b \qquad 2C.6$$

Thus the torsional deflection along the load line direction at any of the Gauss integration points ($0<z<b$), and the end points ($z=0,b$) may be obtained theoretically.

An alternative to the assumption of a concentrated mid-face load is that of a uniformly distributed load across the tooth face-width, giving a linear torque variation across the tooth face with

$$\delta_{stn} = \frac{T.r_b.\cos\beta_b}{G} \left[\frac{\ell_1}{J_1} + \frac{z(2.b-z)}{2.b.J_2} \right]$$

b) Shaft Transverse Shear Deflection

At any transverse section, the cross sectional area is given by

$$A = \pi d^2/4 \qquad 2C.7$$

the shear slope at any section "i" is given by

$$\gamma_{si} = 4F_i/3A_iG \qquad 2C.8a$$

$$\gamma_{si} = (16/3\pi G) \cdot \frac{F_i}{d_i^2} \qquad 2C.8b$$

$$\gamma_{si} = 2.1119 \times 10^{-5} \cdot \frac{F_i}{d_i^2} \qquad 2C.8c$$

where G is taken as the modulus of rigidity for steel, and d is the shaft or gear root diameter at any section. By referring to Figure 2C.2:

$$M_f = F_z.r_f.\sin(\alpha_{ft}) = F.\cos\alpha_n.\sin\beta.r_f.\sin\alpha_{ft} \qquad 2C.9$$

where M_f is a concentrated moment at $z = z_f$

$$F_1 = \frac{F.\cos(\beta_b).(\ell - z_f - \ell_1) + M_f}{\ell} \qquad 2C.10$$

$$F_2 = F \cdot \cos(\beta_b) - F_1 \qquad 2C.11$$

Considering sections ℓ_1, ℓ_2, ℓ_3, and ℓ_4 separately, the shear slope in each section is,

$$\frac{\gamma_{s1}}{F} = 2.1119 \times 10^{-5} \times \frac{F_1}{(d_1)^2} \qquad 2C.12$$

$$\frac{\gamma_{s2}}{F} = 2.1119 \times 10^{-5} \times \frac{F_1}{(d_2)^2} \qquad 2C.13$$

$$\frac{\gamma_{s3}}{F} = -2.1119 \times 10^{-5} \times \frac{F_2}{(d_3)^2} \qquad 2C.14$$

$$\frac{\gamma_{s4}}{F} = -2.1119 \times 10^{-5} \times \frac{F_2}{(d_4)^2} \qquad 2C.15$$

where $d_1 = d_4$ = shaft diameter

and $d_2 = d_3$ = gear root diameter.

The shear deflection in each section is

$$\frac{\delta_{ss1}}{F} = \frac{\gamma_{s1}}{F} \times \ell_1 \qquad 2C.16$$

$$\frac{\delta_{ss2}}{F} = \frac{\gamma_{s2}}{F} \times \ell_2 \qquad 2C.17$$

$$\frac{\delta_{ss3}}{F} = \frac{\gamma_{s3}}{F} \times \ell_3 \qquad 2C.18$$

$$\frac{\delta_{ss4}}{F} = \frac{\gamma_{s4}}{F} \times \ell_4 \qquad 2C.19$$

Referring to Figure 2C.2, the total deflection at the right hand end, with the left hand end kept torsionally and axially restrained is

$$\frac{\delta_{RH}}{F} = (\delta_{ss1} + \delta_{ss2} + \delta_{ss3} + \delta_{ss4})/F \qquad 2C.20$$

and to obtain zero right hand bearing deflection, the deflected shaft must be rotated by an angle equal to

$$\theta = -\left[\frac{\delta_{RH}}{F}\right]/\ell \qquad 2C.21$$

We are interested in the shaft deflection across the gear face width b (at the end points and Gauss points) and so for $0 \leqslant z \leqslant z_f$ we have

$$\frac{\delta_{ss}}{F} = \frac{\delta_{ss1}}{F} + \frac{\gamma_{ss2}}{F} \cdot z + \theta(z+\ell_1) \qquad 2C.22$$

and for $z_f \leqslant z \leqslant b$ we have

$$\frac{\delta_{ss}}{F} = \frac{\delta_{ss1}}{F} + \frac{\delta_{ss2}}{F} + \frac{\gamma_{ss3}}{F} \cdot (z-z_f) + \theta.(z+\ell_1) \qquad 2C.23$$

Finally, to determine the shear deflection along the load line of F, simply multiply equations 2C.22 and 2C.23 by $\cos(\beta_b)$.

c) Shaft Bending Deflection

Using simple engineering theory, the bending deflections of the gear shaft centre were derived for $0 \leqslant z \leqslant b$ (see Figures 2C.1 and 2C.2)
For $0 \leqslant z \leqslant z_f$ we have

$$\delta_{sb} = \frac{F_1.\ell_1^2}{6E.I_1}(3z+\ell_1) + \frac{F_1}{6EI_2}.(z)^2.(z+3\ell_1) + \theta_A.(z+\ell_1) \qquad 2C.24$$

for $z_f \leqslant z \leqslant b$

$$\delta_{sb} = \frac{F_1.\ell_1^2}{6E.I_1}(3z+\ell_1) + \frac{F_1}{6E.I_2}.\left[3\ell_2(z-\ell_2).(2\ell_1+\ell_2) + \ell_2^2.(\ell_2+3\ell_1)\right]$$

$$+ \frac{F_2}{6EI_2}\left[(z-\ell_2)^2.(3\ell_3+3\ell_4+\ell_2-z)\right] + \theta_A.(z+\ell_1) \qquad 2C.25$$

Where

$$\theta_A = -\frac{1}{\ell.E.I_1}\left[\frac{F_2.\ell_4^3}{3} + \frac{F_1.\ell_1^2}{6}.(3\ell-2\ell_1)\right] -$$

$$\frac{1}{\ell.E.I_2}\left[\frac{F_1.\ell_2}{2}.(2\ell_1+\ell_2).(\ell_3+\ell_4)+\frac{F_1.\ell_2^2}{6}.(3\ell_1+\ell_2) +\right.$$

$$\left.\frac{F_2.\ell_3.\ell_4}{2}.(2\ell_4+\ell_3)+\frac{F_2.\ell_3^2}{6}.(3\ell_4+2\ell_3)\right] \qquad 2C.26$$

$$I_1 = \pi . d_1^4/64 \qquad 2C.27$$

$$I_2 = \pi . d_2^4/64 \qquad 2C.28$$

$$d_1 = d_{sh} \text{ (shaft diameter)} \qquad 2C.29$$

$$d_2 = (d_{gtip} + d_{groot})/2 \qquad 2C.30$$

with d_{gtip} - gear tip diameter
and d_{groot} - gear root diameter.

Clearly the expressions for the deflections given by equations 2C.24 and 2C.25 are in the direction of F.cos(β_b). To obtain the deflections in the direction of the tooth normal load F, these equations are simply multiplied by cos(β_b).

The torsional and transverse shear shaft deflections are obtained from the developed micro computer program "S-T". The developed micro computer program "BENDDEFN" calculates the shaft bending deflections.

Note that the shaft "centre" bending deflections were used, and not those in the base tangent plane at the contacting points. This is because in the FE analysis (Ch.2), the shaft "centre" bending deflections were removed from the overall gear tooth deformations. Anyway, the corresponding slopes (accounting for shaft bending deflections at the gear contact surface) are small, particularly on smaller gears and may be ignored.

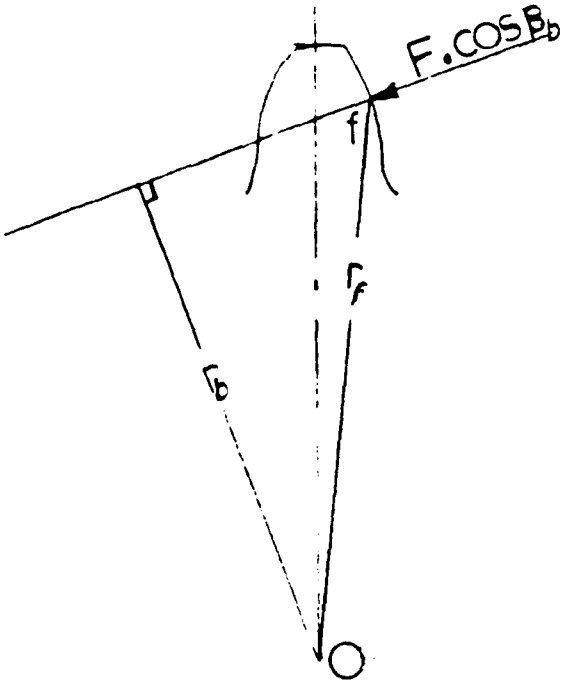

a) transverse section through loaded point "f"

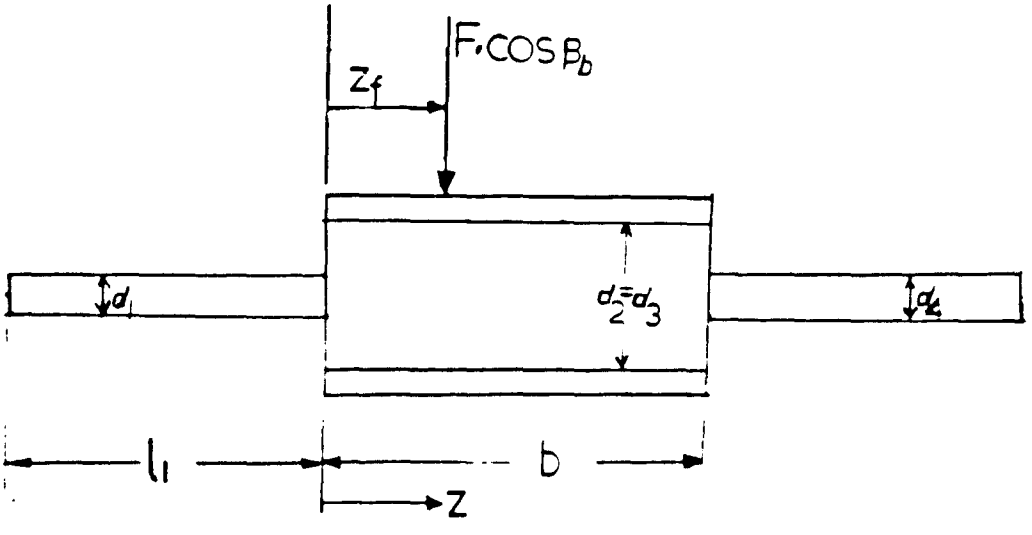

b) view in a direction normal to the plane contained by "z" & the force "F.cosβ_b"

Fig. 2C.1 Shaft Torsional Deflection

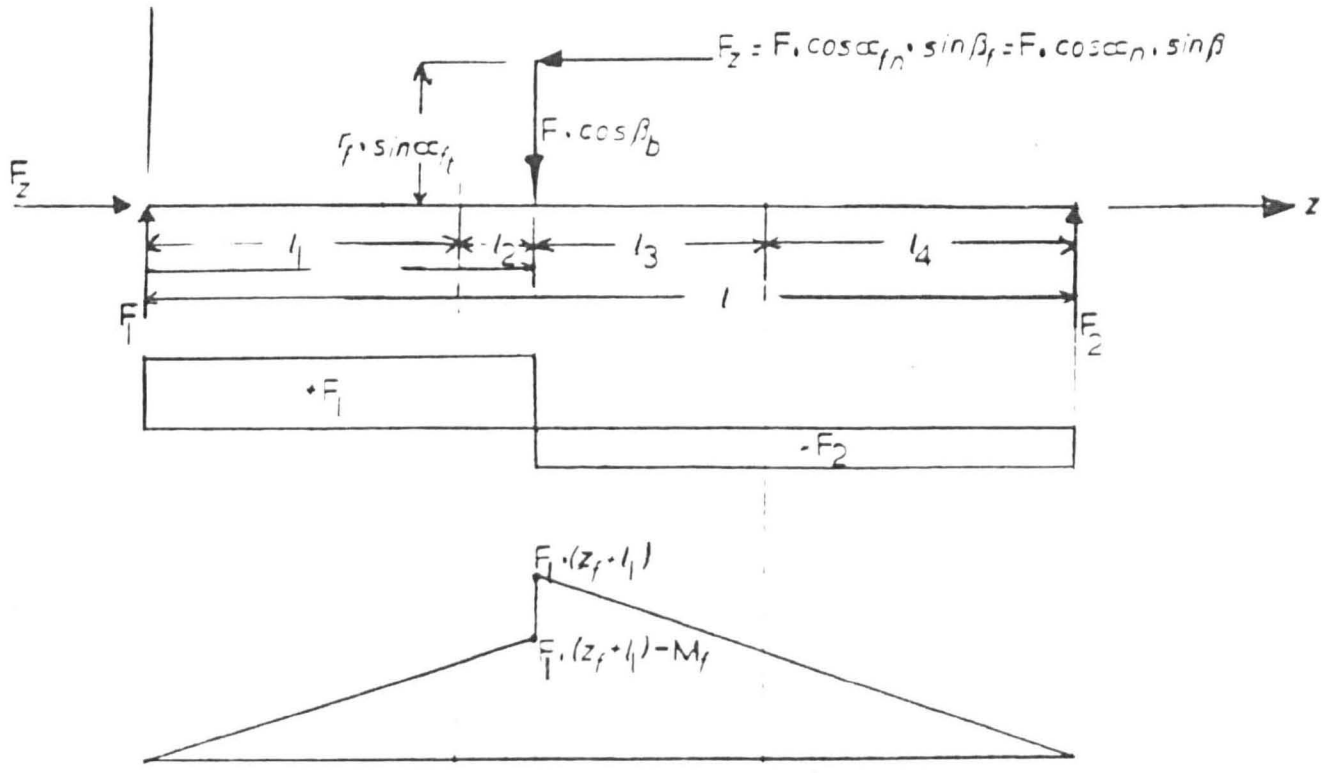

a) load, shear & moment diagrams

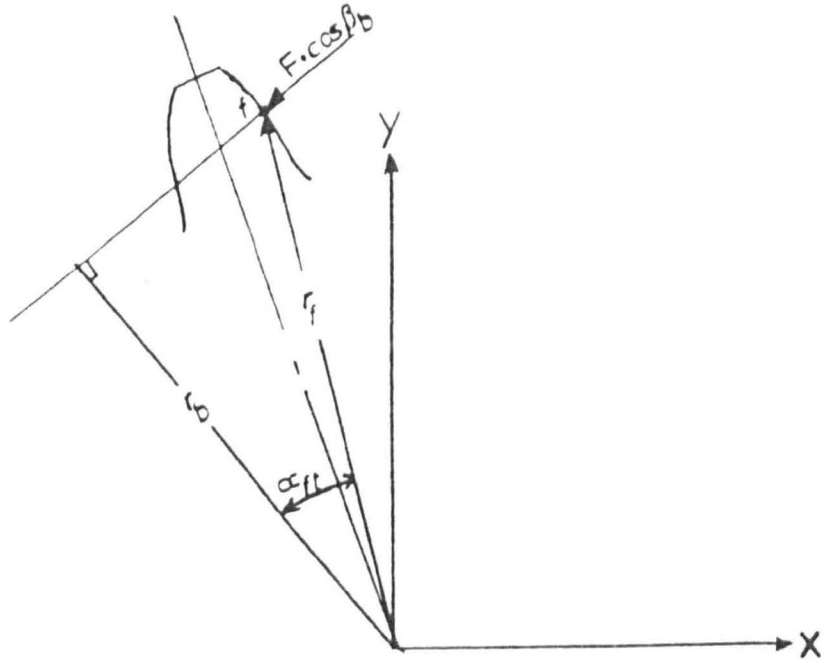

b) a transverse section of the gear through point "f"

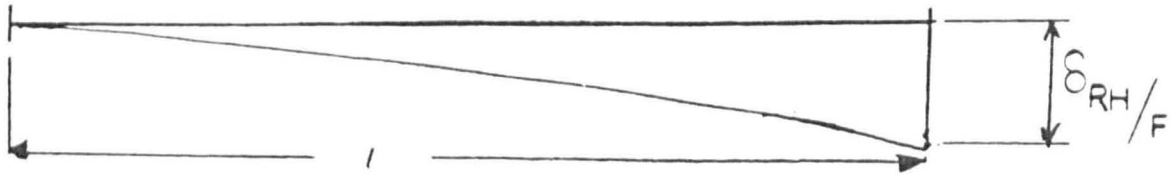

c) determination of Θ

Fig. 2C.2 Shaft Transverse Shear Deflection

APPENDIX 4A

SAMPLE OUTPUTS FROM LOAD DISTRIBUTION PROGRAM "HELICALDIST"

This Appendix lists some sample outputs from the load distribution program for the gear set described in Section 4.1. In all the sample cases listed, except where end-spikes are shown, the same phase of mesh is used in order to show the effect of introducing tooth deviations on the general load distribution at a particular phase. In sample outputs null-b, null-c, and 9b, the phases which produce end-spikes have been chosen for comparison purposes. These phases will not be exactly at the starting or ending geometric phase due to elastic deformations and introduced deviations. Due to space limitations, only three sample cases with spike-effect have been listed. The amount and type of deviation(s) introduced is described before each listing. The peak contact loads and stresses used to plot the graphs of Chapter Four were obtained by producing similar outputs but for about sixty phases for each gear-set. Then the peaks from all sixty phases were taken and compared. Finally the peak of the sixty or so peaks was chosen for the calculations of the load distribution factor. As for the end-spikes, it is known that these occur near the start and end of mesh only, and are thus obtained by trial and error, until the output gives one of the engaged teeth as a single contact point. This is the spike generally producing the worst contact load and stress. Start and end of mesh load spikes are of the same order of magnitude for all practical purposes. The worst stress however is at the start of mesh for the particular gear-set used due to the smaller radius of curvature there (see Eqn. 1.7).

Output null-a This output is that of a perfect (error-free) gear-set at an arbitrary reference phase of mesh 1.01 pbt.

```
**********************************************************************
*HELICALDIST: Design Unit Newcastle University. Version 07 (25-04-89)*
**********************************************************BY C.D. HADDAD**
```

GEAR GEOMETRY & LOADING DATA

		Driver	Driven
Number of teeth	z	18	54
Facewidth	b	120.000	120.000
Ref.circle dia	d	207.846	623.538
Base circle dia	db	191.611	574.834
Tip dia	da	227.846	643.538
Add.mod.factor	x	0.00000	0.00000
Normal module	mn	10.00000000	
Driver Tool Add.	hao1	1.24999988	
Driven Tool Add.	hao2	1.24999988	
Crest Rounding Rad	pan1	0.00000000	
Crest Rounding Rad	pan2	0.00000000	
Working centres	aw	415.69220662	
Helix angle	beta	30.00000000	
Base Helix angle	betab	28.02432072	
Ref.pr.angle	alphan	20.00000000	
Ref.pr.angle	alphat	22.79507719	
Trans.cont.rat	epsalph	1.35286069	
Trans.cont.rat	epsalph0	2.05286068	
Overlap ratio	epsbeta	1.90985939	
Driver torque	T1	1014.86791992	
Tooth load/Lcon	wbm	42.94868259	
Tooth load/b	wbm0	99.99998096	
Max tooth load	max_wb	79.06741242	
Max contact stress	max_sigmaH	365.99906677	
Load factor	kloac	1.84097410	
Load factor	kload0	0.79067421	
Trans. error	ft	8.33224863	
Max no. teeth	MaxTeeth	4	
Matrix order	mat_ord	25	
Max no. intervals	MaxIrrs	3	
Reference phase	phi0	1.0997979	

Tooth num.	Distance along tooth [mm]	Tooth error [mu]	Tooth contact defn. [mu]	Tooth bending defn. [mu]	Normal tooth load [N/mm]	Contact stress [N/mm2]
3	96.000	0.000	0.000	3.908	0.000	0.000
3	101.072	0.000	0.000	3.978	0.000	0.000
3	114.928	0.000	0.000	4.168	0.000	0.000
3	120.000	0.000	0.000	4.238	0.000	0.000
4	48.000	0.000	0.000	3.960	0.000	0.000
4	53.072	0.000	0.000	4.142	0.000	0.000
4	66.928	0.000	0.000	5.066	0.000	0.000
4	77.072	0.000	1.721	6.613	68.381	365.999
4	90.928	0.000	1.674	6.659	66.599	313.946
4	101.072	0.000	1.943	6.390	79.067	317.693
4	114.928	0.000	1.559	6.774	62.202	261.106
4	120.000	0.000	1.352	6.980	53.208	236.121
5	0.000	0.000	0.000	5.584	0.000	0.000
5	5.072	0.000	0.000	5.978	0.000	0.000
5	18.928	0.000	1.535	6.798	60.254	325.493
5	29.072	0.000	1.671	6.662	66.500	311.225
5	42.928	0.000	1.912	6.421	77.926	306.327
5	53.072	0.000	1.914	6.419	78.408	291.830
5	66.928	0.000	1.904	6.429	79.000	277.318
5	77.072	0.000	1.789	6.544	74.828	261.772
5	90.928	0.000	1.813	6.520	79.025	260.749
5	101.072	0.000	0.000	5.180	0.000	0.000
5	114.928	0.000	0.000	4.772	0.000	0.000
5	120.000	0.000	0.000	4.798	0.000	0.000
6	0.000	0.000	1.362	6.970	53.937	232.485
6	5.072	0.000	1.507	6.826	60.759	242.411
6	18.928	0.000	1.711	6.622	71.876	253.541
6	29.072	0.000	1.735	6.598	75.466	254.355
6	42.928	0.000	0.000	4.537	0.000	0.000
6	53.072	0.000	0.000	3.906	0.000	0.000
6	66.928	0.000	0.000	3.413	0.000	0.000
6	72.000	0.000	0.000	3.228	0.000	0.000

Output null-b This output is that of a perfect (error-free) gear-set at a reference phase of mesh 0.4079 pbt chosen to produce the start of mesh spike-effect.

```
**********************************************************************
*HELICALDIST: Design Unit Newcastle University. Version 07 (25-04-89)*
**********************************************BY C.D. HADDAD**
```

GEAR GEOMETRY & LOADING DATA

			Driver	Driven
Number of teeth	z		18	54
Facewidth	b		120.000	120.000
Ref.circle dia	d		207.846	623.538
Base circle dia	db		191.611	574.834
Tip dia	da		227.846	643.538
Add.mod.factor	x		0.00000	0.00000
Normal module	mn	10.00000000		
Driver Tool Add.	hao1	1.24999988		
Driven Tool Add.	hao2	1.24999988		
Crest Rounding Rad	pan1	0.00000000		
Crest Rounding Rad	pan2	0.00000000		
Working centres	aw	415.69220662		
Helix angle	beta	30.00000000		
Base Helix angle	betat	28.02472072		
Ref.pr.angle	alphan	20.00000000		
Ref.pr.angle	alphat	22.79587719		
Trans.cont.rat	epsalph	1.35286069		
Trans.cont.rat	epsalph0	2.05286068		
Overlap ratio	epsbeta	1.90983939		
Driver torque	T1	1014.86791992		
Tooth load/Lcon	wbm	42.94868259		
Tooth load/b	wbm0	99.99998296		
Max tooth load	max_wb	202.64722518		
Max contact stress	max_sigmaH	674.38314466		
Load factor	kloas	4.71835719		
Load factor	kload0	2.02647248		
Trans. error	tt	8.77575952		
Max no. teeth	MaxTeeth	4		
Matrix order	mat_ord	27		
Max no. intervals	MaxInts	5		
Reference phase	ph.z0	0.40790000		

Tooth num.	Distance along tooth [mm]	Tooth error [mu]	Tooth contact defn. [mu]	Tooth bending defn. [mu]	Normal tooth load [N/mm]	Contact stress [N/mm2]
4	72.000	0.000	0.000	3.756	0.000	0.000
4	77.072	0.000	0.000	3.754	0.000	0.000
4	90.928	0.000	0.000	3.774	0.000	0.000
4	101.072	0.000	0.000	3.884	0.000	0.000
4	114.928	0.000	0.000	4.169	0.000	0.000
4	120.000	0.000	4.492	4.283	202.647	634.383
5	24.000	0.000	0.000	3.925	0.000	0.000
5	29.072	0.000	0.000	4.112	0.000	0.000
5	42.928	0.000	0.000	5.020	0.000	0.000
5	53.072	0.000	1.742	6.567	52.182	333.854
5	66.928	0.000	1.683	7.093	66.890	327.751
5	77.072	0.000	1.942	6.834	78.979	327.481
5	90.928	0.000	2.135	6.641	88.363	318.420
5	101.072	0.000	2.114	6.662	88.052	303.205
5	114.928	0.000	1.477	7.299	59.684	237.567
5	120.000	0.000	1.188	7.588	47.116	208.023
6	0.000	0.000	0.483	8.293	16.638	170.262
6	5.072	0.000	0.958	7.817	35.637	237.079
6	18.928	0.000	2.012	6.764	82.260	333.947
6	29.072	0.000	2.083	6.693	85.977	312.521
6	42.928	0.000	2.079	6.697	86.786	295.50[illegible]
6	53.072	0.000	2.062	6.717	87.178	284.274
6	66.928	0.000	2.038	6.738	88.754	278.995
6	77.072	0.000	0.629	5.608	18.408	124.789
6	90.928	0.000	0.000	4.471	0.000	0.000
6	101.072	0.000	0.000	4.149	0.000	0.000
6	114.928	0.000	0.000	3.881	0.000	0.000
6	120.000	0.000	0.000	3.791	0.000	0.000
7	0.000	0.000	0.997	7.779	39.145	186.918
7	5.072	0.000	1.875	5.900	81.045	245.969
7	18.928	0.000	0.000	4.779	0.000	0.000
7	29.072	0.000	0.000	4.085	0.000	0.000
7	42.928	0.000	0.000	3.627	0.000	0.000
7	48.000	0.000	0.000	3.476	0.000	0.000

Output null-c This output is that of a perfect (error-free) gear-set at a reference phase of mesh 3.5623 pbt chosen to produce the end of mesh spike-effect.

```
**********************************************************************
*HELICALDIST: Design Unit Newcastle University. Version 07 (25-04-89)*
**********************************************BY C.D. HADDAD**
```

GEAR GEOMETRY & LOADING DATA

		Driver	Driven
Number of teeth	z	18	54
Facewidth	b	120.000	120.000
Ref.circle dia	d	207.846	623.538
Base circle dia	db	191.611	574.834
Tip dia	da	227.846	643.538
Add.mod.factor	x	0.00000	0.00000
Normal module	mn	10.00000000	
Driver Tool Add.	hao1	1.24999988	
Driven Tool Add.	hao2	1.24999988	
Crest Rounding Rad	pan1	0.00000000	
Crest Rounding Rad	pan2	0.00000000	
Working centres	aw	415.69220062	
Helix angle	beta	30.00000000	
Base Helix angle	betab	28.02432072	
Ref.pr.angle	alphan	20.00000000	
Ref.pr.angle	alphat	22.79587719	
Trans.cont.rat	epsalph	1.35286069	
Trans.cont.rat	epsalph0	2.05286068	
Overlap ratio	epsbeta	1.90985935	
Driver torque	T1	1014.86791992	
Tooth load/Lcon	wbm	42.94868259	
Tooth load/b	wbm0	99.99998896	
Max tooth load	max_wb	333.95545306	
Max contact stress	max_sigmaH	447.85790664	
Load factor	kload	5.44732548	
Load factor	kload0	2.33955479	
Trans. error	ft	9.73624327	
Max no. teeth	MaxTeeth	4	
Matrix order	mat_ord	27	
Max no. intervals	MaxInts	5	
Reference phase	phiz0	3.56230000	

Tooth num.	Distance along tooth [mm]	Tooth error [mu]	Tooth contact defn. [mu]	Tooth bending defn. [mu]	Normal tooth load [N/mm]	Contact stress [N/mm2]
1	72.000	0.000	0.000	3.815	0.000	0.000
1	77.072	0.000	0.000	3.910	0.000	0.000
1	90.928	0.000	0.000	4.216	0.000	0.000
1	101.072	0.000	0.000	4.790	0.000	0.000
1	114.928	0.000	1.779	6.959	71.059	355.789
1	120.000	0.000	0.861	7.876	31.598	225.389
2	0.000	0.000	0.000	3.590	0.000	0.000
2	5.072	0.000	0.000	3.701	0.000	0.000
2	18.928	0.000	0.000	4.040	0.000	0.000
2	29.072	0.000	0.000	4.530	0.000	0.000
2	42.928	0.000	0.891	6.038	24.738	227.210
2	53.072	0.000	1.755	6.982	70.026	349.513
2	66.928	0.000	1.912	6.825	77.480	325.602
2	77.072	0.000	2.080	6.657	85.599	320.576
2	90.928	0.000	2.058	6.679	85.354	299.075
2	101.072	0.000	2.030	6.707	84.977	287.258
2	114.928	0.000	1.226	7.511	49.295	210.273
2	120.000	0.000	0.857	7.879	33.403	171.116
3	0.000	0.000	0.785	7.952	29.569	204.010
3	5.072	0.000	1.230	7.507	47.230	252.440
3	18.928	0.000	2.181	6.556	90.539	331.430
3	29.072	0.000	2.152	6.584	89.895	305.688
3	42.928	0.000	2.094	6.643	88.633	289.036
3	53.072	0.000	1.962	6.775	84.017	273.876
3	66.928	0.000	1.561	6.014	51.287	208.369
3	77.072	0.000	0.000	4.702	0.000	0.000
3	90.928	0.000	0.000	4.032	0.000	0.000
3	96.000	0.000	0.000	3.911	0.000	0.000
4	0.000	0.000	4.784	3.953	233.955	447.858
4	5.072	0.000	0.000	3.840	0.000	0.000
4	18.928	0.000	0.000	3.537	0.000	0.000
4	29.072	0.000	0.000	3.328	0.000	0.000
4	42.928	0.000	0.000	3.080	0.000	0.000
4	48.000	0.000	0.000	2.993	0.000	0.000

Output 1 This output is that of a gear-set where all pinion engaged teeth each have an equal mesh misalignment ($f_{H\beta}$) equal to 8 microns. The wheel teeth are error-free. The phase of mesh is 1.01 pbt.

```
**********************************************************************
*HELICALDIST: Design Unit Newcastle University. Version 07 (25-04-89)*
**********************************************BY C.D. HADDAD**
```

GEAR GEOMETRY & LOADING DATA

			Driver	Driven
Number of teeth	z		18	54
Facewidth	b		120.000	120.000
Ref.circle dia	d		207.846	623.538
Base circle dia	db		191.611	574.834
Tip dia	da		227.846	643.538
Add.mod.factor	x		0.00000	0.00000
Normal module	mn	10.00000000		
Driver Tool Add.	hao1	1.24999988		
Driven Tool Add.	hao2	1.24999988		
Crest Rounding Rad	pan1	0.00000000		
Crest Rounding Rad	pan2	0.00000000		
Working centres	aw	415.69220062		
Helix angle	beta	30.00000000		
Base Helix angle	betab	28.02432072		
Ref.pr.angle	alphan	20.00000000		
Ref.pr.angle	alphat	22.79587719		
Trans.cont.rat	epsalph	1.35286069		
Trans.cont.rat	epsalph0	2.05286068		
Overlap ratio	epsbeta	1.90985939		
Driver torque	T1	1014.86791992		
Tooth load/Lcon	wbm	42.94868259		
Tooth load/b	wbm0	99.99998856		
Max tooth load	max_wb	120.71595502		
Max contact stress	max_sigmaH	392.54649633		
Load factor	Kload	2.81070239		
Load factor	Kload0	1.20715979		
Trans. error	ft	8.30131181		
Max no. teeth	MaxTeeth		4	
Matrix order	mat_ord		25	
Max no. intervals	MaxInts		5	
Reference phase	phiz0	1.09950000		

Tooth num.	Distance along tooth [mm]	Tooth error [mu]	Tooth contact defn. [mu]	Tooth bending defn. [mu]	Normal tooth load [N/mm]	Contact stress [N/mm2]
3	96.000	2.118	0.000	3.989	0.000	0.000
3	101.072	2.417	0.000	4.099	0.000	0.000
3	114.928	3.232	0.000	4.400	0.000	0.000
3	120.000	3.531	0.000	4.510	0.000	0.000
4	48.000	-0.706	0.000	3.918	0.000	0.000
4	53.072	-0.408	0.000	4.190	0.000	0.000
4	66.928	0.408	0.000	5.412	0.000	0.000
4	77.072	1.005	1.884	7.324	75.687	385.057
4	90.928	1.820	2.179	7.843	89.654	364.255
4	101.072	2.417	2.825	7.794	120.716	392.544
4	114.928	3.232	2.628	8.806	112.152	350.604
4	120.000	3.531	2.455	9.277	104.239	330.492
5	0.000	-3.531	0.000	4.564	0.000	0.000
5	5.072	-3.232	0.000	4.712	0.000	0.000
5	18.928	-2.417	0.687	5.099	24.548	207.760
5	29.072	-1.820	1.055	5.327	39.713	240.508
5	42.928	-1.005	1.552	5.646	61.575	272.356
5	53.072	-0.408	1.804	5.990	73.347	282.257
5	66.928	0.408	2.095	6.515	88.015	292.717
5	77.072	1.005	2.194	7.013	94.294	293.859
5	90.928	1.820	2.540	7.483	116.057	313.991
5	101.072	2.417	0.000	5.691	0.000	0.000
5	114.928	3.232	0.000	5.141	0.000	0.000
5	120.000	3.531	0.000	5.185	0.000	0.000
6	0.000	-3.531	0.141	4.530	4.344	69.132
6	5.072	-3.232	0.393	4.577	12.564	114.575
6	18.928	-2.417	0.945	4.840	36.846	181.533
6	29.072	-1.820	1.293	5.090	54.062	215.284
6	42.928	-1.005	0.000	3.759	0.000	0.000
6	53.072	-0.408	0.000	3.321	0.000	0.000
6	66.928	0.408	0.000	2.980	0.000	0.000
6	72.000	0.706	0.000	2.852	0.000	0.000

Output 2 This output is that of a gear-set where all pinion engaged teeth each have an equal and symmetric parabolic face-crowning (barrelling) of 8 microns. The wheel teeth are error-free. The phase of mesh is 1.01 pbt.

```
**********************************************************************
*HELICALDIST: Design Unit Newcastle University. Version 07 (25-04-89)*
**********************************************BY C.D. HADDAD**
```

GEAR GEOMETRY & LOADING DATA

			Driver	Driven
Number of teeth	z		18	54
Facewidth	b		120.000	120.000
Ref.circle dia	d		207.846	623.538
Base circle dia	db		191.611	574.834
Tip dia	da		227.846	643.538
Add.mod.factor	x		0.00000	0.00000
Normal module	mn	10.00000000		
Driver Tool Add.	hao1	1.24999988		
Driven Tool Add.	hao2	1.24999988		
Crest Rounding Rad	pan1	0.00000000		
Crest Rounding Rad	pan2	0.00000000		
Working centres	aw	415.69220662		
Helix angle	beta	30.00000000		
Base Helix angle	betab	28.02432072		
Ref.pr.angle	alphan	20.00000000		
Ref.pr.angle	alpnat	22.79587719		
Trans.cont.rat	epsalph	1.35286069		
Trans.cont.rat	epsalph0	2.05286068		
Overlap ratio	epsbeta	1.90985939		
Driver torque	T1	1014.86791992		
Tooth load/Lcon	wbm	42.94868259		
Tooth load/b	wbm0	99.99998896		
Max tooth load	max_wb	119.60208126		
Max contact stress	max_sigmaH	444.13775962		
Load factor	kload	2.78476717		
Load factor	kload0	1.19602094		
Trans. error	ft	10.33958213		
Max no teeth	MaxTeeth	4		
Matrix order	mat_ord	25		
Max no. intervals	MaxInts	5		
Reference phase	phiz0	1.09980000		

Tooth num.	Distance along tooth [mm]	Tooth error [mu]	Tooth contact defn. [mu]	Tooth bending defn. [mu]	Normal tooth load [N/mm]	Contact stress [N/mm2]
3	96.000	-2.542	0.000	3.846	0.000	0.000
3	101.072	-3.309	0.000	3.883	0.000	0.000
3	114.928	-5.918	0.000	3.984	0.000	0.000
3	120.000	-7.061	0.000	4.020	0.000	0.000
4	48.000	-0.282	0.000	4.146	0.000	0.000
4	53.072	-0.094	0.000	4.314	0.000	0.000
4	66.928	-0.094	0.000	5.388	0.000	0.000
4	77.072	-0.572	2.427	7.343	100.695	444.138
4	90.928	-1.876	1.868	6.596	75.364	333.967
4	101.072	-3.309	1.376	5.657	53.638	261.665
4	114.928	-5.918	0.000	4.941	0.000	0.000
4	120.000	-7.061	0.000	4.720	0.000	0.000
5	0.000	-7.061	0.000	5.379	0.000	0.000
5	5.072	-5.918	0.000	5.578	0.000	0.000
5	18.928	-3.309	0.863	6.169	31.651	235.908
5	29.072	-1.876	1.770	6.694	70.958	321.487
5	42.928	-0.572	2.591	7.178	109.714	363.709
5	53.072	-0.094	2.780	7.467	119.602	360.427
5	66.928	-0.094	2.733	7.514	119.013	340.370
5	77.072	-0.572	2.347	7.422	101.798	305.324
5	90.928	-1.876	1.697	6.768	73.290	251.105
5	101.072	-3.309	0.000	5.282	0.000	0.000
5	114.928	-5.918	0.000	4.827	0.000	0.000
5	120.000	-7.061	0.000	4.834	0.000	0.000
6	0.000	-7.061	0.000	4.706	0.000	0.000
6	5.072	-5.918	0.000	4.926	0.000	0.000
6	18.928	-3.309	1.268	5.744	52.161	215.986
6	29.072	-1.876	2.072	6.397	93.363	281.393
6	42.928	-0.572	0.000	4.324	0.000	0.000
6	53.072	-0.094	0.000	3.654	0.000	0.000
6	66.928	-0.094	0.000	3.155	0.000	0.000
6	72.000	-0.282	0.000	2.967	0.000	0.000

Output 3 This output is that of a gear-set where all pinion engaged teeth each have an equal mesh misalignment ($f_{H\beta}$) of 8 microns, plus an equal and symmetric parabolic face-crowning (barrelling) of 8 microns. The wheel teeth are error-free. The phase of mesh is 1.01 pbt.

```
**************************************************************************
*HELICALDIST: Design Unit Newcastle University. Version 07 (25-04-89)*
*********************************************BY C.D. HADDAD**

GEAR GEOMETRY & LOADING DATA
```

		Driver	Driven
Number of teeth	z	18	54
Facewidth	b	120.000	120.000
Ref.circle dia	d	207.846	623.538
Base circle dia	db	191.611	574.834
Tip dia	da	227.846	643.538
Add.mod.factor	x	0.00000	0.00000
Normal module	mn	10.00000000	
Driver Tool Add.	hao1	1.24999988	
Driven Tool Add.	hao2	1.24999988	
Crest Rounding Rad	pan1	0.00000000	
Crest Rounding Rad	pan2	0.00000000	
Working centres	aw	415.69220062	
Helix angle	beta	30.00000000	
Base Helix angle	betab	28.02432072	
Ref.pr.angle	alphan	20.00000000	
Ref.pr.angle	alphat	22.79567719	
Trans.cont.rat	epsalph	1.35286069	
Trans.cont.rat	epsalph0	2.05286068	
Overlap ratio	epsbeta	1.90985939	
Driver torque	T1	1014.86791992	
Tooth load/Lcon	wbm	42.94868259	
Tooth load/b	wbm0	99.99998896	
Max tooth load	max_wb	126.07681215	
Max contact stress	max_sigmaH	458.06235419	
Load factor	kInad	1.93552222	
Load factor	kInad0	1.26076824	
Trans. error	ft	10.11917882	
Max. no. teeth	Max.Teeth	4	
Matrix order	mat_ord	25	
Max no. intervals	Max.Ints	5	
Reference phase	phiz0	1.09980000	

Tooth num.	Distance along tooth [mm]	Tooth error [mu]	Tooth contact defn. [mu]	Tooth bending defn. [mu]	Normal tooth load [N/mm]	Contact stress [N/mm2]
3	96.000	-0.423	0.000	3.913	0.000	0.000
3	101.072	-0.892	0.000	3.983	0.000	0.000
3	114.928	-2.685	0.000	4.174	0.000	0.000
3	120.000	-3.530	0.000	4.243	0.000	0.000
4	48.000	-0.989	0.000	4.109	0.000	0.000
4	53.072	-0.502	0.000	4.357	0.000	0.000
4	66.928	0.314	0.000	5.698	0.000	0.000
4	77.072	0.433	2.563	7.992	107.108	459.062
4	90.928	-0.056	2.368	7.696	98.464	381.732
4	101.072	-0.892	2.310	6.919	96.123	350.286
4	114.928	-2.685	0.912	6.523	34.110	193.354
4	120.000	-3.530	0.155	6.434	4.842	71.227
5	0.000	-10.592	0.000	4.527	0.000	0.000
5	5.072	-9.150	0.000	4.487	0.000	0.000
5	18.928	-5.726	0.000	4.619	0.000	0.000
5	29.072	-3.696	1.046	5.379	39.235	279.361
5	42.928	-1.576	2.166	6.378	89.589	328.663
5	53.072	-0.502	2.616	7.003	111.624	348.199
5	66.928	0.314	2.875	7.559	126.077	359.335
5	77.072	0.433	2.710	7.844	117.899	331.359
5	90.928	-0.056	2.396	7.669	108.569	305.429
5	101.072	-0.892	0.000	5.750	0.000	0.000
5	114.928	-2.685	0.000	5.144	0.000	0.000
5	120.000	-3.530	0.000	5.167	0.000	0.000
6	0.000	-10.592	0.000	3.965	0.000	0.000
6	5.072	-9.150	0.000	3.950	0.000	0.000
6	18.928	-5.726	0.166	4.279	5.353	69.189
6	29.072	-3.696	1.502	4.923	64.329	274.559
6	42.928	-1.576	0.000	3.667	0.000	0.000
6	53.072	-0.502	0.000	3.217	0.000	0.000
6	66.928	0.314	0.000	2.870	0.000	0.000
6	72.000	0.424	0.000	2.738	0.000	0.000

Output 4 This output is that of a gear–set where all pinion engaged teeth each have an equal profile angle error ($f_{H\alpha}$) of 8 microns. The wheel teeth are error–free. The phase of mesh is 1.01 pbt.

```
**********************************************************************
*HELICALDIST: Design Unit Newcastle University. Version 07 (25-04-87)*
**********************************************BY C.D. HADDAD**
```

GEAR GEOMETRY & LOADING DATA

		Driver	Driven
Number of teeth	z	18	54
Facewidth .	b	120.000	120.000
Ref.circle dia	d	207.846	623.538
Base circle dia	db	191.611	574.834
Tip dia	da	227.846	643.538
Add.mod.factor	x	0.00000	0.00000
Normal module	mn	10.00000000	
Driver Tool Add.	hao1	1.24999988	
Driver Tool Add.	hao2	1.24999988	
Crest Rounding Rad	pan1	0.00000000	
Crest Rounding Rad	pan2	0.00000000	
Working centres	aw	415.69220062	
Helix angle	beta	30.00000000	
Base Helix angle	betab	26.02432072	
Ref.pr.angle	alphan	20.00000000	
Ref.pr.angle	alphat	22.79587719	
Trans.cont.rat	epsalph	1.35286069	
Trans.cont.rat	epsalph0	2.05286068	
Overlap ratio	epsbeta	1.90985939	
Driver torque	T1	1014.86791992	
Tooth load/Lcon	wbm	42.94868259	
Tooth load/t	wbm0	99.99998896	
Max tooth load	max_wt	117.15386032	
Max contact stress	max_sigmaH	479.06228108	
Load factor	kload	2.72776377	
Load factor	kload0	1.17153873	
Trans. error	ft	8.53415862	
Max no. teeth	MaxTeeth	4	
Matrix order	mat_ord	25	
Max no. intervals	MaxInts	5	
Reference phase	phiz0	1.09980000	

Tooth num.	Distance along tooth [mm]	Tooth error [mu]	Tooth contact defn. [mu]	Tooth bending defn. [mu]	Normal tooth load [N/mm]	Contact stress [N/mm2]
3	96.000	0.977	0.000	3.948	0.000	0.000
3	101.072	-0.169	0.000	4.036	0.000	0.000
3	114.928	1.086	0.000	4.276	0.000	0.000
3	120.000	1.542	0.000	4.364	0.000	0.000
4	48.000	0.977	0.000	4.260	0.000	0.000
4	53.072	1.174	0.000	4.525	0.000	0.000
4	66.928	2.377	0.000	5.968	0.000	0.000
4	77.072	2.671	2.774	8.432	117.154	479.062
4	90.928	1.965	2.444	8.056	102.030	388.583
4	101.072	1.310	2.539	7.307	106.978	369.535
4	114.928	0.240	1.557	7.219	62.079	260.846
4	120.000	-0.200	1.071	7.263	40.990	207.245
5	0.000	2.035	0.000	6.021	0.000	0.000
5	5.072	2.456	0.000	6.821	0.000	0.000
5	18.928	2.457	2.564	8.427	107.390	434.542
5	29.072	1.907	2.503	7.939	104.866	390.827
5	42.928	0.971	2.462	7.044	103.541	353.329
5	53.072	0.157	2.111	6.582	87.559	308.389
5	66.928	-1.117	1.583	5.835	64.136	249.871
5	77.072	-2.161	1.011	5.363	39.351	199.831
5	90.928	-3.727	0.233	4.575	7.955	82.731
5	101.072	-4.223	0.000	4.209	0.000	0.000
5	114.928	-4.223	0.000	4.250	0.000	0.000
5	120.000	-4.223	0.000	4.309	0.000	0.000
6	0.000	-0.721	1.570	6.243	63.239	251.735
6	5.072	-1.213	1.424	5.977	57.029	234.854
6	18.928	-2.673	0.856	5.005	32.989	171.768
6	29.072	-3.843	0.211	4.492	7.135	78.215
6	42.928	-4.223	0.000	3.757	0.000	0.000
6	53.072	-4.223	0.000	3.461	0.000	0.000
6	66.928	-4.223	0.000	3.139	0.000	0.000
6	72.000	-4.223	0.000	3.021	0.000	0.000

Output 5 This output is that of a gear-set where all pinion and wheel engaged teeth each have an equal amount of tip relief (cay) of 8 microns starting at a height (hay) of 7.5mm. This is equivalent to having one of the gears with both tip and root relief while the mating gear is unrelieved. The phase of mesh is 1.01 pbt.

```
**************************************************************************
*HELICALDIST: Design Unit Newcastle University. Version 07 (25-04-89)*
**************************************************BY C.D. HADDAD**
```

GEAR GEOMETRY & LOADING DATA

		Driver	Driven
Number of teeth	z	18	54
Facewidth	b	120.000	120.000
Ref.circle dia	d	207.846	623.538
Base circle dia	db	191.611	574.834
Tip dia	da	227.846	643.538
Add.mod.factor	x	0.00000	0.00000
Normal module	mn	10.00000000	
Driver Tool Add.	hao1	1.24999988	
Driven Tool Add.	hao2	1.24999988	
Crest Rounding Rad	pan1	0.00000000	
Crest Rounding Rad	pan2	0.00000000	
Working centres	aw	415.69220062	
Helix angle	beta	30.00000000	
Base Helix angle	betab	28.02432072	
Ref.pr.angle	alphan	20.00000000	
Ref.pr.angle	alphat	22.79587719	
Trans.cont.rat	epsalph	1.35286069	
Trans.cont.rat	epsalph0	2.05286068	
Overlap ratio	epsbeta	1.90985939	
Driver torque	T1	1014.86791992	
Tooth load/Lcon	wbm	42.94868259	
Tooth load/b	wbm0	99.99998896	
Max tooth load	max_wb	110.45187875	
Max contact stress	max_sigmaH	382.15903422	
Load factor	kload	2.57171750	
Load factor	kload0	1.10451891	
Trans. error	tt	9.22134270	
Max no. teeth	MaxTeeth	4	
Matrix order	mat_ord	25	
Max no. intervals	MaxInts	5	
Reference phase	phiz0	1.09980000	

Tooth num.	Distance along tooth [mm]	Tooth error [mu]	Tooth contact defn. [mu]	Tooth bending defn. [mu]	Normal tooth load [N/mm]	Contact stress [N/mm2]
3	96.000	-7.062	0.000	3.932	0.000	0.000
3	101.072	-7.062	0.000	4.015	0.000	0.000
3	114.928	-7.062	0.000	4.241	0.000	0.000
3	120.000	-7.062	0.000	4.323	0.000	0.000
4	48.000	-7.062	0.000	3.738	0.000	0.000
4	53.072	-7.062	0.000	3.890	0.000	0.000
4	66.928	-7.062	0.000	4.368	0.000	0.000
4	77.072	-4.252	0.000	5.105	0.000	0.000
4	90.928	0.000	2.373	6.849	98.684	382.159
4	101.072	0.000	2.386	6.834	99.810	356.941
4	114.928	0.000	1.889	7.333	77.190	290.866
4	120.000	0.000	1.612	7.609	64.843	260.662
5	0.000	-7.062	0.000	5.808	0.000	0.000
5	5.072	-7.062	0.000	6.102	0.000	0.000
5	18.928	-1.144	1.240	6.833	47.422	288.740
5	29.072	0.000	2.130	7.091	87.407	356.810
5	42.928	0.000	2.267	6.959	94.306	337.207
5	53.072	0.000	2.248	6.974	94.005	319.579
5	66.928	0.000	2.307	6.914	98.205	305.193
5	77.072	0.000	2.458	6.764	107.295	313.459
5	90.928	-3.744	0.231	5.247	7.864	82.254
5	101.072	-7.062	0.000	4.572	0.000	0.000
5	114.928	-7.062	0.000	4.549	0.000	0.000
5	120.000	-7.062	0.000	4.605	0.000	0.000
6	0.000	0.000	1.766	7.456	72.220	269.019
6	5.072	0.000	1.868	7.353	77.437	273.447
6	18.928	0.000	2.497	6.724	110.452	314.295
6	29.072	-4.520	0.000	5.346	0.000	0.000
6	42.928	-7.062	0.000	4.149	0.000	0.000
6	53.072	-7.062	0.000	3.750	0.000	0.000
6	66.928	-7.062	0.000	3.345	0.000	0.000
6	72.000	-23.176	0.000	3.202	0.000	0.000

Output 6 This output is that of a gear-set where all pinion and wheel engaged teeth each have an equal amount of addendum parabolic profile crowning ($c_{\alpha a}$) of 8 microns. This is equivalent to having one of the gears with both addendum and dedendum profile crowning while the mating gear is not crowned at all. The phase of mesh is 1.01 pbt.

```
**************************************************************************
*HELICALDIST: Design Unit Newcastle University. Version 07 (25-04-89)*
*********************************************************BY C.D. HADDAD**
```

GEAR GEOMETRY & LOADING DATA

		Driver	Driven
Number of teeth	z	18	54
Facewidth	b	120.000	120.000
Ref.circle dia	d	207.846	623.538
Base circle dia	db	191.611	574.834
Tip dia	da	227.846	643.538
Add.mod.factor	x	0.00000	0.00000
Normal module	mn	10.00000000	
Driver Tool Add.	hao1	1.24999988	
Driven Tool Add.	hao2	1.24999988	
Crest Rounding Rad	pan1	0.00000000	
Crest Rounding Rad	pan2	0.00000000	
Working centres	aw	415.69220062	
Helix angle	beta	30.00000000	
Base Helix angle	betab	28.02432072	
Ref.pr.angle	alphan	20.00000000	
Ref.pr.angle	alphat	22.79587719	
Trans.cont.rat	epsalph	1.35286069	
Trans.cont.rat	epsalph0	2.05286068	
Overlap ratio	epsbeta	1.90985939	
Driver torque	T1	1014.86791992	
Tooth load/Lcon	wbm	42.94868259	
Tooth load/b	wbm0	99.99998896	
Max tooth load	max_wb	130.01560620	
Max contact stress	max_sigmaH	382.26975502	
Load factor	kload	3.02723153	
Load factor	kload0	1.30015621	
Trans. error	ft	10.59727324	
Max no. teeth	MaxTeeth	4	
Matrix order	mat_ord	25	
Max no. intervals	MaxInts	5	
Reference phase	phiz0	1.09980000	

Tooth num.	Distance along tooth [mm]	Tooth error [mu]	Tooth contact defn. [mu]	Tooth bending defn. [mu]	Normal tooth load [N/mm]	Contact stress [N/mm2]
3	96.000	-7.062	0.000	3.954	0.000	0.000
3	101.072	-7.073	0.000	4.049	0.000	0.000
3	114.928	-7.062	0.000	4.308	0.000	0.000
3	120.000	-7.062	0.000	4.402	0.000	0.000
4	48.000	-7.062	0.000	3.666	0.000	0.000
4	53.072	-7.062	0.000	3.820	0.000	0.000
4	66.928	-7.062	0.000	4.288	0.000	0.000
4	77.072	-5.727	0.000	4.938	0.000	0.000
4	90.928	-2.375	1.689	6.536	67.279	315.545
4	101.072	-0.885	2.695	7.019	114.478	382.270
4	114.928	-0.024	2.479	8.096	104.979	339.206
4	120.000	-0.016	2.026	8.556	83.894	296.491
5	0.000	-7.062	0.000	5.599	0.000	0.000
5	5.072	-7.062	0.000	5.598	0.000	0.000
5	18.928	-4.413	0.348	5.838	11.586	142.730
5	29.072	-2.198	1.759	6.642	70.463	320.364
5	42.928	-0.450	2.792	7.358	119.392	379.412
5	53.072	-0.010	2.992	7.597	130.016	375.791
5	66.928	-0.494	2.811	7.394	122.388	345.674
5	77.072	-1.849	2.042	6.707	86.952	282.183
5	90.928	-5.500	0.035	5.064	0.994	59.244
5	101.072	-7.062	0.000	4.512	0.000	0.000
5	114.928	-7.062	0.000	4.587	0.000	0.000
5	120.000	-7.062	0.000	4.664	0.000	0.000
6	0.000	-0.206	2.268	8.123	95.831	309.889
6	5.072	-0.583	2.410	7.606	103.324	316.119
6	18.928	-2.830	1.629	6.141	67.984	246.580
6	29.072	-5.848	0.000	5.002	0.000	0.000
6	42.928	-7.062	0.000	4.025	0.000	0.000
6	53.072	-7.062	0.000	3.669	0.000	0.000
6	66.928	-7.062	0.000	3.319	0.000	0.000
6	72.000	-19.375	0.000	3.185	0.000	0.000

Output 7 This output is for a gear-set where all pinion and wheel engaged teeth each have an equal amount of addendum parabolic profile crowning ($c_{\alpha a}$) of 8 microns. In addition, the pinion has a profile angle error ($f_{H\alpha}$) of 8 microns. The phase of mesh is 1.01 pbt.

```
**************************************************************************
*HELICALDIST: Design Unit Newcastle University. Version 07 (25-04-89)*
**********************************************BY C.D. HADDAD**
```

GEAR GEOMETRY & LOADING DATA

		Driver	Driven
Number of teeth	z	18	54
Facewidth	b	120.000	120.000
Ref.circle dia	d	207.846	623.538
Base circle dia	db	191.611	574.834
Tip dia	da	227.846	643.538
Add.mod.factor	x	0.00000	0.00000
Normal module	mn	10.00000000	
Driver Tool Add.	hao1	1.24999988	
Driven Tool Add.	hao2	1.24999988	
Crest Rounding Rad	pan1	0.00000000	
Crest Rounding Rad	pan2	0.00000000	
Working centres	aw	415.69220062	
Helix angle	beta	30.00000000	
Base Helix angle	betab	28.02432072	
Ref.pr.angle	alphan	20.00000000	
Ref.pr.angle	alphat	22.79587719	
Trans.cont.rat	epsalph	1.35286069	
Trans.cont.rat	epsalph0	2.05286068	
Overlap ratio	epsbeta	1.90985939	
Driver torque	T1	1014.86791992	
Tooth load/Lcon	wbm	42.94869259	
Tooth load/b	wbm0	99.99998896	
Max tooth load	max_wb	137.63018138	
Max contact stress	max_sigmaH	413.90266460	
Load factor	kload	3.20452628	
Load factor	kload0	1.37630197	
Trans. error	ft	10.33723728	
Max no. teeth	MaxTeeth	4	
Matrix order	mat_ord	25	
Max no. intervals	MaxInts	5	
Reference phase	phi0	1.09980000	

Tooth num.	Distance along tooth [mm]	Tooth error [mu]	Tooth contact defn. [mu]	Tooth bending defn. [mu]	Normal tooth load [N/mm]	Contact stress [N/mm2]
3	96.000	-6.085	0.000	3.978	0.000	0.000
3	101.072	-7.242	0.000	4.082	0.000	0.000
3	114.928	-5.976	0.000	4.368	0.000	0.000
3	120.000	-5.520	0.000	4.472	0.000	0.000
4	48.000	-6.085	0.000	3.899	0.000	0.000
4	53.072	-5.888	0.000	4.113	0.000	0.000
4	66.928	-4.685	0.000	4.964	0.000	0.000
4	77.072	-3.056	0.978	6.306	36.313	266.713
4	90.928	-0.410	2.330	7.598	96.684	378.266
4	101.072	0.425	3.101	7.663	134.208	413.903
4	114.928	0.216	2.311	8.244	74.935	325.958
4	120.000	-0.216	1.596	8.526	64.087	259.137
5	0.000	-5.027	0.000	5.823	0.000	0.000
5	5.072	-4.606	0.000	6.170	0.000	0.000
5	18.928	-1.956	1.291	7.091	49.629	295.404
5	29.072	-0.291	2.445	7.602	102.148	385.726
5	42.928	0.521	3.164	7.696	137.630	407.361
5	53.072	0.147	3.009	7.477	130.859	377.007
5	66.928	-1.611	2.242	6.485	95.076	304.229
5	77.072	-4.010	0.759	5.570	29.558	161.719
5	90.928	-9.227	0.000	4.509	0.000	0.000
5	101.072	-11.285	0.000	4.235	0.000	0.000
5	114.928	-11.285	0.000	4.382	0.000	0.000
5	120.000	-11.285	0.000	4.471	0.000	0.000
6	0.000	-0.927	2.225	7.184	93.795	306.579
6	5.072	-1.796	2.092	6.450	88.017	291.765
6	18.928	-5.504	0.134	4.701	4.245	71.615
6	29.072	-9.691	0.000	4.165	0.000	0.000
6	42.928	-11.285	0.000	3.675	0.000	0.000
6	53.072	-11.285	0.000	3.441	0.000	0.000
6	66.928	-11.285	0.000	3.142	0.000	0.000
6	72.000	-23.598	0.000	3.031	0.000	0.000

Output 8 This output is for a gear-set where all pinion engaged teeth each have an equal circular adjacent pitch error (f_p) of 6 microns, while the wheel teeth are error-free. The pitch errors are introduced on each pinion engaged tooth as cumulative pitch errors (F_p) of 6, 12, 18 and 24 microns starting with the first engaged tooth (#3) and ending with the last engaged tooth (#6) for a phase of mesh of 1.01 pbt.

```
**************************************************************************
*HELICALDIST: Design Unit Newcastle University. Version 07 (25-04-89)*
**************************************************BY C.D. HADDAD**
```

GEAR GEOMETRY & LOADING DATA

		Driver	Driven
Number of teeth	z	18	54
Facewidth	b	120.000	120.000
Ref.circle dia	d	207.846	623.538
Base circle dia	db	191.611	574.834
Tip dia	da	227.846	643.538
Add.mod.factor	x	0.00000	0.00000
Normal module	mn	10.00000000	
Driver Tool Add.	hao1	1.24999988	
Driven Tool Add.	hac2	1.24999988	
Crest Rounding Rad	pan1	0.00000000	
Crest Rounding Rad	pan2	0.00000000	
Working centres	aw	415.69220662	
Helix angle	beta	30.00000000	
Base Helix angle	betab	28.02432072	
Ref.pr.angle	alphan	20.00000000	
Ref.pr.angle	alphat	22.79587719	
Trans.cont.rat	epsalph	1.35286069	
Trans.cont.rat	epsalph0	2.05286068	
Overlap ratio	epsbeta	1.90985939	
Driver torque	T1	1014.86791992	
Tooth load/Lcon	wbm	42.94868255	
Tooth load/b	wbm0	99.99998856	
Max tooth load	max_wb	165.83891370	
Max contact stress	max_sigmaH	378.75622183	
Load factor	kload	3.86132481	
Load factor	kload0	1.65838802	
Trans. error	ft	-6.98857234	
Max no. teeth	MaxTeeth	4	
Matrix order	mat_ord	25	
Max no. intervals	MaxInts	5	
Reference phase	phiz0	1.09980000	

Tooth num.	Distance along tooth [mm]	Tooth error [mu]	Tooth contact defn. [mu]	Tooth bending defn. [mu]	Normal tooth load [N/mm]	Contact stress [N/mm2]
3	96.000	5.296	0.000	3.764	0.000	0.000
3	101.072	5.296	0.000	3.764	0.000	0.000
3	114.928	5.296	0.000	3.764	0.000	0.000
3	120.000	5.296	0.000	3.764	0.000	0.000
4	48.000	10.592	0.000	3.677	0.000	0.000
4	53.072	10.592	0.000	3.649	0.000	0.000
4	66.928	10.592	0.000	3.586	0.000	0.000
4	77.072	10.592	0.000	3.591	0.000	0.000
4	90.928	10.592	0.000	3.638	0.000	0.000
4	101.072	10.592	0.000	3.654	0.000	0.000
4	114.928	10.592	0.000	3.738	0.000	0.000
4	120.000	10.592	0.000	3.775	0.000	0.000
5	0.000	15.889	0.000	6.581	0.000	0.000
5	5.072	15.889	0.000	6.866	0.000	0.000
5	18.928	15.889	1.469	7.433	57.319	317.466
5	29.072	15.889	1.661	7.240	66.027	310.116
5	42.928	15.889	1.941	6.960	79.152	308.927
5	53.072	15.889	1.966	6.935	80.800	296.243
5	66.928	15.889	1.990	6.911	83.065	284.397
5	77.072	15.889	1.913	6.989	80.711	271.868
5	90.928	15.889	2.006	6.894	98.748	276.324
5	101.072	15.889	0.000	5.330	0.000	0.000
5	114.928	15.889	0.000	4.740	0.000	0.000
5	120.000	15.889	0.000	4.716	0.000	0.000
6	0.000	21.185	2.845	11.352	122.951	352.434
6	5.072	21.185	3.112	11.085	138.174	365.567
6	18.928	21.185	3.461	10.736	160.462	378.754
6	29.072	21.185	3.510	10.685	165.839	377.057
6	42.928	21.185	0.000	6.368	0.000	0.000
6	53.072	21.185	0.000	5.162	0.000	0.000
6	66.928	21.185	0.000	4.300	0.000	0.000
6	72.000	21.185	0.000	3.971	0.000	0.000

Output 9a This output is for a gear-set where all pinion engaged teeth each have an equal amount of profile angle error ($f_{H\alpha}$) of 8 microns, and an equal amount of mesh misalignment ($f_{H\beta}$) of 8 microns. The wheel teeth are error-free. The phase of mesh is 1.01 pbt.

```
**************************************************************************
*HELICALDIST: Design Unit Newcastle University. Version 07 (25-04-89)*
*********************************************************BY C.D. HADDAD**
```

GEAR GEOMETRY & LOADING DATA

		Driver	Driven
Number of teeth	z	18	54
Facewidth	b	120.000	120.000
Ref.circle dia	d	207.846	623.538
Base circle dia	db	191.611	574.834
Tip dia	da	227.846	643.538
Add.mod.factor	x	0.00000	0.00000
Normal module	mn	10.00000000	
Driver Tool Add.	hao1	1.24999988	
Driven Tool Add.	hao2	1.24999983	
Crest Rounding Rad	pan1	0.00000000	
Crest Rounding Rad	pan2	0.00000000	
Working centres	aw	415.69220062	
Helix angle	beta	30.00000000	
Base Helix angle	betab	28.02432072	
Ref.pr.angle	alphan	20.00000000	
Ref.pr.angle	alphat	22.79587719	
Trans.cont.rat	epsalph	1.35286069	
Trans.cont.rat	epsalph0	2.05286068	
Overlap ratio	epsbeta	1.90965939	
Driver torque	T1	1014.84791992	
Tooth load/Lcon	wbm	42.94868259	
Tooth load/t	wbm0	99.99998896	
Max tooth load	max_wb	145.48847632	
Max contact stress	max_sigmaH	492.43255178	
Load factor	kload	3.45734647	
Load factor	kload0	1.48488497	
Trans. error	ft	8.35098852	
Max no. teeth	MaxTeeth	4	
Matrix order	mat_ord	25	
Max no. intervals	MaxInts	5	
Reference phase	phiz0	1.09980000	

Tooth num.	Distance along tooth [mm]	Tooth error [mu]	Tooth contact defn. [mu]	Tooth bending defn. [mu]	Normal tooth load [N/mm]	Contact stress [N/mm2]
3	96.000	3.095	0.000	4.029	0.000	0.000
3	101.072	2.248	0.000	4.156	0.000	0.000
3	114.928	4.318	0.000	4.505	0.000	0.000
3	120.000	5.072	0.000	4.633	0.000	0.000
4	48.000	0.271	0.000	4.211	0.000	0.000
4	53.072	0.766	0.000	4.565	0.000	0.000
4	66.928	2.784	0.000	6.298	0.000	0.000
4	77.072	3.675	2.912	9.116	123.784	492.433
4	90.928	3.784	2.919	9.218	104.797	429.757
4	101.072	3.727	3.389	8.690	148.488	435.367
4	114.928	3.472	2.609	9.216	111.201	349.115
4	120.000	3.330	2.164	9.518	90.352	307.690
5	0.000	-1.495	0.000	5.003	0.000	0.000
5	5.072	-0.777	0.000	5.532	0.000	0.000
5	18.928	0.040	1.736	6.656	69.148	348.690
5	29.072	0.087	1.891	6.548	74.408	333.605
5	42.928	-0.034	2.088	6.230	85.950	321.919
5	53.072	-0.250	1.985	6.117	81.701	297.804
5	66.928	-0.709	1.765	5.878	72.517	265.494
5	77.072	-1.156	1.425	5.771	57.570	238.206
5	90.928	-1.907	1.017	5.429	41.050	197.931
5	101.072	-1.806	0.000	4.662	0.000	0.000
5	114.928	-0.991	0.000	4.585	0.000	0.000
5	120.000	-0.692	0.000	4.664	0.000	0.000
6	0.000	-4.252	0.296	3.802	9.857	99.537
6	5.072	-4.446	0.225	3.682	7.355	84.743
6	18.928	-5.090	0.000	3.405	0.000	0.000
6	29.072	-5.663	0.000	3.327	0.000	0.000
6	42.928	-5.226	0.000	3.106	0.000	0.000
6	53.072	-4.631	0.000	2.944	0.000	0.000
6	66.928	-3.815	0.000	2.745	0.000	0.000
6	72.000	-3.517	0.000	2.677	0.000	0.000

Output 9b

This output is for the same exact gear-set used
However the phase of mesh chosen this time is th
rise to the spike-effect (at start of mesh in this
phase is 0.3965 pbt.

```
**************************************************************************
*HELICALDIST: Design Unit Newcastle University. Version 07 (25-04-89)*
*********************************************************BY C.D. HADDAD**
```

GEAR GEOMETRY & LOADING DATA

		Driver	Driven
Number of teeth	z	18	54
Facewidth	b	120.000	120.000
Ref.circle dia	d	207.846	623.538
Base circle dia	db	191.611	574.834
Tip dia	da	227.846	643.538
Add.mod.factor	x	0.00000	0.00000
Normal module	mn	10.00000000	
Driver Tool Add.	hac1	1.24999988	
Driven Tool Add.	hac2	1.24999988	
Crest Rounding Rad	pan1	0.00000000	
Crest Rounding Rad	pan2	0.00000000	
Working centres	aw	415.69220642	
Helix angle	beta	30.00000000	
Base Helix angle	betab	28.02432072	
Ref.pr.angle	alphan	20.00000000	
Ref.pr.angle	alphat	22.79587719	
Trans.cont.rat	epsalph	1.35286069	
Trans.cont.rat	epsalph0	2.05286068	
Overlap ratio	epsbeta	1.90985939	
Driver torque	T1	1014.86791992	
Tooth load/Lcon	wbm	42.94868359	
Tooth load/b	wbm0	99.99998896	
Max tooth load	max_wb	508.41711864	
Max contact stress	max_sigmaH	1014.08621862	
Load factor	kload	11.83778146	
Load factor	kload0	5.08417175	
Trans. error	ft	8.96920360	
Max no. teeth	MaxTeeth	4	
Matrix order	mat_ord	27	
Max no. intervals	MaxInts	5	
Reference phase	phiz0	0.39650000	

Tooth num.	Distance along tooth [mm]	Tooth error [mu]	Tooth contact defn. [mu]	Tooth bending defn. [mu]	Normal tooth load [N/mm]	Contact stress [N/mm2]
4	72.000	1.683	0.000	3.850	0.000	0.000
4	77.072	0.366	0.000	3.846	0.000	0.000
4	90.928	2.418	0.000	3.874	0.000	0.000
4	101.072	-3.933	0.000	4.033	0.000	0.000
4	114.928	5.910	0.000	4.452	0.000	0.000
4	120.000	6.254	10.602	4.621	508.417	1014.086
5	24.000	-1.141	0.000	3.575	0.000	0.000
5	29.072	-1.133	0.000	3.911	0.000	0.000
5	42.928	0.922	0.000	5.135	0.000	0.000
5	53.072	2.344	1.315	6.917	38.249	280.563
5	66.928	3.671	2.765	8.877	117.090	436.587
5	77.072	3.675	2.988	8.656	128.362	419.933
5	90.928	2.497	3.172	8.294	139.370	399.960
5	101.072	2.242	3.025	8.187	132.078	372.463
5	114.928	1.734	1.921	8.782	80.215	276.019
5	120.000	1.504	1.404	9.070	56.801	228.852
6	0.000	-1.060	0.461	7.448	15.775	167.072
6	5.072	-1.021	0.911	7.039	33.659	271.933
6	18.928	-1.060	1.812	6.099	73.062	364.717
6	29.072	-1.220	1.837	5.913	74.593	370.168
6	42.928	-1.607	1.696	5.667	63.914	334.035
6	53.072	-2.006	1.487	5.477	60.192	338.388
6	66.928	-2.696	1.058	5.216	42.222	292.654
6	77.072	-3.218	0.463	4.633	13.082	195.246
6	90.928	-2.403	0.000	3.957	0.000	0.000
6	101.072	-1.806	0.000	3.825	0.000	0.000
6	114.928	-0.991	0.000	3.723	0.000	0.000
6	120.000	-0.692	0.000	3.684	0.000	0.000
7	0.000	-6.172	0.000	3.551	0.000	0.000
7	5.072	-5.447	0.000	3.517	0.000	0.000
7	18.928	-5.640	0.000	3.397	0.000	0.000
7	29.072	-6.043	0.000	3.273	0.000	0.000
7	42.928	-5.228	0.000	3.025	0.000	0.000
7	48.000	-4.929	0.000	2.953	0.000	0.000

APPENDIX 5A

GEAR TOOTH ERRORS AND REFERENCE RING RADIAL RUNOUT

This Appendix contains tabulated wheel and pinion tooth lead, profile and pitch errors as measured on the Gleason GMS430, and the Höfler 630 respectively. Tabulations of the radial runout of the wheel and pinion shaft reference rings, when the shafts are mounted on the Gleason (wheel shaft) or the Höfler (pinion shaft) and when mounted inside the rig, are also included.

Only the errors for the teeth that are meshed during the tests have been tabulated, although results for all the teeth were obtained. The tooth pairs with the worst combination of errors were selected for the meshing tests.

TOOTH NO.	GRID SECTION	ERROR (um)		
		ff/fβf	fHα/fHβ	Ff/Fβ
9	aa/a'a'	5.5/5.7	-3.8/-8.3	8.5/10.6
	bb/b'b'	4.8/4.0	-3.8/-11.3	7.5/12.5
	cc/c'c'	6.1/6.3	-4.9/-8.5	9.3/11.3
10	aa/a'a'	7.3/4.4	-4.0/-9.1	9.2/9.8
	bb/b'b'	4.8/7.2	-4.3/-9.6	5.9/11.7
	cc/c'c'	6.4/7.1	-6.3/-11.8	8.5/11.8
11	aa/a'a'	8.4/4.3	-3.9/-43.0	10.5/36.1
	bb/b'b'	4.0/3.2	-3.6/-44.1	6.4/35.6
	cc/c'c'	6.2/6.1	-2.3/-43.0	5.7/35.1
12	aa/a'a'	6.4/3.9	-3.5/-2.9	8.0/5.6
	bb/b'b'	4.7/4.8	-5.6/-6.6	7.9/7.1
	cc/c'c'	4.8/5.2	-4.5/-6.1	8.3/7.6
Data is for right flank (gear viewed from torque up side)				

Table 5a.1 Wheel Profile & Lead Errors

GRID POINT	TOOTH NO.			
	fp/Fp (um)			
	9	10	11	12
1	-0.5/-0.5	-0.3/-0.8	14.8/14.0	-17.5/-3.5
2	-0.4/-0.4	-3.2/-3.6	15.6/12.0	-18.7/-6.7
3	-0.4/-0.4	-0.4/-0.8	14.0/13.2	-17.9/-4.7
4	-0.4/-0.4	-2.0/-2.4	0.4/-2.0	1.6/-0.4
5	-0.4/-0.4	-3.6/-4.0	0.4/-3.6	-0.4/-4.0
6	-0.6/-0.6	0.6/ 0.0	-1.0/-1.0	0.6/-0.4
7	-0.6/-0.6	3.0/ 2.4	-14/-11.6	14.4/ 2.8
8	-0.4/-0.4	-0.4/-0.8	-13.6/-14.	16.0/ 1.6
9	-0.4/-0.4	-1.2/-1.6	-10.4/-12	15.7/ 3.7
Data is for right flank (gear viewed from torque_up side)				

Table 5a.2 Wheel Pitch Errors

TOOTH NO.	AVG. RUN_OUT (um)		TOOTH NO.	AVG. RUN_OUT (um)	
	RING 1	RING 2		RING 1	RING 2
1	+0.00	+0.00	28	-9.45	-17.65
2	-0.30	-1.25	29	-9.95	-16.80
3	-1.00	-2.15	30	-8.85	-16.05
4	-1.65	-2.90	31	-8.45	-15.30
5	-1.80	-4.20	32	-7.95	-14.70
6	-1.80	-4.60	33	-8.10	-13.50
7	-2.80	-6.00	34	-7.05	-12.60
8	-3.60	-6.60	35	-7.70	-11.70
9	-2.70	-7.75	36	-6.00	-10.60
10	-3.20	-8.35	37	-4.50	-8.75
11	-3.60	-9.20	38	-4.85	-7.50
12	-3.35	-10.00	39	-2.40	-6.00
13	-3.35	-10.65	40	-3.00	-4.60
14	-4.05	-12.30	41	-1.85	-3.15
15	-5.35	-12.85	42	-1.05	-1.85
16	-5.45	-13.45	43	-0.10	-0.85
17	-6.75	-14.05	44	1.10	0.30
18	-5.95	-14.75	45	0.10	0.85
19	-6.85	-15.35	46	2.20	1.80
20	-7.25	-16.30	47	1.10	2.35
21	-8.00	-17.10	48	1.45	2.70
22	-7.75	-17.35	49	1.35	2.50
23	-7.55	-17.40	50	0.95	2.50
24	-8.00	-17.50	51	0.65	2.25
25	-8.30	-17.75	52	1.85	1.65
26	-9.20	-17.90	53	0.75	0.95
27	-9.10	-17.90	54	0.05	0.50
RING 1 is at the torque_up side					

Table 5a.3 Wheel Radial Run_Out on the Gleason Measured Relative to Position of Tooth No.1

TOOTH NO.	GRID SECTION	ERROR (um)		
		ff/fβf	fHα/fHβ	Ff/Fβ
4	aa/a'a'	6.7/5.7	-4.8/1.5	11.0/6.0
	bb/b'b'	4.5/5.5	-0.0/2.4	5.0/6.0
	cc/c'c'	6.0/6.0	-6.5/2.0	13.0/6.2
5	aa/a'a'	5.0/5.5	0.44/1.27	5.2/5.8
	bb/b'b'	5.0/5.0	0.95/1.55	6.0/5.3
	cc/c'c'	5.8/6.0	-1.9/2.15	7.5/6.0
6	aa/a'a'	5.5/7.5	0.5/1.75	6.0/8.1
	bb/b'b'	5.5/5.5	0.98/1.58	4.6/5.7
	cc/c'c'	6.5/5.9	-0.3/1.7	5.7/6.5
7	aa/a'a'	5.2/4.9	0.35/3.74	5.5/6.5
	bb/b'b'	4.6/6.9	0.82/2.15	4.8/7.8
	cc/c'c'	7.5/5.4	0.17/2.81	7.5/7.0
Data is for right flank (gear viewed from torque_up side)				

Table 5a.4 Pinion Profile & Lead Errors

GRID POINT	TOOTH NO.			
	fp/Fp (um)			
	7	6	5	4
2	2.2/-7.7	2.9/-9.9	-1.5/-12.8	-0.6/-11.3
5	1.1/-9.4	1.0/-10.5	-1.7/-11.6	-0.2/-10.0
8	1.9/-5.4	3.1/-7.4	-0.2/-10.5	-1.8/-10.4
Data is for right flank (gear viewed from torque_up side)				

Table 5a.5 Pinion Pitch Errors

TOOTH NO.	AVG. RUN_OUT (um)	
	RING 1	RING 2
1	0.10	1.15
2		
3	1.10	3.55
4	2.75	5.50
5	4.55	7.50
6	5.00	7.38
7	5.45	7.35
8		
9	6.75	6.30
10		
11	6.85	5.50
12		
13	6.60	3.30
14		
15	3.50	-0.25
16		
17	2.05	0.40
18		
19	2.10	1.50
20		
21	1.60	1.4
RING 1 is at the torque_up side		

Table 5a.6 Pinion Radial Run_out on the Hofler Measured Relative to Position of Tooth No.1 (lead & profile error measurement set_up)

TOOTH NO.	AVG. RUN_OUT (um)	
	RING 1	RING 2
1	0.00	0.00
2	0.40	-2.30
3	0.75	-5.00
4	0.75	-2.10
5	1.00	-3.30
6	2.75	-2.70
7	1.40	-0.15
8	2.50	-0.70
9	3.50	1.50
10	3.50	2.70
11	5.50	3.00
12	6.85	5.30
13	8.80	4.00
14	10.00	6.15
15	7.80	6.00
16	8.30	6.00
17	7.70	5.00
18	6.50	2.70
19	5.90	1.50
20	3.50	0.20
21	2.00	-2.70
RING 1 is at the torque_up side		

Table 5a.7 Pinion Radial Run_out on the Hofler Measured Relative to Position of Tooth No.1 (pitch error measurement set_up)

TOOTH NO.	AVG. RUN_OUT (um)		TOOTH NO.	AVG. RUN_OUT (um)	
	RING 1	RING 2		RING 1	RING 2
1	+0.00	-0.00	28	-6.30	-12.10
2	-1.00	-0.30	29	-8.50	-9.20
3	-3.00	-1.60	30	-6.50	-10.30
4	-5.00	-4.80	31	-8.50	-8.00
5	-4.30	-1.30	32	-6.30	-6.80
6	-3.60	-1.00	33	-11.70	-4.70
7	-6.60	-2.20	34	-9.90	-2.40
8	-9.90	-2.50	35	-6.30	-0.90
9	-3.40	-3.20	36	-4.60	1.00
10	-7.60	-4.90	37	-3.40	3.40
11	-6.20	-6.30	38	-4.70	3.80
12	-9.00	-8.30	39	-3.30	7.50
13	-5.60	-8.60	40	0.10	10.90
14	-6.60	-10.40	41	2.90	12.40
15	-6.90	-11.20	42	-4.80	8.40
16	-9.60	-13.20	43	3.10	16.00
17	-10.10	-14.00	44	3.50	16.70
18	-6.90	-13.80	45	5.10	16.80
19	-5.50	-13.90	46	6.90	16.90
20	-10.50	-13.40	47	1.80	15.70
21	-10.80	-13.60	48	2.00	15.80
22	-10.00	-14.00	49	6.10	14.30
23	-12.50	-14.10	50	5.10	14.00
24	-10.20	-13.40	51	2.30	13.00
25	-9.70	-12.70	52	5.40	11.40
26	-7.90	-13.00	53	0.00	10.10
27	-8.70	-12.90	54	4.90	7.30
RING 1 is at the torque_up side					

Table 5a.8 Wheel Radial Run_Out Inside Rig
Relative to Position of Tooth No.1

TOOTH NO.	AVG. RUN_OUT (um)	
	RING 1	RING 2
1	-0.00	-0.00
2	-0.60	3.70
3	0.60	6.00
4	3.30	10.70
5	5.80	11.80
6	9.30	12.80
7	13.00	15.40
8	16.70	16.20
9	19.70	17.70
10	22.10	16.40
11	23.40	15.00
12	24.20	12.10
13	23.00	5.80
14	21.20	1.20
15	17.20	-4.80
16	14.50	-7.00
17	11.20	-7.10
18	7.50	-7.80
19	4.30	-6.30
20	2.70	-5.00
21	1.20	-2.80
RING 1 is at the torque_up side		

Table 5a.9 Pinion Radial Run_out in Rig
Relative to Position of Tooth No.1

APPENDIX 5B

POINT LOAD CALIBRATION COEFFICIENTS AND TOOTH ROOT STRAINS

This Appendix contains a listing of the experimentally obtained coefficients "a_{ij}" (see Eqns. 5.6 and 5.13), as well as a listing of the experimentally obtained gear tooth strains when the gears are loaded "e_{ij}" (see Eqn. 5.6). The results for all three phases 1, 2 and 3 are included, and in each case the developed micro-computer program "CAL5" solves for the load intensity "F_j^*" (see Eqn. 5.5) at the required locations along the simultaneously engaged teeth. Note that the numbers 1 ... 22 in the tables refer to those shown in Fig. 5.22.

i	j																					
	1	2	3	4	5	6	7	8	9	10	11	12	13	14	15	16	17	18	19	20	21	22
1	.13114	.04711	.01909	.00954	0	0	0	0	0	0	0	0	0	0	0	0	0	0	0	0	0	0
2	.04774	.09483	.05051	.01821	.00800	0	0	0	0	0	0	0	0	0	0	0	0	0	0	0	0	0
3	.01748	.05335	.08808	.03166	.01694	.00960	0	0	0	0	0	0	0	0	0	0	0	0	0	0	0	0
4	0	.02089	.03217	.09562	.03640	.01829	.00606	0	0	0	0	0	0	0	0	0	0	0	0	0	0	0
5	0	.00932	.01681	.05063	.10327	.03489	.01313	0	0	0	0	0	0	0	0	0	0	0	0	0	0	0
6	0	0	0	.01740	.03321	.10559	.03232	0	0	0	0	0	0	0	0	0	0	0	0	0	0	0
7	0	0	0	.00793	.01370	.03771	.11209	0	0	0	0	0	0	0	0	0	0	0	0	0	0	0
8	0	0	0	0	0	0	0	.21252	.09651	.03402	.00953	0	0	0	0	0	0	0	0	0	0	0
9	0	0	0	0	0	0	0	.09414	.14557	.10204	.04052	.01227	0	0	0	0	0	0	0	0	0	0
10	0	0	0	0	0	0	0	.04597	.09889	.12320	.07309	.02918	.00750	0	0	0	0	0	0	0	0	0
11	0	0	0	0	0	0	0	.01508	.03877	.07256	.11598	.07992	.02929	.01230	0	0	0	0	0	0	0	0
12	0	0	0	0	0	0	0	0	.01978	.03628	.08578	.10373	.05782	.02537	.00831	0	0	0	0	0	0	0
13	0	0	0	0	0	0	0	0	0	.01210	.03256	.05764	.09915	.06769	.02574	.00836	0	0	0	0	0	0
14	0	0	0	0	0	0	0	0	0	0	.01667	.02843	.07361	.10079	.05529	.02055	0	0	0	0	0	0
15	0	0	0	0	0	0	0	0	0	0	0	.00841	.02554	.05620	.09470	.05253	.01731	.00824	0	0	0	0
16	0	0	0	0	0	0	0	0	0	0	0	0	.00977	.02463	.06061	.08906	.04369	.01948	.00603	0	0	0
17	0	0	0	0	0	0	0	0	0	0	0	0	0	.00693	.02349	.05176	.08669	.05176	.02258	0	0	0
18	0	0	0	0	0	0	0	0	0	0	0	0	0	0	.01060	.02437	.05656	.10422	.05867	0	0	0
19	0	0	0	0	0	0	0	0	0	0	0	0	0	0	0	0	.01809	.06296	.13761	0	0	0
20	0	0	0	0	0	0	0	0	0	0	0	0	0	0	0	0	0	0	0	.12933	.09222	.04459
21	0	0	0	0	0	0	0	0	0	0	0	0	0	0	0	0	0	0	0	.10491	.14119	.11337
22	0	0	0	0	0	0	0	0	0	0	0	0	0	0	0	0	0	0	0	.04655	.10326	.21710

Table 5b.1 Coefficients aij at Test Phase 1

i	j																					
	1	2	3	4	5	6	7	8	9	10	11	12	13	14	15	16	17	18	19	20	21	22
1	.11743	.03934	.01637	.00644	0	0	0	0	0	0	0	0	0	0	0	0	0	0	0	0	0	0
2	.03762	.10214	.04098	.01748	.01027	0	0	0	0	0	0	0	0	0	0	0	0	0	0	0	0	0
3	.01359	.04678	.10095	.03129	.01679	0	0	0	0	0	0	0	0	0	0	0	0	0	0	0	0	0
4	0	.01932	.02868	.10583	.03824	0	0	0	0	0	0	0	0	0	0	0	0	0	0	0	0	0
5	0	.01048	.01473	.04877	.10998	0	0	0	0	0	0	0	0	0	0	0	0	0	0	0	0	0
6	0	0	0	0	0	.20231	.08083	.02865	.00944	0	0	0	0	0	0	0	0	0	0	0	0	0
7	0	0	0	0	0	.08677	.11965	.08508	.03384	.01068	0	0	0	0	0	0	0	0	0	0	0	0
8	0	0	0	0	0	.04298	.08053	.10519	.06058	.02604	.00834	0	0	0	0	0	0	0	0	0	0	0
9	0	0	0	0	0	.01406	.03397	.06188	.10301	.07053	.02590	.01155	0	0	0	0	0	0	0	0	0	0
10	0	0	0	0	0	0	.01618	.02941	.07620	.09435	.05030	.02234	.00684	0	0	0	0	0	0	0	0	0
11	0	0	0	0	0	0	0	.00933	.02905	.05139	.09080	.05698	.02203	.00686	0	0	0	0	0	0	0	0
12	0	0	0	0	0	0	0	0	.01493	.02450	.06409	.08935	.04641	.01678	.00527	0	0	0	0	0	0	0
13	0	0	0	0	0	0	0	0	0	.00761	.02213	.04780	.08665	.04582	.01595	.00528	0	0	0	0	0	0
14	0	0	0	0	0	0	0	0	0	0	.00763	.02082	.05098	.08624	.03879	.01366	.00547	0	0	0	0	0
15	0	0	0	0	0	0	0	0	0	0	0	.00695	.01977	.04351	.08757	.03806	.01941	0	0	0	0	0
16	0	0	0	0	0	0	0	0	0	0	0	0	.00836	.02137	.05030	.10368	.05193	0	0	0	0	0
17	0	0	0	0	0	0	0	0	0	0	0	0	0	0	.01445	.05344	.14091	0	0	0	0	0
18	0	0	0	0	0	0	0	0	0	0	0	0	0	0	0	0	0	.12771	.08745	.02717	.01211	0
19	0	0	0	0	0	0	0	0	0	0	0	0	0	0	0	0	0	.09839	.12886	.07552	.03251	.01025
20	0	0	0	0	0	0	0	0	0	0	0	0	0	0	0	0	0	.04362	.09261	.13002	.08735	.03517
21	0	0	0	0	0	0	0	0	0	0	0	0	0	0	0	0	0	.01543	.03858	.10522	.13515	.09528
22	0	0	0	0	0	0	0	0	0	0	0	0	0	0	0	0	0	0	.01046	.04615	.09944	.19497

Table 5b.2 Coefficients aij at Test Phase 2

i \ j	1	2	3	4	5	6	7	8	9	10	11	12	13	14	15	16	17	18	19	20	21	22
1	.11146	.03294	.01279	0	0	0	0	0	0	0	0	0	0	0	0	0	0	0	0	0	0	0
2	.03290	.11416	.03591	0	0	0	0	0	0	0	0	0	0	0	0	0	0	0	0	0	0	0
3	.01206	.04127	.09356	0	0	0	0	0	0	0	0	0	0	0	0	0	0	0	.0	0	0	0
4	0	0	0	.18301	.07383	.02638	.00684	0	0	0	0	0	0	0	0	0	0	0	0	0	0	0
5	0	0	0	.07229	.10848	.07982	.02962	.01106	0	0	0	0	0	0	0	0	0	0	0	0	0	0
6	0	0	0	.03305	.07308	.10018	.05391	.02215	.00513	0	0	0	0	0	0	0	0	0	0	0	0	0
7	0	0	0	.00996	.02846	.05649	.09644	.06128	.02135	.00978	0	0	0	0	0	0	0	0	0	0	0	0
8	0	0	0	0	.01383	.02865	.06911	.08787	.04274	.01758	.00587	0	0	0	0	0	0	0	0	0	0	0
9	0	0	0	0	0	.00987	.02734	.04433	.08329	.05198	.01840	.00681	0	0	0	0	0	0	0	0	0	0
10	0	0	0	0	0	0	.01519	.03215	.05311	.09117	.04050	.01513	0	0	0	0	0	0	0	0	0	0
11	0	0	0	0	0	0	0	.00662	.01769	.04070	.08982	.04013	.01343	.00610	0	0	0	0	0	0	0	0
12	0	0	0	0	0	0	0	0	.00591	.01810	.04348	.09229	.03799	.01221	0	0	0	0	0	0	0	0
13	0	0	0	0	0	0	0	0	0	.00527	.01693	.03862	.09652	.03613	.01186	0	0	0	0	0	0	0
14	0	0	0	0	0	0	0	0	0	0	.00734	.01816	.04669	.12117	.03652	0	0	0	0	0	0	0
15	0	0	0	0	0	0	0	0	0	0	0	0	.01424	.04777	.13570	0	0	0	0	0	0	0
16	0	0	0	0	0	0	0	0	0	0	0	0	0	0	0	.13850	.09714	.03353	.01166	0	0	0
17	0	0	0	0	0	0	0	0	0	0	0	0	0	0	0	.09622	.11806	.06493	.02552	.00785	0	0
18	0	0	0	0	0	0	0	0	0	0	0	0	0	0	0	.04297	.08592	.12843	.07807	.02720	.01051	0
19	0	0	0	0	0	0	0	0	0	0	0	0	0	0	0	.01591	.03662	.09418	.11747	.06303	.02942	.00908
20	0	0	0	0	0	0	0	0	0	0	0	0	0	0	0	0	.01272	.03925	.08463	.11463	.07773	.03081
21	0	0	0	0	0	0	0	0	0	0	0	0	0	0	0	0	0	.01285	.03428	.08525	.11768	.08340
22	0	0	0	0	0	0	0	0	0	0	0	0	0	0	0	0	0	0	.00873	.03438	.08476	.18158

Table 5b.3 Coefficients aij at Test Phase 3

GAUGE No.	TEST PHASE		
	-1-	-2-	-3-
1	8.0	9.5	11.0
2	13.0	10.5	12.0
3	21.0	11.0	12.5
4	43.0	10.5	10.5
5	58.0	9.5	12.5
6	53.5	10.0	13.0
7	21.5	11.5	15.5
8	8.5	12.5	18.5
9	9.5	19.0	32.0
10	12.5	27.5	51.5
11	22.5	52.5	81.5
12	38.0	75.0	96.0
13	81.5	94.0	92.5
14	129.5	120.5	93.0
15	162.0	150.0	95.5
16	177.5	149.5	69.0
17	218.5	177.5	110.5
18	252.0	185.0	218.5
19	286.5	348.0	336.5
20	297.0	548.5	526.5
21	554.0	682.0	663.5
22	692.0	724.5	744.0

Table 5b.4 Meshing Test Tooth Root Strains (in microstrain)

APPENDIX 5C

MODIFICATIONS TO MEASURED TOOTH ERRORS

In this Appendix, the gear tooth errors as measured on the Gleason/Höfler are quoted, and then corrected to account for misalignments of the loaded shafts in the rig (since the shaft axes will not be aligned with the Gleason/Höfler axis). Since the ground circular rings (section 5.2.2.1) are used to measure shaft misalignments in the rig, then any ring irregularities (radial runout and eccentricity) must also be accounted for.

These corrected tooth errors are crucial to the comparison of the experimental load distribution results with the theoretical ones, and must be input to the load distribution program "HELICALDIST" correctly as will be discussed in Chapter 6.

Shaft misalignments will only have an effect on the tooth misalignment errors "$f_{H\beta}$" (tooth profile and pitch errors are not affected). Referring to table 5A.1 and Chapter 6 (section 6.2.2), the averaged uncorrected wheel misalignments for the teeth to be meshed 9, 10 and 11 are respectively −0.13009, −0.14120 and −0.60231 μm/mm. Similarly, referring to table 5A.4 and Chapter 6 (section 6.2.2.), the averaged uncorrected pinion misalignments for the teeth to be meshed 5, 6 and 7 respectively are 0.02303, 0.02327 and 0.04027 μm/mm where the meshing pairs of wheel with pinion are 11 with 5, 10 with 6 and 9 with 7.

Next, the measured shaft vertical misalignments δ_v for the three test phases 1, 2 and 3 respectively are −29.9, −30.3 and −31.0 μm and using equations 5.15 and 5.16, these are converted into angular misalignments along the base tangent "θ_{vt}" and are −0.28023, −0.28397 and −0.29054 μm/mm all measured at the torque-up end, where ℓ = 100mm, $\alpha_t = 20.41^\circ$.

The horizontal shaft misalignments are somewhat more complicated and are expressed in stages. First consider phase 1, from equation 5.17

$$\delta_{h1} = 2.625(-430+394) = -94.5 \ \mu m$$

and from equation 5.18

$$\delta_{h2} = 2.625(-438+372) = -173.25 \ \mu m$$

and finally from equations 5.19, 5.20 and 5.21 the angular misalignment along the base tangent is

$$\theta_{ht} = -0.27463 \ \mu m/mm \text{ (at the other end).}$$

Similarly for phase 2,

$$\delta_{h1} = 2.625(-432+394) = -99.75 \ \mu m$$

$$\delta_{h2} = 2.625(-440+374) = -173.25 \ \mu m$$

$$\theta_{ht} = -0.25634 \ \mu m/mm \text{ (at the other end)}$$

and for phase 3,

$$\delta_{h1} = 2.625(-430+393) = -97.125 \ \mu m$$

$$\delta_{h2} = 2.625(-438+373) = -170.625 \ \mu m$$

$$\theta_{ht} = -0.25634 \ \mu m/mm \text{ (at the other end)}$$

Finally from equation 5.22, the total shaft misalignments along the base tangent "θ_t" for phases 1, 2 and 3 respectively are -0.00560, -0.02764 and -0.03422 μm/mm all at the torque-up end. These misalignments may be added to only the pinion tooth errors as discussed in section 5.5.3.2, but must first be further corrected as discussed below.

As mentioned above, the shaft misalignments calculated so far must be corrected for ring eccentricity and runout, and so "Δr_i", in equation 5.23 must first be calculated. To do that, the points "i" where the alignment measuring devices contact the reference rings must be located by means of the tooth numbering on the gears. Thus for each of the phases 1, 2 and 3, these points on all four rings are determined in the rig. The angle between the tooth at "i" and the tooth at maximum eccentricity "e" is thus the angle $(\theta_i - \varphi)$ in equation 5.23 (see Fig. 5.26).

For the vertical alignment measurements, "i" is at the top surfaces of the rings at 90° from the line of centres of the gears and for the horizontal measurements, "i" is on a line parallel to the line of centres of the gears, as can be clearly seen in Fig. 5.25. Table 5C.1 shows all the variables of equation 5.23 for phases 1, 2 and 3 for both the horizontal and vertical measurments where:

ring 1A - ring on wheel shaft at torque-up end
ring 2A - ring on wheel shaft at other end
ring 1B - ring on pinion shaft at torque-up end
ring 2B - ring on pinion shaft at other end.

The value of "Δr_{im}" at "i" for any case is determined from tables 5A.3 and 5A.6 where interpolation was carried out in cases when "i" did not coincide with a tooth number. The tables list the calculated values of "Δr_i" (Eqn. 5.23), "δr" (Eqn.

5.25) and "θ_t" (Eqn. 5.22), where $2\bar{r}_o$ in equation 5.25 was measured at 10° intervals along the circumference of each ring and these measured values were averaged to be 120.9709, 120.9712, 120.9725 and 120.9713 for rings 1A, 2A, 1B and 2B respectively (recall that $2r_{th}$ is 121.0000mm). Finally, from equation 5.24, $(\theta_t)_{mod}$ for phases 1, 2 and 3 respectively is −0.012786, −0.011245 and −0.020011 μm/mm all at the torque-up end where the results for "δr" in table 5C.2 were used.

PHASE	RING	$\Delta\bar{r}$ [um]	Δrim [um]	e [um]	$\lvert\theta i-\phi\rvert$ [degree]
1	1A	-3.85926	0.9500	4.975	20.000
	2A	-8.12685	2.5000	9.950	0.000
	1B	3.69545	6.6938	3.375	21.430
	2B	3.42727	4.1250	3.875	124.286
2	1A	-3.85926	0.8862	4.975	18.582
	2A	-8.12685	2.4468	9.950	1.418
	1B	3.69545	6.7203	3.375	17.785
	2B	3.42727	4.3589	3.875	120.641
3	1A	-3.85926	0.8224	4.975	17.164
	2A	-8.12685	2.3937	9.950	2.836
	1B	3.69545	6.7470	3.375	14.138
	2B	3.42727	4.5929	3.875	116.994

Table 5c.1a Variables in Eq.5.23 Needed to Get Δri (Vertical)

PHASE	RING	$\Delta\bar{r}$ [um]	Δrim [um]	e [um]	$\lvert\theta i-\phi\rvert$ [degree]
1	1A	-3.85926	-2.9500	4.975	70.000
	2A	-8.12685	-8.0500	9.950	90.000
	1B	3.69545	5.4500	3.375	68.570
	2B	3.42727	7.3500	3.875	34.286
2	1A	-3.85926	-3.0564	4.975	71.417
	2A	-8.12685	-8.1776	9.950	88.582
	1B	3.69545	5.3543	3.375	72.215
	2B	3.42727	7.3564	3.875	30.641
3	1A	-3.85926	-3.1627	4.975	72.836
	2A	-8.12685	-8.3052	9.950	87.164
	1B	3.69545	5.2586	3.375	75.862
	2B	3.42727	7.3628	3.875	26.994

Table 5c.1b Variables in Eq.5.23 Needed to Get Δri (Horiz.)

PHASE	RING	Δri [um]	δr [um]	θt [um/mm]
1	1A	0.13429	-14.41571	-0.00560
	2A	0.67685	-13.72315	
	1B	-0.14332	-13.89332	
	2B	2.88060	-11.4694	
2	1A	0.02981	-14.52019	-0.02764
	2A	0.62670	-13.77330	
	1B	-0.18886	-13.93886	
	2B	2.90660	-11.4434	
3	1A	-0.07177	-14.62177	-0.03422
	2A	0.58274	-13.81726	
	1B	-0.22122	-13.97122	
	2B	2.92448	-11.42552	

Table 5c.2a Calculation of Δri, δr and θt (Vertical)

PHASE	RING	Δri [um]	δr [um]	θt [um/mm]
1	1A	-0.79229	-15.34229	-0.00560
	2A	0.07685	-14.32315	
	1B	0.52144	-13.22856	
	2B	0.72107	-13.62893	
2	1A	-0.78260	-15.33260	-0.02764
	2A	-0.29698	-14.69698	
	1B	0.62797	-13.12203	
	2B	0.59517	-13.75483	
3	1A	-0.77160	-15.32160	-0.03422
	2A	-0.67065	-15.07065	
	1B	0.73883	-13.01117	
	2B	0.48270	-13.86730	

Table 5c.2b Calculation of Δri, δr and θt (Horizontal)

APPENDIX 6A

AVERAGE TOOTH ERRORS

This Appendix contains a listing of the averaged pinion and wheel tooth errors as discussed in section 6.2.2.

WHEEL TOOTH	(Fp)avg (um)	PINION TOOTH	(Fp)avg (um)
9	-0.4560	7	1.7333
10	-1.2889	6	4.0667
11	-0.6000	5	2.9330

Table 6A.1 Average Measured Comulative Pitch Error

WHEEL TOOTH	$(fH\beta)$avg/11 (um/mm)	PINION TOOTH	$(fH\beta)$avg/11 (um/mm)
9	-0.13009	7	0.04027
10	-0.14120	6	0.02327
11	-0.60231	5	0.02303

Table 6A.2 Average Measured Helix Angle Error
(11 _ test range across face width)

WHEEL TOOTH	(fH_α) avg/12 (um/mm)	PINION TOOTH	(fH_α) avg/12 (um/mm)
9	-0.69444	7	0.07417
10	-0.81111	6	0.09729
11	-0.54444	5	-0.03000

Table 6A.3 Average Measured Profile Angle Error
(12 _ test range along tooth height)

WHEEL TOOTH	(fyz)avg/(l1*l2) (um/mm2)	PINION TOOTH	(fyz)avg/(l1*l2) (um/mm2)
9	0.0015065	7	0.0012920
10	0.0057870	6	0.0003303
11	-0.0018520	5	0.0017225

Table 6A.4 Average Twist

PHASE	WHEEL TOOTH	($f_{H\beta}$)mod [um/mm]	PINION TOOTH	($f_{H\beta}$)mod [um/mm]
1	9	-0.130090	7	0.023726
	10	-0.141200	6	0.006726
	11	-0.602310	5	0.006486
2	9	-0.130090	7	0.001426
	10	-0.141200	6	-0.015574
	11	-0.602310	5	-0.015814
3	9	-0.130090	7	-0.005508
	10	-0.141200	6	-0.022508
	11	-0.602310	5	-0.022748

Table 6a.5 Modified Gear_Tooth Misalignments

APPENDIX 6B

THEORETICAL SHAFT DEFORMATIONS

This Appendix contains a listing of the theoretically determined test shaft deformations as discussed in Section 6.3.

z [mm]	WHEEL(2) [um]			PINION(1) [um]			TOTAL [um]
	TORS	SHEAR	BEND	TORS	SHEAR	BEND	
0.00	0	0.543	0.179	14.10	1.233	0.820	16.055
3.17	0	0.546	0.180	14.30	1.319	0.870	17.215
11.83	0	0.552	0.185	14.83	1.556	0.990	18.113
18.17	0	0.557	0.189	15.22	1.730	1.070	18.766
26.83	0	0.546	0.193	15.76	1.967	1.155	19.639
33.17	0	0.569	0.196	16.15	2.140	1.200	20.255
41.83	0	0.575	0.199	16.68	2.377	1.240	21.071
48.17	0	0.570	0.201	16.88	2.376	1.247	21.274
56.83	0	0.549	0.204	16.88	2.138	1.232	21.003
63.17	0	0.543	0.205	16.88	1.964	1.203	20.786
71.83	0	0.514	0.207	16.88	1.726	1.143	20.470
78.17	0	0.498	0.208	16.88	1.552	1.085	20.223
86.83	0	0.478	0.209	16.88	1.313	0.989	19.869
90.00	0	0.470	0.210	16.88	1.226	0.950	19.736

Table 6b.1 Approximate Theoretical Shaft Deflections